UNIVERSITÉ SAVOIE MONT BLANC

THÈSE

Pour obtenir le grade de

DOCTEUR DE L'UNIVERSITÉ SAVOIE MONT BLANC

Spécialité : **Physique théorique**

Arrêté ministériel : 25 Mai 2016

Présentée par

Maël CAVAN

Thèse dirigée par **Diego GUADAGNOLI**

préparée au sein du **Laboratoire d'Annecy-le-vieux de Physique Théorique – LAPTh**
dans **l'École Doctorale de physique de Grenoble**

Nouvelle stratégie pour la recherche de nouvelles particules légères dans les collisionneurs et des objets stellaires

Thèse soutenue publiquement le **10 octobre 2025**,
devant le jury composé de :

Björn Herrmann
Université Savoie Mont Blanc, Président
Francesca Gulminelli
Université de Caen Normandie, Rapporteuse
Marc Knecht
CNRS - Délégation Provence et Corse, Rapporteur
Martino Borsato
Università degli Studi di MILANO-BICOCCA, Examinateur
Francesca Calore
CNRS - Délégation Alpes, Examinatrice
Luca Di Luzio
Istituto Nazionale de Fisica Nucleare, Examinateur
Dominique Duchesneau
CNRS - Délégation Alpes, Examinateur

Abstract

The Standard Model (SM) of particle physics is a remarkably successful theoretical framework. It describes, with unmatched precision, the electromagnetic, weak, and strong interactions among the fundamental constituents of matter. Its predictions have been consistently confirmed by numerous experiments, culminating in the discovery of the Higgs boson by the ATLAS and CMS collaborations in 2012. However, despite its success, several experimental and theoretical indications suggest the existence of physics Beyond the Standard Model (BSM): the origin of dark matter, the matter-antimatter asymmetry, the neutrino masses, and the strong CP problem, to name a few. The latter refers to the observed absence of CP violation in strong interactions, even though such violation is permitted in the Quantum Chromodynamics (QCD) sector of the SM. One of the most elegant theoretical solutions to this issue is the Peccei–Quinn mechanism, which predicts the existence of a new pseudo-scalar particle – the QCD axion – that is also a particularly appealing dark matter candidate.

The QCD axion is a well-studied BSM particle, particularly in its so-called "invisible" version, where its interactions with matter are extremely weak, governed by a symmetry-breaking scale f_a typically above 10^9 GeV. These interactions are proportional to $\partial_\mu a/f_a$, making the physical effects increasingly suppressed as f_a grows. This property renders the QCD axion difficult to detect in laboratory experiments. By extension, similar particles not necessarily linked to solving the strong CP problem – known as Axion Like Particles (ALPs) – have been proposed. ALPs allow a decoupling between their mass and their coupling scale f_a, which may lie near or above the TeV scale, making them more accessible to collider-based experiments.

In this context, this manuscript adopts a multi-probe approach to explore the physics of axions by exploiting the complementarities between astrophysical phenomena, neutrino detection experiments, and collider searches. After introducing the theoretical framework of the QCD axion and showing how it simultaneously addresses the strong CP problem and the dark matter problem, an effective description of its interactions is developed using Chiral Perturbation Theory (ChPT), which enables the study of low-energy hadronic phenomena.

A first contribution focuses on axion emission in Supernovæ, particularly SN 1987A. The cooling of the stellar core via axion emission provides a powerful, albeit indirect, detection channel. By extending calculations to strange baryons and mesons, we present the first quantitative study of axionic emissivity beyond the first generation. The results allow, for the first time, constraints on the axion-strange-strange coupling and set the strongest bounds to date on the axial axion-down-strange coupling, reaching limits of order $\mathcal{O}(10^{-2})$ for $f_a = 10^9$ GeV.

The second focus of this manuscript explores the potential detection of an astrophysical axion flux on Earth in water Cherenkov detectors such as Hyper-Kamiokande. We compute the spectra of the processes $a + N \to N + \gamma$ and $a + N \to N + \pi^0$, where N denotes a nucleon in the water tank. Even for the QCD axion, which is known to be very weakly coupled, detectable signals emerge – notably via π^0 production, whose di-γ energy spectrum proves more favorable than the single-γ counterpart. An extension of this analysis to include axion interactions with strange matter may also give potentially detectable signatures if the interaction with the first generation is suppressed.

Finally, the last part of this manuscript addresses axion searches at colliders. After reviewing current constraints from rare decays, we propose exploring new three-body decay channels such as $K \to \pi\pi a$ and $K \to \mu\mu a$, leveraging the excellent tracking capabilities of the LHCb detector. We show that these channels are particularly accessible experimentally, as reconstruction efficiencies tend to align with the most populated regions of the Dalitz plots.

This work thus demonstrates the potential of combining diverse experimental environments to probe the properties of axions across different energy scales and detection strategies. It opens new perspectives on their potential role in solving fundamental problems of the SM, by establishing novel limits across a variety of experimental settings – collider, neutrino, and astrophysical.

Résumé en français

Motivation

Le Modèle Standard de la physique des particules est l'une des théories les plus abouties et vérifiées de l'histoire des sciences. Il représente la théorie quantique des champs locale et renormalisable la plus générale compatible avec la relativité restreinte et le groupe de jauge $G_{\rm SM} = SU(3)_c \times SU(2)_L \times U(1)_Y$, ainsi qu'avec le contenu de matière connu. Le Modèle Standard inclut les quarks (qui se combinent pour former des hadrons comme les nucléons—protons et neutrons—et les pions), les leptons (comme l'électron), le boson de Higgs (qui confère la masse aux particules élémentaires via le mécanisme de Higgs), et les bosons de jauge associés à chaque interaction fondamentale : les gluons (G) pour l'interaction forte (Chromodynamique Quantique, QCD), le photon (γ) pour l'électromagnétisme (Électrodynamique Quantique, QED), et les bosons $W^{\pm}$ et Z pour l'interaction faible. Le Modèle Standard décrit avec une grande précision les interactions électromagnétiques, faibles et fortes entre toutes les particules connues. La découverte du boson de Higgs en 2012 a confirmé l'exceptionnelle capacité prédictive de ce modèle, validant ainsi le mécanisme de Higgs.

Cependant, malgré son succès, le Modèle Standard présente des limites notables. Il ne parvient pas à expliquer certains phénomènes observés, tels que l'asymétrie matière-antimatière, la masse des neutrinos et, surtout, la nature de la matière noire, une forme de matière exotique et invisible interagissant gravitationnellement. L'un des problèmes théoriques les plus intrigants du Modèle Standard est celui du problème CP fort, c'est-à-dire l'absence de violation de la symétrie CP[1] dans l'interaction forte, alors que cette violation est permise et attendue par la structure même de l'interaction forte. Une solution élégante à la fois pour le problème de la matière noire et le problème CP fort est l'introduction de l'axion QCD, une particule pseudo-scalaire légère issue de la brisure spontanée d'une symétrie de Peccei-Quinn $U(1)_{\rm PQ}$, garantissant ainsi la résolution du problème CP fort.

En ce qui concerne le problème CP fort, toutes les symétries de l'interaction forte permettent une interaction du type $\theta G\tilde{G}$, avec θ un paramètre libre. Cette interaction viole la symétrie CP, mais les mesures expérimentales du moment dipolaire électrique du neutron contraignent ce paramètre à être extrêmement petit, $|\theta| < 10^{-10}$. Le problème CP fort se reformule alors en : pourquoi ce paramètre θ est-il aussi petit, alors qu'aucune loi physique ne l'impose ?

Pour résoudre ce problème sans ajustement fin du paramètre θ, une symétrie $U(1)_{\rm PQ}$ peut être appliquée à θ. Cela conduit à l'introduction de l'axion comme champ dynamique, $a = f_a\theta$, décrit par le potentiel :

$$V(a) \propto 1 - \cos\left(\frac{a}{f_a}\right) = \frac{a^2}{2f_a^2} + \mathcal{O}\left(\frac{a^4}{f_a^4}\right) \ , \tag{1}$$

dont le minimum est $\langle\theta\rangle = \frac{\langle a\rangle}{f_a} = 0$, résolvant ainsi dynamiquement le problème CP fort.

L'existence de la matière noire est désormais confirmée par de multiples observations astrophysiques et cosmologiques, telles que les courbes de rotation des galaxies, les lentilles gravitationnelles, les anisotropies du fond diffus cosmologique (CMB), et la structure à grande échelle de l'Univers. Ces données convergent vers la présence d'une composante non lumineuse, non baryonique, stable, froide et faiblement interagissante, représentant environ 80% de la masse totale de l'Univers. Le Modèle Standard, bien qu'extrêmement précis dans la description des interactions fondamentales, ne fournit aucun candidat pour expliquer ce constituant dominant de la matière. Dans ce contexte, l'axion, initialement proposé pour résoudre le problème CP fort, se révèle être un excellent candidat pour la matière noire. L'axion acquiert les propriétés de la matière noire froide, nécessaire pour résoudre ce problème, non pas de manière thermique avec une masse importante, comme les solutions classiques, mais par un processus appelé le mécanisme de désalignement du vide dans l'Univers primordial. Ce mécanisme permet à l'axion de générer une densité relique compatible avec les observations cosmologiques, sans nécessiter d'interactions fortes avec d'autres particules. Sa faible masse et ses couplages extrêmement faibles le rendent stable à l'échelle cosmologique et difficile à détecter par les moyens classiques, tout en restant potentiellement testable par des expériences dédiées en astrophysique et dans les collisionneurs de particules.

Ainsi, l'axion offre une solution élégante à deux problèmes majeurs du Modèle Standard : la conservation de la symétrie CP dans l'interaction forte et l'origine de la matière noire.

L'axion à hautes énergies

Pour étudier une particule au-delà du Modèle Standard, il est essentiel de comprendre comment

[1] La transformation C correspond à l'échange d'une particule avec son antiparticule, tandis que la transformation P correspond à un changement de signe des vecteurs spatiaux.

elle interagit avec les autres particules. L'interaction de l'axion QCD avec les particules du Modèle Standard peut être décrite de manière générale dans le Lagrangien suivant :

$$\begin{aligned}\mathcal{L}_{axion-SM} =& \frac{1}{2}\partial_\mu a \partial^\mu a + \frac{1}{2}m_a^2 a^2 + c_{aGG}\frac{\alpha_s}{4\pi}\frac{a}{f_a}G\tilde{G} + c_{a\gamma\gamma}\frac{\alpha_{e.m.}}{4\pi}\frac{a}{f_a}F\tilde{F} \\ &+ \frac{\partial_\mu a}{f_a}\bar{q}\gamma^\mu\left(k_V^q + k_A^q\gamma_5\right)q + \frac{\partial_\mu a}{f_a}\bar{\ell}\gamma^\mu\left(k_V^\ell + k_A^\ell\gamma_5\right)\ell \ ,\end{aligned} \tag{2}$$

où m_a est la masse de l'axion, f_a est sa constante caractéristique, et c_{aGG}, $c_{a\gamma\gamma}$, k_V^q, k_A^q et k_V^ℓ, k_A^ℓ sont des couplages respectivement associés aux gluons, aux photons, aux quarks et aux leptons. Ces couplages dépendent du modèle théorique générant l'axion QCD. De même que pour les couplages de Yukawa dans le Modèle Standard, les couplages axioniques sont attendus non nuls.

En utilisant la Théorie des Perturbations Chirales, c'est-à-dire la QCD effective à basse énergie, l'axion acquiert une masse non nulle :

$$m_a \simeq 6 \text{ meV}\left(\frac{10^9 \text{ GeV}}{f_a}\right) \ . \tag{3}$$

ce qui établit une relation entre m_a et f_a, avec $f_a \gtrsim 10^9$ GeV pour être expérimentalement viable.

Une généralisation de l'axion QCD est l'ALP (Axion-like Particle), qui conserve la même structure que l'axion QCD dans la formule formule (2). Toutefois, les paramètres libres de l'ALP ne sont pas fournis par un modèle théorique, mais sont à mesurer expérimentalement. Les valeurs possibles pour la masse m_a sont comprises entre le MeV et le GeV, et $f_a \gtrsim 1$ TeV est un paramètre libre, indépendant de la masse.

Il existe plusieurs modèles théoriques pour expliquer l'axion QCD :

- **Modèle PQWW (Peccei-Quinn-Weinberg-Wilczek)** : C'est le premier modèle introduit, il a fait appel à deux doublets de Higgs. Cependant, ce modèle souffre d'un problème : f_a est trop faible pour être expérimentalement viable, car il est lié à la vev du mécanisme de Higgs, qui est de l'ordre de quelques centaines de GeV, bien en dessous de 10^9 GeV.

- **Modèle DFSZ (Dine-Fischler-Srednicki-Zhitnitsky)** : Ce modèle introduit également deux doublets de Higgs, mais dissocie f_a des vevs, permettant ainsi d'obtenir un f_a suffisamment grand pour être expérimentalement pertinent. Dans ce cadre, les quarks de type up (u, c, t) et down (d, s, b) obtiennent leur masse via des doublets de Higgs différents. Il existe deux variantes du modèle DFSZ, selon que les leptons chargés (e, μ, τ) acquièrent leur masse par le premier ou le deuxième doublet de Higgs.

  Les valeurs des couplages dans les modèles DFSZ sont :

Couplages	**DFSZ-I**	**DFSZ-II**
c_{aGG}	$-\frac{1}{2}$	$-\frac{1}{2}$
$c_{a\gamma\gamma}$	$-\frac{4}{3}$	$-\frac{1}{3}$
$(k_A^q)_{uu}$	$\frac{1}{3}\cos^2\beta$	$\frac{1}{3}\cos^2\beta$
$(k_A^q)_{dd}$	$\frac{1}{3}\sin^2\beta$	$\frac{1}{3}\sin^2\beta$
$(k_A^\ell)_{ee}$	$\frac{1}{3}\sin^2\beta$	$\frac{1}{3}\cos^2\beta$

  avec $\tan(\beta) \in [0.25, 170]$ un paramètre libre et f_a également non fixé.

- **Modèle KSVZ (Kim-Shifman-Vainshtein-Zakharov)** : Ce modèle introduit une paire de quarks lourds, et toutes les interactions avec l'axion passent par ces quarks lourds. Cela fait en sorte que les autres couplages sont extrêmement faibles, à l'exception du couplage $c_{aGG} = -\frac{1}{2}$, nécessaire pour résoudre le problème CP fort.

L'axion à basses énergies

À basse énergie, les quarks ne peuvent plus être traités comme des degrés de liberté libres : ils s'assemblent en mésons et baryons. Leur dynamique est décrite par une théorie effective, la Théorie des Perturbations Chirales (ChPT), qui encode les symétries chirales de la QCD. Les champs mésoniques

et baryoniques sont regroupés dans des multiplets U et B, dont le Lagrangien respecte ces symétries et permet d'exprimer systématiquement les interactions avec l'axion. Les expressions complètes sont données dans l'Appendice C.5.

Cette procédure nous permet d'obtenir des interactions axion-hadrons de manière non ambiguë. Cependant, un point subtil est que nous avons toujours une interaction axion-gluon, qui n'a pas de sens dans une théorie effective de l'interaction forte à basse énergie, où ce type d'interaction doit être encodé dans l'interaction avec les autres particules via des couplages effectifs. La méthode canonique pour résoudre ce problème est d'introduire une rotation chirale des quarks, ce qui donne $c_{aGG} \to \hat{c}_{aGG} = 0$.

Cette procédure engendre la masse de l'axion (voir la formule (3)) et modifie le couplage avec le photon :

$$c_{a\gamma\gamma} \to \hat{c}_{a\gamma\gamma} = c_{a\gamma\gamma} + 1.01(5) \tag{4}$$

et avec les quarks, nous obtenons :

$$\begin{pmatrix} (k_A^q)_{11} \\ (k_A^q)_{22} \\ (k_A^q)_{33} \end{pmatrix} \to \begin{pmatrix} (\hat{k}_A^q)_{11} \\ (\hat{k}_A^q)_{22} \\ (\hat{k}_A^q)_{33} \end{pmatrix} = \begin{pmatrix} (k_A^q)_{11} \\ (k_A^q)_{22} \\ (k_A^q)_{33} \end{pmatrix} - \begin{pmatrix} 0.67(5) \\ 0.31(5) \\ 0.016(3) \end{pmatrix} \ , \tag{5}$$

et pour les leptons, l'effet est extrêmement faible, de l'ordre de 10^{-5}.

Procédure

Sachant que les couplages axioniques sont proportionnels à $(\partial_\mu a/f_a)$, cela implique que les observables sont toutes proportionnelles à $([\text{impulsions externes}]/f_a)^2$. Or, pour l'axion QCD, f_a est extrêmement grand ($\gtrsim 10^9$ GeV), rendant les observables très faibles et rendant ainsi les détections directes impossibles. Cependant, si au lieu de mesures énergétiques, nous procédons à des mesures temporelles en mesurant la durée d'un processus, il devient possible d'acquérir des informations sur l'axion QCD. Les deux principales approches sont les suivantes :

- **Temps de vie** : Le temps de vie d'une particule dépend des canaux de désintégration accessibles. Si un nouveau canal impliquant l'axion est ajouté, alors le temps de vie de la particule devrait être réduit par rapport à la prédiction du Modèle Standard.
- **Refroidissement d'objets astrophysiques** : Les objets astrophysiques denses (et chauds), tels que les supernovæ et les étoiles à neutrons, peuvent émettre des axions. Cette émission d'axions accélère le refroidissement de l'objet astrophysique, rendant la perte d'énergie plus rapide que ce qui est attendu avec les émissions classiques, comme l'émission de neutrinos.

Avec le formalisme définissant les interactions entre l'axion et les particules du Modèle Standard à faible énergie, en fonction des paramètres libres, il est possible d'étudier la phénoménologie de l'axion dans une approche multifacette. Cette approche repose sur l'idée que la combinaison de différents domaines d'observation peut fournir des contraintes complémentaires et robustes sur les propriétés des axions. En particulier, nous explorons la phénoménologie des axions dans trois contextes distincts :

1. **Les objets astrophysiques compacts**, où les axions peuvent être émis via des processus hadroniques dans des conditions thermodynamiques extrêmes.
2. **Les détecteurs Cherenkov à grand volume**, où des axions issus de sources astrophysiques pourraient être détectés via leurs interactions avec la matière de l'eau.
3. **Les expériences de désintégrations rares en collisionneurs**, où les axions peuvent médier des désintégrations rares de hadrons via des courants neutres changeant de saveur.

Recherche de l'émission de l'axion QCD provenant des objets stellaires

Pour contraindre les couplages hadroniques, nous avons utilisé le refroidissement des supernovæ, en particulier la mesure de la supernova SN 1987A, qui a permis une estimation approximative de l'émissivité (la puissance rayonnée par unité de volume) en neutrinos :

$$Q_\nu \sim 3 \times 10^{33} \text{ erg.cm}^{-3}\text{.s}^{-1} \ . \tag{6}$$

Il est possible de calculer l'émissivité en axions à partir de la formule suivante :

$$Q_a = \int \begin{bmatrix} \text{Énergie} \\ \text{de l'axion} \end{bmatrix} \begin{bmatrix} \text{Espace} \\ \text{des phases} \end{bmatrix} \left| \begin{bmatrix} \text{Amplitude} \\ \text{de Feynman} \end{bmatrix} \right|^2 \begin{bmatrix} \text{Statistiques quantiques} \\ \text{des états externes} \end{bmatrix} \ . \tag{7}$$

L'énergie de l'axion est utilisée pour calculer la puissance du flux d'axions, l'espace des phases permet de prendre en compte l'ensemble des impulsions cinématiquement autorisées, l'amplitude de Feynman permet d'incorporer les interactions quantiques entre les particules, incluant les couplages, et les statistiques quantiques des états externes (initiaux et finaux) tiennent compte du fait que l'on travaille à température finie.

La méthode canonique pour contraindre l'émissivité au-delà du Modèle Standard consiste à imposer une borne, selon laquelle l'émissivité axionique ne doit pas dépasser celle issue du Modèle Standard, soit $Q_\nu \gtrsim Q_a$.

Pour calculer l'amplitude de Feynman, il suffit d'utiliser les outils de la ChPT+a décrite précédemment. Toutefois, pour les statistiques quantiques, il est nécessaire de faire quelques hypothèses supplémentaires :

1. **Statistiques quantiques dans le milieu dense** : Les statistiques quantiques dans un milieu dense ne sont pas connues, et les statistiques les mieux maîtrisées sont celles issues de l'approximation des gaz parfaits, c'est-à-dire Fermi-Dirac pour les fermions (comme les baryons) et Bose-Einstein pour les bosons (comme les mésons). Par conséquent, nous utiliserons l'approximation des gaz parfaits pour obtenir les statistiques quantiques.

2. **Interactions dans un milieu dense et chaud** : Le calcul exact des interactions dans un milieu dense et chaud, comme le cœur d'une supernova, est extrêmement complexe, notamment à cause des effets de diffusion multiple. Pour simplifier ces calculs, nous adoptons l'approche du champ moyen, permettant d'utiliser les procédures de calcul dans le vide, qui sont beaucoup plus simples. Cela se fait au prix de travailler avec des grandeurs effectives pour la masse $m_j \to m_j^*$, l'énergie $E_j \to E_j^* = \sqrt{(m_j^*)^2 + p_j^2}$ et le potentiel chimique $\mu_j \to \mu_j^* = \mu_j - U_j$, où U_j est le potentiel d'interaction du champ moyen.

Ces hypothèses sont couramment utilisées dans la littérature et ne posent pas de problème majeur, étant donné que la valeur de l'émissivité en neutrinos admet une grande incertitude. En effet, puisque nous comparons $Q_\nu \gtrsim Q_a$, si Q_ν n'est pas précis, il n'y a pas d'intérêt à obtenir Q_a avec une grande précision. Les hypothèses permettant de calculer Q_a sont donc raisonnables.

Pour calculer les quantités effectives, il est nécessaire de choisir une équation d'état et des conditions thermodynamiques. Nous avons utilisé deux équations d'état, $DD2Y$ et $SFHoY$, qui ont été sélectionnées pour leur disponibilité publique, leur compatibilité avec les contraintes actuelles, et leur capacité à prédire différentes quantités de particules étranges. Pour les conditions thermodynamiques, nous avons choisi $T \in \{30; 40\}$ MeV, $n_B \in \{1; 1.5\}\ n_{\text{sat}}$ et $Y_{Q_B} = 0.3$, représentant une variation autour de conditions réalistes. L'intérêt de l'utilisation de deux équations d'état et de plusieurs conditions thermodynamiques est de garantir que nos résultats ne dépendent pas uniquement de conditions très spécifiques, mais sont aussi aussi généraux que possible.

Dans la littérature, les processus les plus étudiés sont la diffusion nucléon-nucléon $N_1N_2 \to N_3N_4a$. Cependant, des études récentes suggèrent que les processus dominants pourraient être la diffusion pion-nucléon $\pi N_i \to N_f a$, car, suivant quelques hypothèses, la fraction de π^- pourrait être plus importante que prévu. De plus, pour contraindre les couplages de changement de saveur, le processus $\Lambda \to na$ est particulièrement intéressant.

Notre objectif étant d'étudier la contribution de la matière étrange, en plus de la première génération, dans l'émission d'axions, nous avons étudié les octets légers complets de mésons et de baryons, en analysant la diffusion méson-baryon $MB_i \to B_f a$ et la désintégration de baryon $B_i \to B_f a$. Toutefois, la diffusion baryon-baryon $B_1B_2 \to B_3B_4a$ a été laissée pour une étude ultérieure. L'argument intuitif pour étudier les octets complets est que, bien que les fractions de matière étrange soient faibles ($< 1\%$), le grand nombre de processus peut néanmoins induire une contribution significative, car les émissivités s'ajoutent.

Si nous posons $f_a = 10^9$ GeV, ce qui ne compromet pas la généralité des résultats, les contraintes dans les études autres que celles utilisant les supernovæ étaient les suivantes :

- $|(\hat{k}_A)_{11}| \lesssim 2.7$ et $|(\hat{k}_A)_{22}| \lesssim 2.5$ par le refroidissement d'étoiles à neutrons.
- $|(\hat{k}_A)_{23}| \lesssim 30$ et $|(\hat{k}_V)_{23}| \lesssim 2 \times 10^{-3}$ par les désintégrations rares de hadrons.
- $(\hat{k}_A)_{33}$ n'était pas contraint.

Grâce à notre procédure, nous pouvons améliorer considérablement la contrainte sur $(\hat{k}_A)_{23}$ et obtenir une nouvelle contrainte sur $(\hat{k}_A)_{33}$. Bien que les valeurs exactes dépendent des conditions thermody-

namiques, en ordre de grandeur, nous obtenons

$$|(\hat{k}_A)_{23}| \lesssim 0.1 \ , \quad |(\hat{k}_A)_{33}| \lesssim 10 \ . \tag{8}$$

Recherche sur l'absorption de l'axion QCD par des objets stellaires dans des expériences Cherenkov à eau

Si une supernova proche explose, en plus du flux de neutrinos, si l'axion existe, on peut s'attendre à un flux d'axions $\frac{dN_a}{dE_a}$ tel que :

$$Q_a \sim \frac{\rho}{M\Delta t} \int_{m_a}^{+\infty} dE_a E_a \frac{dN_a}{dE_a} \ , \tag{9}$$

où ρ est la densité du cœur de l'étoile, M sa masse et Δt la durée de l'explosion. Ainsi, les outils utilisés pour calculer l'émissivité Q_a peuvent être réutilisés pour déterminer le spectre axionique.

À partir de ce spectre axionique, on peut calculer le spectre d'absorption avec les noyaux d'hydrogène de l'eau dans la cuve Cherenkov. Le processus d'absorption est modélisé par la réaction $ap \to pX$, où X représente un parton Cherenkov entraînant une cascade qui génère un signal. Ce spectre d'absorption est donné par :

$$\frac{dN_X}{dE_X} = \frac{N_t}{4\pi d^2} \int_{m_a}^{+\infty} \frac{d\sigma}{dE_X} \frac{dN_a}{dE_a} dE_a \ , \tag{10}$$

avec N_t le nombre de cibles dans la cuve, d la distance entre la supernova et la Terre, et σ la section efficace du processus.

Ce spectre doit être comparé au spectre issu des neutrinos du Modèle Standard, $\bar{\nu}p \to ne^+$, qui est très important mais de faible énergie, avec l'énergie des e^+, les partons produits par les neutrinos, étant de l'ordre de 10 MeV.

Dans notre étude, nous avons examiné les cas du photon ($X = \gamma$) et du pion neutre ($X = \pi^0$). Nous avons constaté que le spectre issu des pions est plus prometteur, car le nombre de partons produits est plus élevé et le spectre est mieux distinguable de celui du Modèle Standard. Pour une supernova proche, à une distance de $d = 0,2$ kpc (comme Betelgeuse), le nombre de partons produits pourrait atteindre la centaine d'événements distinguables du Modèle Standard, ce qui serait largement mesurable. Même pour les modèles DFSZ et KSVZ, réputés difficiles à atteindre, un signal mesurable pourrait être observé. Cependant, les supernovæ sont des événements extrêmement rares, dans la Voie lactée seulement 2 à 3 supernovæ sont attendues par siècle. Augmenter le rayon de mesurabilité permettrait d'avoir plus de candidats et, par conséquent, d'espérer des explosions mesurables plus fréquemment. Nous avons montré que le flux d'axions pourrait être mesurable jusqu'au kpc (en comparaison, la distance au centre galactique est d'environ 8 kpc). Nous avons également montré, à travers des simulations Monte Carlo, que 80% des partons produits donnent un signal reconstruit expérimentalement, ce qui reflète une excellente sensibilité et démontre que le spectre est bien séparé de celui du Modèle Standard.

Enfin, nous avons étudié des processus au-delà de la première génération, comme $ap \to \Sigma^+ \to p\pi^0$, et bien que ce signal soit moins prometteur que celui de la première génération, il reste détectable et pertinent, notamment si les couplages de première génération sont fortement supprimés.

Recherche de l'axion QCD et des ALP dans les collisions

Les rapports de branchement des canaux de désintégration peuvent être des outils pertinents pour contraindre les couplages axioniques, notamment ceux permettant le changement de saveur $(k_{A,V})_{23}$.

Pour les baryons $B_i \to B_f a$, nous pouvons collecter tous les rapports de branchement expérimentaux. La somme des ratios de branchement doit être égale à 1. Si la somme des valeurs expérimentales est inférieure à 1, cela signifie soit que certaines désintégrations du Modèle Standard n'ont pas pu être mesurées, soit qu'il existe des désintégrations supplémentaires avec des particules au-delà du Modèle Standard. Si la somme des valeurs expérimentales est $1 \pm \delta$, alors les sources de désintégrations au-delà du Modèle Standard ne peuvent pas excéder δ, ce qui permet de contraindre les couplages.

En utilisant cette procédure, pour l'axion QCD avec $f_a = 10^9$ GeV, nous avons montré, via les désintégrations $\Xi^0 \to \Sigma^0 a$ et $\Xi^0 \to \Lambda a$, que

$$|(k_V)_{23}| \lesssim 10 \ , \quad |(k_A)_{23}| \lesssim 20 \ . \tag{11}$$

Pour les mésons, le même principe pourrait être utilisé. Cependant, des études dédiées existent pour des processus tels que $K^+ \to \pi^+ a$, $K_L \to \pi^0 a$, $K_L \to \pi^0\pi^0 a$ et $K^+ \to \pi^+\pi^0 a$. Les désintégrations

à deux corps permettent de contraindre $(k_V)_{23}$, tandis que les désintégrations à trois corps permettent de contraindre $(k_A)_{23}$, ce qui rend les deux types de désintégration complémentaires.

La méthode pour obtenir une contrainte consiste à étudier la désintégration où l'axion est remplacé par une paire $\nu\bar{\nu}$. Expérimentalement, on mesure une impulsion p_{vis}, supposée reconstruite, et l'impulsion invisible p_{inv} doit satisfaire la condition cinématique :

$$(p_{\text{vis}} + p_{\text{inv}})^2 = m_K^2 \ , \tag{12}$$

permettant ainsi de reconstruire l'impulsion manquante. Dans le cas de l'axion, $p_{\text{inv}}^2 = m_a^2$, une constante inconnue, tandis que dans le cas de la paire $\nu\bar{\nu}$, p_{inv}^2 n'est pas constant et peut varier en fonction de l'espace des phases disponible. Pour chaque valeur de p_{inv}^2 de la paire $\nu\bar{\nu}$, un axion de masse $m_a^2 = p_{\text{inv}}^2$ peut apparaître comme un bruit de fond, mais ne peut pas excéder certaines valeurs mesurables. Cela permet d'obtenir une contrainte sur les rapports de branchement, que l'on peut ensuite transférer aux couplages.

Avec cette méthodologie, pour l'axion QCD avec $f_a = 10^9$ GeV, nous obtenons

$$|(k_V)_{23}| \lesssim 2 \times 10^{-3} \ , \quad |(k_A)_{23}| \lesssim 40 \ . \tag{13}$$

On remarque que $(k_V)_{23}$ est bien mieux contraint que $(k_A)_{23}$, ce qui justifie de se concentrer sur les désintégrations mésoniques à trois corps. Cependant, dans la littérature, il n'y a pas eu d'études spécifiques sur K_S, qui pourrait très bien être étudié au LHCb, notamment via la production secondaire, avec les désintégrations $K_S \to \mu^+\mu^- a$ et $K_S \to \pi^+\pi^- a$.

Nous avons mené une étude théorique pour déterminer une méthodologie permettant d'identifier les processus intéressants à examiner dans une étude expérimentale. Cette méthodologie consiste à utiliser les rapports de branchement expérimentaux des bruits de fond potentiels pour estimer une sensibilité S_{eff}, telle que les rapports de branchement théoriques BR_{th} incluant l'axion vérifient $BR_{th} < S_{eff}$, ce qui permet de contraindre les couplages axioniques. En revanche, notre procédure ne peut pas se substituer à une étude spécifique ; elle sert uniquement d'indication pour savoir s'il serait intéressant de mener une étude dédiée sur un processus donné.

Nous avons appliqué cette procédure à la désintégration $K^+ \to \pi^+\pi^0 a$ pour vérifier sa consistance avec les études dédiées, et nous avons étudié les désintégrations de K_S pour déterminer si une étude spécifique pourrait être pertinente. Nous avons trouvé que pour $m_a \simeq m_\pi$, une telle étude pourrait effectivement être intéressante.

Nous avons également tracé les diagrammes de Dalitz du rapprochement de branchement différentiel $\frac{d^2BR}{ds\,dt}$, afin d'observer s'il existe des régions de l'espace des phases surpeuplées. Nous avons constaté que la non-uniformité peut être naturellement alignée avec les sensibilités expérimentales, ce qui suggère qu'une étude non pas sur les rapports de branchement, mais directement sur $\frac{d^2BR}{ds\,dt}$, pourrait fournir des résultats plus précis.

Conclusion

En résumé, ce travail met en évidence la puissance et la nécessité d'une approche multifacette pour la recherche des axions. En établissant systématiquement des liens entre la modélisation théorique et les opportunités expérimentales à travers différentes échelles d'énergie et secteurs, nous avons mis en lumière de nouvelles sensibilités aux propriétés et aux couplages des axions — en particulier ceux impliquant la matière étrange — et posé les bases pour des investigations futures orientées vers la découverte. Les résultats soutiennent l'idée que l'axion QCD et les ALP demeurent parmi les candidats les plus réalistes et théoriquement motivés pour de nouvelles découvertes en physique, dont les effets indirects pourraient bientôt être mesurables grâce à nos installations expérimentales les plus avancées.

Remerciements

Je commence forcément par remercier ma femme. Elle m'a aidé à tenir le coup pendant toutes ces années de thèse, elle a toujours été là, dans les bons comme dans les moments un peu plus durs, avec sa patience et son soutien indéfectible. C'est vraiment grâce à elle que j'ai pu avancer sereinement. Et puis, il y a ma petite Willow, qui a soufflé ses 4 bougies cette année. Elle est une vraie source de bonheur et de motivation, une petite boule d'énergie qui me rappelle chaque jour ce qui compte vraiment dans la vie.

Je souhaite évidemment remercier le reste de ma famille, qui a toujours été un pilier pour moi, en croyant toujours en moi, et ça, c'est un cadeau inestimable. Leur présence, même à distance, a été une source de force et de motivation tout au long de ce parcours.

Je ne peux pas passer à côté de Diego sans lui dire un immense merci. Dès le début, il a été énormément à l'écoute, toujours compréhensif, et il a su créer un environnement de travail vraiment agréable, où j'ai pu m'épanouir. On nous dit souvent que choisir son directeur de thèse, c'est presque aussi important que le sujet lui-même, et franchement, je mesure la chance que j'ai eue d'être encadré par Diego.

Bien sûr, je voudrais remercier toutes les personnes avec qui j'ai eu la chance de collaborer lors des différents projets. En particulier, Ludovico qui a toujours été bienveillant et de bons conseils.

Mes collègues de bureau, Ugo et Axel, je vous dois un grand merci. Vous avez su rendre l'espace de travail convivial et agréable, et nos échanges m'ont souvent aidé à clarifier mes idées et à avancer dans mes recherches. Franchement, ça fait toute la différence.

Je pense aussi à mes collègues doctorants et doctorantes – Cervane, Cyann, Léo, Matthis, Nathan et la coloc LYM (Léo, Yann, Margo[2]) – vous avez été bien plus que des collègues, les moments passés ensemble ont vraiment allégé le quotidien. Un petit clin d'œil spécial à Joshua et Maël pour nos matchs de ping-pong endiablés, toujours un bon moment pour décompresser.

Je tiens également à exprimer ma profonde gratitude à mon jury de thèse, en particulier à Marc Knecht et Francesca Gulminelli, rapporteur et rapporteuse de cette thèse, pour avoir accepté d'en évaluer le contenu et pour la qualité de leurs retours, qui ont contribué à l'amélioration de ce manuscrit. Mais également à Martino Borsato, Francesca, Calore, Luca Di Luzio, Dominique Duchesneau et Björn Herrmann pour le temps pris pour moi et pour leurs questions pertinentes.

Je n'oublie pas les membres de mon Comité de Suivi Individuel – Pasquale Serpico, Christopher Smith et Ana Teixeira – pour leurs conseils avisés, leurs questions pertinentes et leur regard extérieur qui m'ont permis de prendre du recul.

Un grand merci à toute l'administration, qui a fait preuve d'une patience incroyable, que ce soit pour gérer les papiers, les inscriptions, ou tout ce qui peut paraître compliqué mais qui est indispensable. Vous êtes souvent dans l'ombre, mais c'est grâce à vous que tout peut tourner rond.

Je n'oublie pas Christopher, mon fidèle compagnon de galères et de physique depuis la L3 à Grenoble. Nos discussions, souvent longues et passionnées, ont toujours été une vraie source d'enrichissement personnel et scientifique.

Matthias, mon ami et témoin de mariage, je te remercie aussi. Tu as traversé la France avec moi pour les études, et ta présence a vraiment compté dans ce parcours.

Enfin, je pense à mes ami·e·s de la licence à Brest — Yvonne, Gwénolé, Ingrid — avec qui j'ai partagé plein de beaux souvenirs.

Voilà, je pourrais continuer encore longtemps, mais je crois que l'essentiel est là. Merci à toutes et à tous d'avoir fait partie de cette incroyable aventure !

[2] ooooooo

Contents

Introduction **13**

1 The axion and its problem-solving potential **17**
1.1 The Standard Model of particle physics . . . 18
1.2 General axion-Standard Model Lagrangian . . . 20
1.3 The strong CP problem . . . 20
1.4 Dark Matter candidate . . . 27
1.5 The flavor puzzle : the axiflavon/flaxion model . . . 33
1.6 The hierarchy problem : the Relaxion model . . . 34

2 Chiral Perturbation Theory – ChPT **41**
2.1 Motivation . . . 42
2.2 Effective Field Theory vs. Renormalizable Theory . . . 43
2.3 Fermi's theory . . . 43
2.4 The CCWZ formalism . . . 45
2.5 Chiral Currents and Noether's theorem . . . 46
2.6 QCD symmetries . . . 47
2.7 ChPT for mesons . . . 48
2.8 ChPT for baryons . . . 51
2.9 Lagrangian mediating weak processes . . . 56
2.10 Axionic Lagrangian . . . 58
2.11 State-of-the-art in axion-quark coupling bounds . . . 68

3 Search for QCD axion emission from stellar objects **71**
3.1 Motivation . . . 72
3.2 Study of the axion-photon-photon coupling . . . 72
3.3 Axion emission from first generation in Neutron Stars . . . 73
3.4 Axion emission from strange matter in core-collapse Supernovæ . . . 75
3.5 The dominant axion production channels . . . 88

4 Search for QCD axion absorption from stellar objects in water Cherenkov experiments **99**
4.1 Axion interaction with first-generation particles . . . 100
4.2 Axion interaction with strange matter . . . 117
4.3 Outlook . . . 127

5 Search for QCD axion and Axion-like Particles at colliders **131**
5.1 Constraints from non-observable hadron decays and $K^0 - \bar{K}^0$ mixing . . . 132
5.2 Probing QCD Axion or Axion-like Particles in three-body K decays . . . 141

Conclusion **163**

A Basic tools and conventions **165**
A.1 Conventions . . . 165
A.2 Pauli and Gell-Mann matrices . . . 165

B Observables and specific calculations **167**
B.1 Calculations of observables . . . 167
B.2 Regularization of loop integrals . . . 174
B.3 Resonance . . . 178
B.4 $g-2$ anomaly calculation and axion contribution . . . 179
B.5 Extraction of F_0, D, and F from experimental data in ChPT . . . 182
B.6 $K \to \ell^+\ell^-\pi$ calculation . . . 183
B.7 Calculation of $\hat{c}_{aGG}$ and $\hat{c}_{a\gamma\gamma}$ . . . 191
B.8 Axion emissivity calculation . . . 194
B.9 SN core effective quantities . . . 204

C Field theory and Lagrangians **207**
C.1 Zoology of Standard Model particle physics . . . 207
C.2 Higgs mechanism . . . 208
C.3 Quark Model . . . 211
C.4 Meson masses and explicit symmetry breaking . . . 216
C.5 Chiral Perturbation Theory with an axion Lagrangian . . . 217
C.6 Axion-mesons vertices . . . 219
C.7 Axiflavon/flaxion interactions with quarks . . . 220

D Computational framework for axion emission **223**
D.1 Overview . . . 223
D.2 Structure and Usage . . . 223
D.3 Example Input . . . 224
D.4 Availability . . . 224

E Scientific Communication **225**
E.1 Conference presentations . . . 225
E.2 Science outreach . . . 225

List of Figures **231**

List of Tables **235**

List of Acronyms **237**

Bibliography **239**

Introduction

The Standard Model (SM) of particle physics stands as one of the most successful and thoroughly tested theories in the history of science. With a structure built upon gauge invariance, Quantum Field Theory (QFT), and the principles of special relativity, it provides an exceptionally precise description of the electromagnetic, weak, and strong interactions among the fundamental constituents of matter. Its predictions, ranging from cross sections to decay rates and particle masses, have been verified through decades of experimental efforts across a variety of energy scales. The discovery of the Higgs boson in 2012 by the ATLAS and CMS collaborations at CERN confirmed the last missing piece of the SM and validated the Higgs mechanism for electroweak symmetry breaking.

However, the success of the SM also presents a fundamental limitation: being a renormalizable theory, it offers no direct clue of the scale at which it may possibly break. For their part as well, its internal consistency, predictivity, and agreement with experimental data make it challenging to identify clear signs of new physics at accessible energy scales. Yet we know that the SM is not a complete theory. It has major shortcomings from both observational and conceptual viewpoints. These include the existence of Dark Matter (DM), the matter-antimatter asymmetry, the origin of neutrino masses, the hierarchy problem associated with the Higgs boson mass, and the so-called strong CP problem. This is the observed absence of CP violation in the strong interaction, despite the fact that the Quantum Chromodynamics (QCD) Lagrangian allows for a CP-violating term proportional to $G\tilde{G}$. Its coupling originates from two conceptually distinct sources within the SM Lagrangian, and there is no anthropic reason for it to be as small as current experimental bounds require.

The Peccei-Quinn (PQ) mechanism offers a remarkably elegant solution to the strong CP problem. It introduces a new global $U(1)_{PQ}$ symmetry that is spontaneously broken at a scale f_a, giving rise to a pseudo-Nambu-Goldstone boson: the QCD axion. In its "invisible" versions—such as the Kim-Shifman-Vainshtein-Zakharov (KSVZ) and Dine-Fischler-Srednicki-Zhitnitsky (DFSZ) models—the axion is a light, weakly coupled particle whose interactions are suppressed by powers of $1/f_a$. These properties render it not only compatible with current experimental constraints but also a viable cold DM candidate, whose relic abundance can naturally arise from vacuum misalignment during the early Universe.

In recent years, interest in QCD axions and their generalizations–Axion-like Particles (ALPs)–has grown considerably. While ALPs are not necessarily tied to the strong CP problem, they share many of the axion's phenomenological features, especially their coupling structure and potential cosmological roles. ALPs appear in a wide range of theoretical frameworks, including string theory compactifications, and can address other open questions in the SM. Importantly, both QCD axion and ALPs are characterized by the possibility of probing extremely high energy scales indirectly, through their suppressed but structured interactions with SM fields. This makes them ideal targets for exploration across experimental frontiers, including astrophysical observations, underground detectors, and high-energy colliders.

This manuscript adopts a multi-probe approach to the study of axion phenomenology, based on the idea that combining independent observational domains can lead to complementary and robust constraints on axion properties. In particular, we investigate the phenomenology of axions in three distinct settings:

1. Compact astrophysical objects, where axions can be emitted via hadronic processes in high-temperature, high-density environments.

2. Large-volume Cherenkov detectors, where axions fluxes from astrophysical sources may be de-

tected through their interactions with hadronic matter.

3. Flavor experiments at colliders, where QCD axion and ALPs can mediate rare meson decays via Flavor-Changing Neutral Currents (FCNCs).

To enable a consistent and predictive description of axion interactions in these environments, we develop and employ a low-energy Effective Field Theory (EFT) based on Chiral Perturbation Theory (ChPT), which provides a systematic expansion of QCD in terms of mesons and baryons. By embedding axion interactions within the ChPT framework, we construct an effective Lagrangian that describes the couplings of axions to hadronic degrees of freedom–including interactions with hadrons–across a broad range of energy scales and experimental conditions.

The structure of the manuscript is as follows.

In Chapter 1, we review the theoretical foundations of the axion, from its emergence as a solution to the strong CP problem to its cosmological and phenomenological implications. After presenting the Peccei-Quinn-Weinberg-Wilczek (PQWW), KSVZ, and DFSZ models that address the strong CP problem, as well as the misalignment mechanism as a solution to the DM problem, we explore how axions can also provide insights into other SM puzzles, including the flavor puzzle hierarchy, and the Higgs mass hierarchy problem. This chapter establishes the axion as a compelling and versatile Beyond the Standard Model (BSM) candidate.

In Chapter 2, we develop the technical tools required to describe axion interactions with hadronic matter. We begin by reviewing the logic of EFTs and the Callan-Coleman-Wess-Zumino (CCWZ) formalism for constructing effective Lagrangians based on symmetry-breaking patterns. We then formulate the ChPT Lagrangian for mesons and baryons and derive the relevant Noether currents. Finally, we incorporate axionic degrees of freedom into this formalism and construct the low-energy axion-hadron Lagrangian, which becomes a central ingredient for all subsequent phenomenological analyses.

Chapter 3 presents the first original contribution of this manuscript: a detailed calculation of axion emissivities from core-collapse Supernovæ (SNe), including contributions from strange matter. Using the effective Lagrangian developed in Chapter 2, we model axion production via baryon-meson scattering and baryon decay processes in realistic Supernova (SN) core conditions, considering multiple Equation of State (EoS) and temperature-density profiles. For the first time, we derive quantitative estimates of axion emission from hyperons and strange mesons in a consistent EFT framework, resulting in new constraints on the axion-strange-strange and axial axion-down-strange couplings. In particular, we establish the strongest current bounds on the latter coupling, reaching sensitivities at the level of $\mathcal{O}(10^{-2})$ for $f_a = 10^9\,\text{GeV}$.

Building on these results, Chapter 4 explores the terrestrial detection of astrophysical axions using water Cherenkov detectors such as Hyper-Kamiokande (HK). We consider the propagation of axions emitted from nearby SNe and compute their expected flux and spectral distribution. We then study the processes $a + N \to N + \gamma$ and $a + N \to N + \pi^0$, which can produce Cherenkov-visible signatures through the decay of π^0 or γ emission. Our analysis shows that even the QCD axion, despite its suppressed interactions, may lead to detectable signals in the π^0 channel, which is substantially enhanced with respect to the γ channel on which existing literature has been focused. We further generalize the framework to include axion interactions with strange baryons, which–although less visible–could become relevant if the first-generation couplings are suppressed.

Finally, in Chapter 5, we investigate the role of rare hadronic decays at colliders in probing QCD axion and ALPs. We begin by reviewing existing bounds from unobserved baryon and meson decays, as well as K^0-$\bar{K}^0$ mixing. We then present a novel analysis of three-body kaon decays, such as $K \to \pi\pi a$ and $K \to \mu\mu a$, which can be mediated by QCD axions or ALPs with flavor-violating couplings. These decay modes are particularly well-suited for detection at Large Hadron Collider beauty (LHCb). We compute Branching Ratios (BRs), Dalitz distributions, and reconstruction efficiencies, and demonstrate that these processes can probe axion decay constants in the range $f_a \sim 10^7 - 10^9\,\text{GeV}$, thereby covering parameter regions complementary to astrophysical and cosmological searches.

The appendices contain supplementary material that is not essential for the main discussion but may be useful for readers seeking additional details. References to this material will be made where appropriate. For instance, the notations and conventions used throughout this manuscript are collected in Appendix A.1.

In summary, this manuscript demonstrates the power of a multi-probe strategy in exploring axion physics across different experimental domains. By developing a unified theoretical framework rooted in EFT and applying it to distinct physical systems and detection setups–compact stars, neutrino obser-

vatories, and particle colliders–we uncover new regions of parameter space and place novel constraints on previously unexplored couplings, particularly involving strange matter. The results presented here, some of which are based on original research published [Cav+24; Cav+25b; Cav+25a], open new avenues for the discovery of light pseudoscalar particles and strengthen the case for axions as a realistic component of physics BSM.

References

[Cav+24] Mael Cavan-Piton et al. *Axion Emission from Strange Matter in Core-Collapse SNe*. In: *Phys. Rev. Lett.* 133.12 (2024), p. 121002. DOI: 10.1103/PhysRevLett.133.121002. arXiv: 2401.10979 [hep-ph].

[Cav+25a] Mael Cavan-Piton et al. *Probing QCD Axions or axion-like particles in three-body K decays*. In: *JHEP* 06 (2025), p. 039. DOI: 10.1007/JHEP06(2025)039. arXiv: 2411.04170 [hep-ph].

[Cav+25b] Mael Cavan-Piton et al. *Probing the general axion-nucleon interaction in water Cherenkov experiments*. In: *JHEP* 07 (2025), p. 070. DOI: 10.1007/JHEP07(2025)070. arXiv: 2503.17490 [hep-ph].

Chapter 1

The axion and its problem-solving potential

Contents

1.1 The Standard Model of particle physics 18
1.2 General axion-Standard Model Lagrangian 20
1.3 The strong CP problem 20
1.3.1 General considerations 20
1.3.2 The PQWW model 22
1.3.3 The KSVZ model 24
1.3.4 The DFSZ model 25
1.4 Dark Matter candidate 27
1.4.1 The Dark Matter problem 27
1.4.2 Axion field in cosmological context 28
1.4.3 Solving the equation–the misalignment mechanism 29
1.5 The flavor puzzle : the axiflavon/flaxion model 33
1.6 The hierarchy problem : the Relaxion model 34

In this chapter, we first review the structure and content of the Standard Model (SM) of particle physics in Section 1.1, emphasizing its gauge symmetries, particle content, and Lagrangian formulation. Despite its remarkable success, the SM leaves several key questions unanswered, such as the strong CP problem and the nature of Dark Matter (DM).

We then introduce the axion in Section 1.2, discussing its couplings to the SM fields. This leads us to a detailed exploration of specific axion models in Section 1.3, including the original Peccei-Quinn-Weinberg-Wilczek (PQWW) model, and its "invisible" versions: the Kim-Shifman-Vainshtein-Zakharov (KSVZ) and Dine-Fischler-Srednicki-Zhitnitsky (DFSZ) models.

In Section 1.4, we study how the axion may act as a viable DM candidate. This includes the cosmological evolution of the axion field and the misalignment mechanism.

Finally, in Sections 1.5, and 1.6, we review the axion's potential role in solving other puzzles of the SM: the fermion flavor, and the Higgs mass hierarchy, respectively.

Altogether, this chapter outlines the axion's versatility as a solution to multiple problems in particle physics, motivating its study in the broader context of SM physics.

1.1 The Standard Model of particle physics

To construct a Quantum Field Theory (QFT) for particle physics, we need to introduce the fields and their symmetries; define the Lagrangian[1] $\mathcal{L}$, which governs the dynamics of the fields; specify the values of the parameters in the Lagrangian; describe how observable quantities can be computed from the theory (see Appendix B.1).

The SM is the most general local and renormalizable[2] QFT compatible with special relativity (i.e., invariant under the Poincaré group, including Lorentz transformations and space-time translations), consistent with the gauge symmetry group $G_{SM} = SU(3)_c \times SU(2)_L \times U(1)_Y$, and incorporating all known particles as well as the Higgs mechanism.

In G_{SM}, $SU(3)_c$ describes the strong interaction, while $SU(2)_L \times U(1)_Y$ describes the electroweak interaction, which is spontaneously broken down to $U(1)_{e.m.}$ (electromagnetism).

Particle representations under the gauge symmetry group are denoted as $(\underline{c};\underline{L})_Y$, where $\underline{c}$ is the representation under $SU(3)_c$, $\underline{L}$ is the representation under $SU(2)_L$, and Y is the hypercharge under $U(1)_Y$.

The particle content of the SM is as follows[3]:

- Quark doublet:
$$Q^f = \begin{pmatrix} u_L^f \\ d_L^f \end{pmatrix} \sim (\underline{3};\underline{2})_{1/3} \ . \tag{1.1.1}$$
Right-handed singlets:
$$u_R^f \sim (\underline{3};\underline{1})_{4/3}, \quad d_R^f \sim (\underline{3};\underline{1})_{-2/3} \ . \tag{1.1.2}$$
with the three generations $u^f = (u \ , \ c \ , \ t)$ and $d^f = (d \ , \ s \ , \ b)$.

- Lepton doublet:
$$L^f = \begin{pmatrix} \nu_L^f \\ e_L^f \end{pmatrix} \sim (\underline{1};\underline{2})_{-1} \ . \tag{1.1.3}$$
Right-handed singlets:
$$e_R^f \sim (\underline{1};\underline{1})_{-2}, \quad \nu_R^f \sim (\underline{1};\underline{1})_0 \ . \tag{1.1.4}$$
with the three generations $e^f = (e \ , \ \mu \ , \ \tau)$ and $\nu^f = (\nu_e \ , \ \nu_\mu \ , \ \nu_\tau)$.

  Note: The right-handed neutrino ν_R^f remains hypothetical, as it does not couple to the gauge fields.

- Higgs doublet:
$$H = \begin{pmatrix} H^+ \\ H^0 \end{pmatrix} \sim (\underline{1};\underline{2})_1 \ . \tag{1.1.5}$$

- Gauge bosons:
$$B \sim (\underline{1};\underline{1})_0 \quad \text{for } U(1)_Y \ , \tag{1.1.6}$$
$$W \sim (\underline{1};\underline{3})_0 \quad \text{for } SU(2)_L \ , \tag{1.1.7}$$
$$G \sim (\underline{8};\underline{1})_0 \quad \text{for } SU(3)_c \ . \tag{1.1.8}$$

After electroweak symmetry breaking $SU(2)_L \times U(1)_Y \to U(1)_{e.m.}$, the physical gauge bosons are described, in the Glashow-Salam-Weinberg model, by:

$$W_\mu^\pm = \frac{W_\mu^1 \mp i W_\mu^2}{\sqrt{2}} \ , \quad \begin{pmatrix} Z_\mu \\ A_\mu \end{pmatrix} = \begin{pmatrix} \cos(\theta_W) & -\sin(\theta_W) \\ \sin(\theta_W) & \cos(\theta_W) \end{pmatrix} \begin{pmatrix} W_\mu^3 \\ B_\mu \end{pmatrix} \ , \tag{1.1.9}$$

with the weak mixing angle:

$$\cos(\theta_W) = \frac{g}{\sqrt{g^2 + g'^2}} \ , \quad \sin(\theta_W) = \frac{g'}{\sqrt{g^2 + g'^2}} \ , \tag{1.1.10}$$

[1] Strictly speaking, it is a Lagrangian density. However, since in particle physics we only deal with Lagrangian densities, I will, for convenience, refer to them simply as Lagrangians.

[2] That is, it includes only operators of mass dimension $d \leq 4$ in four-dimensional space-time.

[3] For a visual representation of the particle content, see Appendix C.1.

satisfying $\cos(\theta_W) = m_W/m_Z$. g is the gauge coupling of $SU(2)_L$, g' is the gauge coupling of $U(1)_Y$, and g_s is the gauge coupling of $SU(3)_c$. The electric charge is then defined as:

$$e = \frac{gg'}{\sqrt{g^2 + g'^2}} \ . \tag{1.1.11}$$

The full Lagrangian of the SM (before gauge fixing) is:

$$\mathcal{L}_{SM} = \mathcal{L}_B + \mathcal{L}_M + \mathcal{L}_H + \mathcal{L}_Y, \tag{1.1.12}$$

where:

- The gauge field Lagrangian is:

$$\mathcal{L}_B = -\frac{1}{4} G^a_{\mu\nu} G^{a\,\mu\nu} - \frac{1}{4} W^b_{\mu\nu} W^{b\,\mu\nu} - \frac{1}{4} B_{\mu\nu} B^{\mu\nu} \ . \tag{1.1.13}$$

- The fermion Lagrangian is:

$$\mathcal{L}_M = i\bar{Q}^f \not{D} Q^f + i\bar{u}^f_R \not{D} u^f_R + i\bar{d}^f_R \not{D} d^f_R + i\bar{L}^f \not{D} L^f + i\bar{e}^f_R \not{D} e^f_R \ , \tag{1.1.14}$$

  where the covariant derivative, describing interaction with gauge bosons, is:

$$D_\mu = \partial_\mu + i g_s G_\mu + i g W_\mu + i g' \frac{Y}{2} B_\mu \ . \tag{1.1.15}$$

- The Higgs sector Lagrangian is:

$$\mathcal{L}_H = (D_\mu H)^\dagger D^\mu H - V(H) \ , \tag{1.1.16}$$

  with the Higgs potential taking the form of a Mexican hat:

$$V(H) = \lambda \left(H^\dagger H - v^2/2 \right)^2 \ . \tag{1.1.17}$$

- The Yukawa interaction Lagrangian is:

$$\mathcal{L}_Y = -Y_u^{ff'} \bar{Q}^f \tilde{H} u^{f'}_R - Y_d^{ff'} \bar{Q}^f H d^{f'}_R - Y_e^{ff'} \bar{L}^f H e^{f'}_R \ , \tag{1.1.18}$$

  where $Y_{u,d,e}$ are complex 3×3 matrices, and:

$$H = \begin{pmatrix} H^+ \\ H^0 \end{pmatrix}, \quad \tilde{H} = \epsilon H^* = \begin{pmatrix} H^0 \\ -H^- \end{pmatrix} \ . \tag{1.1.19}$$

  This yields the fermion couplings:

$$\bar{Q}\tilde{H} = \bar{u}_L H^0 - \bar{d}_L H^-, \quad \bar{Q} H = \bar{u}_L H^+ + \bar{d}_L H^0 \ . \tag{1.1.20}$$

  After electroweak symmetry breaking, the Higgs field acquires a Vacuum Expectation Value (vev) via the Higgs mechanism, and one sets: $H^0 = \frac{1}{\sqrt{2}}(v + h)$, $H^+ = H^- = 0$, with v being the vev responsible for mass generation. For more details on the Higgs mechanism, see Appendix C.2.

Despite the successes of the SM, several fundamental problems remain unresolved, requiring the development of Beyond the Standard Model (BSM) physics. Among the most prominent are:

- The strong CP problem: the term $G^a_{\mu\nu} \tilde{G}^{a,\mu\nu}$, where $\tilde{G}^{a,\mu\nu} = \frac{1}{2} \epsilon^{\mu\nu\alpha\beta} \tilde{G}^a_{\alpha\beta}$, is allowed by SM symmetries and renormalizability. It leads to CP violation in Quantum Chromodynamics (QCD) that is not observed experimentally (see Section 1.3). This is problematic because the coupling of this operator arises from two conceptually distinct interactions in the SM Lagrangian, and there is no rationale – not even anthropic – to set it to zero;
- The DM problem: astronomical and cosmological observations suggest the existence of non-baryonic matter not accounted for within the SM (see Section 1.4).

Among the candidates proposed to solve these issues, a particularly elegant and compelling one is the axion – a light pseudo-scalar particle, which will be the central subject of the rest of this work. A comprehensive review of how the axion can solve these two major problems can be found in [Mar16].

In addition to these, the axion may also offer insights or partial solutions to other outstanding puzzles in the SM, including:

- The hierarchical flavor structure of quarks and leptons (see Section 1.5).
- The Higgs mass hierarchy (see Section 1.6).

1.2 General axion-Standard Model Lagrangian

The general Lagrangian describing the interaction between the axion and the SM particles can be written as:

$$\begin{aligned}\mathcal{L}_{axion-SM} =& \frac{1}{2}\partial_\mu a \partial^\mu a + \frac{1}{2}m_a^2 a^2 + c_{aGG}\frac{\alpha_s}{4\pi}\frac{a}{f_a}G\tilde{G} + c_{a\gamma\gamma}\frac{\alpha_{e.m.}}{4\pi}\frac{a}{f_a}F\tilde{F} \\ &+ \frac{\partial_\mu a}{f_a}\bar{q}\gamma^\mu\left(k_V^q + k_A^q\gamma_5\right)q + \frac{\partial_\mu a}{f_a}\bar{\ell}\gamma^\mu\left(k_V^\ell + k_A^\ell\gamma_5\right)\ell \ ,\end{aligned} \tag{1.2.1}$$

where $\ell = (e\ \mu\ \tau)^T$ denotes the vector of charged leptons, and $q = (u\ d\ s\ c\ b\ t)^T$ the vector of quarks ordered by increasing mass. The Lagrangian must be real, which requires the matrices $k_{A,V}^{q,\ell}$ to be Hermitian. Moreover, electric charge conservation forbids couplings between particles of different electric charge, which constrains the matrices' structure. In full generality, the lepton coupling matrices can be written as:

$$k_{A,V}^\ell = \begin{pmatrix} (k^\ell)_{ee} & (k^\ell)_{e\mu} & (k^\ell)_{e\tau} \\ (k^\ell)_{e\mu}^* & (k^\ell)_{\mu\mu} & (k^\ell)_{\mu\tau} \\ (k^\ell)_{e\tau}^* & (k^\ell)_{\mu\tau}^* & (k^\ell)_{\tau\tau} \end{pmatrix}_{A,V} \ , \tag{1.2.2}$$

and the quark coupling matrices are given by:

$$k_{A,V}^q = \begin{pmatrix} (k^q)_{uu} & 0 & 0 & (k^q)_{uc} & 0 & (k^q)_{ut} \\ 0 & (k^q)_{dd} & (k^q)_{ds} & 0 & (k^q)_{db} & 0 \\ 0 & (k^q)_{ds}^* & (k^q)_{ss} & 0 & (k^q)_{sb} & 0 \\ (k^q)_{uc}^* & 0 & 0 & (k^q)_{cc} & 0 & (k^q)_{ct} \\ 0 & (k^q)_{db}^* & (k^q)_{sb}^* & 0 & (k^q)_{bb} & 0 \\ (k^q)_{ut}^* & 0 & 0 & (k^q)_{ct}^* & 0 & (k^q)_{tt} \end{pmatrix}_{A,V} \ . \tag{1.2.3}$$

These matrices allow for flavor-changing interactions, which are not forbidden by any symmetry.

Axion-matter couplings are not fundamentally required to vanish and, similarly to Yukawa couplings, are generally expected to be present.

1.3 The strong CP problem

1.3.1 General considerations

In non-Abelian gauge theories, the presence of Euclidean solutions associated with a topological quantum number requires a treatment that goes beyond naïve vacuum-state perturbation theory. These solutions, labeled by a parameter θ, correspond to distinct vacua in the Hilbert space of the theory. Importantly, there are no transitions between states belonging to different θ-sectors.

The vacuum-to-vacuum transition amplitude in a theory described by the Lagrangian $\mathcal{L}(A, \Phi)$, evaluated in the θ-vacuum, is given by:

$$\langle 0|0\rangle_\theta = \sum_{q=-\infty}^{\infty}\int (dA_\mu)_q \int d\Phi \left[\int d^4x\, \mathcal{L}_E(A,\Phi)\right] e^{iq\theta} \ . \tag{1.3.1}$$

Here, A denotes the non-Abelian gauge field and Φ represents other fields in the theory.

The integral $\int (dA_\mu)_q$ is taken over all gauge configurations satisfying:

$$\frac{g^2}{16\pi^2}\int d^4x\, F_{\mu\nu}^a \widetilde{F}^{a,\mu\nu} = q \ , \tag{1.3.2}$$

where $\widetilde{F}^{a,\mu\nu} = \frac{1}{2}\epsilon^{\mu\nu\alpha\beta}F_{\alpha\beta}^a$ is the dual of the field strength tensor $F_{\mu\nu}^a = \partial_\mu A_\nu^a - \partial_\nu A_\mu^a + g f^{abc} A_\mu^b A_\nu^c$.

Although the integrand in Eq. (1.3.2) can be written as a total divergence,

$$F_{\mu\nu}^a \widetilde{F}^{a,\mu\nu} = \partial_\mu\left(2\epsilon^{\mu\nu\alpha\beta}\left(A_\nu^a\partial_\alpha A_\beta^a + \frac{1}{3}g f^{abc}A_\nu^a A_\alpha^b A_\beta^c\right)\right) \ , \tag{1.3.3}$$

with the corresponding current being the Hodge dual of the Chern-Simons 3-form, the integral does not vanish due to the presence of instanton configurations. Instantons are non-perturbative, finite-action

solutions of the Euclidean equations of motion that are globally defined and topologically nontrivial; they interpolate between distinct vacuum sectors labeled by different winding numbers. Each integer q labels a topologically distinct sector.

In naïve perturbation theory, only the $q = 0$ sector contributes to $\langle 0|0\rangle_\theta$. The term $e^{iq\theta}$ can be interpreted as arising from an effective Lagrangian:

$$\mathcal{L}_{eff} = \mathcal{L} + \theta \frac{g^2}{32\pi^2} F^a_{\mu\nu} \widetilde{F}^{a,\mu\nu} = \mathcal{L} + \theta \frac{\alpha}{8\pi} F^a_{\mu\nu} \widetilde{F}^{a,\mu\nu} \ . \tag{1.3.4}$$

When applied to QCD, this leads to the effective term:

$$\mathcal{L} \supset \theta \frac{\alpha_s}{8\pi} G^a_{\mu\nu} \widetilde{G}^{a,\mu\nu} \ . \tag{1.3.5}$$

In addition to the purely gluonic topological term, the QCD Lagrangian acquires a similar effective contribution from the Yukawa sector after electroweak symmetry breaking. Specifically, when quark mass matrices are diagonalized through chiral rotations of the quark fields, the chiral anomaly implies that these field redefinitions shift the θ-angle. As a result, the physical θ-parameter becomes:

$$\theta_{phys} = \theta_{QCD} + \arg(\det(M_q)) \ . \tag{1.3.6}$$

where M_q is the complex quark mass matrix. The phase of the determinant of M_q, originates from the Yukawa couplings. One thus sees that the physical θ term is the result of two conceptually distinct mechanisms.

The Lagrangian term in Eq. (1.3.5) violates the CP symmetry.

To justify this, we define, by analogy with electromagnetism, the chromoelectric and chromomagnetic fields as:

$$G^a_{0i} = E^a_i \ , \quad G^a_{ij} = -\epsilon_{ijk} B^a_k \ . \tag{1.3.7}$$

Here, $\vec{E}^a$ is C-odd and P-odd, while $\vec{B}^a$ is C-odd and P-even[4].

We compute:

$$\tilde{G}^a_{0i} = \epsilon_{0ijk} G^{a,ij} = \epsilon_{ijk}(-\epsilon_{ijl} B^a_l) = -B^a_i \ , \tag{1.3.8}$$

$$\tilde{G}^a_{ij} = 2\epsilon_{ij0k} G^{a,0k} = 2\epsilon_{ijk} E^a_k \ . \tag{1.3.9}$$

Then, the scalar quantities are:

$$G^a_{\mu\nu} G^{a,\mu\nu} = G^a_{ij} G^{a,ij} + G^a_{0i} G^{a,0i} + G^a_{i0} G^{a,i0} = 2(\vec{B}^a \cdot \vec{B}^a - \vec{E}^a \cdot \vec{E}^a) \ , \tag{1.3.10}$$

which is even under both C- and P-even, and therefore CP-even.

In contrast,

$$G^a_{\mu\nu} \tilde{G}^{a,\mu\nu} = G^a_{0i} \tilde{G}^{a,0i} + G^a_{i0} \tilde{G}^{a,i0} + G^a_{ij} \tilde{G}^{a,ij} = (E^a_i)(-B^a_i) + (-E^a_i)(B^a_i) + (-\epsilon^{ijl} B^a_l)(2\epsilon_{ijk} E^a_k) = -4\vec{E}^a \cdot \vec{B}^a \ , \tag{1.3.11}$$

which is C-even and P-odd, and thus violates CP.

This CP-violating term has physical consequences, even if the rest of the QCD Lagrangian is constructed to conserve CP. In particular, it contributes to the neutron Electric Dipole Moment (nEDM), with an effective interaction:

$$\mathcal{L}_{nEDM} = -\frac{i}{2} d_n \bar{n} \sigma^{\mu\nu} \gamma_5 n F_{\mu\nu} \ , \tag{1.3.12}$$

where the nEDM is approximately

$$d_n \simeq 2.4(1.0) \times 10^{-16}\, \theta_{phys}\, e\,\text{cm} \ . \tag{1.3.13}$$

with e is the elementary electric charge.

Experimental limits set $|d_n| < 2.9 \times 10^{-26}\, e\,\text{cm}$ at 90% confidence level [Bak+06], implying $|\theta_{phys}| < 10^{-10}$. This remarkably small number reflects an unexpectedly tiny amount of CP-violation in QCD.

The key question is: How can QCD yield such a small value of θ?

[4]This follows from the properties of the field strength $G^a_{\mu\nu} = \partial_\mu G^a_\nu - \partial_\nu G^a_\mu + g_s f^{abc} G^b_\mu G^c_\nu$, which is C-odd due to the color charge. Since ∂_μ and G^a_μ are P-even for $\mu = 0$, and P-odd otherwise, it follows that G^a_{0i} is P-odd, while G^a_{ij} is P-even.

One possible answer is to treat θ_{phys} as a free parameter, adjusted to match experimental results. While this is formally valid, it is considered unsatisfying from a theoretical standpoint–it appears as a fine-tuning problem. Ideally, one would prefer a natural mechanism that dynamically explains why θ_{phys} is so small.

A priori, one might consider invoking the anthropic principle, which argues that parameters incompatible with the emergence of life are excluded by the fact that we observe them. However, even within this principle, the tiny value of θ_{phys} remains unexplained [Uba10; Din+18].

The most elegant, compelling solution to the strong CP problem, proposed by Peccei and Quinn [PQ77a], introduces a global chiral symmetry $U(1)_{PQ}$, under which $\theta_{phys} = a/f_a$ becomes a dynamical field:

$$\mathcal{L} \supset \frac{a}{f_a}\frac{\alpha_s}{8\pi}G_{\mu\nu}\widetilde{G}^{\mu\nu} \ , \tag{1.3.14}$$

where a is the QCD axion field and f_a is the axion decay constant. The $U(1)_{PQ}$ motivates the potential:

$$V(a) \propto 1 - \cos\left(\frac{a}{f_a}\right) = \frac{a^2}{2f_a^2} + \mathcal{O}\left(\frac{a^4}{f_a^4}\right) \ , \tag{1.3.15}$$

whose minimum is located at $\langle a \rangle = 0$, implying

$$\theta_{phys} = \frac{\langle a \rangle}{f_a} = 0 \ , \tag{1.3.16}$$

thereby dynamically eliminating the θ_{phys} term and resolving the strong CP problem.

The QCD axion is a pseudo-Goldstone boson characterized by its couplings to SM particles, its mass m_a, and the decay constant f_a. The axion mass generated by QCD dynamics, derived from Chiral Perturbation Theory augmented with an axion (ChPT+a) (see Section 2.10), is approximately:

$$m_a \simeq 6 \text{ meV}\left(\frac{10^9 \text{ GeV}}{f_a}\right) \ . \tag{1.3.17}$$

This relation shows that larger f_a implies a lighter axion.

Two important classes of axion models include:

- The QCD axion [Kim79; SVZ80; DFS81; Zhi80; PQ77b; PQ77a; Wei78; Wil78], where $m_a \lesssim 10$ meV and $f_a \gtrsim 10^9$ GeV are linked by Eq. (1.3.17).
- The more general Axion-like Particle (ALP), where $m_a \in [1, 10^3]$ MeV and $f_a \gtrsim 1$ TeV, constrained by experiment (see [SW06; Arv+10] for UV completions).

In the QCD axion case, the couplings to SM particles depend strongly on the model and are constrained by a wide array of laboratory and astrophysical observations (see [IR18; Sik21; Raf90; Raf08; RC24]). For cosmological implications, see [Mar16], and for theoretical overviews, refer to [KC10; Gri+16; Di +20; CIS21].

Popular QCD axion models include:

- The PQWW model [PQ77a; Wei78], which introduces a complex scalar coupled to the electroweak Higgs sector; the PQ scalar, or axion, in this model is ruled out by experimental constraints. One can however introduce extra matter, or enlarge the Higgs sector, to make the axion "invisible", as in the next two models.
- The KSVZ model [Kim79; SVZ80], which introduces heavy vector-like quarks coupled to the PQ scalar.
- The DFSZ model [DFS81; Zhi80], which includes an additional Higgs doublet and PQ scalar field.

1.3.2 The PQWW model

The PQWW model introduces an additional complex scalar field, denoted by ϕ, alongside the Higgs doublet. In this framework, one Higgs field gives mass to up-type quarks, while another gives mass to down-type quarks[5]. This setup determines the representation of ϕ under the $SU(2)_L \times U(1)_Y$ gauge

[5] For more details on the Higgs mechanism in the SM, see Appendix C.2.

group. The Lagrangian must be invariant under a global chiral symmetry $U(1)_{PQ}$, associated with a chiral rotation $e^{i\alpha\gamma_5}$, which shifts the angular component of ϕ by a constant. The PQ field couples to the SM through Yukawa interactions responsible for fermion masses via the Higgs mechanism. The global $U(1)_{PQ}$ symmetry also fixes the PQ charges of the fermions.

To address the strong CP problem, the scalar sector is extended to include two Higgs doublets:

$$H_u = \begin{pmatrix} H_u^+ \\ H_u^0 \end{pmatrix}, \quad H_d = \begin{pmatrix} H_d^+ \\ H_d^0 \end{pmatrix} . \tag{1.3.18}$$

These doublets preserve a global $SU(2)_L \times U(1)_Y \times U(1)_{PQ}$ symmetry, and is spontaneously broken to $U(1)_{e.m.}$. The vevs are defined as $v_1 = \langle 0|H_u|0\rangle/\sqrt{2}$ and $v_2 = \langle 0|H_d|0\rangle/\sqrt{2}$, with $v^2 = v_1^2 + v_2^2$ being the electroweak scale.

The Yukawa sector takes the form:

$$\mathcal{L}_{Yukawa} = -\bar{Q}Y_u u_R \tilde{H}_u - \bar{Q}Y_d d_R H_d - \bar{L}Y_e e_R H_d + \text{h.c.} . \tag{1.3.19}$$

A basis rotation can be applied to make the Goldstone bosons explicit and align the electroweak vev into a single doublet. Using a rotation matrix $R(\beta)$, the Higgs doublets become:

$$H_u = \frac{1}{\sqrt{2}} e^{i\vec{\sigma}\cdot\vec{G}(x)} \begin{pmatrix} 0 \\ v+h \end{pmatrix}, \quad H_d = \frac{1}{\sqrt{2}} \begin{pmatrix} \sqrt{2}H^+ \\ \phi \end{pmatrix} . \tag{1.3.20}$$

Here, $\phi = \sigma e^{ia/f_a}$ reside in the second doublet, with the massive radial field σ and the pseudoscalar axion a. The PQ symmetry is anomalous under both Quantum Electrodynamics (QED) and QCD, giving rise to effective couplings with gauge bosons.

The scalar field ϕ, like the Higgs, possesses a symmetry-breaking potential:

$$V(\phi) = \lambda \left(|\phi|^2 - \frac{f_a^2}{2} \right)^2 . \tag{1.3.21}$$

At the electroweak phase transition, ϕ acquires a vev:

$$\langle \phi \rangle = \frac{f_a}{\sqrt{2}} . \tag{1.3.22}$$

In the PQWW model, this sets the PQ breaking scale to $f_a \simeq 250\,\text{GeV}$, close to the electroweak scale.

After symmetry breaking, four neutral scalar degrees of freedom remain: one contributes to the Z-boson mass, one corresponds to the SM Higgs boson, one is a heavy radial mode from ϕ, and one is the angular mode (the axion). The latter appears as $\langle\phi\rangle e^{ia/f_a}$ after normalization of the kinetic term.

The axion couples to SM fermions via chiral rotations determined by their PQ charges. For instance, expanding the coupling to quarks gives a leading interaction of the form $(m_q/f_a)\, a\, i\bar{q}\gamma_5 q$. The chiral anomaly generates effective couplings to gauge bosons via triangle diagrams, yielding interactions $\propto a\, G\widetilde{G}/f_a$ and $\propto a\, F\widetilde{F}/f_a$. The gluon coupling is essential to solving the strong CP problem via the Peccei-Quinn mechanism.

However, in the PQWW model, the value of f_a is too small, resulting in axion couplings that are too strong to be consistent with experimental constraints, such as those from beam dump experiments [Kim87]. The model is also excluded by collider experiments such as LEP (see the compilation in [MS14]). Axion decays into two gauge bosons would be observable at experiments like those at CERN, yet no such signals have been detected. As a result, the original PQWW model is ruled out.

In contrast, the KSVZ and DFSZ models introduce the PQ field ϕ independently of the electroweak scale. This decouples the PQ breaking scale from electroweak symmetry breaking, allowing f_a to be a freely tunable parameter. In such models, f_a can be large enough to suppress axion interactions below current experimental sensitivity–hence the name "invisible" axions.

In any of the above constructions, and even for general ALPs, the decay constant f_a is bounded from above by constraints such as black hole superradiance [Arv+17], which excludes ultralight axions that would form clouds around spinning black holes, implying $m_a > 10^{-10}$ eV and hence $f_a < 10^{17}$ GeV for the QCD axion, and by cosmological overproduction of axion DM via the misalignment mechanism [PWW83b; AS83b] unless the initial field value is fine-tuned, which requires $f_a < 10^{16}$ GeV for the QCD axion (see Fig. 1.2 for more details).

1.3.3 The KSVZ model

We now turn to the KSVZ model, as reviewed in [Mar16; Di +20].

The KSVZ model introduces a pair of heavy quarks, Q_L and Q_R, which transform as triplets under $SU(3)_c$ but are singlets under the electroweak gauge group. The subscripts L and R denote their transformation properties under chiral rotations. A complex scalar field ϕ, singlet under the entire SM gauge group, is also introduced. This field carries a chiral PQ charge of 2 and interacts with the heavy quarks via a Yukawa term that is invariant under the global $U(1)_{PQ}$ symmetry:

$$\mathcal{L}_Y = -Y_Q \, \phi \, \bar{Q}_L Q_R + \text{h.c.} \; . \tag{1.3.23}$$

Here, Y_Q is a dimensionless Yukawa coupling and a free parameter of the model.

The full KSVZ Lagrangian, including the SM and new fields, is:

$$\begin{aligned} \mathcal{L}_{KSVZ} = \mathcal{L}_{SM} + i \, \bar{Q}_L \not{D} Q_L + i \, \bar{Q}_R \not{D} Q_R - \left(Y_Q \, \phi \, \bar{Q}_L Q_R + \text{h.c.} \right) \\ + \partial_\mu \phi^\dagger \partial^\mu \phi - \lambda_\phi \left(|\phi|^2 - v_a^2/2 \right)^2 \; . \end{aligned} \tag{1.3.24}$$

At low energies, the PQ symmetry is spontaneously broken when ϕ acquires a vev $\langle \phi \rangle = v_a/\sqrt{2}$. We can parameterize the field as:

$$\phi = \frac{1}{\sqrt{2}} (v_a + \rho) e^{ia/v_a} \; . \tag{1.3.25}$$

where a is the axion field, which is massless at tree level and plays the role of a pseudo-Goldstone boson, and ρ is a heavy radial excitation with mass $m_\rho = \sqrt{2\lambda_\phi} v_a$. The heavy quark acquires a mass $m_Q = Y_Q v_a/\sqrt{2}$.

Expanding the Yukawa term leads to an axion-heavy quark interaction:

$$\mathcal{L} \supset -m_Q \, \bar{Q}_L Q_R \, e^{ia/v_a} + \text{h.c.} \; . \tag{1.3.26}$$

This interaction induces an effective coupling between the axion and gluons through a quark triangle loop, shown in Fig. 1.1, and generates the anomaly-mediated coupling:

$$\mathcal{L}_{aGG} = N \, \frac{a}{v_a} \cdot \frac{\alpha_s}{4\pi} \, G^b_{\mu\nu} \, \tilde{G}^{b \, \mu\nu} = c_{aGG} \, \frac{a}{f_a} \cdot \frac{\alpha_s}{4\pi} \, G^b_{\mu\nu} \, \tilde{G}^{b \, \mu\nu} \tag{1.3.27}$$

with $N < 0$. The sign differs from [Di +23]; this is due to the sign convention for the Levi-Civita tensor, which induces a change of sign in

$$\tilde{G}^{\alpha\beta} = \frac{1}{2} \epsilon^{\alpha\beta\mu\nu} G_{\mu\nu} \; , \tag{1.3.28}$$

where in [Di +23] the convention $\epsilon^{0123} = -1$ is used, while we adopt the convention $\epsilon^{0123} = +1$, as in [Bau+21].

To match the normalization $c_{aGG} = -\frac{1}{2}$, we define $f_a = v_a c_{aGG}/N$.

Through this anomalous coupling, the axion dynamically cancels the QCD θ-term. Under a shift of the axion field $a \to a + f_a \theta$, which solves the strong CP problem dynamically.

At tree level, the axion does not couple to SM fermions or gauge bosons directly; its interactions arise only through loop effects and are thus highly suppressed. Furthermore, the additional heavy fields Q and ρ acquire large masses and are expected to lie beyond the reach of current experiments.

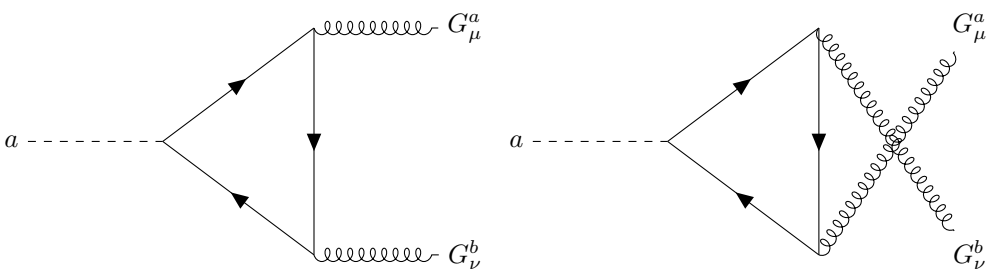

Figure 1.1: Feynman diagram for axion-gluon-gluon coupling via a heavy quark triangle loop.

1.3.4 The DFSZ model

We briefly present the DFSZ model, as described in references [Mar16; Di +20; QS19; QS20].

The DFSZ axion model couples to the SM via the Higgs sector[6]. It includes two Higgs doublets, $H_u \sim (\underline{1},\underline{2})_{-1/2}$ and $H_d \sim (\underline{1},\underline{2})_{+1/2}$, similar to the PQWW model. In addition, a complex scalar field $\phi \sim (\underline{1},\underline{1})_0$, which contains the axion as an angular degree of freedom. The global $U(1)_{PQ}$ symmetry is imposed and spontaneously broken by the potential in Eq. (1.3.21). The scalar sector Lagrangian reads:

$$\mathcal{L}^{scalar}_{DFSZ} = (D_\mu H_u)^\dagger D^\mu H_u + (D_\mu H_d)^\dagger D^\mu H_d + \partial_\mu \phi^\dagger \partial^\mu \phi - V(H_u; H_d; \phi) \ . \tag{1.3.29}$$

The PQ and Higgs fields interact through the scalar potential:

$$V = \lambda (\phi^\dagger)^2 H_u \cdot H_d + \text{h.c.} \ . \tag{1.3.30}$$

The Higgs doublets must also couple to all SM fermions to generate their masses via standard Yukawa interactions. The model contains a degree of freedom in the assignment of PQ charges to leptons, which determines whether they couple to H_u or H_d. This leads to two DFSZ variants:

$$\mathcal{L}^{Y}_{DFSZ-I} = -Y_u \bar{Q} \tilde{H}_u u_R - Y_d \bar{Q} H_d d_R - Y_e \bar{L} H_d e_R \ , \tag{1.3.31}$$

$$\mathcal{L}^{Y}_{DFSZ-II} = -Y_u \bar{Q} \tilde{H}_u u_R - Y_d \bar{Q} H_d d_R - Y_e \bar{L} H_u e_R \ , \tag{1.3.32}$$

with $\tilde{H}_u = i\sigma_2 H_u$.

The vevs are given by:

$$H_u \supset \frac{v_u}{\sqrt{2}} e^{i a_u / v_u} \begin{pmatrix} 0 \\ 1 \end{pmatrix} \ , \quad H_d \supset \frac{v_d}{\sqrt{2}} e^{i a_d / v_d} \begin{pmatrix} 0 \\ 1 \end{pmatrix} \ , \quad \phi \supset \frac{v_\phi}{\sqrt{2}} e^{i a_\phi / v_\phi} \ , \tag{1.3.33}$$

with $v_\phi \gg v_{u,d}$.

To identify the axion in terms of the Goldstone bosons $a_{u,d,\phi}$, we use the PQ current:

$$J^{PQ}_\mu = -\chi_\phi \phi^\dagger i \overleftrightarrow{\partial}_\mu \phi - \chi_u H_u^\dagger i \overleftrightarrow{\partial}_\mu \Phi_u - \chi_d H_d^\dagger i \overleftrightarrow{\partial}_\mu \Phi_d + ... \supset J^{PQ}_\mu|_a = \sum_{i \in \{u;d;\phi\}} \chi_i v_i a_i \ , \tag{1.3.34}$$

where the dots refers to fermionic contributions.

To recover the canonical Goldstone boson relation $\langle 0 | J^{PQ}_\mu |_a | a \rangle = i v_a p_\mu$ with $J^{PQ}_\mu|_a = v_a \partial_\mu a$, we write:

$$a = \frac{1}{v_a} \sum_{i \in \{u;d;\phi\}} \chi_i v_i a_i \ , \quad v_a^2 = \sum_{i \in \{u;d;\phi\}} \chi_i^2 v_i^2 \ . \tag{1.3.35}$$

In the DFSZ model, the different vevs break the symmetry as:

$$U(1)_u \times U(1)_d \times U(1)_\phi \to U(1)_Y \times U(1)_{PQ} \ . \tag{1.3.36}$$

The PQ charges χ are determined by imposing:

1. PQ invariance of the operator $(\phi^\dagger)^2 H_u \cdot H_d$, leading to the condition: $\chi_u + \chi_d - 2\chi_\phi = 0$.
2. Orthogonality between the PQ current $J^{PQ}_\mu|_a = \sum_{i \in \{u;d;\phi\}} \chi_i v_i \partial_\mu a_i$ and the hypercharge current $J^{Y}_\mu|_a = \sum_{i \in \{u;d;\phi\}} Y_i v_i \partial_\mu a_i$ to avoid kinetic mixing with the Z-boson: $0 = \sum_{i \in \{u;d;\phi\}} 2 Y_i \chi_i v_i^2 = -\chi_u v_u^2 + \chi_d v_d^2$.

These conditions yield:

$$\chi_u = 2 \frac{v_d^2}{v_u^2 + v_d^2} \chi_\phi \ , \quad \chi_d = 2 \frac{v_u^2}{v_u^2 + v_d^2} \chi_\phi \ . \tag{1.3.37}$$

Since the PQ charges are only defined up to a global normalization, we can set $\chi_\phi = 1$ without loss of generality, which gives:

$$\chi_u = 2 \cos^2(\beta) \ , \quad \chi_d = 2 \sin^2(\beta) \ , \tag{1.3.38}$$

with $\sin(\beta) = v_u / v$, $\cos(\beta) = v_d / v$, and $v = \sqrt{v_u^2 + v_d^2} \simeq 246$ GeV.

[6] For more details on the Higgs mechanism in the SM, see Appendix C.2.

To find the axion-fermion couplings, we insert the axion field into the Yukawa terms in Eqs. (1.3.31)-(1.3.32) and isolate the physical axion contribution:

$$\mathcal{L}^{Y}_{DFSZ-I} \supset -m_u \bar{u}_L u_R e^{i\chi_u a/v_a} - m_d \bar{d}_L d_R e^{i\chi_d a/v_a} - m_e \bar{e}_L e_R e^{i\chi_d a/v_a} + \text{h.c.} \,, \tag{1.3.39}$$

$$\mathcal{L}^{Y}_{DFSZ-II} \supset -m_u \bar{u}_L u_R e^{i\chi_u a/v_a} - m_d \bar{d}_L d_R e^{i\chi_d a/v_a} - m_e \bar{e}_L e_R e^{-i\chi_u a/v_a} + \text{h.c.} \,. \tag{1.3.40}$$

The axion can be removed from the mass terms via chiral fermion redefinitions:

- For DFSZ-I:

$$u \to e^{-i\gamma_5 \chi_u a/(2v_a)} u \,, \quad d \to e^{-i\gamma_5 \chi_d a/(2v_a)} d \,, \quad e \to e^{-i\gamma_5 \chi_d a/(2v_a)} e \,. \tag{1.3.41}$$

- For DFSZ-II:

$$u \to e^{-i\gamma_5 \chi_u a/(2v_a)} u \,, \quad d \to e^{-i\gamma_5 \chi_d a/(2v_a)} d \,, \quad e \to e^{i\gamma_5 \chi_u a/(2v_a)} e \,. \tag{1.3.42}$$

Due to QCD and QED anomalies, this induces couplings of the form $aG\tilde{G}$ and $aF\tilde{F}$:

$$\mathcal{L}_{axion-gauge} = N \frac{\alpha_s}{4\pi} \frac{a}{v_a} G\tilde{G} + E \frac{\alpha_{e.m.}}{4\pi} \frac{a}{v_a} F\tilde{F} \,, \tag{1.3.43}$$

with:

- For DFSZ-I:

$$N = -N_g \left(\frac{1}{2}\chi_u + \frac{1}{2}\chi_d \right) = -3 \,, \tag{1.3.44}$$

$$E = -N_g \left(N_c \left(\frac{2}{3}\right)^2 \chi_u + N_c \left(\frac{-1}{3}\right)^2 \chi_d + (-1)^2 \chi_d \right) = -8 \,. \tag{1.3.45}$$

- For DFSZ-II:

$$N = -N_g \left(\frac{1}{2}\chi_u + \frac{1}{2}\chi_d \right) = -3 \,, \tag{1.3.46}$$

$$E = -N_g \left(N_c \left(\frac{2}{3}\right)^2 \chi_u + N_c \left(\frac{-1}{3}\right)^2 \chi_d - (-1)^2 \chi_u \right) = -2 \,, \tag{1.3.47}$$

where $N_g = 3$ is the number of generations and $N_c = 3$ is the number of QCD colors. The difference in sign with [Di +23] comes from the sign convention of the Levi-Civita tensor, as in the KSVZ case.

To match the normalization $c_{aGG} = -\frac{1}{2}$, we define $f_a = v_a c_{aGG}/N$, which allows us to write the terms of the general Lagrangian (see Section 1.2) as[7]:

- For DFSZ-I:

$$c_{aGG} = -\frac{1}{2} \,, \tag{1.3.48}$$

$$c_{a\gamma\gamma} = \frac{c_{aGG} E}{N} = -\frac{4}{3} \,, \tag{1.3.49}$$

$$(k^q_A)_{uu} = \frac{1}{3}\cos^2(\beta) \,, \tag{1.3.50}$$

$$(k^q_A)_{dd} = (k^\ell_A)_{ee} = \frac{1}{3}\sin^2(\beta) \,. \tag{1.3.51}$$

- For DFSZ-II:

$$c_{aGG} = -\frac{1}{2} \,, \tag{1.3.52}$$

$$c_{a\gamma\gamma} = \frac{c_{aGG} E}{N} = -\frac{1}{3} \,, \tag{1.3.53}$$

$$(k^q_A)_{uu} = (k^\ell_A)_{ee} = \frac{1}{3}\cos^2(\beta) \,, \tag{1.3.54}$$

$$(k^q_A)_{dd} = \frac{1}{3}\sin^2(\beta) \,. \tag{1.3.55}$$

[7] In [CR20], it is shown that $|g_{aee}| < 1.6 \times 10^{-13}$, where $g_{aee} = (k^\ell_A)_{ee} \cdot m_e/f_a$. For $f_a \simeq 10^9$ GeV, this implies $(k^\ell_A)_{ee} \lesssim 0.31$. In DFSZ models, where $(k^\ell_A)_{ee} \sim \mathcal{O}(10^{-1})$ depending on $\tan(\beta)$, this constraint is satisfied for $f_a \gtrsim 10^9$ GeV and moderate values of $\tan(\beta)$, leaving the DFSZ axion still viable.

Here, we have written the formulas for the first generation, but the results generalize immediately to the other generations, and no flavor-changing terms are present[8].

It is possible to constrain β by requiring that the Yukawa couplings in the DFSZ model satisfy $y_{t,b}^{DFSZ} < \sqrt{16\pi/3}$ [Bjö+20], together with the relations:

$$y_t^{SM} = \sqrt{2} m_t / v = y_t^{DFSZ} \sin(\beta) \ , \quad y_b^{SM} = \sqrt{2} m_b / v = y_b^{DFSZ} \cos(\beta) \ . \tag{1.3.56}$$

This leads to the following constraints:

$$\sin(\beta) > \sqrt{\frac{3}{16\pi}} y_t^{SM} \ , \quad \cos(\beta) > \sqrt{\frac{3}{16\pi}} y_b^{SM} \ . \tag{1.3.57}$$

Using $m_t = 173.1$ GeV, $m_b = 4.18$ GeV and $v = 246$ GeV, we find:

$$\tan(\beta) \in [0.25; 170] \ . \tag{1.3.58}$$

Using the Higgs sector in the DFSZ model has several important consequences that distinguish it from the KSVZ model:

1. In the DFSZ model, the axion couples at tree level to SM fermions via chiral mass terms.
2. The electroweak sector is extended by an additional pseudoscalar Higgs boson, with a mass of the order of the electroweak scale. This is constrained by collider data and could potentially be observed at the Large Hadron Collider (LHC).

1.4 Dark Matter candidate

This section examines how the axion could potentially address the DM problem [PWW83a; AS83a; DF83], drawing on insights from comprehensive reviews [JRW22; Mar16].

1.4.1 The Dark Matter problem

Observations across various observations–the Virialization of galaxy cluster ; the galaxy rotation curves ; the CMB-based and primordial nucleosynthesis evidence ; the Bullet Cluster–with various scales–galactic, galaxy clusters, and cosmological–reveal a consistent ratio between total matter and ordinary (baryonic) matter $\Omega_m \simeq 6\Omega_B$. Upon recognizing discrepancies between observations and theoretical predictions, one is faced with the need to either revise existing theories or gain a deeper understanding of why these discrepancies arise. The CMB-based evidence is particularly compelling because it reveals the presence of DM before the formation of the first atoms. As a result, any explanation involving conventional baryonic matter formed after the CMB was emitted cannot account for the DM problem. The spatial offset between the gravitational and baryonic mass distributions, in the Bullet Cluster, presents a major challenge to modified gravity theories that attempt to explain galactic dynamics without invoking DM [Clo+06]. Instead, it strongly suggests the presence of an additional, non-luminous mass component that contributes to the gravitational potential–namely, DM.

Although the true nature of DM remains unknown, certain properties can be inferred if it consists of particles:

1. **Stability:** DM particles must be stable on cosmological timescales to persist until the present day.
2. **Neutrality:** They must be electrically neutral, as otherwise they would interact with electromagnetic radiation and would have already been detected.

Historically, early considerations focused on Massive Compact Halo Objects (MACHOs)–such as black holes, brown dwarfs, or neutron stars–which do not emit light but can influence visible matter through gravity. However, this hypothesis conflicts with cosmological constraints, which indicate that DM cannot be composed of baryonic particles. As a result, the MACHO hypothesis has largely

[8] Tree-level Flavor-Changing Neutral Currents (FCNCs) are generally present in the most generic Two Higgs Doublet Model (2HDM), and are known to be phenomenologically "problematic" [Bra+12]. For this reason, viable 2HDM constructions typically exclude such terms. Since the DFSZ model is a particular case of a 2HDM, it inherits this feature and does not contain tree-level FCNCs.

fallen out of favor. This does not rule out the existence of primordial black holes formed before nucleosynthesis, which remains actively investigated as a potential DM candidate [VMP21].

Currently, the leading theoretical candidates are Weakly Interacting Massive Particles (WIMPs). One possibility is that they are extremely heavy right-handed neutrinos arising from the seesaw mechanism, though this idea lacks experimental confirmation. Another possibility involves supersymmetric particles, such as the lightest neutralino or sneutrino. However, the lack of evidence for supersymmetry at current collider energies weakens the appeal of this framework. Extensions of the SM provide additional DM candidates.

For a time, it was proposed that DM could be made of classical neutrinos, since they interact weakly. However, their small mass classifies them as hot DM, which is incompatible with the observed formation of large-scale structures: being thermally produced, they remain relativistic for too long and cannot cluster efficiently. In general, light particles struggle to satisfy the cold DM Equation of State (EoS). An important exception is the axion, which can be produced non-thermally through the misalignment mechanism. In this case, the axion field is initially frozen by Hubble friction, and when $H \ll m_a$, it begins to oscillate coherently, behaving as cold DM despite its tiny mass, making it a viable DM candidate.

1.4.2 Axion field in cosmological context

We begin by formulating the action of the axion field in curved space-time, as appropriate for the early Universe. In a Friedmann-Lemaître-Robertson-Walker (FLRW) geometry, the action reads:

$$\mathcal{S} = \int d^4x\sqrt{-g}\left(\frac{1}{2}g^{\mu\nu}\nabla_\mu a(x)\nabla_\nu a(x) - V(a(x))\right) . \tag{1.4.1}$$

Here, ∇_μ denotes the covariant derivative in general relativity, distinct from D_μ typically used for gauge covariant derivatives. The determinant $g := \det(g_{\mu\nu})$ is negative, ensuring $\sqrt{-g}$ is well defined[9].

Varying this action with respect to the axion field yields the Euler-Lagrange equation:

$$\Box a + \frac{\partial V}{\partial a} = 0 , \tag{1.4.2}$$

where $\Box$ is the d'Alembertian operator in curved space-time:

$$\Box a = g^{\mu\nu}\nabla_\mu\nabla_\nu a = \frac{1}{\sqrt{-g}}\partial_\mu(\sqrt{-g}g^{\mu\nu}\partial_\nu a) . \tag{1.4.3}$$

The axion potential $V(a)$ arises from non-perturbative QCD effects and typically takes the form:

$$V(a) = \chi(T)\left(1 - \cos\left(\frac{a}{f_a}\right)\right) = \chi(T)\frac{a^2}{2f_a^2} + \mathcal{O}\left(\frac{a^4}{f_a^4}\right) . \tag{1.4.4}$$

Here, $\chi(T)$ is the topological susceptibility of QCD, which depends on the temperature T of the early Universe. In the small-field limit, this potential becomes approximately quadratic, resembling a mass term for a scalar field with effective temperature-dependent mass:

$$m_a^2(T) = \frac{\chi(T)}{f_a^2} . \tag{1.4.5}$$

To analyze the axion field dynamics in an expanding Universe, we now consider the FLRW metric:

$$ds^2 = g_{\mu\nu}dx^\mu dx^\nu = dt^2 - R^2(t)(dx^2 + dy^2 + dz^2) , \tag{1.4.6}$$

where $R(t)$ is the scale factor describing the Universe's expansion.

Assuming that the axion field is spatially homogeneous and isotropic–i.e., $a = a(t)$–spatial derivatives vanish, and the curved-space d'Alembertian reduces to:

$$\Box a = \frac{1}{R^3}\partial_t(R^3\partial_t)a = \left(\partial_t^2 + 3\frac{\dot{R}}{R}\partial_t\right)a , \tag{1.4.7}$$

[9]Note that in four-dimensional space-time, this determinant is invariant under signature changes: both $\eta = \mathrm{diag}(1,-1,-1,-1)$ and $\eta = \mathrm{diag}(-1,1,1,1)$ yield $\det(\eta) = -1$.

where $H = \dot{R}/R$ represents the Hubble parameter, characterizing the Universe's expansion.

Substituting into the equation of motion, we obtain the axion field evolution in the cosmological background:

$$\ddot{a} + 3H\dot{a} + m_a^2 a = 0 \ . \tag{1.4.8}$$

Throughout the history of the Universe, the axion equation of motion undergoes two distinct regimes: first when $H \gg m_a$, and later when $H \ll m_a$. The time evolution of the Hubble parameter H, along with QCD effects governed by the topological susceptibility $\chi(T)$, play key roles in driving this transition.

1.4.3 Solving the equation–the misalignment mechanism

The primary goal of solving Eq. (1.4.8) is to compute the energy density of the axion field, which can then be compared to the relic density required for DM.

1.4.3.1 Equation of State calculation

In a FLRW Universe, a cosmological fluid is assumed to be a perfect fluid, and therefore follows an EoS:

$$P = \varpi\rho \ , \tag{1.4.9}$$

where P is the pressure, ρ the energy density, and ϖ a constant characteristic of the fluid.

Using the first law of thermodynamics under adiabatic conditions, we track how ρ and P evolve with the scale factor R:

$$\begin{aligned} dU = \delta W + \delta Q = \delta W &\Leftrightarrow d(\rho R^3) = -Pd(R^3) \\ &\Leftrightarrow 3R^2 dR + R^3 d\rho = -3R^2\varpi\rho dR \\ &\Leftrightarrow \frac{d\rho}{\rho} = -3(\varpi+1)\frac{dR}{R} \\ &\Leftrightarrow \rho(R) \propto R^{-3(\varpi+1)} \ . \end{aligned} \tag{1.4.10}$$

In statistical physics, the phase space distribution function is given by:

$$f = \frac{g}{(2\pi)^3}\left(e^{E/T} + \epsilon\right)^{-1} \ , \tag{1.4.11}$$

where $\epsilon = 1$ for fermions (Fermi-Dirac statistic) and $\epsilon = -1$ for bosons (Bose-Einstein statistic). Here, T is the temperature, $E = \sqrt{m^2 + p^2}$ is the relativistic energy, and g is the number of spin states.

From this distribution, one obtains:

$$P = \iiint_{\mathbb{R}^3} f\frac{pv}{3}d^3\vec{p} \ , \quad \rho = \iiint_{\mathbb{R}^3} fEd^3\vec{p} \ . \tag{1.4.12}$$

There are three main cosmological cases:

- For ultra-relativistic particles, where $E \simeq p$ and $v \simeq 1$, we have $\varpi = 1/3$, which leads to $\rho(R) \propto R^{-4}$.
- For cold matter particles, where $E > p$ and $v \ll 1$, we have $\varpi = 0$,[10] resulting in $\rho(R) \propto R^{-3}$.
- For dark energy fluids, according to Friedmann's equation, the exponent of the scale factor in the energy density remains zero ($\rho(R) \propto R^0$), implying $-3(\varpi+1) = 0$ and therefore $\varpi = -1$.

To derive ρ and P from field theory, we use the energy-momentum tensor derived from Noether's theorem:

$$T_{\mu\nu} = \frac{\partial\mathcal{L}}{\partial(\partial^\mu\varphi_a)}\partial_\nu\varphi_a - \mathcal{L}\eta_{\mu\nu} \ . \tag{1.4.13}$$

[10] For a degenerate Fermi gas, deviations from the $\varpi = 0$ approximation can arise from non-thermal e.m.degeneracy pressure due to the Pauli exclusion principle. This effect is not relevant on cosmological scales for cold DM, which is accurately modeled by $\varpi = 0$.

Specifically for the axion, this becomes:

$$T_{\mu\nu} = \nabla_\mu a \nabla_\nu a - g_{\mu\nu}\left(\frac{1}{2}g^{\alpha\beta}\nabla_\alpha a \nabla_\beta a - V(a)\right) . \tag{1.4.14}$$

For a perfect fluid, the energy-momentum tensor is given by:

$$T_{\mu\nu} = (\rho + P)u_\mu u_\nu - P g_{\mu\nu} , \tag{1.4.15}$$

where u is the speed of the fluid, thus in the co-moving coordinates, this yields:

$$(T_{\mu\nu}) = \mathrm{diag}(\rho; R^2(t)P; R^2(t)P; R^2(t)P) . \tag{1.4.16}$$

We can determine P and ρ by evaluating T_{ii} and T_{00}, respectively, from Eq. (1.4.14). Taking only the time derivatives, we obtain:

$$\rho = \frac{1}{2}\dot{a}^2 + V(a) = \frac{1}{2}\dot{a}^2 + \frac{1}{2}m_a^2 a^2 \tag{1.4.17}$$

$$P = \frac{1}{2}\dot{a}^2 - V(a) = \frac{1}{2}\dot{a}^2 - \frac{1}{2}m_a^2 a^2 . \tag{1.4.18}$$

Thus, ϖ is:

$$\varpi = \left\langle \frac{P}{\rho} \right\rangle = \left\langle \frac{\dot{a}^2 - m_a^2 a^2}{\dot{a}^2 + m_a^2 a^2} \right\rangle . \tag{1.4.19}$$

Here, the angular brackets $\langle\cdot\rangle$ indicate a time average over many oscillations of the axion field, used to extract the effective macroscopic behavior of the system, encoded in the EoS.

1.4.3.2 High-temperature phase: $H \gg m_a$

In the early Universe, temperatures are extremely high, rendering QCD effects negligible. As a result, the axion remains effectively massless during this epoch.

The dominant energy density in the Friedmann's equation comes from radiation, which scales as $\rho(t) \propto R^{-4}(t)$. In this regime, the Friedmann's equation reads:

$$\left(\frac{\dot{R}}{R}\right)^2 = H_0^2 \frac{\Omega_r^0}{R^4} \Leftrightarrow R\dot{R} = H_0\sqrt{\Omega_r^0} , \tag{1.4.20}$$

where H_0 is the present-day Hubble constant, and Ω_r^0 is the current radiation density parameter.

Solving this yields:

$$\int_0^R R' dR' = H_0\sqrt{\Omega_r^0}\int_0^t dt' \Leftrightarrow R(t) = \sqrt{2H_0\sqrt{\Omega_r^0}t} , \tag{1.4.21}$$

and therefore, using Eq. (1.4.20),

$$H = \frac{\dot{R}}{R} = \frac{H_0\sqrt{\Omega_r^0}}{R^2(t)} = \frac{1}{2t} . \tag{1.4.22}$$

This allows us to rewrite the axion field's equation of motion (Eq. (1.4.8)) as:

$$\ddot{a} + \frac{3}{2t}\dot{a} = 0 . \tag{1.4.23}$$

The axion field a is related to the angular variable θ by $\theta = a/f_a$, then the Cauchy problem for θ becomes:

$$\ddot{\theta} + \frac{3}{2t}\dot{\theta} = 0 , \tag{1.4.24}$$
$$\theta(t_{PQ}) = \theta_{PQ} , \quad \dot{\theta}(t_{PQ}) = \dot{\theta}_{PQ} .$$

Here t_{PQ} represents the time when $U(1)_{PQ}$ is spontaneously broken, and the time for the axion field dynamics, with $\theta(t_{PQ}) = \theta_{PQ}$ being the initial misalignment angle, a key parameter in subsequent relic density calculations.

Its value is typically determined as $t_{PQ} \sim \frac{M_P}{f_a^2}$ in natural units.

Solving for $\dot{\theta}$ gives:

$$\int \frac{d\dot{\theta}}{\dot{\theta}} = -\int \frac{3dt}{2t} \Leftrightarrow \ln|\dot{\theta}(t)| = C_0 - \frac{3}{2}\ln|t| \Leftrightarrow \dot{\theta}(t) = C_1 t^{-3/2} = \dot{\theta}_{PQ}\left(\frac{t_{PQ}}{t}\right)^{3/2} , \tag{1.4.25}$$

and consequently,

$$\theta(t) = \int \dot{\theta}(t)dt = \dot{\theta}_{PQ} t_{PQ}^{3/2}\frac{-2}{\sqrt{t}} + C_2 = \theta_{PQ} + 2\dot{\theta}_{PQ}t_{PQ}\left(1 - \sqrt{\frac{t_{PQ}}{t}}\right) . \tag{1.4.26}$$

If $\dot{\theta}_{PQ} = 0$, then θ remains constant over time. In such a scenario, the EoS parameter is $\varpi = -1$ (see Eq. (1.4.19)), implying that the axion behaves similarly to an inflaton or a dark energy component.

In the limit where the axion mass m_a is exactly zero, θ quickly settles to:

$$\lim_{t\to+\infty} \theta(t) = \theta_{PQ} + 2\dot{\theta}_{PQ}t_{PQ} . \tag{1.4.27}$$

1.4.3.3 QCD phase transition: $H \ll m_a$

As the Universe cools to temperatures where QCD effects become significant, the Hubble parameter H becomes much smaller than the axion mass m_a.

In this regime, the evolution of the axion field θ is governed by a harmonic oscillator equation:

$$\ddot{\theta} + m_a^2\theta = 0 . \tag{1.4.28}$$

The solution to this equation, starting from the time t_{osc} when the axion field begins to oscillate, is straightforward:

$$\theta(t) = \theta_{osc}\cos(m_a t + \varphi_{osc}) , \tag{1.4.29}$$

$$\dot{\theta}(t) = m_a\theta_{osc}\sin(m_a t + \varphi_{osc}) , \tag{1.4.30}$$

where $\theta(t_{osc}) = \theta_{osc}$.

To resolve the strong CP problem, one must explain why the parameter θ is experimentally observed to be extremely small:

$$\langle\theta\rangle = \theta_{osc}\langle\cos(m_a t + \varphi_{osc})\rangle = 0 , \tag{1.4.31}$$

which naturally solves the strong CP problem.

In this scenario, the energy density ρ_a and pressure P_a of the axion field are given by:

$$\begin{aligned}\rho_a &= \frac{1}{2}\dot{a}^2 + V(a) = \frac{m_a^2\theta_{osc}^2 f_a^2}{2}\sin^2(m_a t + \varphi_{osc}) + \frac{m_a^2\theta_{osc}^2 f_a^2}{2}\cos^2(m_a t + \varphi_{osc}) \\ &= \frac{m_a^2\theta_{osc}^2 f_a^2}{2} ,\end{aligned} \tag{1.4.32}$$

$$\begin{aligned}P_a &= \frac{1}{2}\dot{a}^2 - V(a) = \frac{m_a^2\theta_{osc}^2 f_a^2}{2}\sin^2(m_a t + \varphi_{osc}) - \frac{m_a^2\theta_{osc}^2 f_a^2}{2}\cos^2(m_a t + \varphi_{osc}) \\ &= -\frac{m_a^2\theta_{osc}^2 f_a^2}{2}\cos(2m_a t + \varphi_{osc}) .\end{aligned} \tag{1.4.33}$$

Thus, the EoS parameter ϖ is:

$$\varpi = \left\langle\frac{P_a}{\rho_a}\right\rangle = -\langle\cos(2m_a t + \varphi_{osc})\rangle = 0 . \tag{1.4.34}$$

This corresponds to the EoS for cold matter, regardless of the specific value of the axion mass. The fact that the axion naturally acquires these properties as the Universe expands strongly supports its role as a DM candidate. Notably, this mechanism is non-thermal, meaning it does not arise from a statistical distribution or thermal equilibrium.

This result is both robust and general, applying across various scenarios for the Hubble parameter H, further reinforcing the axion's potential as a viable DM component.

1.4.3.4 Relic density calculation

The relic density of axions, crucial for evaluating their viability as DM candidates, is determined by the initial conditions at the onset of their oscillations and the subsequent dilution due to the expansion of the Universe.

At the onset of oscillations (t_{osc}), the axion energy density is given by Eq. (1.4.32). The present-day energy density ρ_a^0 is obtained by accounting for the dilution due to expansion:

$$\rho_a^0 = \rho_a(t_{osc}) \left(\frac{R(t_{osc})}{R(t_0)} \right)^3 = \frac{1}{2} m_a^2 \theta_{osc}^2 f_a^2 R_{osc}^3 \ , \tag{1.4.35}$$

where R_{osc} is the scale factor at the onset of oscillations, and $R(t_0) = 1$ today. The cubic dilution factor arises because the axion behaves as cold matter, with an EoS $\varpi = 0$.

Using the Friedmann's equation, the present-day axion density parameter Ω_a^0 is:

$$\Omega_a^0 H_0^2 = \frac{8\pi G}{3} \rho_a^0 = \frac{8\pi}{3M_P^2} \rho_a^0 \Leftrightarrow \Omega_a^0 = \frac{4\pi m_a^2 \theta_{osc}^2 f_a^2 R_{osc}^3}{3M_P^2 H_0^2} \ , \tag{1.4.36}$$

where M_P is the Planck mass.

To estimate R_{osc}, we note that axion oscillations begin when $m_a \gg H$, which holds during the radiation-dominated era. At matter-radiation equality:

$$\frac{\Omega_r^0}{R_{eq}^4} = \frac{\Omega_m^0}{R_{eq}^3} \ \Rightarrow \ R_{eq} = \frac{\Omega_r^0}{\Omega_m^0} \simeq 1.7 \times 10^{-4} \ , \tag{1.4.37}$$

and the Hubble parameter at equality is:

$$H_{eq} = \frac{H_0 \sqrt{\Omega_r^0}}{R} \simeq 10^{-27} \ \mu\text{eV} \ll m_a \ . \tag{1.4.38}$$

The onset of axion oscillations occurs when the condition $H \ll m_a$ becomes valid, indicating that the axion mass m_a dominates over the Hubble parameter H during the Universe's evolution. To estimate R_{osc}, the scale factor at the onset of oscillations, we consider the scenario where $3H_{osc} = \alpha m_a$, with α being a parameter.

For a more rigorous approach, we use the general solution of the axion field Eq. (1.4.8):

$$\theta(t) = \sqrt{\frac{t}{t_i R^3(t)}} \left(C_1 J_n(m_a t) + C_2 Y_n(m_a t) \right) \ , \tag{1.4.39}$$

where J_n and Y_n are Bessel functions of the first and second kind, t_i is an initial time, and for a power-law scale factor $R(t) \propto t^{-p}$, the index is $n = (3p-1)/2$. In the radiation-dominated era ($p = 1/2$), this gives $n = 1/4$.

Relating to the Hubble parameter during radiation domination in Eq. (1.4.22):

$$t_{osc} = \frac{1}{2H_{osc}} \simeq \frac{3}{2\alpha m_a} \Rightarrow R_{osc} = \sqrt{2H_0 \sqrt{\Omega_t^0} t_{osc}} \simeq \sqrt{\frac{3H_0 \sqrt{\Omega_r^0}}{\alpha m_a}} \ . \tag{1.4.40}$$

Inserting this into the expression for Ω_a^0, we obtain:

$$\Omega_a^0 \simeq \frac{4\pi \sqrt{3} (\Omega_r^0)^{3/4} m_a^{1/2} f_a^2}{M_P^2 H_0^{1/2} \alpha^{3/2}} \theta_{osc}^2 \ . \tag{1.4.41}$$

A more refined computation [Mar16] confirms this result with $\alpha = 1$.

To match the observed DM density $\Omega_a^0 = \Omega_{DM}$, one can solve for θ_{osc}:

$$\theta_{osc} \simeq \sqrt{\frac{\Omega_{DM} M_P^2 H_0^{1/2}}{4\pi \sqrt{3} (\Omega_r^0)^{3/4} m_a^{1/2} f_a^2}} \ . \tag{1.4.42}$$

Alternatively, one obtains a constraint on m_a:

$$m_a \simeq \frac{M_P^4 H_0 \alpha^3 \Omega_{DM}^2}{48\pi^2 (\Omega_r^0)^{3/2} \theta_{osc}^4 f_a^4} \simeq 7.4 \ \text{meV} \frac{1}{\theta_{osc}^4} \left(\frac{10^{12} \ \text{GeV}}{f_a} \right)^4 \ . \tag{1.4.43}$$

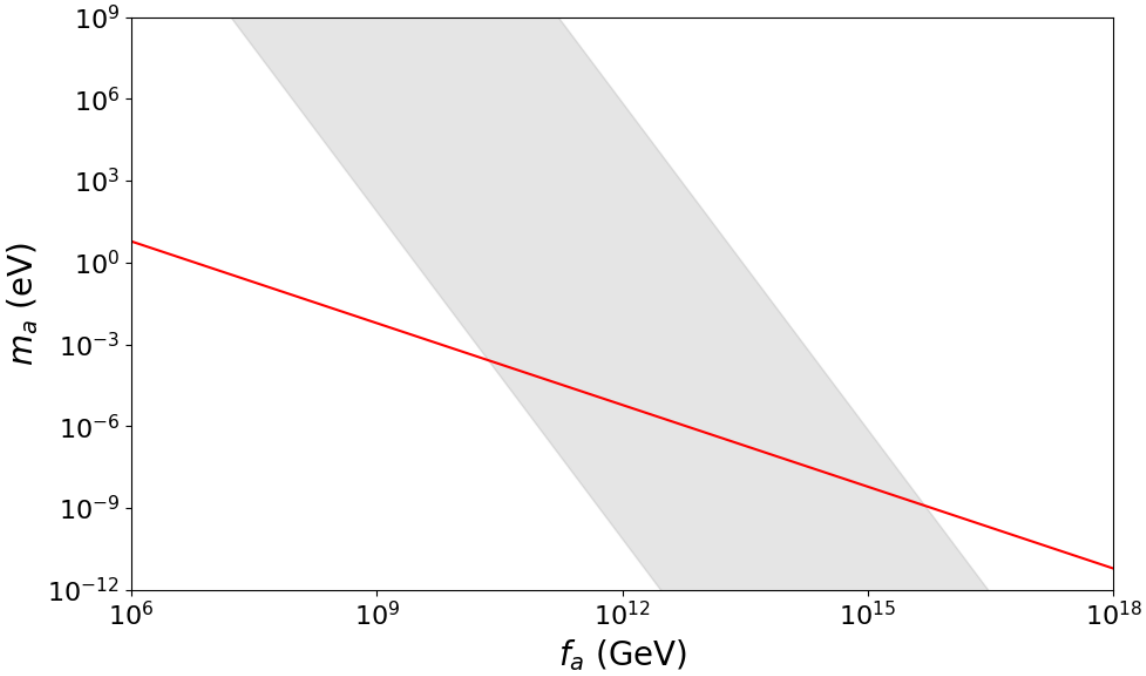

Figure 1.2: The gray region in the f_a-m_a plane corresponds to values consistent with the axion accounting for DM, assuming $\theta_{osc} \in [10^{-2}, 10^2]$. The red line indicates the QCD axion relation.

For the QCD axion (after the QCD phase transition), we have (see Eq. (1.3.17)):

$$m_a \simeq 6\ \mu\text{eV} \left(\frac{10^{12}\ \text{GeV}}{f_a} \right) . \tag{1.4.44}$$

Therefore, given a value for θ_{osc}, one can deduce values for m_a and f_a. However, θ_{osc} is a free parameter, not fixed by the theory. To avoid fine-tuning, it is generally assumed to lie within a reasonable range, for intense we can take $\theta_{osc} \in [10^{-2}, 10^2]$. Avoiding fine-tuning is crucial, as the motivation for introducing the axion stems from resolving the strong CP problem without invoking unnatural parameters.

Fig. 1.2 shows the region of the f_a-m_a plane compatible with axion DM (gray area), with the red line corresponding to the QCD axion.

We observe that the QCD axion can account for DM if $m_a \in [10^{-3}, 10^2]$ μeV and $f_a \in [2 \times 10^{10}, 5 \times 10^{15}]$ GeV. In contrast, ALPs with $m_a \in [1, 10^3]$ MeV are compatible for $f_a \in [10^7, 10^{12}]$ GeV.[11]

1.5 The flavor puzzle : the axiflavon/flaxion model

In the SM, fermion masses and mixings originate from Yukawa couplings, but their observed pattern is highly hierarchical and seemingly *ad hoc*: quark and charged-lepton masses span many order-of-magnitude (oom) and the Cabibbo-Kobayashi-Maskawa (CKM) entries display a pronounced hierarchy, while the SM offers no organizing principle for these numbers. This is the so-called flavor puzzle.

The axiflavon/flaxion model [Ema+17; Cal+17] (see [Rei82; Wil82] for pioneering work and [Ahn15; BCK18] for related constructions) proposes a minimal framework to address the flavor puzzle of quarks and leptons. In other words, it offers a dynamical explanation of the observed pattern of fermion masses and mixings, by explaining the underlying Yukawa couplings as powers of suitable ratios of scales. To do so, this model introduces a global $U(1)_H$ flavor symmetry and a complex scalar Φ containing the axion.

In this model, the masses of SM fermions originate from the vev $v = 246$ GeV of the SM Higgs field H, while the hierarchy in Yukawa couplings is attributed to the global horizontal symmetry $U(1)_H$.

[11] Allowing for more extreme values of θ_{osc} expands the parameter space. If no limit is imposed on θ_{osc}, then in principle, all values of m_a and f_a could be compatible with axion DM.

The Yukawa sector of the resulting effective theory takes the form:

$$\mathcal{L} = a^u_{ij} Q_i U^c_j H(\Phi/\Lambda)^{[q]_i+[u]_j} + a^d_{ij} Q_i D^c_j \tilde{H}(\Phi/\Lambda)^{[q]_i+[d]_j} + a^e_{ij} L_i E^c_j \tilde{H}(\Phi/\Lambda)^{[l]_i+[e]_j} + \text{h.c.} \,, \tag{1.5.1}$$

where $a^{u,d,e}_{ij}$ are coefficients of order $\mathcal{O}(1)$. When Φ acquires a vev $\langle\Phi\rangle = V_\Phi/\sqrt{2}$, the SM Yukawa couplings become $Y^{ij}_{u,d,e} = a^{u,d,e}_{ij}\epsilon^{[L]_i+[R]_j}$ with $\epsilon = V_\Phi/(\sqrt{2}\Lambda)$, where $[L]_i = [q]_i$ and $[R]_j = [u]_j, [d]_j$ for quarks, and $[L]_i = [l]_i$, $[R]_j = [e]_j$ for charged leptons. The small parameter ϵ controls the suppression of effective Yukawa operators, so that hierarchies follow from $U(1)_H$ charge sums rather than from arbitrary small numbers.

The fermion mass hierarchy thus arises from the $U(1)_H$ charge assignments. The Yukawa matrices scale as $Y^{ij}_f \sim \hat{V}_{ij} m^f_j/v$, where m^f_i are the SM fermion masses and $\hat{V}_{ij} = V_{ij}$ for $i < j$, and $\hat{V}_{ij} = 1/V_{ij}$ for $i \geqslant j$. Here, V refers to the CKM matrix in the quark sector and the Pontecorvo-Maki-Nakagawa-Sakata (PMNS) matrix in the lepton sector. The observed CKM structure corresponds to $\epsilon \sim 0.23$, of the same order as the Cabibbo angle. The $U(1)_H$ charges can be determined by fitting the fermion masses and mixings. Although the uncertainty on the $\mathcal{O}(1)$ coefficients $a^{u,d,e}_{ij}$ limits the precision, it has negligible impact on underlying picture.

The field Φ contains two excitations: a CP-even flavon ϕ and a CP-odd axiflavon/flaxion a,

$$\Phi = \frac{1}{\sqrt{2}}(V_\Phi + \phi)e^{ia/V_\Phi} \,. \tag{1.5.2}$$

The flavon ϕ has a mass $m_\phi \sim \mathcal{O}(V_\Phi)$, rendering it irrelevant at low energies. The axiflavon/flaxion a, being a pseudo Goldstone boson, is initially massless but acquires a mass through the QCD anomaly associated with the $U(1)_H$ breaking.

In this model, the axiflavon/flaxion couplings to quarks satisfy:

$$(k^q_V)_{ij} = 0 \,, \qquad |(k^q_A)_{ij}|_{i\neq j} = \mathcal{O}(0.1) \,, \qquad (k^q_A)_{ii} = \mathcal{O}(1) \,. \tag{1.5.3}$$

Details of the derivation can be found in Appendix C.7.

1.6 The hierarchy problem : the Relaxion model

This model introduces an axion-like field whose dynamics resemble those of the QCD axion but are designed to solve the electroweak hierarchy problem by leveraging an unspecified inflationary period, as detailed in [GKR15].

The modifications to the QCD axion include endowing it with an extremely large (non-compact) field range and introducing a soft symmetry-breaking coupling to the Higgs field.

The axion retains its characteristic periodic potential, but with a field range that spans many periods–effectively exceeding the cutoff scale and potentially even the Planck scale.

The Lagrangian for this model is given by:

$$\mathcal{L} = \mathcal{L}_{SM} - (M^2 - g\phi)H^\dagger H + V(g\phi) \supset \frac{g_s}{32\pi^2}\frac{\phi}{f} G^a_{\mu\nu}\tilde{G}^{a,\mu\nu} \,, \tag{1.6.1}$$

where M denotes the cutoff scale, H is the Higgs doublet, and g is a dimensionful coupling. For simplicity, all order-one coefficients are omitted.

Aligned with the hierarchy problem, the most natural expectation is for the Higgs mass to be of the same order as the cutoff scale M.

In the limit $g \to 0$, the Lagrangian exhibits a shift symmetry $\phi \to \phi + 2\pi f$, which is only softly broken by non-perturbative QCD effects. In this framework, g acts as a spurion that completely breaks the shift symmetry, generating small potential terms for ϕ via an expansion in powers of $g\phi$. Meanwhile, QCD instantons generate an additional potential for ϕ, which respects the shift symmetry. Below the QCD scale, the potential takes the form:

$$V(g\phi) = gM^2\phi + g^2\phi^2 + o(g\phi/M^2) + \Lambda^4\cos(\phi/f) \,. \tag{1.6.2}$$

The cosine term approximates the periodic function required to preserve the shift symmetry. Both g and Λ are expected to be much smaller than the cutoff M, in accordance with the principle of technical naturalness.

To address the hierarchy problem, the model's behavior during the early universe is crucial. Specifically, the value of ϕ must ensure that the Higgs's effective mass squared m_h^2 remains positive. During inflation, ϕ undergoes slow-roll dynamics, effectively scanning the physical Higgs mass.

As the Higgs vev increases, the height of the effective potential barriers Λ^4 also increases. When Λ^4 becomes large enough, it halts the rolling of ϕ shortly after m_h^2 crosses zero. This mechanism naturally results in a Higgs mass that is much smaller than the cutoff scale. Near the SM Higgs vev, the barrier height is approximately:

$$\Lambda^4 \sim f_\pi^2 m_\pi^2 \times [\text{dimensionless ratios of quark masses}] \ . \tag{1.6.3}$$

Since m_π^2 scales linearly with the quark masses, it is directly proportional to the Higgs vev, leading to a linear increase of Λ^4 with the vev. In other words, the QCD barrier height grows with the Higgs vev, which feeds back into the relaxion potential and is essential to stop the rolling.

The success of this mechanism does not depend on the initial condition of ϕ, as its dynamics are driven by Hubble friction during slow-roll. This imposes the following constraints: $g \lesssim H_i$ and $g \lesssim (H_i^2 M_P/M^2)$, where H_i is the Hubble parameter during inflation and M_P is the reduced Planck mass. Over N e-folds of inflation, the change in ϕ is approximately:

$$\Delta\phi \sim (\dot{\phi}/H_i)N \sim (V'_\phi/H_i^2)N \sim (gM^2/H_i^2)N \ . \tag{1.6.4}$$

Requiring $\Delta\phi \gtrsim (M^2/g)$, we derive:

$$N \gtrsim \frac{H_i^2}{g^2} \ . \tag{1.6.5}$$

Inflationary viability requires 3 conditions:

1. **Vacuum energy dominance:** The vacuum energy during inflation must exceed the energy variation along the ϕ direction, i.e.,
$$H_i > \frac{M^2}{M_P} \ . \tag{1.6.6}$$

2. **Formation of barriers:** The Hubble scale must be below the QCD scale:
$$H_i < \Lambda_{\text{QCD}}. \tag{1.6.7}$$
Here, Λ_{QCD} is the scale where instanton contributions to the axion potential become significant. It is natural to expect $\Lambda \sim \Lambda_{\text{QCD}}$.

3. **Classical rolling dominance:** The evolution of ϕ must be dominated by classical motion rather than quantum fluctuations, ensuring all inflated regions reach the electroweak vacuum:
$$\frac{\delta\phi_{\text{quant}}}{\delta t} \sim H_i^2 < \dot{\phi}_{\text{classical}} \sim \frac{V'(\phi)}{H_i} \ , \tag{1.6.8}$$
which gives the standard condition:
$$H_i^3 < V'(\phi) \Rightarrow H_i < (gM^2)^{1/3} \ . \tag{1.6.9}$$

The slow-roll stops when Λ becomes large enough that the barrier slope Λ^4/f matches the slope of the linear term gM^2:

$$\Lambda^4 \sim gM^2 f \ . \tag{1.6.10}$$

By combining Eqs. (1.6.6), (1.6.9), and (1.6.10), we obtain an upper bound on the cutoff M, and hence on the Higgs mass:

$$M < \left(\frac{\Lambda^4 M_P^3}{f}\right)^{1/6} \sim 10^7\,\text{GeV} \times \left(\frac{10^9\,\text{GeV}}{f}\right)^{1/6} \ . \tag{1.6.11}$$

Although this upper bound may initially seem too high, it does not yet account for the specific properties of the QCD axion. Solving the strong CP problem requires adjusting $g \sim \bar{g}\sqrt{\theta}$, using the

CP-violating angle $\theta < 10^{-10}$. Incorporating this constraint, Eqs. (1.6.6)-(1.6.10) become:

$$N \gtrsim \theta \frac{H_i^2}{g^2} \ , \tag{1.6.12}$$

$$H_i > \frac{M^2}{M_P \sqrt{\theta}} \ , \tag{1.6.13}$$

$$H_i < \left(\frac{g M^2}{\theta} \right)^{1/3} \tag{1.6.14}$$

$$\Lambda^4 \theta \sim g M^2 f \ . \tag{1.6.15}$$

This leads to a refined constraint on the cutoff scale:

$$M < \left(\frac{\Lambda^4 M_P^3}{f} \right)^{1/6} \theta^{1/4} \sim 30 \, \text{TeV} \times \left(\frac{\theta}{10^{-10}} \right)^{1/4} \left(\frac{10^9 \, \text{GeV}}{f} \right)^{1/6} \ . \tag{1.6.16}$$

This yields an upper bound on the cutoff scale–and thus the Higgs mass–whose oom is consistent with the experimentally observed value $m_h = 0.125$ TeV.

References

[Ahn15] Y. H. Ahn. *Flavored Peccei-Quinn symmetry*. In: *Phys. Rev. D* 91 (2015), p. 056005. DOI: 10.1103/PhysRevD.91.056005. arXiv: 1410.1634 [hep-ph].

[Arv+10] Asimina Arvanitaki et al. *String Axiverse*. In: *Phys. Rev. D* 81 (2010), p. 123530. DOI: 10.1103/PhysRevD.81.123530. arXiv: 0905.4720 [hep-th].

[Arv+17] Asimina Arvanitaki et al. *Black hole mergers and the QCD axion at Advanced LIGO*. In: *Phys. Rev. D* 95 (4 Feb. 2017), p. 043001. DOI: 10.1103/PhysRevD.95.043001. URL: https://link.aps.org/doi/10.1103/PhysRevD.95.043001.

[AS83a] L. F. Abbott and P. Sikivie. *A Cosmological Bound on the Invisible Axion*. In: *Phys. Lett. B* 120 (1983). Ed. by M. A. Srednicki, pp. 133–136. DOI: 10.1016/0370-2693(83)90638-X.

[AS83b] L.F. Abbott and P. Sikivie. *A cosmological bound on the invisible axion*. In: *Physics Letters B* 120.1 (1983), pp. 133–136. ISSN: 0370-2693. DOI: https://doi.org/10.1016/0370-2693(83)90638-X. URL: https://www.sciencedirect.com/science/article/pii/037026938390638X.

[Bak+06] C. A. Baker et al. *Improved Experimental Limit on the Electric Dipole Moment of the Neutron*. In: *Physical Review Letters* 97.13 (Sept. 2006). DOI: 10.1103/physrevlett.97.131801. URL: https://doi.org/10.1103%2Fphysrevlett.97.131801.

[Bau+21] Martin Bauer et al. *Consistent Treatment of Axions in the Weak Chiral Lagrangian*. In: *Phys. Rev. Lett.* 127.8 (2021), p. 081803. DOI: 10.1103/PhysRevLett.127.081803. arXiv: 2102.13112 [hep-ph].

[BCK18] Fredrik Björkeroth, Eung Jin Chun, and Stephen F. King. *Accidental Peccei–Quinn symmetry from discrete flavour symmetry and Pati–Salam*. In: *Phys. Lett. B* 777 (2018), pp. 428–434. DOI: 10.1016/j.physletb.2017.12.058. arXiv: 1711.05741 [hep-ph].

[Bjö+20] Fredrik Björkeroth et al. *Axion-electron decoupling in nucleophobic axion models*. In: *Physical Review D* 101.3 (Feb. 2020). ISSN: 2470-0029. DOI: 10.1103/physrevd.101.035027. URL: http://dx.doi.org/10.1103/PhysRevD.101.035027.

[Bra+12] G.C. Branco et al. *Theory and phenomenology of two-Higgs-doublet models*. In: *Physics Reports* 516.1–2 (July 2012), pp. 1–102. ISSN: 0370-1573. DOI: 10.1016/j.physrep.2012.02.002. URL: http://dx.doi.org/10.1016/j.physrep.2012.02.002.

[Cal+17] Lorenzo Calibbi et al. *Minimal axion model from flavor*. In: *Phys. Rev. D* 95.9 (2017), p. 095009. DOI: 10.1103/PhysRevD.95.095009. arXiv: 1612.08040 [hep-ph].

[CIS21] Kiwoon Choi, Sang Hui Im, and Chang Sub Shin. *Recent Progress in the Physics of Axions and Axion-Like Particles*. In: *Ann. Rev. Nucl. Part. Sci.* 71 (2021), pp. 225–252. DOI: 10.1146/annurev-nucl-120720-031147. arXiv: 2012.05029 [hep-ph].

[Clo+06] Douglas Clowe et al. *A Direct Empirical Proof of the Existence of Dark Matter*. In: *The Astrophysical Journal* 648.2 (Aug. 2006), pp. L109–L113. DOI: 10.1086/508162. URL: https://doi.org/10.1086%2F508162.

[CR20] Francesco Capozzi and Georg Raffelt. *Axion and neutrino bounds improved with new calibrations of the tip of the red-giant branch using geometric distance determinations*. In: *Physical Review D* 102.8 (Oct. 2020). ISSN: 2470-0029. DOI: 10.1103/physrevd.102.083007. URL: http://dx.doi.org/10.1103/PhysRevD.102.083007.

[DF83] Michael Dine and Willy Fischler. *The Not So Harmless Axion*. In: *Phys. Lett. B* 120 (1983). Ed. by M. A. Srednicki, pp. 137–141. DOI: 10.1016/0370-2693(83)90639-1.

[DFS81] Michael Dine, Willy Fischler, and Mark Srednicki. *A Simple Solution to the Strong CP Problem with a Harmless Axion*. In: *Phys. Lett. B* 104 (1981), pp. 199–202. DOI: 10.1016/0370-2693(81)90590-6.

[Di +20] Luca Di Luzio et al. *The landscape of QCD axion models*. In: *Phys. Rept.* 870 (2020), pp. 1–117. DOI: 10.1016/j.physrep.2020.06.002. arXiv: 2003.01100 [hep-ph].

[Di +23] Luca Di Luzio et al. *Running into QCD axion phenomenology*. In: (May 2023). arXiv: 2305.11958 [hep-ph].

[Din+18] Michael Dine et al. *Some Remarks on Anthropic Approaches to the Strong CP Problem*. In: *JHEP* 05 (2018), p. 171. DOI: 10.1007/JHEP05(2018)171. arXiv: 1801.03466 [hep-th].

[Ema+17] Yohei Ema et al. *Flaxion: a minimal extension to solve puzzles in the standard model*. In: *JHEP* 01 (2017), p. 096. DOI: 10.1007/JHEP01(2017)096. arXiv: 1612.05492 [hep-ph].

[GKR15] Peter W. Graham, David E. Kaplan, and Surjeet Rajendran. *Cosmological Relaxation of the Electroweak Scale*. In: *Physical Review Letters* 115.22 (Nov. 2015). ISSN: 1079-7114. DOI: 10.1103/physrevlett.115.221801. URL: http://dx.doi.org/10.1103/PhysRevLett.115.221801.

[Gri+16] Giovanni Grilli di Cortona et al. *The QCD axion, precisely*. In: *JHEP* 01 (2016), p. 034. DOI: 10.1007/JHEP01(2016)034. arXiv: 1511.02867 [hep-ph].

[IR18] Igor G. Irastorza and Javier Redondo. *New experimental approaches in the search for axion-like particles*. In: *Prog. Part. Nucl. Phys.* 102 (2018), pp. 89–159. DOI: 10.1016/j.ppnp.2018.05.003. arXiv: 1801.08127 [hep-ph].

[JRW22] J. Jaeckel, G. Rybka, and L. Winslow. *Axion Dark Matter*. 2022. DOI: 10.48550/ARXIV.2203.14923. URL: https://arxiv.org/abs/2203.14923.

[KC10] Jihn E. Kim and Gianpaolo Carosi. *Axions and the Strong CP Problem*. In: *Rev. Mod. Phys.* 82 (2010). [Erratum: Rev.Mod.Phys. 91, 049902 (2019)], pp. 557–602. DOI: 10.1103/RevModPhys.82.557. arXiv: 0807.3125 [hep-ph].

[Kim79] Jihn E. Kim. *Weak Interaction Singlet and Strong CP Invariance*. In: *Phys. Rev. Lett.* 43 (1979), p. 103. DOI: 10.1103/PhysRevLett.43.103.

[Kim87] J. E. Kim. *Light pseudoscalars, particle physics and cosmology*. In: *Physics Reports* 150.1 (Jan. 1987), pp. 1–177. DOI: 10.1016/0370-1573(87)90017-2.

[Mar16] David J. E. Marsh. *Axion Cosmology*. In: *Phys. Rept.* 643 (2016), pp. 1–79. DOI: 10.1016/j.physrep.2016.06.005. arXiv: 1510.07633 [astro-ph.CO].

[MS14] Ken Mimasu and Verónica Sanz. *ALPs at Colliders*. In: (2014). DOI: 10.48550/arxiv.1409.4792. URL: https://arxiv.org/abs/1409.4792.

[PQ77a] R. D. Peccei and Helen R. Quinn. *Constraints imposed by CP conservation in the presence of pseudoparticles*. In: *Phys. Rev. D* 16 (6 Sept. 1977), pp. 1791–1797. DOI: 10.1103/PhysRevD.16.1791. URL: https://link.aps.org/doi/10.1103/PhysRevD.16.1791.

[PQ77b] R. D. Peccei and Helen R. Quinn. *CP Conservation in the Presence of Instantons*. In: *Phys. Rev. Lett.* 38 (1977), pp. 1440–1443. DOI: 10.1103/PhysRevLett.38.1440.

[PWW83a] John Preskill, Mark B. Wise, and Frank Wilczek. *Cosmology of the Invisible Axion*. In: *Phys. Lett. B* 120 (1983). Ed. by M. A. Srednicki, pp. 127–132. DOI: 10.1016/0370-2693(83)90637-8.

[PWW83b] John Preskill, Mark B. Wise, and Frank Wilczek. *Cosmology of the invisible axion*. In: *Physics Letters B* 120.1 (1983), pp. 127–132. ISSN: 0370-2693. DOI: https://doi.org/10.1016/0370-2693(83)90637-8. URL: https://www.sciencedirect.com/science/article/pii/0370269383906378.

[QS19] Jérémie Quevillon and Christopher Smith. *Axions are blind to anomalies*. en. In: *The European Physical Journal C* 79.10 (Oct. 2019), p. 822. ISSN: 1434-6044, 1434-6052. DOI: 10.1140/epjc/s10052-019-7304-4. URL: http://link.springer.com/10.1140/epjc/s10052-019-7304-4 (visited on 06/28/2022).

[QS20] Jérémie Quevillon and Christopher Smith. *Baryon and lepton number intricacies in axion models*. en. In: *Physical Review D* 102.7 (Oct. 2020), p. 075031. ISSN: 2470-0010, 2470-0029. DOI: 10.1103/PhysRevD.102.075031. URL: https://link.aps.org/doi/10.1103/PhysRevD.102.075031 (visited on 06/28/2022).

[Raf08] Georg G. Raffelt. *Astrophysical axion bounds*. In: *Lect. Notes Phys.* 741 (2008). Ed. by Markus Kuster, Georg Raffelt, and Berta Beltran, pp. 51–71. DOI: 10.1007/978-3-540-73518-2_3. arXiv: hep-ph/0611350.

[Raf90] Georg G. Raffelt. *Astrophysical methods to constrain axions and other novel particle phenomena*. In: *Phys. Rept.* 198 (1990), pp. 1–113. DOI: 10.1016/0370-1573(90)90054-6.

[RC24] G. Raffelt and A. Caputo. *Astrophysical Axion Bounds: The 2024 Edition*. In: *Proceedings of 1st General Meeting and 1st Training School of the COST Action COSMIC WSIPers — PoS(COSMICWISPers). COSMICWISPers*. Sissa Medialab, Mar. 2024. DOI: 10.22323/1.454.0041. URL: http://dx.doi.org/10.22323/1.454.0041.

[Rei82] David B. Reiss. *Can the Family Group Be a Global Symmetry?* In: *Phys. Lett. B* 115 (1982), pp. 217–220. DOI: 10.1016/0370-2693(82)90647-5.

[Sik21] Pierre Sikivie. *Invisible Axion Search Methods*. In: *Rev. Mod. Phys.* 93.1 (2021), p. 015004. DOI: 10.1103/RevModPhys.93.015004. arXiv: 2003.02206 [hep-ph].

[SVZ80] Mikhail A. Shifman, A. I. Vainshtein, and Valentin I. Zakharov. *Can Confinement Ensure Natural CP Invariance of Strong Interactions?* In: *Nucl. Phys. B* 166 (1980), pp. 493–506. DOI: 10.1016/0550-3213(80)90209-6.

[SW06] Peter Svrcek and Edward Witten. *Axions In String Theory*. In: *JHEP* 06 (2006), p. 051. DOI: 10.1088/1126-6708/2006/06/051. arXiv: hep-th/0605206.

[Uba10] Lorenzo Ubaldi. *Effects of theta on the deuteron binding energy and the triple-alpha process*. In: *Phys. Rev. D* 81 (2010), p. 025011. DOI: 10.1103/PhysRevD.81.025011. arXiv: 0811.1599 [hep-ph].

[VMP21] Pablo Villanueva-Domingo, Olga Mena, and Sergio Palomares-Ruiz. *A Brief Review on Primordial Black Holes as Dark Matter*. In: *Frontiers in Astronomy and Space Sciences* 8 (May 2021). ISSN: 2296-987X. DOI: 10.3389/fspas.2021.681084. URL: http://dx.doi.org/10.3389/fspas.2021.681084.

[Wei78] Steven Weinberg. *A New Light Boson?* In: *Phys. Rev. Lett.* 40 (4 Jan. 1978), pp. 223–226. DOI: 10.1103/PhysRevLett.40.223. URL: https://link.aps.org/doi/10.1103/PhysRevLett.40.223.

[Wil78] Frank Wilczek. *Problem of Strong P and T Invariance in the Presence of Instantons*. In: *Phys. Rev. Lett.* 40 (1978), pp. 279–282. DOI: 10.1103/PhysRevLett.40.279.

[Wil82] Frank Wilczek. *Axions and Family Symmetry Breaking*. In: *Phys. Rev. Lett.* 49 (1982), pp. 1549–1552. DOI: 10.1103/PhysRevLett.49.1549.

[Zhi80] A P Zhitnitskii. *Possible suppression of axion-hadron interactions*. In: *Sov. J. Nucl. Phys. (Engl. Transl.); (United States)* 31 (Feb. 1980). URL: https://www.osti.gov/biblio/7063072.

Chapter 2

Chiral Perturbation Theory – ChPT

Contents

2.1 Motivation **42**
2.2 Effective Field Theory vs. Renormalizable Theory **43**
2.3 Fermi's theory **43**
2.4 The CCWZ formalism **45**
2.5 Chiral Currents and Noether's theorem **46**
2.6 QCD symmetries **47**
2.7 ChPT for mesons **48**
2.7.1 The u- and U-basis 48
2.7.2 Mesonic Lagrangian 50
2.7.3 Mesonic currents 51
2.8 ChPT for baryons **51**
2.8.1 $SU(2)$ limit 52
2.8.2 $SU(3)$ limit 52
2.8.3 Baryonic currents 53
2.9 Lagrangian mediating weak processes **56**
2.10 Axionic Lagrangian **58**
2.10.1 Axion-quark interaction 58
2.10.2 Axion-hadron interaction 63
2.10.3 Interactions with nucleons 65
2.10.4 Axion-quark vs. axion-hadron couplings 66
2.10.5 Lagrangian mediating weak processes 67
2.11 State-of-the-art in axion-quark coupling bounds **68**

In this chapter, we develop the theoretical tools required to describe axion interactions at low energies, using the framework of Chiral Perturbation Theory (ChPT). As an Effective Field Theory (EFT) of low-energy Quantum Chromodynamics (QCD), ChPT provides a systematic expansion in momenta and quark masses, enabling a model-independent treatment of hadronic processes.

We begin in Section 2.1 by motivating the need for an EFT approach to non-perturbative QCD. We then contrast renormalizable theories with EFTs in Section 2.2, before reviewing Fermi's theory as a historical example of a successful low-energy EFT in Section 2.3.

The general construction of EFTs based on symmetry principles is presented in Section 2.4, where we introduce the Callan-Coleman-Wess-Zumino (CCWZ) formalism. We then discuss chiral symmetries and their associated Noether currents in Section 2.5, followed by an overview of QCD's global symmetry structure in Section 2.6.

In Sections 2.7 and 2.8, we present the leading-order chiral Lagrangian for mesons and baryons, and derive the corresponding Noether currents. The inclusion of weak interactions is discussed in Section 2.9.

Finally, in Section 2.10, we incorporate axionic couplings into this framework, constructing the low-energy effective Lagrangian for the axion and analyzing its interactions with hadrons.

Taken together, this chapter establishes the low-energy effective description of axion dynamics in hadronic environments, forming the foundation for later chapters focused on axion phenomenology in both collider and astrophysical settings.

For an in-depth treatment of EFT methods and their application to low-energy QCD, see the reviews [Man; Sch03].

2.1 Motivation

In QCD, the strong coupling constant α_s is not truly constant; it varies with the energy scale μ due to renormalization. This variation is governed by the renormalization group equation, which describes how α_s evolves with μ. The running of α_s is determined by the β-function:

$$\mu \frac{d\alpha_s}{d\mu} = \beta(\alpha_s) \ . \tag{2.1.1}$$

At one-loop order, the β-function for QCD is given by:

$$\beta(\alpha_s) = -\beta_0 \frac{\alpha_s^2}{2\pi} \ , \tag{2.1.2}$$

where $\beta_0 = \frac{11N_c - 2N_f}{3}$, with $N_c = 3$ (number of colors) and $N_f \geq 3$ (number of active quark flavors).

Solving the renormalization group equation and imposing the condition $\lim_{\mu \to \Lambda_{\rm QCD}} \alpha_s(\mu) = +\infty$, we obtain:

$$\alpha_s(\mu) = \frac{2\pi}{\beta_0 \ln(\mu/\Lambda_{\rm QCD})} \ . \tag{2.1.3}$$

In Fig. 2.1, α_s is plotted as a function of $\mu/\Lambda_{\rm QCD}$. The plot highlights three distinct regions:

- **perturbative QCD (pQCD) region** (green): At high energies, α_s becomes small (< 1), allowing perturbative calculations in terms of quarks and gluons.
- **ChPT region** (brown): At low energies, it is necessary to use EFT such as ChPT to work directly with hadrons.
- **Intermediate region**: The domain between the pQCD and ChPT regimes, where neither pQCD nor ChPT strictly applies, posing theoretical challenges for calculating strong-interaction effects.

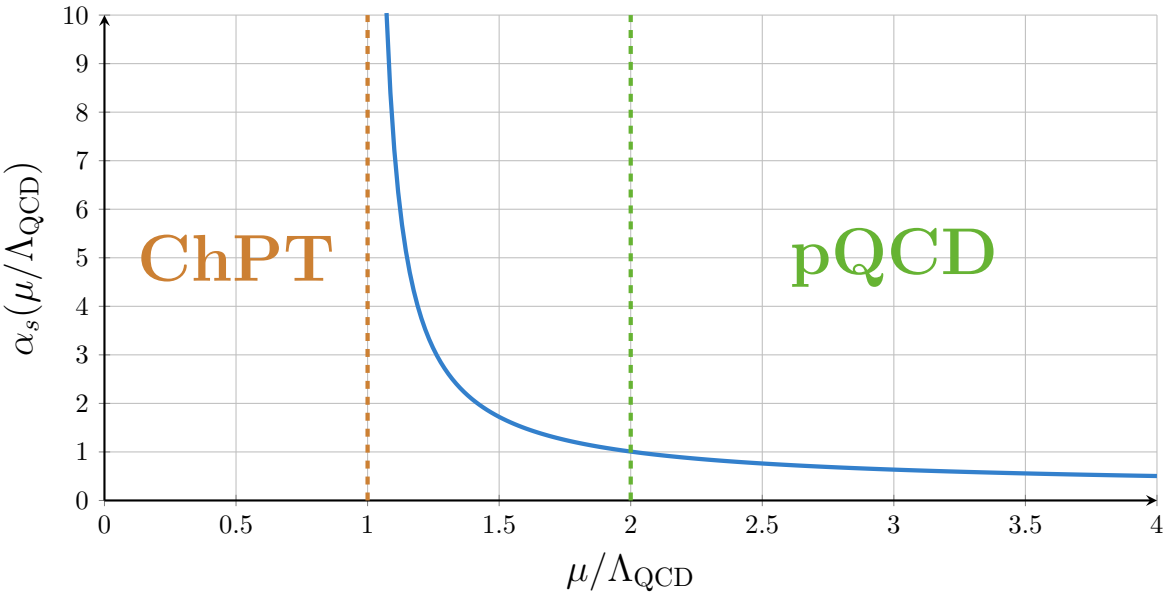

Figure 2.1: α_s as a function of $\mu/\Lambda_{\rm QCD}$ with ChPT limit in brown and pQCD limit in green.

This subdivision underscores the need for different theoretical tools to study strong interactions across various energy scales. ChPT offers a systematic framework to describe low-energy hadronic physics, while remaining consistent with the symmetries and dynamics of QCD.

2.2 Effective Field Theory vs. Renormalizable Theory

In Quantum Field Theory (QFT), a theory defined in a space-time of dimension d is considered renormalizable if its Lagrangian contains only operators of mass dimension less than or equal to d. Operators of dimension greater than d require an infinite number of counterterms to absorb divergences during renormalization. If the number of counterterm couplings at a given order in the mass expansion is n, the theory is fully predictive only after using n measurements to fix these couplings.

An EFT Lagrangian can be expanded as follows:

$$\mathcal{L}_{eff} = \mathcal{L}_{\leq d} + \sum_{k=1}^{+\infty} \mathcal{L}_{d+k} \ . \tag{2.2.1}$$

Here, $\mathcal{L}_{\leq d}$ includes all operators of dimension up to d, while $\mathcal{L}_{d+k}$ contains operators of dimension $d+k$. A renormalizable theory would only involve $\mathcal{L}_{\leq d}$. Although $\mathcal{L}_{eff}$ is not renormalizable, it is predictive at any finite order in k.

An EFT is a systematic low-energy approximation to a more fundamental, often unknown, theory. It is built from field-theoretic principles: one identifies the relevant degrees of freedom at the scale of interest, imposes the appropriate symmetries, and organizes interactions as an expansion in operators suppressed by powers of a cutoff scale Λ. This makes EFTs predictive in a *controlled* way: the error on a prediction to a given order k in the expansion is at least of order $(p/\Lambda)^{k+1}$, where p is the typical scale of the process, e.g. the mass of a decaying particle. By contrast, a phenomenological model is an empirical mathematical description designed to capture observed behavior, through *ad hoc* assumptions, parametrizations, or simplified dynamics, without necessarily being derived from underlying symmetries or principles. While phenomenological models can be highly successful in practice, they lack the systematic expansion that distinguish EFTs. In particular, the error to be attached to a prediction within a phenomenological model is not calculable.

In summary, EFTs can be just as predictive as renormalizable theories for low-energy calculations, as long as a finite (but controllable) level of precision is acceptable.

2.3 Fermi's theory

To illustrate EFTs, let us consider a historically emblematic example from the Standard Model (SM): the Fermi's theory, the EFT of the weak interaction that allows, for instance, the calculation of the decay width of $n \to p\, e^-\, \bar{\nu}_e$ at scales much below the electroweak one.

The weak interaction Lagrangian is given by

$$\mathcal{L}_{qqW} = \frac{g}{\sqrt{2}} \left(\bar{u}_i \gamma^\mu P_L d_i + \bar{\nu}_i \gamma^\mu P_L \ell_i\right) W^-_\mu + \text{h.c.} \ , \tag{2.3.1}$$

where the indices label the fermion generations. Here, the un-hatted quark fields u_i, d_i are defined in the interaction basis, in which the weak charged current is diagonal. To move to the mass eigenbasis, where the quark mass matrices are diagonal, one performs unitary transformations on the left-handed up- and down-type quark fields:

$$u_L \to \hat{u}_L = U_L u_L \ , \quad d_L \to \hat{d}_L = D_L d_L \ , \tag{2.3.2}$$

where U_L and D_L are unitary matrices diagonalizing the up- and down-type quark mass matrices, respectively.

In this mass basis, the charged current interaction becomes

$$\mathcal{L}_{qqW} = \frac{g}{\sqrt{2}} \left(\bar{\hat{u}}_i (V_{\text{CKM}})_{ij} \gamma^\mu P_L \hat{d}_j + \bar{\nu}_i \gamma^\mu P_L \ell_i\right) W^-_\mu + \text{h.c.} \ , \tag{2.3.3}$$

where the Cabibbo-Kobayashi-Maskawa (CKM) matrix is defined as[1]

$$V_{\text{CKM}} = U_L^\dagger D_L \ . \tag{2.3.4}$$

[1] In the case of neutral currents, the unitary rotations cancel out, since $U_L^\dagger U_L = 1$ and $D_L^\dagger D_L = 1$. As a result, the CKM matrix does not appear in neutral current interactions and only contributes to charged currents.

The Feynman rule for the vertex $d_j \to u_i W^-$ is then:

$$i\frac{g}{\sqrt{2}}(V_{CKM})_{ij}\gamma^\mu P_L \ , \tag{2.3.5}$$

and for $\ell_i \to \nu_i W^-$:

$$i\frac{g}{\sqrt{2}}\gamma^\mu P_L \ . \tag{2.3.6}$$

Fermi's theory relies on the mass hierarchy:

$$m_{u,d,s,c,b,e,\mu,\tau} \ll m_{W,Z,t} \ . \tag{2.3.7}$$

The idea is to build a theory by integrating out heavy degrees of freedom. Remarkably, such an effective theory allowed for precise decay predictions well before the electroweak theory was established.

The amplitude for $\ell_i \to \nu_i \, \ell_j \, \bar{\nu}_j$ (with $i > j$) is:

$$i\mathcal{M}_{fi} = \left(i\frac{g}{\sqrt{2}}\bar{u}_{\nu_i}\gamma^\alpha P_L u_{\ell_i}\right)\frac{-i\eta_{\alpha\beta}}{k^2 - m_W^2}\left(i\frac{g}{\sqrt{2}}\bar{u}_{\ell_j}\gamma^\beta P_L v_{\nu_j}\right) \ . \tag{2.3.8}$$

At low energies, one can expand the propagator:

$$\frac{1}{k^2 - m_W^2} = \frac{-1}{m_W^2} + \mathcal{O}\left(\frac{k^2}{m_W^4}\right) \ , \tag{2.3.9}$$

leading to the approximate amplitude:

$$i\mathcal{M}_{fi} \simeq -i\frac{g^2}{2m_W^2}(\bar{u}_{\nu_i}\gamma^\alpha P_L u_{\ell_i})(\bar{u}_{\ell_j}\gamma_\alpha P_L v_{\nu_j}) = i\langle \ell_j \bar{\nu}_j \nu_i | \mathcal{L}_{eff} | \ell_i \rangle \ , \tag{2.3.10}$$

which allows us to write the effective Lagrangian as:

$$\mathcal{L}_{eff} = -\frac{g^2}{2m_W^2}(\bar{\nu}_j\gamma^\alpha P_L \ell_j)(\bar{\ell}_i\gamma_\alpha P_L \nu_i) \ . \tag{2.3.11}$$

The above effective Lagrangian features a local four-fermion interaction (see Fig. 2.2) of mass dimension 6, making the theory non-renormalizable.

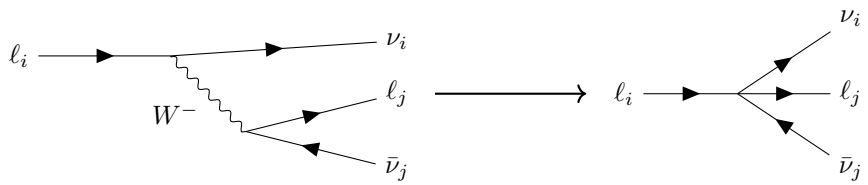

Figure 2.2: Feynman diagram for $\ell_i \to \nu_i \, \ell_j \, \bar{\nu}_j$.

We define the Fermi coupling constant G_F via:

$$\frac{4G_F}{\sqrt{2}} = \frac{g^2}{2m_W^2} \ . \tag{2.3.12}$$

The Fermi's constant G_F can be measured in one process (e.g., $\mu^- \to \nu_\mu e^- \bar{\nu}_e$) and then used to predict the rates of other weak decays.

The same procedure can be applied to any process with four external fermions, as long as none of them involves the top quark (which is too heavy, actually heavier than the W boson mass, and would make the neglect of W propagation unjustified). For example, in the case of $d_j \to u_i \, \ell_k \, \bar{\nu}_k$, the effective Lagrangian becomes:

$$\mathcal{L}_{eff} = -\frac{4G_F}{\sqrt{2}}(V_{CKM})_{ij}(\bar{u}_i\gamma^\alpha P_L d_j)(\bar{\ell}_k\gamma_\alpha P_L \nu_k) \ . \tag{2.3.13}$$

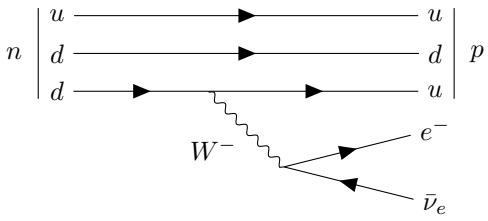

Figure 2.3: Feynman diagram for $n \to p\, e^-\, \bar{\nu}_e$ at the quark level.

This gives the amplitude for neutron beta decay $n \to p\, e^-\, \bar{\nu}_e$ (see Fig. 2.3):

$$i\mathcal{M}_{fi} = \langle e^- \bar{\nu}_e p | i\mathcal{L}_{eff} | n \rangle = -i\frac{4G_F}{\sqrt{2}} V_{ud} \bar{u}_e \gamma_\alpha P_L v_{\nu_e} \langle p | \bar{u}\gamma^\alpha P_L d | n \rangle \ . \tag{2.3.14}$$

Since G_F is measured independently, $V_{ud} = (V_{CKM})_{11} = 0.97 \simeq 1$, and the hadronic matrix element $\langle p|\bar{u}\gamma^\alpha P_L d|n\rangle$ is computable, the neutron decay rate can be accurately predicted.

Historically, things unfolded differently: Fermi's theory was introduced before the weak interaction was incorporated into the SM. However, presenting Fermi's theory in this way helps us better understand how to construct an effective theory – e.g., in the context of the strong interaction.

The central idea of the procedure is to write an effective Lagrangian with free parameters – in the case of Fermi's theory, G_F and V_{CKM} – which are determined from selected processes and then used to make predictions for others. This can be done without knowing the Ultraviolet (UV) theory – that is, without explicitly introducing the gauge bosons of the interaction, which are effectively integrated out and replaced by local interaction vertices.

With this general context on EFTs, we now introduce the formalism for ChPT, with one important conceptual caveat. The discussion above described an EFT built by integrating out heavy degrees of freedom, leading to the Fermi theory, which retains only a subset of the full SM fields. By contrast, ChPT rests on entirely different premises: it does not arise from integrating out heavy fields, but from *replacing* the UV degrees of freedom of QCD with those more appropriate below the confinement scale– namely, hadrons. In other words, quarks and gluons are traded for hadrons as dynamical degrees of freedom.

Accordingly, the guiding principle for constructing the interactions is not the decoupling of heavy scales, but a spontaneously broken global symmetry: the chiral symmetry of QCD. This symmetry implies that light mesons (pions, and to a lesser extent kaons) are Goldstone bosons in the limit of exact symmetry. In reality, it is explicitly broken by quark masses, but in the light-quark sector the breaking is mild, quantified by $m_q \ll \Lambda_{\rm QCD}$.

Baryons are included only because the symmetry can be generalized to them; otherwise, they behave as heavy degrees of freedom ($m_{n,p} \sim \Lambda_{\rm QCD}$) and are not massless in the exact-symmetry limit.

In summary, the logic behind EFT power counting differs completely between the Fermi theory and ChPT. Yet both are valid EFTs, each with a consistent expansion: $p^2 G_F^2$ in the Fermi theory, and $p^2/\Lambda_{\rm QCD}^2$ in ChPT, with p the typical external momentum of the process.

2.4 The CCWZ formalism

The most comprehensive framework for constructing effective Lagrangians in the presence of spontaneously broken symmetries is known as the CCWZ formalism.

Consider a theory with a global symmetry group G, spontaneously broken down to a subgroup H. The set of degenerate vacuum states is then described by the coset space G/H.

To describe the local fluctuations around the vacuum, we introduce a set of coordinates parameterizing these fluctuations. Let $\Xi(x) \in G$ be a group-valued field[2] that transforms the reference vacuum configuration into the local field configuration. This matrix is not unique: any transformation of the form Ξh, with $h \in H$, corresponds to the same physical configuration, since the vacuum is invariant under H.

[2]By this we mean a representation of a general group element, where the parameters along the different generator directions are space-time functions.

Using the Lie algebra structure, the CCWZ formalism prescribes the construction of $\Xi(x)$ from the broken generators X as:

$$\Xi(x) = \exp(iX \cdot \phi(x)) \ , \tag{2.4.1}$$

where $\phi(x)$ denotes the Goldstone boson fields.

Under a global transformation $g \in G$, the field $\Xi(x)$ transforms as:

$$\Xi(x) \to g\Xi(x)h^{-1} \ , \tag{2.4.2}$$

where $h \in H$ implicitly depends on both g and $\Xi(x)$. Eqs. (2.4.1) and (2.4.2) provide the CCWZ prescription for the Goldstone boson fields and their transformation laws.

It is important to note that while any choice of $\Xi(x)$ constructed in this way leads to the same physical observables, different parameterizations may yield different off-shell Green's functions. Nonetheless, the CCWZ formalism provides a systematic and consistent method to describe the low-energy dynamics of Goldstone bosons arising from spontaneous symmetry breaking.

2.5 Chiral Currents and Noether's theorem

Noether's theorem states that for every continuous *global*[3] symmetry of a Lagrangian, there corresponds a conserved quantity.

Let us consider a Lagrangian $\mathcal{L}$ depending on a set of n independent fields Φ_i and their first derivatives:

$$\mathcal{L} = \mathcal{L}(\Phi_i, \partial_\mu \Phi_i) \ . \tag{2.5.1}$$

The Euler-Lagrange equations of motion for each field are

$$\frac{\partial \mathcal{L}}{\partial \Phi_i} - \partial_\mu \left(\frac{\partial \mathcal{L}}{\partial(\partial_\mu \Phi_i)} \right) = 0 \ . \tag{2.5.2}$$

Suppose the Lagrangian is invariant under an infinitesimal global transformation of the form

$$\Phi_i(x) \to \Phi_i'(x) = \Phi_i(x) + \delta\Phi_i(x) = \Phi_i(x) - i\epsilon_b F_i^b[\Phi_j(x)] \ , \tag{2.5.3}$$

where ϵ_b are small (constant) parameters, and F_i^b represents the infinitesimal generator of the symmetry acting on Φ_i.

The variation of the Lagrangian is then

$$\begin{aligned}
\delta\mathcal{L} &= \mathcal{L}(\Phi_i'; \partial_\mu \Phi_i') - \mathcal{L}(\Phi_i; \partial_\mu \Phi_i) \\
&= \frac{\partial \mathcal{L}}{\partial \Phi_i}\delta\Phi_i + \frac{\partial \mathcal{L}}{\partial \partial_\mu \Phi_i}\partial_\mu \delta\Phi_i \\
&= -i\epsilon_b \frac{\partial \mathcal{L}}{\partial \Phi_i} F_i^b - i\epsilon_b \frac{\partial \mathcal{L}}{\partial \partial_\mu \Phi_i}\partial_\mu F_i^b + \mathcal{O}(\epsilon^2) \\
&= -i\epsilon_b \left(\partial_\mu \frac{\partial \mathcal{L}}{\partial \partial_\mu \Phi_i} \right) F_i^b - i\epsilon_b \frac{\partial \mathcal{L}}{\partial \partial_\mu \Phi_i}\partial_\mu F_i^b + \mathcal{O}(\epsilon^2) \\
&= \partial_\mu \left(-i\epsilon_b \frac{\partial \mathcal{L}}{\partial \partial_\mu \Phi_i} F_i^b \right) + \mathcal{O}(\epsilon^2) \ .
\end{aligned} \tag{2.5.4}$$

This leads to the identification of the conserved Noether currents in each direction:

$$J^{\mu,b} = -i \frac{\partial \mathcal{L}}{\partial(\partial_\mu \Phi_i)} F_i^b \ , \tag{2.5.5}$$

which satisfy the conservation law $\partial_\mu J^{\mu,b} = 0$ as a consequence of the invariance of the Lagrangian, i.e., $\delta\mathcal{L} = 0$ for arbitrary values of ϵ_b.

The associated conserved charges are given by

$$Q^b = \int_V J^{0,b}(\vec{x}, t) d^3V \ , \tag{2.5.6}$$

[3]For local (gauge) symmetries, Noether's second theorem applies, and the consequences are different (e.g., identities between equations of motion rather than conserved currents).

and remains conserved in time since

$$\partial_0 Q^b(t) = \int_V \partial_0 J^{0,b}(\vec{x};t) d^3V = -\int_V \nabla \cdot \vec{J}^b(\vec{x};t) d^3V = -\int_{\partial V} \vec{J}^b(\vec{x};t) \cdot d^2\vec{S} = 0 \ . \tag{2.5.7}$$

Although the symmetry is global, a useful trick to extract the conserved currents is to temporarily promote the transformation parameter ϵ_b to a spacetime-dependent function $\epsilon_b(x)$. Under such a *local* transformation, the variation of the Lagrangian becomes

$$\delta\mathcal{L} = \partial_\mu \left(\epsilon_b(x) J^{\mu,b}(x)\right) = J^{\mu,b}(x)\partial_\mu \epsilon_b(x) + \epsilon_b(x)\partial_\mu J^{\mu,b}(x) \ . \tag{2.5.8}$$

From this expression, the current can be extracted via:

$$J^{\mu,b}(x) = \frac{\partial(\delta\mathcal{L})}{\partial(\partial_\mu \epsilon_b(x))} \ . \tag{2.5.9}$$

This method is computationally convenient, but it is important to emphasize that the underlying symmetry remains global.

2.6 QCD symmetries

The QCD Lagrangian takes the form:

$$\mathcal{L}_{QCD} = \bar{q}\left(i\not{D} - M_q\right) q = i\bar{q}_L \not{D} q_L + i\bar{q}_R \not{D} q_R - \bar{q}_L M_q q_R - \bar{q}_R M_q^\dagger q_L \ , \tag{2.6.1}$$

where q denotes the vector of quark fields and M_q is the diagonal quark mass matrix.

In the limit $M_q \to 0$, the left- and right-handed components decouple, leading to an approximate global symmetry:

$$q_L \to q'_L = L q_L \ , \quad q_R \to q'_R = R q_R \ , \tag{2.6.2}$$

with $(L;R) \in G = U(n)_L \times U(n)_R$, where n is the number of quark flavors considered. For $n = 2$, the symmetry applies to systems involving pions and nucleons composed of u and d quarks. For $n = 3$, it extends to kaons and hyperons, involving u, d and s quarks.

The full symmetry group G can be decomposed as:

$$U(n)_L \times U(n)_R = U(1)_L \times U(1)_R \times SU(n)_L \times SU(n)_R \ . \tag{2.6.3}$$

We write the left- and right-handed transformation

$$L = \exp\left(-i\theta_L^b \tau^b/2\right) \ , \quad R = \exp\left(-i\theta_R^b \tau^b/2\right) \tag{2.6.4}$$

where $b \geq 1$ corresponds to the $SU(n)_{L/R}$ generators and $b = 0$ to the $U(1)_{L/R}$ generator. The matrices τ^b are Hermitian matrices known as the group generators. For $n = 2$ it is customary to use Pauli matrices and for $n = 3$ Gell-Mann matrices, normalized such that $\mathrm{Tr}(\tau^a \tau^b) = 2\delta^{ab}$. The Pauli and Gell-Mann matrices form a basis for traceless Hermitian matrices. To obtain a complete basis of Hermitian matrices in n dimensions, we also include $\tau^0 \propto I_n$, with the proper normalization given by $\tau^0 = \frac{\sqrt{2}}{\sqrt{n}} I_n$. The Pauli and Gell-Mann matrices are given in Appendix A.2.

We now apply the procedure outlined in Section 2.5 to determine the Noether currents. In particular, we use the trick of promoting the global symmetry transformations to local ones, which allows us to extract the currents from the linear dependence of $\delta\mathcal{L}$ on $\partial_\mu \theta_{L,R}(x)$.

For a left- or right-handed transformation, this yields:

$$\delta\mathcal{L} = i\bar{q}_{L/R}\left(\gamma^\mu \partial_\mu (L/R)\right) q_{L/R} = \partial_\mu \theta^b_{L/R} \bar{q}_{L/R} \gamma^\mu \frac{\tau^b}{2} q_{L/R} \ . \tag{2.6.5}$$

Therefore, we derive the corresponding conserved currents:

- For $U(1)_L \times U(1)_R$:

$$J^{\mu;0}_{L/R} = \frac{\sqrt{2}}{2\sqrt{n}} \bar{q}_{L/R} \gamma^\mu q_{L/R} \ . \tag{2.6.6}$$

  The vector transformation corresponds to $\alpha_L = \alpha_R$, while the axial transformation corresponds to $\alpha_L = -\alpha_R$, leading to:

$$J^{\mu;0}_V = J^{\mu;0}_R + J^{\mu;0}_L = \frac{\sqrt{2}}{\sqrt{n}} \bar{q}\gamma^\mu q \ , \quad J^{\mu;0}_A = J^{\mu;0}_R - J^{\mu;0}_L = \frac{\sqrt{2}}{\sqrt{n}} \bar{q}\gamma^\mu\gamma_5 q \ . \tag{2.6.7}$$

- For $SU(n)_L \times SU(n)_R$:

$$J^b_{L/R} = \bar{q}_{L/R}\gamma^\mu \frac{\tau^b}{2} q_{L/R} \ , \tag{2.6.8}$$

and their vector and axial combinations are:

$$J^{\mu;b}_V = \bar{q}\gamma^\mu \frac{\tau^b}{2} q \ , \quad J^{\mu;b}_A = \bar{q}\gamma^\mu\gamma_5 \frac{\tau^b}{2} q \ . \tag{2.6.9}$$

Using the Dirac equation, the divergences of these currents can be computed:

$$\partial_\mu J^{\mu;0}_V = 0 \ , \quad \partial_\mu J^{\mu;b}_V = \frac{i}{2}\bar{q}[M_q;\tau^b]q \ , \quad \partial_\mu J^{\mu;0}_A = i\frac{\sqrt{2}}{\sqrt{n}}\bar{q}M_q\gamma_5 q \ , \quad \partial_\mu J^{\mu;b}_A = \frac{i}{2}\bar{q}\{M_q;\tau^b\}\gamma_5 q \ , \tag{2.6.10}$$

Thus, $J^{\mu;0}_V$ is always a conserved current, while $J^{\mu;b}_V$ is conserved only in the limit $M_q \to 0$ or if $M_q \propto I_n$. This limit should be understood in units of the hadronization scale, Λ_{QCD}. For $n = 2$, it corresponds to the isospin limit, which holds to a much better approximation than the $n = 3$ counterpart.

Although $\partial_\mu J^{\mu;0}_A = 0$ at tree level in the limit $M_q \to 0$, quantum corrections generate an anomaly that explicitly breaks this symmetry:

$$\partial_\mu J^{\mu;0}_A = \frac{\alpha_s}{8\pi} G^a_{\mu\nu}\tilde{G}^{\mu\nu,a} + \frac{\alpha_{e.m.}}{8\pi} F_{\mu\nu}\tilde{F}^{\mu\nu} \ , \tag{2.6.11}$$

with the diagrams:

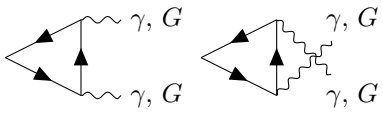

This anomaly reflects an explicit breaking of the classical symmetry at the quantum level.

The divergence $\partial_\mu J^{\mu;b}_A$ vanishes only in the chiral limit $M_q \to 0$, indicating that it is a symmetry of the massless QCD Lagrangian. However, this symmetry is also spontaneously broken by the QCD vacuum. In QCD, q_i and $\bar{q}_i$ experience strong attractive interactions. When the quark mass m_{q_i} is small with respect to Λ_{QCD}, the energy cost to produce them from the vacuum is also small, leading to the formation of a quark condensate $\langle\bar{q}q\rangle \neq 0$. Specifically, $\langle\bar{q}q\rangle = \langle 0_q|\bar{q}_R q_L + \bar{q}_L q_R|0_q\rangle$, then $\langle\bar{q}q\rangle \neq 0$ breaks the axial symmetry spontaneously while preserving the vector symmetry.

Consequently, in the limit of small quark masses, the global symmetry group $G = U(n)_L \times U(n)_R$ is spontaneously broken down to the subgroup $H = U(n)_V$. The Goldstone bosons associated with this breaking parametrize the coset space: $U(n)_L \times U(n)_R/U(n)_V = U(n)$.

This spontaneous symmetry breaking allows for the application of the CCWZ formalism to construct the corresponding low-energy effective theory. The generators of G are denoted T^b_L and T^b_R, acting on the left- and right-handed quarks, respectively. The unbroken generators of H are $T^b_L + T^b_R$.

2.7 ChPT for mesons

2.7.1 The u- and U-basis

In the context of the chiral Lagrangian of QCD, two commonly used parametrizations of the Goldstone boson fields are the u- and U-basis. We now examine both in detail.

2.7.1.1 The u-basis

The chiral symmetry group $U(n)_L \times U(n)_R$ can be expressed in block matrix form as:

$$g = \begin{pmatrix} L & 0 \\ 0 & R \end{pmatrix} \ , \tag{2.7.1}$$

where $L \in U(n)_L$ and $R \in U(n)_R$. The unbroken transformation corresponds to $K = L = R$, leading to:

$$h = \begin{pmatrix} K & 0 \\ 0 & K \end{pmatrix} \ . \tag{2.7.2}$$

If one choose the broken generators as $X^b = T_R^b - T_L^b$, the field Ξ in Eq. (2.4.1) becomes:

$$\Xi(x) = \exp(iX \cdot \phi(x)) = \exp\left[i \begin{pmatrix} -T \cdot \phi & 0 \\ 0 & T \cdot \phi \end{pmatrix}\right] = \begin{pmatrix} u^\dagger(x) & 0 \\ 0 & u(x) \end{pmatrix} , \tag{2.7.3}$$

with

$$u = \exp(iT \cdot \phi) , \tag{2.7.4}$$

corresponding to the lower block of $\Xi(x)$.

Under the general transformation law (as in Eq. (2.4.2)), we have:

$$\begin{pmatrix} u^\dagger(x) & 0 \\ 0 & u(x) \end{pmatrix} \to \begin{pmatrix} L & 0 \\ 0 & R \end{pmatrix} \begin{pmatrix} u^\dagger(x) & 0 \\ 0 & u(x) \end{pmatrix} \begin{pmatrix} K^\dagger & 0 \\ 0 & K^\dagger \end{pmatrix} , \tag{2.7.5}$$

which implies the transformation law:

$$u(x) \to Ru(x)K^\dagger = Ku(x)L^\dagger , \tag{2.7.6}$$

where K is determined in terms of L, R and u to satisfy the previous equality.

2.7.1.2 The U-basis

An alternative is the U-basis, defined as $U = u^2$, which leads to the transformation

$$U(x) = u^2(x) \to Ru(x)K^\dagger \cdot Ku(x)L^\dagger = Ru^2(x)L^\dagger = RU(x)L^\dagger . \tag{2.7.7}$$

This definition arises naturally from the CCWZ construction when one chooses the broken generators as $X^a = T_R^a$.[4] In this case, the field $\Xi(x)$ in Eq. (2.4.1) becomes:

$$\Xi(x) = \exp(iX \cdot \phi(x)) = \exp\left[i \begin{pmatrix} 0 & 0 \\ 0 & T \cdot \phi \end{pmatrix}\right] = \begin{pmatrix} 1 & 0 \\ 0 & U \end{pmatrix} , \tag{2.7.8}$$

where

$$U = \exp(iT \cdot \phi) , \tag{2.7.9}$$

corresponds to the lower block of $\Xi(x)$.

Under the symmetry transformation (as in Eq. (2.4.2)), we have:

$$\begin{pmatrix} 1 & 0 \\ 0 & U(x) \end{pmatrix} \to \begin{pmatrix} L & 0 \\ 0 & R \end{pmatrix} \begin{pmatrix} 1 & 0 \\ 0 & U(x) \end{pmatrix} \begin{pmatrix} K^\dagger & 0 \\ 0 & K^\dagger \end{pmatrix} , \tag{2.7.10}$$

resulting in $K = L$ and

$$U(x) \to RU(x)L^\dagger . \tag{2.7.11}$$

By comparing this with the transformation in Eq. (2.7.6), we see that the two parametrizations are related via:

$$U(x) = u^2(x) . \tag{2.7.12}$$

This relation highlights the connection between the u- and U-basis within the framework of ChPT for mesons.

[4] At first glance, choosing the broken generators as $X^a = T_R^a$ may seem inconsistent, since the left-handed symmetry appears to commute with all other elements. However, this apparent issue disappears once one works in the coset space G/H, where $G = SU(n)_L \times SU(n)_R$ and $H = SU(n)_V$ is the preserved vector subgroup. In this framework, left-handed transformations can be represented as combinations of right-handed transformations and elements of the preserved subgroup. Specifically, a left transformation $(L, 1)$ can be written as $(1, L^\dagger) \cdot (L, L) = (L, 1)$, with $(1, L^\dagger)$ a right-handed transformation and $(L, L) \in H$. Thus, any linear combination $X^a = \alpha T_R^a + \beta T_L^a$ with $\alpha \neq \beta$ (and at least one of them nonzero) defines a valid choice of broken generators.

2.7.2 Mesonic Lagrangian

The Goldstone boson fields are angular variables and hence dimensionless. However, it is often convenient to work with fields of mass dimension one, similar to conventional scalar fields. A standard choice to achieve this normalization is:

$$u = \exp(i\phi/(2F_0)) \quad ; \quad U = u^2 = \exp(i\phi/F_0) \ , \tag{2.7.13}$$

where $F_0 = 93$ MeV is the pion decay constant[5]. The matrix ϕ contains the pseudoscalar meson fields and is defined as $\phi = \phi^a \sigma^a$ for $U(2)$, and $\phi = \phi^a \lambda^a$ for $U(3)$, where λ^a are the Gell-Mann matrices normalized such that[6]:

$$\mathrm{Tr}(\lambda^a \lambda^b) = 2\delta^{ab} \ . \tag{2.7.14}$$

In the following, we adopt the $n = 3$ framework, which is more general. To recover the $n = 2$ case, one simply selects the upper-left 2×2 submatrix, discarding the third row and column, and removing the non-pion components accordingly.

The matrix ϕ, containing the meson fields[7], is given by[8]:

$$\phi = \sqrt{2} \begin{pmatrix} \frac{1}{\sqrt{2}}\pi^0 + \frac{1}{\sqrt{6}}\eta_8 + \frac{1}{\sqrt{3}}\eta_0 & \pi^+ & K^+ \\ \pi^- & -\frac{1}{\sqrt{2}}\pi^0 + \frac{1}{\sqrt{6}}\eta_8 + \frac{1}{\sqrt{3}}\eta_0 & K^0 \\ K^- & \bar{K}^0 & -\frac{2}{\sqrt{6}}\eta_8 + \frac{1}{\sqrt{3}}\eta_0 \end{pmatrix} \ . \tag{2.7.15}$$

To construct a Lagrangian invariant under the chiral transformation $U \to LUR^\dagger$, one may consider general expressions like $\mathrm{Tr}[UU^\dagger \dots UU^\dagger]$. However, since $UU^\dagger = I_3$, such terms are constant and do not depend on the meson fields.

The only non-trivial invariant term involving two derivatives is:

$$\mathcal{L} = \frac{F_0^2}{4} \mathrm{Tr}(D_\mu U D^\mu U^\dagger) \ , \tag{2.7.16}$$

where the covariant derivative[9] is defined as:

$$D_\mu U = \partial_\mu U - ieA_\mu [Q; U] \ , \tag{2.7.17}$$

with $Q = \mathrm{diag}(q_u; q_d; q_s) = \mathrm{diag}(2; -1; -1)/3$ being the quark charge matrix.

The previous Lagrangian treats the mesons as true Goldstone bosons. However, experimental evidence shows that mesons are actually pseudo-Goldstone bosons, acquiring mass through explicit symmetry breaking (see Appendix C.4). This leads to the full Lagrangian up to two derivatives:

$$\mathcal{L}_U = \frac{F_0^2}{4} \mathrm{Tr}(D_\mu U D^\mu U^\dagger) + \frac{F_0^2 B_0}{2} \mathrm{Tr}(U^\dagger M_q + M_q^\dagger U) \ . \tag{2.7.18}$$

Expanding U as a series, we obtain:

$$\mathcal{L}_U = \frac{1}{4} \mathrm{Tr}(D_\mu \phi D^\mu \phi) + \frac{1}{12F_0^2} \mathrm{Tr}([\phi; D_\mu \phi][\phi; D^\mu \phi]) + \dots \tag{2.7.19}$$

$$= \frac{1}{2} \partial_\mu \pi^0 \partial_\mu \pi^0 + \partial_\mu \pi^+ \partial_\mu \pi^- + \dots \tag{2.7.20}$$

The normalization of kinetic term in Eq. (2.7.18) is chosen such that the kinetic terms for the pions in Eq. (2.7.20) match the canonical normalization for real and imaginary scalar fields. Importantly, only even powers of meson fields appear in the expansion of Eq. (2.7.18), consistent with the pseudoscalar nature of the Goldstone bosons.

This Lagrangian determines all multi-meson scattering amplitudes at leading order in the chiral expansion, relying on two parameters : F_0 and B_0. We extract F_0 from the decay $\pi^- \to \mu^- \bar{\nu}_\mu$,

[5] In the literature, one often uses the symbol f_π, numerically equal to $\sqrt{2} \cdot F_0$.

[6] The indices $a \geq 1$ correspond to the $SU(n)$ part, while $a = 0$ corresponds to the $U(1)$ component. To satisfy the normalization in Eq. (2.7.14), one defines $\sigma^0 = I_2$ and $\lambda^0 = \sqrt{2/3} I_3$. For explicit expressions of the Pauli and Gell-Mann matrices, see Appendix A.2.

[7] For a detailed understanding of the quark model underlying mesons, see Appendix C.3.

[8] The factor of $\sqrt{2}$ outside the matrix is included to match a commonly used normalization in the literature. It is not directly incorporated into the matrix in order to highlight the similarity with the baryon octet matrix in Eq. (2.8.8).

[9] Respecting the Leibniz rule $D_\mu U^2 = U D_\mu U + (D_\mu U) U$, since $[Q; U^2] = U[Q; U] + [Q; U]U$.

whose experimentally measured branching ratio is close to one (see Appendix B.5.1 for details). By expanding Eq. (2.7.18), we obtain

$$B_0 = \frac{m_{\pi^0}^2}{m_u + m_d} \ . \tag{2.7.21}$$

For further discussion, see Appendix C.4.

2.7.3 Mesonic currents

In this section, we compute the mesonic currents following the Noether procedure presented in Section 2.5, treating the transformations as if they were local for computational convenience. These currents are essential for describing certain weak processes, such as the decay $\pi^- \to \mu^- \bar{\nu}_\mu$ mediated by a W^- exchange (see Appendix B.5.1). However, for us, they will play a more central role in defining the interactions between the axion and mesons (see Section 2.10.2.2).

To obtain the mesonic current, we need to apply the field transformation

$$U \to U' = RUL^\dagger \ , \tag{2.7.22}$$

to the leading-order mesonic Lagrangian in Eq. (2.7.18).

By performing a left-handed infinitesimal transformation on this Lagrangian, we obtain:

$$\delta\mathcal{L}_U = \frac{F_0^2}{4}\mathrm{Tr}\left[iU(\partial_\mu\theta_L^b)\frac{\lambda^b}{2}(D^\mu U)^\dagger - (D_\mu U)i(\partial^\mu\theta_L^b)\frac{\lambda^b}{2}U^\dagger\right] \ . \tag{2.7.23}$$

Thus, the left-handed Noether current is:

$$J_L^{b,\mu} = +i\frac{F_0^2}{4}\mathrm{Tr}[\lambda^b(D^\mu U)^\dagger U] \ , \tag{2.7.24}$$

where we used the identity $U^\dagger(D_\mu U) = -(D_\mu U)^\dagger U$. [10]

Similarly, by performing a right-handed infinitesimal transformation, we find:

$$\delta\mathcal{L}_U = \frac{F_0^2}{4}\mathrm{Tr}\left[-i(\partial_\mu\theta_b^R)\frac{\lambda^b}{2}U(\partial_\mu(D^\mu U)^\dagger + (D_\mu U)U^\dagger i(\partial^\mu\theta_R^b)\frac{\lambda^b}{2}\right] \ . \tag{2.7.25}$$

Thus, the right-handed Noether current is:

$$J_R^{b,\mu} = -i\frac{F_0^2}{4}\mathrm{Tr}[\lambda^b U(D^\mu U)^\dagger] \ . \tag{2.7.26}$$

2.8 ChPT for baryons

As spelled out earlier at the end of Section 2.3, baryons are included in ChPT because one can consistently define baryon fields transforming under a conserved subgroup of the chiral symmetry. Their interactions can then be incorporated via the Noether procedure. However, they are not chiral states: they behave as heavy degrees of freedom ($m_N \sim \Lambda_{\mathrm{QCD}}$) and are not massless in the exact-symmetry limit.

The question then arises, *which* baryon multiplets should be included. The first decuplet of states is only moderately heavier than the octet containing nucleons, which can slow the convergence of the chiral series for some observables. This is not a concern here, since our observable of interest–emissivity (see Section 3.4 for more details)–is accessible only at the order-of-magnitude (oom) level. In fact, emissivities are not measured directly but inferred from stellar properties (mass, radiated fraction, dynamics), themselves known only within an oom. We therefore restrict our calculations to the first baryonic octet, as including the decuplet will not alter the oom of our estimate.

Having settled this point, ChPT can be generalized beyond Goldstone bosons to include interactions with other particles, referred to as matter fields–such as baryons and heavy mesons. While Goldstone bosons transform under the full chiral symmetry group $SU(n)_L \times SU(n)_R$, matter fields like baryons transform only under the conserved vector subgroup $SU(n)_V$ and therefore do not form chiral representations of $SU(n)_L \times SU(n)_R$.

To describe interactions involving matter fields, particularly baryons, it is advantageous to work in the u-basis introduced in Section 2.7.1. We focus here on the interactions between the scalar meson octet and the baryon octet, although this framework can be straightforwardly extended to other types of matter fields.

[10] $U^\dagger(D_\mu U) + (D_\mu U)^\dagger U = D_\mu(U^\dagger U) = D_\mu I_d = 0$.

2.8.1 $SU(2)$ limit

In the $SU(2)$ limit, the relevant baryons are the nucleons, which form an isospin doublet,

$$\Psi = \begin{pmatrix} p \\ n \end{pmatrix} \ , \tag{2.8.1}$$

transforming under chiral symmetry as

$$\Psi \to \Psi' = K\Psi \ , \tag{2.8.2}$$

where K is defined in terms of L and R via Eq. (2.7.6).

The most general Lagrangian involving nucleons and pions, consistent with chiral symmetry and containing the lowest number of derivatives, is given by

$$\mathcal{L}_{N\pi} = \bar{\Psi}\left(i\not{D} - M_N - \frac{g_A}{2}\gamma^\mu\gamma_5 u_\mu\right)\Psi + \mathcal{L}_\pi \ , \tag{2.8.3}$$

where $\mathcal{L}_\pi$ denotes the purely pionic part defined at leading order in Eq. (2.7.18). The covariant derivative is given by

$$D_\mu\Psi = \partial_\mu\Psi + \Gamma_\mu\Psi \ , \tag{2.8.4}$$

with

$$\begin{aligned} \Gamma_\mu &= \frac{1}{2}\left(u(\partial_\mu - il_\mu)u^\dagger + u^\dagger(\partial_\mu - ir_\mu)u\right) = \frac{1}{2F_0}[\phi;\partial^\mu\phi] + \dots \ , \\ u_\mu &= i\left(u^\dagger(\partial_\mu - ir_\mu)u - u(\partial_\mu - il_\mu)u^\dagger\right) = 2\frac{\partial_\mu\phi}{F_0} + \dots \ , \\ r_\mu &= l_\mu = -eQA_\mu \ , \end{aligned} \tag{2.8.5}$$

which transform under $SU(2)_L \times SU(2)_R$ as

$$\begin{aligned} u_\mu &\to K u_\mu K^\dagger \ , \\ \Gamma_\mu &\to K\Gamma_\mu K^\dagger - \partial_\mu K K^\dagger \ , \\ D_\mu\Psi &\to K D_\mu\Psi \ . \end{aligned} \tag{2.8.6}$$

2.8.2 $SU(3)$ limit

Following the CCWZ prescription, the transformation of baryon fields is given by

$$B \to KBK^\dagger \tag{2.8.7}$$

where K is again defined via Eq. (2.7.6). The baryon octet B is represented as[11]

$$B = \begin{pmatrix} \frac{1}{\sqrt{2}}\Sigma^0 + \frac{1}{\sqrt{6}}\Lambda & \Sigma^+ & p \\ \Sigma^- & -\frac{1}{\sqrt{2}}\Sigma^0 + \frac{1}{\sqrt{6}}\Lambda & n \\ \Xi^- & \Xi^0 & -\frac{2}{\sqrt{6}}\Lambda \end{pmatrix} \ , \tag{2.8.8}$$

which transforms as an adjoint of $SU(3)_V$. Any transformation that reduces to the adjoint representation of $SU(3)_V$ is acceptable. For instance:

$$B \to RBR^\dagger \ , \quad B \to KBL^\dagger \ \dots \tag{2.8.9}$$

These various choices are equivalent and simply correspond to different field redefinitions of the baryonic degrees of freedom.

The covariant derivative acting on the baryon octet is defined as

$$D^\mu B = \partial^\mu B + [\Gamma^\mu; B] \ , \tag{2.8.10}$$

which transform as

$$D^\mu B \to K D^\mu B K^\dagger \ . \tag{2.8.11}$$

[11] For a detailed understanding of the quark model underlying baryons, see Appendix C.3.

The general baryonic Lagrangian at leading order is expressed as

$$\mathcal{L}_{BU} = \mathrm{Tr}[\bar{B}(i\not{D} - M_B)B] - \frac{D}{2}\,\mathrm{Tr}[\bar{B}\gamma^\mu\gamma_5\{u_\mu; B\}] - \frac{F}{2}\,\mathrm{Tr}[\bar{B}\gamma^\mu\gamma_5[u_\mu; B]] + \mathcal{L}_U \ , \tag{2.8.12}$$

where $\mathcal{L}_U$ represents the purely mesonic part, defined at leading order in Eq. (2.7.18).

Here, M_B denotes the baryon mass matrix, while D and F are the usual axial coupling constants. Their values can be extracted by fitting semi-leptonic decays of the form $B_i \to B_f e^- \bar{\nu}_e$, yielding $D \simeq 0.8$ and $F \simeq 0.5$ [Sch03]. For more details, see Appendix B.5.2.

In the $SU(2)$ limit, the identifications

$$B \to \begin{pmatrix} 0 & \Psi \\ 0 & 0 \end{pmatrix} \ , \quad u_{SU(3)} \to \begin{pmatrix} u & 0 \\ 0 & 0 \end{pmatrix} \ , \tag{2.8.13}$$

reduce the Lagrangian in Eq. (2.8.12) to

$$\mathcal{L}_{BU} \to \bar{\Psi}\left(i\not{D} - M_N - \frac{D+F}{2}\gamma^\mu\gamma_5 u_\mu\right)\Psi \ , \tag{2.8.14}$$

which precisely matches with Eq. (2.8.3) for $g_A = D + F$.

2.8.3 Baryonic currents

As was done for mesons (see Section 2.7.3), we now derive the baryonic currents, which will serve as the foundation for introducing axion couplings to baryons in Section 2.10.2.3.

2.8.3.1 Explicit determination of K

To derive the baryonic currents, we first need to understand how K can be expressed in terms of the transformations L and R. We define K as

$$K := \exp\left(-iv^a\frac{\lambda^a}{2}\right) \ , \tag{2.8.15}$$

where it is implicitly defined through the relation

$$u \to u' = KuL^\dagger = RuK^\dagger \ . \tag{2.8.16}$$

This relation is difficult to invert explicitly to isolate K, since matrix exponentials do not commute in general. To tackle this, we expand the matrix $v := v^a\lambda^a/2$ as a series:

$$v = \sum_{k=0}^{+\infty} v_k \ , \quad v_k \propto \phi^k \ , \tag{2.8.17}$$

where the proportionality only refers to a scalar multiplication ($\phi \to \lambda\phi \Rightarrow v_k \to \lambda^k v_k$).

The procedure will first consist in determining v_0 by setting $v = v_0 + \mathcal{O}(\phi)$ and using $u = I_d + \mathcal{O}(\phi)$ in Eq. (2.8.16). Then, the idea is to iteratively determine v_n from all v_k with $k < n$, by eliminating all terms of order $\mathcal{O}(\phi^{n+1})$ in the series expansion of Eq. (2.8.16).

Determination of v_0

$$\begin{aligned} & KuL^\dagger = RuK^\dagger \\ \Leftrightarrow\ & (I_d - iv_0 + \mathcal{O}(\phi))\,(I_d + \mathcal{O}(\phi))\left(I_d + i\theta_L^a\frac{\lambda^a}{2}\right) = \left(I_d - i\theta_R^a\frac{\lambda^a}{2}\right)(I_d + \mathcal{O}(\phi))\,(I_d + iv_0 + \mathcal{O}(\phi)) \\ \Leftrightarrow\ & I_d - iv_0 + i\theta_L^a\frac{\lambda^a}{2} = I_d - i\theta_R^a\frac{\lambda^a}{2} + iv_0 + \mathcal{O}(\phi) \\ \Leftrightarrow\ & v_0 = \frac{\theta_R^a + \theta_L^a}{2}\frac{\lambda^a}{2} \ . \end{aligned} \tag{2.8.18}$$

Since the λ^a form a basis, we deduce:

$$v^a = \frac{\theta_L^a + \theta_R^a}{2} + \mathcal{O}(\phi) \ . \tag{2.8.19}$$

Recurrence relation

We use the relation

$$KuL^\dagger = RuK^\dagger \ , \tag{2.8.20}$$

with

$$\begin{aligned} KuL^\dagger &= \left(I_d - i\sum_{k=0}^{n} v_k + \mathcal{O}(\phi^{n+1})\right)\left(\sum_{j=0}^{+\infty}\left(\frac{i}{2F_0}\right)^j \frac{\phi^j}{j!}\right)\left(I_d + i\theta_L^a \frac{\lambda^a}{2}\right) \\ &= -i\sum_{k=0}^{n}\sum_{j=0}^{n-k}\left(\frac{i}{2F_0}\right)^j v_k \frac{\phi^j}{j!} + i\theta_L^a \sum_{j=0}^{n}\left(\frac{i}{2F_0}\right)^j \frac{\phi^j}{j!}\frac{\lambda^a}{2} + \mathcal{O}(\phi^{n+1}) \ , \end{aligned} \tag{2.8.21}$$

and

$$\begin{aligned} RuK^\dagger &= \left(I_d - i\theta_R^a \frac{\lambda^a}{2}\right)\left(\sum_{j=0}^{+\infty}\left(\frac{i}{2F_0}\right)^j \frac{\phi^j}{j!}\right)\left(I_d + i\sum_{k=0}^{n} v_k + \mathcal{O}(\phi^{n+1})\right) \\ &= i\sum_{k=0}^{n}\sum_{j=0}^{n-k}\left(\frac{i}{2F_0}\right)^j \frac{\phi^j}{j!} v_k - i\theta_R^a \sum_{j=0}^{n}\left(\frac{i}{2F_0}\right)^j \frac{\lambda^a}{2}\frac{\phi^j}{j!} + \mathcal{O}(\phi^{n+1}) \ . \end{aligned} \tag{2.8.22}$$

This allows us to write

$$v_n = -\frac{1}{2}\sum_{k=0}^{n-1}\sum_{j=0}^{n-k}\left(\frac{i}{2F_0}\right)^j \frac{\{v_k;\phi^j\}}{j!} + \frac{\theta_L^a}{2}\sum_{j=0}^{n}\left(\frac{i}{2F_0}\right)^j \frac{\phi^j}{j!}\frac{\lambda^a}{2} + \frac{\theta_R^a}{2}\sum_{j=0}^{n}\left(\frac{i}{2F_0}\right)^j \frac{\lambda^a}{2}\frac{\phi^j}{j!} + \mathcal{O}(\phi^{n+1}) \ . \tag{2.8.23}$$

In the previous equation, it seems that v_n is not proportional to ϕ^n. However, this is because simplifications occur among the terms involving v_k. Keeping only the terms proportional to ϕ^n, we find

$$v_n = -\frac{1}{2}\sum_{k=0}^{n-1}\left(\frac{i}{2F_0}\right)^{n-k} \frac{\{v_k;\phi^{n-k}\}}{(n-k)!} + \frac{\theta_L^a}{2}\left(\frac{i}{2F_0}\right)^n \frac{\phi^n}{n!}\frac{\lambda^a}{2} + \frac{\theta_R^a}{2}\left(\frac{i}{2F_0}\right)^n \frac{\lambda^a}{2}\frac{\phi^n}{n!} \ . \tag{2.8.24}$$

Determination of v_1

$$\begin{aligned} v_1 &= \frac{i}{4F_0}\left(-2\{v_0;\phi\} + \theta_L^a \phi\lambda^a + \theta_R^a \lambda^a \phi\right) = \frac{i}{4F_0}\left(-\frac{\theta_R^a + \theta_L^a}{2}\{\lambda^a;\phi\} + \theta_L^a \phi\lambda^a + \theta_R^a \lambda^a\phi\right) \\ &= \frac{i}{8F_0}(\theta_L^a - \theta_R^a)[\phi;\lambda^a] = \frac{i}{8F_0}(\theta_L^a - \theta_R^a)\phi^b[\lambda^b;\lambda^a] \\ &= \frac{1}{4F_0}(\theta_R^a - \theta_L^a) f^{cba}\phi^b\lambda^c \ . \end{aligned} \tag{2.8.25}$$

This allows us to write

$$v^a\lambda^a = 2(v_0 + v_1) + \mathcal{O}(\phi^2) = \frac{\theta_L^a}{2}\left(\lambda^a - \frac{f^{\lambda\phi a}}{2F_0}\right) + \frac{\theta_R^a}{2}\left(\lambda^a + \frac{f^{\lambda\phi a}}{2F_0}\right) + \mathcal{O}(\phi^2) \tag{2.8.26}$$

where

$$f^{\lambda\phi a} = f^{cba}\lambda^c\phi^b = \frac{i}{2}[\lambda^a;\phi] \ . \tag{2.8.27}$$

It is possible to determine the v_k for $k > 1$ in the same way. However, since they will not be needed in the following, we will restrict ourselves to the expression obtained in Eq. (2.8.26).

2.8.3.2 Kinetic part

Under an infinitesimal transformation, the baryon field B transforms as

$$B \to KBK^\dagger = \left(1 + iv^b\frac{\lambda^b}{2}\right)B\left(1 - i\frac{v^b\lambda^b}{2}\right) = B + iv^b\left[\frac{\lambda^b}{2};B\right], \tag{2.8.28}$$

$$\bar{B} \to K^\dagger\bar{B}K = \bar{B} - iv^b\left[\bar{B};\frac{\lambda^b}{2}\right]. \tag{2.8.29}$$

We now consider the variation of the kinetic term under this transformation:

$$\begin{aligned}\delta\left(\mathrm{Tr}\left[\bar{B}i\not{D}B\right]\right) &\supset \mathrm{Tr}\left[\bar{B}i\not{D}\delta B\right] + \mathrm{Tr}\left[\bar{B}i\delta\not{D}B\right] \\ &\supset \mathrm{Tr}\left(\bar{B}i\gamma^\mu i\partial_\mu v^b\left[\frac{\lambda^b}{2},B\right]\right) + \mathrm{Tr}\left(\bar{B}i\gamma^\mu[\delta\Gamma_\mu,B]\right) \\ &\supset \mathrm{Tr}\left(\bar{B}i\gamma^\mu i\partial_\mu v^b\left[\frac{\lambda^b}{2},B\right]\right) + \mathrm{Tr}\left(\bar{B}i\gamma^\mu\left[\delta\left(\frac{u^\dagger\partial_\mu u + u\partial_\mu u^\dagger}{2}\right),B\right]\right)\ .\end{aligned} \tag{2.8.30}$$

Applying the infinitesimal transformations of u as given in Eq. (2.8.16), we obtain:

$$u^\dagger\partial_\mu u \to u^\dagger(\partial_\mu K)u + \partial_\mu L^\dagger\ , \tag{2.8.31}$$
$$u^\dagger\partial_\mu u \to u^\dagger(\partial_\mu R)u + \partial_\mu K^\dagger\ , \tag{2.8.32}$$

and similarly,

$$u\partial_\mu u^\dagger \to u(\partial_\mu L)u^\dagger + \partial_\mu K^\dagger\ , \tag{2.8.33}$$
$$u\partial_\mu u^\dagger \to u(\partial_\mu K)u^\dagger + \partial_\mu R^\dagger\ . \tag{2.8.34}$$

Using Eqs. (2.8.31) and (2.8.33), we find

$$u^\dagger\partial_\mu u + u\partial_\mu u^\dagger \to u^\dagger(\partial_\mu K)u + (\partial_\mu L^\dagger) + u(\partial_\mu L)u^\dagger + (\partial_\mu K^\dagger)\ . \tag{2.8.35}$$

Similarly, from Eqs. (2.8.32) and (2.8.34),

$$u^\dagger\partial_\mu u + u\partial_\mu u^\dagger \to u^\dagger(\partial_\mu R)u + (\partial_\mu K^\dagger) + u(\partial_\mu K)u^\dagger + (\partial_\mu R^\dagger)\ . \tag{2.8.36}$$

For a left transformation, using the relation (2.8.26) in Eq. (2.8.36), we obtain

$$u^\dagger\partial_\mu u + u\partial_\mu u^\dagger \to \frac{i}{2}\frac{\partial_\mu\theta_L^b}{2}\left(\lambda^b - \frac{f^{\lambda\phi b}}{2F_0}\right) + u\left(-\frac{i}{2}\frac{\partial_\mu\theta_L^b}{2}\left(\lambda^b - \frac{f^{\lambda\phi b}}{2F_0}\right)\right)u^\dagger\ . \tag{2.8.37}$$

Thus, the left current reads:

$$(J_K)_L^{b,\mu} = \frac{1}{4}\mathrm{Tr}\left(\bar{B}\gamma^\mu\left[\lambda^b - \frac{f^{\lambda\phi b}}{2F_0};B\right]\right) - \frac{1}{8}\mathrm{Tr}\left(\bar{B}\gamma^\mu\left[\left(\lambda^b - \frac{f^{\lambda\phi b}}{2F_0}\right) - u\left(\lambda^b - \frac{f^{\lambda\phi b}}{2F_0}\right)u^\dagger;B\right]\right)\ . \tag{2.8.38}$$

Similarly, for a right transformation, using relation (2.8.26) in Eq. (2.8.35), we find

$$(J_K)_R^{b,\mu} = \frac{1}{4}\mathrm{Tr}\left(\bar{B}\gamma^\mu\left[\lambda^b + \frac{f^{\lambda\phi b}}{2F_0};B\right]\right) - \frac{1}{8}\mathrm{Tr}\left(\bar{B}\gamma^\mu\left[\left(\lambda^b + \frac{f^{\lambda\phi b}}{2F_0}\right) - u\left(\lambda^b + \frac{f^{\lambda\phi b}}{2F_0}\right)u^\dagger;B\right]\right)\ . \tag{2.8.39}$$

2.8.3.3 D and F parts

For the D and F parts, the relevant terms are

$$\mathcal{L}_B \supset -\frac{D}{2}\mathrm{Tr}\left(\bar{B}\gamma^\mu\gamma_5\{u_\mu,B\}\right) - \frac{F}{2}\mathrm{Tr}\left(\bar{B}\gamma^\mu\gamma_5[u_\mu,B]\right)\ , \tag{2.8.40}$$

where

$$u_\mu \supset i\left[u^\dagger\partial_\mu u - u\partial_\mu u^\dagger\right], \tag{2.8.41}$$

Using the transformations derived earlier (Eqs. (2.8.31), (2.8.33), (2.8.32), and (2.8.34)), we find:

$$u^\dagger\partial_\mu u - u\partial_\mu u^\dagger \to u^\dagger(\partial_\mu K)u + (\partial_\mu L^\dagger) - u(\partial_\mu L)u^\dagger - (\partial_\mu K^\dagger)\ , \tag{2.8.42}$$
$$u^\dagger\partial_\mu u - u\partial_\mu u^\dagger \to u^\dagger(\partial_\mu R)u + (\partial_\mu K^\dagger) - u(\partial_\mu K)u^\dagger - (\partial_\mu R^\dagger)\ . \tag{2.8.43}$$

Proceeding analogously to the kinetic part, for a left transformation, we obtain:

$$u^\dagger\partial_\mu u - u\partial_\mu u^\dagger \to \frac{i}{4}\partial_\mu\theta_b^L\left(\left(\lambda^b - \frac{f^{\lambda\phi b}}{2F_0}\right) + u\left(\lambda^b - \frac{f^{\lambda\phi b}}{2F_0}\right)u^\dagger\right)\ , \tag{2.8.44}$$

thus leading to the left-handed currents:

$$(J_D)^{b,\mu}_L = +\frac{D}{8}\mathrm{Tr}\left(\bar{B}\gamma^\mu\gamma_5\left\{\left(\lambda^b - \frac{f^{\lambda\phi b}}{2F_0}\right) + u\left(\lambda^b - \frac{f^{\lambda\phi b}}{2F_0}\right)u^\dagger; B\right\}\right) , \tag{2.8.45}$$

$$(J_F)^{b,\mu}_L = +\frac{F}{8}\mathrm{Tr}\left(\bar{B}\gamma^\mu\gamma_5\left[\left(\lambda^b - \frac{f^{\lambda\phi b}}{2F_0}\right) + u\left(\lambda^b - \frac{f^{\lambda\phi b}}{2F_0}\right)u^\dagger; B\right]\right) . \tag{2.8.46}$$

Similarly, for a right transformation, we find:

$$u^\dagger\partial_\mu u - u\partial_\mu u^\dagger \to -\frac{i}{4}\partial_\mu\theta^R_b\left(\left(\lambda^b + \frac{f^{\lambda\phi b}}{2F_0}\right) + u^\dagger\left(\lambda^b + \frac{f^{\lambda\phi b}}{2F_0}\right)u\right) , \tag{2.8.47}$$

resulting in the right-handed currents:

$$(J_D)^{b,\mu}_R = -\frac{D}{8}\mathrm{Tr}\left(\bar{B}\gamma^\mu\gamma_5\left\{\left(\lambda^b + \frac{f^{\lambda\phi b}}{2F_0}\right) + u^\dagger\left(\lambda^b + \frac{f^{\lambda\phi b}}{2F_0}\right)u; B\right\}\right) , \tag{2.8.48}$$

$$(J_F)^{b,\mu}_R = -\frac{F}{8}\mathrm{Tr}\left(\bar{B}\gamma^\mu\gamma_5\left[\left(\lambda^b + \frac{f^{\lambda\phi b}}{2F_0}\right) + u^\dagger\left(\lambda^b + \frac{f^{\lambda\phi b}}{2F_0}\right)u; B\right]\right) . \tag{2.8.49}$$

The transformations (2.8.42) and (2.8.43) can alternatively be combined, making use of Eqs. (2.8.34) and (2.8.32), yielding:

$$u^\dagger\partial_\mu u - u\partial_\mu u^\dagger \to u^\dagger(\partial_\mu R)u + \partial_\mu K^\dagger - u(\partial_\mu L)u^\dagger - \partial_\mu K^\dagger = u^\dagger(\partial_\mu R)u - u(\partial_\mu L)u^\dagger . \tag{2.8.50}$$

Substituting this into the expressions for the currents, we obtain:

$$(J_D)^{b,\mu}_{L/R} + (J_F)^{b,\mu}_{L/R} = \pm\frac{D}{4}\mathrm{Tr}\left(\bar{B}\gamma^\mu\gamma_5\left\{u^\dagger\lambda^b u; B\right\}\right) \pm \frac{F}{4}\mathrm{Tr}\left(\bar{B}\gamma^\mu\gamma_5\left[u^\dagger\lambda^b u; B\right]\right) . \tag{2.8.51}$$

These procedures are theoretically equivalent. However, when comparing the two approaches, their difference does not vanish exactly, but rather:

$$\Delta(J_{D,F})^{b,\mu}_{L/R} = \mathcal{O}(\phi^2) , \tag{2.8.52}$$

which is consistent with the fact that the computation of K was performed only up to $\mathcal{O}(\phi^2)$.

For currents involving two baryons and more than two mesons, a higher-order expansion of K in ϕ would be necessary.

Importantly, the expression in Eq. (2.8.51) does not explicitly depend on the detailed form of K. This independence results from a cancellation of terms involving $\partial_\mu K^\dagger$ in Eq. (2.8.50). In contrast, the kinetic part of the Lagrangian explicitly depends on K, introducing an $\mathcal{O}(\phi^2)$ correction to the total baryonic Lagrangian.

2.8.3.4 Baryonic currents: sum of all terms

The total current is thus given by

$$J^{b,\mu}_{L/R} = (J_K)^{b,\mu}_{L/R} + (J_D)^{b,\mu}_{L/R} + (J_F)^{b,\mu}_{L/R} . \tag{2.8.53}$$

2.9 Lagrangian mediating weak processes

In addition to the strong interaction contributions, the SM includes a Lagrangian that mediates weak processes [Cor+24; Cro67; KMW90].

The non-leptonic weak interaction is constructed to preserve the same chiral symmetry properties as the underlying quark-level interaction. The dominant contributions at low energy arise from effective operators transforming as $(\underline{8}_L,\ \underline{1}_R)$ and $(\underline{27}_L,\ \underline{1}_R)$ under chiral symmetry. At leading order $\mathcal{O}(p^2)$, the weak chiral Lagrangian can be written as

$$\mathcal{L}_{weak} = G_8 O_8 + G'_8 O'_8 + G^{(1/2)}_{27} O^{(1/2)}_{27} + G^{(3/2)}_{27} O^{(3/2)}_{27} + \text{h.c.} . \tag{2.9.1}$$

Using L_μ and S, which are the chiral representations of the left-handed current $\bar{q}\gamma_\mu P_L q$ and the scalar current $\bar{q}_L M_q q_R + \text{h.c.}$, respectively, we define for the mesonic sector:

$$L_\mu = i\frac{F_0^2}{2}(D_\mu U)^\dagger U \ , \tag{2.9.2}$$

$$S = B_0 F_0^2 (U^\dagger M_q + M_q^\dagger U) \ . \tag{2.9.3}$$

To derive L_μ, we consider the Noether current associated with $SU(3)_L$:[12]

$$J_L^{b,\mu} = \frac{\partial \delta\mathcal{L}}{\partial \partial_\mu \epsilon_L^b} \ , \tag{2.9.4}$$

and make the substitution $\lambda^b/2 \to \lambda_{ij}$ with $(\lambda_{ij})_{ab} = \delta_{ia}\delta_{jb}$, leading to

$$(L^\mu)_{ji} = (J_L^{b,\mu})|_{\lambda^b/2 \to \lambda_{ij}} \ . \tag{2.9.5}$$

For mesons, this gives

$$\begin{aligned}(L^\mu)_{ji} &= i\frac{F_0^2}{2}\ \text{Tr}\left[\frac{\lambda^b}{2}(D^\mu U)^\dagger U\right]\Big|_{\lambda^b/2\to\lambda_{ij}} = i\frac{F_0^2}{2}\text{Tr}\left[\lambda_{ij}(D^\mu U)^\dagger U\right] = i\frac{F_0^2}{2}(\lambda_{ij})_{ab}((D^\mu U)^\dagger U)_{ba} \\ &= i\frac{F_0^2}{2}\delta_{ia}\delta_{jb}((D^\mu U)^\dagger U)_{ba} = i\frac{F_0^2}{2}((D^\mu U)^\dagger U)_{ji} \ .\end{aligned} \tag{2.9.6}$$

The effective coefficients G_i are defined as

$$G_i = -\frac{4G_F}{\sqrt{2}}V_{ud}^* V_{us}\left(g_i - \frac{V_{tb}^* V_{ts}}{V_{ud}^* V_{us}} g_i^t\right) \simeq -\frac{4G_F}{\sqrt{2}}V_{ud}^* V_{us}\, g_i \ , \tag{2.9.7}$$

where G_F is the Fermi constant, and $V_{ud}^* V_{us}$ is the relevant CKM factor associated with the $s \to d$ transition. The parameter g_i is a low-energy constant encoding non-perturbative QCD effects.

The $(\underline{8}_L,\ \underline{1}_R)$ operators are given by

$$O_8 = (L_\mu L^\mu)_{32} \ , \quad O_8' = S_{32} \ . \tag{2.9.8}$$

The $(\underline{27}_L,\ \underline{1}_R)$ operators with isospin change $\Delta I = \frac{1}{2}$ and $\Delta I = \frac{3}{2}$ take the form

$$O_{27}^{(1/2)} = (L_\mu)_{32}(L^\mu)_{11} + (L_\mu)_{31}(L^\mu)_{12} + 2(L_\mu)_{32}(L^\mu)_{22} - 3(L_\mu)_{32}(L^\mu)_{33} \ , \tag{2.9.9}$$

$$O_{27}^{(3/2)} = (L_\mu)_{32}(L^\mu)_{11} + (L_\mu)_{31}(L^\mu)_{12} - (L_\mu)_{32}(L^\mu)_{22} \ . \tag{2.9.10}$$

Using the relation $g_{27} = 9g_{27}^{(1/2)} = \frac{9}{5}g_{27}^{(3/2)}$, we obtain the equivalent compact expression:

$$G_{27}^{(1/2)}O_{27}^{(1/2)} + G_{27}^{(1/2)}O_{27}^{(1/2)} = G_{27}\left((L_\mu)_{32}(L^\mu)_{11} + \frac{2}{3}(L_\mu)_{31}(L^\mu)_{12} - \frac{1}{3}(L_\mu)_{32}\text{Tr}[L^\mu]\right) \tag{2.9.11}$$

and since $\text{Tr}[L^\mu] = 0$, the last term vanishes.

The constants g_8 and g_{27} must be extracted from experimental data or computed non-perturbatively [BGI10]. From the decay $K \to 2\pi$, one finds:

$$|g_8| \simeq 5.1 \ , \quad \arg(g_8) \simeq -1.7 \times 10^{-4} \ , \quad |g_{27}| \simeq 0.3 \ . \tag{2.9.12}$$

Since $|g_8| \simeq 17 \times |g_{27}|$, one can neglect the 27-plet contribution when an octet contribution is present.

The weak Lagrangian is also suppressed relative to the strong interaction by a factor of $G_F F_0^2 \sim 10^{-7}$. Therefore, whenever strong interactions contribute, weak effects are typically negligible.

The scalar term S can be absorbed into a redefinition of the meson masses, slightly shifting them relative to their purely strong-interaction values. This has no significant impact at leading order.

In conclusion, the leading weak Lagrangian is well approximated by:

$$\mathcal{L}_{aBU}^w = \frac{4G_F}{\sqrt{2}}V_{us}V_{ud}^* g_8 (L_\mu L^\mu)_{32} + \text{h.c.} \ , \tag{2.9.13}$$

with

$$(L^\mu)_{ji} = (J_L^{(U)})_{ij}^\mu + (J_L^{(BU)})_{ij}^\mu = \left((J_L^{(U)})^{b,\mu} + (J_L^{(BU)})^{b,\mu}\right)|_{\lambda^b/2\to\lambda_{ij}} \ . \tag{2.9.14}$$

[12] Using the trick of promoting the global symmetry transformations to local ones.

2.10 Axionic Lagrangian

2.10.1 Axion-quark interaction

2.10.1.1 General expression

Before defining axion-hadron interactions, we begin with the general form of the axion-quark interaction for light quarks, as given in [Bau+21]:

$$\begin{aligned}\mathcal{L} =&\mathcal{L}_{QCD} + \frac{1}{2}(\partial_\mu a)(\partial^\mu a) - \frac{1}{2}m_a^2 a^2 + c_{aGG}\frac{\alpha_s}{4\pi}\frac{a}{f_a}G^b_{\mu\nu}\tilde{G}^{\mu\nu,b} + c_{a\gamma\gamma}\frac{\alpha_{e.m.}}{4\pi}\frac{a}{f_a}F_{\mu\nu}\tilde{F}^{\mu\nu} \\ &+ \frac{\partial_\mu a}{f_a}\left(\bar{q}_L k_L \gamma^\mu q_L + \bar{q}_R k_R \gamma^\mu q_R\right) \ .\end{aligned} \tag{2.10.1}$$

The axion-quark couplings are encoded in the matrices $k_{R,L}$. Imposing charge conservation and Hermiticity, these matrices can be generically written as:

$$k_{R,L} = \begin{pmatrix} k_{11} & 0 & 0 \\ 0 & k_{22} & k_{23} \\ 0 & \bar{k}_{23} & k_{33} \end{pmatrix}_{R,L} \ . \tag{2.10.2}$$

We do not use the most general Lagrangian from Section 1.2, since we are working within ChPT, i.e., below the QCD confinement scale Λ_{QCD}. Consequently, only the three lightest quarks contribute. For notational simplicity, we label them $1, 2, 3$ instead of u, d, s, respectively.

All axionic couplings are normalized by f_a. Therefore, multiplying all couplings by a constant is equivalent to rescaling f_a by that same constant. Exploiting this freedom, we can normalize f_a such that $|c_{aGG}| = \frac{1}{2}$, without loss of generality.

For standard theoretical models such as Kim-Shifman-Vainshtein-Zakharov (KSVZ) and Dine-Fischler-Srednicki-Zhitnitsky (DFSZ), the value is $c_{aGG} = -\frac{1}{2}$,[13] however in an agnostic framework, $c_{aGG} = +\frac{1}{2}$ is also possible. Nevertheless, as we will see later, axion-matter couplings can be written as $\hat{k} = k^{(\text{IR})} + k^{(\text{UV})}$, where $k^{(\text{UV})}$ denotes the UV contribution and $k^{(\text{IR})}$ the Infrared (IR) contribution, proportional to c_{aGG}, which we will compute explicitly. Therefore, for a specific model providing $k^{(\text{UV})}$, one can predict $\hat{k}$; but for a model agnostic to the UV contribution, one can work directly with $\hat{k}$, thereby eliminating the ambiguity between $c_{aGG} = \pm\frac{1}{2}$, which only arises when the UV and IR pieces are treated separately.

2.10.1.2 Vector and axial decomposition

The axion-quark interaction can be rewritten in terms of vector and axial matrices:

$$\begin{aligned}\mathcal{L}_{aqq} =&\frac{\partial_\mu a}{f_a}\left(\bar{q}_L k_L \gamma^\mu q_L + \bar{q}_R k_R \gamma^\mu q_R\right) = \frac{\partial_\mu a}{f_a}\bar{q}\left(k_L P_R \gamma^\mu P_L + k_R P_L \gamma^\mu P_R\right) q \\ =&\frac{\partial_\mu a}{f_a}\bar{q}\gamma^\mu\left(k_L P_L^2 + k_R P_R^2\right) q = \frac{\partial_\mu a}{f_a}\bar{q}\gamma^\mu\left(k_L P_L + k_R P_R\right) q \\ =&\frac{\partial_\mu a}{2f_a}\bar{q}\gamma^\mu\left((k_R + k_L) + (k_R - k_L)\gamma_5\right) q \ .\end{aligned} \tag{2.10.3}$$

We define:

$$k_V = k_R + k_L, \quad k_A = k_R - k_L \ . \tag{2.10.4}$$

Using the Dirac equation, the Lagrangian $\mathcal{L}_{aqq}$ can also be expressed as:

$$\mathcal{L}_{aqq} = \partial_\mu\left(\frac{a}{f_a}\bar{q}\gamma^\mu\left(k_V + k_A\gamma_5\right) q\right) + i\frac{a}{f_a}\bar{q}\left([M_q; k_V] + \{M_q; k_A\}\gamma_5\right) q \ . \tag{2.10.5}$$

The total derivative term does not affect the dynamics. Since M_q is diagonal, the diagonal part of k_V in the commutator vanishes from the Lagrangian. This leaves 7 parameters:

1. Three diagonal axial couplings $(k_A)_{ii}$.
2. Four off-diagonal couplings: $|(k_{V,A})_{23}|$ and $\arg((k_{V,A})_{23})$.

[13] The sign difference with [Di +23] originates from the sign convention for ϵ^{0123}, as mentioned in Section 1.3.3.

The objective of this work is to constrain these 7 parameters in two benchmark scenarios:

- QCD axion: $m_a \ll m_q$ and $f_a \gtrsim 10^9$ GeV.
- Axion-like Particle (ALP): $m_a \sim 1$ MeV $-$ GeV and $f_a \gtrsim 1$ TeV.

2.10.1.3 Chiral rotation to eliminate c_{aGG}

Below the hadronization scale, it is convenient to eliminate the $aG\tilde{G}$ term in favor of an axion-dependent quark mass matrix [GKR86]. This can be achieved through a chiral rotation of the quark fields:

$$q(x) \to q'(x) = \exp\left(-i(\delta + \kappa\gamma_5)c_{aGG}\frac{a(x)}{f_a}\right) q(x) \ . \tag{2.10.6}$$

where δ and κ are Hermitian matrices, which can be chosen diagonal in the quark mass basis. This rotation will induce IR contributions proportional to c_{aGG}. This transformation modifies all Lagrangians involving quarks:

$$\mathcal{L} = \bar{q}i\not{D}q - \bar{q}_R(M_q)^\dagger q_L - \bar{q}_L M_q q_R + \frac{\partial_\mu a}{f_a}(\bar{q}_L k_L \gamma^\mu q_L + \bar{q}_R k_R \gamma^\mu q_R) \ . \tag{2.10.7}$$

Differentiating the rotated field, we obtain:

$$\partial_\mu q' = \partial_\mu \left(\exp(-i(\delta + \kappa\gamma_5)c_{aGG}a/f_a)q\right) = \exp(-i(\delta + \kappa\gamma_5)c_{aGG}a/f_a)\partial_\mu q - ic_{aGG}\frac{\partial_\mu a}{f_a}(\delta + \kappa\gamma_5)q' \ . \tag{2.10.8}$$

This leads to:

$$\begin{aligned}
\bar{q}'i\not{D}q' &= \bar{q}i\not{D}q + c_{aGG}\frac{\partial_\mu a}{f_a}\bar{q}'\gamma^\mu(\delta + \kappa\gamma_5)q' \\
&= \bar{q}i\not{D}q + c_{aGG}\frac{\partial_\mu a}{f_a}\left(\bar{q}'_L\gamma^\mu(\delta + \kappa\gamma_5)q'_L + \bar{q}'_R\gamma^\mu(\delta + \kappa\gamma_5)q'_R\right) \\
&= \bar{q}i\not{D}q + c_{aGG}\frac{\partial_\mu a}{f_a}\left(\bar{q}'_L\gamma^\mu(\delta - \kappa)q'_L + \bar{q}'_R\gamma^\mu(\delta + \kappa)q'_R\right) \ ,
\end{aligned} \tag{2.10.9}$$

where we used:

$$(\delta + \kappa\gamma_5)P_{R/L} = (\delta + \kappa\gamma_5)\frac{1 \pm \gamma_5}{2} = \frac{\delta + \kappa\gamma_5 \pm \delta\gamma_5 \pm \kappa}{2} = (\delta \pm \kappa)\frac{1 \pm \gamma_5}{2} = (\delta \pm \kappa)P_{R/L} \ , \tag{2.10.10}$$

and the identity:

$$P_{R/L}e^{a+b\gamma_5} = e^{a\pm b}P_{R/L} \ , \tag{2.10.11}$$

which follows from the series expansion of the exponential and the property $\gamma_5^2 = 1$.

Defining $\Phi^\pm = c_{aGG}(\delta \pm \kappa)$, the Lagrangian after the chiral rotation becomes:

$$\begin{aligned}
\mathcal{L} =& \bar{q}'i\not{D}q' - \bar{q}'_R(M_q)^\dagger q'_L - \bar{q}'_L M_q q'_R + \frac{\partial_\mu a}{f_a}(\bar{q}'_L k_L \gamma^\mu q'_L + \bar{q}'_R k_R \gamma^\mu q'_R) \\
=& \bar{q}i\not{D}q - \bar{q}'_R(M_q)^\dagger q'_L - \bar{q}'_L M_q q'_R + \frac{\partial_\mu a}{f_a}(\bar{q}'_L(k_L + \Phi^-)\gamma^\mu q'_L + \bar{q}'_R(k_R + \Phi^+)\gamma^\mu q'_R) \ .
\end{aligned} \tag{2.10.12}$$

To express everything in terms of the original quark field q, we define:

$$\mathcal{L} = \bar{q}i\not{D}q - \bar{q}_R\hat{M}_q^\dagger(a)q_L - \bar{q}_L\hat{M}_q(a)q_R + \frac{\partial_\mu a}{f_a}(\bar{q}_L\hat{k}_L(a)\gamma^\mu q_L + \bar{q}_R\hat{k}_R(a)\gamma^\mu q_R) \ . \tag{2.10.13}$$

This leads to the following expressions for the field-dependent couplings:

$$\begin{aligned}
\hat{k}_L(a) &= \exp\big(i\Phi^- a/f_a\big)(k_L + \Phi^-)\exp\big(-i\Phi^- a/f_a\big) \ , \\
\hat{k}_R(a) &= \exp\big(i\Phi^+ a/f_a\big)(k_R + \Phi^+)\exp\big(-i\Phi^+ a/f_a\big) \ , \\
\hat{M}_q(a) &= \exp(-2i\kappa c_{aGG}a/f_a)M_q \ .
\end{aligned} \tag{2.10.14}$$

To obtain these expressions one can use Eq. (2.10.11), which allows us to eliminate γ_5 from the exponentials.

Using standard properties of matrix exponentials, one finds:

$$(\hat{k}_{R/L})_{ii} = (k_{R/L})_{ii} + (\Phi^{\pm})_{ii} \ , \quad (\hat{k}_{R/L})_{23} = e^{i((\Phi^{\pm})_{22}-(\Phi^{\pm})_{33})a/f_a}(k_{R/L})_{23} \ . \tag{2.10.15}$$

The modification to the axion-quark couplings arises directly from the chiral rotation. However, this change also induces loop-level corrections to the axion-gluon-gluon and axion-photon-photon couplings, as illustrated in Fig. 2.4.

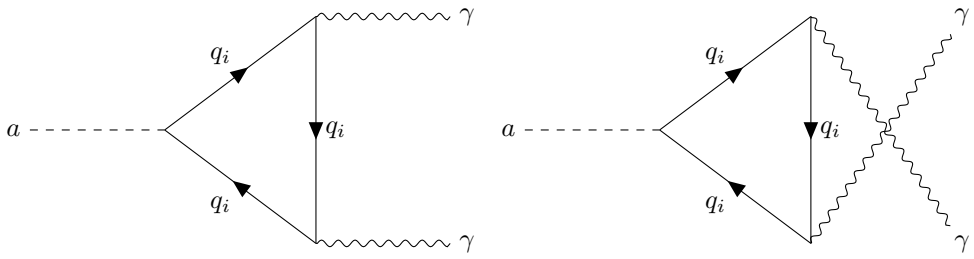

Figure 2.4: One-loop Feynman diagrams contributing to the coupling $\hat{c}_{a\gamma\gamma}$ via the process $a \to \gamma\gamma$.

The resulting effective couplings are:[14]

$$\hat{c}_{aGG} = c_{aGG}(1 - \mathrm{Tr}[\kappa]) \tag{2.10.16}$$

$$\hat{c}_{a\gamma\gamma} = c_{a\gamma\gamma} - 2N_c c_{aGG}\mathrm{Tr}(Q^2\kappa) = c_{a\gamma\gamma} - 6c_{aGG}\mathrm{Tr}(Q^2\kappa) \tag{2.10.17}$$

where $Q = \mathrm{diag}(q_u; q_d; q_s)$ is the quark electric charge matrix. The derivation is given in Appendix B.7. As seen in Eq. (2.10.16), by imposing $\mathrm{Tr}(\kappa) = 1$, the axion-gluon-gluon coupling is eliminated as wanted.

By considering the interaction between charged leptons and photons, we obtain an additional contribution to the axion-lepton-lepton interaction via the diagram shown in Fig. 2.5.

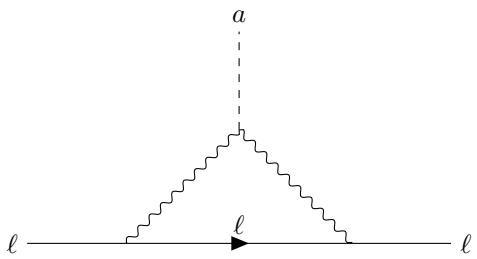

Figure 2.5: One-loop Feynman diagram contributing to the axion-lepton-lepton coupling.

This results in a correction to the axial coupling of the lepton $i \in \{e, \mu, \tau\}$:

$$(\hat{k}_A^{\ell})_{ii} = (k_A^{\ell})_{ii} - \frac{3\alpha^2}{8\pi^2}\left(c_{a\gamma\gamma}\ln\left(\frac{f_a}{\mu}\right) - 6c_{aGG}\mathrm{Tr}(Q^2\kappa)\ln\left(\frac{\Lambda_{\mathrm{QCD}}}{\mu}\right)\right) \ . \tag{2.10.18}$$

This correction consists of three terms:

1. the tree-level UV contribution $(k_A^{\ell})_{ii}$,
2. the one-loop UV contribution proportional to $c_{a\gamma\gamma}$, and
3. the one-loop IR contribution proportional to c_{aGG}[15].

[14] The sign of the loop contribution depends on the convention adopted for the Levi-Civita tensor. In our case, we use $\epsilon^{0123} = +1$, as in [Bau+21]. However, adopting the opposite convention, $\epsilon^{0123} = -1$, as in [Di +23], leads to a sign flip, which does not affect the final results.

[15] This IR term must be removed from the high-energy expression, i.e., when the renormalization scale μ is above the QCD confinement scale Λ_{QCD}.

The loop calculation yields a logarithmic divergence with natural UV cutoff f_a[16] and a natural IR cutoff $\Lambda_{\rm QCD} \sim 200\,\text{MeV}$. Moreover, the renormalization scale μ should be chosen to match the relevant energy of the physical process considered. In this context, a natural choice is $\mu = m_i$, implying that the IR contribution does not affect the τ lepton, since $\Lambda_{\rm QCD} < m_\tau$. Finally, note that the one-loop correction in Eq. (2.10.18) is suppressed by the factor $\frac{3\alpha^2}{8\pi^2} \simeq 2 \times 10^{-6}$.

Expanding the quark mass matrix $\hat{M}_q(a)$ from Eq. (2.10.15) in the mesonic Lagrangian,

$$\mathcal{L}_U = \frac{F_0^2}{4}\text{Tr}[D_\mu U (D^\mu U)^\dagger] + \frac{F_0^2 B_0}{2}\text{Tr}[\hat{M}_q(a) U^\dagger + U \hat{M}_q^\dagger(a)] \,, \tag{2.10.19}$$

one finds that the axion mass receives a shift:

$$\hat{m}_a^2 = m_a^2 + 2c_{aGG}^2 \frac{F_0^2 B_0}{f_a^2}\text{Tr}[\{\kappa^2; M_q\}] \,. \tag{2.10.20}$$

To choose a convenient value of κ, we aim to eliminate any mixing between the axion and the neutral pion. Starting from the mixing Lagrangian:

$$\mathcal{L}_{a\pi^0} = \frac{1}{2}\partial_\mu a \partial^\mu a + \frac{1}{2}\partial_\mu \pi^0 \partial^\mu \pi^0 + \epsilon_{\pi a}^K \partial_\mu a \partial^\mu \pi^0 - \frac{1}{2} m_{\pi^0}^2 (\pi^0)^2 - \frac{1}{2} m_a^2 a^2 - \epsilon_{\pi a}^M \pi^0 a \,, \tag{2.10.21}$$

$$\mathcal{L}_{a\pi^0} = \frac{1}{2}\partial_\mu a_{phys} \partial^\mu a_{phys} + \frac{1}{2}\partial_\mu \pi^0_{phys} \partial^\mu \pi^0_{phys} - \frac{1}{2} m_{\pi^0}^2 (\pi^0_{phys})^2 - \frac{1}{2} m_a^2 a_{phys}^2 \,. \tag{2.10.22}$$

We perform a field rotation to diagonalize the kinetic and mass terms:

$$\pi^0_{phys} = \frac{\pi^0 + \theta_{\pi a} a}{\sqrt{1+\theta_{\pi a}^2}} = \pi^0 + \theta_{\pi a} a + o(\theta_{\pi a}) \,, \tag{2.10.23}$$

$$a_{phys} = \frac{a + \theta_{a\pi} \pi^0}{\sqrt{1+\theta_{a\pi}^2}} = a + \theta_{a\pi} \pi^0 + o(\theta_{a\pi}) \,, \tag{2.10.24}$$

Substituting these fields into Eq. (2.10.22) yields:

$$\mathcal{L}_{a\pi^0} = \frac{1}{2}\partial_\mu a \partial^\mu a + \frac{1}{2}\partial_\mu \pi^0 \partial^\mu \pi^0 + (\theta_{\pi a} + \theta_{a\pi}) \partial_\mu a \partial^\mu \pi^0 - \frac{1}{2} m_{\pi^0}^2 (\pi^0)^2 - \frac{1}{2} m_a^2 a^2 - (\theta_{a\pi} m_a^2 + \theta_{\pi a} m_{\pi^0}^2) \pi^0 a \,. \tag{2.10.25}$$

By comparing with Eq. (2.10.21), we identify:

$$\epsilon_{\pi a}^K = \theta_{\pi a} + \theta_{a\pi} \,, \quad \epsilon_{\pi a}^M = \theta_{\pi a} m_{\pi^0}^2 + \theta_{a\pi} m_a^2 \,, \tag{2.10.26}$$

which can be inverted to:

$$\theta_{\pi a} = \frac{1}{m_{\pi^0}^2 - m_a^2} \epsilon_{\pi a}^M - \frac{m_a^2}{m_{\pi^0}^2 - m_a^2} \epsilon_{\pi a}^K \,, \tag{2.10.27}$$

$$\theta_{a\pi} = \frac{-1}{m_{\pi^0}^2 - m_a^2} \epsilon_{\pi a}^M + \frac{m_{\pi^0}^2}{m_{\pi^0}^2 - m_a^2} \epsilon_{\pi a}^K \,. \tag{2.10.28}$$

To ensure that $\pi^0_{phys} \simeq \pi^0$, we require $\theta_{\pi a} \simeq 0$. In the case of the QCD axion, where $m_a \ll m_{\pi^0}$, this condition is satisfied as long as $\epsilon_{\pi a}^M$ remains small.

Expanding the mesonic Lagrangian in Eq. (2.10.19) using the axion-dependent quark mass matrix from Eq. (2.10.15), we obtain:

$$\epsilon_{\pi a}^M = 2 c_{aGG} F_0 B_0 (\kappa_{11} m_u - \kappa_{22} m_d) \,, \tag{2.10.29}$$

$$\epsilon_{\eta_8 a}^M = \frac{2}{\sqrt{3}} c_{aGG} F_0 B_0 (\kappa_{11} m_u + \kappa_{22} m_d - 2\kappa_{33} m_s) \,. \tag{2.10.30}$$

Eliminating the axion-π^0 and axion-η_8 mixing by imposing $\epsilon_{\pi a}^M = \epsilon_{\eta_8 a}^M = 0$, along with the condition $\text{Tr}[\kappa] = 1$ (required to eliminate the $aG\tilde{G}$ term), leads to a unique solution:

$$\kappa = \frac{M_q^{-1}}{\text{Tr}[M_q^{-1}]} \,. \tag{2.10.31}$$

[16] The fact that the coupling $\hat{k}_{ii}^\ell$ grows logarithmically with f_a may seem surprising, since as $f_a \to \infty$, axion-matter couplings should vanish. This is indeed the case here, because the physical coupling is $\hat{k}_{ii}^\ell/(2f_a)$ (see Section 1.2), which tends to zero when $f_a \to \infty$.

With this choice, setting $c_{aGG} = -\frac{1}{2}$ to remain consistent with KSVZ and DFSZ, we obtain the following numerical values:

$$((\hat{k}_V)_{11}, (\hat{k}_V)_{22}, (\hat{k}_V)_{33}) = ((k_V)_{11}, (k_V)_{22}, (k_V)_{33}) - (\delta_{11}, \delta_{22}, \delta_{33}) \tag{2.10.32}$$

$$\begin{aligned}((\hat{k}_A)_{11}, (\hat{k}_A)_{22}, (\hat{k}_A)_{33}) &= ((k_A)_{11}, (k_A)_{22}, (k_A)_{33}) - (\kappa_{11}, \kappa_{22}, \kappa_{33}) \\ &= ((k_A)_{11}, (k_A)_{22}, (k_A)_{33}) - (0.67(5), 0.31(5), 0.016(3))\end{aligned} \tag{2.10.33}$$

$$\begin{aligned}(\hat{k}_V)_{23} &= e^{i(\delta_{33}-\delta_{22})a/f_a}\,(\cos((\kappa_{33}-\kappa_{22})a/f_a)(k_V)_{23} + i\sin((\kappa_{33}-\kappa_{22})a/f_a)(k_A)_{23}) \\ &= e^{i(\delta_{33}-\delta_{22})a/f_a}\,(\cos(0.30(5)\ a/f_a)(k_V)_{23} + i\sin(0.30(5)\ a/f_a)(k_A)_{23}) \\ &= (k_V)_{23} + \mathcal{O}\left(\frac{a}{f_a}\right)\end{aligned} \tag{2.10.34}$$

$$\begin{aligned}(\hat{k}_A)_{23} &= e^{i(\delta_{33}-\delta_{22})a/f_a}\,(\cos((\kappa_{33}-\kappa_{22})a/f_a)(k_A)_{23} + i\sin((\kappa_{33}-\kappa_{22})a/f_a)(k_V)_{23}) \\ &= e^{i(\delta_{33}-\delta_{22})a/f_a}\,(\cos(0.30(5)\ a/f_a)(k_A)_{23} + i\sin(0.30(5)\ a/f_a)(k_V)_{23}) \\ &= (k_A)_{23} + \mathcal{O}\left(\frac{a}{f_a}\right)\end{aligned} \tag{2.10.35}$$

$$\hat{m}_a^2 = m_a^2 + \frac{F_0^2 m_{\pi^0}^2 m_u m_d}{f_a^2 (m_u+m_d)(m_u+m_d+m_u m_d/m_s)} = m_a^2 + \left(5.8\ \text{meV}\ \frac{10^9\ \text{GeV}}{f_a}\right)^2 \tag{2.10.36}$$

$$\hat{c}_{a\gamma\gamma} = c_{a\gamma\gamma} + \frac{4\kappa_{11}+\kappa_{22}+\kappa_{33}}{3} = c_{a\gamma\gamma} + 1.01(5) \tag{2.10.37}$$

$$\hat{k}_{ee}^{\ell} = k_{ee}^{\ell} - 10^{-5} \times \left(1.2 + \left(5.7 + \ln\left(\frac{f_a}{10^9\ \text{GeV}}\right)\right) c_{a\gamma\gamma}\right) \tag{2.10.38}$$

$$\hat{k}_{\mu\mu}^{\ell} = k_{\mu\mu}^{\ell} - 10^{-5} \times \left(0.13 + \left(4.7 + \ln\left(\frac{f_a}{10^9\ \text{GeV}}\right)\right) c_{a\gamma\gamma}\right) \tag{2.10.39}$$

$$\hat{k}_{\tau\tau}^{\ell} = k_{\tau\tau}^{\ell} - 10^{-5} \times \left(4.1 + \ln\left(\frac{f_a}{10^9\ \text{GeV}}\right)\right) c_{a\gamma\gamma} \tag{2.10.40}$$

Since interactions involving two axions are highly suppressed relative to single-axion couplings due to the large value of f_a, we are primarily interested in processes where the axion dependence of $\hat{k}_{V,A}(a)$ can be neglected. Thus, in Eqs. (2.10.34)-(2.10.35), the $\mathcal{O}(a/f_a)$ terms can be safely neglected.

The hatted couplings can be viewed as composed of two distinct parts: a UV model-dependent component (unhatted), and a universal IR contribution arising from the c_{aGG}-driven chiral rotation. If the UV theory is unspecified, the precise value of the hat couplings remains unknown. However, since the UV and IR sectors are independent, it is highly unlikely that they cancel each other. For instance, if we write $(\hat{k}_A)_{11} = (k_A)_{11} - 0.67(5)$, one cannot know $(\hat{k}_A)_{11}$ without specifying the UV theory. But for the UV term to accidentally cancel out the IR term, some (scale-dependent) fine-tuning would be required. To avoid such fine-tuning, it is reasonable to assume $(k_A)_{11} \neq 0.67(5)$, which implies: $|(\hat{k}_A)_{11}| \gtrsim 0.67(5)$.

In this sense, the model-independent IR contribution provides a lower bound on the physical axion coupling, offering a way to constrain f_a independently of the UV theory.

2.10.1.4 Application to UV models: KSVZ and DFSZ

We now apply the above framework to two common UV completions: KSVZ and DFSZ models [Cho+21; Cho+22].

For more details on the UV aspects, please refer to Sections 1.3.3-1.3.4.

- KSVZ model:
$$(k_A)_{ii} = \mathcal{O}(10^{-2}) \Rightarrow (\hat{k}_A)_{ii} = -(0.67(5), 0.31(5), 0.02(5)) \ . \tag{2.10.41}$$
- DFSZ model:
$$(k_A)_{11} = \frac{1}{3}\cos^2(\beta) + \mathcal{O}(10^{-3}) \ , \quad \forall i \in \{2;3\}, \ (k_A)_{ii} = \frac{1}{3}\sin^2(\beta) + \mathcal{O}(10^{-3}) \ , \tag{2.10.42}$$
with $\tan(\beta) \in [0.5; 170]$, giving:
$$(\hat{k}_A)_{11} = \frac{1}{3}\cos^2(\beta) - 0.67(5) \ , \quad (\hat{k}_A)_{22} = \frac{1}{3}\sin^2(\beta) - 0.31(5) \ , \quad (\hat{k}_A)_{33} = \frac{1}{3}\sin^2(\beta) - 0.016(3) \tag{2.10.43}$$

Off-diagonal couplings and vector couplings are vanishing in both models.

2.10.2 Axion-hadron interaction

2.10.2.1 General procedure

We now introduce the axion field into the hadronic Lagrangian, following the procedure developed in [GKR86].

The idea is to replace the quark-level currents with their hadronic counterparts:
$$J^{b,\mu}_{L/R}(q) \to J^{b,\mu}_{L/R}(U, B) \ , \tag{2.10.44}$$
where the currents are computed via the Noether procedure, using the left- and right-chiral transformations[17]:
$$L = \exp\left(-i\theta^L_b \frac{\lambda^b}{2}\right) \ , \quad R = \exp\left(-i\theta^R_b \frac{\lambda^b}{2}\right) \ . \tag{2.10.45}$$

As shown in Section 2.6, the quark-level left and right currents are given by
$$J^{b,\mu}_{L/R}(q) = \bar{q}_{L/R}\gamma^\mu \frac{\lambda^b}{2} q_{L/R} \ . \tag{2.10.46}$$

Accordingly, the axion-quark interaction Lagrangian can be written as
$$\mathcal{L}_{aqq} = \frac{\partial_\mu a}{f_a} \sum_{i\in\{L;R\}} x^b_i J^{b,\mu}_{L/R}(q) = \frac{\partial_\mu a}{f_a} \sum_{i\in\{L;R\}} \bar{q}_{L/R}\gamma^\mu x^b_i \frac{\lambda^b}{2} q_{L/R} \ . \tag{2.10.47}$$

Alternatively, it can be expressed as
$$\mathcal{L}_{aqq} = \frac{\partial_\mu a}{f_a} \sum_{i\in\{L;R\}} \bar{q}_{L/R}\gamma^\mu \hat{k}_i q_{L/R} \ , \tag{2.10.48}$$

which justifies expanding $\hat{k}_{L/R}$ in the λ^b basis. By identification, one obtains
$$\hat{k}_{L/R} = x^b_{L/R} \frac{\lambda^b}{2} \ , \tag{2.10.49}$$
implying
$$x^b_{L/R} = \mathrm{Tr}[\hat{k}_{L/R}\lambda^b] \ , \tag{2.10.50}$$
using the identity $\mathrm{Tr}[\lambda^a\lambda^b] = 2\delta^{ab}$.

As previously mentioned, the Gell-Mann matrices form a basis for the space of traceless Hermitian 3×3 matrices. To complete the basis for all Hermitian matrices, one adds a component proportional to the identity. We define $\lambda^0 = aI_3$ such that $\mathrm{Tr}[\lambda^0\lambda^0] = 2$, which leads to $\lambda^0 = \sqrt{\frac{2}{3}}I_3$. This yields
$$x^0_{L/R} = \sqrt{\frac{2}{3}}\mathrm{Tr}[\hat{k}_{L/R}] \ . \tag{2.10.51}$$

In the decomposition $U(3)_{L/R} = U(1)_{L/R} \times SU(3)_{L/R}$, the index $b = 0$ corresponds to the $U(1)_{L/R}$ component, while $b \geq 1$ runs over the $SU(3)_{L/R}$ directions.

[17] The precise sign or normalization inside L and R is irrelevant for the final Lagrangian, as it appears both at the quark and hadronic levels and thus cancels out.

2.10.2.2 Mesonic part

Using the mesonic currents computed in Section 2.7.3,

$$J_L^{b,\mu} = +i\frac{F_0^2}{4}\mathrm{Tr}[\lambda^b (D^\mu U)^\dagger U] \ , J_R^{b,\mu} = -i\frac{F_0^2}{4}\mathrm{Tr}[\lambda^b U (D^\mu U)^\dagger] \ , \tag{2.10.52}$$

the axion-mesons Lagrangian is therefore given by:

$$\mathcal{L}_{aU} = \frac{\partial_\mu a}{f_a}(x_L^b J_L^{b,\mu,} + x_R^b J_R^{b,\mu}) = i\frac{F_0^2}{2}\frac{\partial_\mu a}{f_a}\mathrm{Tr}\left[\frac{\lambda^b}{2}\left(x_L^b (D^\mu U)^\dagger U - x_R^b U (D^\mu U)^\dagger\right)\right] \ . \tag{2.10.53}$$

Using the identities $U^\dagger (D^\mu U) = -(D^\mu U)^\dagger U$, $(D^\mu U)U^\dagger = -U(D^\mu U)^\dagger$, and $x_{L/R}^b \lambda^b/2 = \hat{k}_{L/R}$, we can rewrite Eq. (2.10.53) as

$$\mathcal{L}_{aU} = \frac{F_0^2}{4}\mathrm{Tr}\left[-i\frac{\partial_\mu a}{f_a}\left(\hat{k}_R U - U\hat{k}_L\right)(D^\mu U)^\dagger + i\frac{\partial_\mu a}{f_a}(D^\mu U)\left(\hat{k}_R U - U\hat{k}_L\right)^\dagger\right] \ . \tag{2.10.54}$$

This motivates the definition of the covariant derivative,

$$D_\mu U = \partial_\mu U - ieA_\mu[Q;U] - i\frac{\partial_\mu a}{f_a}(\hat{k}_R U - U\hat{k}_L) \ , \tag{2.10.55}$$

so that the axion-mesons interaction is absorbed into the general mesonic Lagrangian:

$$\mathcal{L}_U = \frac{F_0^2}{4}\mathrm{Tr}\left[(D_\mu U)(D^\mu U)^\dagger\right] \ . \tag{2.10.56}$$

This Lagrangian includes a term quadratic in the axion field; however, since f_a is very large, such processes are highly suppressed and are usually neglected in phenomenological studies.

For a systematic expansion of the axion-mesons Lagrangian involving an arbitrary number of mesons and the corresponding vertices, see Appendix C.6.

2.10.2.3 Baryonic part

Using the currents developed in Section 2.8.3, we can write

$$\mathcal{L}_{aBU} = \frac{\partial_\mu a}{f_a}\left\{x_L^b (J_L^{(BU)})^{b,\mu} + x_R^b (J_R^{(BU)})^{b,\mu} + \mathrm{Tr}(\hat{k}_A)\frac{S}{6}\mathrm{Tr}(\bar{B}\gamma^\mu\gamma_5 B)\right\} \ , \tag{2.10.57}$$

where

$$\begin{aligned}(J_L^{(BU)})^{b,\mu} = &\frac{1}{4}\mathrm{Tr}\left(\bar{B}\gamma^\mu\left[\left(\lambda^b - \frac{f^{\lambda\phi b}}{2F_0}\right);B\right]\right)\\ &-\frac{1}{8}\mathrm{Tr}\left(\bar{B}\gamma^\mu\left[\left(\lambda^b - \frac{f^{\lambda\phi b}}{2F_0}\right) - u\left(\lambda^b - \frac{f^{\lambda\phi b}}{2F_0}\right)u^\dagger;B\right]\right)\\ &+\frac{D}{4}\mathrm{Tr}\left(\bar{B}\gamma^\mu\gamma_5\left\{u\lambda^b u^\dagger;B\right\}\right) + \frac{F}{4}\mathrm{Tr}\left(\bar{B}\gamma^\mu\gamma_5\left[u\lambda^b u^\dagger;B\right]\right) \ ,\end{aligned} \tag{2.10.58}$$

and

$$\begin{aligned}(J_R^{(BU)})^{b,\mu} = &\frac{1}{4}\mathrm{Tr}\left(\bar{B}\gamma^\mu\left[\left(\lambda^b + \frac{f^{\lambda\phi b}}{2F_0}\right);B\right]\right)\\ &-\frac{1}{8}\mathrm{Tr}\left(\bar{B}\gamma^\mu\left[\left(\lambda^b + \frac{f^{\lambda\phi b}}{2F_0}\right) - u^\dagger\left(\lambda^b + \frac{f^{\lambda\phi b}}{2F_0}\right)u;B\right]\right)\\ &-\frac{D}{4}\mathrm{Tr}\left(\bar{B}\gamma^\mu\gamma_5\left\{u\lambda^b u^\dagger;B\right\}\right) - \frac{F}{4}\mathrm{Tr}\left(\bar{B}\gamma^\mu\gamma_5\left[u\lambda^b u^\dagger;B\right]\right) \ .\end{aligned} \tag{2.10.59}$$

The previous expressions apply for $b \geq 1$, corresponding to the $SU(3)_{L/R}$ components of $U(3)_{L/R}$. To account for the $U(1)_{L/R}$ contribution, one replaces the Gell-Mann matrices by a matrix proportional to the identity. Adopting the same normalization as in the literature [CC93], one obtains

$$\mathcal{L}_{aB}^S = \mathrm{Tr}(\hat{k}_A)\frac{S}{6}\frac{\partial_\mu a}{f_a}\mathrm{Tr}(\bar{B}\gamma^\mu\gamma_5 B) \ . \tag{2.10.60}$$

Our results are in perfect agreement with the existing literature [GKR86; CC93]. We note that we are not concerned by vertices involving one axion, two baryons, and at least two mesons. In the transformation of the baryon fields via the matrix K, we have accordingly neglected terms involving two or more mesons.

2.10.3 Interactions with nucleons

Following the approach of [VGM21], we compare the results obtained from Chiral Perturbation Theory augmented with an axion (ChPT+a) with those derived from Lattice QCD (LQCD).

The axion-nucleon-nucleon Lagrangian can be written as

$$\mathcal{L}_{aNN} = C_{aNN}\frac{\partial_\mu a}{2f_a}\bar{N}\gamma^\mu\gamma_5 N \ . \tag{2.10.61}$$

In ChPT+a, expanding the Lagrangian in Eq. (2.10.57), the coefficients C_{app} and C_{ann} are given by

$$C_{app} = -\frac{(\hat{k}_A)_{11} - 2(\hat{k}_A)_{22} + (\hat{k}_A)_{33}}{3}D - ((\hat{k}_A)_{11} - (\hat{k}_A)_{33})F + \frac{(\hat{k}_A)_{11} + (\hat{k}_A)_{22} + (\hat{k}_A)_{33}}{3}S \tag{2.10.62}$$

$$= \frac{-D-3F+S}{3}(\hat{k}_A)_{11} + \frac{2D+S}{3}(\hat{k}_A)_{22} + \frac{-D+3F+S}{3}(\hat{k}_A)_{33} \ , \tag{2.10.63}$$

$$C_{ann} = \frac{2(\hat{k}_A)_{11} - (\hat{k}_A)_{22} - (\hat{k}_A)_{33}}{3}D - ((\hat{k}_A)_{22} - (\hat{k}_A)_{33})F + \frac{(\hat{k}_A)_{11} + (\hat{k}_A)_{22} + (\hat{k}_A)_{33}}{3}S \tag{2.10.64}$$

$$= \frac{2D+S}{3}(\hat{k}_A)_{11} + \frac{-D-3F+S}{3}(\hat{k}_A)_{22} + \frac{-D+3F+S}{3}(\hat{k}_A)_{33} \ . \tag{2.10.65}$$

To derive the LQCD Lagrangian, we use the matching condition

$$\langle N|\mathcal{L}_{aqq}|N\rangle = \langle N|\mathcal{L}_{aNN}|N\rangle \ , \tag{2.10.66}$$

with

$$\left\langle N'|\bar{N}\gamma^\mu\gamma_5 N|N'\right\rangle := s^\mu/2\delta_{NN'} \ , \tag{2.10.67}$$

where s^μ denotes the nucleon spin vector.

For $q = (u \ \ d \ \ s)^T$, the LQCD parameters $\Delta_{u,d,s}$ are defined as

$$\langle p|\bar{q}\gamma^\mu\gamma_5 q|p\rangle := (\Delta_u \ \ \Delta_d \ \ \Delta_s)^T s^\mu/2 \ , \tag{2.10.68}$$

where isospin symmetry[18] implies

$$\langle n|\bar{q}\gamma^\mu\gamma_5 q|n\rangle = (\Delta_d \ \ \Delta_u \ \ \Delta_s)^T s^\mu/2 \ . \tag{2.10.69}$$

The matching condition (2.10.66) for the proton becomes

$$\begin{aligned} & C_{app}\frac{\partial_\mu a}{2f_a}\langle p|\bar{p}\gamma^\mu\gamma_5 p|p\rangle = \frac{\partial_\mu a}{2f_a}(\hat{k}_A)_{ii}\langle p|\bar{q}_i\gamma^\mu\gamma_5 q_i|p\rangle \\ \Leftrightarrow \ & C_{app}\frac{\partial_\mu a}{2f_a}\frac{s^\mu}{2} = \frac{\partial_\mu a}{2f_a}(\hat{k}_A)_{ii}\Delta_i\frac{s^\mu}{2} \\ \Leftrightarrow \ & C_{app} = (\hat{k}_A)_{11}\Delta_u + (\hat{k}_A)_{22}\Delta_d + (\hat{k}_A)_{33}\Delta_s \ . \end{aligned} \tag{2.10.70}$$

Similarly, for the neutron, or by interchanging $u \leftrightarrow d$, we find

$$C_{ann} = (\hat{k}_A)_{11}\Delta_d + (\hat{k}_A)_{22}\Delta_u + (\hat{k}_A)_{33}\Delta_s \ . \tag{2.10.71}$$

Requiring that the LQCD and ChPT+a results coincide for all values of $(\hat{k}_A)_{ii}$ imposes the relations:

$$\begin{aligned} \Delta_u &= \frac{-D-3F+S}{3} \ , \\ \Delta_d &= \frac{2D+S}{3} \ , \\ \Delta_s &= \frac{-D+3F+S}{3} \ . \end{aligned} \tag{2.10.72}$$

[18] $n \leftrightarrow p \Leftrightarrow u \leftrightarrow d$.

Inverting these relations yields:

$$\begin{aligned} D &= -\Delta_u/2 + \Delta_d - \Delta_s/2 \ , \\ F &= -\Delta_u/2 + \Delta_s/2 \ , \\ S &= \Delta_u + \Delta_d + \Delta_s \ . \end{aligned} \tag{2.10.73}$$

Using the LQCD results from [Aok+20],

$$\Delta_u = 0.847(50) \ , \quad \Delta_d = -0.407(34) \ , \quad \Delta_s = -0.035(13) \ , \tag{2.10.74}$$

we find

$$D = -0.813(43) \ , \quad F = -0.441(26) \ , \quad S = 0.405(62) \ , \tag{2.10.75}$$

which is in very good agreement with the values of D and F obtained from semi-leptonic decays (see Appendix B.5.2).

Taking $c_{aGG} = -1/2$, we obtain

$$C_{app} = -0.452(28) + 0.847(50)\ (k_A)_{11} - 0.407(34)\ (k_A)_{22} - 0.035(13)\ (k_A)_{33} \ , \tag{2.10.76}$$

$$C_{ann} = 0.012(28) - 0.407(34)\ (k_A)_{11} + 0.847(50)\ (k_A)_{22} - 0.035(13)\ (k_A)_{33} \ , \tag{2.10.77}$$

which is consistent with [Di +23].

These results apply to theoretical models:

- **KSVZ model:** In this model, the axion-quark-quark couplings $(k_A)_{ii}$ arise only from running effects at $\mathcal{O}(10^{-2})$ [Cho+22], leading to

$$C_{app}^{KSVZ} = -0.45(3) \ , \quad C_{ann}^{KSVZ} = 0.01(3) \ . \tag{2.10.78}$$

- **DFSZ model:** In this model, $(k_A)_{11} \simeq \frac{1}{3}\cos^2(\beta)$ and $(k_A)_{22} \simeq (k_A)_{33} \simeq \frac{1}{3}\sin^2(\beta)$, where $\tan(\beta) \in [0.25, 170]$, this leads to

$$C_{app}^{DFSZ} = -0.170(30) - 0.430(21)\sin^2(\beta) \in [-0.6; -0.17] \ , \tag{2.10.79}$$

$$C_{ann}^{DFSZ} = -0.124(30) + 0.407(21)\sin^2(\beta) \in [-0.12; 0.28] \ , \tag{2.10.80}$$

  which is also consistent with [Di +23].

2.10.4 Axion-quark vs. axion-hadron couplings

As we have seen, all axion-hadron couplings can be expressed in terms of the axion-quark couplings $\hat{k}_{A,V}$, which correspond to the UV couplings. However, from a phenomenological point of view, it may be more convenient to work directly with the axion-hadron couplings, i.e., the IR couplings.

The axion-hadron couplings are not independent: while there are many possible axion-hadron couplings, they can all be rewritten in terms of a reduced set of effective couplings. For example, two couplings describe the first generation (C_{ann}, C_{app}), one describes a strange-strange transition ($C_{a\Lambda\Lambda}$), and two describe a strange-down transition ($C_{a\Lambda n}^A$, $C_{a\Lambda n}^V$). These are defined such that:

$$\mathcal{L}_{aUB} \supset \frac{\partial_\mu a}{2f_a} \sum_{B\in\{n,p,\Lambda\}} C_{aBB}\bar{B}\gamma^\mu\gamma_5 B + \frac{\partial_\mu a}{2f_a}\left(\bar{n}\gamma^\mu\left(C_{a\Lambda n}^V + C_{a\Lambda n}^A\gamma_5\right)\Lambda + \text{h.c.}\right) \ . \tag{2.10.81}$$

Expanding the chiral Lagrangian leads to the following expressions:

$$\begin{aligned} C_{ann} &= \frac{2D+S}{3}(\hat{k}_A)_{11} + \frac{-3F-D+S}{3}(\hat{k}_A)_{22} + \frac{3F-D+S}{3}(\hat{k}_A)_{33} \\ &= -0.407\ (k_A)_{11} + 0.847\ (k_A)_{22} - 0.035\ (k_A)_{33} \ , \end{aligned} \tag{2.10.82}$$

$$\begin{aligned} C_{app} &= \frac{-3F-D+S}{3}(\hat{k}_A)_{11} + \frac{2D+S}{3}(\hat{k}_A)_{22} + \frac{3F-D+S}{3}(\hat{k}_A)_{33} \\ &= 0.847\ (k_A)_{11} - 0.407\ (k_A)_{22} - 0.035\ (k_A)_{33} \ , \end{aligned} \tag{2.10.83}$$

$$C_{a\Lambda\Lambda} = \frac{D+S}{3}(\hat{k}_A)_{11} + \frac{D+S}{3}(\hat{k}_A)_{22} + \frac{-2D+S}{3}(\hat{k}_A)_{33} \tag{2.10.84}$$
$$= -0.136\ (k_A)_{11} - 0.136\ (k_A)_{22} + 0.677\ (k_A)_{33}\ ,$$

$$C^V_{an\Lambda} = -\sqrt{6}(\hat{k}_V)_{23} = -2.45\ (\hat{k}_V)_{23}\ , \tag{2.10.85}$$

$$C^A_{an\Lambda} = \frac{3F+D}{\sqrt{6}}(\hat{k}_A)_{23} = -0.872\ (\hat{k}_A)_{23}\ . \tag{2.10.86}$$

These expressions can be inverted to yield:

$$(\hat{k}_A)_{11} = \frac{D^2+DF+FS}{S(D^2+4DF+3F^2)}C_{ann} + \frac{D^2+DF-DS-2FS}{S(D^2+4DF+3F^2)}C_{app} + \frac{-D+3F+S}{S(D+3F)}C_{a\Lambda\Lambda}\ , \tag{2.10.87}$$
$$= 0.775\ C_{ann} + 1.573\ C_{app} + 0.121\ C_{a\Lambda\Lambda}$$

$$(\hat{k}_A)_{22} = \frac{D^2+DF-DS-2FS}{S(D^2+4DF+3F^2)}C_{ann} + \frac{D^2+DF+FS}{S(D^2+4DF+3F^2)}C_{app} + \frac{-D+3F+S}{S(D+3F)}C_{a\Lambda\Lambda} \tag{2.10.88}$$
$$= 1.573\ C_{ann} + 0.775\ C_{app} + 0.121\ C_{a\Lambda\Lambda}\ ,$$

$$(\hat{k}_A)_{33} = \frac{D+S}{S(D+3F)}C_{ann} + \frac{D+S}{S(D+3F)}C_{app} + \frac{-D+3F-2S}{S(D+3F)}C_{a\Lambda\Lambda} \tag{2.10.89}$$
$$= 0.472\ C_{ann} + 0.472\ C_{app} + 1.53\ C_{a\Lambda\Lambda}\ ,$$

$$(\hat{k}_A)_{23} = \frac{\sqrt{6}}{3F+D}C^A_{an\Lambda} = -1.15\ C^A_{an\Lambda}\ , \tag{2.10.90}$$

$$(\hat{k}_V)_{23} = -\frac{1}{\sqrt{6}}C^V_{an\Lambda} = -0.408\ C^V_{an\Lambda}\ . \tag{2.10.91}$$

Thus, all axion-hadron couplings, which are derived from the matrices $\hat{k}_{A,V}$, can be expressed in terms of the five effective couplings C_{ann}, C_{app}, $C_{a\Lambda\Lambda}$, $C^V_{an\Lambda}$, and $C^A_{an\Lambda}$,[19] instead of the original axion-quark couplings.

2.10.5 Lagrangian mediating weak processes

The SM Lagrangian governing weak processes (see Section 2.9) can be extended to include axion interactions. In this context, the covariant derivative is

$$D_\mu U = \partial_\mu U - ieA_\mu[Q,U] - i\frac{\partial_\mu a}{f_a}\left(\hat{k}_R(a)U - U\hat{k}_L(a)\right)\ . \tag{2.10.92}$$

To account for the chiral rotation of quarks and eliminate terms like $aG\tilde{G}$, the chiral rotation must be incorporated directly into the Lagrangian, leading to the expression

$$(L^\mu)^{ji} = \exp\left(i\frac{a}{f_a}(\Phi_i^- - \Phi_j^-)\right)\left((J_L^{(U)})^\mu_{(ij)} + (J_L^{(BU)})^\mu_{(ij)}\right)\ , \tag{2.10.93}$$

where the J_L currents include both purely mesonic and baryonic-mesonic contributions, and $\Phi_i^\pm = c_{aGG}(\delta \pm \kappa)_{ii}$.

The resulting weak Lagrangian reads [Cor+24]

$$\mathcal{L}^w_{aBU} = G_8(L_\mu L^\mu)_{32} + G_8^\theta\frac{\partial_\mu a}{f_a}(L^\mu)_{32}$$
$$+ G_{27}\left((L_\mu)_{32}(L^\mu)_{11} + \frac{2}{3}(L_\mu)_{31}(L^\mu)_{12} - \frac{1}{3}(L_\mu)_{32}\mathrm{Tr}[L^\mu]\right) + \text{h.c.}\ . \tag{2.10.94}$$

[19] The couplings $C^V_{an\Lambda}$ and $C^A_{an\Lambda}$ are complex, as are $(\hat{k}_V)_{23}$ and $(\hat{k}_A)_{23}$; consequently, one must determine both their absolute values and their phases.

In the SM, $\mathrm{Tr}[L^\mu] = 0$; however, in the presence of an axion, one finds $\mathrm{Tr}[L^\mu] = -\dfrac{\partial^\mu a}{f_a}$.

The parameter G_8^θ is unknown, as it is absent in the pure SM. Nevertheless, its contribution could be phenomenologically relevant in processes involving both axions and weak interactions.

Similar to the SM case, this interaction is suppressed by a factor $G_F F_0^2 \sim 10^{-7}$, moreover, due to the additional $1/f_a$ suppression from the axion coupling, the effects predicted by this Lagrangian are expected to be doubly suppressed and thus experimentally unobservable.

2.11 State-of-the-art in axion-quark coupling bounds

Axion-quark interactions[20] are given by

$$\mathcal{L}_{aqq} = \frac{\partial_\mu a}{2f_a}\bar{q}\gamma^\mu\left(\hat{k}_V + \hat{k}_A\gamma_5\right)q \ , \tag{2.11.1}$$

where, by hermiticity and charge conservation,

$$\hat{k}_{A,V} = \begin{pmatrix} (\hat{k}_{A,V})_{11} & 0 & 0 \\ 0 & (\hat{k}_{A,V})_{22} & (\hat{k}_{A,V})_{23} \\ 0 & (\hat{k}_{A,V})^*_{23} & (\hat{k}_{A,V})_{33} \end{pmatrix} \ . \tag{2.11.2}$$

The bounds on axion-quark couplings are summarized in Table 2.1.

Table 2.1: Bounds on axion-quark couplings for the QCD axion ($m_a \ll m_q$). We define $(F_{A,V})_{ij} := 2f_a/(\hat{k}_{A,V})_{ij}$ [Mar+20]. For $(\hat{k}_A)_{23}$ two numbers appear in a cell as $x \mid y$, they correspond to collider | astrophysical bounds, respectively.

Couplings	$\lvert(\hat{k}_A)_{11}\rvert$	$\lvert(\hat{k}_A)_{22}\rvert$	$\lvert(\hat{k}_A)_{33}\rvert$	$\lvert(\hat{k}_A)_{23}\rvert$	$\lvert(\hat{k}_V)_{23}\rvert$
Upper bounds at $f_a = 10^9$ GeV	2.7	2.5	10	$32 \mid 10^{-1}$	2×10^{-3}
Couplings	$\lvert(F_A)_{11}\rvert$	$\lvert(F_A)_{22}\rvert$	$\lvert(F_A)_{33}\rvert$	$\lvert(F_A)_{23}\rvert$	$\lvert(F_V)_{23}\rvert$
Lower bounds (GeV)	7.4×10^8	8.0×10^8	10^8	$6.3 \times 10^7 \mid 10^{10}$	1×10^{12}

Constraints on $(\hat{k}_A)_{11}$ and $(\hat{k}_A)_{22}$ follow from C_{ann} and C_{app} inferred from Neutron Star (NS) cooling [Bus+22] (see Section 3.3).

The bound on $(\hat{k}_A)_{33}$ comes from core-collapse Supernovæ (SNe) with strange matter [Cav+24], correlating the diagonal axial couplings and exploiting the first-generation bounds (see Section 3.4.9).

For $|(\hat{k}_A)_{23}|$, we quote both collider bounds [Mar+20] (baryon decays, $K \to \pi\pi a$, and $K^0 - \bar{K}^0$ mixing; see Section 5.1.5) on the left and astrophysical bounds from core-collapse SNe [Cav+24; Mar+20; Cam+21] (see Section 3.4.9) on the right. Taking astrophysical constraints into account leads to significantly stronger bounds – up to two oom stronger than the collider results. It is worth clarifying the relative status of these constraints. Collider-derived bounds benefit from the high level of control inherent to laboratory collisions, where the limiting factor is statistics rather than modeling. By contrast, astrophysical bounds necessarily rely on interpreting signals from complex, unprepared sources. In SNe, for instance, emissivity (energy radiated by unit of time and volume, see Section 3.4.3) is not directly measurable: it is inferred from the proto-NS mass, the radiated fraction, and the assumed density profile, each only known to about an oom. There is currently no clear avenue to reduce this intrinsic uncertainty, even for future nearby Supernova (SN) explosions. NSs and their mergers may eventually allow improvements thanks to multimessenger observations (e.g. interferometry), but strange-matter contributions there are less pronounced than in SNe, and their modeling presents additional challenges, including the hyperon puzzle and reliable estimates of Fermi blocking. Astrophysical constraints should therefore be viewed as highly complementary to laboratory ones: they probe diagonal (flavor-conserving) couplings largely better than flavor physics, and in selected cases–such as the $(\hat{k}_A)_{23}$ coupling–achieve oom sensitivities at levels unmatched even by precision observables such as hadron decays and $K^0 - \bar{K}^0$ mixing.

The vector off-diagonal $|(\hat{k}_V)_{23}|$ is bounded by $K^+ \to \pi^+ a$ [Mar+20] (see Section 5.1.5).

[20] Only the single-axion Lagrangian is shown; interactions with multiple axions are suppressed by an additional factor of $1/f_a$ for each extra axion.

Phases of $(\hat{k}_{A,V})_{23}$ are harder to access, but can appear, for example, in K_S and K_L decays (see Section 5.2.4.1).

Finally, diagonal vector couplings $(\hat{k}_V)_{ii}$ do not contribute via the strong interaction, only weak effects probe them and are suppressed by $G_F F_0^2 \sim 10^{-7}$ (see Section 2.10.5), making meaningful bounds extremely challenging.

References

[Aok+20] S. Aoki et al. *FLAG Review 2019: Flavour Lattice Averaging Group (FLAG)*. In: *The European Physical Journal C* 80.2 (Feb. 2020). ISSN: 1434-6052. DOI: 10.1140/epjc/s10052-019-7354-7. URL: http://dx.doi.org/10.1140/epjc/s10052-019-7354-7.

[Bau+21] Martin Bauer et al. *Consistent Treatment of Axions in the Weak Chiral Lagrangian*. In: *Phys. Rev. Lett.* 127.8 (2021), p. 081803. DOI: 10.1103/PhysRevLett.127.081803. arXiv: 2102.13112 [hep-ph].

[BGI10] Andrzej J. Buras, Diego Guadagnoli, and Gino Isidori. *On ϵ_K Beyond Lowest Order in the Operator Product Expansion*. In: *Phys. Lett. B* 688 (2010), pp. 309–313. DOI: 10.1016/j.physletb.2010.04.017. arXiv: 1002.3612 [hep-ph].

[Bus+22] Malte Buschmann et al. *Upper Limit on the QCD Axion Mass from Isolated Neutron Star Cooling*. In: *Phys. Rev. Lett.* 128.9 (2022), p. 091102. DOI: 10.1103/PhysRevLett.128.091102. arXiv: 2111.09892 [hep-ph].

[Cam+21] Jorge Martin Camalich et al. *Supernova Constraints on Dark Flavored Sectors*. In: *Phys. Rev. D* 103.12 (2021), p. L121301. DOI: 10.1103/PhysRevD.103.L121301. arXiv: 2012.11632 [hep-ph].

[Cav+24] Mael Cavan-Piton et al. *Axion Emission from Strange Matter in Core-Collapse SNe*. In: *Phys. Rev. Lett.* 133.12 (2024), p. 121002. DOI: 10.1103/PhysRevLett.133.121002. arXiv: 2401.10979 [hep-ph].

[CC93] Sanghyeon Chang and Kiwoon Choi. *Hadronic axion window and the big bang nucleosynthesis*. In: *Phys. Lett. B* 316 (1993), pp. 51–56. DOI: 10.1016/0370-2693(93)90656-3. arXiv: hep-ph/9306216.

[Cho+21] Kiwoon Choi et al. *Precision axion physics with running axion couplings*. In: *JHEP* 08 (2021), p. 058. DOI: 10.1007/JHEP08(2021)058. arXiv: 2106.05816 [hep-ph].

[Cho+22] Kiwoon Choi et al. *Axion emission from supernova with axion-pion-nucleon contact interaction*. In: *JHEP* 02 (2022), p. 143. DOI: 10.1007/JHEP02(2022)143. arXiv: 2110.01972 [hep-ph].

[Cor+24] Claudia Cornella et al. *$K^{\pm} \to \pi^{\pm} a$ at Next-to-Leading Order in Chiral Perturbation Theory and Updated Bounds on ALP Couplings*. 2024. arXiv: 2308.16903 [hep-ph]. URL: https://arxiv.org/abs/2308.16903.

[Cro67] Jeremiah A. Cronin. *Phenomenological model of strong and weak interactions in chiral $U(3)\times U(3)$*. In: *Phys. Rev.* 161 (1967), pp. 1483–1494. DOI: 10.1103/PhysRev.161.1483.

[Di +23] Luca Di Luzio et al. *Running into QCD axion phenomenology*. In: (May 2023). arXiv: 2305.11958 [hep-ph].

[GKR86] Howard Georgi, David B. Kaplan, and Lisa Randall. *Manifesting the Invisible Axion at Low-energies*. In: *Phys. Lett. B* 169 (1986), pp. 73–78. DOI: 10.1016/0370-2693(86)90688-X.

[KMW90] J. Kambor, John H. Missimer, and D. Wyler. *The Chiral Loop Expansion of the Nonleptonic Weak Interactions of Mesons*. In: *Nucl. Phys. B* 346 (1990), pp. 17–64. DOI: 10.1016/0550-3213(90)90236-7.

[Man] Aneesh V. Manohar. *Effective field theories*. In: *Perturbative and Nonperturbative Aspects of Quantum Field Theory*. Springer Berlin Heidelberg, pp. 311–362. DOI: 10.1007/bfb0104294. URL: https://doi.org/10.1007%2Fbfb0104294.

[Mar+20] Jorge Martin Camalich et al. *Quark Flavor Phenomenology of the QCD Axion*. In: *Phys. Rev. D* 102.1 (2020), p. 015023. DOI: 10.1103/PhysRevD.102.015023. arXiv: 2002.04623 [hep-ph].

[Sch03] Stefan Scherer. *Introduction to chiral perturbation theory*. In: *Adv. Nucl. Phys.* 27 (2003). Ed. by John W. Negele and E. W. Vogt, p. 277. arXiv: hep-ph/0210398.

[VGM21] Thomas Vonk, Feng-Kun Guo, and Ulf-G. Meißner. *The axion-baryon coupling in SU(3) heavy baryon chiral perturbation theory*. In: *JHEP* 08 (2021), p. 024. DOI: 10.1007/JHEP08(2021)024. arXiv: 2104.10413 [hep-ph].

Chapter 3

Search for QCD axion emission from stellar objects

Contents

3.1 Motivation . . . 72
3.2 Study of the axion-photon-photon coupling . . . 72
3.2.1 Model-independant bounds on f_a and m_a . . . 72
3.2.2 Axion lifetime . . . 72
3.3 Axion emission from first generation in Neutron Stars . . . 73
3.4 Axion emission from strange matter in core-collapse Supernovæ . . . 75
3.4.1 Introduction . . . 75
3.4.2 Constraints from SN 1987A . . . 76
3.4.3 Neutrino emissivity estimation . . . 77
3.4.4 Axion emissivity estimation . . . 78
3.4.5 Supernova core modeling . . . 79
3.4.6 Axion-hadron modeling . . . 81
3.4.7 Studied processes . . . 82
3.4.8 General procedure to compute emissivity . . . 82
3.4.9 Results . . . 85
3.4.10 Conclusion . . . 87
3.5 The dominant axion production channels . . . 88

In this chapter, we explore the phenomenology of Quantum Chromodynamics (QCD) axions in astrophysical environments, focusing on their potential emission from compact stellar objects such as Neutron Stars (NSs) and core-collapse Supernovæ (SNe). These extreme settings, characterized by high densities and, for SNe, temperatures as well, provide a unique laboratory for probing axion couplings to hadronic matter, particularly in regimes inaccessible to terrestrial experiments.

We begin in Section 3.1 by outlining the motivations for studying axion production in compact stellar objects. In Section 3.2, we review the axion-photon-photon coupling and its role in axion stability.

In Section 3.3, we summarize existing results on axion emission from NSs, driven by couplings to nucleons. The main focus of this chapter, however, lies in the detailed study presented in Section 3.4, where we examine axion production in core-collapse SNe. This analysis, based on original work [Cav+24], consistently incorporates the full baryon and meson octets and computes axion emissivities from both baryon-meson scattering and baryon decay processes involving strange matter. We model the relevant Supernova (SN) core conditions across different Equation of State (EoS) as well as thermodynamic scenarios, ultimately deriving new, world-leading constraints on axion couplings to strange quarks. We conclude this chapter with Section 3.5, which outlines a general procedure to identify the dominant axion production processes beyond the first generation.

Altogether, this chapter highlights the potential of astrophysical probes–notably those containing strange hadronic matter–to constrain previously unexplored regions of axion parameter space, and establishes a framework for future studies of axion emission in astrophysical environments.

3.1 Motivation

We have seen in previous chapters that axion couplings are proportional to $(\partial_\mu a/f_a)$ (see Eq. (2.10.1)), implying that observable effects scale as $([\text{external momenta}]/f_a)^2$.

For the QCD axion, the decay constant f_a is very large ($\gtrsim 10^9$ GeV), making observable effects extremely small. As a result, direct detection of QCD axions at particle colliders is possible only in very special circumstances, which will be explored in Chapter 5. On the other hand, dense and hot astrophysical objects, such as SNe, could radiate axions, accelerating their cooling relative to expectations based on standard mechanisms such as neutrino emission. Although both the calculations and the measurements involved in testing this possibility are limited—primarily due to the inherently poor knowledge of the emitter—the resulting bounds are still meaningful, in the following sense. Because of the above uncertainties—many of which irreducible at the moment—these bounds are to be interpreted as order-of-magnitude (oom) estimates, with uncertainties of order $\mathcal{O}(100\%)$. Nevertheless, their central values turn out to be highly significant.

3.2 Study of the axion-photon-photon coupling

3.2.1 Model-independant bounds on f_a and m_a

The axion-photon-photon interaction is given by

$$\mathcal{L}_{a\gamma\gamma} = -\frac{g_{a\gamma\gamma}}{4} a F_{\mu\nu}\tilde{F}^{\mu\nu} = \frac{\hat{c}_{a\gamma\gamma}}{f_a}\frac{\alpha_{e.m.}}{4\pi} a F_{\mu\nu}\tilde{F}^{\mu\nu} \ . \tag{3.2.1}$$

As shown in the left panel of Fig. 3.1, the strongest model-independent constraint on the axion-photon-photon coupling, obtained from globular cluster stellar evolution [DHV22], without assuming a specific axion mass, is:

$$|g_{a\gamma\gamma}| < 0.47 \times 10^{-10} \text{ GeV}^{-1} \ . \tag{3.2.2}$$

As discussed in Section 2.10.1.3, the model-independent contribution to the axion-photon-photon coupling is given by

$$\hat{c}_{a\gamma\gamma} = -6 c_{GG} \text{Tr}[Q^2\kappa] \simeq 1 \ , \tag{3.2.3}$$

and thus, in the model-independent case, we obtain:

$$f_a = \frac{|\hat{c}_{a\gamma\gamma}|}{|g_{a\gamma\gamma}|}\frac{\alpha_{e.m.}}{\pi} \gtrsim 5 \times 10^7 \text{ GeV} \ . \tag{3.2.4}$$

Furthermore, still in the model-independent case, we have[1] (Eq. (2.10.36)

$$m_a^2 = 4 c_{GG} \frac{F_0^2 m_\pi^2}{f_a^2} \frac{m_u m_d}{(m_u + m_d)^2} \ , \tag{3.2.5}$$

which implies

$$m_a \lesssim 0.16 \text{ eV} \ . \tag{3.2.6}$$

3.2.2 Axion lifetime

For the QCD axion to be a viable Dark Matter (DM) candidate, it must be sufficiently stable; otherwise, DM would have already decayed.

The only kinematically allowed decay channel for the QCD axion (due to its low mass) is $a \to \gamma\gamma$, with an amplitude given by

$$\mathcal{M}_{fi}(a \to \gamma\gamma) = 4 g_{a\gamma\gamma} \epsilon^{\alpha\lambda\beta\nu} k_\alpha p_\beta \epsilon_\lambda(k) \epsilon_\nu(p) \ , \tag{3.2.7}$$

which yields

$$\begin{aligned} |\mathcal{M}_{fi}|^2(a \to \gamma\gamma) &= 16 g_{a\gamma\gamma}^2 \epsilon^{\alpha_1\lambda_1\beta_1\nu_1} k_{\alpha_1} p_{\beta_1} \epsilon_{\lambda_1}(k) \epsilon_{\nu_1}(p) \epsilon^{\alpha_2\lambda_2\beta_2\nu_2} k_{\alpha_2} p_{\beta_2} \epsilon_{\lambda_2}(k) \epsilon_{\nu_2}(p) \\ &= 16 g_{a\gamma\gamma}^2 \epsilon^{\alpha_1\lambda\beta_1\nu} \epsilon^{\alpha_2}{}_{\lambda_2\nu}{}^{\beta_2} k_{\alpha_1} p_{\beta_1} k_{\alpha_2} p_{\beta_2} \\ &= 16 g_{a\gamma\gamma}^2 \epsilon^{\alpha_1\lambda\beta_1\nu} 2(\eta^{\alpha_1\beta_2}\eta^{\beta_1\alpha_2} - \eta^{\alpha_1\alpha_2}\eta^{\beta_1\beta_2}) k_{\alpha_1} p_{\beta_1} k_{\alpha_2} p_{\beta_2} \\ &= 32 g_{a\gamma\gamma}^2 (p \cdot k)^2 \\ &= 8 g_{a\gamma\gamma}^2 m_a^4 \ . \end{aligned} \tag{3.2.8}$$

[1] This relation follows from Eq. (2.10.36) in the limit $m_s \gg m_{u,d}$.

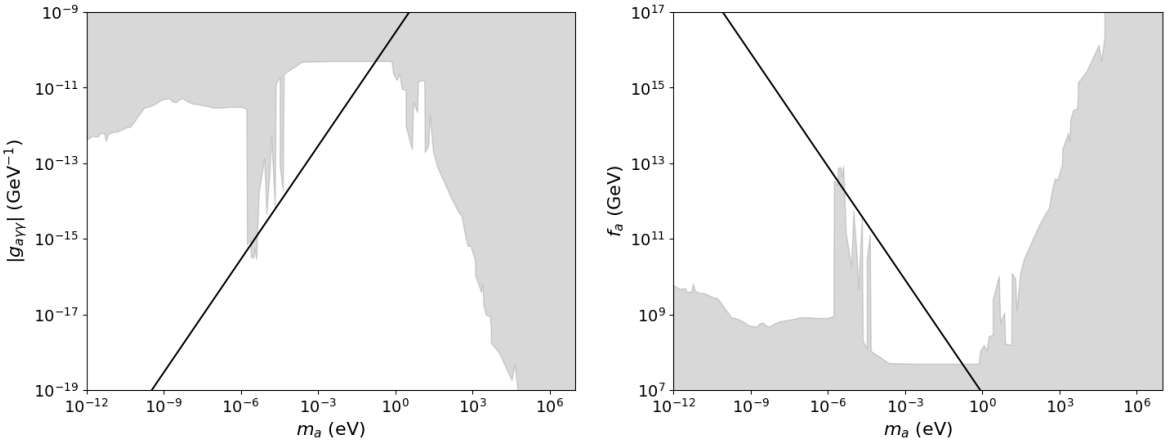

Figure 3.1: The left panel shows in gray the excluded region in the $g_{a\gamma\gamma} - m_a$ plane (see [OHa20]), while the right panel shows in gray the excluded region in the $f_a - m_a$ plane in the model-independent case, see the text for more details. The black lines correspond to the model-independent theoretical prediction derived from Eq. (3.2.5).

The corresponding decay width is

$$\Gamma(a \to \gamma\gamma) = \frac{|\mathcal{M}_{fi}|^2}{16\pi m_a} = \frac{g_{a\gamma\gamma}^2}{2\pi} m_a^3 = \frac{\alpha_{e.m.}^2}{32\pi^3 f_a^2} \hat{c}_{a\gamma\gamma}^2 m_a^3 \ . \tag{3.2.9}$$

In the model-independent case, this becomes

$$\Gamma(a \to \gamma\gamma) = \frac{\alpha_{e.m.}^2}{72\sqrt{2}\pi^3} \frac{z^{3/2}(z+4)^2}{(z+1)^5} \frac{F_0^3 m_\pi^3}{f_a^5} \ , \tag{3.2.10}$$

where $z = m_u/m_d$.

Therefore, the axion lifetime can be expressed as

$$\tau_a = \tau_U \times \left(\frac{f_a}{4.6 \times 10^5 \text{ GeV}} \right)^5 \ , \tag{3.2.11}$$

where τ_U is the age of the Universe. Hence, to ensure axion stability as a dark matter candidate, we require

$$f_a \gtrsim 10^5 \text{ GeV} \ , \tag{3.2.12}$$

a condition clearly satisfied by the bound in Eq. (3.2.4).

Fig. 3.2 generalizes the axion lifetime ratio τ_a/τ_U to the case where no specific relation between m_a and f_a is assumed, corresponding to so-called Axion-like Particles (ALPs). These particles are "just-so" generalizations of the QCD axion: they are parametric extensions amenable to phenomenological considerations but otherwise lack strong theoretical motivation. For sufficiently large m_a and $|g_{a\gamma\gamma}|$ (top right), the ALP becomes unstable. However, as shown in Fig. 3.1, this region is already excluded by observational constraints.

This implies that the axion-photon-photon coupling is always weak enough to prevent axions from decaying into photons on cosmological timescales.

3.3 Axion emission from first generation in Neutron Stars

The couplings C_{app} and C_{ann} (see Section 2.10.3 for more details) are constrained by NS cooling data [Bus+22].

These bounds are derived by solving the energy balance and transport equations in full general relativity, considering both the core and the crust of the NS. Alternatively, an envelope model is employed to relate the interior and surface temperatures, denoted by T_b and T_s, respectively. After

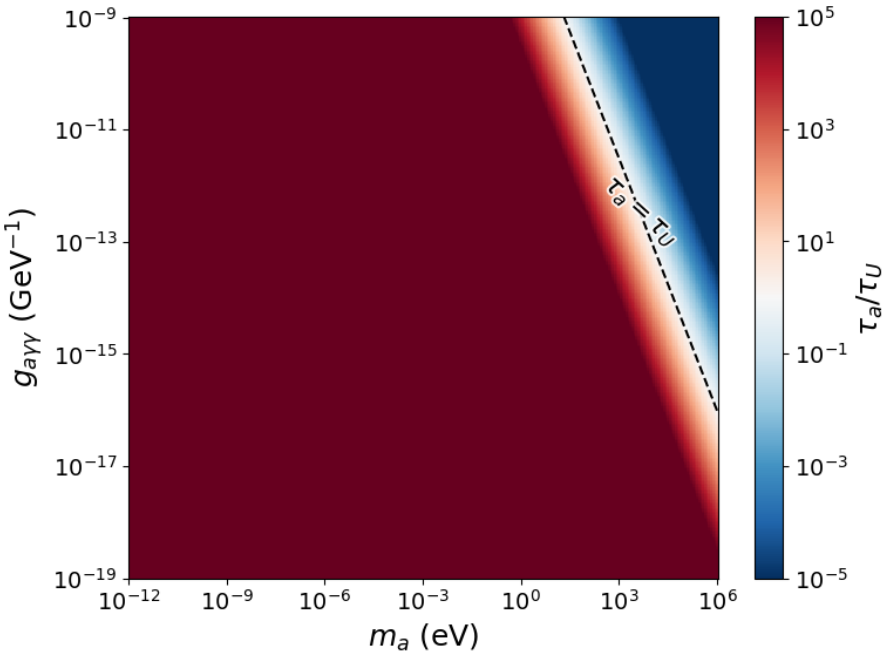

Figure 3.2: Lifetime constraint on axions in the $m_a - |g_{a\gamma\gamma}|$ plane. The color map shows the ratio τ_a/τ_U, where $\tau_a = \tau(a \to \gamma\gamma)$ and τ_U is the age of the universe. The dashed black line corresponds to $\tau_a = \tau_U$, marking the boundary of cosmological stability.

thermal relaxation is achieved, ensuring a uniform core temperature throughout the NS, integrating the energy balance equation over the stellar interior yields the cooling equation for a distant observer:

$$L_\gamma^\infty = -C\frac{dT_b^\infty}{dt} - L_\nu^\infty - L_a^\infty + H \ , \tag{3.3.1}$$

where $L_\gamma^\infty = 4\pi R_{*,\infty}^2 (T_s^\infty)^4$ is the photon luminosity, and t denotes time. The heat capacity of the NS is C, while L_ν^∞ and L_a^∞ correspond to the neutrino and axion luminosities, respectively. The term H accounts for possible heating sources, such as magnetic field decay, which is set to zero in [Bus+22] because magnetic-field-induced heating seems to play a subdominant role in the thermal evolution of isolated NSs.

The solution to this equation defines the NS cooling curve $L_\gamma^\infty(t;\theta)$, where θ parameterizes specific axion and NS properties. The axion is characterized by its mass m_a and its axion-nucleon-nucleon couplings C_{aNN}, while the NS parameters include its mass, EoS, superfluidity model ΔT_b, and envelope model parameterized by the mass of light elements ΔM.

The analysis of [Bus+22] solves the cooling equation using the publicly available code `NSCool`[2], which provides a robust framework for simulating the thermal evolution of NSs under various physical assumptions.

The left panel of Fig. 3.3 shows the region in the $C_{ann} - C_{app}$ plane that is consistent with NS cooling data, while the right panel presents the corresponding constraints in the $(\hat{k}_A)_{11} - (\hat{k}_A)_{22}$ plane.

These constraints are derived using the following relations:

$$C_{app} = 0.847(50)\ (\hat{k}_A)_{11} - 0.407(34)\ (\hat{k}_A)_{22} - 0.035(13)\ (\hat{k}_A)_{33} \ , \tag{3.3.2}$$

$$C_{ann} = -0.407(34)\ (\hat{k}_A)_{11} + 0.847(50)\ (\hat{k}_A)_{22} - 0.035(13)\ (\hat{k}_A)_{33} \ , \tag{3.3.3}$$

as derived in Section 2.10.3.

Notably, within C_{aNN}, the coefficient of $(\hat{k}_A)_{33}$ (-0.035) is significantly smaller than those of $(\hat{k}_A)_{11}$ and $(\hat{k}_A)_{22}$ (0.847 and -0.407, respectively). Thus, if $(\hat{k}_A)_{11,22}$ are non-negligible compared to $(\hat{k}_A)_{33}$, the latter can be neglected in C_{app} and C_{ann}. This is expected since neutrons and protons are composed primarily of first-generation quarks, leading to a weak dependence on $(\hat{k}_A)_{33}$, which

[2]Available at: `https://www.astroscu.unam.mx/neutrones/NSCool/`

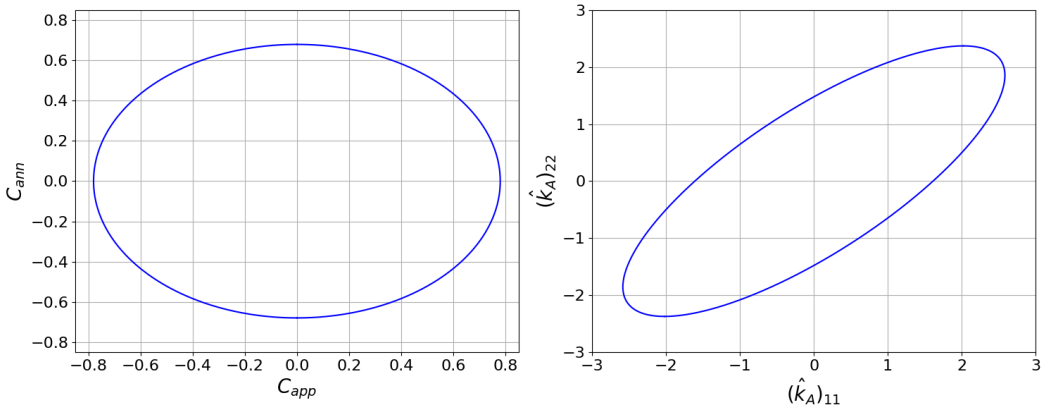

Figure 3.3: The left panel shows 95% one-sided upper limits in the $C_{ann} - C_{app}$ plane for the reference value $f_a = 10^9$ GeV, with the shaded region consistent with NS cooling. The right panel presents the equivalent constraints in the $(\hat{k}_A)_{11} - (\hat{k}_A)_{22}$ plane. See [Bus+22].

corresponds to the strange quark. As part of the quark sea, $(\hat{k}_A)_{33}$ naturally has a much smaller coefficient, justifying its omission to first approximation.

The constraint on C_{app} and C_{ann} for the reference value $f_a = 10^9$ GeV:[3]

$$\left(\frac{C_{app}}{1.6}\right)^2 + \left(\frac{C_{ann}}{1.4}\right)^2 \lesssim 1 \,, \tag{3.3.4}$$

translates into constraints on $(\hat{k}_A)_{11}$ and $(\hat{k}_A)_{22}$:

$$\left(\frac{\cos(\theta)(\hat{k}_A)_{11} + \sin(\theta)(\hat{k}_A)_{22}}{3.315}\right)^2 + \left(\frac{-\sin(\theta)(\hat{k}_A)_{11} + \cos(\theta)(\hat{k}_A)_{22}}{1.154}\right)^2 \lesssim 1 \,, \tag{3.3.5}$$

where $\theta \simeq 0.23\ \pi$.

As a result, we obtain the bounds $|(\hat{k}_A)_{11}| \lesssim 2.7$ and $|(\hat{k}_A)_{22}| \lesssim 2.5$.

Although it may appear surprising that such stringent bounds can be extracted from NS cooling–given that the modeling still faces challenges, such as the possible presence of strange degrees of freedom and the possibly significant impact of superfluidity at low temperatures–the situation offers clear advantages. Thermodynamics is comparatively well understood, a wealth of observational data is available, and the cooling dynamics are much better constrained than in the case of core-collapse SN. It would therefore be highly interesting to revisit the NS cooling calculation including strange matter and supefluidity-suppressed cooling, in order to assess whether the resulting bound on the axial axion-strange-strange coupling $(\hat{k}_A)_{33}$ is compatible with, or possibly even stronger than, that obtained from core-collapse SN (see Section 3.4.9).

3.4 Axion emission from strange matter in core-collapse Supernovæ

This section details the calculations leading to the results presented in [Cav+24].

3.4.1 Introduction

Astrophysical observations of core-collapse SNe, such as SN 1987A, play a crucial role in constraining the existence of axions. The neutrino burst associated with SN 1987A, observed as expected [Hir+87; Bio+87; Bur00; WJ05], places strong constraints on non-standard cooling mechanisms, including free-streaming axions coupled to hadrons [Tur88; RS88; BTB89]. The hypothesis of free-streaming is verified *a posteriori* in Sections 4.1.3.3 and 4.2.2.3. A commonly used criterion is that axion emissivity–that is, the energy-loss rate per unit volume, the local analogue of luminosity–should not

[3] $|g_{app}| < 1.5 \times 10^{-9}$ and $|g_{ann}| < 1.3 \times 10^{-9}$ at 95% confidence, where $g_{aNN} = C_{aNN} m_N / f_a$.

exceed neutrino emissivity, a condition quantified by Raffelt's bound,[4] $Q_a \lesssim Q_\nu$ [Raf90; BTB89] (see Sections 3.4.3 and 3.4.4 for further details). The motivation for using both the free-streaming approximation and the Raffelt's bound is discussed in Section 3.4.2.

In the literature, the most established constraints arise from nucleon-nucleon scattering processes, $N+N \to N+N+a$ [EM89; Car+19; RC24]. However, recent studies suggest that pion-nucleon scattering reactions, $N + \pi \to N + a$, may well be comparable or even dominate axion production [Car+21; Fis+21; Cho+22]. This is the case if the π^- number density within SNe is as large as suggested in [FR20].[5] This suggestion rests on a well-defined physical argument, based on beta equilibrium, charge neutrality, and the virial approximation. The first two conditions relate the chemical potential of π^- to that of electrons, which is itself fixed by the neutron-proton chemical potential difference. Given this, the π^- density is estimated using a virial expansion in fugacity $z = e^{(\mu-m)/T}$, valid when the medium is sufficiently dilute. This assumes that π^- follow a quasi-Boltzmann distribution with only weak two-body corrections. However, at SN core densities and chemical potentials, this dilute limit may break down, rendering the expansion unreliable. As a result, the actual π^- abundance under SN conditions remains an open question, see e.g. [Car23; Raf90]. For further developments, see [Lel+23; Ho+23; VGM22; Lel+24]. In our study, we use particle number densities Y inferred from simulations within the CompOSE framework [TOK15; Typ+22] and obtain Y_{π^-} very much in line with the results suggested by [FR20].

Despite these advances, several aspects of axion emission from SNe remain poorly understood, including:

- Hydrodynamic modeling of SNe, in particular the coherent treatment of axion emission dynamics and possible deviations from spherical symmetry [Fis+21; Mor+22; BO22; Mor+23].
- The impact of in-medium effects on the leading axion-emission processes. These effects are inherently multi-body and as such difficult to capture with full confidence. One approach, applied to the case of neutrinos, is to perform core-dynamical simulations [Mar+12; RRS12]. These effects may then be captured—as in a mean-field picture—by a suitable redefinition of particle masses, energies and chemical potentials by obtaining the latter in terms of the simulated number densities.
- The potential role of axionic interactions with matter components inside the SN volume, beyond first-generation matter [Oer+16; Sil+20; MBB21; KRT22; Rad22; SLW23]. This is well-motivated, because of the large temperature of the emitter, and because of the related facts that fractional densities of certain strange hadrons are "large", around 10^{-2} and that the processes they can mediate are also large, $\mathcal{O}(100)$.

Our study focuses on the last point.

3.4.2 Constraints from SN 1987A

The argument presented below follows the reasoning developed in [Raf90], which examines the constraints imposed by SN 1987A on hypothetical light particles that could be thermally produced in the SN core.

We assume the existence of a new particle X, light enough to be thermally produced, i.e., $m_X \lesssim 10$ MeV. It is also assumed to interact more weakly with matter than neutrinos. Let g_X denote the effective coupling of X to matter[6]. The larger g_X is, the stronger the interaction. A particle X produced in the SN core has some probability of being reabsorbed before escaping; this probability is governed by its mean free path, $l_X \propto g_X^{-2}$. If $l_X > R_{\rm core}$, the particle escapes freely: this is the *free-streaming* regime, and emission occurs throughout the entire volume of the SN core. In this case, the luminosity scales as $L_X \propto g_X^2$, increasing with the coupling. Conversely, if $l_X < R_{\rm core}$, the particles are trapped and escape from an emission sphere of radius $R_X = R_{\rm core} - l_X$. They are then emitted thermally as blackbody radiation, with luminosity given by the Stefan–Boltzmann law:

[4] The original condition is on the luminosity rather than the emissivity. However, since emissivity is more straightforward to compute and we are only working at the oom level, we follow the very standard assumption in the literature that $L_a \lesssim L_\nu$ is, to order of magnitude, approximately equivalent to $Q_a \lesssim Q_\nu$.

[5] In this respect, NS cooling may be simpler to model, since free pions are strongly suppressed at NS temperatures–at least in *mature* stars–and pion condensation is generally disfavored at early stages, when densities are lower, compared with the appearance of hyperons under typical equilibrium conditions.

[6] In general, there are multiple couplings, but for simplicity, we consider a single one, as this does not affect the main argument.

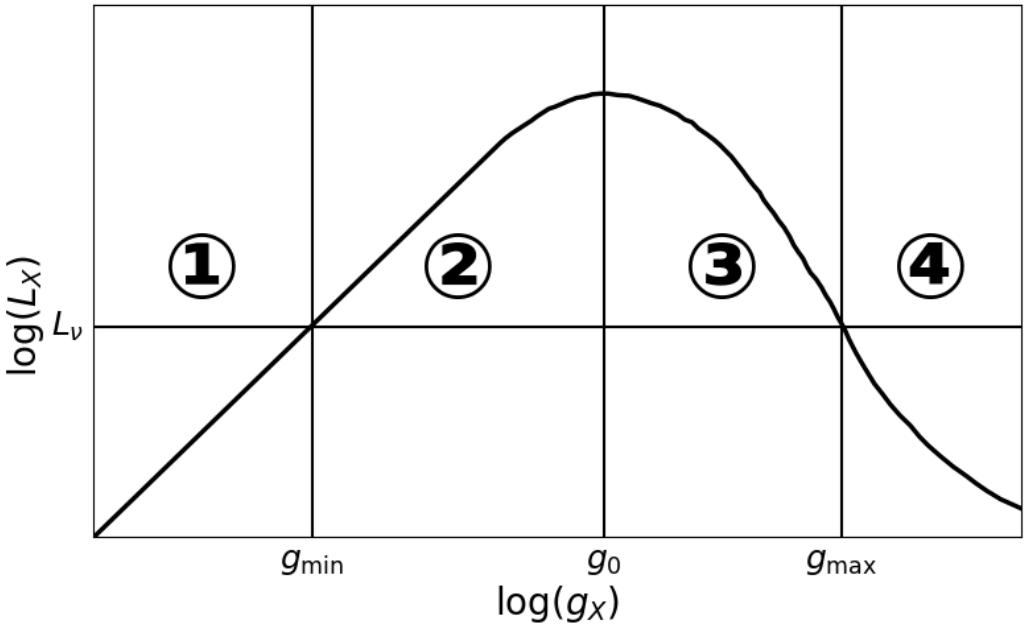

Figure 3.4: Schematic illustration of the luminosity L_X of a hypothetical light particle X as a function of its coupling g_X to matter, adapted from [Raf90]. The plot is divided into four regions: regions 1 and 2 correspond to the free-streaming regime ($l_X > R_{\rm core}$), where L_X increases with g_X, while regions 3 and 4 correspond to the trapped regime ($l_X < R_{\rm core}$), where L_X decreases with g_X.

$L_X \propto R_X^2 T^4(R_X)$. Since $R^2T^4(R)$ is a decreasing function of R in a nascent NS, L_X decreases with g_X in this regime.[7] Moreover, since X is assumed to interact more weakly than neutrinos, its mean free path is larger: $l_X > l_\nu$, which implies that in the trapped regime, $R_X < R_\nu$. Because $R^2T^4(R)$ decreases with R, it is possible to have $L_X > L_\nu$ even if X interacts more weakly than neutrinos.

The total neutrino energy emission is only mildly affected by the presence of X, as about half of this energy is released very rapidly–immediately after the shock wave passes through the neutrinosphere–when heavy nuclei dissociate, causing a sharp increase in the neutrino mean free path. However, particle X can extract energy from the SN core more efficiently during the slow cooling phase (the "cooling tail"), potentially shortening the duration of the neutrino signal. As a result, the signal duration is a more sensitive observable than the total emitted energy for constraining the properties of X. Finally, since the free-streaming regime allows X to escape rapidly, it has the most significant impact on the signal duration. This justifies using a simple criterion such as $L_X \lesssim L_\nu$ to efficiently constrain the free-streaming regime, whereas no simple criterion exists in the trapped regime, where the impact on the burst duration is more indirect.

An illustrative plot of the luminosity as a function of the coupling is shown in Fig. 3.4. Four regions can be identified: regions 1 and 2 correspond to the free-streaming regime (where L_X increases with g_X), while regions 3 and 4 correspond to the trapped regime (where L_X decreases with g_X). Region 4 is excluded by the assumption that X interacts more weakly than neutrinos. Region 3 remains unconstrained. In the free-streaming regime, region 2 is excluded by the condition $L_X \lesssim L_\nu$, whereas region 1 is still compatible with SN 1987A observations. The original argument was first presented in [EO83].

3.4.3 Neutrino emissivity estimation

To apply the condition $Q_a \lesssim Q_\nu$, it is necessary to estimate both the axion and neutrino emissivities.

Estimating the neutrino emissivity from observations is inherently challenging, as direct emissivity measurements are not available. Instead, Q_ν can only be inferred indirectly by estimating the duration of the neutrino burst ($\Delta t_\nu \sim 10$ s) and using an estimation of the core mass ($M \sim M_\odot$) and the density ($\rho \sim 3 - 8$ g/cm^3) of the SN core. This results in an oom estimate for Q_ν, which we summarize next.

[7] More precisely, if g_X increases, then l_X decreases, implying that $R_X = R_{\rm core} - l_X$ increases. Because $R^2T^4(R)$ is a rapidly decreasing function of R, the luminosity L_X decreases.

To determine Q_ν, we begin with the gravitational binding energy,

$$E_b \sim \frac{GM^2}{r} = G\rho^{1/3}M^{5/3} \sim 6 \times 10^{53} \text{ erg} , \tag{3.4.1}$$

and assume that approximately half of this energy is radiated in neutrinos over a timescale Δt_ν. This leads to a neutrino luminosity [Bur00; WJ05]

$$L_\nu \sim \frac{E_b}{2\Delta t_\nu} \sim \frac{G\rho^{1/3}M^{5/3}}{2\Delta t_\nu} \sim 3 \times 10^{52} \text{ erg.s}^{-1} . \tag{3.4.2}$$

The corresponding energy-loss rate per unit mass is estimated as

$$\epsilon_\nu \sim \frac{L_\nu}{M} \sim \frac{G\rho^{1/3}M^{2/3}}{2\Delta t_\nu} \sim 10^{19} \text{ erg.g}^{-1}\text{.s}^{-1} . \tag{3.4.3}$$

Thus, the neutrino emissivity is approximately

$$Q_\nu = \epsilon_\nu \rho \sim \frac{GM^{2/3}\rho^{4/3}}{2\Delta t_\nu} \sim 3 \times 10^{33} \text{ erg.cm}^{-3}\text{.s}^{-1} . \tag{3.4.4}$$

From this argument, it is clear that emissivity estimates can only be trusted to within an oom, and that this uncertainty is irreducible, because neither the luminosity, nor the core mass, nor the actual fraction of the core mass lost in radiation are, at the moment, measured directly. With this important qualification in mind, any constraint on axion couplings derived from SN emissivity will thus carry an associated uncertainty of about 50% since Q_a depends quadratically on the axionic couplings.

Therefore, to improve the robustness of axion bounds, refining the precision of Q_a calculations alone may not be sufficient. Future observations of core-collapse SNe, similar to SN 1987A, will be crucial toward statistically reducing these uncertainties.

3.4.4 Axion emissivity estimation

In astrophysical systems, the emissivity [CR24; Tam+17] of a particle,[8] produced in a process $n_i \to n_f$, quantifies the energy radiated by this particle per unit volume and per unit time. Taking the axion a for definiteness, we have, by definition,

$$dQ_a = \frac{E_a}{V} d\dot{n} , \tag{3.4.5}$$

where the differential event rate $d\dot{n}$, given in Eq. (B.1.24) in Appendix B.1, determines how physical observables are derived. The resulting expression for the emissivity is:

$$dQ_a = E_a |\mathcal{M}_{fi}|^2 (2\pi)^4 \delta^4(P_i - P_f) \left(\prod_{b=1}^{n_i} \frac{f_b d^3\vec{p}_b}{2E_b(2\pi)^3} \right) \left(\prod_{c=1}^{n_f} \frac{\bar{f}_c d^3\vec{p}_c}{2E_c(2\pi)^3} \right) . \tag{3.4.6}$$

The relevant phase space calculations for the emissivity are presented in Appendix B.8.

In Eq. (3.4.6), f_b and $\bar{f}_c$ denote the statistical distribution functions for incoming and outgoing particles, respectively:

$$f_b = \left(e^{(E_b - \mu_b)/T} + \epsilon_b \right)^{-1} , \quad \bar{f}_c = 1 - \epsilon_c f_c = \left(1 + \epsilon_c e^{-(E_c - \mu_c)/T} \right)^{-1} , \tag{3.4.7}$$

where $\epsilon = +1$ for fermions (Fermi-Dirac distribution) and $\epsilon = -1$ for bosons (Bose-Einstein distribution). When $E - \mu \gg T$, ϵ becomes negligible compared to the exponential, and the quantum distribution reduces to the classical Maxwell-Boltzmann distribution:

$$f_b = e^{-(E_b - \mu_b)/T} , \quad \bar{f}_c = 1 . \tag{3.4.8}$$

Non-thermal particles, such as axions, which interact weakly and do not thermalize with the surrounding medium, typically have $f_b \simeq 0$ and $\bar{f}_c \simeq 1$. This means that the probability for them to interact as incoming particles inside the core is assumed to be nearly zero. This free-streaming regime can be verified *a posteriori*.

[8] Here we consider the axion, but the procedure is general and not limited to axions.

The distribution formulas require knowledge of the chemical potential. To determine it, one uses the particle number density:

$$n_b = \int_{\mathbb{R}^3} f(E) \frac{d^3\vec{p}}{(2\pi)^3} = \frac{1}{2\pi^2} \int_0^{+\infty} \frac{p^2}{e^{(E-\mu)/T} + \epsilon} dp \ . \tag{3.4.9}$$

If the chemical potential μ is known, the density n can be deduced. Conversely, if the density n is known, the chemical potential μ can be determined, for instance, by using a dichotomy method.

The luminosity L_a associated with particle a corresponds to the total energy radiated via this particle per unit time. It is computed by integrating the emissivity over the entire volume:

$$L_a = \int_V Q_a(\vec{r}) d^3\vec{r} \ . \tag{3.4.10}$$

Assuming spherical symmetry, this simplifies to:

$$L_a = 4\pi \int_0^R Q_a(r) r^2 dr \ . \tag{3.4.11}$$

It is also possible to express the emissivity as

$$Q_a = \int_{m_a}^{+\infty} E_a \frac{d\dot{n}_a}{dE_a} dE_a \ , \tag{3.4.12}$$

which allows us to define the spectrum

$$\frac{dN_a}{dE_a} = \int_V d^3\vec{r} \int_{t_i}^{t_f} dt \frac{d\dot{n}_a}{dE_a} \simeq V \Delta t \frac{d\dot{n}_a}{dE_a} \ , \tag{3.4.13}$$

where V is the volume of emission and Δt is the emission duration.

The spectrum is related to the luminosity by

$$\int_{t_i}^{t_f} L_a dt = \int_{m_a}^{+\infty} E_a \frac{dN_a}{dE_a} dE_a \quad \Leftrightarrow \quad L_a \simeq \frac{N_a \langle E_a \rangle}{\Delta t} \ , \tag{3.4.14}$$

where

$$N_a = \int_{m_a}^{+\infty} \frac{dN_a}{dE_a} dE_a \ , \tag{3.4.15}$$

is the total number of emitted a particles, and

$$\langle E_a \rangle = \frac{1}{N_a} \int_{m_a}^{+\infty} E_a \frac{dN_a}{dE_a} dE_a \ , \tag{3.4.16}$$

is their average energy.

In summary, while emissivity quantifies the local energy emission rate of particle a, luminosity describes the total energy emitted by a across the entire volume per unit time. These quantities are fundamental in modeling energy transfer and cooling dynamics in astrophysical systems, where particle interactions drive the evolution and observable signatures of stellar and compact object environments.

3.4.5 Supernova core modeling

To model the SN core, we make the following assumptions:

- The absence of muons. Although muons are typically included in EoSs for cold NSs, most SN simulations to date have not treated heavy charged leptons explicitly. Their influence is expected to remain small owing to their comparatively large rest masses [Oer+17].
- Weak equilibrium for strangeness-changing reactions, i.e., reactions where $|\Delta S| \neq 0$.

Under these conditions, the state of matter is fully characterized by three thermodynamic parameters, that may be chosen as:

- the temperature T,

- the baryon number density n_B, and
- the electron fraction $Y_e = (n_{e^-} - n_{e^+})/n_B$.

These parameters determine the abundances of all relevant particles entering the EoS [Jan+07; Oer+17].

In the standard approach [Bru85], local values of these parameters are obtained by solving the hydrodynamic equations coupled with neutrino transport, ensuring the conservation of energy-momentum, baryon number, and lepton number. When axions are included, additional energy and momentum losses due to axion emission must be incorporated into the core-collapse SN dynamics, as discussed in [Fis+21; Mor+22; BO22; Mor+23].

Ideally, thermodynamic parameters should be obtained through such procedure. However, in this study, as in much of the existing literature on exotic sources of cooling, we estimate axion emission *a posteriori*, assuming typical thermodynamic conditions inside the SN core as adopted in [Car+21; Mar+20]. The reference values we use are:

- $T \in \{30, 40\}$ MeV. This choice is consistent with typical values adopted in the literature for *fiducial*[9] calculations of axion emissivity [Car+21].[10] Although proto-NSs quickly cool below these temperatures [Pon+99; Rob12; PNO22], the emissivity grows steeply with T,[11] so the luminosity is dominated by the hottest phases. Evaluating the Raffelt bound at such temperatures therefore provides a good approximation without requiring a full treatment of the thermal evolution;
- $n_B \in \{1, 1.5\}\ n_{\rm sat}$, with $n_{\rm sat} = 0.16\ \text{fm}^{-3}$;
- As a third thermodynamic parameter, we use the total charged baryon fraction

$$Y_{Q_B} = \sum_{i \in \text{baryons}} q_i n_i / n_B = 0.3\ . \tag{3.4.17}$$

  This choice corresponds to the standard fiducial value $Y_{Q_B} = 0.3$ used in SN axion-emissivity studies [Car+21], motivated by charge equilibrium conditions at $\rho \simeq \rho_{\rm sat}$. While somewhat on the upper side of values encountered during the evolution, it provides a conventional benchmark, especially for comparisons with the literature. We note that smaller Y_{Q_B} values would reduce the emissivity.

The exact distribution functions of the various particles within the core are not known. The best-controlled distributions stem from the ideal-gas approximation (i.e., Fermi-Dirac or Bose-Einstein statistics), and we adopt this assumption, consistent with much of the existing literature. However, in-medium effects in hot and dense matter significantly modify charged-current neutrino interactions, thereby affecting the resulting emission spectra [Mar+12; RRS12]. In particular, nucleon mean-field effects alter the single-particle energies, as the interaction potentials of neutrons and protons differ in asymmetric matter where neutron and proton densities are unequal.

These distributions require knowledge of parameters such as chemical potentials and particle masses. In dense and hot systems like the SN core, calculating the exact interactions between each pair of particles is a daunting task, due to, for example, multiple scattering effects. The mean-field approach alleviates this complexity by replacing microscopic interactions with an average potential. This approximation often leads to simpler, more tractable mathematical equations. We apply the formalism developed in [RPL98] to compute axion emissivities. While mean-field effects are expected to be weaker under the less dense conditions we consider, a detailed analysis of these corrections is left for future work. In this formalism, baryon masses and chemical potentials are replaced by their effective counterparts, incorporating medium interactions at the mean-field level (see e.g. [Mar+12; RRS12; RPL98; Oer+20]):

$$m_j \to m_j^*\ , \quad \mu_j \to \mu_j^* = \mu_j - U_j\ , \tag{3.4.18}$$

where the effective chemical potential μ_j^* includes the mean-field interaction potential U_j.

In our analysis, we assume that meson effective masses remain equal to their vacuum masses, and the only nonzero meson chemical potentials are $\mu_{\pi^\pm} = \mu_{K^\pm} = \pm\mu_q$. This approximation is standard in

[9] As opposed to full SN simulations, see e.g. [Fis+14].

[10] $T = 40$ MeV, though somewhat high, is included as an exploratory scenario for assessing stronger constraints.

[11] This can be understood intuitively, given the high dimensionality of the phase space, and the fact that powers of momenta are ultimately normalized by the temperature.

mean-field models: mesons are introduced as auxiliary fields whose couplings are fitted to reproduce bulk nuclear-matter properties, so mesons' in-medium modifications are effectively encoded in the baryonic self-energies. For global thermodynamic quantities such as the EoS and particle abundances, this treatment is sufficient: a more refined description of meson propagation would be required only for observables directly sensitive to meson spectral functions.

We consider two well-established EoS models, referred to as $DD2Y$ and $SFHoY$ [FOP18; Mar+17], which provide the relevant chemical potentials and effective masses for the hadronic species included in our calculations. This choice is motivated by several factors: these models predict different amounts of strangeness in hot and dense matter; they are publicly available; and they are compatible with astrophysical and nuclear physics constraints [FOP18; Mar+17].

In summary, we have seen in this section that calculating the axion emissivity requires making certain assumptions about the SN-core modeling, which introduces a sizeable uncertainty on Q_a and on Q_ν. However, notwithstanding this uncertainty, the inequality $Q_a \lesssim Q_\nu$ still provides formidable bounds on axion interactions.

Considering different EoS models and thermodynamic conditions (with numerical values given in Appendix B.9) allows us to explore the range of variation of our results, and ascertain that they are not restricted to a specific scenario but remain of general validity.

3.4.6 Axion-hadron modeling

In the literature, axion emissivity is typically used to constrain axion-nucleon or axion-neutron-Λ couplings independently. However, a comprehensive framework for broadly constraining axion-hadron couplings is still lacking. In this section, we incorporate strange matter effects and analyze the full meson and baryon octets within a consistent Effective Field Theory (EFT) approach.

To achieve robust results in axion-hadron modeling, we employ Chiral Perturbation Theory augmented with an axion (ChPT+a), which defines axion-hadron interactions in terms of fundamental axion-quark couplings. This Lagrangian is specified in Section 2.10. Some qualification is in order as concerns the purely hadronic vertices. These vertices depend, besides F_0, on the chiral $SU(3)$ low-energy constants D, F, and S, which are fixed from Lattice QCD (LQCD) data. The amplitudes thereby obtained are then modified parametrically: masses and chemical potentials are replaced by their effective counterparts, following a Relativistic Mean-Field (RMF) picture. These effective quantities are, in turn, determined through separate simulations describing the macroscopic properties of the medium, with built-in EoSs such as $DD2Y$ and $SFHoY$, chosen to satisfy astrophysical constraints (e.g. a maximum NS mass exceeding $2M_\odot$).

We assume the QCD axion constant at the reference value $f_a = 10^9$ GeV. This choice does not restrict generality, as the emissivity Q_a scales as $1/f_a^2$. Thus, if f_a is multiplied by a factor x_f, the resulting Q_a scales as $1/x_f^2$. To maintain generality, we do not assume any specific frameworks such as Kim-Shifman-Vainshtein-Zakharov (KSVZ) or Dine-Fischler-Srednicki-Zhitnitsky (DFSZ). Instead, we rely exclusively on experimental constraints that are independent of SN observations.

The axion-quark couplings are encoded in the matrices $\hat{k}_{A/V}$, which, under charge conservation and hermiticity, take the form:

$$\hat{k}_{A/V} = \begin{pmatrix} \hat{k}_{11} & 0 & 0 \\ 0 & \hat{k}_{22} & \hat{k}_{23} \\ 0 & \hat{k}_{23}^* & \hat{k}_{33} \end{pmatrix}_{A/V} . \tag{3.4.19}$$

However, not all elements contribute significantly to the relevant processes:

- The diagonal vector couplings $(\hat{k}_V)_{ii}$ do not contribute to strong interactions, only to weak interactions, which are suppressed by a factor $G_F F_0^2 \sim 10^{-7}$ (see Section 2.10.5).
- The phases $\arg((\hat{k}_{A/V})_{23})$ do not affect the processes studied here, as the initial and final states involved in the relevant transitions have the same parity.
- The off-diagonal vector coupling $|(\hat{k}_V)_{23}|$ is negligible due to its stringent experimental limit of 2×10^{-3} (see Section 5.1).

As a result, the only relevant parameters to constrain are the diagonal axial couplings $(\hat{k}_A)_{ii}$ and the absolute value of the off-diagonal axial coupling $|(\hat{k}_A)_{23}|$.

Existing bounds from the literature are summarized in Table 3.1.

Table 3.1: Bounds on axion-quark couplings. Constraints on $(\hat{k}_A)_{ii}$ are discussed in Section 3.3, and those on $|(\hat{k}_{V/A})_{23}|$ in Section 5.1.

Couplings	$\lvert(\hat{k}_A)_{11}\rvert$	$\lvert(\hat{k}_A)_{22}\rvert$	$\lvert(\hat{k}_A)_{33}\rvert$	$\lvert(\hat{k}_A)_{23}\rvert$	$\lvert(\hat{k}_V)_{23}\rvert$
Bounds	2.7	2.5	unknown	22	2×10^{-3}

3.4.7 Studied processes

The literature has primarily focused on first-generation processes, particularly nucleon-nucleon scattering, $N_1N_2 \to N_3N_4a$ [EM89; Car+19; CR24]. However, recent studies suggest that pion-nucleon scattering, $N_i\pi \to N_fa$, could be the dominant channel [Car+21; Fis+21; Cho+22], due to the non-negligible fraction of π^- calculated in [FR20], as described above. The decay process $\Lambda \to na$ was considered in [Mar+20].

The motivation for including the complete baryon and meson octets, as we do in our study, lies in the additive nature of the emissivity. Although the fraction of strange matter is small ($< 10^{-2}$), the large number of possible processes may still yield a non-negligible total contribution. In particular, baryon decay involves 7 processes, while meson-baryon scattering includes 134. All considered processes must satisfy kinematic constraints, electric charge conservation, and the condition $|\Delta S| \leq 1$, since the axion can mediate flavor-changing interactions. We neglect flavor changes induced by weak interactions.

It is important to emphasize that, since emissivity is additive, neglecting any additional channel beyond those we consider does not invalidate our results. Rather, it makes our bounds more conservative, as we may underestimate the total emissivity. Moreover, the goal of this study is not to provide a comprehensive prediction of the axion emission spectrum, but rather to assess whether hadrons beyond the first generation–particularly strange hadrons–can significantly contribute to axion emission.

The Feynman diagrams for baryon-meson scattering are shown in Fig. 3.5. These include all diagrams with the appropriate external fields, a single axion vertex, and no loops. Diagram 1 corresponds to a local vertex. Diagrams 2 and 3 involve baryon propagators and are the only ones retained if one merely requires the presence of axion-baryon couplings (e.g. C_{aNN}) [Car+21], without adopting a consistent EFT framework. Diagram 4 features a meson-meson-axion vertex, involving only $\hat{k}_V$. However, its diagonal components are unobservable under strong interactions, so this diagram contributes only through flavor-changing processes. Consequently, it vanishes for the first generation. Diagrams 5, 6, and 7 include axion-meson mixing, which is proportional to m_a^2. Since we focus on the QCD axion, this contribution is negligible and is not considered here.

The Feynman diagrams for baryon decay are shown in Fig. 3.6. They include all diagrams with the appropriate external fields, a single axion vertex, and no loops. Diagram 2 involves axion-meson mixing, proportional to m_a^2. Again, since we study the QCD axion, we neglect this contribution and retain only Diagram 1.

3.4.8 General procedure to compute emissivity

For a generic process $n_i \to n_f$, the full phase space is $3(n_i + n_f)$-dimensional. However, the conservation of the total four-momentum reduces the number of independent variables by 4. Additional symmetries (e.g., isotropy) allow for a further reduction by $n_{\text{sym}} \geq 2$.[12] For example, in a $1 \to 2$ process, we have $3(1+2)-4-3 = 2$ dimensions left (see Appendix B.8.1), whereas a $2 \to 2$ process results in $3(2+2)-4-3 = 5$ dimensions (see Appendix B.8.2). While 2-dimensional integrals pose no numerical difficulty, the 5-dimensional case requires careful treatment. In the literature (see e.g. [Car+21]), the strategy to handle such high-dimensional integrals has been to apply approximations that further reduce the dimensionality. For example, assuming baryons are nearly at rest ($E \sim m$) simplifies the integration to a product of two 1-dimensional integrals (see Appendix B.8.2.4), which is numerically straightforward. We performed a numerical comparison between this approximation and the full, unapproximated calculation. For first-generation particles, the difference turns out to be minimal (see Appendix B.8.2.5 for details). However, it is not clear whether this remains true when considering the full baryon and meson octet. For instance, in a process such as $\Sigma\pi \to Na$, assuming the nucleon

[12] This follows from the fact that only relative angles enter the calculation, allowing one to choose $\vec{p}_a$ as the reference direction and perform the integration directly over $d\Omega_a$.

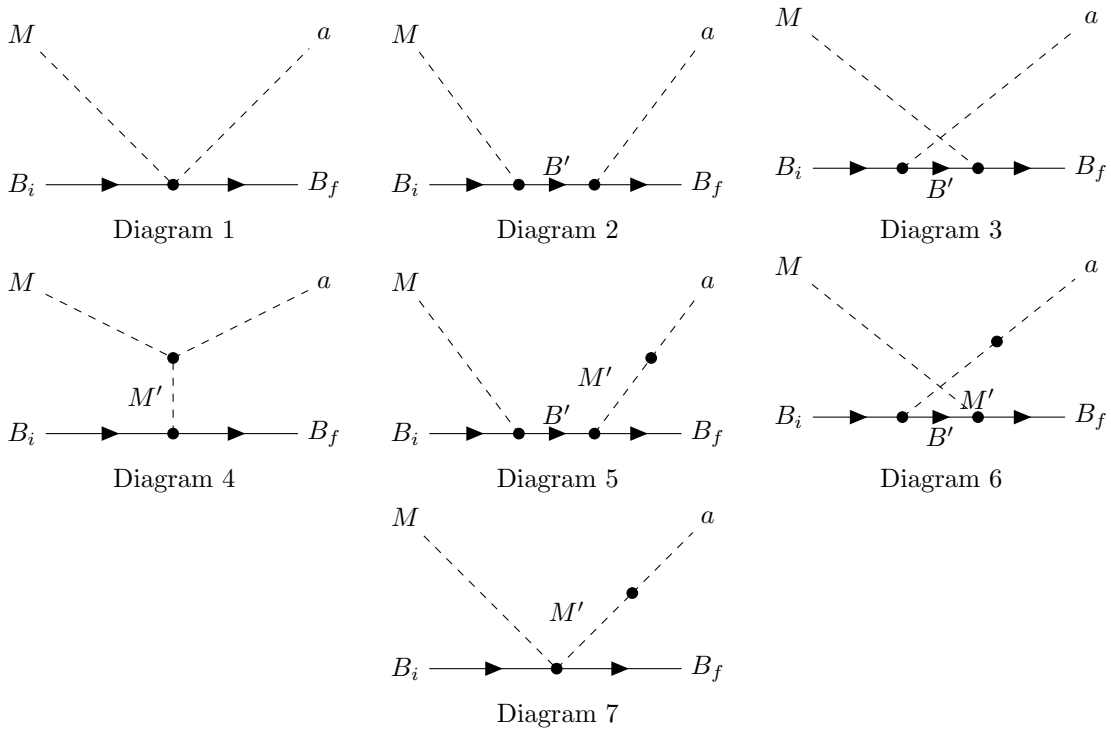

Figure 3.5: Leading-order Feynman diagrams contributing to baryon-meson scattering $B_i M \to B_f a$.

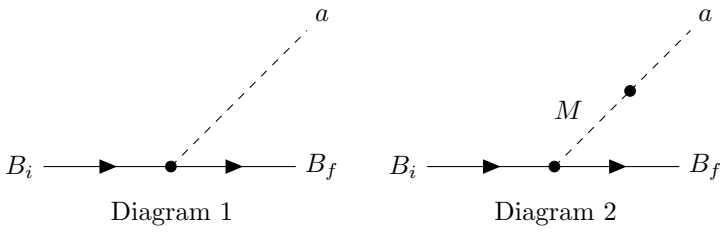

Figure 3.6: Leading-order Feynman diagrams contributing to baryon decay $B_i \to B_f a$.

to be at rest may no longer be valid, since it can carry away a significant portion of the Σ's rest mass energy.

In our calculations, axion and mesons are treated relativistically using the full energy-momentum relation ($E^2 = m^2 + |\vec{p}|^2$), since the temperature is not negligible compared to their masses ($m_a \ll T$, $T/m_\pi \sim 25\%$). Conversely, baryons are much heavier than the temperature ($T/m_N < 5\%$), which justifies using the non-relativistic approximation ($E = m + |\vec{p}|^2/(2m)$). As a consequence, in high-dimensional phase space processes such as $MB_i \to B_f a$, we adopt the non-relativistic treatment for baryons to simplify the calculation. However, in simpler kinematic cases such as $B_i \to B_f a$, we retain the full relativistic treatment. Further details can be found in Appendix B.8.

We thus need a general procedure to compute the axion emissivity, Q_a, in high-dimensional phase space. In general, we write:

$$Q_a = \int_D g(\vec{p}) |\mathcal{M}_{fi}|^2(\vec{p})\, d^n\vec{p}\,, \tag{3.4.20}$$

where g is a general function depending on the external states' momenta, $\mathcal{M}_{fi}$ is the Feynman amplitude of the process, and n is the integration dimension, taking into account energy-momentum conservation and symmetries.

For our specific integrations, we express

$$|\mathcal{M}_{fi}|^2(\vec{p}) = \sum_{b=1}^{N} P_b(\vec{p})\, C_b\,, \tag{3.4.21}$$

where $P_b(\vec{p})$ depends on the SN core model, the particle masses, and their momenta, while C_b depends

solely on couplings Beyond the Standard Model (BSM). Importantly, C_b remains invariant under integration, so that

$$Q_a = \sum_{b=1}^{N} C_b \, I_b \ , \tag{3.4.22}$$

with

$$I_b = \int_D g(\vec{p}) \, P_b(\vec{p}) \, d^n\vec{p} \ . \tag{3.4.23}$$

The integrals can thus be performed independently of the axion couplings, allowing us to compute the numerous integrations once and for all, and then vary the axion couplings as needed. Without this method, each change in the couplings $\hat{k}_{A/V}$ would require redoing the entire integration.

Ultimately, Q_a manifests as a quadratic form in the components of $\hat{k}_{A/V}$. Defining $\vec{k}$ as the vector containing these components, we can write

$$Q_a = \vec{k}^{\dagger} \cdot A \cdot \vec{k} \ , \tag{3.4.24}$$

where A is a Hermitian matrix, ensuring it is diagonalizable with real eigenvalues. Since Q_a must be positive, all eigenvalues of A are positive as well, providing a straightforward consistency check of our integral calculations.

To implement the procedure outlined above, it is necessary to perform high-dimensional integrals. For this purpose, we use a Monte Carlo method [Wei00].

The method involves introducing a probability density $f_{\vec{X}}$ over the domain D, so that

$$I = \int_D F(\vec{x}) \, d^n\vec{x} = \int_D \frac{F(\vec{x})}{f_{\vec{X}}(\vec{x})} f_{\vec{X}}(\vec{x}) \, d^n\vec{x} = \mathbb{E}\left(\frac{F(\vec{X})}{f_{\vec{X}}(\vec{X})}\right) \ . \tag{3.4.25}$$

By generating a pseudo-random sample $(\vec{x}_b)_{b\in[\![1;N]\!]}$ according to the density $f_{\vec{X}}$, we approximate the expectation with the mean:

$$I \simeq \frac{1}{N} \sum_{b=1}^{N} \frac{F(\vec{x}_b)}{f_{\vec{X}}(\vec{x}_b)} \ . \tag{3.4.26}$$

To estimate the uncertainty, we apply the central limit theorem, which implies that the standard deviation of the confidence interval at significance level α is

$$\Delta I = q_\alpha \sqrt{\frac{V}{N}} \ , \tag{3.4.27}$$

where the variance V is

$$V := \mathrm{Var}\left(\frac{F(\vec{X})}{f_{\vec{X}}(\vec{X})}\right) = \mathbb{E}\left(\left(\frac{F(\vec{X})}{f_{\vec{X}}(\vec{X})}\right)^2\right) - \left(\mathbb{E}\left(\frac{F(\vec{X})}{f_{\vec{X}}(\vec{X})}\right)\right)^2 \ , \tag{3.4.28}$$

and

$$\mathbb{E}\left(\left(\frac{F(\vec{X})}{f_{\vec{X}}(\vec{X})}\right)^2\right) = \int_D \left(\frac{F(\vec{x})}{f_{\vec{X}}(\vec{x})}\right)^2 f_{\vec{X}}(\vec{x}) \, d^n\vec{x} = \int_D \frac{(F(\vec{x}))^2}{f_{\vec{X}}(\vec{x})} \, d^n\vec{x} \ , \tag{3.4.29}$$

is also estimated by a mean[13].

Additionally, we apply a strategy to compactify the integrals by performing a change of variables, $x = t/(1-t)$, yielding

$$\int_0^{+\infty} f(x) \, dx = \int_0^1 f\left(\frac{t}{1-t}\right) \frac{dt}{(1-t)^2} \ . \tag{3.4.30}$$

[13] For convergence of this method, it is crucial that the integral in Eq. (3.4.29) converges, emphasizing the importance of an appropriate choice for the density $f_{\vec{X}}$. Moreover, a judicious choice of $f_{\vec{X}}$ can accelerate the computation time to reach a given precision; the closer $f_{\vec{X}}$ is in form to F, the faster the convergence will be.

3.4.9 Results

The procedure consists in taking, as priors for the k-couplings, samples uniformly distributed over the values compatible with experimental data–namely K decays and potentially NS cooling–and obtaining a posterior by applying the condition $Q_a \lesssim Q_\nu$.

The results are presented in Figs. 3.7, 3.8, 3.9, and 3.10. However, the coupling $(\hat{k}_V)_{23}$ is omitted, as $K \to \pi a$ decays already provide significantly stronger constraints on this quantity, and the emissivity does not improve them.

The results are expressed in terms of $\hat{k}_A$ rather than k_A,[14] since the emissivity depends quadratically on $\hat{k}_A$, making the interpretation of the results more straightforward. Once bounds on $\hat{k}_A$ are established, the corresponding bounds on k_A can be deduced using the relation $\hat{k}_A = k_A + 2c_{aGG}M_q^{-1}/\mathrm{Tr}[M_q^{-1}]$.

Each figure consists of four panels corresponding to different thermodynamic conditions. Within each panel, nine plots are arranged in a triangular layout: the diagonal plots show the one-dimensional marginalized posteriors for each coupling, while the off-diagonal plots display two-dimensional projections to highlight potential correlations.

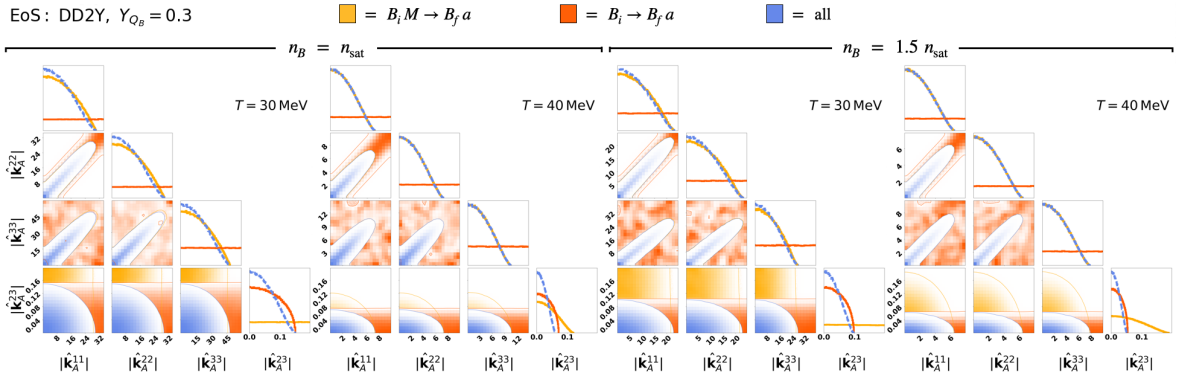

Figure 3.7: Allowed regions for $|(\hat{k}_A)_{ij}|$, with $ij \in \{11, 22, 33, 23\}$, obtained from $Q_a(B_i M \to B_f a)$, $Q_a(B_i \to B_f a)$, and their combination, for $T \in \{30, 40\}$ MeV, $n_B \in \{1, 1.5\}\ n_{\rm sat}$, and $Y_{Q_B} = 0.3$. The EoS $DD2Y$ with $f_a = 10^9$ GeV is used. The diagonal plots display the marginalized posterior distributions for the respective k-couplings.

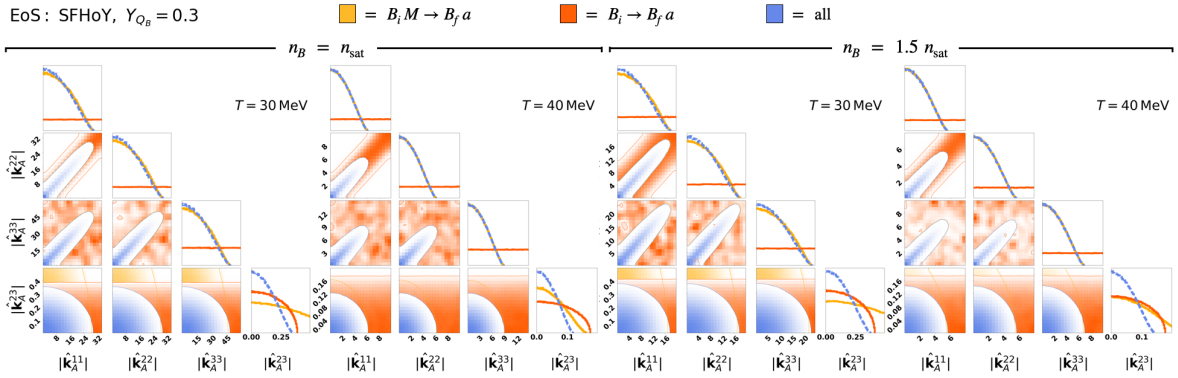

Figure 3.8: Same as Fig. 3.7, but for $SFHoY$.

Figs. 3.7 and 3.8 present the results considering only emissivity constraints. In these cases, $|(\hat{k}_A)_{23}|$ is primarily constrained by $B_i \to B_f a$ decays (and marginally by $B_i M \to B_f a$ scatterings), while the diagonal couplings $(\hat{k}_A)_{ii}$ are bounded through $B_i M \to B_f a$ scatterings. Significant correlations between diagonal couplings are also visible.

Figs. 3.9 and 3.10 additionally include NS cooling constraints. While NS cooling does not affect $|(\hat{k}_A)_{23}|$, it significantly improves the bounds on the diagonal couplings $(\hat{k}_A)_{11}$ and $(\hat{k}_A)_{22}$. Through emissivity-induced correlations, the constraint on $(\hat{k}_A)_{33}$ is also strengthened.

[14] See Section 2.10.1, where k_A and $\hat{k}_A$ are defined.

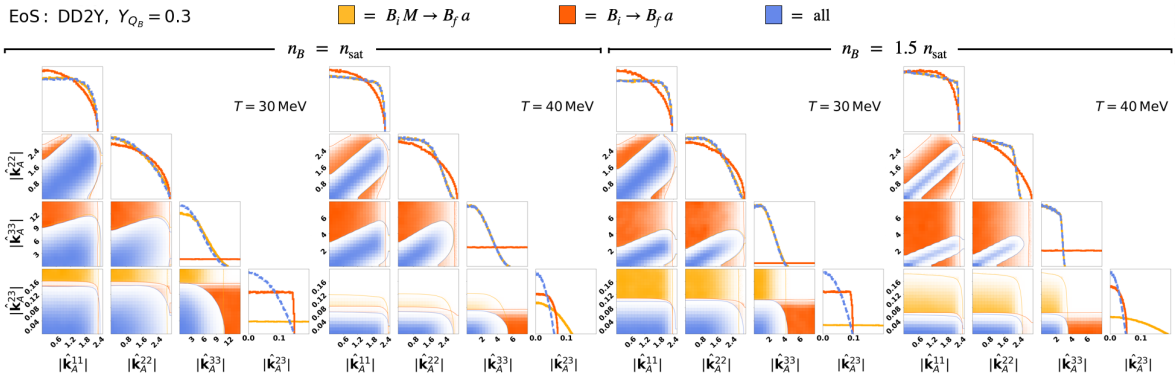

Figure 3.9: Same as Fig. 3.7, but incorporating the NS cooling constraint.

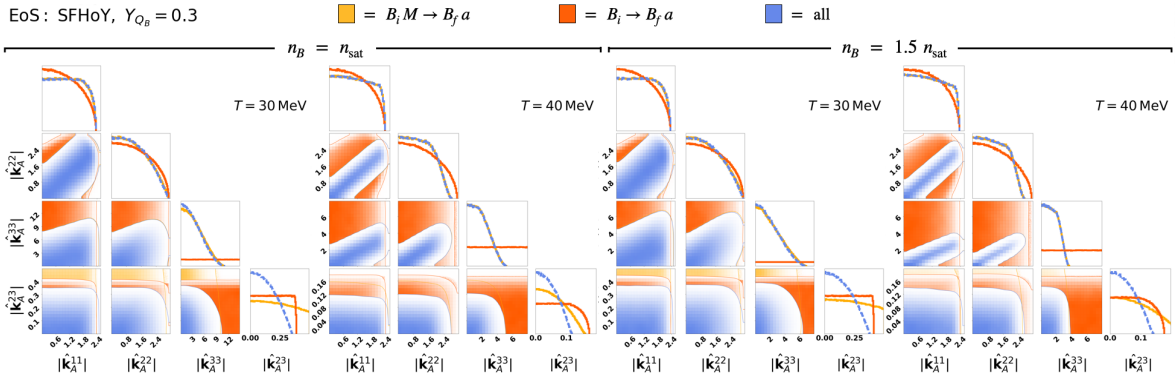

Figure 3.10: Same as Fig. 3.9, but for $SFHoY$.

The previous results can be understood by considering the general form of the emissivity for the processes under study,

$$Q_a = \alpha_V |(\hat{k}_V)_{23}|^2 + \alpha_A |(\hat{k}_A)_{23}|^2 + \sum_{i=1}^{3} \alpha_i \left(\sum_{j=1}^{3} \beta_{ij} (\hat{k}_A)_{jj} \right)^2 , \tag{3.4.31}$$

where $\alpha_{V,A,i} \geq 0$. This structure naturally leads to direct bounds on $|(\hat{k}_{V,A})_{23}|$ and both bounds and correlations among the diagonal elements $(\hat{k}_A)_{ii}$[15].

The numerical values of the bounds are provided in Tables 3.2 and 3.3. [16]

It can be observed that $|(\hat{k}_A)_{23}|$ is constrained to be of order 0.1, depending on the EoS and thermodynamic parameters. However, since we rely on neutrino emissivity, which carries significant uncertainties, the exact numerical values listed in the tables are less important; only the oom matters. This oom is consistent across the different SN core models, demonstrating the relative robustness of the result. It also represents a substantial improvement compared to bounds without SN, which were of order 20, even though the collider bounds quoted here originate from a controlled environment and are therefore free of the oom uncertainties affecting astrophysical constraints (for more details, see Section 2.11).

[15] If we consider only the $SU(3)_L \times SU(3)_R$ symmetry ($S = 0$ in the axion-hadron Lagrangian, see Eq. (2.10.57)), then the couplings involve only the Gell-Mann matrices, which are traceless. This implies that for all $i \in \{1, 2, 3\}$, we have $\sum_{j=1}^{3} \beta_{ij} = 0$. However, from the diagonalization of Eq. (3.4.24), the combinations $\sum_{j=1}^{3} \beta_{ij} (\hat{k}_A)_{jj}$ must form a basis, which would require that at least for some i, say $i = 3$, the sum $\sum_{j=1}^{3} \beta_{ij} \neq 0$. To resolve this apparent contradiction, it is necessary that $\alpha_3 = 0$. As a result, the $S = 0$ case preserves correlations among the diagonal couplings, but no direct bounds can be obtained without incorporating the NS cooling constraint.

[16] Figs. 3.9-3.10 and Table 3.3 differ from their counterparts in [Cav+24]. In our initial estimates, we adopted the assumption $S = 0$ in Eq. (2.10.57), following the standard choice in early literature such as [CC93], where experimental extractions yielded values of S compatible with zero–for example, the EMC measurement of the polarized proton structure function reported $S = 0.13 \pm 0.20$ [JM90], and the elastic neutral-current experiment found $S = 0.09 \pm 0.24$ [KM88]. Recent LQCD computations [VGM21], however, provide much improved precision and indicate a non-vanishing value, $S = 0.405 \pm 0.062$ (see Section 2.10.3). The updated results shown here incorporate this value. The numerical differences are modest and do not alter any oom conclusions.

Table 3.2: SN bounds on $|(\hat{k}_A)_{23,11,22,33}|$ depending on the SN core modeling. The lower (resp. upper) value in each entry corresponds to $DD2Y$ (resp. $SFHoY$). Bounds assume $f_a = 10^9$ GeV.

k-coupling	$n_B = n_{\rm sat}$		$n_B = 1.5\ n_{\rm sat}$	
	$T = 30$ MeV	$T = 40$ MeV	$T = 30$ MeV	$T = 40$ MeV
$\lvert(\hat{k}_A)_{23}\rvert$	0.35 0.15	0.12 0.061	0.38 0.097	0.14 0.052
$\lvert(\hat{k}_A)_{11}\rvert$	30 30	6.1 7.2	18 23	5.5 6.5
$\lvert(\hat{k}_A)_{22}\rvert$	30 30	6.0 7.2	18 23	5.7 6.4
$\lvert(\hat{k}_A)_{33}\rvert$	49 48	8.8 11	23 28	6.8 7.7

Table 3.3: Same as Table 3.2, but including NS cooling.

k-coupling	$n_B = n_{\rm sat}$		$n_B = 1.5\ n_{\rm sat}$	
	$T = 30$ MeV	$T = 40$ MeV	$T = 30$ MeV	$T = 40$ MeV
$\lvert(\hat{k}_A)_{23}\rvert$	0.35 0.15	0.12 0.061	0.38 0.097	0.14 0.052
$\lvert(\hat{k}_A)_{11}\rvert$	2.7 2.7	2.7 2.7	2.7 2.7	2.6 2.6
$\lvert(\hat{k}_A)_{22}\rvert$	2.5 2.5	2.5 2.5	2.5 2.5	2.5 2.4
$\lvert(\hat{k}_A)_{33}\rvert$	11 12	5.3 5.6	6.7 4.3	3.5 3.2

The constraints $|(\hat{k}_A)_{11}| < 2.7$ and $|(\hat{k}_A)_{22}| < 2.5$ are solely derived from NS data. Emissivity does not directly improve these bounds, but it enhances the correlations, as seen in Figs. 3.9-3.10. In particular, incorporating baryon-meson scattering results strengthens the correlation (blue) compared to the case of decay processes (yellow) combined with NS cooling, indicating its contribution.

Although for the terms $(\hat{k}_A)_{11}$ and $(\hat{k}_A)_{22}$ there is no major improvement from emissivity, the correlations allow us to derive an upper bound on $(\hat{k}_A)_{33}$ in the range of 1-10, which is also new. In fact, $(\hat{k}_A)_{33}$ used to be unconstrained since strange matter contributions were not considered. This new bound is particularly important, as it highlights the non-negligible contribution of strange matter to the emissivity, even without strangeness-changing processes.

Finally, for the KSVZ and DFSZ axion models, where $|(\hat{k}_A)_{ii}| < 1$, the current constraints remain compatible with these theoretical frameworks.

3.4.10 Conclusion

In this work, we have presented the first study of SN axion emissivity, Q_a, that consistently quantifies the potential role of matter beyond the first generation. Specifically, we have computed all baryon-meson to baryon-axion processes, as well as baryon decay processes, involving the lightest baryon and meson octets. The emissivity Q_a provides a strong constraint on axion interactions with strange matter. In particular, we derive the first bound on the axion-strange-strange coupling, and the strongest existing bound on the axial axion-down-strange coupling, of order 0.1. Our study assumes $f_a = 10^9$ GeV and $m_a \ll m_\pi$, conditions applicable to the QCD axion – the most difficult axion type to constrain.

Our results suggest several potential applications, including extensions to other compact objects such as NSs containing strange matter. We have shown that including strange matter in core-collapse SNe yields new and significant bounds. The constraints from NS cooling (see Section 3.3) are highly competitive for first-generation couplings. By contrast, the role of strange matter in NSs and NS mergers may be more limited, since the typical temperatures involved are much lower. (This point remains debated, and is an interesting line of inquiry in its own right.) Nevertheless, NS mergers remain interesting laboratories for axion emission [FI22; Dev+24; Zha+21; Lec+25; Har+20], not least because they constitute comparatively well-controlled systems. Current constraints from these

channels are weaker than those from core-collapse SNe and NS cooling,[17] but future detections could significantly improve their competitiveness.

A possible avenue for future investigation is the extension of our results to ALPs with masses m_a comparable to those of the external states.[18]

Importantly, we aim to further investigate the dependence of our results on SN dynamics and the EoS, particularly in regard to the predicted particle abundances. As a first step, one could explore the impact of varying the interaction potentials, which affect the effective masses–and thus particle abundances–within physically reasonable ranges. Ultimately, the goal is to develop a comprehensive SN simulation that includes axion losses in the dynamics, in analogy to how neutrino losses are treated. Such a simulation would also allow exploration of the spatial dependence (radial and beyond) of thermodynamic quantities, the effects of different nuclear-matter EoSs, and the influence of baryon-meson couplings. [19]

3.5 The dominant axion production channels

To identify the relevant axion-emitting processes, we first determine the particles present in the medium. The three most abundant species are electrons, protons, and neutrons. However, hyperons and mesons also play a role in the dense environment of a SN core.

Therefore, the processes that can, in principle, contribute to axion production are:

1. $B_1B_2 \to B_3B_4a$ – baryon-baryon scattering, listed in Table 3.4
2. $B_iM \to B_fa$ – baryon-meson scattering, listed in Table 3.6
3. $B_i \to B_fa$ – baryon decay, listed in Table 3.5
4. $\ell\ell \to \ell\ell a$ – lepton-lepton scattering
5. $\ell B \to \ell Ba$ – lepton-baryon scattering, listed in Table 3.7
6. $\ell M \to \ell Ma$ – lepton-meson scattering, listed in Table 3.8
7. $M_i \to M_fa$ – meson decay, listed in Table 3.9
8. $M_1M_2 \to M_3a$ – meson-meson scattering, listed in Table 3.10

The luminosity associated with a given process is given by

$$L_a = \frac{N_a\langle E_a\rangle}{\Delta t} \,, \tag{3.5.1}$$

where N_a is the number of axions produced by the process, $\langle E_a\rangle$ is the average axion energy, and $\Delta t \sim \mathcal{O}(10\text{ s})$ is the duration of the axion burst.

To contribute significantly to the luminosity, a process must have both a large N_a and a large $\langle E_a\rangle$:

- A large N_a requires that the initial-state particles have non-negligible abundances. The more abundant the particles in the SN core, the larger N_a will be.
- A large $\langle E_a\rangle$ requires that the initial mass energy (M_i) be larger than the final mass energy (M_f). The axion energy will be approximately $\Delta M = M_i - M_f$, plus a contribution from the thermal energy. If $\Delta M \lesssim T$, the axion energy is primarily determined by the thermal energy of the system, although the available phase space may be reduced, if $\Delta M < 0$, thereby also suppressing N_a. In contrast, if $\Delta M \gg T$, the axion energy can be significantly enhanced.

[17] An exception concerns ultralight axions with $m_a < 10^{-11}$ eV, for which $f_a \in [1.6 \times 10^{16}, 10^{18}]$ GeV is excluded at the 3σ confidence level [Zha+21].

[18] The generalization to an ALP is straightforward for $m_a \ll m_\pi$, as one simply rescales by f_a. For example, to obtain bounds for $f_a = 1$ TeV, one multiplies the bounds by 10^{-6}. However, for $m_a \simeq m_\pi$, a new analysis is required, as the dependence of the emissivity on the axion mass becomes non-trivial.

[19] It goes without saying that interaction potentials and baryon-meson couplings jointly determine the nuclear-matter EoS, so these quantities are not independent. This consistency reduces the actual uncertainty compared to varying every parameter freely. Moreover, recent Bayesian estimates of the strangeness contribution in dense matter (so far with Λ hyperons at $T = 0$) already provide valuable constraints [MP22].

Table 3.4: List of processes of the type $B_1B_2 \to B_3B_4a$.

Class	Number of processes
$NN \to NNa$	3
$NN \to N\Lambda a$ & $N\Lambda \to NNa$	4
$NN \to N\Sigma a$ & $N\Sigma \to NNa$	10
$N\Lambda \to N\Lambda a$	2
$N\Lambda \to N\Sigma a$ & $N\Sigma \to N\Lambda a$	8
$N\Lambda \to N\Xi a$ & $N\Xi \to N\Lambda a$	6
$N\Lambda \to \Lambda\Lambda a$ & $\Lambda\Lambda \to N\Lambda a$	2
$N\Lambda \to \Lambda\Sigma a$ & $N\Sigma \to \Lambda\Lambda a$ & $\Lambda\Lambda \to N\Sigma a$ & $\Lambda\Sigma \to N\Lambda a$	8
$N\Lambda \to \Sigma\Sigma a$ & $N\Sigma \to \Lambda\Sigma a$ & $\Lambda\Sigma \to N\Sigma a$ & $\Sigma\Sigma \to N\Lambda a$	16
$N\Sigma \to N\Sigma a$	10
$N\Sigma \to N\Xi a$ & $N\Xi \to N\Sigma a$	14
$N\Sigma \to \Sigma\Sigma a$ & $\Sigma\Sigma \to N\Sigma a$	16
$N\Xi \to N\Xi a$	6
$N\Xi \to \Lambda\Lambda a$ & $\Lambda\Lambda \to N\Xi a$	4
$N\Xi \to \Lambda\Sigma a$	4
$N\Xi \to \Lambda\Xi a$ & $\Lambda\Xi \to N\Xi a$	6
$N\Xi \to \Sigma\Sigma a$ & $\Sigma\Sigma \to N\Xi a$	12
$N\Xi \to \Sigma\Xi a$ & $\Sigma\Xi \to N\Xi a$	14
$\Lambda\Lambda \to \Lambda\Lambda a$	1
$\Lambda\Lambda \to \Lambda\Sigma a$ & $\Lambda\Sigma \to \Lambda\Lambda a$	2
$\Lambda\Lambda \to \Lambda\Xi a$ & $\Lambda\Xi \to \Lambda\Lambda a$	2
$\Lambda\Lambda \to \Sigma\Sigma a$ & $\Lambda\Sigma \to \Lambda\Sigma a$ & $\Sigma\Sigma \to \Lambda\Lambda a$	7
$\Lambda\Lambda \to \Sigma\Xi a$ & $\Lambda\Sigma \to \Lambda\Xi a$ & $\Lambda\Xi \to \Lambda\Sigma a$	6
$\Lambda\Sigma \to N\Xi a$	4
$\Lambda\Sigma \to \Sigma\Sigma a$ & $\Sigma\Sigma \to \Lambda\Sigma a$	8
$\Lambda\Sigma \to \Sigma\Xi a$ & $\Lambda\Xi \to \Sigma\Sigma a$ & $\Sigma\Sigma \to \Lambda\Xi a$ & $\Sigma\Xi \to \Lambda\Sigma a$	16
$\Lambda\Xi \to \Lambda\Xi a$	2
$\Lambda\Xi \to \Sigma\Xi a$ & $\Sigma\Xi \to \Lambda\Xi a$	8
$\Lambda\Xi \to \Xi\Xi a$ & $\Xi\Xi \to \Lambda\Xi a$	4
$\Sigma\Sigma \to \Sigma\Sigma a$	8
$\Sigma\Sigma \to \Sigma\Xi a$ & $\Sigma\Xi \to \Sigma\Sigma a$	16
$\Sigma\Xi \to \Lambda\Lambda a$	2
$\Sigma\Xi \to \Sigma\Xi a$	10
$\Sigma\Xi \to \Xi\Xi a$ & $\Xi\Xi \to \Sigma\Xi a$	10
$\Xi\Xi \to \Xi\Xi a$	3
$B_1B_2 \to B_3B_4a$	254

Table 3.5: List of processes of the type $B_i \to B_f a$.

Class	Number of processes
$\Lambda \to na$	1
$\Sigma \to \Lambda a$	1
$\Sigma \to Na$	2
$\Xi \to \Lambda a$	1
$\Xi \to \Sigma a$	2
$B_i \to B_f a$	7

Table 3.6: List of processes of the type $B_iM \to B_fa$.

Class	Number of processes
$N\pi \to Na$	4
$NK \to Na$	6
$N\eta \to Na$	2
$N\pi \to \Lambda a$ & $\Lambda\pi \to Na$	4
$NK \to \Lambda a$ & $\Lambda K \to Na$	4
$N\eta \to \Lambda a$ & $\Lambda\eta \to Na$	2
$N\pi \to \Sigma a$ & $\Sigma\pi \to Na$	10
$NK \to \Sigma a$ & $\Sigma K \to Na$	8
$N\eta \to \Sigma a$ & $\Sigma\eta \to Na$	4
$NK \to \Xi a$ & $\Xi K \to Na$	6
$\Lambda\pi \to \Lambda a$	1
$\Lambda K \to \Lambda a$	2
$\Lambda\eta \to \Lambda a$	1
$\Lambda\pi \to \Sigma a$ & $\Sigma\pi \to \Lambda a$	6
$\Lambda K \to \Sigma a$ & $\Sigma K \to \Lambda a$	8
$\Lambda\eta \to \Sigma a$ & $\Sigma\eta \to \Lambda a$	2
$\Lambda\pi \to \Xi a$ & $\Xi\pi \to \Lambda a$	4
$\Lambda K \to \Xi a$ & $\Xi K \to \Lambda a$	4
$\Lambda\eta \to \Xi a$ & $\Xi\eta \to \Lambda a$	2
$\Sigma\pi \to \Sigma a$	7
$\Sigma K \to \Sigma a$	10
$\Sigma\eta \to \Sigma a$	3
$\Sigma\pi \to \Sigma a$ & $\Xi\pi \to \Sigma a$	10
$\Sigma K \to \Xi a$ & $\Xi K \to \Sigma a$	8
$\Sigma\eta \to \Xi a$ & $\Xi\eta \to \Sigma a$	4
$\Xi\pi \to \Xi a$	4
$\Xi K \to \Xi a$	6
$\Xi\eta \to \Xi a$	2
$B_iM \to B_fa$	134

Table 3.7: List of processes of the type $\ell B_i \to \ell B_f a$.

Class	Number of processes
$\ell p \to \ell pa$	1
$\ell p \to \ell\Sigma^+ a$ & $\ell\Sigma^+ \to \ell pa$	2
$\ell\Sigma^\pm \to \ell\Sigma^\pm a$	2
$\ell\Xi^- \to \ell\Sigma^- a$ & $\ell\Sigma^- \to \ell\Xi^- a$	2
$\ell\Xi^- \to \ell\Xi^- a$	1
$B_iM \to B_fa$	8

Table 3.8: List of processes of the type $\ell M_i \to \ell M_f a$.

Class	Number of processes
$\ell\pi^\pm \to \ell\pi^\pm a$	2
$\ell K^\pm \to \ell K^\pm a$	2
$\ell K^\pm \to \ell\pi^\pm a$ & $\ell\pi^\pm \to \ell K^\pm a$	4
$\ell M \to \ell Ma$	8

Table 3.9: List of processes of the type $M_i \to M_f a$.

Class	Number of processes
$K \to \pi a$	4
$\eta \to \pi a$	1
$\eta \to Ka$	2
$M_i \to M_f a$	7

Table 3.10: List of processes of the type $M_1M_2 \to M_3a$.

Class	Number of processes
$\pi\pi \to \pi a$	3
$\pi\pi \to Ka$ & $\pi K \to \pi a$	16
$\pi K \to Ka$ & $KK \to \pi a$	12
$\pi\eta \to Ka$ & $K\eta \to \pi a$& $\pi K \to \eta a$	12
$KK \to Ka$	10
$KK \to \eta a$ & $K\eta \to Ka$	6
$K\eta \to \eta a$ & $\eta\eta \to Ka$	4
$M_1M_2 \to M_3a$	63

Table 3.11: Particle fractions (in percent) for the $DD2Y$ EoS at $T = 40$ MeV, $n_B = n_{\rm sat}$, and $Y_{Q_B} = 0.3$.

Y_e	Y_n	Y_p	Y_Λ	Y_{Σ^-}	Y_{Σ^0}	Y_{Σ^+}	Y_{Ξ^-}	Y_{Ξ^0}
28.9	68.0	30.2	1.40	0.20	0.06	0.02	0.05	0.02
	Y_{π^-}	Y_{π^0}	Y_{π^+}	Y_{K^-}	Y_{K^+}	Y_{K^0}	$Y_{\bar{K}^0}$	Y_η
	1.14	0.23	0.04	7×10^{-4}	3×10^{-5}	1×10^{-4}	1×10^{-4}	4×10^{-5}

Based on the previous discussion, we can understand why pion-nucleon scattering, $\pi N_i \to N_f a$, can dominate over nucleon-nucleon scattering, $N_1N_2 \to N_3N_4a$, even though nucleons are much more abundant than pions. This is due to the mass difference:

$$m_\pi + m_{N_i} - m_{N_f} \gg T \gg m_{N_1} + m_{N_2} - m_{N_3} - m_{N_4} \ . \tag{3.5.2}$$

For a process of the type $n_i \to n_f$, the number of interactions N_a will be proportional to the product of the particle fractions (Y) of the initial-state particles, with a significant phase space suppression if $\Delta M < 0$. As a result, processes with $\Delta M < 0$ will not contribute significantly. Among the remaining processes, given that $\langle E_a \rangle \sim \max\{T; \Delta M\}$, we can expect the luminosity to scale as

$$L_a \propto \max\{T; \Delta M\} \times \prod_{i=1}^{n_i} Y_i \ . \tag{3.5.3}$$

Eq. (3.5.3) only accounts for the phase space, without including the interaction amplitudes that determine the actual probabilities. One would also need to consider the coupling strengths between the particles. Nevertheless, Eq. (3.5.3) provides a first estimate of which processes can contribute significantly based on the available phase space.

Before proceeding further, let us verify Eq. (3.5.3) with a numerical application using a SN core modelization based on the $DD2Y$ EoS at $T = 40$ MeV, $n_B = n_{\rm sat}$, and $Y_{Q_B} = 0.3$. The particle fractions are provided in Table 3.11.

We will test the validity of the formula in the case of baryon-meson scattering, assuming constant amplitudes $|\mathcal{M}_{fi}|^2$. This choice allows us to disregard the specific values of the coupling constants, which are free parameters, and focus solely on the phase space contribution, as Eq. (3.5.3) is meant to capture only this aspect.

Eq. (3.5.3) will be validated if and only if the following ratio holds:

$$\frac{Q_a(MB_i \to B_f a)}{Q_a(\pi^- p \to n a)} \simeq \frac{Y_M Y_{B_i}, \max\{T, m_M + m_{B_i} - m_{B_f}\}}{Y_{\pi^-} Y_p (m_{\pi^-} + m_p - m_n)} \ . \tag{3.5.4}$$

The verification of Eq. (3.5.4) in the case of constant $|\mathcal{M}_{fi}|^2$ is shown in Fig. 3.11, with three color codes: blue for $\Delta M > T$, green for $\Delta M \in [0, T]$, and red for $\Delta M < 0$. We observe that the formula provides a very good approximation when $\Delta M > T$, but fails when $\Delta M < 0$. This is expected, since the available phase space is strongly suppressed by the mass difference, significantly reducing the emissivity.

This comparison validates Eq. (3.5.3) as a useful tool for identifying dominant processes when $\Delta M > T$. If $\Delta M < 0$, the contribution is negligible. If $\Delta M \in [0, T]$, as in the case of processes like $N_1N_2 \to N_3N_4a$, then only a large number of interactions N_a can lead to a significant luminosity. In such cases, only processes involving very abundant initial particles, such as electrons or nucleons, can contribute meaningfully.

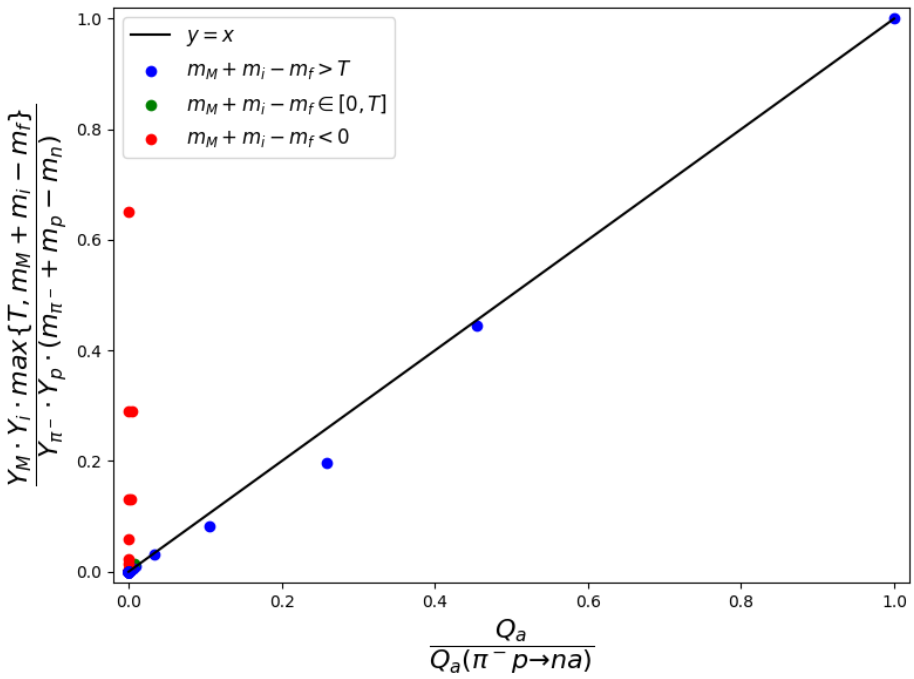

Figure 3.11: Verification of Eq. (3.5.3) for baryon-meson scattering $MB_i \to B_f a$, assuming a constant amplitude $|\mathcal{M}_{fi}|^2$. The SN core is modeled according to Table 3.11. Colors indicate different regimes of the mass difference $\Delta M = m_M + m_{B_i} - m_{B_f}$: blue for $\Delta M > T$, green for $\Delta M \in [0, T]$, and red for $\Delta M < 0$.

The previous numerical verification was carried out in a specific case, but Eq. (3.5.3) is quite general: it can be applied to other astrophysical objects, different EoS, and various thermodynamic conditions.

At least formally, Eq. (3.5.3) can be used for different types of processes. For instance, one could use it to compare $\Lambda \to na$ with $\pi^- p \to na$, which leads to:

$$\frac{Q_a(\Lambda \to na)}{Q_a(\pi^- p \to na)} \overset{?}{\simeq} \frac{Y_\Lambda (m_\Lambda - m_n)}{Y_{\pi^-} Y_p (m_{\pi^\pm} + m_p - m_n)} \simeq 10 \ . \tag{3.5.5}$$

However, in practice, this comparison is more complicated. We cannot assume a constant $|\mathcal{M}_{fi}|^2$, because the phase spaces differ significantly and $|\mathcal{M}_{fi}|^2$ does not have the same dimensionality in each case. For such comparisons, a more detailed analysis is necessary. Typically, from Section 3.4.9, constraints on diagonal terms are of order 1, while constraints on non-diagonal terms are of order 0.1. This means that for the same coupling values, the process $\Lambda \to na$ contributes about 100 times more than the $B_i M \to B_f a$ terms – an oom higher than the estimate from Eq. (3.5.5). Therefore, Eq. (3.5.3) appears to be effective when comparing processes with similar phase spaces, but not when the phase spaces are significantly different.

It is possible, for each type of process, to select a reference reaction – for example, $\pi^0 \Lambda \to na$ for meson-baryon scattering, $\Lambda \to na$ for baryon decay, and $\Lambda n \to nna$ for baryon-baryon scattering – and then compute the ratios:

$$\alpha := \frac{Q_a(\Lambda \to na)}{Q_a(\pi^0 \Lambda \to na)} \ , \quad \beta := \frac{Q_a(\Lambda n \to nna)}{Q_a(\pi^0 \Lambda \to na)} \ , \tag{3.5.6}$$

Given that experimentally $|(k_V)_{23}| \lesssim 10^{-3}$ and $|(k_A)_{23}| \lesssim 10^{-1}$, we can take $(k_V)_{23} = 0$. In this case, all flavor-changing axion emissivities are proportional to $|(k_A)_{23}|^2$, and this dependence cancels out in the ratios defined in (3.5.6), allowing for a comparison that is independent of the couplings.

From Eq. (3.5.6), one can deduce:

$$\frac{Q_a(B_i \to B_f a)}{Q_a(\pi^0 \Lambda \to na)} = \frac{Q_a(B_i \to B_f a)}{Q_a(\Lambda \to na)} \cdot \frac{Q_a(\Lambda \to na)}{Q_a(\pi^0 \Lambda \to na)} \simeq \frac{Y_{B_i}(m_{B_i} - m_{B_f})}{Y_\Lambda (m_\Lambda - m_n)} \cdot \alpha \ , \tag{3.5.7}$$

Table 3.12: List of dominant processes as predicted by Eq. (3.5.3), with numerical input from Table 3.11. The contributions are normalized to the maximum within each type (Transition + Process type). Only relative contributions greater than 10% are shown.

Transition type	**Process type**	**Reaction**	**Relative value (%)**
First-generation transitions	$B_i M \to B_f a$	$\pi^- p \to n a$	100
		$\pi^0 n \to n a$	44
		$\pi^0 p \to p a$	20
Strange–strange transitions	$B_i M \to B_f a$	$\pi^0 \Lambda \to n a$	100
		$\pi^+ \Lambda \to p a$	18
	$B_1 B_2 \to B_3 B_4 a$	$p\Sigma^- \to n\Lambda a$	100
		$n\Sigma^0 \to n\Lambda a$	72
		$n\Sigma^+ \to p\Lambda a$	23
		$p\Sigma^0 \to p\Lambda a$	32
Strange–down transitions	$B_i \to B_f a$	$\Lambda \to n a$	100
	$B_i M \to B_f a$	$\pi^0 \Lambda \to n a$	100
		$\pi^+ \Lambda \to p a$	18
	$B_1 B_2 \to B_3 B_4 a$	$n\Lambda \to nna$	100
		$p\Lambda \to npa$	44

and

$$\frac{Q_a(B_1B_2 \to B_3B_4a)}{Q_a(\pi^0\Lambda \to na)} = \frac{Q_a(B_1B_2 \to B_3B_4a)}{Q_a(\Lambda n \to nna)} \cdot \frac{Q_a(\Lambda n \to nna)}{Q_a(\pi^0\Lambda \to na)} \simeq \frac{Y_{B_1}Y_{B_2}(m_{B_1}+m_{B_2}-m_{B_3}-m_{B_4})}{Y_\Lambda Y_n(m_\Lambda - m_n)} \cdot \beta \,. \tag{3.5.8}$$

With this procedure, all types of processes can be compared to each other, thereby generalizing Eq. (3.5.3), even when the phase spaces differ significantly.

The processes that can potentially contribute to the luminosity for $\Delta M \in [0; T]$ are those involving particles that are abundantly present, namely the electron, the proton, and the neutron. This leads to the five processes[20]:

- $pp \to ppa$
- $nn \to nna$
- $np \to npa$
- $pe^- \to pe^-a$
- $e^-e^- \to e^-e^-a$

Leptonic or semi-leptonic processes must involve a photon as a propagator; however, the electromagnetic interaction is weaker than hadronic interactions. As a result, processes involving electrons are expected to be subdominant, unless $C_{aee} := (k_A^\ell)_{ee}$ is significantly larger than C_{aNN}.

By applying Eq. (3.5.3), we can compare different processes in the regime $\Delta M > T$. The dominant processes are listed in Table 3.12, grouped into three categories:

- first-generation transitions, which constrain $(k_A)_{11,22}$,
- strange-strange transitions, which constrain $(k_A)_{33}$, and
- strange-down transitions, which constrain $(k_{V,A})_{23}$.

In total, this adds 14 processes[21] in addition to the 5 processes with a small ΔM.

With this methodology, we reduce the number of relevant processes from the full set of $7 + 134 + 254 = 395$ to just 19 key processes.

It is important to note that the dominant processes listed here depend on the particle fractions. In other astrophysical conditions, a different set of processes may dominate. The goal here is not to provide an exhaustive list of dominant processes for all scenarios, but rather to propose a general framework that can be applied to identify the leading processes in any specific context.

[20] If one aims to constrain only axion-quark couplings, the process $e^-e^- \to e^-e^-a$ should not be considered. However, for a comprehensive study including all contributing processes, it must be included.

[21] The exact number depends on the chosen threshold; here we use 10%.

References

[Bio+87] R. M. Bionta et al. *Observation of a Neutrino Burst in Coincidence with Supernova SN 1987a in the Large Magellanic Cloud*. In: *Phys. Rev. Lett.* 58 (1987), p. 1494. DOI: 10.1103/PhysRevLett.58.1494.

[BO22] Aurore Betranhandy and Evan O'Connor. *Neutrino driven explosions aided by axion cooling in multidimensional simulations of core-collapse supernovae*. In: *Phys. Rev. D* 106.6 (2022), p. 063019. DOI: 10.1103/PhysRevD.106.063019. arXiv: 2204.00503 [astro-ph.HE].

[Bru85] Stephen W. Bruenn. *Stellar core collapse: Numerical model and infall epoch*. In: *Astrophys. J. Suppl.* 58 (1985), pp. 771–841. DOI: 10.1086/191056.

[BTB89] Adam Burrows, Michael S. Turner, and R. P. Brinkmann. *Axions and SN 1987A*. In: *Phys. Rev. D* 39 (1989), p. 1020. DOI: 10.1103/PhysRevD.39.1020.

[Bur00] A. Burrows. *Supernova explosions in the universe*. In: *Nature* 403 (2000), pp. 727–733. DOI: 10.1038/35001501.

[Bus+22] Malte Buschmann et al. *Upper Limit on the QCD Axion Mass from Isolated Neutron Star Cooling*. In: *Phys. Rev. Lett.* 128.9 (2022), p. 091102. DOI: 10.1103/PhysRevLett.128.091102. arXiv: 2111.09892 [hep-ph].

[Car+19] Pierluca Carenza et al. *Improved axion emissivity from a supernova via nucleon-nucleon bremsstrahlung*. In: *Journal of Cosmology and Astroparticle Physics* 2019.10 (Oct. 2019), p. 016. DOI: 10.1088/1475-7516/2019/10/016. URL: https://dx.doi.org/10.1088/1475-7516/2019/10/016.

[Car+21] Pierluca Carenza et al. *Enhanced Supernova Axion Emission and its Implications*. In: *Phys. Rev. Lett.* 126.7 (2021), p. 071102. DOI: 10.1103/PhysRevLett.126.071102. arXiv: 2010.02943 [hep-ph].

[Car23] Pierluca Carenza. *Axion emission from supernovae: a cheatsheet*. In: *The European Physical Journal Plus* 138.9 (2023), p. 836. DOI: 10.1140/epjp/s13360-023-04484-2. URL: https://doi.org/10.1140/epjp/s13360-023-04484-2.

[Cav+24] Mael Cavan-Piton et al. *Axion Emission from Strange Matter in Core-Collapse SNe*. In: *Phys. Rev. Lett.* 133.12 (2024), p. 121002. DOI: 10.1103/PhysRevLett.133.121002. arXiv: 2401.10979 [hep-ph].

[CC93] Sanghyeon Chang and Kiwoon Choi. *Hadronic axion window and the big bang nucleosynthesis*. In: *Phys. Lett. B* 316 (1993), pp. 51–56. DOI: 10.1016/0370-2693(93)90656-3. arXiv: hep-ph/9306216.

[Cho+22] Kiwoon Choi et al. *Axion emission from supernova with axion-pion-nucleon contact interaction*. In: *JHEP* 02 (2022), p. 143. DOI: 10.1007/JHEP02(2022)143. arXiv: 2110.01972 [hep-ph].

[CR24] Andrea Caputo and Georg Raffelt. *Astrophysical Axion Bounds: The 2024 Edition*. In: *PoS* COSMICWISPers (2024), p. 041. DOI: 10.22323/1.454.0041. arXiv: 2401.13728 [hep-ph].

[Dev+24] P. S. Bhupal Dev et al. *First Constraints on the Photon Coupling of Axionlike Particles from Multimessenger Studies of the Neutron Star Merger GW170817*. In: *Phys. Rev. Lett.* 132 (10 Mar. 2024), p. 101003. DOI: 10.1103/PhysRevLett.132.101003. URL: https://link.aps.org/doi/10.1103/PhysRevLett.132.101003.

[DHV22] Matthew J. Dolan, Frederick J. Hiskens, and Raymond R. Volkas. *Advancing globular cluster constraints on the axion-photon coupling*. In: *Journal of Cosmology and Astroparticle Physics* 2022.10 (Oct. 2022), p. 096. ISSN: 1475-7516. DOI: 10.1088/1475-7516/2022/10/096. URL: http://dx.doi.org/10.1088/1475-7516/2022/10/096.

[EM89] T.E.O. Ericson and J.-F. Mathiot. *Axion emission from SN1987A. Nuclear physics constraints*. In: *Physics Letters B* 219.4 (1989), pp. 507–514. ISSN: 0370-2693. DOI: https://doi.org/10.1016/0370-2693(89)91103-9. URL: https://www.sciencedirect.com/science/article/pii/0370269389911039.

[EO83] John Ellis and Keith A. Olive. *Constraints on light particles from stellar evolution*. In: *Nuclear Physics B* 223.1 (1983), pp. 252–268. ISSN: 0550-3213. DOI: https://doi.org/10.1016/0550-3213(83)90104-9. URL: https://www.sciencedirect.com/science/article/pii/0550321383901049.

[FI22] Damiano F. G. Fiorillo and Fabio Iocco. *Axions from neutron star mergers*. In: *Phys. Rev. D* 105 (12 June 2022), p. 123007. DOI: 10.1103/PhysRevD.105.123007. URL: https://link.aps.org/doi/10.1103/PhysRevD.105.123007.

[Fis+14] Tobias Fischer et al. *Symmetry energy impact in simulations of core-collapse supernovae*. In: *The European Physical Journal A* 50.2 (2014), p. 46. DOI: 10.1140/epja/i2014-14046-5. URL: https://doi.org/10.1140/epja/i2014-14046-5.

[Fis+21] Tobias Fischer et al. *Observable signatures of enhanced axion emission from protoneutron stars*. In: *Phys. Rev. D* 104.10 (2021), p. 103012. DOI: 10.1103/PhysRevD.104.103012. arXiv: 2108.13726 [hep-ph].

[FOP18] M. Fortin, M. Oertel, and C. Providência. *Hyperons in hot dense matter: what do the constraints tell us for equation of state?* In: *Publ. Astron. Soc. Austral.* 35 (2018), p. 44. DOI: 10.1017/pasa.2018.32. arXiv: 1711.09427 [astro-ph.HE].

[FR20] Bryce Fore and Sanjay Reddy. *Pions in hot dense matter and their astrophysical implications*. In: *Phys. Rev. C* 101.3 (2020), p. 035809. DOI: 10.1103/PhysRevC.101.035809. arXiv: 1911.02632 [astro-ph.HE].

[Har+20] Steven P. Harris et al. *Axions in neutron star mergers*. In: *Journal of Cosmology and Astroparticle Physics* 2020.07 (July 2020), pp. 023–023. ISSN: 1475-7516. DOI: 10.1088/1475-7516/2020/07/023. URL: http://dx.doi.org/10.1088/1475-7516/2020/07/023.

[Hir+87] K. Hirata et al. *Observation of a Neutrino Burst from the Supernova SN 1987a*. In: *Phys. Rev. Lett.* 58 (1987). Ed. by K. C. Wali, pp. 1490–1493. DOI: 10.1103/PhysRevLett.58.1490.

[Ho+23] Shu-Yu Ho et al. *Supernova axion emissivity with $\Delta(1232)$ resonance in heavy baryon chiral perturbation theory*. In: *Phys. Rev. D* 107.7 (2023), p. 075002. DOI: 10.1103/PhysRevD.107.075002. arXiv: 2212.01155 [hep-ph].

[Jan+07] Hans-Thomas Janka et al. *Theory of Core-Collapse Supernovae*. In: *Phys. Rept.* 442 (2007), pp. 38–74. DOI: 10.1016/j.physrep.2007.02.002. arXiv: astro-ph/0612072.

[JM90] R.L. Jaffe and Aneesh Manohar. *The g1 problem: Deep inelastic electron scattering and the spin of the proton*. In: *Nuclear Physics B* 337.3 (1990), pp. 509–546. ISSN: 0550-3213. DOI: https://doi.org/10.1016/0550-3213(90)90506-9. URL: https://www.sciencedirect.com/science/article/pii/0550321390905069.

[KM88] David B. Kaplan and Aneesh Manohar. *Strange matrix elements in the proton from neutral-current experiments*. In: *Nuclear Physics B* 310.3 (1988), pp. 527–547. ISSN: 0550-3213. DOI: https://doi.org/10.1016/0550-3213(88)90090-9. URL: https://www.sciencedirect.com/science/article/pii/0550321388900909.

[KRT22] Hristijan Kochankovski, Angels Ramos, and Laura Tolos. *Equation of state for hot hyperonic neutron star matter*. In: *Mon. Not. Roy. Astron. Soc.* 517.1 (2022). [Erratum: Mon.Not.Roy.Astron.Soc. 518, 6376], pp. 507–517. DOI: 10.1093/mnras/stac2671. arXiv: 2206.11266 [astro-ph.HE].

[Lec+25] Francesca Lecce et al. *Probing axionlike particles with multimessenger observations of neutron star mergers*. In: *Physical Review D* 112.2 (July 2025). ISSN: 2470-0029. DOI: 10.1103/krf3-lm4s. URL: http://dx.doi.org/10.1103/krf3-lm4s.

[Lel+23] Alessandro Lella et al. *Protoneutron stars as cosmic factories for massive axionlike particles*. In: *Phys. Rev. D* 107.10 (2023), p. 103017. DOI: 10.1103/PhysRevD.107.103017. arXiv: 2211.13760 [hep-ph].

[Lel+24] Alessandro Lella et al. *Getting the most on supernova axions*. In: *Phys. Rev. D* 109.2 (2024), p. 023001. DOI: 10.1103/PhysRevD.109.023001. arXiv: 2306.01048 [hep-ph].

[Mar+12] G. Martinez-Pinedo et al. *Charged-current weak interaction processes in hot and dense matter and its impact on the spectra of neutrinos emitted from proto-neutron star cooling*. In: *Phys. Rev. Lett.* 109 (2012), p. 251104. DOI: 10.1103/PhysRevLett.109.251104. arXiv: 1205.2793 [astro-ph.HE].

[Mar+17] Miguel Marques et al. *New temperature dependent hyperonic equation of state: Application to rotating neutron star models and $I-Q$ relations*. In: *Phys. Rev. C* 96.4 (2017), p. 045806. DOI: 10.1103/PhysRevC.96.045806. arXiv: 1706.02913 [nucl-th].

[Mar+20] Jorge Martin Camalich et al. *Quark Flavor Phenomenology of the QCD Axion*. In: *Phys. Rev. D* 102.1 (2020), p. 015023. DOI: 10.1103/PhysRevD.102.015023. arXiv: 2002.04623 [hep-ph].

[MBB21] Tuhin Malik, Sarmistha Banik, and Debades Bandyopadhyay. *New equation of state involving Bose-Einstein condensate of antikaon for supernova and neutron star merger simulations*. In: *Eur. Phys. J. ST* 230.2 (2021), pp. 561–566. DOI: 10.1140/epjs/s11734-021-00006-2. arXiv: 2012.10127 [astro-ph.HE].

[Mor+22] Kanji Mori et al. *Shock revival in core-collapse supernovae assisted by heavy axionlike particles*. In: *Phys. Rev. D* 105.6 (2022), p. 063009. DOI: 10.1103/PhysRevD.105.063009. arXiv: 2112.03613 [astro-ph.HE].

[Mor+23] Kanji Mori et al. *Multimessenger signals of heavy axionlike particles in core-collapse supernovae: Two-dimensional simulations*. In: *Phys. Rev. D* 108.6 (2023), p. 063027. DOI: 10.1103/PhysRevD.108.063027. arXiv: 2304.11360 [astro-ph.HE].

[MP22] Tuhin Malik and Constan ça Providência. *Bayesian inference of signatures of hyperons inside neutron stars*. In: *Phys. Rev. D* 106 (6 Sept. 2022), p. 063024. DOI: 10.1103/PhysRevD.106.063024. URL: https://link.aps.org/doi/10.1103/PhysRevD.106.063024.

[Oer+16] Micaela Oertel et al. *Hyperons in neutron stars and supernova cores*. In: *Eur. Phys. J. A* 52.3 (2016), p. 50. DOI: 10.1140/epja/i2016-16050-1. arXiv: 1601.00435 [nucl-th].

[Oer+17] M. Oertel et al. *Equations of state for supernovae and compact stars*. In: *Rev. Mod. Phys.* 89.1 (2017), p. 015007. DOI: 10.1103/RevModPhys.89.015007. arXiv: 1610.03361 [astro-ph.HE].

[Oer+20] M. Oertel et al. *Improved neutrino-nucleon interactions in dense and hot matter for numerical simulations*. In: *Physical Review C* 102.3, 035802 (Sept. 2020), p. 035802. DOI: 10.1103/PhysRevC.102.035802. arXiv: 2003.02152 [astro-ph.HE].

[OHa20] C. O'Hare. *Axion Limits*. Accessed: 2025-03-07. 2020. URL: https://cajohare.github.io/AxionLimits/docs/ap.html.

[PNO22] A. Pascal, J. Novak, and M. Oertel. *Proto-neutron star evolution with improved charged-current neutrino–nucleon interactions*. In: *Mon. Not. Roy. Astron. Soc.* 511.1 (2022), pp. 356–370. DOI: 10.1093/mnras/stac016. arXiv: 2201.01955 [nucl-th].

[Pon+99] J. A. Pons et al. *Evolution of protoneutron stars*. In: *Astrophys. J.* 513 (1999), p. 780. DOI: 10.1086/306889. arXiv: astro-ph/9807040.

[Rad22] Adriana R. Raduta. *Equations of state for hot neutron stars-II. The role of exotic particle degrees of freedom*. In: *Eur. Phys. J. A* 58.6 (2022), p. 115. DOI: 10.1140/epja/s10050-022-00772-0. arXiv: 2205.03177 [nucl-th].

[Raf90] Georg G. Raffelt. *Astrophysical methods to constrain axions and other novel particle phenomena*. In: *Phys. Rept.* 198 (1990), pp. 1–113. DOI: 10.1016/0370-1573(90)90054-6.

[RC24] G. Raffelt and A. Caputo. *Astrophysical Axion Bounds: The 2024 Edition*. In: *Proceedings of 1st General Meeting and 1st Training School of the COST Action COSMIC WSIPers — PoS(COSMICWISPers). COSMICWISPers*. Sissa Medialab, Mar. 2024. DOI: 10.22323/1.454.0041. URL: http://dx.doi.org/10.22323/1.454.0041.

[Rob12] L. F. Roberts. *A New Code for Proto-Neutron Star Evolution*. In: *Astrophys. J.* 755 (2012), p. 126. DOI: 10.1088/0004-637X/755/2/126. arXiv: 1205.3228 [astro-ph.HE].

[RPL98] Sanjay Reddy, Madappa Prakash, and James M Lattimer. *Neutrino interactions in hot and dense matter*. In: *Phys. Rev.* D58 (1998), p. 013009. DOI: 10.1103/PhysRevD.58.013009.

[RRS12] L. F. Roberts, Sanjay Reddy, and Gang Shen. *Medium modification of the charged current neutrino opacity and its implications*. In: *Phys. Rev. C* 86 (2012), p. 065803. DOI: 10.1103/PhysRevC.86.065803. arXiv: 1205.4066 [astro-ph.HE].

[RS88] Georg Raffelt and David Seckel. *Bounds on Exotic Particle Interactions from SN 1987a*. In: *Phys. Rev. Lett.* 60 (1988), p. 1793. DOI: 10.1103/PhysRevLett.60.1793.

[Sil+20] André da Silva Schneider et al. *Equation of State and Progenitor Dependence of Stellar-mass Black Hole Formation*. In: *Astrophys. J.* 894.1 (2020), p. 4. DOI: 10.3847/1538-4357/ab8308. arXiv: 2001.10434 [astro-ph.HE].

[SLW23] Armen Sedrakian, Jia-Jie Li, and Fridolin Weber. *Heavy baryons in compact stars*. In: *Prog. Part. Nucl. Phys.* 131 (2023), p. 104041. DOI: 10.1016/j.ppnp.2023.104041. arXiv: 2212.01086 [nucl-th].

[Tam+17] Irene Tamborra et al. *Flavor-dependent neutrino angular distribution in core-collapse supernovae*. In: *Astrophys. J.* 839 (2017), p. 132. DOI: 10.3847/1538-4357/aa6a18. arXiv: 1702.00060 [astro-ph.HE].

[TOK15] S. Typel, M. Oertel, and T. Klähn. *CompOSE CompStar online supernova equations of state harmonising the concert of nuclear physics and astrophysics compose.obspm.fr*. In: *Phys. Part. Nucl.* 46.4 (2015), pp. 633–664. DOI: 10.1134/S1063779615040061. arXiv: 1307.5715 [astro-ph.SR].

[Tur88] Michael S. Turner. *Axions from SN 1987A*. In: *Phys. Rev. Lett.* 60 (1988), p. 1797. DOI: 10.1103/PhysRevLett.60.1797.

[Typ+22] S. Typel et al. *CompOSE Reference Manual*. In: *Eur. Phys. J. A* 58.11 (2022), p. 221. DOI: 10.1140/epja/s10050-022-00847-y. arXiv: 2203.03209 [astro-ph.HE].

[VGM21] Thomas Vonk, Feng-Kun Guo, and Ulf-G. Meißner. *The axion-baryon coupling in SU(3) heavy baryon chiral perturbation theory*. In: *JHEP* 08 (2021), p. 024. DOI: 10.1007/JHEP08(2021)024. arXiv: 2104.10413 [hep-ph].

[VGM22] Thomas Vonk, Feng-Kun Guo, and Ulf-G. Meißner. *Pion axioproduction: The Δ resonance contribution*. In: *Phys. Rev. D* 105.5 (2022), p. 054029. DOI: 10.1103/PhysRevD.105.054029. arXiv: 2202.00268 [hep-ph].

[Wei00] Stefan Weinzierl. *Introduction to Monte Carlo methods*. 2000. arXiv: hep-ph/0006269 [hep-ph]. URL: https://arxiv.org/abs/hep-ph/0006269.

[WJ05] Stan Woosley and Thomas Janka. *The physics of core-collapse supernovae*. In: *Nature Phys.* 1 (2005), p. 147. DOI: 10.1038/nphys172. arXiv: astro-ph/0601261.

[Zha+21] Jun Zhang et al. *First Constraints on Nuclear Coupling of Axionlike Particles from the Binary Neutron Star Gravitational Wave Event GW170817*. In: *Physical Review Letters* 127.16 (Oct. 2021). ISSN: 1079-7114. DOI: 10.1103/physrevlett.127.161101. URL: http://dx.doi.org/10.1103/PhysRevLett.127.161101.

Chapter 4

Search for QCD axion absorption from stellar objects in water Cherenkov experiments

Contents

4.1 Axion interaction with first-generation particles 100
4.1.1 Introduction 100
4.1.2 Existing Literature 100
4.1.3 Axion Spectrum 100
4.1.4 Parton spectrum 104
4.1.5 Results 107
4.1.6 Conclusion 116
4.2 Axion interaction with strange matter 117
4.2.1 Introduction 117
4.2.2 Axion spectrum 117
4.2.3 Parton spectrum 119
4.2.4 Results 125
4.2.5 Conclusion 126
4.3 Outlook 127

In this chapter, we investigate the potential detection of Quantum Chromodynamics (QCD) axions through their absorption in terrestrial detectors, focusing in particular on the axion-induced production of Cherenkov light in large water-based neutrino observatories. Building on the axion emission spectra derived in Section 3.4, we consider the scenario in which axions emitted from a nearby core-collapse Supernova (SN) reach Earth and interact with nucleons in a water Cherenkov detector such as Hyper-Kamiokande (HK). These interactions can lead to final states containing photons or neutral pions, whose subsequent decay products may yield detectable Cherenkov light.

We begin in Section 4.1 by studying axion interactions with first-generation matter. We compute the axion flux spectrum and its associated final-state parton spectra from the processes $aN \to N\gamma$ and $aN \to N\pi^0$. This analysis, based on original work [Cav+25b], accounts for general axion-quark interactions and explores a range of coupling scenarios constrained either by experimental bounds or specific theoretical frameworks. The resulting photon and pion energy distributions are then used to evaluate the detectability of the axion signal in Cherenkov detectors.

In Section 4.2, we generalize this framework to include axion interactions with strange hadronic matter. We model the resulting modifications to the partonic spectra induced by processes involving strange baryons, extending the detection prospects to a broader class of axion couplings.

Altogether, this chapter provides a novel perspective on the detection of astrophysical axions via their hadronic interactions in terrestrial detectors. By connecting the physics of SN core to that of large-scale observatories, it opens up new avenues for probing the QCD axion in upcoming neutrino experiments.

4.1 Axion interaction with first-generation particles

This section details the calculations leading to the results presented in [Cav+25b].

4.1.1 Introduction

In Supernovæ (SNe), as discussed in Section 3.4, the cooling mechanism leading to the formation of a young Neutron Star (NS) is known to provide one of the strongest constraints on exotic cooling sources such as axions, in addition to standard neutrino emission. Once produced by the SN, the axion flux may be detectable on Earth using neutrino-detection facilities, such as the planned HK water Cherenkov detector [Abe+11; Abe+18]. The main challenge is to distinguish the axion-induced signal from the neutrino background.

In this section, we consider the most general interactions of the QCD axion with nucleons. As extensively discussed in Chapter 2, these interactions can be formulated as an extension of Chiral Perturbation Theory (ChPT) for nucleons via the Noether procedure, with axion-hadron coupling strengths inheriting from (i.e. functions of) the fundamental axion-quark couplings [GKR86]. Based on the resulting nucleonic chiral Lagrangian, we analyze axion absorption processes in water that produce final-state "Cherenkov partons"–i.e., particles that initiate Cherenkov light cascades. We find that π^0 are particularly promising, as their number spectrum peaks at higher values and is more clearly separated in energy than the corresponding photon spectrum. In both cases, we compare the peak structure and energy separation with those of the reference Cherenkov spectrum expected from neutrino absorption events.

4.1.2 Existing Literature

Several papers in the literature have explored different physics mechanisms for axion detection at neutrino Cherenkov experiments. Examples we are aware of include:

1. The coupling of the QCD axion to matter induced by the nucleon Electric Dipole Moment portal interaction, a model-independent feature of QCD axions, as discussed in [Luc+22];
2. Investigations into the axion-photon-photon coupling and the nucleon Electric Dipole Moment portal interaction for Axion-like Particles (ALPs) produced from primordial black hole evaporation [LZ22];
3. Studies of the coupling responsible for axion photo-production through the anomaly-induced Wess-Zumino-Witten term, see [CGV24];
4. Constraints on the axion-photon-photon and the axion-electron-electron couplings for ALPs originating from neutrino-boosted fluxes [CFJ24];
5. Studies of the couplings of axions with electrons, protons, and neutrons for both solar and SN axions, focusing on processes such as inverse Compton scattering, the axio-electric effect, and axion-induced pair production [Ari+24];
6. The coupling of glueball ALPs with protons, as investigated in [CPW24];
7. The coupling between protons and ALPs from a diffuse galactic flux via photo-production, as discussed in [Alo+24b; Alo+24a];
8. Axion-absorption induced excitation of oxygen nuclei, leading to the emission of de-excitation photons, potentially providing detectable signals at Cherenkov detectors [ESH90; Car+24].

All these mechanisms underscore the versatility of Cherenkov experiments in probing a wide range of axion interactions, as well as their astrophysical implications.

4.1.3 Axion Spectrum

4.1.3.1 Generalities

To determine the axion spectrum, we follow the procedure described in Section 3.4, using

$$Q_a = \int dE_a \, E_a \, \frac{d\dot{n}_a}{dE_a} \, . \tag{4.1.1}$$

The axion emission spectrum associated with a given process is defined by

$$\frac{dN_a}{dE_a} := \int dt \int d^3\vec{r} \frac{d\dot{n}_a}{dE_a} \simeq V\Delta t \frac{d\dot{n}_a}{dE_a} = \frac{M}{\rho}\Delta t \frac{d\dot{n}_a}{dE_a} \ , \tag{4.1.2}$$

where $\Delta t \simeq 10$ s is the duration of the burst, $M \simeq M_\odot$ is the mass of the SN core, and $\rho \simeq \rho_{\rm core} \simeq 2.6 \times 10^{14}$ g/cm^3 is its average density.

Each point of the spectrum requires one fewer integration than the emissivity, which simplifies the calculation. However, to obtain the full spectrum, the integration must be performed over the entire domain, so the total computational time remains similar.

Since we aim to determine the axion spectrum associated with first-generation matter, we focus on nucleon-pion scattering processes, $N_i\pi \to N_f a$, where π denotes a pion, N_i and N_f are nucleons, and a is an axion. Fig. 4.1 shows all first-generation diagrams contributing to the QCD axion, with the appropriate external fields, containing a single axion vertex and no loops.

There are three relevant interaction vertices:

- $\mathcal{L}_{aNN} = \dfrac{\partial_\mu a}{2f_a} C_{aNN} \bar{N}\gamma^\mu\gamma_5 N$;
- $\mathcal{L}_{\pi NN'} = \dfrac{D+F}{2F_0}\left(\partial_\mu\pi^0(\bar{p}\gamma^\mu\gamma_5 p - \bar{n}\gamma^\mu\gamma_5 n) + \sqrt{2}\partial_\mu\pi^+(\bar{p}\gamma^\mu\gamma_5 n) + \sqrt{2}\partial_\mu\pi^-(\bar{n}\gamma^\mu\gamma_5 p)\right)$;
- $\mathcal{L}_{a\pi NN'} = -iC_{a\pi NN'}\dfrac{\partial_\mu a}{f_a}\dfrac{\pi^-}{F_0}\bar{n}\gamma^\mu p + \text{h.c.}$,

where $D + F = -1.26(5)$ and

$$C_{a\pi NN'} = \frac{C_{ann} - C_{app}}{2\sqrt{2}(D+F)} \ . \tag{4.1.3}$$

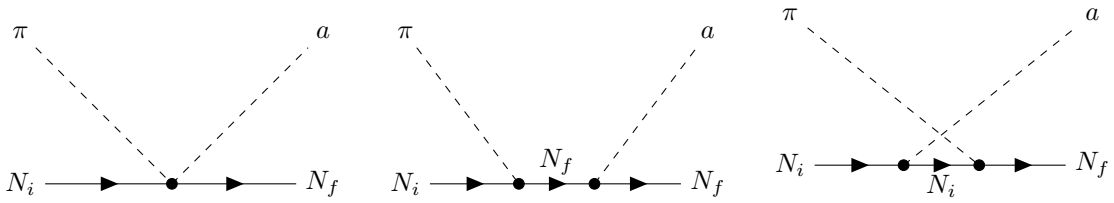

Figure 4.1: Leading-order Feynman diagrams contributing to nucleon-pion scattering $N_i\pi \to N_f a$.

We neglect nucleon-nucleon scattering processes, $N_1N_2 \to N_3N_4a$, because they are expected to peak at lower energies compared to nucleon-pion scattering – around 100 MeV versus 300 MeV [Car+21]. As we will discuss later, the contributions that are most suitable for detectability come from the highest-energy axions, whose spectrum is more clearly separated in energy from the SN neutrino counterpart, which is less energetic. Stated simply, the strategy is to detect the axion in zero-background regions[1].

As regards the emitter of the axion flux, we adopt assumptions in line with previous work: thermodynamic conditions $T \in \{30, 40\}$ MeV, $n_B \in \{1, 1.5\}\ n_{\rm sat}$, and $Y_p = 0.3$[2]; as regards the Equation of State (EoS) models, instead of using the $DD2Y$ and $SFHoY$ EoS models (which include the full hadron octets, i.e. also hyperons), we consider their first-generation equivalents, $DD2$ and $SFHo$.

We conclude this discussion by enumerating the main sources of uncertainty that are neglected in our study:

- First, our discussion concerns SN-like events that have not yet been observed, and the relevant quantities for predicting spectra may vary across different astrophysical sources.

[1] Although, in general, neutrino detectors also cope with other experimental backgrounds such as cosmic-ray muons and their secondary showers, the dominant background in the $\sim$ 300 MeV region comes from *atmospheric neutrinos* [Gai19]. For a SN burst of duration $\mathcal{O}(10\,\text{s})$, the expected number of atmospheric neutrino events in this short time window is significantly smaller than one for detectors of current or near-future size, so the background remains negligible for the purposes of this analysis.

[2] In previous work, the charged baryon fraction was denoted Y_{Q_B}. However, for first-generation matter, only the proton is charged, so $Y_{Q_B} = Y_p$.

- Second, even within a detected SN event, neither the emitter's mass, the exact emission time, nor the fraction of mass lost to radiation is known to better than order-of-magnitude (oom) precision. Therefore, only the oom of $\kappa = M\Delta t/\rho$ in Eq. (4.1.2) can be reasonably estimated.

- Third, spatial and temporal inhomogeneities during the emission interval, such as radial density variations or deviations from spherical symmetry [Fis+21; Mor+22; BO22; Mor+23], may significantly affect the emitted flux.

- Fourth, the flux propagating from the SN to Earth is subject to gravitational redshift, observer-time redshift, each encoded in a factor ξ, and Doppler shift effects due to the radial velocity v_r of the emitting medium. These corrections are incorporated into a multiplicative factor $\xi^2(r)(1+2v_r)$ [CRV22; Cap+22], collectively reducing the observed luminosity by approximately 20-30% [CRV22].

In our study, the key observables are the *relative* positions of the Cherenkov parton spectrum peaks induced by axions and neutrinos, respectively, as well as the oom of the corresponding spectra. Our goal is to determine whether, under typical SN emission parameters on one side and realistic water Cherenkov detector conditions on the other, the axion-induced spectrum can be distinguished from the neutrino one. The neglected effects mentioned above are not expected to significantly shift the peak positions or alter the spectrum amplitudes beyond the oom. Therefore, they should not affect our main conclusions.

4.1.3.2 Constraints and scenarios

By definition, the luminosity is the volume integral of the emissivity:

$$L_a = \int_V Q_a d^3\vec{r}\,, \tag{4.1.4}$$

which implies that

$$L_a \Delta t = \int_V E_a \frac{dN_a}{dE_a} dE_a = N_a \langle E_a \rangle \ . \tag{4.1.5}$$

Therefore, once the axion spectrum has been calculated as a function of the couplings, it becomes possible to use the Raffelt's bound – not on the emissivity as in the previous chapter, but directly on the luminosity – requiring namely $L_a \lesssim L_\nu$ with $L_\nu \sim 3 \times 10^{52}$ erg/s [Bur00; WJ05].

Restricting to first-generation matter, the calculation depends only on the couplings C_{app} and C_{ann}. The axion luminosity can be expressed as

$$L_a(C_{app}, C_{ann}) = L_a^{pp}|C_{app}|^2 + L_a^{nn}|C_{ann}|^2 + L_a^{pn}\mathrm{Re}[C_{app}C_{ann}^*]\,, \tag{4.1.6}$$

where L_a^{pp}, L_a^{nn}, and L_a^{pn} are numbers.

As a result, lines of constant luminosity correspond to ellipses in the (C_{app}, C_{ann}) plane, with axes not necessarily aligned with the C_{app} and C_{ann} directions.

We collect all the values of the upper bounds on the axion couplings. These results are shown in Table 4.1 and represent the strongest constraints coming from axion luminosity.

Comparing with bounds obtained from NS cooling studies, where $|C_{app}| < 1.16$ and $|C_{ann}| < 1.22$, we find that for $T = 30$ MeV, NS cooling provides stronger constraints than SN bounds. However, for $T = 40$ MeV, SN bounds become more stringent.

We define three scenarios for the couplings C_{app} and C_{ann}:

Table 4.1: Constraints on the absolute values of the axion couplings to nucleons, $|C_{app}|$ and $|C_{ann}|$, for different EoS models and thermodynamic conditions in the SN core.

		DD2		**SFHo**	
T (MeV)	n_B	$\lvert C_{app}\rvert$	$\lvert C_{ann}\rvert$	$\lvert C_{app}\rvert$	$\lvert C_{ann}\rvert$
30	n_{sat}	2.1	2.0	1.8	1.7
30	$1.5\,n_{\mathrm{sat}}$	2.0	1.9	1.5	1.5
40	n_{sat}	0.80	0.76	0.67	0.64
40	$1.5\,n_{\mathrm{sat}}$	0.76	0.74	0.59	0.56

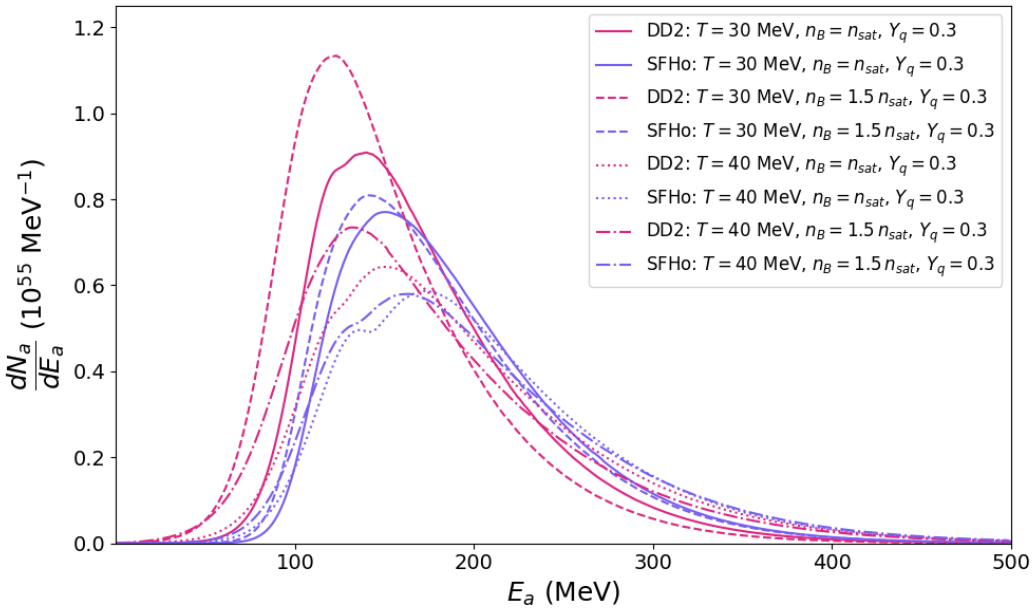

Figure 4.2: Axion emission spectra from $\pi N \to N' a$ processes in the agnostic case. The line style encodes different temperature and density configurations: solid line ($T = 30$ MeV, $n_B = n_{\rm sat}$, $Y_p = 0.3$), dashed line ($T = 30$ MeV, $n_B = 1.5\ n_{\rm sat}$, $Y_p = 0.3$), dotted line ($T = 40$ MeV, $n_B = n_{\rm sat}$, $Y_p = 0.3$), and dash-dotted line ($T = 40$ MeV, $n_B = 1.5\ n_{\rm sat}$, $Y_p = 0.3$). Colors distinguish between the EoS: pink for $DD2$ and purple for $SFHo$.

- **Agnostic scenario**: no theoretical model is assumed, and couplings are only constrained by experimental data.
- **Kim-Shifman-Vainshtein-Zakharov (KSVZ) model**: $C_{app}^{KSVZ} = -0.45(3)$ and $C_{ann}^{KSVZ} = 0.01(3)$.
- **Dine-Fischler-Srednicki-Zhitnitsky (DFSZ) model**: $C_{app}^{DFSZ} = -0.170(30) - 0.430(21)\sin^2(\beta)$ and $C_{ann}^{DFSZ} = -0.124(30) + 0.407(21)\sin^2(\beta)$ with $\tan(\beta) \in [0.5, 170]$.

For the KSVZ model, there is no ambiguity in the coupling values. In contrast, for the agnostic and DFSZ scenarios, unless otherwise specified, numerical values and associated plots correspond to the maximum coupling values allowed.

The emission spectra for the agnostic scenario are shown in Fig. 4.2.

4.1.3.3 Free-streaming approximation

In our calculations, we have assumed that the axion-matter interaction is sufficiently weak for axions to escape from the SN core. We now verify *a posteriori* whether this assumption holds. This can be quantified by computing the mean free path, $l_a = \Gamma_a^{-1}$, and comparing it to the SN core radius, R. If the axion-matter couplings are too strong, l_a becomes smaller than R. The key question is whether the experimentally allowed values of these couplings are sufficiently small to satisfy the free-streaming condition. Our *a posteriori* check is then clear: the free-streaming assumption holds if l_a is larger than R.

Following the prescription of [Raf96], we write

$$Q_a = \int E_a e^{E_a/T} \frac{d^3\vec{p}_a}{(2\pi)^3} \Gamma_a = \int dE_a \frac{|p_a| E_a^2}{2\pi^2} e^{E_a/T} \Gamma_a \ . \tag{4.1.7}$$

Using the definition of Q_a, we obtain

$$\Gamma_a = 2\pi^2 \frac{e^{-E_a/T}}{E_a |p_a|} \frac{d\dot{n}_a}{dE_a} \simeq \frac{2\pi^2}{V \Delta t} \frac{e^{-E_a/T}}{E_a |p_a|} \frac{dN_a}{dE_a} \ , \tag{4.1.8}$$

where $V = M/\rho$ is the volume of the SN core.

Thus, the condition for free streaming is

$$l_a > R \quad \Leftrightarrow \quad \frac{e^{-E_a/T}}{E_a|p_a|}\frac{dN_a}{dE_a} < \left(\frac{3V}{4\pi}\right)^{1/3}\frac{V\Delta t}{2\pi^2} = 1.2\times 10^{55}\ \text{MeV}^{-3}\ . \tag{4.1.9}$$

Since the function $e^{-E_a/T}/(E_a|p_a|)$ decreases with energy, and the spectrum becomes negligible below[3] $E_a \sim 20$ MeV (see Fig. 4.2), we estimate that for $T \in \{30, 40\}$ MeV:

$$e^{-E_a/T}/(E_a|p_a|) \lesssim 10^{-3}\ \text{MeV}^{-2}\ . \tag{4.1.10}$$

Therefore, to satisfy the free-streaming condition, it is sufficient that

$$\frac{dN_a}{dE_a} \ll 10^{58}\ \text{MeV}^{-1}\ . \tag{4.1.11}$$

From Fig. 4.2, we observe that the peak value of the spectrum is of order 10^{55} MeV^{-1}, well below the critical threshold of 10^{58} MeV^{-1}. This confirms that we are indeed in the free-streaming regime.

4.1.4 Parton spectrum

4.1.4.1 Generalities

The energy spectrum of a particle B_1 emitted via the process $aN \to \sum_{k=1}^{n_f} B_k$ can be computed using the following formula:

$$\frac{dN_{B_1}}{dE_{B_1}}(E_{B_1}) = \frac{1}{4\pi d^2}\int \frac{d\cos(\theta_{aN})}{2} dE_a \frac{dN_a}{dE_a}(E_a) dE_N \frac{dN_N}{dE_N}(E_N)\frac{d\sigma}{dE_{B_1}}(E_a; E_N; \cos(\theta_{aN}); E_{B_1})\ , \tag{4.1.12}$$

where d is the distance to the source.

This formula can be understood as follows: for a given point in phase space, the cross-sectional probability for an interaction is given, by definition, by the cross section σ. However, axion emission from the source is diluted over a surface $4\pi d^2$ (with $d^2 \gg \sigma$), so the probability for a process to occur is $p = \sigma/(4\pi d^2)$. This corresponds to a Bernoulli probability, and for N possible interactions, it becomes a binomial distribution with mean $Np = N\sigma/(4\pi d^2)$.[4] Taking into account the energy spectra of the initial particles, the number of expected events becomes[5]

$$N_{B_1} = \int \frac{d\cos(\theta_{aN})}{2} dE_a \frac{dN_a}{dE_a}(E_a) dE_N \frac{dN_N}{dE_N}(E_N)\frac{\sigma}{4\pi d^2}\ , \tag{4.1.13}$$

and differentiating Eq. (4.1.13) with respect to E_{B_1} gives Eq. (4.1.12).

In our cases of interest, the nucleon in the medium is at rest in the laboratory frame of reference, so

$$\frac{dN_N}{dE_N}(E_N) \simeq N_t \delta(E_N - m_N)\ , \tag{4.1.14}$$

where N_t is the number of target nucleons. This approximation holds because the nucleon mass ($m_N \sim 940$ MeV) is much larger than the thermal energy scale ($T \sim 25$ meV).

To justify this rigorously, we consider the Boltzmann distribution for non-relativistic particles of mass m at temperature T:

$$f_v(v) = \sqrt{\frac{2}{\pi}}\left(\frac{m}{T}\right)^{3/2} v^2 e^{-mv^2/(2T)}\ . \tag{4.1.15}$$

The kinetic energy is $K = \frac{1}{2}mv^2$, leading to the energy distribution

$$f_K(K) = 2\sqrt{\frac{K}{\pi T^3}} e^{-K/T}\ , \tag{4.1.16}$$

[3] Strictly speaking, the spectrum support is $\mathbb{R}_+^*$. However, for $E_a < 20$ MeV, it becomes negligible.

[4] Since $p \ll 1$ and $N \gg 1$, we can approximate the binomial distribution $\mathcal{B}(p; N)$ by a Poisson distribution $\mathcal{P}(\lambda = pN)$ because

$$\binom{N}{k} p^k (1-p)^{N-k} = \frac{(pN)^k}{k!} e^{-pN}\left(1 + \mathcal{O}\left(\frac{1}{N}\right)\right)\ .$$

[5] Dividing $d\cos(\theta_{aN})$ by 2 gives the probability density of $\cos(\theta_{aN})$, which is uniformly distributed between -1 and 1.

with mean and standard deviation[6]

$$\langle K\rangle = \frac{3}{2}T \ , \quad \sigma_K = \sqrt{\langle K^2\rangle - \langle K\rangle^2} = \sqrt{\frac{3}{2}}T \ . \tag{4.1.17}$$

Since $E = m + K$, we have $\langle E\rangle = m + \langle K\rangle$ and $\sigma_E = \sigma_K$, leading to a relative dispersion $\sigma_E/\langle E\rangle \sim 3 \times 10^{-11}$, thereby justifying the approximation in Eq. (4.1.14).

Thus, for a process $aN \to N'X$ with X a Cherenkov parton, the resulting spectrum is

$$\frac{dN_X}{dE_X}(E_X) = \frac{N_t}{4\pi d^2}\int dE_a \frac{d\sigma}{dE_X}(E_X; E_a)\frac{dN_a}{dE_a}(E_a) \ , \tag{4.1.18}$$

where the number of target nucleons is

$$N_t = 10^9 N_N \mathcal{N}_A \frac{m_{det}}{1 \text{ kton}} \frac{1 \text{ g.mol}^{-1}}{M_{water}} \ , \tag{4.1.19}$$

with $N_N = 2$ the number of the nucleon N (in hydrogen or deuterium), $\mathcal{N}_A$ Avogadro's number, m_{det} the detector mass, and M_{water} the molar mass of water ($M_{H_2O} = 18$ g.mol^{-1} or $M_{D_2O} = 20$ g.mol^{-1}). We note that $N_N = 2$ is the most significant approximation in our approach (as in much of the literature): we do not consider the nucleons bound in oxygen nuclei, as their binding energy is significant, around ~ 10 MeV, so they cannot be treated as free, static particles when they interact with axions. In contrast, for hydrogen, the molecular binding energy–approximately ~ 10 eV–is entirely negligible compared to typical axion energies of ~ 100 MeV. Inclusion of the interaction with oxygen nucleons thus requires knowledge of non-perturbative matrix elements, and is an important task left for future work. We note that neglect of this contribution does not invalidate our conclusions, it only makes them more conservative. In fact, interaction with oxygen will result in an increase of the Cherenkov spectrum induced by axion absorption.

Using $\int d\sigma\delta(E_X - E) = \dfrac{\partial\sigma}{\partial E_X}(E_X = E; E_a)$, we can write

$$\begin{aligned}
\frac{dN_X}{dE_X}(E_X = E) =& \frac{N_t}{4\pi d^2}\int dE_a \frac{\partial\sigma}{\partial E_X}(E_X = E; E_a)\frac{dN_a}{dE_a}(E_a) \\
=& \frac{N_t}{4\pi d^2}\int dE_a d\sigma\delta(E_X - E)\frac{dN_a}{dE_a}(E_a) \\
\simeq& \frac{N_t}{4\pi d^2}\int dE_a d\sigma\delta(E_a - E)\frac{dN_a}{dE_a}(E_a) \\
=& \frac{N_t\sigma(E)}{4\pi d^2}\frac{dN_a}{dE_a}(E) \\
=& \frac{N_t\sigma(E_a)}{4\pi d^2}\frac{dN_a}{dE_a}(E_a)|_{E_a=E} \ ,
\end{aligned} \tag{4.1.20}$$

where the exchange between E_a and E_X is a valid approximation if $E_a \simeq E_X$.

For the process $aN_i \to N_f X$, with $E_{N_i} = m_{N_i}$ and negligible axion mass, the kinematic relation reads:

$$E_a = \frac{E_X + (m_{N_f}^2 - m_{N_i}^2 - m_X^2)/(2m_{N_i})}{1 - (E_X - |p_X|\cos(\theta_{aX}))/m_{N_i}} \ . \tag{4.1.21}$$

Given that $m_{N_i} \simeq m_{N_f} \gg m_X$, $E_a \ll m_{N_i}$ (see Fig. 4.2), and $E_X \lesssim E_a$, it follows that Eq. (4.1.21) simplifies to $E_a \simeq E_X$.

Eq. (4.1.20) is the form used in [Luc+22] for $X = \gamma$. In the following, we will use the exact formula without this approximation.

[6]The moments are computed as

$$\langle K^n\rangle = \int_0^{+\infty} dK\, K^n\, 2\sqrt{\frac{K}{\pi T^3}}e^{-K/T} = \frac{2}{\sqrt{\pi}}T^n\Gamma(n+3/2) = \frac{(2n+2)!}{2^{2n+1}(n+1)!}T^n \ .$$

In the laboratory frame, where the initial nucleon N_i is at rest, the cross section can be written as

$$\begin{aligned} d\sigma =& \frac{1}{4m_{N_i}E_a}\frac{d^3\vec{p}_X}{(2\pi)^3 2E_X}\frac{d^3\vec{p}_{N_f}}{(2\pi)^3 2E_{N_f}}\overline{|\mathcal{M}_{fi}|^2}(2\pi)^4\delta^4(P_i - P_f) \\ =& \frac{1}{4m_{N_i}E_a}\frac{(2\pi)|p_X|d\cos(\theta_{aX})dE_X}{(2\pi)^3 2}\overline{|\mathcal{M}_{fi}|^2}(2\pi)\delta((p_{N_i}+p_a-p_X)^2 - m_{N_f}^2) \\ =& \frac{1}{4m_{N_i}E_a}\frac{(2\pi)|p_X|dE_X}{(2\pi)^3 2}\overline{|\mathcal{M}_{fi}|^2}(2\pi)\frac{1}{2E_a|p_X|} \\ =& dE_X\frac{\overline{|\mathcal{M}_{fi}|^2}}{32\pi m_{N_i}E_a^2} \ , \end{aligned} \tag{4.1.22}$$

with

$$\cos(\theta_{aX}) = \frac{E_aE_X + m_N(E_X - E_a) - (m_X^2 + m_a^2)/2}{|p_a||p_X|} \ . \tag{4.1.23}$$

Thus,

$$\frac{d\sigma}{dE_X} = \frac{\overline{|\mathcal{M}_{fi}|^2}}{32\pi m_{N_i}E_a^2} \ , \tag{4.1.24}$$

which finally leads to

$$\frac{dN_X}{dE_X}(E_X) = \frac{N_t}{128\pi^2 d^2 m_{N_i}}\int_\Omega dE_a\frac{\overline{|\mathcal{M}_{fi}|^2}}{E_a^2}\frac{dN_a}{dE_a}(E_a) \ , \tag{4.1.25}$$

where the domain is defined by $\Omega = \{E_a \in [m_a; +\infty[\ | \ \cos(\theta_{aX}) \in [-1; 1]\}$.

4.1.4.2 Neutrino spectrum

The neutrino contribution is primarily due to the process $\bar{\nu}p \to ne^+$ [Fog+05]. Based on this study, the positron energy spectrum is given by

$$\frac{dN_{e^+}}{dE_{e^+}}(E_{e^+}) = N_{e^+}\left(\frac{0.2 \text{ kpc}}{d}\right)^2\frac{(1+\beta)^{1+\beta}}{\Gamma(1+\beta)\langle E\rangle}\left(\frac{E_{e^+}}{\langle E\rangle}\right)^\beta e^{-(1+\beta)E_{e^+}/\langle E\rangle} \ , \tag{4.1.26}$$

where $\langle E\rangle = 18.2$ MeV is the average positron energy, $\beta = 3$ is a spectral shape parameter, d is the SN-Earth distance, and $N_{e^+} = 2.9 \times 10^8$ corresponds to the total number of positrons for a source distance $d = 0.2$ kpc.

4.1.4.3 Photon spectrum

At tree level, the diagrams consistent with Chiral Perturbation Theory augmented with an axion (ChPT+a) are shown in Fig. 4.3. There are three vertices:

- $\mathcal{L}_{app} = \frac{\partial_\mu a}{2f_a}C_{app}\bar{p}\gamma^\mu\gamma_5 p$;
- $\mathcal{L}_{\gamma pp} = -ie\bar{p}\gamma_\mu p A^\mu$;
- $\mathcal{L}_{a\gamma\gamma} = \hat{c}_{a\gamma\gamma}\frac{\alpha_{e.m.}}{4\pi}aF\tilde{F}$.

We will not consider diagram (c), since the factor $\alpha_{e.m.}/(4\pi) < 10^{-3}$ is expected to suppress its contribution compared to the other diagrams.

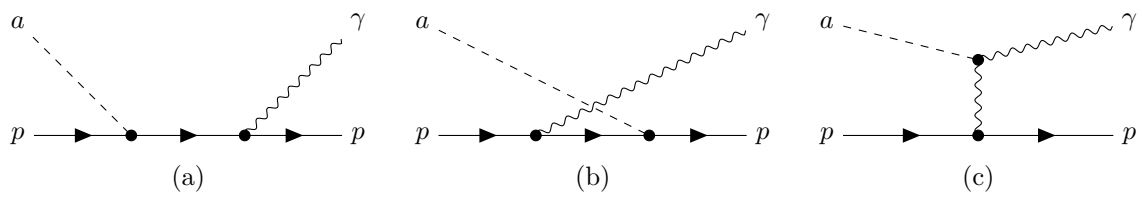

Figure 4.3: Leading-order Feynman diagrams contributing to $pa \to p\gamma$.

The total amplitude squared, averaged over the initial states, is given by

$$\overline{|\mathcal{M}_{fi}(ap \to p\gamma)|^2} = \frac{8\pi\alpha_{e.m.}|C_{app}|^2 m_N^2 (p_a \cdot p_{N_f} - p_a \cdot p_{N_i})^2}{f_a^2 (p_a \cdot p_{N_f})(p_a \cdot p_{N_i})} \,. \tag{4.1.27}$$

Since $p_a \cdot p_{N_i} = E_a m_N$ in the laboratory frame, it is worth noting that in the elastic limit, namely for $E_f = m_N$ and $p_a \cdot p_{N_f} = E_a m_N$, the amplitude vanishes.

4.1.4.4 Pion spectrum

At tree level, the diagrams consistent with ChPT+a are shown in Fig. 4.4, where the local diagram is absent because it only exists for the charged pions. There are two vertices:

- $\mathcal{L}_{aNN} = \dfrac{\partial_\mu a}{2f_a} C_{aNN} \bar{N}\gamma^\mu\gamma_5 N$;
- $\mathcal{L}_{\pi^0 NN} = \dfrac{D+F}{2F_0} \partial_\mu \pi^0 (\bar{p}\gamma^\mu\gamma_5 p - \bar{n}\gamma^\mu\gamma_5 n)$,

where $D + F = -1.26(5)$.

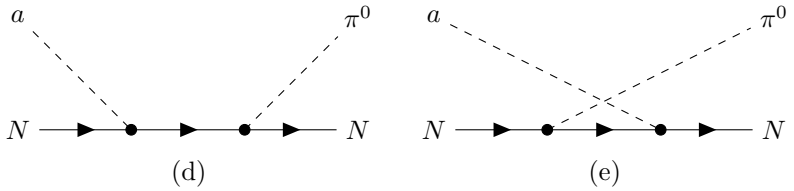

Figure 4.4: Leading-order Feynman diagrams contributing to $Na \to N\pi^0$.

The total amplitude squared, averaged over the initial states, is given by

$$\overline{|\mathcal{M}_{fi}(aN \to N\pi^0)|^2} = \frac{(D+F)^2 |C_{aNN}|^2 [2(p_a \cdot p_{N_i})(p_a \cdot p_{N_i})(p_{N_i} \cdot p_{N_f}) - m_N^2 (p_a \cdot p_{N_i})^2 - m_N^2 (p_a \cdot p_{N_f})^2]}{F_0^2 f_a^2 (p_a \cdot p_{N_f})(p_a \cdot p_{N_i})} \,. \tag{4.1.28}$$

Similarly to the $ap \to p\gamma$ case, this amplitude vanishes in the elastic approximation.

4.1.5 Results

4.1.5.1 Axion- vs. neutrino-absorption spectra

The previous discussion allows us to calculate the Cherenkov-parton number spectrum, see Eq. (4.1.25), where the particle absorbed in the Cherenkov-light producing process is an axion.

The spectra calculations are performed for a detector of the HK type, i.e., with a proposed fiducial mass of $M_{det} = 374$ kton [Abe+11], and for a source similar to Betelgeuse, located at a distance of approximately $d \simeq 0.2$ kpc [HBG08].

4.1.5.1.1 Physical spectra

In the plots shown in Fig. 4.5,[7] we compare the calculated axion and neutrino number spectra.

The two rows correspond to the $DD2$ and $SFHo$ EoS models, respectively, while the left and right columns correspond to $T = 30$ and 40 MeV. All plots use $n_B = n_{\rm sat}$, and we omit the $n_B = 1.5\, n_{\rm sat}$ counterparts since the differences are not significant.

Each panel in Fig. 4.5 displays three groups of number spectra for the different Cherenkov partons:

- Dashed blue lines: the e^+ number spectrum from the $\bar{\nu}p \to ne^+$ process [Fog+05], peaking at the lowest energies in all panels;

[7] The spectra shown in Fig. 4.5 differ by a factor of 2 in normalization compared to their counterparts in [Cav+25b]. This discrepancy arises from a typo identified after publication. The typo has no impact on our conclusions, as it does not affect the oom–the only information of relevance, as explained at the end of Section 4.1.3.1. The corrected formulas are provided in Eqs. (4.1.27)-(4.1.28). We thank Matías M. Reynoso for bringing this discrepancy to our attention.

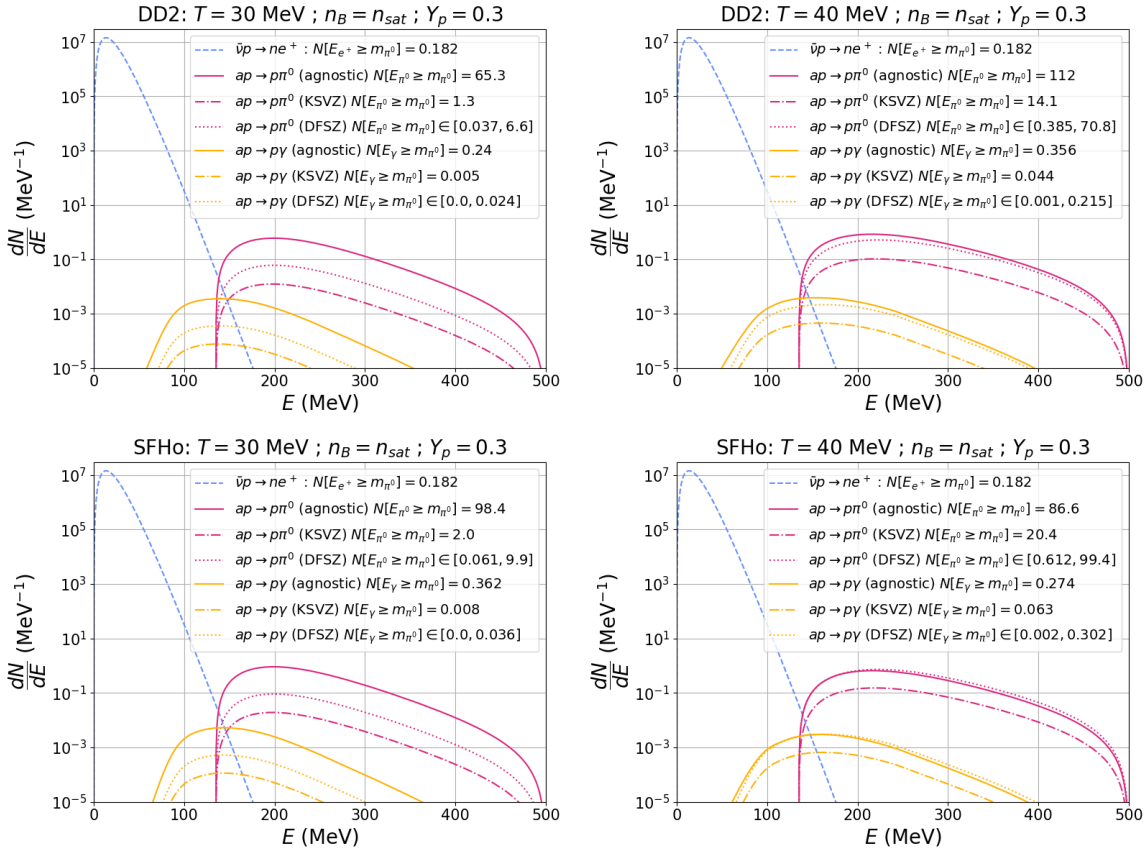

Figure 4.5: Comparison between the Cherenkov-light spectra induced by neutrino (dashed blue) vs. axion absorption. The latter includes either a photon (yellow) or a π^0 (purple) as Cherenkov partons, with different line styles denoting the various theoretical scenarios discussed in Section 4.1.3.2—see the legend, which also specifies the total number of events above the π^0 threshold. The first (second) row corresponds to the $DD2$ ($SFHo$) EoS models, while the first (second) column corresponds to $T = 30$ (40) MeV. The remaining thermodynamic parameters are fixed to reference values, as their variations within motivated ranges are imperceptible.

- Purple lines (with different styles): the π^0 spectrum from $ap \to p\pi^0$, peaking at the highest energies in all panels;
- Yellow lines (with different styles): the photon spectrum from $ap \to p\gamma$, exhibiting the lowest peak in all panels.

The spectra for axion-absorbing processes depend on the axion-nucleon-nucleon couplings C_{ann} and C_{app}, which are fixed according to the three benchmark scenarios outlined in Section 4.1.3.2. These cases are represented by different line styles (solid, dot-dashed, dotted) as detailed in the legend.

We also display, in the legend, the integral of each spectrum above $E_X \geq m_{\pi^0}$, where X denotes the relevant Cherenkov parton. This choice for the lower integration boundary is a practical approximation to the intersection point between the $\bar{\nu}p \to ne^+$ and $ap \to p\pi^0$ spectra, as seen in all panels. The numbers reported in the legend suggest that the π^0 channel would yield about a hundred events above m_{π^0}, essentially free of background from the $\bar{\nu}p \to ne^+$ process. Conversely, the $ap \to p\gamma$ channel would contribute at most $\mathcal{O}(10^{-1})$ events in this region, making it significantly less promising compared to the π^0 channel. These conclusions are expected to hold even after accounting for the effects discussed in the concluding paragraph of Section 4.1.3.1.

It is also worth noting that the number of expected events increases with temperature in the KSVZ and DFSZ scenarios, as anticipated. However, this trend does not necessarily hold when only experimental bounds are imposed (the "agnostic" case). For example, within the $SFHo$ model, an increase in temperature causes the Raffelt's bound to be saturated at lower values of C_{aNN}, leading to a reduced number of events.

4.1.5.1.2 Detector-response-corrected spectra

In this section, we assess the expected reconstruction efficiency for the π^0 spectra in Fig. 4.5, based on a realistic simulation of the detector response. The underlying motivation for this line of inquiry is the fact that, unlike positrons emitted from inverse-β decay of SN antineutrinos, π^0s, being electromagnetically neutral, do not directly produce Cherenkov radiation and are instead detected via their electromagnetic decay into two high-energy photons. The latter provide a distinct signature with respect to the Cherenkov cascade initiated by the e^+ originating from antineutrino absorption. Furthermore, if both photons are reconstructed, it is possible to calculate the invariant mass of the π^0, adding additional validation to the signal. The study in this section provides the context towards addressing these two questions in an actual experimental analysis.

To estimate the reconstruction performance and signal detection at HK, we simulate the π^0 decays using the `PYTHIA8` software [Bie+22] and adapt the existing and validated Monte-Carlo simulations and tools of atmospheric neutrinos [Fer+23]. Since the $\bar{\nu}$ signal lies just at the 100 MeV threshold for atmospheric neutrino analyses [Abe+18; Wes+24], we extend the detector response to lower energies and relax the energy cuts applied in these analyses. This adjustment improves the efficiency of the *2-ring π^0-like* sample. Furthermore, given that the expected signal is confined to a few seconds, this modification has virtually no impact on contamination from lower-energy events or accidental coincidences with cosmic rays.

According to the sample definitions, there are four different topologies in which these events can be classified:

- *2-ring π^0-like*: Two photons are reconstructed, and their invariant mass falls between 85 MeV and 215 MeV.
- *1-ring π^0-like*: A single Cherenkov cascade is reconstructed and satisfies specific selection criteria based on likelihoods computed under the assumption that it originates from a π^0 decay with a small opening angle between the two gammas.
- *1-ring e-like*: A single Cherenkov cascade is reconstructed but is found to be incompatible with the π^0 decay hypothesis.
- *1-ring μ-like*: A single Cherenkov ring is reconstructed and identified as compatible with a muon signal. This sample primarily consists of events with misidentified particle types.
- *2-ring other*: Additionally, we consider events with two reconstructed photons that do not satisfy the π^0-like criteria. These events correspond to poorly reconstructed π^0 decays that remain distinguishable from the neutrino signal.

Table 4.2 shows the expected efficiency and purity of each sample. The energy cut at 150 MeV– slightly above the π^0 mass– is sufficient to reduce drastically the contamination from the neutrino emission. Most of the π^0 events fall under the *2-ring π^0-like* category, as expected from lowering the detection threshold in the simulations and due to the low energy of the neutral pions, which implies large opening angles between the decay gammas and enables a good separation and reconstruction. The events with poorer reconstruction populate the 1-ring samples, with a small fraction also classified as *2-ring other*, in which at least one of the Cherenkov rings is misidentified. Any other contribution

Table 4.2: Fractions of axion-induced Cherenkov events reconstructed at HK, categorized according to the event types discussed in the main text. Axion emission follows the SN $DD2$ model with $T = 30$ or 40 MeV. The corresponding fractions of $\bar{\nu}$-induced Cherenkov events are omitted as they are always smaller than $\mathcal{O}(10^{-11})$.

	Reconstructed as π^0	
Selection	**T = 30** MeV	**T = 40** MeV
$E_{\text{reco}} > 150$ MeV	0.973	0.984
$E_{\text{reco}} > 150$ MeV, 2-ring π^0-like	0.675	0.582
$E_{\text{reco}} > 150$ MeV, 1-ring π^0-like	0.146	0.201
$E_{\text{reco}} > 150$ MeV, 1-ring e-like	0.084	0.134
$E_{\text{reco}} > 150$ MeV, 1-ring μ-like	0.007	0.013
$E_{\text{reco}} > 150$ MeV, 2-ring other	0.061	0.053

to the event rate, such as atmospheric neutrinos, is expected to be negligible due to the reduced time window of the signal.

Table 4.2 confirms that the π^0 signal overwhelmingly dominates for reconstructed energies above 150 MeV. More importantly, they indicate that the π^0 reconstruction efficiency is expected to be high, around 80%, though not perfect, as about 20% of the rings will not exhibit a π^0-like shape.

The signal above 150 MeV is essentially background-free. Thus, accurately assessing the reconstruction efficiency will be relevant when distinguishing between axion-induced signals and other potential physical sources such as those considered in [Mas+20; FRV23], whose spectra partially overlap with our signal.

4.1.5.2 Number of events as a function of the axion-matter couplings

Eq. (4.1.25) allows one to calculate the expected number of signal events, $\langle N_X^{(R)} \rangle$. This total number spectrum is obtained by integrating over a specified energy range R.

Since the $\frac{dN_X}{dE_X}$ spectra for Cherenkov partons induced by neutrinos ($X = e^+$) and axions ($X = \gamma$ or π^0) peak at well-separated energies–around 10 MeV for e^+ and 100-200 MeV for γ or π^0–it is generally convenient to define the energy range as $R := [E^*, \infty[$, where E^* is the energy at which $\frac{dN_X^{(a)}}{dE_X}$ overtakes $\frac{dN_{e^+}^{(\nu)}}{dE_{e^+}}$.

However, as shown in the previous sections, the π^0 component dominates overwhelmingly. For this component, it is sufficient to set $E^* \simeq m_{\pi^0}$, and we will henceforth restrict our numerical analysis to this case by taking $R = [m_{\pi^0}, \infty[$. This choice is also justified by the fact that the transition point $\frac{dN_X^{(a)}}{dE_X}(E) = \frac{dN_{e^+}^{(\nu)}}{dE_{e^+}}(E)$ is not experimentally accessible, and thus a cutoff that is both physically motivated and experimentally well-defined–such as $E^* = m_{\pi^0}$–is preferable.

The expected number of signal events can then be estimated as

$$\lambda_{\pi^0}(C_{app}, C_{ann}) \;:=\; \langle N_{\pi^0}^{(R)} \rangle \;=\; \int_R dE_{\pi^0} \frac{dN_{\pi^0}^{(a)}}{dE_{\pi^0}}(C_{app}, C_{ann}) \;. \tag{4.1.29}$$

The probability of observing n events follows a Poisson distribution with mean λ_{π^0}, denoted $P(n; \lambda_{\pi^0})$. Thus, the observed number of events can be approximated as $\lambda_{\pi^0} \pm \delta(\alpha)$, where $\delta(\alpha)$ depends on the confidence level $CL = 1 - \alpha$, with the significance level α, and is defined by

$$P(k \in [\lambda_{\pi^0} - \delta(\alpha),\ \lambda_{\pi^0} + \delta(\alpha)]; \lambda_{\pi^0}) \;=\; \sum_{k \in [\lambda_{\pi^0} - \delta(\alpha),\ \lambda_{\pi^0} + \delta(\alpha)]} P(k; \lambda_{\pi^0}) \;=\; 1 - \alpha \;. \tag{4.1.30}$$

Now, consider a family of random variables $\{X_\lambda\}_{\lambda \in \mathbb{R}+^*}$, each following a Poisson distribution with mean λ. It is well known that

$$\frac{X_\lambda - \lambda}{\sqrt{\lambda}} \underset{\lambda \to \infty}{\xrightarrow{\mathcal{L}}} \mathcal{N}(0; 1) \;, \tag{4.1.31}$$

which implies that for $\lambda \gg 1$, the Poisson distribution can be approximated by a normal distribution centered at λ with standard deviation $\sqrt{\lambda}$. Consequently, at a confidence level corresponding to $k\sigma$, we have

$$\delta(\alpha) = k\sqrt{\lambda} \;. \tag{4.1.32}$$

Eq. (4.1.32) offers two main advantages over Eq. (4.1.30): it is significantly simpler to use, requiring no summation, and it is continuous.

While Eq. (4.1.32) is theoretically justified for large λ, its validity at smaller λ can be assessed numerically. As shown in Fig. 4.6, the approximation remains acceptable even for moderate event rates. Therefore, in the following analysis, we will adopt Eq. (4.1.32) to estimate uncertainties.

In Fig. 4.7, we display the expected number of events (represented as shades of grey) in the C_{app}-C_{ann} plane. In each panel, the blue segment extending outward corresponds to the DFSZ model as $\tan(\beta)$ varies over $[0.25, 170]$, while the red cross indicates the KSVZ model with its associated uncertainties. Dotted yellow ellipses mark the experimental constraints from NSs and SNe, and the dashed orange lines represent the detectability criterion $\lambda_{\pi^0} \geq 2$ for a SN event at the Galactic center.

The choice of $\lambda_{\pi^0} \geq 2$ as the detectability threshold is motivated by two considerations. First, in a counting experiment, the associated Poisson uncertainty for N events is $\sqrt{N}$, and the smallest

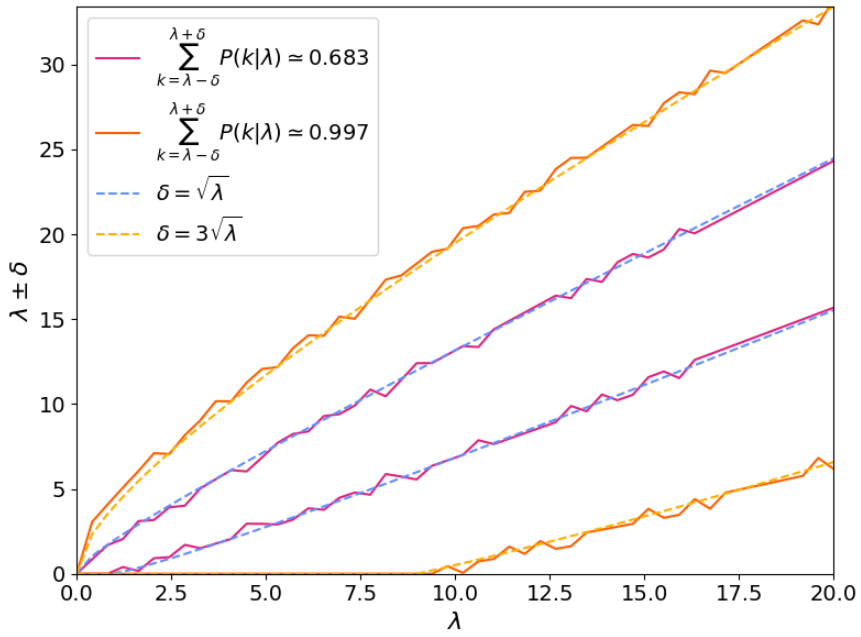

Figure 4.6: Numerical comparison between Eqs. (4.1.30) and (4.1.32).

integer satisfying $N > \sqrt{N}$ is $N = 2$. Second, considering background contributions (e.g., neutrino-induced events), the p-value for observing N or more events under a background-only hypothesis can be calculated. Taking $\lambda = 0.182$ (the neutrino contribution; see Fig. 4.5), the p-value is

$$p = P(X \geq N) = 1 - P(X < N) = 1 - \sum_{k=0}^{N-1} \frac{\lambda^k}{k!} e^{-\lambda} \,, \tag{4.1.33}$$

where X follows a Poisson distribution with mean λ. Table 4.3 shows that a p-value below 5% requires at least $N = 2$ observed events, below 1% requires $N = 3$, and a 5σ detection would require $N = 6$.

The number of signal events is calculated as λ_{π^0} (central panels) or $\lambda_{\pi^0} \mp \sqrt{\lambda_{\pi^0}}$ (left and right panels, respectively), showing only minimal differences. The two rows correspond to $T = 30, 40$ MeV, respectively. Although the shapes of the contours are similar between the two temperatures, the x- and y-axis scales differ by roughly a factor of 2.

The dependence on the choice of EoS model ($DD2$ vs. $SFHo$) and baryon density n_B is less pronounced. Overall, Fig. 4.7 provides a comprehensive overview of the expected variability.

The main trends can be summarized as follows:

- Temperature dependence is by far the most significant: increasing T from 30 to 40 MeV results in approximately a tenfold increase in the number of events[8]. For instance, the KSVZ benchmark predicts ~ 5 events at $T = 30$ MeV and ~ 50 events at $T = 40$ MeV. Thus, predictions at $T = 30$ MeV provide conservative estimates.[9]
- Dependence on EoS model is moderate: switching from $DD2$ to $SFHo$ (at fixed T and n_B) increases the number of events by a factor between 1.5 and 1.8.
- Dependence on baryon density is milder: increasing n_B from $n_{\rm sat}$ to $1.5\, n_{\rm sat}$ increases the number of events by a factor between 1 and 1.3, with slightly larger effects for $SFHo$ than $DD2$.

We emphasize that Fig. 4.7 and the above discussion are intended to provide a preliminary understanding of the sensitivity to SN parameters within reasonable fiducial ranges. A more robust treatment would require detailed SN simulations, which lie beyond the scope of this work.

[8]This scaling can be understood from the emissivity dependence, $Q_a \propto T^{7.5}$, up to a subleading T-dependent prefactor. Neglecting this prefactor gives an expected increase by a factor ~ 8.7.

[9]As already noted earlier (see Section 3.4.5), our T is a fiducial temperature chosen to align with similar non-simulation-based approaches in the literature, starting from [Raf; CR24]. This choice also enables a direct comparison with [Car+21], which adopts T values around 30 MeV in the main text and 40 MeV in its main table. In summary, and as already emphasized in Section 3.4.5, this temperature refers to the SN-core region at the time and place where the bulk of the burst is emitted, and is not representative of the wider SN-core volume and evolution.

Table 4.3: Statistical significance of observing N events assuming a Poisson background with mean $\lambda = 0.182$. The p-value represents the probability of observing N or more events due to background alone. The corresponding number of σ indicates the equivalent significance in a one-sided Gaussian approximation.

Number of observed events N	**p-value (%)**	**Significance (in σ)**
0	100	0.0
1	16.6	1.4
2	1.47	2.4
3	0.09	3.3
4	4×10^{-3}	4.1
5	1×10^{-4}	4.9
6	4×10^{-6}	5.5
7	1×10^{-7}	6.1
8	3×10^{-9}	6.6

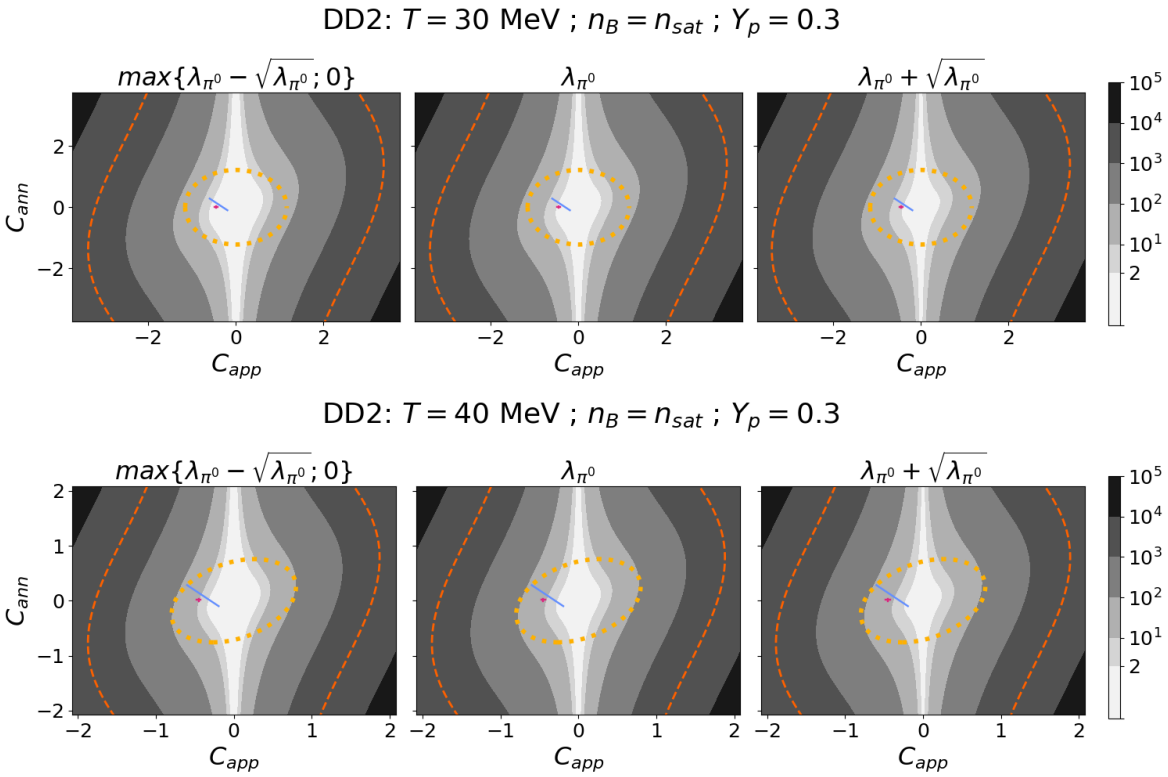

Figure 4.7: Expected number of events (shades of grey) in the C_{app}-C_{ann} plane at a distance of $d = 0.2$ kpc. The blue segment (DFSZ) extends outward with $\tan(\beta) \in [0.25, 170]$, while the red cross represents the KSVZ model with uncertainties. Dotted yellow ellipses and dashed orange lines denote experimental constraints (NSs, SNe) and the detectability criterion ($N_{\pi^0} \geq 2$ for a Galactic center SN), respectively. The expected number of events is calculated as λ_{π^0} (central panels), and as $\lambda_{\pi^0} \mp \sqrt{\lambda_{\pi^0}}$ (left/right panels). Top and bottom rows correspond to $T = 30$ and 40 MeV, respectively.

4.1.5.3 Number of events vs. distance

The calculated number of axion-absorption events for a given SN candidate scales inversely with the square of the distance d from Earth, see Eq. (4.1.25). Beyond a certain distance, the number of signal events falls below the detectability threshold of 2.

Fig. 4.8 illustrates this scaling for the case where the Cherenkov parton is a π^0. The SN models (see plot titles) match those shown in Figs. 4.5-4.7. The expected number of π^0-initiated Cherenkov

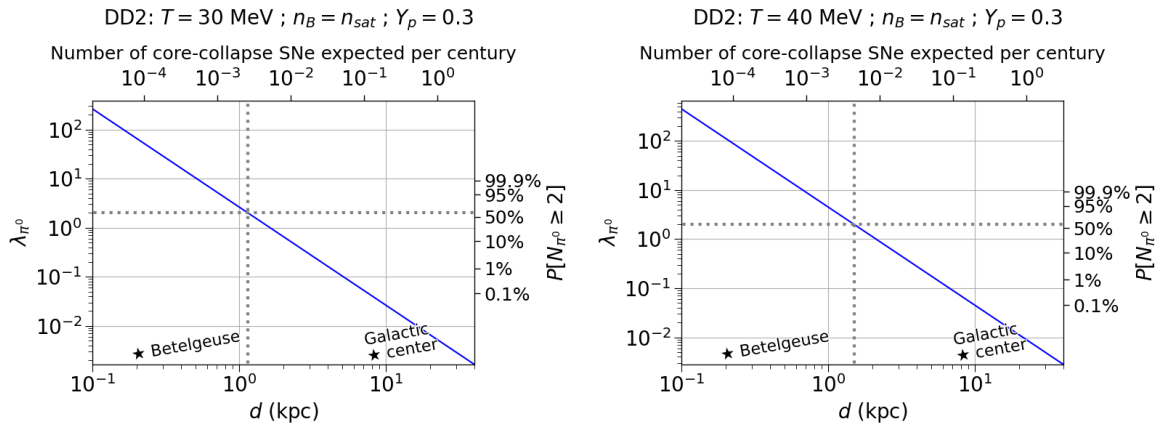

Figure 4.8: Scaling of the expected number of π^0-initiated Cherenkov cascades with the inverse square of the distance d of a SN candidate from Earth. The left y-axis shows the number of expected events as a function of d (lower x-axis), with SN models matching those in Fig. 4.5-4.7. The grey dashed lines indicate the detectability threshold (≥ 2 events), defining the critical distance $d_2^{(a)}$ below which axion absorption remains observable. The upper y-axis maps d onto the expected number of SNe per century, $\dot{N}(d)$, based on the estimation in [TLS94].

cascades is shown on the left y-axis as a function of the distance d (lower x-axis) of the emitting candidate from Earth. The grey dashed lines indicate the critical distance, denoted $d_2^{(a)}$, below which a SN candidate remains above the detectability threshold for axion absorption. The figure suggests $d_2^{(a)} \in [1, 2]$ kpc.

A few important remarks should be made. First, $d_2^{(a)} \in [1, 2]$ kpc refers only to axion-burst detectability: SNe are detectable via their neutrino bursts even from distances of several Mpc, due to the vastly higher total neutrino yield compared to axions. Second, the $d_2^{(a)}$ value results from a calculation considering only axion interactions with hydrogen in water, neglecting oxygen contributions. Including oxygen may significantly increase the estimated axion event yield, but such modeling carries greater uncertainties. Third, only first-generation processes were included; additional reactions (e.g., $aN \to YX$ with X a Cherenkov parton and Y a non-nucleon baryon) could further enhance detectability prospects. We will return to these points in the conclusion.

With these qualifications, the general relationship is clear: the higher the detectability threshold, the longer the expected waiting time for detecting an SN event (via neutrinos). In the Milky Way, this relationship is estimated as [TLS94]

$$\dot{N}(d) = (d/1 \text{ kpc})^2 \times 2.0 \times 10^{-5} \text{ yr}^{-1} \, . \tag{4.1.34}$$

Integrating over the galactic volume yields an expectation of 1-3 SN neutrino events per century in the Milky Way [TLS94; Li+11; RVC21]. However, not all these events will produce detectable axion bursts, since $d_2^{(a)}$ is smaller than the Galactic radius: only sufficiently nearby SNe will yield both neutrino and axion signals.

We display $\dot{N}(d)$ along the upper x-axis of Fig. 4.8. The figure suggests that axion bursts may be detectable for a SN rate of $\lesssim 10^{-2}$ events per century. This scaling estimate is rather crude–it neglects inhomogeneities in the Galactic structure (e.g., core, spiral arms)–but still provides a useful reference point. It is important to keep in mind that this is a statistical estimate; it remains entirely possible that one of the 42 red supergiants listed in Table 4.4[10] could explode as a SN in the coming decades.

Nonetheless, improving the modeling of axion absorption processes in water, especially those producing Cherenkov light, remains crucial for uncovering potential oom enhancements.

[10]Extracted from the compilation provided at https://www.universeguide.com/blogarticle/list-of-red-supergiant-stars

Table 4.4: Selection of nearby red supergiant stars (distance < 2 kpc).

Constellation	**Star Name**	**Distance (kpc)**
Vela	HD 81034	0.023
Cepheus	V419 Cephei	0.054
Orion	Betelgeuse	0.15
Scorpius	Antares	0.17
Cassiopeia	KN Cassiopeiae	0.21
Auriga	Psi1 Aurigae	0.3
Auriga	V408 Aurigae	0.38
Ara	V849 Arae	0.41
Carina	RT Carinae	0.44
Perseus	T Persei	0.47
Cassiopeia	V605 Cassiopeiae	0.48
Taurus	119 Tauri	0.55
Canis Major	VY Canis Majoris	0.56
Monoceros	V926 Monocerotis	0.59
Auriga	NO Aurigae	0.6
Perseus	S Persei	0.6
Auriga	V362 Aurigae	0.61
Cassiopeia	V358 Cassiopeiae	0.61
Centaurus	V412 Centauri	0.64
Carina	BZ Carinae	0.68
Cassiopeia	V595 Cassiopeiae	0.73
Centaurus	V923 Centauri	0.75
Puppis	V407 Puppis	0.77
Cygnus	BC Cygni	0.83
Lacerta	U Lacertae	0.88
Perseus	XX Persei	0.88
Gemini	TV Geminorum	0.95
Vela	V348 Velorum	0.97
Perseus	PR Persei	0.98
Cassiopeia	V778 Cassiopeiae	1.1
Cygnus	RW Cygni	1.1
Perseus	V441 Persei	1.1
Cassiopeia	V704 Cassiopeiae	1.2
Gemini	BU Geminorum	1.3
Perseus	V550 Persei	1.3
Sagitta	V340 Sagittae	1.3
Carina	IX Carinae	1.4
Centaurus	V910 Centauri	1.4
Pyxis	AB Pyxidis	1.4
Centaurus	V772 Centauri	1.6
Cepheus	Herchel's Garnet Star	1.8
Perseus	YZ Persei	1.9

4.1.5.4 Bayesian analysis

Let us assume that in the future, a sufficiently nearby SN is observed, producing a number of events N at energies where the Standard Model (SM) contribution, $\lambda_{SM}(d)$, is small, where d is the distance to the SN. In such a case, the number of axion-induced events would follow a function $\lambda_{BSM}(C_{app}, C_{ann}; d)$. The distance d can be determined independently from the neutrino signal, leaving λ_{BSM} dependent only on the couplings C_{app} and C_{ann}. The total expected number of events would then be $\lambda = \lambda_{SM} + \lambda_{BSM}$.

Applying Bayes' theorem, we write

$$P(C_{app}, C_{ann} \mid N) = \frac{P(N \mid C_{app}, C_{ann}) P(C_{app}, C_{ann})}{P(N)} \ . \tag{4.1.35}$$

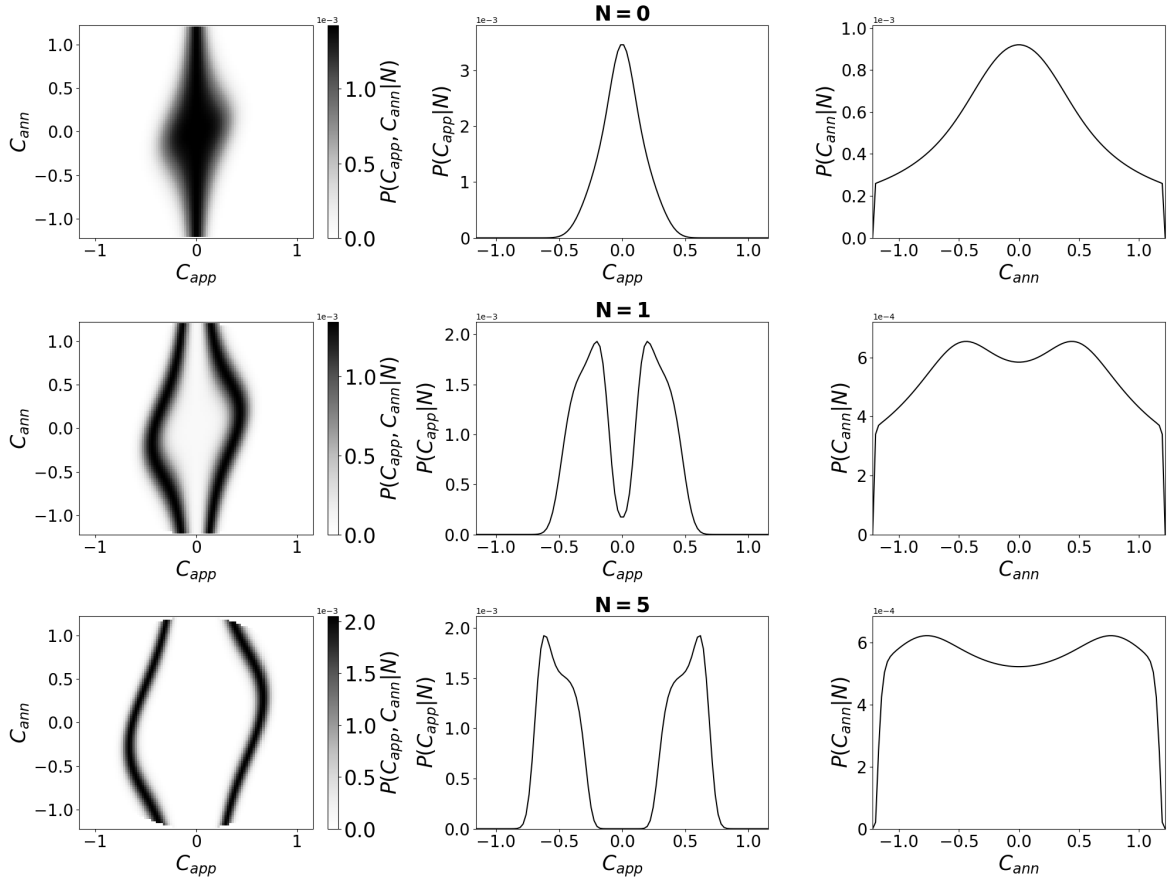

Figure 4.9: Posterior probability densities for the axion couplings C_{app} and C_{ann} as a function of the number of observed events N (each row corresponds to a different $N \in \{0, 1, 5\}$). We assume a SN at a distance $d = 0.2$ kpc, considering only first-generation axion production $\pi N \to N'a$ and absorption $ap \to p\pi^0$. The calculation uses the $DD2$ EoS under thermodynamic conditions $T = 30$ MeV, $n_B = n_{\rm sat}$, and $Y_p = 0.3$. The first column shows the joint 2D posterior $P(C_{app}, C_{ann} \,|\, N)$, the second column shows the marginal posterior $P(C_{app} \,|\, N)$, and the third column shows $P(C_{ann} \,|\, N)$.

Since $P(N)$ is a constant with respect to the parameters, and assuming uniform priors for the couplings (within the domain allowed by current data), the posterior simplifies to

$$P(C_{app}, C_{ann} \mid N) \propto P(N \mid C_{app}, C_{ann}) \propto \lambda^N e^{-\lambda} \ . \tag{4.1.36}$$

The normalization constant is obtained by requiring

$$\int_{\mathbb{R}} dC_{app} \int_{\mathbb{R}} dC_{ann} P(C_{app}, C_{ann} \mid N) = 1 \ . \tag{4.1.37}$$

To obtain the probability density function for C_{aNN} alone, we marginalize over the other variable:

$$P(C_{aNN} \mid N) = \int_{\mathbb{R}} dC_{aN'N'} \, P(C_{app}, C_{ann} \mid N) \ . \tag{4.1.38}$$

Fig. 4.9 shows the resulting posterior distributions as a function of the number of events, assuming a distance $d = 0.2$ kpc. Only the processes involving the emission $\pi N \to N'a$ and the absorption $ap \to p\pi^0$ are considered here. Consequently, the results presented are conservative; the true spectra would require taking into account all relevant processes, and will be much larger.

As seen in the figure, the coupling C_{ann} remains unconstrained by this analysis, while some information on C_{app} can be extracted. This behavior is expected, as in water, axion interactions primarily occur with protons.

When N is small, the analysis allows for an improvement of the upper bound on $|C_{app}|$, whereas for sufficiently large N, a finite confidence interval excluding zero can be obtained.

We applied a Bayesian analysis to the total number of events N. This method is effective for both small and large sample sizes. However, in the case of large N, it may be more appropriate to apply Bayes' theorem directly to the spectrum itself, which could yield more precise results.

4.1.6 Conclusion

The core-collapse and cooling that drive the transition from a SN to a young NS produce a burst of neutrinos. Similarly, this process may also generate fluxes of additional feebly interacting, uncharged particles such as axions. These particles could be detected on Earth by exploiting their interactions with nucleons in reverse, leading to the production of Cherenkov light. These interactions take the form $\alpha N \to N'X$, where the incoming particle α is absorbed by a nucleon N in a water-based detector–such as the planned HK facility–producing a final-state nucleon N' and a "Cherenkov parton" X (such as $e^{\pm}$, γ, or π^0), which initiates an electromagnetic cascade.

Using ChPT+a, we calculated the energy spectra for the reactions $a+p \to p+\gamma$ and $a+p \to p+\pi^0$. Our analysis assumes the most general axion-quark interactions, with coupling strengths constrained either by astrophysical transient observations or by specific theoretical scenarios.

We compared the Cherenkov-light spectra induced by axion absorption with those from neutrino interactions. The axion-absorption spectra depend on the axion-nucleon-nucleon couplings C_{ann}, C_{app}, which are fixed according to the different cases of interest mentioned above. We corroborated these findings by assessing the expected reconstruction efficiency for π^0 spectra based on a realistic HK-like detector simulation. We considered different event categories contributing to π^0 identification and find an intrinsic efficiency around 80%, which, while not perfect, is highly promising.

In addition, we examined how the number of detected events depends on the axion-matter couplings, identifying the regions of the $C_{ann} - C_{app}$ parameter space that can be probed based on the expected number of π^0-initiated signal candidates. Furthermore, we explored how the number of axion-absorption events scales with the number of SN candidates.

4.2 Axion interaction with strange matter

4.2.1 Introduction

In the previous section, we saw that an axionic spectrum interacting with first-generation particles from a sufficiently nearby SN could lead to a detectable signal, even for theoretical models such as KSVZ and DFSZ, which are generally considered difficult to probe.

The question we now address is whether flavor-changing couplings $(k_{V,A})_{23}$ can also make a significant contribution. In other words, while the previous section focused on the case where off-diagonal terms are negligible compared to diagonal ones, we now consider the opposite case, where diagonal terms are negligible in comparison to off-diagonal terms. Moreover, we will not include $(k_V)_{23}$ in our analysis, as its contribution is strongly constrained by the non-observation of the decay $K \to \pi a$ (see Section 5.1).

4.2.2 Axion spectrum

4.2.2.1 Considered processes

Strictly speaking, all flavor-changing processes induced by axion interactions should be taken into account. However, as we saw in the study of axion emission, the decay $\Lambda \to na$ is the dominant contribution. For this reason, we will only consider this decay in our analysis. This approximation will allow us to estimate the oom, though a more precise calculation would require including other flavor-changing processes as well.

4.2.2.2 Spectrum calculation

Using on the one hand:

$$Q_a = \int E_a \frac{d^3\vec{p}_\Lambda}{(2\pi)^3 2E_\Lambda} \frac{d^3\vec{p}_a}{(2\pi)^3 2E_a} \frac{d^3\vec{p}_n}{(2\pi)^3 2E_n} |\mathcal{M}_{fi}|^2 (2\pi)^4 \delta^4(p_\Lambda - p_a - p_n) f_\Lambda (1 - f_n) \ , \tag{4.2.1}$$

and on the other:

$$Q_a = \int dE_a E_a \frac{d\dot{n}_a}{dE_a} \ , \tag{4.2.2}$$

we deduce, through phase space integration (see Appendix B.8), that:

$$\frac{d\dot{n}_a}{dE_a} = \frac{1}{4(2\pi)^3} \int_\Omega |\mathcal{M}_{fi}|^2 f_\Lambda (1 - f_n) dE_\Lambda \ , \tag{4.2.3}$$

where $\Omega = \{E_\Lambda \in [m_\Lambda; +\infty[\ | \ \cos(\theta_{\Lambda a}) \in [-1; 1]\}$ and

$$\cos(\theta_{\Lambda a}) = \frac{m_n^2 - m_\Lambda^2 - m_a^2 + 2E_\Lambda E_a}{2|p_\Lambda||p_a|} \ . \tag{4.2.4}$$

For the QCD axion, the amplitude can be written as:

$$\mathcal{M}_{fi} = \bar{u}_n \not{p}_a (C_V + C_A \gamma_5) u_\Lambda \ , \tag{4.2.5}$$

which leads to:

$$\begin{aligned} |\mathcal{M}_{fi}|^2 =& 4|C_V|^2 (2(p_\Lambda \cdot p_a)(p_n \cdot p_a) + m_a^2((p_\Lambda \cdot p_n) - m_\Lambda m_n)) \\ &+ 4|C_A|^2 (2(p_\Lambda \cdot p_a)(p_n \cdot p_a) - m_a^2((p_\Lambda \cdot p_n) + m_\Lambda m_n)) \ , \end{aligned} \tag{4.2.6}$$

with:

$$p_\Lambda \cdot p_a = \frac{m_\Lambda^2 + m_a^2 - m_n^2}{2} \ , \quad p_n \cdot p_a = \frac{m_\Lambda^2 - m_a^2 - m_n^2}{2} \ , \quad p_\Lambda \cdot p_n = \frac{m_\Lambda^2 - m_a^2 + m_n^2}{2} \ . \tag{4.2.7}$$

For QCD axions ($m_a \ll m_\pi$), this simplifies to:

$$|\mathcal{M}_{fi}|^2 = 2(|C_V|^2 + |C_A|^2)(m_\Lambda^2 - m_n^2)^2 \ . \tag{4.2.8}$$

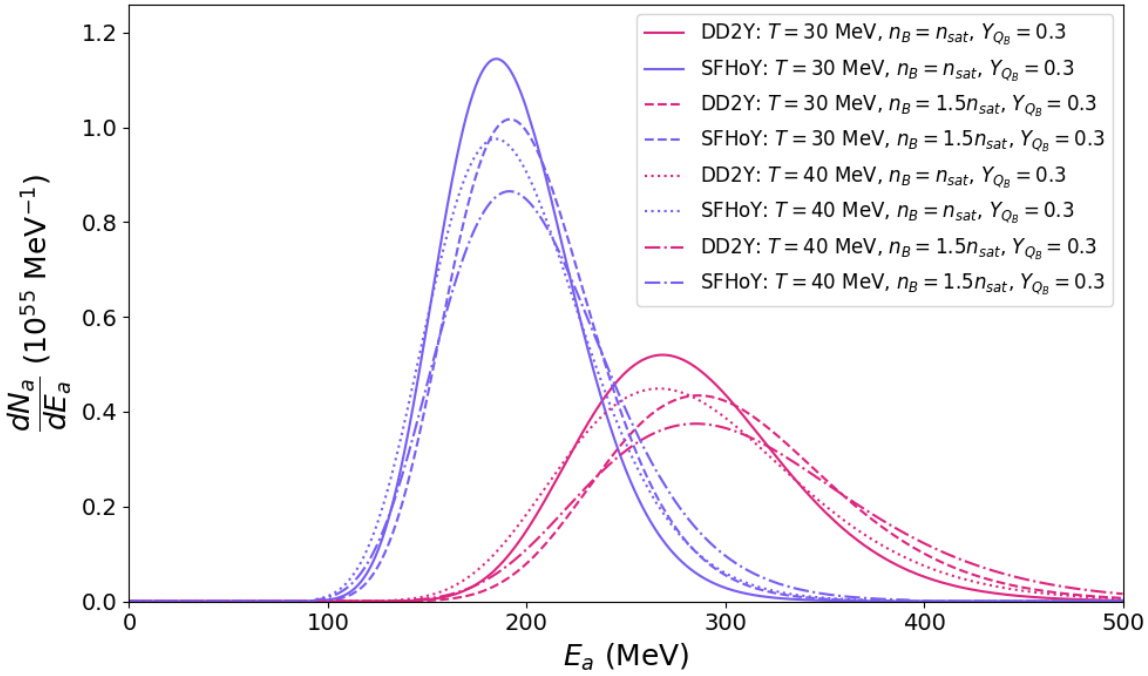

Figure 4.10: Axion spectrum from $\Lambda \to na$ emission for two EoS: $DD2Y$ and $SFHoY$, under different thermodynamic conditions: $T \in \{30, 40\}$ MeV, $n_B \in 1, 1.5\ n_{\rm sat}$, and $Y_{Q_B} = 0.3$.

Furthermore, for the $\Lambda \to na$ process:

$$C_V = \frac{\sqrt{6}}{2}\frac{(k_V)_{23}}{f_a}\ , \quad C_A = -\frac{\sqrt{6}}{12}(D+3F)\frac{(k_A)_{23}}{f_a}\ . \tag{4.2.9}$$

Using the relation:

$$\frac{dN_a}{dE_a} = \int_V d^3\vec{r}\int_{t_i}^{t_f} dt\frac{d\dot{n}_a}{dE_a} \simeq V\Delta t\frac{d\dot{n}_a}{dE_a} = \frac{M}{\rho}\Delta t\frac{d\dot{n}_a}{dE_a}\ , \tag{4.2.10}$$

we can write:

$$\frac{dN_a}{dE_a} \simeq \frac{M\Delta t}{6(4\pi)^3\rho}\frac{36|k_V^{23}|^2 + (D+3F)^2|k_A^{23}|^2}{f_a^2}(m_\Lambda^2 - m_n^2)^2\int_\Omega dE_\Lambda f_\Lambda(1-f_n)\ , \tag{4.2.11}$$

where $\Omega = \{E_\Lambda \in [m_\Lambda; +\infty[\ |\ \cos(\theta_{\Lambda a}) \in [-1, 1]\}$ and $\cos(\theta_{\Lambda a})$ is defined in Eq. (4.2.4).

We normalize the spectra by requiring that they saturate the Raffelt's bound:

$$\int L_\nu dt = \int E_a\frac{dN_a}{dE_a}dE_a\ , \tag{4.2.12}$$

where $L_\nu \sim 3\times 10^{52}$ erg.s^{-1} and $\Delta t \sim 10$ s.

Table 4.5 provides the values of $|(k_A)_{23}|$ required to saturate the Raffelt's bound. As expected, the constraints become more stringent with increasing temperature and density. These values are consistent with those found in Section 3.4. The small differences arise primarily from two aspects: (i) this analysis is based on luminosity rather than emissivity, and (ii) only one flavor-changing process is considered here. Nevertheless, the oom remains consistent, confirming the overall coherence of both approaches.

Fig. 4.10 shows the axion spectra that saturate the Raffelt's bound. We observe that the $DD2Y$ and $SFHoY$ EoSs lead to differences in the average energy. For $SFHoY$, the effective mass difference between the Λ and the neutron lies in the range $m_\Lambda - m_n \in [207.6, 219.8]$ MeV, whereas for $DD2Y$ it lies in the range $m_\Lambda - m_n \in [329.2, 375.6]$ MeV, depending on the thermodynamic conditions (see Appendix B.9). Since the mass difference between the initial and final states provides an estimate of the average energy of the emitted axions (see Section 3.5 for more details), we infer that the

Table 4.5: Constraints on the absolute value of the axion down-strange coupling, $|(k_A)_{23}|$, for different EoS models and thermodynamic conditions in the SN core.

		$\lvert(k_A)_{23}\rvert$	
T (MeV)	n_B	**DD2Y**	**SFHoY**
30	n_{sat}	0.13	0.31
30	$1.5\,n_{\text{sat}}$	0.063	0.23
40	n_{sat}	0.069	0.16
40	$1.5\,n_{\text{sat}}$	0.039	0.12

spectra produced with $DD2Y$ are peaked at higher energies than those obtained with $SFHoY$, even though the effective masses in $SFHoY$ are larger than in $DD2Y$. On the other hand, thermodynamic conditions appear to have a limited effect on the overall shape once normalization is applied.

4.2.2.3 Free-streaming approximation

We now verify the validity of the free-streaming approximation. The procedure is very similar to that used for first-generation couplings: we must check *a posteriori* that the mean free path, $l_a = \Gamma_a^{-1}$, is significantly larger than the SN core radius, R.

The condition for free streaming is given by[11]

$$l_a > R \quad \Leftrightarrow \quad \frac{e^{-E_a/T}}{E_a|p_a|}\frac{dN_a}{dE_a} < 1.2 \times 10^{55}\ \text{MeV}^{-3}\ . \tag{4.2.13}$$

Since the function $e^{-E_a/T}/(E_a|p_a|)$ decreases monotonically with increasing E_a, and the axion spectrum becomes negligible below[12] $E_a \sim 100$ MeV (see Fig. 4.10), we can estimate that for $T \in \{30, 40\}$ MeV:

$$e^{-E_a/T}/(E_a|p_a|) \lesssim 10^{-5}\ \text{MeV}^{-2}\ . \tag{4.2.14}$$

Therefore, the free-streaming condition is satisfied if

$$\frac{dN_a}{dE_a} \ll 10^{60}\ \text{MeV}^{-1}\ . \tag{4.2.15}$$

From Fig. 4.10, we observe that the peak value of the spectrum is on the order of 10^{55}MeV^{-1}, well below the critical threshold of 10^{60} MeV^{-1}. This confirms that our calculation lies safely within the free-streaming regime.

4.2.3 Parton spectrum

4.2.3.1 Studied processes

The idea is similar to the first-generation case: the process begins with an interaction between an incoming axion and a nucleon within the detector, aiming to produce an intermediate hyperon. This hyperon will then decay via the weak interaction.

Strictly speaking, a full calculation should be performed. However, due to the weak interaction couplings, off-shell contributions are negligible. A detailed justification for this on-shell dominance is provided in Section 4.2.3.2.

Therefore, we focus on on-shell hyperons and use known Branching Ratios (BRs) to deduce the final-state particles along with their associated probabilities. As in the first-generation case, we are interested in final states containing either a γ or a π^0. The axionic processes leading to hyperon production that are compatible with ChPT+a are:

- $a + n \to \Lambda$,
- $a + n \to \Sigma^0$,
- $a + p \to \Sigma^+$.

Experimentally, the relevant decay channels are [Nav+24]:

[11] For more details, see Section 4.1.3.3.

[12] Strictly speaking, the support of the spectrum is $\mathbb{R}_+^*$. However, for $E_a < 100$ MeV, the contribution is negligible.

- $ap \to \Sigma^+ \to p\pi^0$,
- $an \to \Lambda \to n\pi^0$,
- $an \to \Sigma^0 \to \gamma\Lambda(\to n\pi^0)$,

with the following BRs:

- $BR[\Sigma^+ \to p\pi^0] = 0.5157$,
- $BR[\Lambda \to n\pi^0] = 0.358$,
- $BR[\Sigma^0 \to \Lambda\gamma] \simeq 1$.

An important point to highlight is that the very high BR of $\Sigma^0 \to \Lambda\gamma$ originates from the fact that this decay does not involve a flavor change. Consequently, it does not require the weak interaction, and the on-shell argument no longer applies. In this case, a full phase space integration must be performed to properly account for all non-negligible configurations in the $an \to \Sigma^0 \to \gamma\Lambda$ process. Once the Λ spectrum is obtained, the on-shell approximation becomes valid again for the decay $\Lambda \to n\pi^0$, which does involve a flavor change.

As in the previous section, and due to the relatively small volume of heavy-water detectors, we will restrict our numerical treatment to interactions involving initial-state protons. Therefore, our primary process of interest is $ap \to \Sigma^+ \to p\pi^0$. We will nonetheless outline the methodology for the other channels to keep the analysis as general as possible. However, numerical results will only be presented for this dominant channel, as the others would lead to event rates that are too low to be relevant in heavy-water detectors.

4.2.3.2 Justification of the on-shell approximation

In a general calculation, all Feynman diagrams leading to the same final state must be considered, without assuming the on-shell approximation, which corresponds to a subspace of the full phase space. However, for the strange matter to appear as an intermediate state, two flavor changes are required. One can be mediated by the axion, but the other must occur via weak interactions, which are suppressed by a factor of $G_F F_0^2 \sim 10^{-7}$ compared to strong interactions.

The Feynman diagrams contributing to the process $ap \to p\pi^0$ with a strange particle in the intermediate state are:

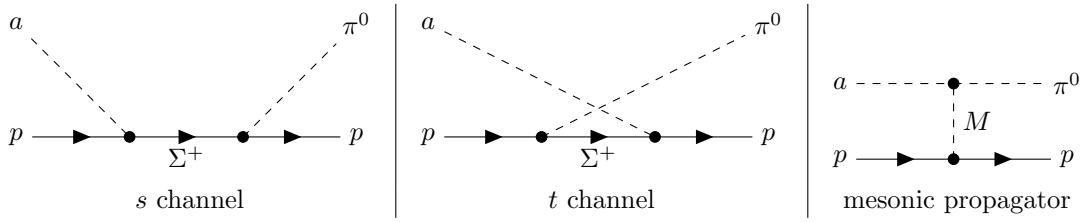

The goal of this section is to demonstrate that

$$d\sigma(ap \to \Sigma^+ \to p\pi^0) \simeq d\sigma(ap \to \Sigma^+)\, dBR(\Sigma^+ \to p\pi^0) \ , \tag{4.2.16}$$

in the narrow width limit $\Gamma_{\Sigma^+} \ll m_{\Sigma^+}$.

We can write, in full generality:

$$\begin{aligned} i\mathcal{M}_{fi}(ap \to \Sigma^+ \to p\pi^0) &= \bar{u}_f V_{\Sigma^+ \to p\pi^0} i \frac{\not{p}_{\Sigma^+} + m_{\Sigma^+}}{s - m_{\Sigma^+}^2 + i m_{\Sigma^+}\Gamma_{\Sigma^+}} V_{ap \to \Sigma^+} u_i \ , \\ i\mathcal{M}_{fi}(ap \to \Sigma^+) &= \bar{u}_{\Sigma^+} V_{ap \to \Sigma^+} u_i \ , \\ i\mathcal{M}_{fi}(\Sigma^+ \to p\pi^0) &= \bar{u}_f V_{\Sigma^+ \to p\pi^0} u_{\Sigma^+} \ , \end{aligned} \tag{4.2.17}$$

which leads to

$$\begin{aligned} \mathcal{M}_{fi}(\Sigma^+ \to p\pi^0)\mathcal{M}_{fi}(ap \to \Sigma^+) &= -\bar{u}_f V_{\Sigma^+ \to p\pi^0} u_{\Sigma^+} \bar{u}_{\Sigma^+} V_{ap \to \Sigma^+} u_i \\ &= -\bar{u}_f V_{\Sigma^+ \to p\pi^0} (\not{p}_{\Sigma^+} + m_{\Sigma^+}) V_{ap \to \Sigma^+} u_i \ . \end{aligned} \tag{4.2.18}$$

Thus, we obtain:

$$\mathcal{M}_{fi}(ap \to \Sigma^+ \to p\pi^0) = -i\frac{\mathcal{M}_{fi}(\Sigma^+ \to p\pi^0)\mathcal{M}_{fi}(ap \to \Sigma^+)}{s - m_{\Sigma^+}^2 + im_{\Sigma^+}\Gamma_{\Sigma^+}} \ , \tag{4.2.19}$$

and therefore, for fixed spin configurations,

$$|\mathcal{M}_{fi}(ap \to \Sigma^+ \to p\pi^0)|^2 = \frac{|\mathcal{M}_{fi}(\Sigma^+ \to p\pi^0)|^2|\mathcal{M}_{fi}(ap \to \Sigma^+)|^2}{|s - m_{\Sigma^+}^2 + im_{\Sigma^+}\Gamma_{\Sigma^+}|^2} \ . \tag{4.2.20}$$

Averaging over initial spins and summing over final spins then gives:

$$\overline{|\mathcal{M}_{fi}(ap \to \Sigma^+ \to p\pi^0)|^2} = \frac{\overline{|\mathcal{M}_{fi}(\Sigma^+ \to p\pi^0)|^2}\,\overline{|\mathcal{M}_{fi}(ap \to \Sigma^+)|^2}}{|s - m_{\Sigma^+}^2 + im_{\Sigma^+}\Gamma_{\Sigma^+}|^2} \ , \tag{4.2.21}$$

because

$$\begin{aligned}
\frac{\overline{|\mathcal{M}_{fi}(\Sigma^+ \to p\pi^0)|^2}\,\overline{|\mathcal{M}_{fi}(ap \to \Sigma^+)|^2}}{|s - m_{\Sigma^+}^2 + im_{\Sigma^+}\Gamma_{\Sigma^+}|^2} &= \frac{\left(\frac{1}{2}\sum\limits_{s_{\Sigma^+}}\sum\limits_{s_{p_f},s_{\pi^0}}|\mathcal{M}_{fi}(\Sigma^+ \to p\pi^0)|^2\right)\left(\frac{1}{2}\sum\limits_{s_{p_i},s_a}\sum\limits_{s_{\Sigma^+}}|\mathcal{M}_{fi}(ap \to \Sigma^+)|^2\right)}{|s - m_{\Sigma^+}^2 + im_{\Sigma^+}\Gamma_{\Sigma^+}|^2} \\
&= \frac{1}{2}\sum_{s_{p_i},s_a}\sum_{s_{p_f},s_{\pi^0}}\frac{\frac{1}{2}\left(\sum\limits_{s_{\Sigma^+}}|\mathcal{M}_{fi}(\Sigma^+ \to p\pi^0)|^2\right)\left(\sum\limits_{s_{\Sigma^+}}|\mathcal{M}_{fi}(ap \to \Sigma^+)|^2\right)}{|s - m_{\Sigma^+}^2 + im_{\Sigma^+}\Gamma_{\Sigma^+}|^2} \\
&= \frac{1}{2}\sum_{s_{p_i},s_a}\sum_{s_{p_f},s_{\pi^0}}\frac{1}{2}\sum_{s_{\Sigma^+}}\frac{|\mathcal{M}_{fi}(\Sigma^+ \to p\pi^0)|^2|\mathcal{M}_{fi}(ap \to \Sigma^+)|^2}{|s - m_{\Sigma^+}^2 + im_{\Sigma^+}\Gamma_{\Sigma^+}|^2} \\
&= \frac{1}{2}\sum_{s_{p_i},s_a}\sum_{s_{p_f},s_{\pi^0}}\frac{1}{2}\sum_{s_{\Sigma^+}}|\mathcal{M}_{fi}(ap \to \Sigma^+ \to p\pi^0)|^2 \\
&= \frac{1}{2}\sum_{s_{p_i},s_a}\sum_{s_{p_f},s_{\pi^0}}|\mathcal{M}_{fi}(ap \to \Sigma^+ \to p\pi^0)|^2 \\
&= \overline{|\mathcal{M}_{fi}(ap \to \Sigma^+ \to p\pi^0)|^2} \ .
\end{aligned} \tag{4.2.22}$$

The transition from two independent sums over s_{Σ^+} to a single sum arises from the narrow-width approximation: the intermediate Σ^+ is quasi on-shell, and the spin appearing in the production is the same as that in the decay.

Using the resonance approximation with the Breit-Wigner distribution, we have:

$$(2\pi)\delta(\sqrt{s} - m_{\Sigma^+}) \simeq \frac{4m_{\Sigma^+}^2\Gamma_{\Sigma^+}}{|s - m_{\Sigma^+}^2 + im_{\Sigma^+}\Gamma_{\Sigma^+}|^2} = \frac{4m_{\Sigma^+}^2\Gamma_{\Sigma^+}}{(s - m_{\Sigma^+}^2)^2 + m_{\Sigma^+}^2\Gamma_{\Sigma^+}^2} \ . \tag{4.2.23}$$

The normalization ensures that both sides integrate to the same value[13]. This approximation is valid only in the narrow width limit $\Gamma_{\Sigma^+} \ll m_{\Sigma^+}$.

Consequently, we obtain:

$$\overline{|\mathcal{M}_{fi}(ap \to \Sigma^+ \to p\pi^0)|^2} \simeq \frac{2\pi}{4m_{\Sigma^+}^2\Gamma_{\Sigma^+}}\delta(\sqrt{s} - m_{\Sigma^+})\overline{|\mathcal{M}_{fi}(\Sigma^+ \to p\pi^0)|^2}\,\overline{|\mathcal{M}_{fi}(ap \to \Sigma^+)|^2} \ . \tag{4.2.24}$$

From this, we get the following cross sections and decay observables:

$$d\sigma(ap \to \Sigma^+ \to p\pi^0) = \frac{1}{2F}\frac{d^3\vec{p}_f}{(2\pi)^3 2E_f}\frac{d^3\vec{p}_\pi}{(2\pi)^3 2E_\pi}(2\pi)^4\delta^4(p_a + p_i - p_p - p_\pi)\overline{|\mathcal{M}_{fi}(ap \to \Sigma^+ \to p\pi^0)|^2} \ , \tag{4.2.25}$$

$$\begin{aligned}
d\sigma(ap \to \Sigma^+) &= \frac{1}{2F}\frac{d^3\vec{p}_{\Sigma^+}}{(2\pi)^3 2E_{\Sigma^+}}(2\pi)^4\delta^4(p_a + p_i - p_{\Sigma^+})\overline{|\mathcal{M}_{fi}(ap \to \Sigma^+)|^2} \\
&= \frac{1}{2F}(2\pi)\delta(s - m_{\Sigma^+}^2)\overline{|\mathcal{M}_{fi}(ap \to \Sigma^+)|^2} \\
&= \frac{1}{2F}\frac{1}{2m_{\Sigma^+}}(2\pi)\delta(\sqrt{s} - m_{\Sigma^+})\overline{|\mathcal{M}_{fi}(ap \to \Sigma^+)|^2} \ ,
\end{aligned} \tag{4.2.26}$$

[13] A proof is provided in Appendix B.3.

$$dBR(\Sigma^+ \to p\pi^0) = \frac{1}{2m_{\Sigma^+}\Gamma_{\Sigma^+}} \frac{d^3\vec{p}_f}{(2\pi)^3 2E_f} \frac{d^3\vec{p}_\pi}{(2\pi)^3 2E_\pi} (2\pi)^4 \delta^4(p_{\Sigma^+} - p_p - p_\pi) \overline{|\mathcal{M}_{fi}(\Sigma^+ \to p\pi^0)|^2} \ . \tag{4.2.27}$$

Using Eq. (4.2.24) in Eq. (4.2.25) directly yields the product of Eqs. (4.2.26) and (4.2.27), which demonstrates the validity of Eq. (4.2.16) in the narrow-width limit $\Gamma_{\Sigma^+}/m_{\Sigma^+} \ll 1$, a condition that is extremely well satisfied here since $\Gamma_{\Sigma^+}/m_{\Sigma^+} \sim 10^{-14}$.

In the t-channel, the vertices $p \to \Sigma^+\pi^0$ and $a\Sigma^+ \to p$ are kinematically forbidden for an on-shell Σ^+. For instance, assuming the vertex $p \to \Sigma^+\pi^0$ in the proton rest frame leads to a contradiction: $m_p = E_{\Sigma^+} + E_{\pi^0} \geq m_{\Sigma^+} + m_{\pi^0} > m_p$.

For the mesonic propagator diagram, we have $p \to pM$ and $aM \to \pi^0$ with $M \in \{K^0, \bar{K}^0\}$. Again, assuming energy conservation in the rest frame of the initial proton, we get $m_p = E_p + E_M \geq m_p + m_M > m_p$, which is impossible.

Hence, all diagrams except for the decay of the intermediate Σ^+ involve strange particles that are far off-shell, resulting in amplitudes suppressed by $G_F F_0^2$. In contrast, for the process $ap \to \Sigma^+ \to p\pi^0$, although the vertex $\Sigma^+ \to p\pi^0$ is weak and contributes a factor $G_F F_0^2$, the quasi-on-shell estimate introduces a division by $\Gamma_{\Sigma^+} \propto (G_F F_0)^2$, canceling this suppression. Therefore, in the on-shell approximation, this channel provides the dominant contribution to the process.

4.2.3.3 Procedure

To obtain the spectra of final-state particles from the initial axion spectrum, the process proceeds in two main steps:

1. Compute the spectra of primary on-shell hyperons produced through axion-nucleon interactions (see Section 4.2.3.4).

2. Propagate these spectra through a cascade of successive decays until stable or detectable final states are reached (see Section 4.2.3.5).

The second step is recursive: at each stage, secondary products may themselves decay, contributing to the final observable spectrum.

4.2.3.4 Primary on-shell hyperon spectrum

Let us consider the generic case $aN \to B$, where an axion a interacts with a nucleon N to produce a hyperon B on its mass shell.

Following exactly the same procedure as in the previous section, one can write:

$$\frac{dN_B}{dE_B}(E_B) = \frac{N_t}{4\pi d^2} \int_{m_a}^{+\infty} \frac{d\sigma}{dE_B}(E_a; E_B) \frac{dN_a}{dE_a}(E_a) dE_a \ . \tag{4.2.28}$$

For a one-body final state, the cross section takes the form:

$$\begin{aligned} \sigma(E_a) =& \int_{\mathbb{R}^3} \frac{1}{4\sqrt{(p_a \cdot p_N)^2 - (m_a m_N)^2}} \frac{d^3\vec{p}_B}{(2\pi)^3 2E_B} \overline{|\mathcal{M}_{fi}|^2} (2\pi)^4 \delta^4(p_a + p_N - p_B) \\ =& \frac{1}{8m_B m_N E_a} \overline{|\mathcal{M}_{fi}|^2} (2\pi) \delta(\sqrt{s} - m_B) H(\sqrt{s}) \ . \end{aligned} \tag{4.2.29}$$

Here, H denotes the Heaviside function.

The issue with Eq. (4.2.29) is that the cross section is proportional to a Dirac delta distribution. This renders the cross section ill-defined from a physical standpoint, as observables must be regular functions, not distributions.

To address this, we employ the resonance framework, where the cross section is redefined using the Breit-Wigner profile. Specifically, we replace:

$$(2\pi)\delta(\sqrt{s} - m_B) \to \frac{4m_B^2 \Gamma_B}{|s - m_B^2 + i m_B \Gamma_B|^2} = \frac{4m_B^2 \Gamma_B}{(s - m_B^2)^2 + m_B^2 \Gamma_B^2} \ . \tag{4.2.30}$$

The denominator arises from the propagator of a quasi-virtual baryon due to the resonance, while the numerator ensures proper normalization such that the integral remains unchanged if $\Gamma_B \ll m_B$.

With this modification, we can rigorously compute N_B using Eq. (4.2.28) as:

$$N_B = \int_{m_B}^{+\infty} \frac{dN_B}{dE_B}(E_B)dE_B = \frac{N_t}{4\pi d^2}\int_{m_a}^{+\infty} \sigma(E_a)\frac{dN_a}{dE_a}(E_a)dE_a \ . \tag{4.2.31}$$

To better understand the situation, let us perform a kinematic calculation. The axion energy is distributed according to a spectrum induced by SN emission, while the nucleon can be considered at rest. Energy and momentum conservation then yield:

$$\begin{cases} m_N + E_a = E_B \\ \vec{p}_a = \vec{p}_B \end{cases} \Rightarrow \begin{cases} E_a^0 = \dfrac{m_B^2 - m_N^2 - m_a^2}{2m_N} \\ E_B^0 = \dfrac{m_B^2 + m_N^2 - m_a^2}{2m_N} \end{cases} \ . \tag{4.2.32}$$

Without the resonance, the probability of the axion having precisely this energy E_a^0 is zero, since the axion energy spectrum is continuous. With the resonance, this probability becomes nonzero.

For example:

- $E_\Lambda^0 = 1132$ MeV and $E_a^0 = 193$ MeV,
- $E_{\Sigma^+}^0 = 1223$ MeV and $E_a^0 = 285$ MeV.

Referring to Fig. 4.10, it appears that the $SFHoY$ EoS favors Λ production, while $DD2Y$ favors Σ^+. However, this must be considered alongside the values of $|(k_A)_{23}|$ given in Table 4.5, which can strongly suppress the interaction rate in the Cherenkov water tank if it is small.

In the case $an \to \Sigma^0 \to \gamma\Lambda(\to n\pi^0)$, the spectrum of the resulting Λ will no longer be a delta function at a fixed energy. Instead, the same procedure as in the first-generation case must be applied: consider all relevant Feynman diagrams to determine the spectra of the intermediate γ and Λ. And then apply a cascade method (discussed in Section 4.2.3.5) to compute the π^0 spectrum assuming an on-shell Λ.

Using the identity:

$$\delta(\sqrt{s} - m_B)H(\sqrt{s}) = \frac{m_B}{m_N}\delta(E_a - E_a^0) \ , \tag{4.2.33}$$

we obtain:

$$N_B = \frac{N_t\overline{|\mathcal{M}_{fi}|^2}}{8d^2 m_N(m_B^2 - m_N^2 - m_a^2)}\frac{dN_a}{dE_a}(E_a^0) \ . \tag{4.2.34}$$

Assuming the matrix element is of the form:

$$\mathcal{M}_{fi} = \bar{u}_B \not{p}_a(C_V + C_A\gamma_5)u_N \ , \tag{4.2.35}$$

then, for QCD axions with $m_a \ll m_\pi$, we find:

$$\overline{|\mathcal{M}_{fi}|^2} = (|C_V|^2 + |C_A|^2)(m_B^2 - m_N^2)^2 \ . \tag{4.2.36}$$

For the process $ap \to \Sigma^+$, the vector and axial couplings are:

$$C_V = -\frac{(k_V)_{23}^*}{f_a} \ , \quad C_A = \frac{D-F}{2}\frac{(k_A)_{23}^*}{f_a} \ , \tag{4.2.37}$$

which allows us to write, for QCD axions:

$$N_{\Sigma^+} = \frac{N_t(m_{\Sigma^+}^2 - m_N^2)(4|(k_V)_{23}|^2 + (D-F)^2|(k_A)_{23}|^2)}{32d^2 m_N f_a^2}\frac{dN_a}{dE_a}(E_a^0) \ . \tag{4.2.38}$$

Table 4.6 shows the expected maximum number of produced particles, ranging between 0.3 and 6 depending on the EoS and thermodynamic conditions. These estimates carry substantial uncertainty due to the application of the Raffelt's bound. We observe that the production yield decreases with increasing temperature or baryon density, which is attributed to the small values of $|(k_A)_{23}|$ (see Table 4.5).

Table 4.6: Maximum average number of particles produced via $ap \to \Sigma^+ \to p\pi^0$, consistent with the Raffelt's bound, for a source at $d = 0.2$ kpc and a detector of the HK type. The result depends on the EoS and the thermodynamic conditions.

		λ_{Σ^+}		$\lambda_{\pi^0} = \lambda_{\Sigma^+} \cdot BR(\Sigma^+ \to p\pi^0)$	
T (MeV)	n_B	$DD2Y$	$SFHoY$	$DD2Y$	$SFHoY$
30	$n_{\rm sat}$	5.5	3.9	2.8	2.0
	$1.5\,n_{\rm sat}$	1.1	3.5	0.56	1.8
40	$n_{\rm sat}$	1.3	1.8	0.66	0.91
	$1.5\,n_{\rm sat}$	0.35	1.5	0.18	0.76

4.2.3.5 Cascade

Once we enter the cascade phase, all decays are assumed to be of the form $A \to B + C$. Our goal is to determine the energy distributions of particles B and C, given the energy distribution of the initial particle A.

In the rest frame of A, the kinematics are governed by:

$$E_B^* + E_C^* = m_A \ , \quad \vec{p}_B^* + \vec{p}_C^* = \vec{0} \ . \tag{4.2.39}$$

These yield the solutions:

$$\begin{aligned} E_B^* &= \frac{m_A^2 + m_B^2 - m_C^2}{2m_A} \ , \\ E_C^* &= \frac{m_A^2 - m_B^2 + m_C^2}{2m_A} \ , \\ p^* = p_B^* = p_C^* &= \frac{\sqrt{(m_A + m_B + m_C)(m_A + m_B - m_C)(m_A - m_B + m_C)(m_A - m_B - m_C)}}{2m_A} \ . \end{aligned} \tag{4.2.40}$$

Applying a Lorentz boost to the lab frame gives:

$$E_B = \frac{E_A}{m_A}\left(E_B^* + zp^*\frac{p_A}{E_A}\right) \ , \tag{4.2.41}$$

$$E_C = \frac{E_A}{m_A}\left(E_C^* - zp^*\frac{p_A}{E_A}\right) \ , \tag{4.2.42}$$

where $z = \cos\theta = \hat{p}_B^* \cdot \hat{p}_A \sim \mathcal{U}([-1,1])$ is uniformly distributed.

The energy distribution of B can be computed analytically. Using the equivalence

$$E_B \le E \Leftrightarrow z \le f(E;E_A) = \left(\frac{Em_A}{E_A} - E_B^*\right)\frac{E_A}{\sqrt{(E_B^*)^2 - m_B^2}\sqrt{E_A^2 - m_A^2}} \ , \tag{4.2.43}$$

we obtain the cumulative distribution function:

$$\begin{aligned} F_B(E) &= P(E_B \le E) = P(z \le f(E;E_A)) \\ &= \int_{m_A}^{+\infty} dE_A\, f_A(E_A)\left(\int_{-1}^{f(E;E_A)} \frac{\chi_{[-1,1]}(f(E;E_A))}{2} dz + \chi_{]1,+\infty[}(f(E;E_A))\right) \ , \end{aligned} \tag{4.2.44}$$

and the corresponding probability density:

$$\begin{aligned} f_B(E) &= \frac{1}{2}\int_{m_A}^{+\infty} dE_A\, f_A(E_A)\frac{\partial f}{\partial E}(E;E_A)\,\chi_{[-1,1]}(f(E;E_A)) \\ &= \frac{1}{2}\int_{m_A}^{+\infty} dE_A\, f_A(E_A)\frac{m_A}{\sqrt{(E_B^*)^2 - m_B^2}\sqrt{E_A^2 - m_A^2}}\,\chi_{[-1,1]}(f(E;E_A)) \\ &= \frac{m_A}{2\sqrt{(E_B^*)^2 - m_B^2}}\int_{E_A^{\rm inf}/m_A}^{E_A^{\rm sup}/m_A} \frac{f_A(m_A x)}{\sqrt{x^2-1}} dx \ , \end{aligned} \tag{4.2.45}$$

with the integration bounds given by:

$$E_A^{\rm inf} = \max\left\{m_A, \frac{2EE_B^* m_A - \sqrt{\Delta}}{2m_B^2}\right\} , \tag{4.2.46}$$

$$E_A^{\rm sup} = \frac{2EE_B^* m_A + \sqrt{\Delta}}{2m_B^2} , \tag{4.2.47}$$

where

$$\Delta = 4m_A^2(E^2 - m_B^2)\left((E_B^*)^2 - m_B^2\right) . \tag{4.2.48}$$

In the limit $m_B \to 0$ (e.g. for photons), the bounds simplify to:

$$E_A^{\rm inf} = \max\left\{m_A, \frac{(E^2 + (E_B^*)^2)m_A}{2EE_B^*}\right\} , \tag{4.2.49}$$

$$E_A^{\rm sup} = +\infty . \tag{4.2.50}$$

This cascade formalism allows us to apply Eq. (4.2.45) recursively:

1. If f_A is a Dirac delta distribution, then f_B is uniform between $E_B^{\rm min} = E_B[z=-1]$ and $E_B^{\rm max} = E_B[z=+1]$.

2. If f_A is uniform over $[E_A^{\rm min}, E_A^{\rm max}]$, then:

$$f_B(E) = \frac{m_A H(\min\{E_A^{\rm max}, E_A^{\rm sup}\} - \max\{E_A^{\rm min}, E_A^{\rm inf}\})}{2(E_A^{\rm max} - E_A^{\rm min})\sqrt{(E_B^*)^2 - m_B^2}} \times \left(\cosh^{-1}\left[\min\left\{\frac{E_A^{\rm max}}{m_A}, \frac{E_A^{\rm sup}}{m_A}\right\}\right] - \cosh^{-1}\left[\max\left\{\frac{E_A^{\rm min}}{m_A}, \frac{E_A^{\rm inf}}{m_A}\right\}\right]\right) , \tag{4.2.51}$$

   with H denotes the Heaviside function.

3. For a general form of f_A, the density f_B is obtained by numerically integrating Eq. (4.2.45).

As a consequence, for the processes $ap \to \Sigma^+ \to p\pi^0$ and $an \to \Lambda \to n\pi^0$, the resulting π^0 spectrum is uniform[14] and independent of the axion spectrum or axion-matter interaction details. Only the normalization $\lambda_{\pi^0} := \langle N_{\pi^0}\rangle$ depends on these parameters.

In contrast, for the process $an \to \Sigma^0 \to \gamma\Lambda(\to n\pi^0)$, one must first compute the spectra of the intermediate γ and Λ, similarly to the first generation case, and then propagate the Λ spectrum through the cascade formalism to obtain the final π^0 spectrum.

An alternative, less analytical method to obtain the spectra of particles B and C consists of generating a random sample of energies E_A according to the density f_A,[15] along with a uniformly distributed sample of $z \in [-1, 1]$. These can be used in Eqs. (4.2.41)-(4.2.42) to generate random lists for E_B and E_C, from which histograms approximating the respective densities can be built. By applying this procedure recursively, vertex by vertex, one can propagate the full cascade down to the spectra of final-state partons. This numerical approach was also used to cross-check the analytical results derived in this section.

4.2.4 Results

The Cherenkov-light spectra induced by neutrinos and axion absorption are shown in Fig. 4.11. The axion-induced contribution is flat over the energy range [194, 284] MeV, with an expected number of events ranging from 0.18 to 2.8, depending on the EoS and thermodynamic conditions (see Table 4.6). These values only affect the overall normalization of the spectrum.

Compared to the first-generation interaction scenario, which yields π^0 mesons with energies in the range [135, 500] MeV (see Fig. 4.5), we note that the axion-induced strange-matter window [194, 284] MeV is fully contained within the first-generation interval. Therefore, if a significant number of π^0 events are detected in the complementary range $[135, 500] \setminus [194, 284]$ MeV, this would strongly

[14] This yields a discontinuous distribution; a more complete treatment–including weak interactions and resonance widths–would produce a slightly modified and smoother profile.

[15] This can be achieved numerically using the generalized inverse transform sampling: define the pseudo-inverse $F_A^*(u) = \inf\{E_A \mid u \le F_A(E_A)\}$. Then, if $U \sim \mathcal{U}[0,1]$, the random variable $F_A^*(U)$ follows the desired distribution f_A.

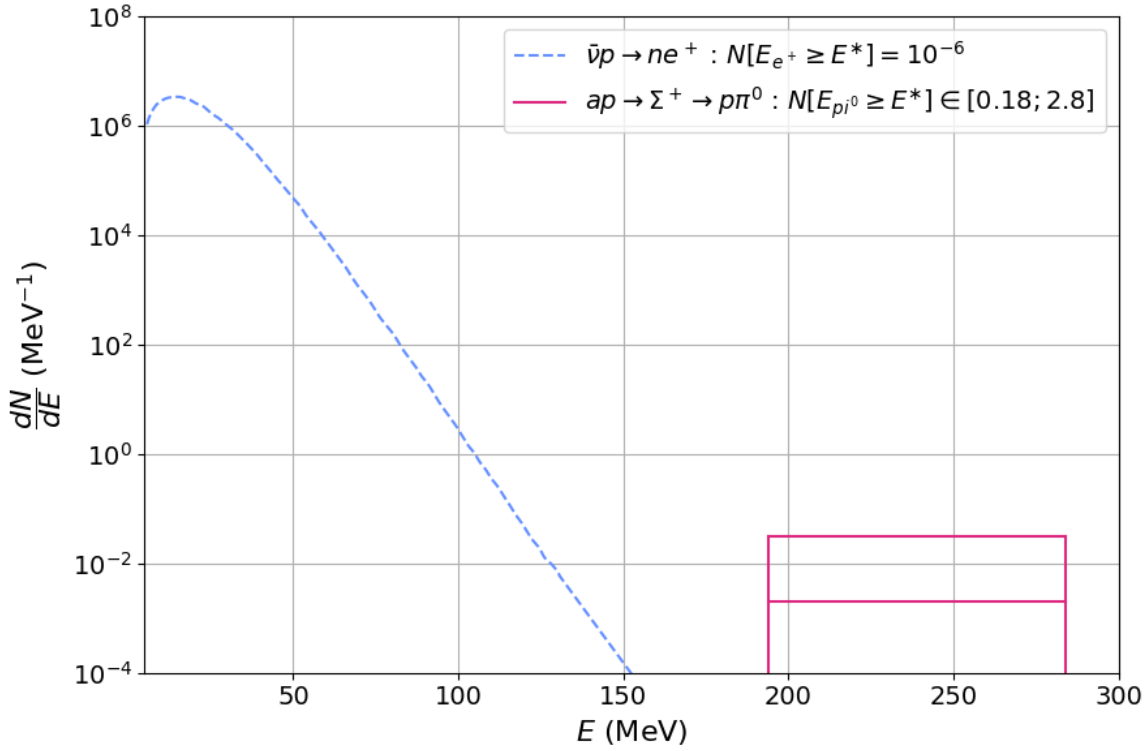

Figure 4.11: Comparison between the Cherenkov-light spectra induced by neutrinos (dashed blue) and axion (solid purple) absorption through $ap \to \Sigma^+ \to p\pi^0$. The legend also specifies the total number of expected events above the detection threshold $E^* = 194$ MeV. The value of $N[E_{\pi^0} \geq E^*]$ depends on the EoS model and thermodynamic conditions–see Table 4.6.

favor a first-generation origin. In contrast, events within $[194, 284]$ MeV are compatible with both first-generation and strange-matter contribution.[16]

A similar analysis to that performed for the first-generation channel (see Section 4.1.5) can be applied here: computing detector-response-corrected spectra, estimating the number of events as a function of axion-matter couplings and distance to the SN, and performing a Bayesian inference of $|(k_A)_{23}|$ from observed event rates. However, the results are expected to be qualitatively similar, but with significantly fewer events. For instance, while the first-generation interaction could yield on the order of 10^2 events at $d = 0.2$ kpc, the strange-matter contribution remains below 3 events. Consequently, detection would only be feasible if the Raffelt's bound is saturated and the SN occurs at short distance.

4.2.5 Conclusion

In the previous section, we showed that axion interactions with first-generation particles can lead to potentially detectable signals in Cherenkov detectors. In this section, we demonstrated that interactions with strange matter can also produce a detectable signal–especially in scenarios where the first-generation contribution is negligible.

We focused in particular on processes involving intermediate hyperons, such as $ap \to \Sigma^+ \to p\pi^0$, which can lead to up to 3 observable events for a SN located at a distance of $d = 0.2$ kpc. Such a signal would be within the reach of current or next-generation neutrino detectors.

A notable strength of these channels lies in the fact that the spectral shape of the resulting signal is entirely independent of both the axion-matter interaction details and the modeling of the SN core. Only the overall normalization–i.e., the expected number of events–is affected by these parameters.

[16] If the strange-matter contribution were sharply localized within a much narrower energy window than that of the first generation, events within such a narrow range could be more confidently attributed to strange matter. However, the strange-matter window $[194, 284]$ MeV covers roughly 25% of the first-generation interval $[135, 500]$ MeV, making it difficult to exclude a first-generation origin, except for a very large number of events.

4.3 Outlook

Our findings lead to several key conclusions, among which we highlight the following two:

1. Even for the QCD axion–which interacts most weakly with matter compared to generic ALPs–the Cherenkov light spectrum from neutrino-nucleon interactions can be modified in a potentially detectable way.

2. Detectability is significantly more promising in the $p+\pi^0$ final state, whose spectrum is not only an oom more intense, but also extends to twice the energy range compared to the $p+\gamma$ channel.

The second point is particularly interesting, as a stronger signal allows for detection at larger distances. SNe are typically discovered through their neutrino bursts, with an expected rate of 2-3 events per century in the Milky Way. However, not all of these will yield detectable axion bursts, since the axion detectability threshold lies well within the Galactic radius. Consequently, only relatively nearby SNe are likely to produce simultaneously detectable neutrino and axion signals. Given the rarity of such dual detections, it is important to identify additional mechanisms that could enhance the axion signal.

In this context, improving the modeling of axion absorption in water Cherenkov detectors is essential, as it may uncover potential oom enhancements.

Beyond identifying dominant processes that can enhance axion signals, it is equally important to establish a predictive framework. If, in the coming decades, a nearby red supergiant such as Betelgeuse were to explode in a SN and no Beyond the Standard Model (BSM) Cherenkov partons were observed, this would allow us to place stronger bounds on axion couplings. Conversely, if an excess of Cherenkov light were observed at energies incompatible with the SM but consistent with axion predictions, it would be essential to provide coupling-dependent predictions to interpret the observation precisely.

In such a case, studying isolated processes while neglecting others would no longer suffice; a comprehensive prediction would be required, incorporating all dominant processes and relevant couplings. A precise prediction will necessitate not only a better understanding of astrophysical sources, but also a calculation framework that accounts for:

- **Free protons (hydrogen nuclei):** Two targets per water molecule. As discussed, the process $ap \to p\pi^0$ dominates over $ap \to p\gamma$, but $ap \to n\pi^+$ has been left for future study. Flavor-changing processes such as $ap \to \Sigma^+ \to p\pi^0$ are also likely to non negligible.

- **Free electrons:** Ten targets per water molecule. This includes processes such as $ae^- \to e^-\gamma$.

- **Bound nucleons in oxygen nuclei:** Sixteen targets per water molecule. Ref. [Car+24] studies processes such as

$$a + {}^{16}O \to {}^{16}O^* \to \begin{cases} {}^{16}O + \gamma \\ {}^{15}N + p + \gamma \\ {}^{15}O + n + \gamma \end{cases} .$$

  However, these reactions involve low-energy axions, with typical energies of order $\mathcal{O}(10\text{ MeV})$, close to nuclear binding energies. As a result, the corresponding spectrum is not well separated from that of neutrino-induced events.

  A dedicated study is therefore needed to assess the contribution of axions with energies well above nuclear binding energies. In this case, nucleons inside oxygen nuclei would behave as quasi-free. While they cannot be treated as truly free–since typical axion energies ($E_a < 500$ MeV, see Figs. 4.2–4.10) are not overwhelmingly larger than nuclear binding energies ($\sim$10 MeV)–their contribution must be estimated, especially considering the large number of such targets in water.

References

[Abe+11] K. Abe et al. *Letter of Intent: The Hyper-Kamiokande Experiment — Detector Design and Physics Potential —*. In: (Sept. 2011). arXiv: 1109.3262 [hep-ex].

[Abe+18] K. Abe et al. *Hyper-Kamiokande Design Report*. In: (May 2018). arXiv: 1805.04163 [physics.ins-det].

[Alo+24a] David Alonso-González et al. *Disentangling axion-like particle couplings to nucleons via a delayed signal in Super-Kamiokande from a future supernova*. In: (Dec. 2024). arXiv: 2412.19890 [hep-ph].

[Alo+24b] David Alonso-González et al. *Probing a diffuse flux of axion-like particles from galactic supernovae with neutrino water Cherenkov detectors*. In: (Dec. 2024). arXiv: 2412.09595 [hep-ph].

[Ari+24] Fernando Arias-Aragón et al. *Axion-induced pair production: a new strategy for axion detection*. In: (Nov. 2024). arXiv: 2411.19327 [hep-ph].

[Bie+22] Christian Bierlich et al. *A comprehensive guide to the physics and usage of PYTHIA 8.3*. In: *SciPost Phys. Codeb.* 2022 (2022), p. 8. DOI: 10.21468/SciPostPhysCodeb.8. arXiv: 2203.11601 [hep-ph].

[BO22] Aurore Betranhandy and Evan O'Connor. *Neutrino driven explosions aided by axion cooling in multidimensional simulations of core-collapse supernovae*. In: *Phys. Rev. D* 106.6 (2022), p. 063019. DOI: 10.1103/PhysRevD.106.063019. arXiv: 2204.00503 [astro-ph.HE].

[Bur00] A. Burrows. *Supernova explosions in the universe*. In: *Nature* 403 (2000), pp. 727–733. DOI: 10.1038/35001501.

[Cap+22] Andrea Caputo et al. *Low-Energy Supernovae Severely Constrain Radiative Particle Decays*. In: *Phys. Rev. Lett.* 128.22 (2022), p. 221103. DOI: 10.1103/PhysRevLett.128.221103. arXiv: 2201.09890 [astro-ph.HE].

[Car+21] Pierluca Carenza et al. *Enhanced Supernova Axion Emission and its Implications*. In: *Phys. Rev. Lett.* 126.7 (2021), p. 071102. DOI: 10.1103/PhysRevLett.126.071102. arXiv: 2010.02943 [hep-ph].

[Car+24] Pierluca Carenza et al. *Cross section for supernova axion observation in neutrino water Čherenkov detectors*. In: *Phys. Rev. C* 109.1 (2024), p. 015501. DOI: 10.1103/PhysRevC.109.015501. arXiv: 2306.17055 [hep-ph].

[Cav+25b] Mael Cavan-Piton et al. *Probing the general axion-nucleon interaction in water Cherenkov experiments*. In: *JHEP* 07 (2025), p. 070. DOI: 10.1007/JHEP07(2025)070. arXiv: 2503.17490 [hep-ph].

[CFJ24] Wei Chao, Jing-Jing Feng, and Mingjie Jin. *Direct detections of the axionlike particle revisited*. In: *Phys. Rev. D* 109.7 (2024), p. 075044. DOI: 10.1103/PhysRevD.109.075044. arXiv: 2311.09547 [hep-ph].

[CGV24] Sabyasachi Chakraborty, Aritra Gupta, and Miguel Vanvlasselaer. *Photoproduction of heavy QCD axions in supernovae*. In: *Phys. Rev. D* 110.6 (2024), p. 063032. DOI: 10.1103/PhysRevD.110.063032. arXiv: 2403.12169 [hep-ph].

[CPW24] Pierluca Carenza, Roman Pasechnik, and Zhi-Wei Wang. *Glueball Axion-Like Particles*. In: (Nov. 2024). arXiv: 2411.11716 [hep-ph].

[CR24] Andrea Caputo and Georg Raffelt. *Astrophysical Axion Bounds: The 2024 Edition*. In: *PoS* COSMICWISPers (2024), p. 041. DOI: 10.22323/1.454.0041. arXiv: 2401.13728 [hep-ph].

[CRV22] Andrea Caputo, Georg Raffelt, and Edoardo Vitagliano. *Muonic boson limits: Supernova redux*. In: *Phys. Rev. D* 105.3 (2022), p. 035022. DOI: 10.1103/PhysRevD.105.035022. arXiv: 2109.03244 [hep-ph].

[ESH90] J. Engel, D. Seckel, and A. C. Hayes. *Emission and detectability of hadronic axions from SN1987A*. In: *Phys. Rev. Lett.* 65 (1990), pp. 960–963. DOI: 10.1103/PhysRevLett.65.960.

[Fer+23] Pablo Fernandez et al. *Atmospheric Neutrino Monte Carlo Simulations*. Version V1. 2023. DOI: 10.7910/DVN/OS5N7U. URL: https://doi.org/10.7910/DVN/OS5N7U.

[Fis+21] Tobias Fischer et al. *Observable signatures of enhanced axion emission from protoneutron stars*. In: *Phys. Rev. D* 104.10 (2021), p. 103012. DOI: 10.1103/PhysRevD.104.103012. arXiv: 2108.13726 [hep-ph].

[Fog+05] G. L. Fogli et al. *Probing supernova shock waves and neutrino flavor transitions in next-generation water-Cerenkov detectors*. In: *JCAP* 04 (2005), p. 002. DOI: 10.1088/1475-7516/2005/04/002. arXiv: hep-ph/0412046.

[FRV23] Damiano F. G. Fiorillo, Georg G. Raffelt, and Edoardo Vitagliano. *Strong Supernova 1987A Constraints on Bosons Decaying to Neutrinos*. In: *Phys. Rev. Lett.* 131.2 (2023), p. 021001. DOI: 10.1103/PhysRevLett.131.021001. arXiv: 2209.11773 [hep-ph].

[Gai19] Thomas K. Gaisser. *Atmospheric Neutrinos*. 2019. arXiv: 1910.08851 [astro-ph.HE]. URL: https://arxiv.org/abs/1910.08851.

[GKR86] Howard Georgi, David B. Kaplan, and Lisa Randall. *Manifesting the Invisible Axion at Low-energies*. In: *Phys. Lett. B* 169 (1986), pp. 73–78. DOI: 10.1016/0370-2693(86)90688-X.

[HBG08] Graham M. Harper, Alexander Brown, and Edward F. Guinan. *A New VLA-Hipparcos Distance to Betelgeuse and its Implications*. In: *The Astronomical Journal* 135.4 (Mar. 2008), p. 1430. DOI: 10.1088/0004-6256/135/4/1430. URL: https://dx.doi.org/10.1088/0004-6256/135/4/1430.

[Li+11] Weidong Li et al. *Nearby Supernova Rates from the Lick Observatory Supernova Search. III. The Rate-Size Relation, and the Rates as a Function of Galaxy Hubble Type and Colour*. In: *Mon. Not. Roy. Astron. Soc.* 412 (2011), p. 1473. DOI: 10.1111/j.1365-2966.2011.18162.x. arXiv: 1006.4613 [astro-ph.SR].

[Luc+22] Giuseppe Lucente et al. *Axion signatures from supernova explosions through the nucleon electric-dipole portal*. In: *Phys. Rev. D* 105.12 (2022), p. 123020. DOI: 10.1103/PhysRevD.105.123020. arXiv: 2203.15812 [hep-ph].

[LZ22] Tong Li and Rui-Jia Zhang. *Axionlike particles from primordial black hole evaporation and their detection in neutrino experiments*. In: *Phys. Rev. D* 106.9 (2022), p. 095034. DOI: 10.1103/PhysRevD.106.095034. arXiv: 2208.02696 [hep-ph].

[Mas+20] Leonardo Mastrototaro et al. *Heavy sterile neutrino emission in core-collapse supernovae: Constraints and signatures*. In: *JCAP* 01 (2020), p. 010. DOI: 10.1088/1475-7516/2020/01/010. arXiv: 1910.10249 [hep-ph].

[Mor+22] Kanji Mori et al. *Shock revival in core-collapse supernovae assisted by heavy axionlike particles*. In: *Phys. Rev. D* 105.6 (2022), p. 063009. DOI: 10.1103/PhysRevD.105.063009. arXiv: 2112.03613 [astro-ph.HE].

[Mor+23] Kanji Mori et al. *Multimessenger signals of heavy axionlike particles in core-collapse supernovae: Two-dimensional simulations*. In: *Phys. Rev. D* 108.6 (2023), p. 063027. DOI: 10.1103/PhysRevD.108.063027. arXiv: 2304.11360 [astro-ph.HE].

[Nav+24] S. Navas et al. *Review of particle physics*. In: *Phys. Rev. D* 110.3 (2024), p. 030001. DOI: 10.1103/PhysRevD.110.030001.

[Raf] Georg G. Raffelt. *Astrophysical Axion Bounds*. In: *Axions*. Springer Berlin Heidelberg, pp. 51–71. ISBN: 9783540735182. DOI: 10.1007/978-3-540-73518-2_3. URL: http://dx.doi.org/10.1007/978-3-540-73518-2_3.

[Raf96] G. G. Raffelt. *Stars as laboratories for fundamental physics: The astrophysics of neutrinos, axions, and other weakly interacting particles*. May 1996. ISBN: 978-0-226-70272-8.

[RVC21] Karolina Rozwadowska, Francesco Vissani, and Enrico Cappellaro. *On the rate of core collapse supernovae in the milky way*. In: *New Astron.* 83 (2021), p. 101498. DOI: 10.1016/j.newast.2020.101498. arXiv: 2009.03438 [astro-ph.HE].

[TLS94] G. A. Tammann, W. Loeffler, and A. Schroder. *The Galactic supernova rate*. In: *Astrophys. J. Suppl.* 92 (1994), pp. 487–493. DOI: 10.1086/192002.

[Wes+24] T. Wester et al. *Atmospheric neutrino oscillation analysis with neutron tagging and an expanded fiducial volume in Super-Kamiokande I-V*. In: *Physical Review D* 109.7 (Apr. 2024). ISSN: 2470-0029. DOI: 10.1103/physrevd.109.072014. URL: http://dx.doi.org/10.1103/PhysRevD.109.072014.

[WJ05] Stan Woosley and Thomas Janka. *The physics of core-collapse supernovae*. In: *Nature Phys.* 1 (2005), p. 147. DOI: 10.1038/nphys172. arXiv: astro-ph/0601261.

Chapter 5

Search for QCD axion and Axion-like Particles at colliders

Contents

5.1 Constraints from non-observable hadron decays and $K^0 - \bar{K}^0$ mixing . 132

5.1.1 Phase space . . . 132

5.1.2 Unobserved baryon decays . . . 133

5.1.3 Unobserved meson decays . . . 134

5.1.4 $K^0 - \bar{K}^0$ mixing . . . 138

5.1.5 Results . . . 139

5.2 Probing QCD Axion or Axion-like Particles in three-body K decays . 141

5.2.1 Motivation . . . 141

5.2.2 Procedure . . . 141

5.2.3 Branching Ratio Calculations . . . 144

5.2.4 Results . . . 153

5.2.5 Conclusion . . . 158

In this chapter, we investigate collider-based strategies to constrain Axion-like Particles (ALPs) through their flavor-violating couplings to quarks, with a particular focus on the axion-down-strange interaction. These couplings can mediate rare hadronic processes that compete with weak interactions, providing a promising avenue for probing ALPs at low masses. Importantly, for sufficiently light ALPs, these constraints become directly applicable to the Quantum Chromodynamics (QCD) axion itself.

Section 5.1 begins with a review of existing bounds derived from the non-observation of rare baryon and meson decays, as well as constraints from $K^0 - \bar{K}^0$ mixing. These processes are sensitive to off-diagonal couplings in the ALP-quark current, in particular the $(k_{V,A})_{23}$ terms, which induce flavor-changing neutral currents Beyond the Standard Model (BSM). While diagonal terms can also be constrained in principle [Bau+21], they are suppressed relative to weak interactions by a factor $G_F F_0^2 \sim 10^{-7}$, rendering their impact negligible in the regime considered here.

In Section 5.2, we present an original study [Cav+25a] of rare three-body kaon decays involving a QCD axion or an ALP, such as $K \to \pi\pi a$ and $K \to \mu\mu a$. These processes offer complementary sensitivity to traditional two-body decays and are particularly well-suited to the detection capabilities of Large Hadron Collider beauty (LHCb). The analysis includes Branching Ratio (BR) calculations, background estimates, and signal reconstruction efficiencies. Our results suggest that dedicated searches could probe f_a scales between 10^7 and 10^9 GeV, with significant discovery potential.

Altogether, this chapter highlights the importance of collider experiments–particularly rare kaon decays and LHCb–in constraining flavor-violating interactions, and illustrates how rare hadron decays can serve as powerful probes of low-mass pseudoscalars BSM.

5.1 Constraints from non-observable hadron decays and $K^0 - \bar{K}^0$ mixing

This section provides an introduction to the existing constraints in the literature, originally obtained in the context of the QCD axion [Mar+20], and extends them to the case of an ALP.

We find that $|(k_V)_{23}| \lesssim 2 \times 10^{-3}$ and $|(k_A)_{23}| \lesssim 32$ for the QCD axion ($m_a \ll m_q$ and $f_a = 10^9$ GeV).

5.1.1 Phase space

We will discuss two-body and three-body decays.

5.1.1.1 $P_i \to P_f a$

$$\begin{aligned}\Gamma &= \int_{(\mathbb{R}^3)^2} \frac{1}{2m_i} \frac{d^3\vec{p}_f}{(2\pi)^3 2E_f} \frac{d^3\vec{p}_a}{(2\pi)^3 2E_a} \overline{|\mathcal{M}_{fi}|^2} (2\pi)^4 \delta^4(p_i - p_f - p_a) \\ &= \int_{m_a}^{+\infty} \frac{1}{2m_i} \frac{4\pi |p_a| E_a dE_a}{(2\pi)^3 2E_a} \overline{|\mathcal{M}_{fi}|^2} (2\pi) \delta(p_f^2 - m_f^2) \\ &= \frac{|p_a|}{8\pi m_i^2} \overline{|\mathcal{M}_{fi}|^2} \ ,\end{aligned} \tag{5.1.1}$$

with $|p_a| = \sqrt{E_a^2 - m_a^2}$ and $E_a = (m_i^2 + m_a^2 - m_f^2)/(2m_i)$.

5.1.1.2 $P_i \to P_1 P_2 a$

$$\begin{aligned}\Gamma &= \int_{(\mathbb{R}^3)^3} \frac{1}{2m_i} \frac{d^3\vec{p}_1}{(2\pi)^3 2E_1} \frac{d^3\vec{p}_2}{(2\pi)^3 2E_2} \frac{d^3\vec{p}_a}{(2\pi)^3 2E_a} \overline{|\mathcal{M}_{fi}|^2} (2\pi)^4 \delta^4(p_i - p_1 - p_2 - p_a) \\ &= \int_0^1 d\cos(\theta_{1a}) \int_{m_1}^{+\infty} dE_1 \int_{m_a}^{+\infty} dE_a \frac{|p_i||p_a|}{4m_i (2\pi)^3} \overline{|\mathcal{M}_{fi}|^2} \delta(p_2^2 - m_2^2) \\ &= \int_{m_1}^{+\infty} dE_1 \int_{m_a}^{+\infty} dE_a \frac{\overline{|\mathcal{M}_{fi}|^2}}{8m_i (2\pi)^3} \ ,\end{aligned} \tag{5.1.2}$$

where we have used

$$p_2^2 - m_2^2 = (p_i - p_1 - p_a)^2 - m_a^2 = m_i^2 + m_a^2 + m_1^2 - m_2^2 - 2m_i(E_1 + E_a) + 2E_1 E_a - 2|p_1||p_a| \cos(\theta_{1a}) \ , \tag{5.1.3}$$

which leads to

$$\cos(\theta_{a1}) = \frac{m_i^2 + m_a^2 + m_1^2 - m_2^2 - 2m_i(E_a + E_1) + 2E_a E_1}{2|p_a||p_1|} \ . \tag{5.1.4}$$

We define the kinematic variables s and t as

$$s = (p_i - p_a)^2 = (p_1 + p_2)^2 \in [(m_1 + m_2)^2, (m_i - m_a)^2] \ , \tag{5.1.5}$$

$$t = (p_i - p_1)^2 = (p_2 + p_a)^2 \in [(m_2 + m_a)^2, (m_i - m_1)^2] \ , \tag{5.1.6}$$

which gives

$$s = m_i^2 + m_a^2 - 2m_i E_a \ , \tag{5.1.7}$$

$$t = m_i^2 + m_1^2 - 2m_i E_1 \ . \tag{5.1.8}$$

Thus,

$$ds dt = 4m_i^2 dE_a dE_1 \tag{5.1.9}$$

allowing us to write

$$\frac{d^2\Gamma}{ds dt} = \frac{\overline{|\mathcal{M}_{fi}|^2}}{(4\pi)^3 4m_i^3} \tag{5.1.10}$$

To determine the total decay width, we then integrate over these two variables. We have

$$(s;t) \in \Omega \subset [(m_1+m_2)^2;(m_i-m_a)^2] \times [(m_2+m_a)^2;(m_i-m_1)^2] \,, \tag{5.1.11}$$

defined such that $\cos(\theta_{a1}) \in [-1;1]$, as given in Eq. (5.1.4). This implies that for a given s, $t \in [t_{\min}(s);t_{\max}(s)]$, where

$$t_{\min/\max}(s) = \frac{(m_K^2-m_X^2)^2}{4s} - \left(\sqrt{\frac{s}{4}-m_{h^+}^2} \pm \sqrt{\frac{(s+m_X^2-m_K^2)^2}{4s}-m_X^2}\right)^2 \,, \tag{5.1.12}$$

and thus

$$\Gamma = \int_\Omega dsdt \frac{d^2\Gamma}{dsdt} = \int_{s_{\min}}^{s_{\max}} ds \int_{t_{\min}(s)}^{t_{\max}(s)} dt \frac{d^2\Gamma}{dsdt} \,. \tag{5.1.13}$$

where $s_{\min} = (m_1+m_2)^2$ and $s_{\max} = (m_i-m_a)^2$.

5.1.2 Unobserved baryon decays

5.1.2.1 Procedure

The PDG [Nav+24] provides a list of BRs for various decay modes.

However, since the sum of all BRs must equal 1, any deviation from this (considering uncertainties) suggests either the presence of significant standard decay modes that have not yet been measured or the existence of new physics introducing additional decay channels.

If the sum of the measured BRs is $1 \pm \delta BR$, then the contribution from new physics cannot exceed δBR, providing an upper bound on BSM decay modes.

By applying this method, we obtain Table 5.1.

Table 5.1: Upper bounds on the BRs for baryons based on data from [Nav+24].

Baryon	Upper bounds
Λ	8.5×10^{-3}
Σ^+	4.9×10^{-3}
Ξ^0	2.3×10^{-4}
Ξ^-	6.4×10^{-4}

5.1.2.2 Amplitude

We consider the decay mode $B_i \to B_f a$, with the corresponding Feynman diagrams shown in Fig. 5.1.

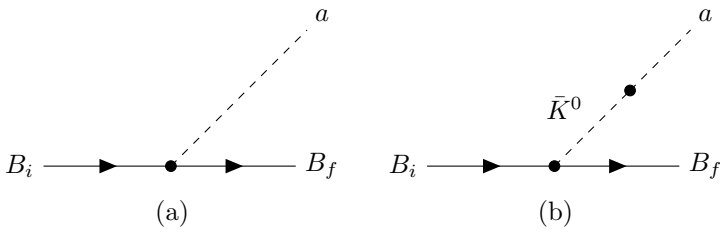

Figure 5.1: Baryon decays with ALP emission.

In general, the amplitude can be written as

$$\mathcal{M}_{fi}^{(a)} = \bar{u}_f \not{p}_a \left(C_V^{(a)} + C_A^{(a)}\gamma_5\right) u_i \quad , \quad \mathcal{M}_{fi}^{(b)} = \bar{u}_f \not{p}_a \left(C_A^{(b)}\gamma_5\right) u_i \,. \tag{5.1.14}$$

Defining $C_V = C_V^{(a)}$ and $C_A = C_A^{(a)} + C_A^{(b)}$, we obtain

$$\begin{aligned} \overline{|\mathcal{M}_{fi}|^2} &= \frac{1}{2}\mathrm{Tr}[(\not{p}_f + m_f)\not{p}_a(C_V + C_A\gamma_5)(\not{p}_i + m_i)\not{p}_a(C_V + C_A\gamma_5)] \\ &= 2\left(|C_V|^2 + |C_A|^2\right)\left(2(p_a\cdot p_i)(p_a\cdot p_f) - m_a^2(p_i\cdot p_f)\right) + 2\left(|C_V|^2 - |C_A|^2\right) m_i m_f m_a^2 \,. \end{aligned} \tag{5.1.15}$$

The coupling constants are defined as

$$\begin{aligned} C_V^{(a)} &= \tilde{C}_V^{(a)} \times \frac{(k_V)_{23}}{f_a} \ , \\ C_A^{(a)} &= \tilde{C}_A^{(a)} \times \frac{(k_A)_{23}}{f_a} \ , \\ C_A^{(b)} &= \tilde{C}_A^{(b)} \times \frac{\sqrt{2}}{4} \frac{m_a^2}{m_a^2 - m_{K^0}^2} \frac{(k_A)_{23}}{f_a} \ . \end{aligned} \tag{5.1.16}$$

Using Chiral Perturbation Theory augmented with an axion (ChPT+a), we compute the parameters listed in Table 5.2.

For the decay of Ξ^0, there are two possible processes, and the sum of their contributions must remain below the experimental bound.

Table 5.2: Couplings for different baryon decays $B_i \to B_f a$.

Process	$\tilde{C}_V^{(a)}$	$\tilde{C}_A^{(a)}$	$\tilde{C}_A^{(b)}$
$\Lambda \to na$	1	$-\sqrt{6}(D/3+F)/4$	$\sqrt{3}(D/3+F)$
$\Sigma^+ \to pa$	$\sqrt{6}/2$	$(D-F)/2$	$-\sqrt{2}(D-F)$
$\Xi^0 \to \Lambda a$	-1	$-\sqrt{6}(D/3-F)/4$	$\sqrt{3}(D/3-F)$
$\Xi^0 \to \Sigma^0 a$	$\sqrt{2}/2$	$-\sqrt{2}(D+F)/4$	$(D+F)$
$\Xi^- \to \Sigma^- a$	$-\sqrt{6}/2$	$(D+F)/2$	$-\sqrt{2}(D+F)$

5.1.2.3 Results

Constraints on $(k_{V,A})_{23}$ from baryonic decays are presented in Fig. 5.2.

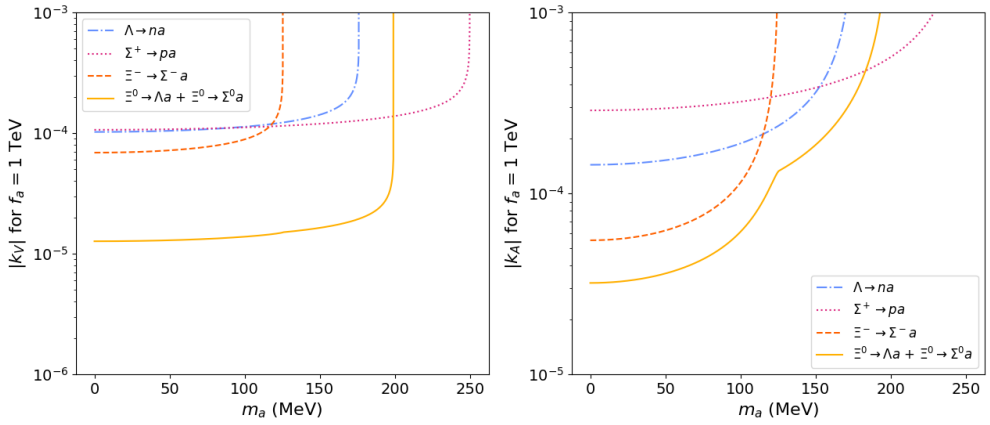

Figure 5.2: Constraints on $|(k_V)_{23}|$ (left panel) and $|(k_A)_{23}|$ (right panel) as a function of the ALP mass, assuming $f_a = 1$ TeV, obtained from $B_i \to B_f a$ decays. The different curves correspond to the processes $\Lambda \to na$ (blue, dash-dotted), $\Sigma^+ \to pa$ (pink, dotted), $\Xi^- \to \Sigma^- a$ (orange, dashed), and $\Xi^0 \to \Lambda a$ (yellow, solid).

Our compuations are in perfect agreement with those of [Mar+20] for $m_a \ll m_q$ and extend the analysis to the case of a massive ALP.

The strongest constraint is provided by the decays of Ξ^0.

5.1.3 Unobserved meson decays

5.1.3.1 Procedure

We could follow the same procedure as for baryons; however, in the case of mesons, dedicated searches exist that allow for significantly stronger constraints.

We will study the processes $K \to \pi a$ (see Fig. 5.3) and $K \to \pi\pi a$ (see Fig. 5.4). The key idea is to compare with existing studies where, instead of an ALP, a neutrino-antineutrino pair $\nu\bar{\nu}$ is present. The reason is that the experimental signature is identical: both the ALP and neutrinos are invisible. However, a crucial difference exists—while the missing 4-momentum squared is fixed for the ALP as $p^2_{\text{inv}} = m^2_a$, for the neutrino pair, it is given by $p^2_{\text{inv}} = (p_\nu + p_{\bar{\nu}})^2$, which is not fixed. In such studies, p^2_{inv} varies within a certain range dictated by kinematics and experimental resolution. Data corresponding to a specific p^2_{inv} value can therefore set constraints on an ALP with $m^2_a = p^2_{\text{inv}}$, where the ALP would appear as an experimental background at that particular value. An important observation is that this method, which relies on analyzing p^2_{inv}, is insensitive to the spin of the invisible particle.

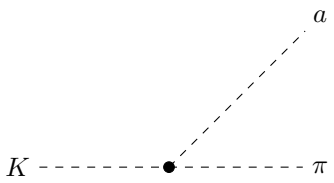

Figure 5.3: $K \to \pi a$ decays with an ALP.

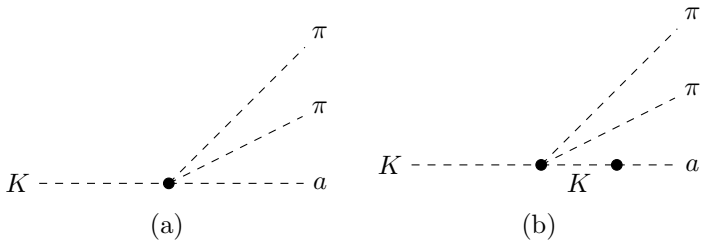

Figure 5.4: $K \to \pi\pi a$ decays with an ALP.

5.1.3.2 $K^+ \to \pi^+ a$

The experimental constraint from [Adl+08] is given by:

$$BR(K^+ \to \pi^+ a) < 7.3 \times 10^{-11} \ . \tag{5.1.17}$$

The amplitude is given by:

$$i\mathcal{M}_{fi}(K^+ \to \pi^+ a) = \frac{(k_V)^*_{23}}{2f_a}(2m_{K^+}E_a - m^2_a) = \frac{(k_V)^*_{23}}{2f_a}(m^2_{K^\pm} - m^2_{\pi^\pm}) \ . \tag{5.1.18}$$

5.1.3.3 $K_L \to \pi^0 a$

The data constraining the BR $BR(K_L \to \pi^0 a)$ from [Ahn+19] is presented in Fig. 5.5.

The amplitude for $K^0 \to \pi^0 a$ is given by:

$$\mathcal{M}_{fi}(K^0 \to \pi^0 a) = i\frac{\sqrt{2}}{4}\frac{(k_V)^*_{23}}{f_a} p_a \cdot (p_{K^0} + p_{\pi^0}) \ . \tag{5.1.19}$$

For the physical eigenstate K_L[1], the amplitude becomes:

$$\mathcal{M}_{fi}(K_L \to \pi^0 a) = \frac{1}{2}\frac{\text{Im}[(k_V)_{23}]}{f_a} p_a \cdot (p_{K_L} + p_{\pi^0}) \ . \tag{5.1.20}$$

5.1.3.4 $K_L \to \pi^0\pi^0 a$

The data constraining the BR $BR(K_L \to \pi^0\pi^0 a)$ from [Oga+11] is provided in Table 5.3.

[1]For a detailed understanding of the transition from the interaction eigenstates K^0 and $\bar{K}^0$ to the mass eigenstates K_S and K_L, see Appendix C.3.5.

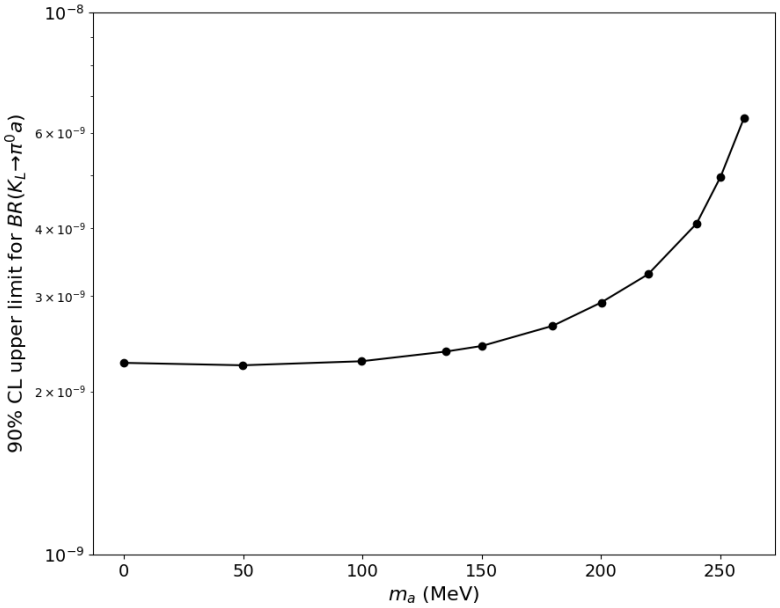

Figure 5.5: The 90% CL upper limits for the $K_L \to \pi^0 a$ BR [Ahn+19].

Table 5.3: Summary of the 90% C.L. upper limit on the BR as a function of the mass of an invisible particle X in the $K_L \to \pi^0\pi^0 X$ decay [Oga+11].

m_a (MeV)	50	75	100	125	150	175	200
BR upper limit (10^{-7})	7.0	7.0	7.1	8.5	12	27	400

The local diagram gives the amplitude:

$$\mathcal{M}_{fi}^{(a)}(K^0 \to \pi^0\pi^0 a) = \frac{\sqrt{2}(k_A)_{23}^*}{12F_0 f_a}\left(2m_a^2 + 3p_a \cdot (p_{\pi^0,1} + p_{\pi^0,2})\right). \tag{5.1.21}$$

The second diagram contributes:

$$\mathcal{M}_{fi}^{(b)}(K^0 \to \pi^0\pi^0 a) = \frac{\sqrt{2}(k_A)_{23}^*}{12F_0 f_a}\frac{m_a^2}{m_a^2 - m_{K^0}^2}\left(m_{\pi^0}^2 - m_a^2 - p_a \cdot (p_{\pi^0,1} + p_{\pi^0,2}) + 2(p_{\pi^0,1} \cdot p_{\pi^0,2})\right). \tag{5.1.22}$$

Thus, the total amplitude is:

$$\begin{aligned}\mathcal{M}_{fi}(K^0 \to \pi^0\pi^0 a) = \frac{\sqrt{2}(k_A)_{23}^*}{12F_0 f_a(m_{K^0}^2 - m_a^2)}[&p_a \cdot (p_{\pi^0,1} + p_{\pi^0,2})(3m_{K^0}^2 - 2m_a^2) \\ &+ m_a^2(2m_{K^0}^2 - m_a^2 - m_{\pi^0}^2 - 2(p_{\pi^0,1} \cdot p_{\pi^0,2}))].\end{aligned} \tag{5.1.23}$$

For the K_L eigenstate, the amplitude simplifies to:

$$\begin{aligned}\mathcal{M}_{fi}(K_L \to \pi^0\pi^0 a) = \frac{\mathrm{Re}[(k_A)_{23}]}{6F_0 f_a(m_{K^0}^2 - m_a^2)}[&p_a \cdot (p_{\pi^0,1} + p_{\pi^0,2})(3m_{K^0}^2 - 2m_a^2) \\ &+ m_a^2(2m_{K^0}^2 - m_a^2 - m_{\pi^0}^2 - 2(p_{\pi^0,1} \cdot p_{\pi^0,2}))].\end{aligned} \tag{5.1.24}$$

Further simplification leads to:

$$\mathcal{M}_{fi}(K_L \to \pi^0\pi^0 a) = \frac{\mathrm{Re}[(k_A)_{23}]}{12F_0 f_a(m_{K^0}^2 - m_a^2)}\left[3m_{K^0}^2(m_{K^0}^2 - s) - m_a^2(m_{K^0}^2 - 2m_{\pi^0}^2)\right]. \tag{5.1.25}$$

The amplitude is real and symmetric under the exchange $p_{\pi^0,1} \leftrightarrow p_{\pi^0,2}$, as expected from CP symmetry and pion indistinguishability.

To see this explicitly:

In general, we can write $\mathcal{M}_{fi} = f_r(p_{\pi^0,1}, p_{\pi^0,2}, p_a) + if_i(p_{\pi^0,1}, p_{\pi^0,2}, p_a)$, where f_r and f_i are real-valued functions. Due to pion indistinguishability, both f_r and f_i must be symmetric under $p_{\pi^0,1} \leftrightarrow p_{\pi^0,2}$. Applying the CP transformation to the process:

$$CP\,|K_L\rangle = -\,|K_L\rangle\,, \quad CP\,\big|\pi^0,\pi^0,a\big\rangle = -\,\big|\pi^0,\pi^0,a\big\rangle$$

implies $CP(\mathcal{M}_{fi}) = \mathcal{M}_{fi}$. However, CP also transforms $\mathcal{M}_{fi}$ as $f_r - if_i$, meaning f_i must vanish, leaving $\mathcal{M}_{fi}$ purely real.

5.1.3.5 $K^+ \to \pi^+\pi^0 a$

The data constraining the BR $BR(K^+ \to \pi^+\pi^0 a)$ from [Sad+24] is provided in Fig. 5.6.

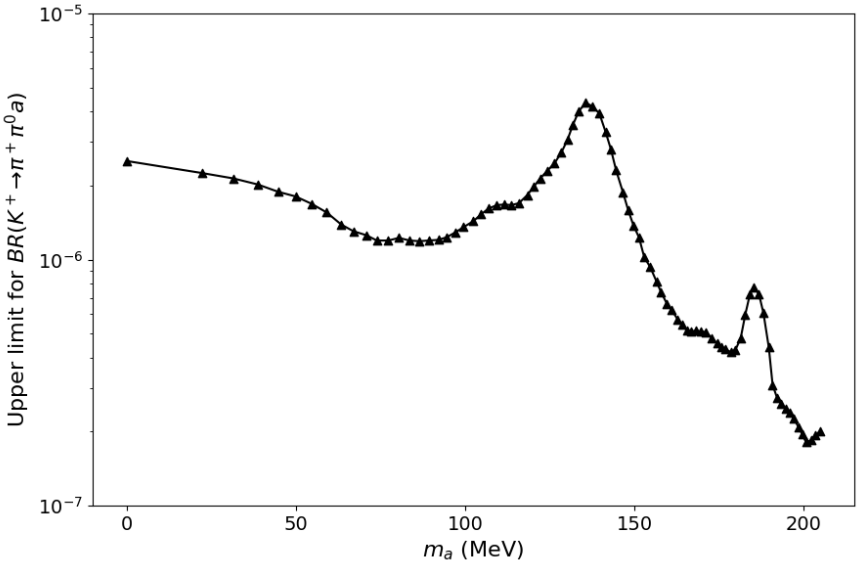

Figure 5.6: The 90% CL upper limits for the $K^+ \to \pi^+\pi^0 a$ BR [Sad+24].

The local diagram contributes:

$$\mathcal{M}_{fi}^{(a)}(K^+ \to \pi^+\pi^0 a) = \frac{(k_A)^*_{23}}{2F_0 f_a}\, p_a \cdot (p_{\pi^0} - p_{\pi^+})\ . \tag{5.1.26}$$

The second diagram gives:

$$\mathcal{M}_{fi}^{(b)}(K^+ \to \pi^+\pi^0 a) = \frac{(k_A)^*_{23}}{4F_0 f_a} \frac{m_a^2}{m_a^2 - m_{K^0}^2} \left(p_{K^+} \cdot p_{\pi^+} - p_{K^+} \cdot p_{\pi^0} + p_a \cdot p_{\pi^+} - p_a \cdot p_{\pi^0}\right)\ . \tag{5.1.27}$$

Thus, the total amplitude is:

$$\mathcal{M}_{fi}(K^+ \to \pi^+\pi^0 a) = \frac{(k_A)^*_{23}}{2F_0 f_a} \frac{m_K^2}{m_K^2 - m_a^2} p_{K^+} \cdot (p_{\pi^0} - p_{\pi^+})\ . \tag{5.1.28}$$

5.1.3.6 Results

The constraints on $(k_{V,A})_{23}$ from meson decays are presented in Fig. 5.7.

Our computations are in perfect agreement with [Mar+20] in the limit $m_a \ll m_q$ and extend the analysis to a massive axion.

The constraints from K_L decays are sensitive only to the real part of $(k_A)_{23}$ and the imaginary part of $(k_V)_{23}$, whereas those from K^+ decays constrain their absolute values.

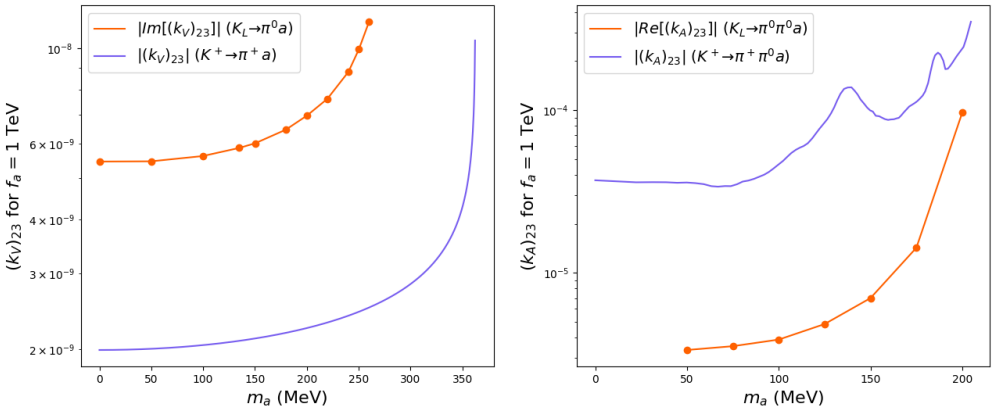

Figure 5.7: Constraints on $|(k_V)_{23}|$ (left panel, for $K \to \pi a$) and $|(k_A)_{23}|$ (right panel, for $K \to \pi\pi a$) as a function of the ALP mass, assuming $f_a = 1$ TeV, derived from meson decays. The different curves correspond to decays of K^+ (blue) and K_L (orange).

5.1.4 $K^0 - \bar{K}^0$ mixing

The contributions to $K^0 - \bar{K}^0$ mixing are illustrated in Fig. 5.8.

By definition,

$$M_{12} = \frac{\mathcal{M}_{fi}}{4m_{K^0}} \,, \tag{5.1.29}$$

to derive constraints on axionic couplings from non-standard CP-violating contributions to $K^0 - \bar{K}^0$ mixing, we define the ratio

$$C_{\epsilon_K} = \frac{|\epsilon_K^{SM+a}|}{|\epsilon_K^{SM}|} \,, \tag{5.1.30}$$

where

$$\epsilon_K = e^{i\phi_c} \sin(\phi_c) \left(\frac{\mathrm{Im}(M_{12})}{\Delta m_K} \right) \,. \tag{5.1.31}$$

We take experimental values from [Nav+24] for $\Delta m_K = m_L - m_S$, $\Delta\Gamma_K = \Gamma_S - \Gamma_L$, and $\phi_c = \arctan(2\Delta m_K/\Delta\Gamma_K)$, along with the Standard Model (SM) prediction for $|\epsilon_K^{SM}|$ from [BGS20].

Defining the deviation from unity,

$$\delta C_{\epsilon_K} = C_{\epsilon_K} - 1, \tag{5.1.32}$$

the UTFit collaboration provides a global CKM fit, yielding $0.87 < C_{\epsilon_K} < 1.39$ at 95% CL [Bon+23], implying $|\delta C_{\epsilon_K}| < 0.39$.

At tree level, the axionic contribution to $K^0 - \bar{K}^0$ mixing is given by

$$\mathcal{M}_{fi}^{(a)} = ((k_A)_{23})^2 \frac{F_0^2}{f_a^2} \frac{m_{K^0}^4}{m_{K^0}^2 - m_a^2} \Rightarrow M_{12}^{(a)} = ((k_A)_{23})^2 \frac{F_0^2}{4f_a^2} \frac{m_{K^0}^3}{m_{K^0}^2 - m_a^2} \,. \tag{5.1.33}$$

Thus,

$$\delta C_{\epsilon_K} = \frac{1}{4} \frac{|\sin(\phi_c)|}{|\epsilon_K^{SM}|} \frac{m_{K^0}}{\Delta m_K} \frac{m_{K^0}^2}{m_{K^0}^2 - m_a^2} \frac{F_0^2}{f_a^2} \left| \mathrm{Im}[((k_A)_{23})^2] \right| \,. \tag{5.1.34}$$

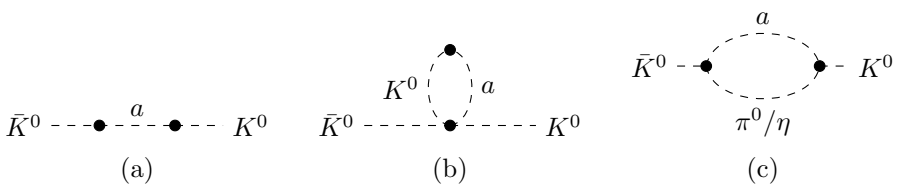

Figure 5.8: Axionic contributions to $K^0 - \bar{K}^0$ mixing up to one loop.

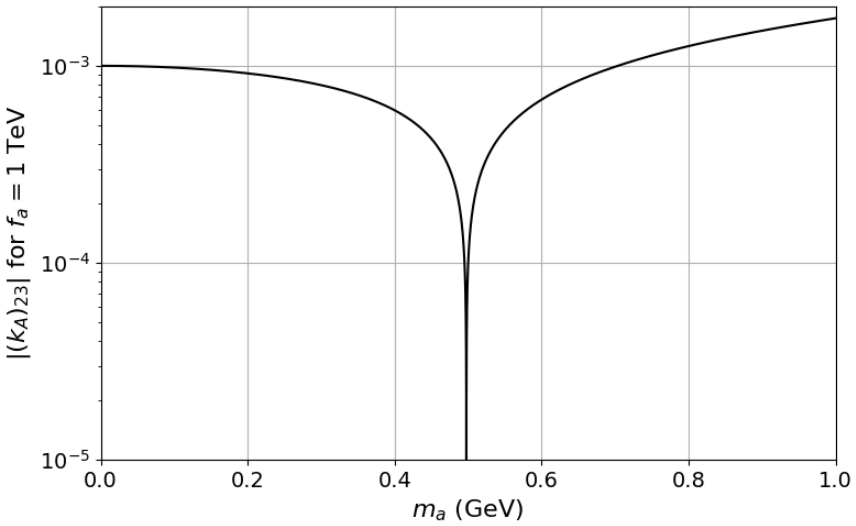

Figure 5.9: Bounds on $(k_A)_{23}$ for ALPs as a function of the axion mass from $K^0 - \bar{K}^0$ mixing.

This leads to the bound

$$\left|\mathrm{Im}[((k_A)_{23})^2]\right| \lesssim \frac{|m_{K^0}^2 - m_a^2|}{m_{K^0}^2} \times 10^4 \times \left(\frac{f_a}{10^9\,\mathrm{GeV}}\right)^2 . \tag{5.1.35}$$

Another way to place constraints is by considering the axionic contribution to $\Delta m_K = 2\,\mathrm{Re}[M_{12}]$, which leads to the following expression:

$$\frac{\Delta m_K}{m_{K^0}} = \mathrm{Re}[((k_A)_{23})^2]\frac{F_0^2}{2f_a^2}\frac{m_{K^0}^2}{m_{K^0}^2 - m_a^2} . \tag{5.1.36}$$

Using the experimentally measured value $\Delta m_K = 3.484(6) \times 10^{-12}\,\mathrm{MeV}$, we obtain the bound:

$$|\,\mathrm{Re}[((k_A)_{23})^2]| \lesssim \frac{\Delta m_K}{m_{K^0}}\frac{|m_{K^0}^2 - m_a^2|}{m_{K^0}^2}\frac{2f_a^2}{F_0^2} = \frac{|m_{K^0}^2 - m_a^2|}{m_{K^0}^2} \times 10^6 \times \left(\frac{f_a}{10^9\,\mathrm{GeV}}\right)^2 . \tag{5.1.37}$$

From the two previous results in Eqs. (5.1.35)-(5.1.37), we can deduce a bound on $|(k_A)_{23}|$ by considering both the real and imaginary parts:

$$|\,\mathrm{Re}[((k_A)_{23})^2]| < \alpha_r \quad \text{and} \quad |\,\mathrm{Im}[((k_A)_{23})^2]| < \alpha_i \quad \Rightarrow \quad |(k_A)_{23}| < (\alpha_r^2 + \alpha_i^2)^{1/4} , \tag{5.1.38}$$

this gives the constraint:

$$|(k_A)_{23}| \lesssim 10^3 \frac{f_a}{10^9\,\mathrm{GeV}}\frac{\sqrt{|m_{K^0}^2 - m_a^2|}}{m_{K^0}} = 10^{-3}\frac{f_a}{1\,\mathrm{TeV}}\frac{\sqrt{|m_{K^0}^2 - m_a^2|}}{m_{K^0}} . \tag{5.1.39}$$

For the QCD axion ($m_a \ll m_q$ and $f_a = 10^9\,\mathrm{GeV}$), we find that $|(k_A)_{23}| \lesssim 10^3$. For the ALP case, the bounds are shown in Fig. 5.9. The forbidden value at $m_a = m_{K^0}$ arises from the fact that, in this case, the propagator diverges.

For a more detailed one-loop analysis, refer to [Mar+20]. In their study, they assume maximization of either the real or imaginary part of the contribution. Here, in order to be as conservative as possible, this assumption has not been made.

5.1.5 Results

It is possible to combine all these results to obtain Fig. 5.10.

For $(k_V)_{23}$, the bound is exclusively related to the decay $K^+ \to \pi^+ a$. In contrast, for $(k_A)_{23}$, for masses below 200 MeV, the dominant contributions come from the decays, while for larger masses, the

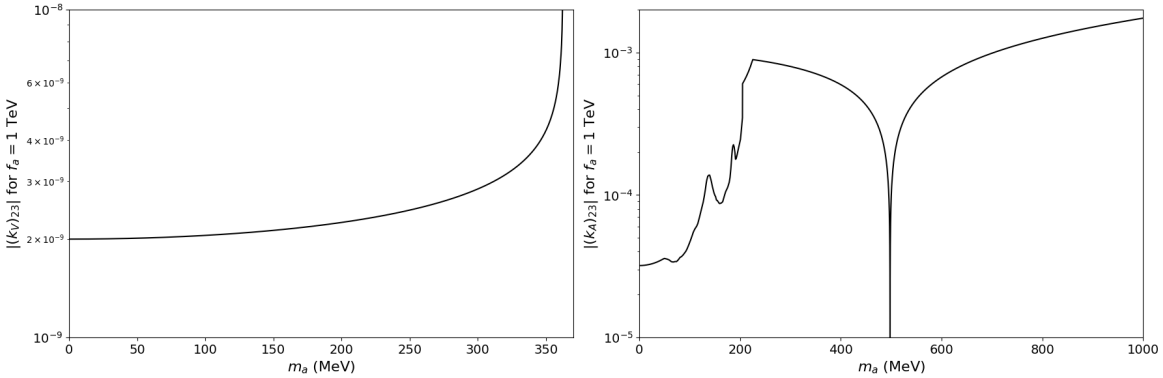

Figure 5.10: Bounds on $|(k_{A/V})_{23}|$ for ALPs as a function of the axion mass, derived from the non-observation of hadron decays and $K^0 - \bar{K}^0$ mixing.

dominant contribution comes from $K^0 - \bar{K}^0$ mixing. In this case, the axion acts as an intermediate state, and kinematically, even large masses are possible.

For low axion masses, the two dominant processes are $K^+ \to \pi^+\pi^0 a$ and decays of the Ξ^0, which are of the same order-of-magnitude (oom). This is particularly notable because the decay $K^+ \to \pi^+\pi^0 a$ has a dedicated study (via $K^+ \to \pi^+\pi^0\nu\bar{\nu}$), whereas for Ξ^0 decays, no such dedicated study exists, as we have only used BR measurements from the SM. Therefore, a specific study on Ξ^0 decays could yield interesting results.

That said, it is important to note that due to Chiral Perturbation Theory (ChPT), mesonic calculations are much more precise than baryonic ones, meaning the results from $K^+ \to \pi^+\pi^0 a$ are more robust than those from Ξ^0 decays.

For a QCD axion ($m_a \ll m_q$ and $f_a = 10^9$ GeV), we obtain the following bounds:

$$|(k_V)_{23}| \lesssim 2 \times 10^{-3} \ , \quad |(k_A)_{23}| \lesssim 32 \ . \tag{5.1.40}$$

5.2 Probing QCD Axion or Axion-like Particles in three-body K decays

In this section, I present the results obtained in [Cav+25a].

5.2.1 Motivation

If we neglect the weak interaction, then in a kaon decay into an axion, the parity of the final pion number determines the dependence on the parameters. If this number is even, the process is sensitive to $(k_A)_{23}$, whereas if it is odd, it is sensitive to $(k_V)_{23}$.[2] This implies that decays of the type $K \to \pi a$ are sensitive to $(k_V)_{23}$, while three-body decays such as $K \to \pi\pi a$ or $K \to \ell\ell a$ are sensitive to $(k_A)_{23}$.

As discussed in the previous section, $(k_V)_{23}$ is already well constrained by the $K^+ \to \pi^+ a$ decay. The advantage of focusing on three-body decays is that they allow us to study $(k_A)_{23}$, which remains less constrained.

Moreover, while previous studies have examined the decays of K^+ and K_L, there has been no dedicated study of K_S decays. The lifetimes of these kaons are:

$$\tau_{K^+} = 1.2379(21) \times 10^{-8} \text{ s}, \quad \tau_{K_L} = 5.116(20) \times 10^{-8} \text{ s}, \quad \tau_{K_S} = 8.954(4) \times 10^{-11} \text{ s} \tag{5.2.1}$$

These significant differences in lifetimes play a crucial role in determining where the kaon decays. For neutral kaons, we focus on the K_S, as it must decay frequently enough within the detector volume to be observable. We investigate processes of the form $K_S \to h^+h^-a$ because, from an experimental perspective, the pair h^+h^- provides a clean trigger. This approach takes advantage of specific strengths at facilities such as LHCb, including high-precision tracking capabilities. Additionally, LHCb benefits from the large number of kaons it produces and detects within a short enough lifetime to allow their decays to be observed. In 2024, LHCb collected an integrated luminosity of 9.56 fb^{-1}, which should enable sensitivities at the 10^{-9} level for the BRs of decays such as $K_S \to \mu^+\mu^- X$.

5.2.2 Procedure

The most immediate test of the constraining power of our considered decays, $K \to h_1 h_2 a$, is the total BRs, $BR(K \to h_1 h_2 a)$. In this section, I will explain the procedure to estimate the sensitivities on the fundamental coupling $(k_A)_{23}$ to understand the potential bounds.

In a dedicated search, the signal of our decays of interest is the total yield (background-subtracted) of h_1h_2 pairs with a total 4-momentum p_{vis} (assumed to be fully reconstructed experimentally), plus the missing 4-momentum p_{inv}, such that the total 4-momentum $p_{\text{vis}} + p_{\text{inv}}$ is consistent with $m_K^2 = (p_{\text{vis}} + p_{\text{inv}})^2$ within an appropriate uncertainty. By definition, this total yield is insensitive to the angular anisotropies of the particle(s) responsible for p_{inv}, and is thus insensitive to the total spin carried by these particles. On the other hand, we can assume that the measurement will generally be sensitive to the invariant mass of the escaping particle(s) via $\sqrt{p_{\text{inv}}^2}$. Thus, in the case of a single escaping particle, this search can generally distinguish between $m_a \ll m_\pi$ and $m_a \simeq m_\pi$.

Given the described signal, we can identify irreducible backgrounds as a function of the ALP mass. For example, for $K_S \to \pi^+\pi^- a$:

- For very low masses, the background is $K_S \to \pi^+\pi^-\gamma$ with an undetected γ. One must also account for processes involving misidentifications of muons as pions, such as $K_S \to \mu^+\mu^-\gamma$ and $K_S \to \pi\mu\nu$ with a misidentification factor $\epsilon_{\mu\pi}$ per misidentified muon. Finally, we must also consider K_L, which may decay inside the detector volume and create background to processes originating from K_S. Such processes contribute a factor A_{K_L}.

- For large masses, $m_a \simeq m_\pi$, the background would come from $K_S \to \pi^+\pi^-\pi^0$. Similarly, we need to account for processes involving muon-to-pion misidentifications and K_L decays.

The factors $\epsilon_{\pi\mu}$, $\epsilon_{\mu\pi}$, and A_{K_L} are suppression factors that may be compensated by a large BR.

The misidentification $\pi \leftrightarrow \mu$ is a critical issue in high-energy physics experiments, arising from the similarities in their detector signatures under certain conditions (same charge and $m_\mu \simeq m_{\pi^\pm}$). In calorimeters, both hadronic and electromagnetic, a pion can deposit energy in a manner closely resembling that of a muon, particularly when its energy deposits create clusters that are difficult

[2] The computation of the couplings between the axion and n mesons is provided in Appendix C.6.

to distinguish from those left by muons. This similarity is exacerbated in scenarios where high-energy pions exhibit minimal energy loss and penetration characteristics akin to those of muons. Because muons are Minimal Ionizing Particles (MIPs), they generally exhibit lower energy loss per unit length compared to other particles. As a result, high-energy pions, which can punch through the detector material similarly to muons, may be misidentified if their energy deposits and trajectories align closely with those expected from muons. Additionally, the limited spatial and energy resolution of the detectors can further contribute to this misidentification, as the distinguishing features between muons and pions may fall within the resolution limits of the detector systems. Accurate particle identification thus relies on robust detection algorithms and precise calibration to minimize such misidentification probabilities and ensure reliable particle tracking and measurement.

The expected yield from the discussed backgrounds has two main sources of uncertainty: the absolute uncertainty on the experimental BR, denoted $\sigma_{\rm bkg}$, and the uncertainty on the normalization channel yield. In our study, the former is taken from the PDG [Nav+24], while the latter is assumed to have a systematic component at the 5% level of the central value of the background BR, denoted $BR_{\rm bkg}$.[3]

As the signal and irreducible background yields are normalized to the same channel, the quantity

$$S_{eff} := \sqrt{(0.05 \times BR_{\rm bkg})^2 + \sigma_{\rm bkg}^2}\ , \tag{5.2.2}$$

appears to realistically quantify the best possible sensitivity in a dedicated search. To include all channels, we sum quadratically:

$$S_{eff}^{tot} = \sqrt{\sum_i S_{eff,i}^2}\ . \tag{5.2.3}$$

In simple terms, the sensitivity to the signal BR can be estimated from the uncertainty on the main irreducible background noise in the search. In other words, the signal can at most be as large as the extent to which its dominant sources of irreducible background noise are controlled. We emphasize that S_{eff} is a sensitivity, not a physical BR limit, which can only be determined by a dedicated search. However, S_{eff} quantifies the efficiency (in terms of the BR limit) of such a search, based on the quality of control over the dominant irreducible backgrounds.

With this important qualification in mind, we then use S_{eff} to place limits on the theoretically calculated BR, denoted BR_{th}. These bounds will be obtained from relations of the form $BR_{th}((k_A)_{23}) \lesssim S_{eff}$ and will show that dedicated searches in each of our considered channels would provide new and very effective probes of the considered couplings. We will show that this is true even for f_a as large as 10^9 GeV and $m_a \ll m_\pi$, namely for ALPs approaching the parameter space of the QCD axion.

To apply this procedure, we begin by collecting the BR measurements relevant to the S_{eff} that we calculate for the $K \to \{\mu\mu; \pi\pi\}a$ channels of interest, assuming that m_a is either negligible or comparable to the pion mass. From [Nav+24], one finds:

$$\begin{aligned}
BR(K_S \to \pi^+\pi^-\gamma) &= (1.79 \pm 0.05) \times 10^{-3}\ , & BR(K_S \to \pi^+\pi^-\pi^0) &= (3.5^{+1.1}_{-0.9}) \times 10^{-7}\ ,\\
BR(K_L \to \pi^+\pi^-\gamma) &= (4.15 \pm 0.15) \times 10^{-5}\ , & BR(K_L \to \pi^+\pi^-\pi^0) &= (12.54 \pm 0.05) \times 10^{-2}\ ,\\
BR(K_S \to \pi\mu\nu) &= (4.56 \pm 0.20) \times 10^{-4}\ , & BR(K_S \to \mu^+\mu^-\pi^0) &= (2.9^{+1.5}_{-1.2}) \times 10^{-9}\ ,\\
BR(K_L \to \pi\mu\nu) &= (27.04 \pm 0.07) \times 10^{-2}\ , & BR(K^+ \to \pi^+\pi^0\pi^0) &= (1.760 \pm 0.023) \times 10^{-2}\ ,\\
BR(K^+ \to \pi^+\pi^0\gamma) &= (6.0 \pm 0.4) \times 10^{-6}\ , & BR(K^+ \to \mu^+\pi^0\nu) &= (3.352 \pm 0.034) \times 10^{-2}\ ,
\end{aligned} \tag{5.2.4}$$

whereas $BR(K_S \to \mu^+\mu^-\gamma)$ is unmeasured.

[3] The value of 5% is an informed assumption, although arbitrary. This protects our S_{eff} definition (see Eq. (5.2.2)) from cases where $\sigma_{\rm bkg}$ is very small, such that without the term $0.05 \times BR_{\rm bkg}$, it would lead to an overly optimistic sensitivity estimate.

Using Eq. (5.2.2) on (5.2.4), we can then establish the following approximate relations:

$$\begin{aligned}
BR_{th}(K_S \to \pi^+\pi^- a)_{m_a \ll m_\pi} &\lesssim S_{eff}(K_S \to \pi^+\pi^-\gamma) &&\simeq 1.0\times10^{-4}\,,\\
BR_{th}(K_S \to \pi^+\pi^- a)_{m_a = m_\pi} &\lesssim S_{eff}(K_L \to \pi^+\pi^-\pi^0, A_{K_L}) &&\simeq 1.3\times10^{-5}\,,\\
BR_{th}(K^+ \to \pi^+\pi^0 a)_{m_a \ll m_\pi} &\lesssim S_{eff}(K^+ \to \pi^+\pi^0\gamma) &&\simeq 5.0\times10^{-7}\,,\\
BR_{th}(K^+ \to \pi^+\pi^0 a)_{m_a = m_\pi} &\lesssim S_{eff}(K^+ \to \pi^+\pi^0\pi^0) &&\simeq 9.1\times10^{-4}\,,\\
BR_{th}(K_S \to \mu^+\mu^- a)_{m_a \ll m_\pi} &\lesssim S_{eff}(K_{S,L} \to \pi\mu\nu, K_S \to \pi\pi\gamma, \epsilon_{\pi\mu}, A_{K_L}) &&\simeq 4.1\times10^{-7},\\
BR_{th}(K_S \to \mu^+\mu^- a)_{m_a = m_\pi} &\lesssim S_{eff}(K_S \to \mu^+\mu^-\pi^0, K_L \to \pi^+\pi^-\pi^0, \epsilon_{\pi\mu}, A_{K_L}) &&\simeq 2.0\times10^{-9}\,.
\end{aligned} \tag{5.2.5}$$

A few comments on the above relations follow:

Regarding the $K_S \to \pi^+\pi^- a$ channel with small m_a (the first in (5.2.5)), the first background comes from $K_S \to \pi^+\pi^-\gamma$ with a hard but undetected photon. Using (5.2.4) and (5.2.2), one finds $S_{eff} \simeq 1\times10^{-4}$. Another background is represented by $K_S \to \pi\mu\nu$ (charge-conjugated modes included in the final state), with one muon misidentified as a pion. Quantifying the μ-to-π misidentification probability at LHCb as $\epsilon_{\mu\pi} = 10^{-2}$ [Aai+15], this channel yields an S_{eff} of order $10^{-5}\times\epsilon_{\mu\pi}$, thus subdominant with respect to $K_S \to \pi^+\pi^-\gamma$. Two additional irreducible backgrounds are the K_L counterparts of the above decays. These yields are suppressed by the small K_L acceptance in LHCb, which is due to the long lifetime of K_L relative to that of K_S. We denote this acceptance factor as A_{K_L}. One finds $A_{K_L} \simeq 2\times10^{-3}$ [Alv+19]. On the other hand, the $K_L \to \pi\mu\nu$ channel has a very large BR, as shown in (5.2.4). Including all factors, one obtains $S_{eff} \simeq 1.4\times10^{-2}\times\epsilon_{\mu\pi}\times A_{K_L}$, which is numerically negligible. A similar conclusion holds for the $K_L \to \pi^+\pi^-\gamma$ channel, which itself has a very small BR. These considerations justify our final value of $S_{eff} \simeq 1.0\times10^{-4}$ in this channel, as shown in (5.2.5).

Following the same logic, we now comment on the $K_S \to \pi^+\pi^- a$ channel with $m_a = m_\pi$. The irreducible background from $K_S \to \pi^+\pi^-\pi^0$ gives $S_{eff} \simeq 1.1\times10^{-7}$. Its K_L counterpart yields $S_{eff} \simeq 1.3\times10^{-5}$, which includes the acceptance suppression by A_{K_L}. We quote the latter as the sensitivity in this channel.

For the $K^+ \to \pi^+\pi^0 a$ channel with small m_a, the most straightforward background comes from $K^+ \to \pi^+\pi^0\gamma$, which gives $S_{eff} \simeq 5.0\times10^{-7}$. Additionally, the channel $K^+ \to \mu^+\pi^0\nu$, with a misidentified muon, has a large BR. However, the μ-to-π misidentification probability at NA62 is as small as 1.3×10^{-8}, making this channel entirely negligible.

For the $K^+ \to \pi^+\pi^0 a$ channel with $m_a = m_\pi$, we have conservatively quoted $K^+ \to \pi^+\pi^0\pi^0$ as the leading irreducible background. Ref. [Lo 21] finds that this background can be largely eliminated by suitable kinematical cuts.

Concerning the $BR(K_S \to \mu^+\mu^- a)$ with small m_a (the penultimate in (5.2.5)). As noted below (5.2.4), $BR(K_S \to \mu^+\mu^-\gamma)$ has not been measured yet. However, several existing channels seem to provide similar information. First, $BR(K_S \to \pi\mu\nu)$ again: taking into account the $\pi \to \mu$ misidentification probability at LHCb, $\epsilon_{\pi\mu}$, we obtain $S_{eff}(K_S \to \pi\mu\nu) \simeq 3\times10^{-7}$. A second channel is $K_S \to \pi^+\pi^-\gamma$ (the first in Eq. (5.2.4)), with two $\epsilon_{\pi\mu}$ factors, yielding $S_{eff} \simeq 1\times10^{-8}$, thus negligible compared to the first channel. A third channel is $K_L \to \pi\mu\nu$. Taking into account the $\epsilon_{\pi\mu}\times A_{K_L}$ factor, we obtain $S_{eff} \simeq 2.7\times10^{-7}$ for this channel. In conclusion, by adding the two larger channels in quadrature, we get $S_{eff} \simeq 4.1\times10^{-7}$, as stated in Eq. (5.2.5).

Regarding the $K_S \to \mu^+\mu^- a$ channel with $m_a = m_\pi$, the $K_S \to \mu^+\mu^-\pi^0$ and $K_L \to \pi^+\pi^-\pi^0$ backgrounds contribute $S_{eff} \simeq \{1.5, 1.3\}\times10^{-9}$, with the latter factor including the $\epsilon^2_{\pi\mu}\times A_{K_L}$ factor, where $\epsilon_{\pi\mu}$ is the $\pi \to \mu$ misidentification probability at LHCb, evaluated at 1%. Adding these two S_{eff} values in quadrature, we obtain the final $S_{eff} \simeq 2.0\times10^{-9}$.

Interestingly, the decay $K_S \to \mu^+\mu^-\pi^0$ can be measured by LHCb, both with and without an explicit π^0 requirement. To separate it from $K_S \to \mu^+\mu^- a$ with $m_a = m_\pi$, we can use the measurement from NA62 as described above and, in the long term, a hypothetical measurement by LHCb with an explicit π^0 requirement. Assuming that the latter reaches 8% precision [Cho+16], the S_{eff} sensitivity in the last line of Eq. (5.2.5) would be around 1.5×10^{-10}, improving by an oom compared to the S_{eff} value quoted in Eq. (5.2.5).

5.2.3 Branching Ratio Calculations

All the processes studied in this section can generically be written as $K \to h^+ \tilde{h} X$, where $K \in \{K^+, K_S\}$ represents a kaon, $(h^+, \tilde{h}) \in \{(\ell^+, \ell^-), (\pi^+, \pi^-), (\pi^+, \pi^0)\}$ denotes a lepton or pion pair, and $X \in \{a, \pi^0\}$ is a pseudoscalar particle.

To obtain explicitly a Lorentz-invariant expression, we define the Mandelstam variables as:

$$s = (p_K - p_X)^2 = (p_{h^+} + p_{\tilde{h}})^2 \ , \quad t = (p_K - p_{h^+})^2 = (p_X + p_{\tilde{h}})^2 \ , \quad u = (p_K - p_{\tilde{h}})^2 = (p_X + p_{h^+})^2 \ . \tag{5.2.6}$$

Using the results from Section 5.1.1, we obtain the following expression for the doubly differential decay rate:

$$\frac{d^2\Gamma}{ds\, dt}[K \to h^+ \tilde{h} X] = \frac{1}{(4\pi)^3} \frac{1}{4m_K^3} \left| \mathcal{M}_{fi}[K \to h^+ \tilde{h} X] \right|^2 \ . \tag{5.2.7}$$

The BR is then given by:

$$BR(K \to h^+ \tilde{h} X) = \frac{1}{\Gamma_{\text{tot}}[K]} \int_{(m_{h^+}+m_{\tilde{h}})^2}^{(m_K - m_X)^2} ds \int_{t_{\min}(s)}^{t_{\max}(s)} dt \, \frac{d^2\Gamma}{ds\, dt}[K \to h^+ \tilde{h} X] \ , \tag{5.2.8}$$

where

$$t_{\min/\max}(s) = \frac{(m_K^2 - m_X^2)^2}{4s} - \left(\sqrt{\frac{s}{4} - m_{h^+}^2} \pm \sqrt{\frac{(s + m_X^2 - m_K^2)^2}{4s} - m_X^2} \right)^2 \ . \tag{5.2.9}$$

Since $\frac{d^2\Gamma}{ds,dt}$ is a polynomial in t, the partial integration over t can be performed analytically to obtain $\frac{d\Gamma}{ds}$, after which the remaining integration is carried out numerically to compute the BR.

From Eq. (5.2.7), it is clear that one only needs to compute the relevant Feynman amplitudes to determine the observables. Therefore, in this section, we will compute the Feynman amplitudes for the processes of interest–first for the SM case with $X = \pi^0$, to validate the method, and then for the axion case with $X = a$.

For processes involving axions, weak interactions will be neglected, as the axion itself induces flavor-changing transitions. In contrast, for SM processes, weak interactions must be included in the calculations. In the Feynman diagrams, weak interaction vertices will be indicated by squares, while strong interaction vertices will be marked with circles.

5.2.3.1 $K_S \to \ell^+ \ell^- \pi^0$

Before computing the amplitude for $K_S \to \ell^+ \ell^- a$, we first consider the analogous process with the axion replaced by a π^0, in order to validate our procedure. This step allows us to recover the results of Ref. [EPR87]; the corresponding calculation is provided in Appendix B.6.

5.2.3.2 $K_S \to \ell^+ \ell^- a$

5.2.3.2.1 Treatment of K_S

Given that

$$K_S = \frac{K^0 - \bar{K}^0}{\sqrt{2}} + \epsilon_K \frac{K^0 + \bar{K}^0}{\sqrt{2}} = \frac{K^0 - \bar{K}^0}{\sqrt{2}} + \mathcal{O}(\epsilon_K) \ , \tag{5.2.10}$$

we find that the amplitude can be written as

$$\mathcal{M}_{fi}[K_S \to \ell^+ \ell^- a] = \frac{1}{\sqrt{2}} \left(\mathcal{M}_{fi}[K^0 \to \ell^+ \ell^- a] + \mathcal{M}_{fi}[\bar{K}^0 \to \ell^+ \ell^- a] \right) + \mathcal{O}(\epsilon_K) \ . \tag{5.2.11}$$

Therefore, we compute the amplitudes for K^0 and $\bar{K}^0$, the interaction eigenstates, from which the result for K_S is obtained. For simplicity, we neglect the term $\epsilon_K \simeq 10^{-3}$ in the following calculations.

5.2.3.2.2 Electromagnetic gauge structure

Mesons do not couple directly to leptons, implying that the interaction must proceed via a bosonic mediator. By charge conservation, the mediator must be either a photon (γ) or a Z boson. In this analysis, we neglect the weak interaction and retain only the virtual photon contribution.

By Lorentz invariance and electromagnetic gauge symmetry, the most general form of the amplitude for the transition $K \to a + \gamma^*$ involves the contraction of the electromagnetic field-strength tensor $F^{\mu\nu}$ with an antisymmetric rank-2 tensor constructed from external momenta. The symmetric part vanishes[4].

This leads to the general structure:

$$\mathcal{M}_{fi} = F_{\mu\nu}(p_\gamma)(p_K^\mu p_a^\nu - p_K^\nu p_a^\mu)\,\phi(p_\gamma^2)\ , \tag{5.2.12}$$

where $F^{\mu\nu}(p_\gamma) = \epsilon^\mu p_\gamma^\nu - \epsilon^\nu p_\gamma^\mu$, and ϵ^μ is the polarization vector of the virtual photon. The function $\phi(p_\gamma^2)$ encapsulates the model-dependent dynamics.

The amplitude can then be rewritten in the form:

$$\mathcal{M}_{fi} = \epsilon_\mu V^\mu\ , \tag{5.2.13}$$

with

$$V^\mu = [-p_\gamma^2(p_K^\mu + p_a^\mu) + (m_K^2 - m_a^2)p_\gamma^\mu]\,\phi(p_\gamma^2)\ , \tag{5.2.14}$$

as derived from:

$$\begin{aligned} F_{\mu\nu}(p_\gamma)(p_K^\mu p_a^\nu - p_K^\nu p_a^\mu) &= (\epsilon^\mu p_\gamma^\nu - \epsilon^\nu p_\gamma^\mu)(p_K^\mu p_a^\nu - p_K^\nu p_a^\mu) \\ &= 2\epsilon_\mu\left[(p_\gamma\cdot p_a)p_K^\mu - (p_\gamma\cdot p_K)p_a^\mu\right] \\ &= \epsilon_\mu\left[(m_K^2 - m_a^2 - p_\gamma^2)p_K^\mu - (m_K^2 - m_a^2 + p_\gamma^2)p_a^\mu\right] \\ &= \epsilon_\mu\left[-p_\gamma^2(p_K^\mu + p_a^\mu) + (m_K^2 - m_a^2)p_\gamma^\mu\right]\ . \end{aligned} \tag{5.2.15}$$

Here, we used the kinematic identities:

$$m_K^2 = (p_\gamma + p_a)^2 = p_\gamma^2 + m_a^2 + 2(p_\gamma\cdot p_a) \Rightarrow p_\gamma\cdot p_a = \tfrac{1}{2}(m_K^2 - m_a^2 - p_\gamma^2)\ , \tag{5.2.16}$$

$$m_a^2 = (p_K - p_\gamma)^2 = m_K^2 + p_\gamma^2 - 2(p_\gamma\cdot p_K) \Rightarrow p_\gamma\cdot p_K = \tfrac{1}{2}(m_K^2 - m_a^2 + p_\gamma^2)\ . \tag{5.2.17}$$

The complete amplitude for the process $K \to a(\gamma^* \to \ell^+\ell^-)$ is then:

$$\mathcal{M}_{fi}(K \to a(\gamma^* \to \ell^+\ell^-)) = V_\mu \frac{-i\eta^{\mu\nu}}{p_\gamma^2 + i\epsilon}(-ie)\,\bar{u}_{\ell^-}\gamma_\nu v_{\ell^+}\ . \tag{5.2.18}$$

An important observation is that the term in V^μ proportional to p_γ^μ does not contribute to the amplitude squared, since:

$$\begin{aligned} |\mathcal{M}_{fi}|^2 &\propto \mathrm{Tr}\left[(\not{p}_{\ell^-} + m_\ell)\not{p}_\gamma(\not{p}_{\ell^+} - m_\ell)\not{p}_\gamma\right] \\ &= \mathrm{Tr}\left[(\not{p}_{\ell^-} + m_\ell)(\not{p}_{\ell^-} + \not{p}_{\ell^+})(\not{p}_{\ell^+} - m_\ell)(\not{p}_{\ell^-} + \not{p}_{\ell^+})\right] \\ &= 4(-2m_\ell^4 - 2m_\ell\, p_{\ell^+}\cdot p_{\ell^-} + 2m_\ell^4 + 2m_\ell\, p_{\ell^+}\cdot p_{\ell^-}) = 0\ . \end{aligned} \tag{5.2.19}$$

Therefore, the only gauge-invariant contribution is:

$$V^\mu = -p_\gamma^2(p_K^\mu + p_a^\mu)\,\phi(p_\gamma^2)\ . \tag{5.2.20}$$

This implies that the diagram for $K \to a\gamma^*$ is proportional to p_γ^2. However, when performing perturbative calculations with a finite number of diagrams, this proportionality may not be manifest. In the full calculation, electromagnetic gauge symmetry ensures cancellation of the unwanted terms. To enforce this symmetry at the perturbative level, we define:

$$\hat{V}^\mu := V^\mu - V^\mu\big|_{p_\gamma^2=0}\ , \tag{5.2.21}$$

so that only the gauge-invariant piece remains.

The final amplitude respecting electromagnetic gauge invariance is therefore:

$$\mathcal{M}_{fi}(K \to a(\gamma^* \to \ell^+\ell^-)) = \hat{V}_\mu \frac{-i\eta^{\mu\nu}}{p_\gamma^2 + i\epsilon}(-ie)\,\bar{u}_{\ell^-}\gamma_\nu v_{\ell^+}\ . \tag{5.2.22}$$

[4]If $A_{\mu\nu}$ is a tensor, it can be decomposed as $A_{\mu\nu} = A^+_{\mu\nu} + A^-_{\mu\nu}$, with $A^\pm_{\mu\nu} := (A_{\mu\nu} \pm A_{\nu\mu})/2$. Since $F^{\mu\nu}$ is antisymmetric, it satisfies $F^{\mu\nu}A^+_{\mu\nu} = 0$.

5.2.3.2.3 Amplitude calculation

The tree-level amplitude vanishes due to charge conservation: any tree-level diagram for $K_S \to a\gamma$ necessarily involves only neutral particles, but there exists no direct coupling between neutral mesons (, the axion), and the photon.

At order $\mathcal{O}(p^2)$ in the chiral expansion, the only possible source of photon couplings comes from the covariant derivative:

$$D_\mu U = \partial_\mu U - ieA_\mu[Q, U] \ . \tag{5.2.23}$$

However, if we restrict to neutral mesons only, the chiral field takes the form:

$$U_{\text{neutral}} = \begin{pmatrix} A & \vec{0}^T \\ \vec{0} & B \end{pmatrix} \ , \tag{5.2.24}$$

with

$$A = \pi^0 + \frac{\eta_8}{\sqrt{3}} + \frac{\sqrt{2}\eta_0}{\sqrt{3}} \ , \tag{5.2.25}$$

$$B = \begin{pmatrix} -\pi^0 + \frac{\eta_8}{\sqrt{3}} + \frac{\sqrt{2}\eta_0}{\sqrt{3}} & \sqrt{2}K^0 \\ \sqrt{2}\bar{K}^0 & -\frac{2\eta_8}{\sqrt{3}} + \frac{\sqrt{2}\eta_0}{\sqrt{3}} \end{pmatrix} \ , \tag{5.2.26}$$

and

$$Q = \frac{1}{3}\begin{pmatrix} 2 & \vec{0}^T \\ \vec{0} & -\mathbb{I}_2 \end{pmatrix} \ . \tag{5.2.27}$$

Both U_{neutral} and Q are block-diagonal, and the blocks of Q are proportional to the identity. This implies that $[Q, U_{\text{neutral}}] = 0$, and therefore, the photon does not couple to (axion-)neutral meson vertices at this order.

At higher orders, additional couplings involving the electromagnetic field-strength tensor $F_{\mu\nu}$ may appear. However, these terms possess a well-defined classical limit, which should also hold at long distances. Even though neutral mesons have an internal charged structure, they are globally neutral, and in the classical limit, they cannot couple to the photon without the presence of charged mesons.[5]

The relevant Feynman diagrams involving loops are shown in Fig. 5.11.

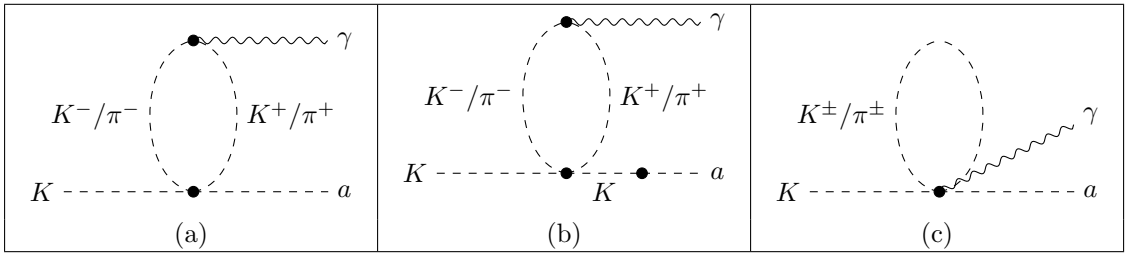

Figure 5.11: Feynman diagrams for $K_S \to a + (\gamma \to \ell^+\ell^-)$.

Let us denote the internal virtual meson as $M \in \{K, \pi\}$ for each diagram. We define $s = p_\gamma^2 = (p_{\ell^+} + p_{\ell^-})^2$, and let p_+ be the momentum of the positively charged meson (K^+ or π^+), so that the negatively charged meson carries momentum $p_- = p_\gamma - p_+$.

Diagram (a)

The amplitude corresponding to diagram (a) reads:

$$\begin{aligned} i\mathcal{M}_{fi}^{(a)} = \int_{\mathbb{R}^d} \frac{\mu^{4-d} d^d p_+}{(2\pi)^d} i \frac{C_{0a} p_a \cdot p_K - C_{+a} p_a \cdot p_+ - C_{-a} p_a \cdot p_-}{12 F_0 f_a} \times \frac{i}{p_+^2 - m_M^2} \frac{i}{p_-^2 - m_M^2} \\ \times i^2 e(-ip_+^\mu + ip_-^\mu) \times \frac{-i\eta_{\mu\nu}}{s} \times \bar{u}_{\ell^-} ie\gamma^\nu v_{\ell^+} \ . \end{aligned} \tag{5.2.28}$$

Here, the coefficients $C^M_{\{0,+,-\}a}$ denote the relevant interaction vertices.

[5] The chiral anomaly that induces the coupling $\pi^0 \to \gamma\gamma$ violates this rule, but it is anomalous in nature. Even taking such anomalies into account, the vertex always involves two photons, and thus cannot generate $K \to a\gamma$ without loop effects.

Using dimensional regularization (See Appendix B.2.5 for general information, and Appendix B.6 for an example calculation of $K \to \pi(\gamma \to \ell^+\ell^-)$.), the amplitude becomes:

$$\begin{aligned} i\mathcal{M}_{fi}^{(a)} =& -i\frac{e^2}{12(4\pi)^2 F_0 f_a s}\bar{u}_{\ell^-}\not{p}_a v_{\ell^+}(C_{-a}-C_{+a}) \\ &\times\left(\left(\frac{-2}{\epsilon}+\gamma-1\right)\int_0^1 \Delta(m_{M^\pm}^2)d\alpha + \int_0^1 \Delta(m_{M^\pm}^2)\ln\left(\frac{\Delta(m_{M^\pm}^2)}{4\pi\mu^2}\right)d\alpha\right) \end{aligned} \tag{5.2.29}$$

$$\begin{aligned} =& -i\frac{e^2}{12(4\pi)^2 F_0 f_a s}\bar{u}_{\ell^-}\not{p}_a v_{\ell^+}(C_{-a}-C_{+a}) \\ &\times\left(\left(\frac{-2}{\epsilon}+\gamma-1\right)\frac{6m_{M^\pm}^2-s}{6} + \int_0^1 \Delta(m_{M^\pm}^2)\ln\left(\frac{\Delta(m_{M^\pm}^2)}{4\pi\mu^2}\right)d\alpha\right) \end{aligned} \tag{5.2.30}$$

where $\Delta(m_{M^\pm}^2) = m_{M^\pm}^2 - \alpha(1-\alpha)s$.

Applying the explicit form of the vertices $C^M_{\{0,+,-\}a}$, we find:

$$\mathcal{M}_{fi}^{(a)}[K^0 \to \ell^+\ell^- a] = \frac{\sqrt{2}e^2}{2(4\pi)^2 F_0 f_a s}\bar{u}_{\ell^-}\not{p}_a v_{\ell^+} I^{(a)}(k_A)^*_{23} \tag{5.2.31}$$

with

$$\begin{aligned} I^{(a)} =& \left(\frac{-2}{\epsilon}+\gamma-1\right)(m_{K^\pm}^2 - m_{\pi^\pm}^2) + \int_0^1 \Delta(m_{K^\pm}^2)\ln\left(\frac{\Delta(m_{K^\pm}^2)}{4\pi\mu^2}\right)d\alpha \\ &- \int_0^1 \Delta(m_{\pi^\pm}^2)\ln\left(\frac{\Delta(m_{\pi^\pm}^2)}{4\pi\mu^2}\right)d\alpha \end{aligned} \tag{5.2.32}$$

Imposing electromagnetic gauge invariance, we obtain:

$$\hat{I}^{(a)} = \int_0^1 \left(m_{K^\pm}^2 \ln\left(\frac{\Delta(m_{K^\pm}^2)}{m_{K^\pm}^2}\right) - m_{\pi^\pm}^2 \ln\left(\frac{\Delta(m_{\pi^\pm}^2)}{m_{\pi^\pm}^2}\right) + \alpha(1-\alpha)s\ln\left(\frac{\Delta(m_{\pi^\pm}^2)}{\Delta(m_{K^\pm}^2)}\right)\right)d\alpha\ . \tag{5.2.33}$$

Taking into account electromagnetic symmetry, the sum of pion and kaon loop contributions yields a finite result. There is no residual dependence on the renormalization scale μ.

Diagram (b)

The amplitude corresponding to diagram (b) is given by:

$$i\mathcal{M}_{fi}^{(b)} = \int_{\mathbb{R}^d}\frac{\mu^{4-d}d^dp_+}{(2\pi)^d} i\frac{-2C_{+-}p_+\cdot p_- + 2C_{0\bar{0}}p_K\cdot p_a + C_{0+}p_K\cdot p_+ - C_{+\bar{0}}p_a\cdot p_+ + C_{0-}p_K\cdot p_- - C_{-\bar{0}}p_a\cdot p_-}{-6F_0^2} \tag{5.2.34}$$

$$\times\frac{i}{m_a^2-m_{K_S}^2}\times i\frac{-F_0C_{0a}}{2f_a}m_a^2\times\frac{i}{p_+^2-m_{M^\pm}^2}\times\frac{i}{p_-^2-m_{M^\pm}^2}\times i^2e(-ip_+^\mu+ip_-^\mu)\times\frac{-i\eta_{\mu\nu}}{s}\times\bar{u}_{\ell^-}(ie\gamma^\nu)v_{\ell^+}\ .$$

Here, the coefficients C_{ij} denote the interaction couplings at the vertices.

Using the same integration techniques and definitions as in diagram (a), the amplitude simplifies to:

$$\mathcal{M}_{fi}^{(b)}[K^0 \to \ell^+\ell^- a] = \frac{\sqrt{2}e^2}{2(4\pi)^2 F_0 f_a s}\frac{m_a^2}{m_{K_S}^2-m_a^2}\bar{u}_{\ell^-}\not{p}_a v_{\ell^+} I^{(b)}(k_A)^*_{23}\ , \tag{5.2.35}$$

with

$$I^{(b)} = I^{(a)}\ . \tag{5.2.36}$$

Diagram (c)

The amplitude takes the form:

$$i\mathcal{M}_{fi}^{(c)} = \int_{\mathbb{R}^d}\frac{\mu^{4-d}\,d^dp}{(2\pi)^d}\,i\frac{eC}{F_0f_a}\,p_a^\mu\times\frac{i}{p^2-m_{M^\pm}^2}\times\frac{-i\eta_{\mu\nu}}{s}\times\bar{u}_{\ell^-}(ie\gamma^\nu)v_{\ell^+}\ , \tag{5.2.37}$$

which evaluates to:

$$\mathcal{M}_{fi}^{(c)}[K^0 \to \ell^+\ell^- a] = I^{(c)}(k_A)^*_{23}\ , \tag{5.2.38}$$

with:

$$I^{(c)} = \frac{e^2}{2(4\pi)^2 F_0 f_a s}\,\bar{u}_{\ell^-}\not{p}_a v_{\ell^+}\left[m_{K^\pm}^2\left(-\frac{2}{\epsilon}+\gamma-1+\ln\left(\frac{m_{K^\pm}^2}{4\pi\mu^2}\right)\right)\right. \\ \left. - m_{\pi^\pm}^2\left(-\frac{2}{\epsilon}+\gamma-1+\ln\left(\frac{m_{\pi^\pm}^2}{4\pi\mu^2}\right)\right)\right]\,. \tag{5.2.39}$$

Imposing electromagnetic gauge invariance leads to the cancellation of the divergence and scale dependence in this term. As a result, the gauge-invariant combination vanishes:

$$\hat{I}^{(c)} = 0\,. \tag{5.2.40}$$

All diagrams

The total amplitude corresponds to the sum of all diagrammatic contributions:

$$\begin{aligned}\mathcal{M}_{fi}[K^0\to\ell^+\ell^- a] &= \mathcal{M}_{fi}^{(a)}[K^0\to\ell^+\ell^- a] + \mathcal{M}_{fi}^{(b)}[K^0\to\ell^+\ell^- a] + \mathcal{M}_{fi}^{(c)}[K^0\to\ell^+\ell^- a] \\ &= \frac{\sqrt{2}e^2}{2(4\pi)^2 F_0 f_a s}\bar{u}_{\ell^-}\not{p}_a v_{\ell^+}\left(1+\frac{m_a^2}{m_{K^0}^2-m_a^2}\right)(k_A)_{23}^*\hat{I}(s) \\ &= \frac{\sqrt{2}e^2}{2(4\pi)^2 F_0 f_a s}\bar{u}_{\ell^-}\not{p}_a v_{\ell^+}\frac{m_{K^0}^2}{m_{K^0}^2-m_a^2}(k_A)_{23}^*\hat{I}(s)\,.\end{aligned} \tag{5.2.41}$$

Here, the loop function $\hat{I}(s)$ is defined as:

$$\hat{I}(s) = \int_0^1\left(m_{K^\pm}^2\ln\left(\frac{\Delta(m_{K^\pm}^2)}{m_{K^\pm}^2}\right) - m_{\pi^\pm}^2\ln\left(\frac{\Delta(m_{\pi^\pm}^2)}{m_{\pi^\pm}^2}\right) + \alpha(1-\alpha)s\ln\left(\frac{\Delta(m_{\pi^\pm}^2)}{\Delta(m_{K^\pm}^2)}\right)\right)d\alpha\,. \tag{5.2.42}$$

with $\Delta(m^2) = m^2 - \alpha(1-\alpha)s$.

We then obtain the amplitude for the physical $K_S\to\ell^+\ell^- a$ decay as:

$$\begin{aligned}\mathcal{M}_{fi}[K_S\to\ell^+\ell^- a] =& \frac{\mathcal{M}_{fi}[K^0\to\ell^+\ell^- a] - \mathcal{M}_{fi}[\bar{K}^0\to\ell^+\ell^- a]}{\sqrt{2}} \\ =& \frac{\sqrt{2}e^2}{2(4\pi)^2 F_0 f_a s}\bar{u}_{\ell^-}\not{p}_a v_{\ell^+}\frac{m_{K^0}^2}{m_{K^0}^2-m_a^2}\hat{I}(s)\frac{(k_A)_{23}^*-(k_A)_{23}}{\sqrt{2}} \\ =& -\frac{e^2}{(4\pi)^2 F_0 f_a s}\bar{u}_{\ell^-}\not{p}_a v_{\ell^+}\frac{m_{K^0}^2}{m_{K^0}^2-m_a^2}\hat{I}(s)\,\mathrm{Im}[(k_A)_{23}]\,.\end{aligned} \tag{5.2.43}$$

5.2.3.2.4 Computation of $\hat{I}(s)$

The calculation of $\hat{I}(s)$ is non-trivial due to the fact that the integrand contains logarithmic terms whose arguments may become negative. This requires careful treatment of the logarithm in the complex plane.

To make the expression dimensionless, we define:

$$\hat{J}(s) := \frac{\hat{I}(s)}{m_K^2} = \int_0^1 d\alpha\left[\ln\left(\frac{\Delta_K}{m_K^2}\right) - \frac{m_\pi^2}{m_K^2}\ln\left(\frac{\Delta_\pi}{m_\pi^2}\right) + \alpha(1-\alpha)\frac{s}{m_K^2}\ln\left(\frac{\Delta_K}{\Delta_\pi}\right)\right]\,, \tag{5.2.44}$$

where we define $\Delta_i := m_i^2 - \alpha(1-\alpha)s$. For a fixed value of s, we have $\Delta_i \in [m_i^2 - s/4,\, m_i^2]$. Therefore:

- $\Delta_K > 0$ over the entire integration domain,
- but Δ_π may become negative for sufficiently large s, even within its domain of definition.

This sign change can cause discontinuities in the logarithm if not handled properly.

Before dealing with the sign ambiguity, it is important to confirm that the logarithmic integrand is integrable at the lower endpoint $x = 0$, where the logarithm becomes divergent. This requires an improper integral, but it can be shown that the divergence is integrable.

Let us now discuss the complex logarithm. The standard real logarithm $\ln : \mathbb{R}_+^* \to \mathbb{R}$ has two equivalent definitions:

- As the primitive of the inverse function vanishing at 1:

$$\forall x \in \mathbb{R}_+^*, \quad \ln(x) = \int_1^x \frac{dt}{t} \; ;$$

- As the inverse of the exponential function:

$$\forall (x, y) \in \mathbb{R} \times \mathbb{R}_+^*, \quad \exp(\ln(y)) = y \quad \text{and} \quad \ln(\exp(x)) = x \; .$$

However, in Eq. (5.2.44), the argument of the logarithm may become negative within the integration range, in which case the real logarithm is no longer well-defined. To proceed, we must extend the logarithm to the complex plane. There are two equivalent approaches:

(i) As a complex integral of the inverse function: One can use the fact that any holomorphic function[6] defined on a star-shaped domain[7] admits a primitive.

The function $1/z$ is holomorphic on $\mathbb{C}^* = \mathbb{C} \setminus \{0\}$, but this domain is not star-shaped. To construct a star-shaped domain containing parts of $\mathbb{C}^*$, one typically removes a branch cut, such as the negative real axis $\mathbb{R}_-$, yielding $\mathbb{C} \setminus \mathbb{R}_-$, which is star-shaped.

On such a domain, the function $1/z$ admits a primitive, and the complex logarithm can be defined by the integral:

$$\ln(z) = \int_\gamma \frac{dz'}{z'} \quad \text{for any path } \gamma : [0,1] \to \mathbb{C} \setminus \mathbb{R}_- \text{ with } \gamma(0) = 1 \text{ and } \gamma(1) = z \; . \tag{5.2.45}$$

If the path γ crosses the branch cut (i.e., the negative real axis), then by the residue theorem, the integral becomes:

$$\int_\gamma \frac{dz'}{z'} = \ln(\gamma(1)) - \ln(\gamma(0)) + 2\pi i k \; , \tag{5.2.46}$$

where $k \in \mathbb{Z}$ is the winding number, which counts (algebraically) the number of times the path winds around the origin.

This construction shows that the complex logarithm is multivalued, with ambiguities that arise from different homotopy classes of paths in $\mathbb{C}^*$. Choosing a particular branch cut amounts to selecting a consistent determination of the logarithm over a star-shaped subset of the complex plane.

(ii) As the inverse of the complex exponential: The complex exponential $\exp : \mathbb{C} \to \mathbb{C}^*$ is $2i\pi$-periodic. Therefore, it does not admit a globally single-valued inverse. However, by restricting the imaginary part of $z \in \mathbb{C}$ to a strip of width 2π, we can define a branch of the complex logarithm:

$$\ln(z) = \ln|z| + i \arg(z) \; , \tag{5.2.47}$$

where $\arg(z) \in]-\pi, \pi[$ (principal branch) is the chosen determination of the argument.

In both cases, we see that the complex logarithm is inherently a multivalued function. This multivalued behavior is naturally understood in the framework of Riemann surfaces, where such functions are lifted to single-valued functions defined over an appropriate branched covering of the complex plane. A schematic representation of the Riemann surface associated with the logarithm is shown in Fig. 5.12.

Consequences for the integral over α: Due to the multivalued nature of the complex logarithm, one cannot evaluate the integral in Eq. (5.2.44) by taking an antiderivative between $\alpha = 0$ and $\alpha = 1$ without tracking branch changes. An evaluation performed in this way produces discontinuities at the branch cut, as seen in Fig. 5.13 (left panel). The right panel shows the correct, continuous result obtained with proper analytic continuation, though the function remains non-differentiable at the branch point.

[6] A function $f : U \to \mathbb{C}$, with U an open subset of the complex plane, is said to be holomorphic if for every point $z \in U$, the limit $\lim_{h \to 0} \frac{f(z+h) - f(z)}{h}$ exists and is finite. This definition resembles real differentiability, but since the complex plane allows infinitely many directions for approaching zero, holomorphy is much more restrictive. For example, any holomorphic function is analytic (i.e., locally expandable into a power series), whereas a real $\mathcal{C}^\infty$ function is not necessarily analytic.

[7] A set $D \subset \mathbb{C}$ is called star-shaped if there exists a point $x \in D$ such that, for every $y \in D$, the line segment between x and y lies entirely within D: $[x, y] = \{x + \beta(y - x) \mid \beta \in [0, 1]\} \subset D$.

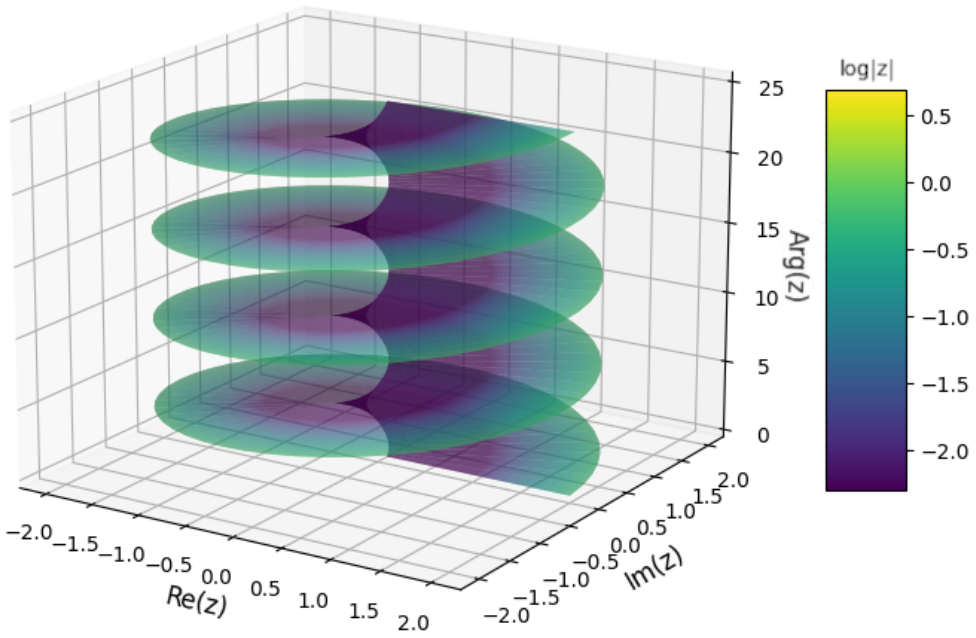

Figure 5.12: Visual representation of the Riemann surface of the complex logarithm. Each sheet corresponds to a different branch of $\arg(z)$.

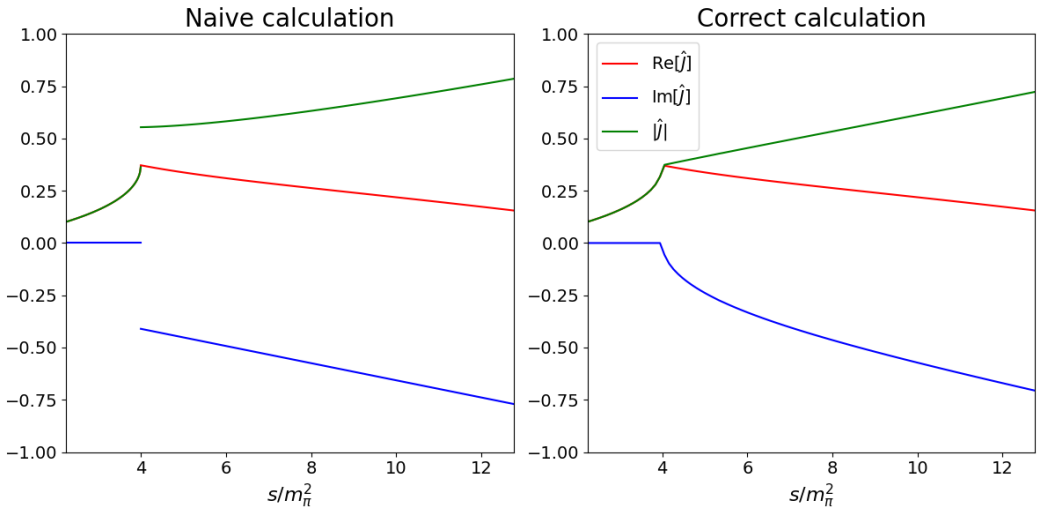

Figure 5.13: Evaluation of $\hat{J}(s)$ with an incorrect treatment of the logarithmic branches (left), leading to a discontinuity at the branch cut $s = 4m_\pi^2$, versus the correct result obtained with proper branch tracking (right).

5.2.3.3 $K_S \to \pi^+\pi^-\pi^0$

The objective of this section is to reproduce the results from [BDB03; FG89] to ensure that we are using the correct procedure for $K_S \to \pi^+\pi^- a$.

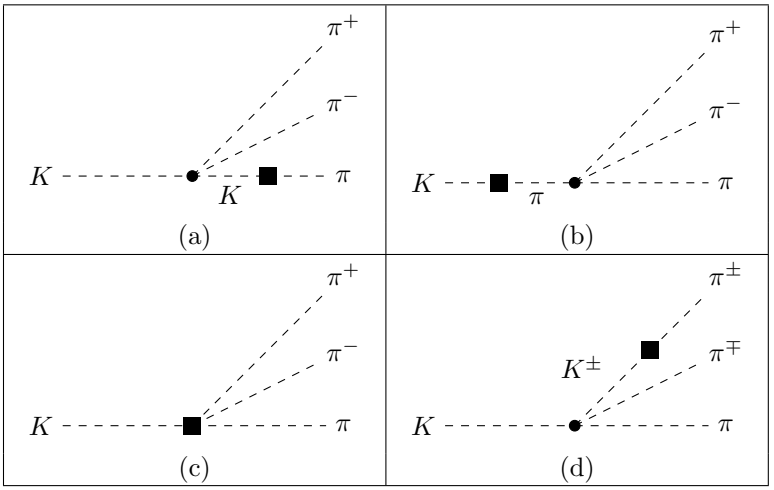

Figure 5.14: Feynman diagrams for $K_S \to \pi^+ + \pi^- + \pi^0$

The Feynman diagrams are given in Fig. 5.14.

If we compute this Feynman diagrams for K^0, we obtain:

$$
\begin{aligned}
i\mathcal{M}_{fi}^{(a)}[K^0 \to \pi^+ + \pi^- + \pi^0] =& -i\frac{1}{6}G_F V_{us}V_{ud}^* g_8 \frac{m_{\pi^0}^2}{m_{\pi^0}^2 - m_{K^0}^2}\begin{pmatrix} -p_{\pi^+}\cdot p_{\pi^-} - p_{\pi^0}\cdot p_{\pi^-} + 2p_{\pi^0}\cdot p_{\pi^+} \\ -2p_{K^0}\cdot p_{\pi^-} + p_{K^0}\cdot p_{\pi^+} + p_{K^0}\cdot p_{\pi^0}\end{pmatrix}, \\
i\mathcal{M}_{fi}^{(b)}[K^0 \to \pi^+ + \pi^- + \pi^0] =& i\frac{1}{3}G_F V_{us}V_{ud}^* g_8 \frac{m_{K^0}^2}{m_{K^0}^2 - m_{\pi^0}^2}\begin{pmatrix} -2p_{K^0}\cdot p_{\pi^0} + p_{K^0}\cdot p_{\pi^-} + p_{K^0}\cdot p_{\pi^+} \\ -p_{\pi^0}\cdot p_{\pi^-} - p_{\pi^0}\cdot p_{\pi^+} + 2p_{\pi^+}\cdot p_{\pi^-}\end{pmatrix}, \\
i\mathcal{M}_{fi}^{(c)}[K^0 \to \pi^+ + \pi^- + \pi^0] =& -i\frac{1}{6}G_F V_{us}V_{ud}^* g_8 \begin{pmatrix} -p_{\pi^0}\cdot p_{\pi^-} - p_{\pi^0}\cdot p_{\pi^+} - 4p_{K^0}\cdot p_{\pi^0} \\ +p_{K^0}\cdot p_{\pi^-} + p_{K^0}\cdot p_{\pi^+}\end{pmatrix}, \\
i\mathcal{M}_{fi}^{(d)}[K^0 \to \pi^+ + \pi^- + \pi^0] =& -i\frac{1}{2}G_F V_{us}V_{ud}^* g_8 \frac{m_{\pi^\pm}^2}{m_{\pi^\pm}^2 - m_{K^\pm}^2}\begin{pmatrix} p_{K^0}\cdot p_{\pi^0} - p_{K^0}\cdot p_{\pi^+} \\ +p_{\pi^0}\cdot p_{\pi^-} - p_{\pi^-}\cdot p_{\pi^+}\end{pmatrix}.
\end{aligned}
\tag{5.2.48}
$$

Which gives

$$
\begin{aligned}
\mathcal{M}_{fi}^{(a)}[K_S \to \pi^+\pi^-\pi^0] =& -\frac{1}{2\sqrt{2}}G_F V_{us}V_{ud}^* g_8 \frac{m_{\pi^0}^2}{m_{\pi^0}^2 - m_{K^0}^2}(p_{\pi^0} + p_K)\cdot(p_{\pi^+} - p_{\pi^-}) \\
\mathcal{M}_{fi}^{(b)}[K_S \to \pi^+\pi^-\pi^0] =& \mathcal{M}_{fi}^{(c)}[K_S \to \pi^+\pi^-\pi^0] = 0 \\
\mathcal{M}_{fi}^{(d)}[K_S \to \pi^+\pi^-\pi^0] =& \frac{1}{2\sqrt{2}}G_F V_{us}V_{ud}^* g_8 \frac{m_{\pi^\pm}^2}{m_{\pi^\pm}^2 - m_{K^\pm}^2}(p_{\pi^0} + p_K)\cdot(p_{\pi^+} - p_{\pi^-})
\end{aligned}
\tag{5.2.49}
$$

which simplifies to

$$
\mathcal{M}_{fi}[K_S \to \pi^+\pi^-\pi^0] = \frac{1}{\sqrt{2}}G_F V_{us}V_{ud}^* g_8 \left(\frac{m_{\pi^\pm}^2}{m_{\pi^\pm}^2 - m_{K^\pm}^2} - \frac{m_{\pi^0}^2}{m_{\pi^0}^2 - m_{K^0}^2}\right) p_K\cdot(p_{\pi^+} - p_{\pi^-}) \tag{5.2.50}
$$

Although this quantity does not vanish exactly, it is strongly suppressed due to the near-degeneracy of the meson masses, $m_{\pi^0} \simeq m_{\pi^\pm}$ and $m_{K^0} \simeq m_{K^\pm}$. As a result, the contribution from the octet representation alone is insufficient, and it becomes necessary to include the 27-plet representation in the chiral expansion.

In this case, we obtain

$$
\begin{aligned}
i\mathcal{M}^{(a)}_{fi}[K^0 \to \pi^+ + \pi^- + \pi^0] =& -i\frac{1}{6}G_F V_{us}V^*_{ud}g_{27}\frac{m^2_{\pi^0}}{m^2_{\pi^0}-m^2_{K^0}}\begin{pmatrix}-p_{\pi^+}\cdot p_{\pi^-} - p_{\pi^0}\cdot p_{\pi^-} + 2p_{\pi^0}\cdot p_{\pi^+}\\ -2p_{K^0}\cdot p_{\pi^-} + p_{K^0}\cdot p_{\pi^+} + p_{K^0}\cdot p_{\pi^0}\end{pmatrix},\\
i\mathcal{M}^{(b)}_{fi}[K^0 \to \pi^+ + \pi^- + \pi^0] =& i\frac{1}{3}G_F V_{us}V^*_{ud}g_{27}\frac{m^2_{K^0}}{m^2_{K^0}-m^2_{\pi^0}}\begin{pmatrix}-2p_{K^0}\cdot p_{\pi^0} + p_{K^0}\cdot p_{\pi^-} + p_{K^0}\cdot p_{\pi^+}\\ -p_{\pi^0}\cdot p_{\pi^-} - p_{\pi^0}\cdot p_{\pi^+} + 2p_{\pi^+}\cdot p_{\pi^-}\end{pmatrix},\\
i\mathcal{M}^{(c)}_{fi}[K^0 \to \pi^+ + \pi^- + \pi^0] =& i\frac{1}{2}G_F V_{us}V^*_{ud}g_{27}\begin{pmatrix}-11p_{\pi^+}\cdot p_{\pi^-} - 9p_{\pi^0}\cdot p_{\pi^-} + p_K\cdot p_{\pi^+}\\ +11p_K\cdot p_{\pi^-} - 26p_K\cdot p_{\pi^0}\end{pmatrix}, \qquad (5.2.51)\\
i\mathcal{M}^{(d)}_{fi}[K^0 \to \pi^+ + \pi^- + \pi^0] =& i\frac{2\sqrt{2}}{3}G_F V_{us}V^*_{ud}g_{27}\frac{m^2_{\pi^\pm}}{m^2_{\pi^\pm}-m^2_{K^\pm}}\begin{pmatrix}p_{K^0}\cdot p_{\pi^0} - p_{K^0}\cdot p_{\pi^+}\\ +p_{\pi^0}\cdot p_{\pi^-} - p_{\pi^-}\cdot p_{\pi^+}\end{pmatrix}.
\end{aligned}
$$

Therefore,

$$
\begin{aligned}
\mathcal{M}^{(a)}_{fi}[K_S \to \pi^+ + \pi^- + \pi^0] =& -\frac{1}{\sqrt{2}}G_F V_{us}V^*_{ud}g_{27}\frac{m^2_{\pi^0}}{m^2_{\pi^0}-m^2_{K^0}}\; p_{K_S}\cdot(p_{\pi^+}-p_{\pi^-}),\\
\mathcal{M}^{(b)}_{fi}[K_S \to \pi^+ + \pi^- + \pi^0] =& \mathcal{M}^{(d)}_{fi}[K_S \to \pi^+ + \pi^- + \pi^0] = 0, \qquad (5.2.52)\\
\mathcal{M}^{(c)}_{fi}[K_S \to \pi^+ + \pi^- + \pi^0] =& -\frac{1}{2\sqrt{2}}G_F V_{us}V^*_{ud}g_{27}\; p_{K_S}\cdot(p_{\pi^-}-p_{\pi^+}).
\end{aligned}
$$

Thus,

$$
\mathcal{M}_{fi}[K_S \to \pi^+ + \pi^- + \pi^0] = -\frac{1}{\sqrt{2}}G_F V_{us}V^*_{ud}g_{27}\left(\frac{1}{2}+\frac{m^2_{\pi^0}}{m^2_{\pi^0}-m^2_{K^0}}\right)p_{K_S}\cdot(p_{\pi^-}-p_{\pi^+}). \qquad (5.2.53)
$$

For a pseudoscalar $X \in \{\pi^0, a\}$, we can exploit the fact that K_S is a CP-even scalar, while $\pi^\pm$, π^0, and a are CP-odd pseudoscalars. Under CP transformation, we have

$$
CP\,|K_S\rangle = |K_S\rangle, \quad CP\left|\pi^+,\pi^-,X\right\rangle = (-1)^3\left|\pi^-,\pi^+,X\right\rangle. \qquad (5.2.54)
$$

Therefore, CP invariance requires the amplitude to be antisymmetric under the exchange $\pi^+ \leftrightarrow \pi^-$.

The amplitude must be constructed from Lorentz-invariant scalar products of the external momenta. Since momentum conservation allows us to eliminate the momentum of the undetected particle X, the only available antisymmetric Lorentz structure is $p_{K_S}\cdot(p_{\pi^+}-p_{\pi^-})$. This is precisely the structure that appears in Eq. (5.2.53).

Numerical comparison:

$$
BR(K_S \to \pi^+\pi^-\pi^0)_{\text{ChPT}} = 2.6\times10^{-7}, \qquad (5.2.55)
$$

$$
BR(K_S \to \pi^+\pi^-\pi^0)_{\text{exp}} = \left(3.5^{+1.1}_{-0.9}\right)\times10^{-7}. \qquad (5.2.56)
$$

The consistency between the theoretical prediction and experimental measurement within uncertainties provides a validation of the method. This confirms that the procedure can be reliably extended to the case of the axion.

5.2.3.4 $K \to \pi^+\pi^- a$

The Feynman diagrams contributing to this process are shown in Fig. 5.15.

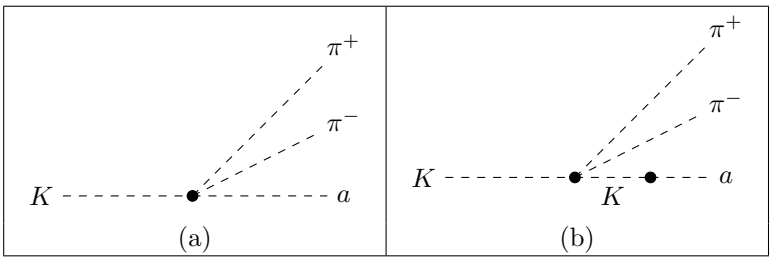

Figure 5.15: Feynman diagrams for $K \to \pi^+\pi^- a$

The amplitudes for K^0 read:

$$i\mathcal{M}_{fi}^{(a)}[K^0] = i\frac{\sqrt{2}(k_A)_{23}^*}{6F_0 f_a}(2p_a\cdot p_{\pi^+} - p_a\cdot p_{\pi^-} + p_a\cdot p_{K^0})\ , \tag{5.2.57}$$

$$\begin{aligned} i\mathcal{M}_{fi}^{(b)}[K^0] = -i\frac{\sqrt{2}(k_A)_{23}^*}{12F_0 f_a}\frac{m_a^2}{m_a^2-m_{K^0}^2}(&-p_{\pi^-}\cdot p_{\pi^+} - p_a\cdot p_{\pi^-} + 2p_a\cdot p_{\pi^+} \\ &- 2p_{K^0}\cdot p_{\pi^-} + p_{K^0}\cdot p_{\pi^+} + p_a\cdot p_{K^0})\ . \end{aligned} \tag{5.2.58}$$

Combining both contributions, we obtain the total amplitude for K_S:

$$\begin{aligned} \mathcal{M}_{fi}[K_S] =& \frac{\mathrm{Re}[(k_A)_{23}]}{2F_0 f_a}\frac{m_{K^0}^2}{m_{K^0}^2-m_a^2}p_{K_S}\cdot(p_{\pi^-}-p_{\pi^+}) \\ &+ i\frac{\mathrm{Im}[(k_A)_{23}]}{6F_0 f_a}\left[\frac{m_{K^0}^2}{m_{K^0}^2-m_a^2}(p_{K_S}\cdot(p_{\pi^-}+p_{\pi^+}) + 2p_{\pi^+}\cdot p_{\pi^-}) - \frac{2m_{K^0}^2-m_a^2}{m_{K^0}^2-m_a^2}(m_{K^0}^2-m_{\pi^\pm}^2)\right]\ . \end{aligned} \tag{5.2.59}$$

Let us verify that this expression indeed respects the CP symmetry. The part proportional to the real component is antisymmetric under the exchange $\pi^+ \leftrightarrow \pi^-$, while the part multiplying the imaginary component is symmetric. However, under a CP transformation, the imaginary part acquires a complex conjugation, effectively flipping its sign. Therefore, the amplitude is thus manifestly antisymmetric under CP, as expected.

5.2.4 Results

5.2.4.1 Branching Ratio formulae

Previously, we introduced the formulae for the doubly differential widths in terms of the amplitude for the different processes under study: $K_S \to \{\mu^+\mu^-;\pi^+\pi^-\}a$ and $K^+ \to \pi^+\pi^0 a$ (see Section 5.2.3). If we write these processes generically as $K \to h^+\tilde{h}a$, we can define the Mandelstam variables as $s = (p_K - p_a)^2$ and $t = (p_K - p_{h^+})^2$. Using the following abbreviations:

$$\begin{aligned} \omega_\pi &:= m_a^2 + m_K^2 + 2m_\pi^2 - s - 2t, \\ \omega_\ell &:= m_a^2(m_\ell^2 + m_K^2 - t) + (m_\ell^2 - t)(m_\ell^2 + m_K^2 - s - t), \\ \kappa_\pi &:= \frac{s-4m_\pi^2}{s}\left[m_a^4 + (m_K^2-s)^2 - 2m_a^2(m_K^2+s)\right], \\ \kappa_\ell &:= \frac{(s-4m_\ell^2)^{1/3}}{s}\left[m_a^4 + (m_K^2-s)^2 - 2m_a^2(m_K^2+s)\right], \\ \eta_\pi &:= 12288\pi^3 F_0^2(m_a^2-m_K^2)^2, \\ \eta_\ell &:= 12288\pi^5 F_0^2(m_a^2-m_K^2)^2 s^2, \\ \rho &:= 3s - 3m_K^2 + m_a^2 - 2\frac{m_a^2 m_\pi^2}{m_K^2}. \end{aligned} \tag{5.2.60}$$

We obtain the following expressions for the doubly differential widths:

$$\begin{aligned} \frac{d^2\Gamma(K_S\to\pi^+\pi^- a)}{ds dt} &= 3m_K\frac{\omega_\pi^2}{\eta_\pi}\left(\frac{\mathrm{Re}(k_A)_{23}}{f_a}\right)^2 + m_K\frac{\rho^2}{3\eta_\pi}\left(\frac{\mathrm{Im}(k_A)_{23}}{f_a}\right)^2\ , \\ \frac{d^2\Gamma(K^+\to\pi^+\pi^0 a)}{ds dt} &= 3m_K\frac{\omega_\pi^2}{\eta_\pi}\left(\frac{|(k_A)_{23}|}{f_a}\right)^2\ , \\ \frac{d^2\Gamma(K_S\to\ell^+\ell^- a)}{ds dt} &= 6m_K\frac{\alpha_{\mathrm{em}}^2|\hat{I}^{(a)}|^2\omega_\ell}{\eta_\ell}\left(\frac{\mathrm{Re}(k_A)_{23}}{f_a}\right)^2\ . \end{aligned} \tag{5.2.61}$$

The variable s is constrained to the range $[2(m_{h^+}+m_{\tilde{h}})^2, (m_K-m_a)^2]$, while $t \in [t_{\min}(s), t_{\max}(s)]$, where the functions $t_{\min,\max}(s)$ are determined by kinematics [Nav+24]. Integrating over t within its kinematic range, we obtain the singly differential widths:

$$\begin{aligned}
\frac{d\Gamma(K_S \to \pi^+\pi^- a)}{ds} &= \frac{\kappa_\pi^{3/2}}{\eta_\pi} m_K \left(\frac{\mathrm{Re}(k_A)_{23}}{f_a}\right)^2 + \frac{\kappa_\pi^{1/2}\rho^2}{3\eta_\pi} m_K \left(\frac{\mathrm{Im}(k_A)_{23}}{f_a}\right)^2 , \\
\frac{d\Gamma(K^+ \to \pi^+\pi^0 a)}{ds} &= \frac{\kappa_\pi^{3/2}}{\eta_\pi} m_K \left(\frac{|(k_A)_{23}|}{f_a}\right)^2 , \\
\frac{d\Gamma(K_S \to \ell^+\ell^- a)}{ds} &= m_K \frac{\alpha_{\mathrm{em}}^2 |\hat{I}^{(a)}|^2 \kappa_\ell^{3/2}(2m_\ell^2 + s)}{\eta_\ell} \left(\frac{\mathrm{Re}(k_A)_{23}}{f_a}\right)^2 .
\end{aligned} \tag{5.2.62}$$

It is worth commenting on the dependence on $(k_A)_{23}$ in (5.2.61). The decay $K_S \to \ell^+\ell^- a$, like $K_S \to \ell^+\ell^-\pi^0$, is dominantly mediated by the CP-even component of the K_S. Since each of the final states is a CP eigenstate, including the $\ell^+\ell^-$ state, which originates from a virtual photon, we find that $\mathcal{M}_{fi}(K_S \to \ell^+\ell^- a) \propto \mathrm{Re}(k_A)_{23}$. On the other hand, in the case of $K_S \to \pi^+\pi^- a$, the $\pi^+\pi^-$ pair has both CP-even and CP-odd components. Consequently, $\mathcal{M}_{fi}(K_S \to \pi^+\pi^- a)$ has contributions from both $\mathrm{Re}(k_A)_{23}$ and $\mathrm{Im}(k_A)_{23}$.

5.2.4.2 Sensitivity

The inequalities in Eq. (5.2.5) can be used to estimate the sensitivity to the ratio $(k_A)_{23}/f_a$ from different channels. By "saturating" these inequalities, i.e., treating them as equalities, we can infer the maximal value of this ratio. The values obtained for each channel are summarized in Table 5.4.

Table 5.4: Constraints on the ratio of the coupling to f_a, in units of $10^{-3}, \mathrm{TeV}^{-1}$, derived from Eq. (5.2.5). A separate constraint is provided for each of the considered channels (table rows), distinguishing between small and large m_a. Constraints on $\mathrm{Re}(k_A)_{23}$, $\mathrm{Im}(k_A)_{23}$, or $|(k_A)_{23}|$ are reported where applicable (table columns). See the text for more details.

	$m_a \ll m_\pi$			$m_a = m_\pi$		
Channel	$\frac{\lvert\mathrm{Re}[(k_A)_{23}]\rvert}{f_a}$	$\frac{\lvert\mathrm{Im}[(k_A)_{23}]\rvert}{f_a}$	$\frac{\lvert(k_A)_{23}\rvert}{f_a}$	$\frac{\lvert\mathrm{Re}[(k_A)_{23}]\rvert}{f_a}$	$\frac{\lvert\mathrm{Im}[(k_A)_{23}]\rvert}{f_a}$	$\frac{\lvert(k_A)_{23}\rvert}{f_a}$
$K_S \to \mu^+\mu^- a$	48	—	—	5.7	—	—
$K_S \to \pi^+\pi^- a$	3.0	1.0		3.7	0.57	
$K^+ \to \pi^+\pi^0 a$	—	—	0.018	—	—	2.6

By fixing the coupling-to-f_a ratio for each channel, we can determine the corresponding f_a value as a function of the assumed coupling. This relation is shown in Fig. 5.16 in the $\mathrm{Re}(k_A)_{23}$ vs. $\mathrm{Im}(k_A)_{23}$ plane. Naturally, both the coupling and f_a scale proportionally. Choosing a reference value for a "large" coupling allows us to determine the maximal f_a scale probed by each channel. We define this scale as the f_a value for which either the real or imaginary part of $(k_A)_{23}$, or its absolute value (depending on the channel), is equal to or closest to 10. The contour with the largest f_a value in each panel of Fig. 5.16 corresponds to this "large" coupling choice.

Our sensitivity study highlights the potential for dedicated experimental analyses. It is interesting to compare our results with existing experimental searches, which, to our knowledge, are available only for the $K^+ \to \pi^+\pi^0 a$ decay. The most recent dedicated search is presented in [Sad+24] for various choices of the ALP mass[8].

For $m_a \ll m_\pi$, the bound on $|(k_A)_{23}|$ inferred from (5.2.5) is only about a factor of ~ 2 stronger than the one obtained in [Sad+24]. For $m_a = m_\pi$, the bound derived from (5.2.5) is still compatible with [Sad+24] but is approximately an oom weaker. This comparison is illustrated in the right panels of Fig. 5.16, which correspond to the K^+ channel. The red dashed lines are obtained by replacing S_{eff} in (5.2.5) with the actual BR limit from [Sad+24], depending on the value of m_a. In these lines, the f_a value is set equal to that of the outermost contour (indicated by a dotted line) in each respective panel, ensuring direct comparability. In short, the red dashed lines represent actual experimental limits, obtained by identifying a ChPT-based BR calculation (without prior assumptions on the axion mass) with the experimental bound from [Sad+24].

[8]The previous best upper limit can be inferred from [Tch+04], while the PDG quotes Ref. [Adl+01]. These earlier searches assumed a pure phase-space distribution, which Ref. [Sad+24] demonstrates to be a rough approximation. See also [Lo 21] for a sensitivity study.

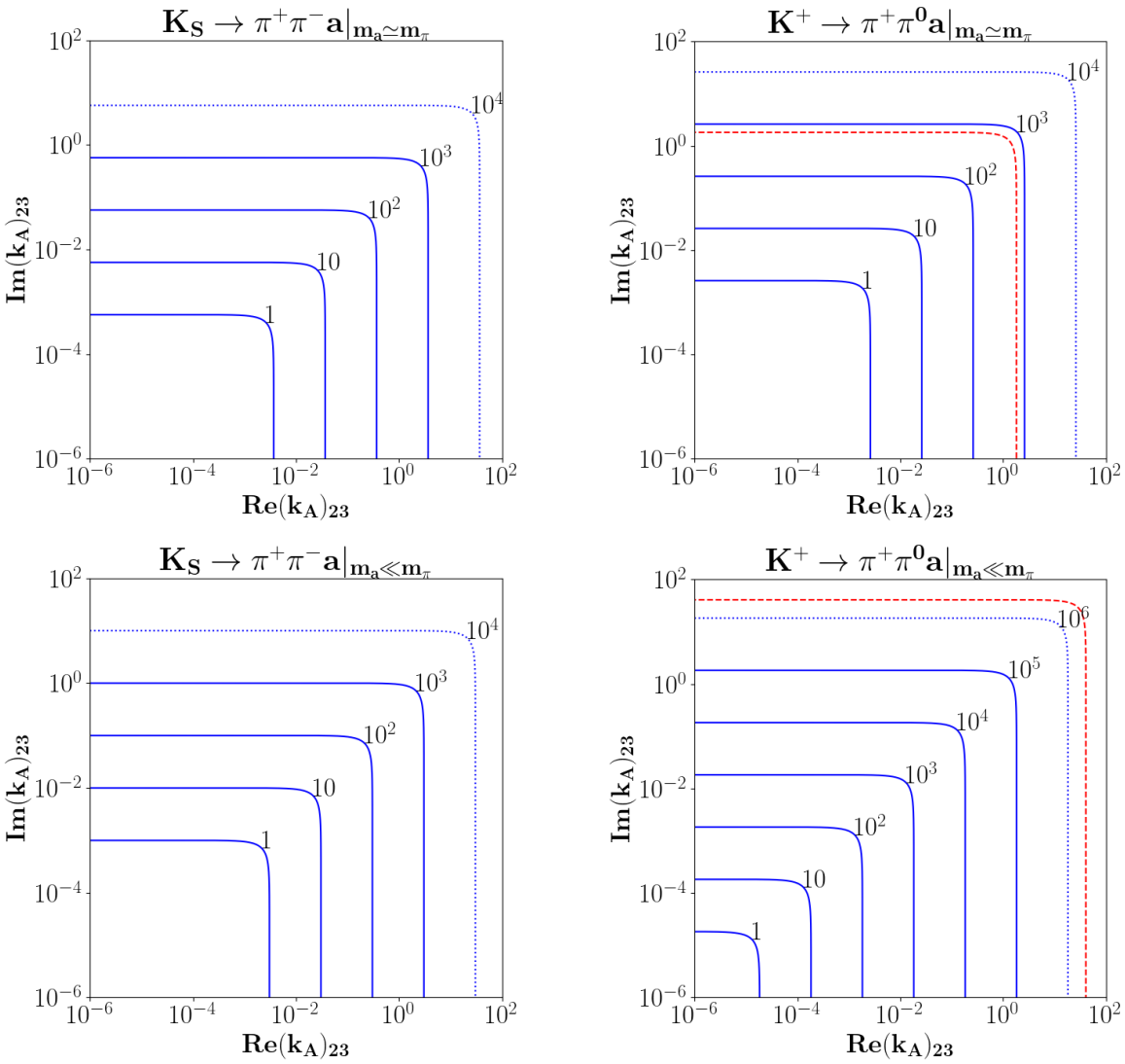

Figure 5.16: Contours of constant f_a (in TeV) in the $\mathrm{Re}(k_A)_{23}$ vs. $\mathrm{Im}(k_A)_{23}$ plane. The upper panels compare $K_S \to \pi^+\pi^- a$ and $K^+ \to \pi^+\pi^0 a$ for $m_a = m_\pi$. The lower panels show the same comparison for $m_a \ll m_\pi$.

These constraints can be rewritten as[9]

$$\frac{|(k_A)_{23}|}{f_a} \leq 10^{-3}\ \mathrm{TeV}^{-1} \times \begin{cases} 0.041 & \text{for } m_a \ll m_\pi \\ 0.18 & \text{for } m_a = m_\pi \end{cases} . \tag{5.2.63}$$

These findings confirm that our approach yields results consistent with existing searches. In cases where a direct comparison is possible (i.e., for $K^+ \to \pi^+\pi^0 a$), our predictions are either of the same oom or slightly weaker, as expected, because we deliberately adopted a conservative approach. Consequently, if dedicated searches for K_S decays were carried out, one would expect similar or even stronger constraints. This makes, for example, the value 0.57 in Table 5.4 particularly interesting. Thus, our results strongly suggest that dedicated searches in the proposed K_S channels could significantly improve constraints on $(k_A)_{23}$, potentially by an oom.

[9]Taking astrophysical constraints into account leads to significantly stronger bounds. For instance, in the limit $m_a \ll m_\pi$, and using the emissivity within Supernovæ (SNe), one obtains: $\frac{|(k_A)_{23}|}{f_a} \leq 10^{-7}\ \mathrm{TeV}^{-1}$, which is two oom stronger than the result in Eq. (5.2.63). However, these inferred constraints depend on numerous assumptions, such as the poorly known fraction of strange matter in the astrophysical source, as well as the limited knowledge of the source's physical properties – including its emission time, total mass, composition, and geometrical structure, and the mass fraction radiated in axions. These assumptions introduce oom uncertainties that are absent in the controlled environment of collider experiments. For further details, see Section 3.4.

5.2.4.3 Branching ratios differential in s

In each of the channels shown in Fig. 5.16, we extract the "maximal" value of the coupling-to-f_a ratio, i.e., the ratio that saturates the corresponding bound in (5.2.5). These values are collected in Table 5.4. We chose to derive a separate ratio for each considered channel, further distinguishing between the cases of small and large m_a.

From (5.2.62), only the $K_S \to \pi^+\pi^- a$ channel depends separately on $\mathrm{Re}(k_A)_{23}$ and $\mathrm{Im}(k_A)_{23}$. In this case, we consider different assumptions for the short-distance coupling, as shown in the table. The constraint on the real (imaginary) part of $(k_A)_{23}$ is obtained by setting the imaginary (real) part to zero. For each bound, we retain only the first two significant digits.

We use the ratios in Table 5.4 to determine the "maximal" spectra predicted for the singly differential BRs, which are shown in Fig. 5.17.

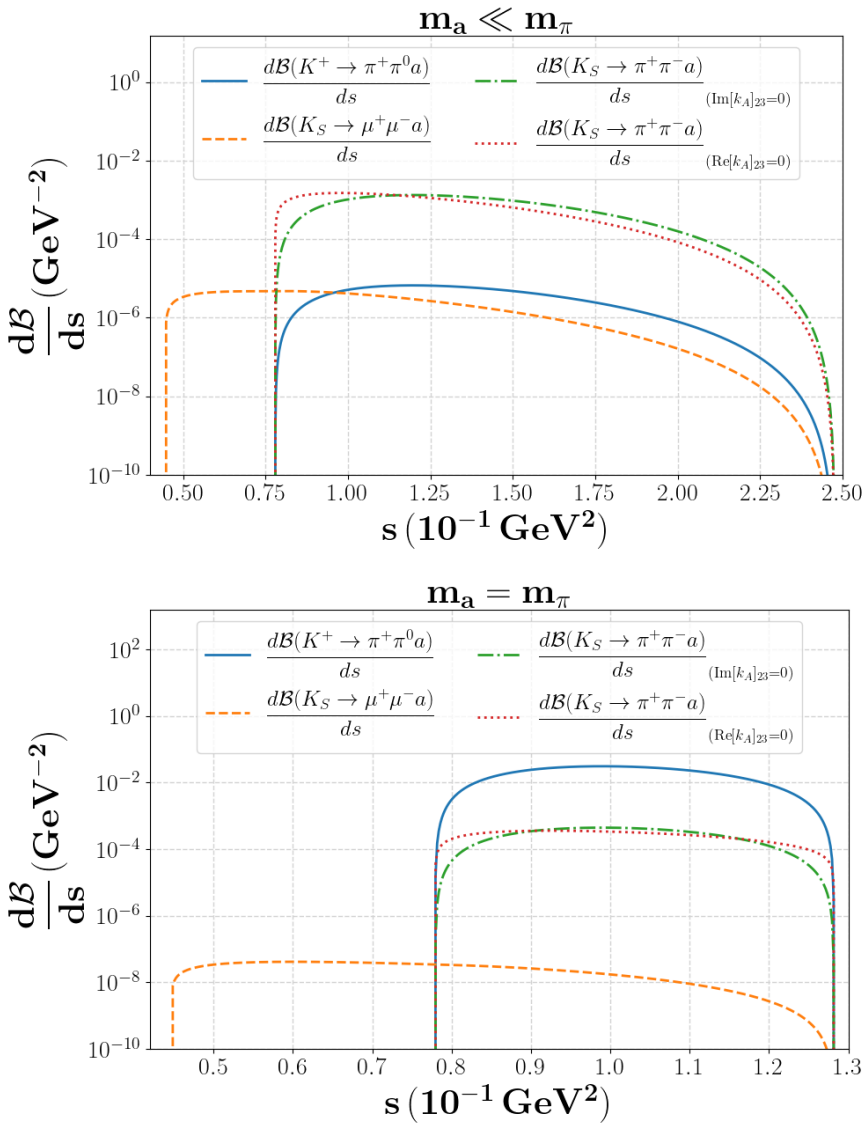

Figure 5.17: Singly differential BRs for the different $K \to \{\pi\pi, \mu\mu\}a$ channels considered. The two panels correspond to $m_a \ll m_\pi$ (upper) or $m_a = m_\pi$ (lower). The couplings are set by assuming saturation of the bounds in (5.2.2), corresponding to a "maximal" coupling value, separately for each channel, as discussed around Table 5.4.

5.2.4.4 Doubly differential widths

The bound that can be inferred from a total BR averages over regions with both smaller and larger sensitivity, producing an overall bound. In this section, we aim to explore the possibility of improving the bound derived from a total BR by considering only the regions in the Dalitz plot ($\frac{d^2BR}{dsdt}$ in the s-t plane) that simultaneously have the largest yield and the largest reconstruction efficiency.

The doubly differential BRs for the channels under consideration are shown in the s vs. t plane in Figures 5.18-5.21. The four figures show the following cases: $K^+ \to \pi^+\pi^0 a$, $K_S \to \pi^+\pi^- a$ from $\mathrm{Re}(k_A)_{23}$ or $\mathrm{Im}(k_A)_{23}$, and $K_S \to \mu^+\mu^- a$, respectively. The two panels in each figure refer to the instances of $m_a \ll m_\pi$ and $m_a = m_\pi$, respectively. We have chosen to use the same axis limits for $m_a \ll m_\pi$ and $m_a = m_\pi$ to properly visualize the reduction in the phase space due to the non-zero mass of m_a.

Figures 5.18-5.19 show that the Dalitz plot is dominated by two relatively narrow regions of phase space. By inspecting (5.2.62), we observe that the BRs in the channels of interest depend on s and t through ω_π^2. The large region in the Dalitz plot with a small local BR corresponds to small ω_π, i.e. $s + 2t \simeq m_a^2 + m_K^2 + 2m_\pi^2$, while the two narrow regions with most of the statistics occur for maximal or minimal $s + 2t$.

On the other hand, Figures 5.20-5.21 suggest that the region of lower s is the most significant, regardless of the t value. However, this preference is less pronounced compared to Figures 5.18-5.19.

In summary, especially for the processes shown in Figures 5.18-5.19, the s vs. t plane is primarily populated in very specific regions. An interesting question is whether the highest reconstruction efficiencies, as a function of s and t, can realistically be found in these most populated regions. Fully addressing this question in a given channel would require a comprehensive search in that channel. Here, we limit ourselves to exploring this question using the fast-simulation tool described in [Cho+20], which is designed to estimate the performance of an LHCb-like detector. Thus, we focus on the $K_S \to \pi^+\pi^- a$ channel in Figures 5.19-5.20, and the $K_S \to \mu^+\mu^- a$ channel in Fig. 5.21, i.e., on the two channels that can be considered at LHCb. We simulate proton-proton collisions according to the current Large Hadron Collider (LHC) setup and sample reconstructed events of the type $K_S \to \{\pi^+\pi^-, \mu^+\mu^-\}$ plus a neutral spinless particle. As detailed in [Cho+20], the detector simulation is an improved version of the fast-simulation framework used in [Alv+19]. We then plot, in (s,t)-plane bins, the number of events where the two charged final states are correctly reconstructed, normalized to the total yield in the same bin. In Fig. 5.22, we provide an explicit example for the di-muon channel and for $m_a = m_\pi$. This plot shows a pattern of efficiencies monotonically decreasing with increasing s and being roughly insensitive to t. Comparing this with the rightmost panel of Fig. 5.21, we see that regions with higher efficiencies matched to regions with larger yields. Similar considerations can be made for all the other cases.

This is particularly interesting because by studying the BRs not in total, but bin by bin, it would be possible - if the efficiency maps are similar to the physical maps - to improve the results.

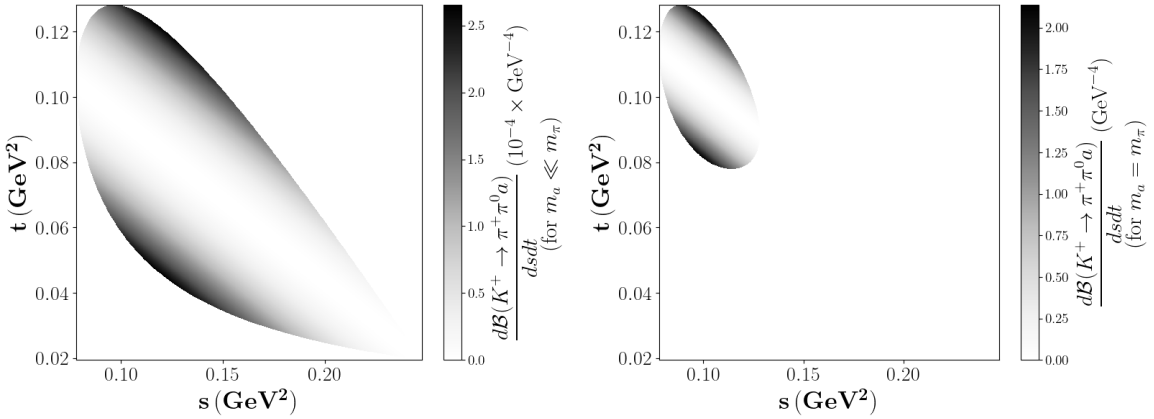

Figure 5.18: Doubly differential $BR(K^+ \to \pi^+\pi^0 a)$ in the $\{s, t\}$ plane, with $m_a \ll m_\pi$ (left) and $m_a = m_\pi$ (right). In either case we assume the axion coupling strength to saturate the relevant inequality in (5.2.2).

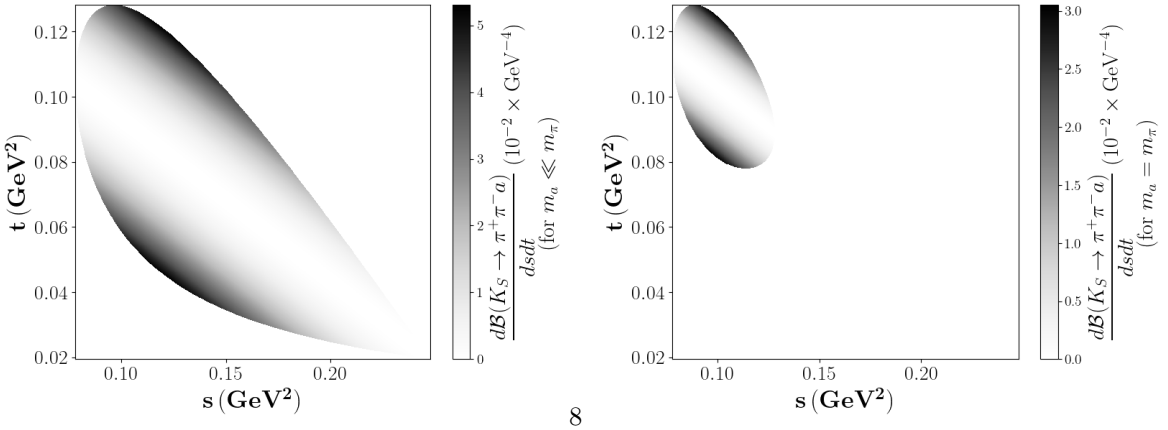

Figure 5.19: Same as Fig. 5.18, but for the contribution to $BR(K_S \to \pi^+\pi^- a)$ proportional to $\mathrm{Re}(k_A)_{23}$.

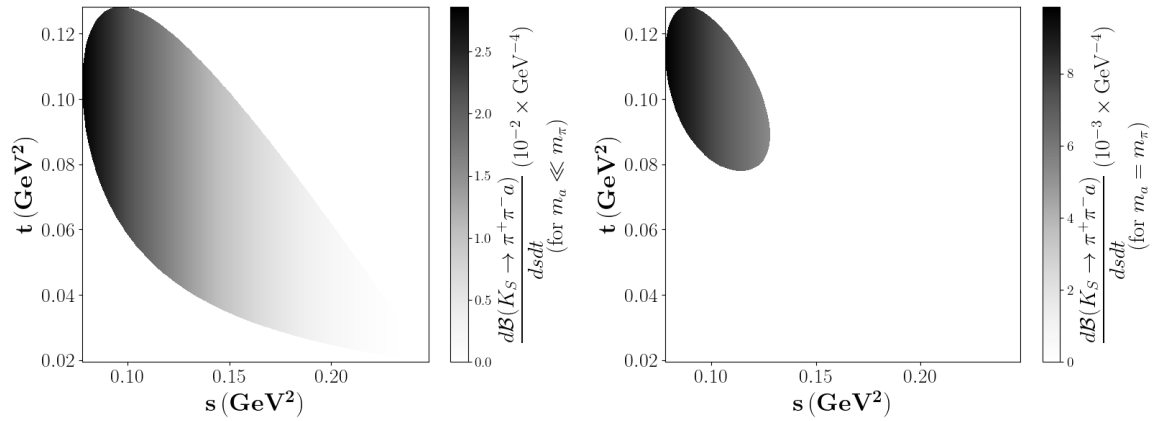

Figure 5.20: Same as Fig. 5.18, but for the contribution to $BR(K_S \to \pi^+\pi^- a)$ proportional to $\mathrm{Im}(k_A)_{23}$.

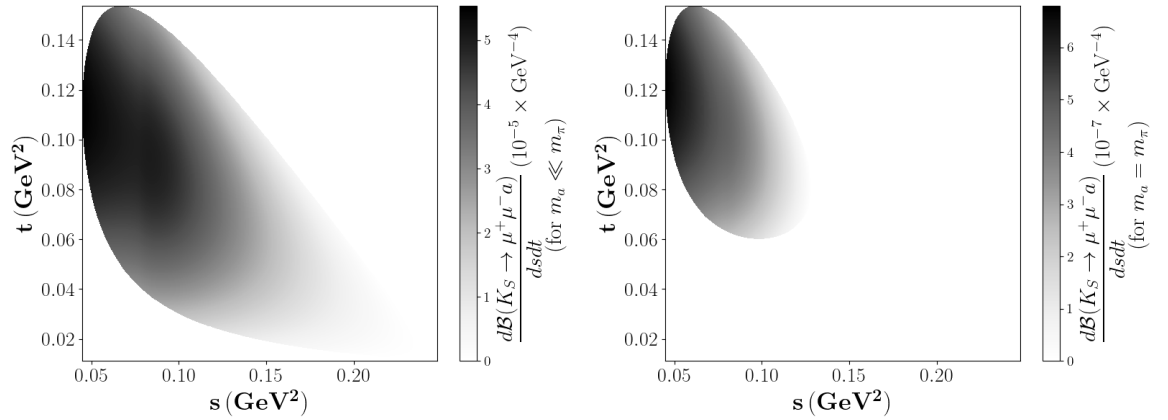

Figure 5.21: Same as Fig. 5.18 but for $BR(K_S \to \mu^+\mu^- a)$.

5.2.5 Conclusion

In this section, we examine three-body kaon decays involving the $\pi\pi a$ or $\mu\mu a$ channels. First, we conducted a comprehensive theoretical analysis within the framework of ChPT extended by the presence of an axion. Based on this theoretical study, we then performed a sensitivity analysis aimed at constraining the ratio between the fundamental axial axion-down-strange coupling and the axion

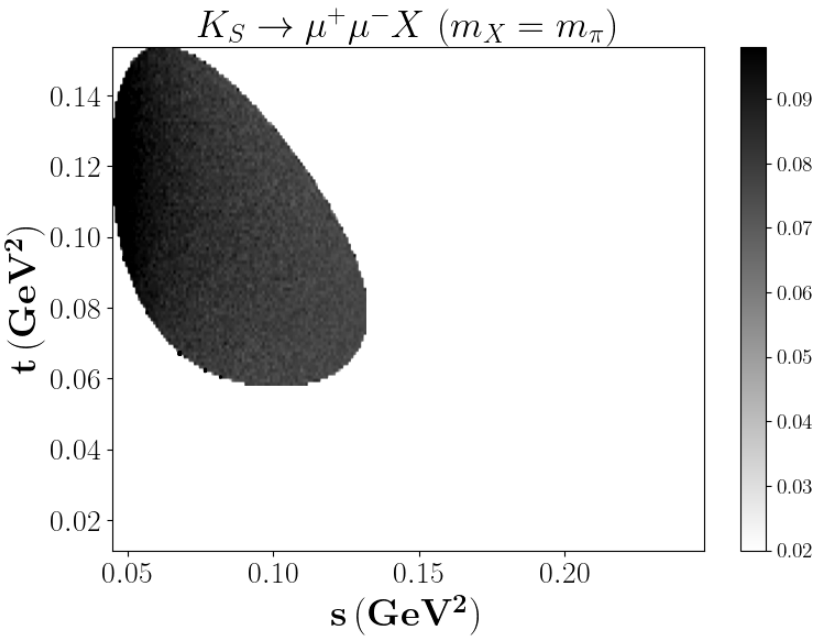

Figure 5.22: Example of a reconstruction efficiency map, obtained through the fast-simulation code [Cho+20] as detailed in the text. This example corresponds to the case of $K_S \to \mu^+\mu^- X$ with $m_X = m_\pi$, where X is a generic spinless particle, i.e. not necessarily an axion.

decay constant f_a.

To estimate the sensitivity of the different channels, we first identified the main sources of irreducible background noise. Then, we quantified the sensitivity based on the uncertainties associated with these backgrounds, specifically by assessing how well these backgrounds can be controlled. Following this methodological approach, we determined that targeted searches could explore values of f_a in the range of 10^4 to 10^6 TeV. This result highlights the strong potential of these channels in the search for axion-related signals.

To validate this conclusion, we specifically examined the case of the decay $K^+ \to \pi^+\pi^0 a$, for which a recent experimental search is available. In this context, we are able to establish an explicit experimental limit, see (5.2.63). This comparison also suggests that our approach provides conservative sensitivity estimates, implying that dedicated searches in these specific channels could achieve significantly better performance than anticipated. If this is the case, three-body kaon decays could become the preferred reference channels for constraining the axial coupling $(k_A)_{23}$.

References

[Aai+15] Roel Aaij et al. *LHCb Detector Performance*. In: *Int. J. Mod. Phys. A* 30.07 (2015), p. 1530022. DOI: 10.1142/S0217751X15300227. arXiv: 1412.6352 [hep-ex].

[Adl+01] S. Adler et al. *Search for the decay $K^+ \to \pi^+\pi^0\nu\bar{\nu}$*. In: *Phys. Rev. D* 63 (2001), p. 032004. DOI: 10.1103/PhysRevD.63.032004. arXiv: hep-ex/0009055.

[Adl+08] S. Adler et al. *Measurement of the $K^+ \to \pi^+\nu\bar{\nu}$ branching ratio*. In: *Physical Review D* 77.5 (Mar. 2008). ISSN: 1550-2368. DOI: 10.1103/physrevd.77.052003. URL: http://dx.doi.org/10.1103/PhysRevD.77.052003.

[Ahn+19] J. K. Ahn et al. *Search for $K_L \to \pi^0\nu\bar{\nu}$ and $K_L \to \pi^0 X^0$ Decays at the J-PARC KOTO Experiment*. In: *Physical Review Letters* 122.2 (Jan. 2019). ISSN: 1079-7114. DOI: 10.1103/physrevlett.122.021802. URL: http://dx.doi.org/10.1103/PhysRevLett.122.021802.

[Alv+19] A. A. Alves Junior et al. *Prospects for Measurements with Strange Hadrons at LHCb*. In: *JHEP* 05 (2019), p. 048. DOI: 10.1007/JHEP05(2019)048. arXiv: 1808.03477 [hep-ex].

[Bau+21] Martin Bauer et al. *Consistent Treatment of Axions in the Weak Chiral Lagrangian*. In: *Phys. Rev. Lett.* 127.8 (2021), p. 081803. DOI: 10.1103/PhysRevLett.127.081803. arXiv: 2102.13112 [hep-ph].

[BDB03] Johan Bijnens, Pierre Dhonte, and Fredrik Borg. *$K \to 3\pi$ decays in chiral perturbation theory*. In: *Nucl. Phys. B* 648 (2003), pp. 317–344. DOI: 10.1016/S0550-3213(02)00970-7. arXiv: hep-ph/0205341.

[BGS20] Joachim Brod, Martin Gorbahn, and Emmanuel Stamou. *Standard-Model Prediction of ϵ_K with Manifest Quark-Mixing Unitarity*. In: *Physical Review Letters* 125.17 (Oct. 2020). ISSN: 1079-7114. DOI: 10.1103/physrevlett.125.171803. URL: http://dx.doi.org/10.1103/PhysRevLett.125.171803.

[Bon+23] Marcella Bona et al. *New UTfit Analysis of the Unitarity Triangle in the Cabibbo-Kobayashi-Maskawa scheme*. In: *Rend. Lincei Sci. Fis. Nat.* 34 (2023), pp. 37–57. DOI: 10.1007/s12210-023-01137-5. arXiv: 2212.03894 [hep-ph].

[Cav+25a] Mael Cavan-Piton et al. *Probing QCD Axions or axion-like particles in three-body K decays*. In: *JHEP* 06 (2025), p. 039. DOI: 10.1007/JHEP06(2025)039. arXiv: 2411.04170 [hep-ph].

[Cho+16] Veronika Georgieva Chobanova et al. *Sensitivity of LHCb and its upgrade in the measurement of $\mathcal{B}(K_S^0 \to \pi^0\mu^+\mu^-)$*. In: *LHCb-PUB-2016-017* (2016).

[Cho+20] Veronika Chobanova et al. *Fast simulation of a forward detector at 50 and 100 TeV proton-proton colliders*. In: (Dec. 2020). arXiv: 2012.02692 [hep-ex].

[EPR87] Gerhard Ecker, Antonio Pich, and Eduardo de Rafael. *$K \to \pi\ell^+\ell^-$ Decays in the Effective Chiral Lagrangian of the Standard Model*. In: *Nucl. Phys. B* 291 (1987), pp. 692–719. DOI: 10.1016/0550-3213(87)90491-3.

[FG89] S. Fajfer and J. M. Gerard. *A Simple Chiral Lagrangian Approach to $K \to \pi\pi\pi$ Decays and ϵ'_{+0-}*. In: *Z. Phys. C* 42 (1989), p. 425. DOI: 10.1007/BF01548447.

[Lo 21] Prisco Lo Chiatto. "Theoretical analysis and sensitivity study for the NA62 experiment of the decay of the K meson into two pions and a pseudoscalar particle". MA thesis. U. Modena (main), Oct. 2021.

[Mar+20] Jorge Martin Camalich et al. *Quark Flavor Phenomenology of the QCD Axion*. In: *Phys. Rev. D* 102.1 (2020), p. 015023. DOI: 10.1103/PhysRevD.102.015023. arXiv: 2002.04623 [hep-ph].

[Nav+24] S. Navas et al. *Review of particle physics*. In: *Phys. Rev. D* 110.3 (2024), p. 030001. DOI: 10.1103/PhysRevD.110.030001.

[Oga+11] R. Ogata et al. *Study of the $K_L^0 \to \pi^0\pi^0\nu\bar{\nu}$ decay*. In: *Physical Review D* 84.5 (Sept. 2011). ISSN: 1550-2368. DOI: 10.1103/physrevd.84.052009. URL: http://dx.doi.org/10.1103/PhysRevD.84.052009.

[Sad+24] A. S. Sadovsky et al. *Searches for the light invisible axion-like particle in $K^+ \to \pi^+\pi^0 a$ decay*. In: *Eur. Phys. J. C* 84.3 (2024), p. 266. DOI: 10.1140/epjc/s10052-024-12444-y. arXiv: 2310.16429 [hep-ex].

[Tch+04] O. G. Tchikilev et al. *Search for light pseudoscalar sgoldstino in K- decays*. In: *Phys. Lett. B* 602 (2004), pp. 149–156. DOI: 10.1016/j.physletb.2004.10.002. arXiv: hep-ex/0308061.

Conclusion

The search for physics Beyond the Standard Model (BSM) spans an increasingly diversified experimental landscape, motivated by a host of unresolved phenomena ranging from the nature of Dark Matter (DM) to the strong CP problem. Among the theoretically compelling and experimentally elusive candidates that could address some of these issues, the Quantum Chromodynamics (QCD) axion and its generalizations–Axion-like Particles (ALPs)–have emerged as versatile mediators of new physics. Their suppressed yet structured interactions with Standard Model (SM) particles, governed by an energy scale f_a often far beyond the reach of direct production, make them prime targets for indirect detection strategies.

In this thesis, we have pursued a multi-pronged investigation of axion phenomenology across three distinct physical environments: compact astrophysical objects, neutrino detection facilities, and high-energy particle colliders. Each of these domains offers a unique window into the axion parameter space and probes complementary couplings and energy regimes. The unifying thread of this work lies in the development and application of a low-energy effective field theory framework, rooted in Chiral Perturbation Theory (ChPT), that consistently describes axion interactions with hadronic matter.

In Chapters 1 and 2, we established the theoretical foundations necessary for this endeavor. We reviewed the construction of the QCD axion from the Peccei–Quinn mechanism and its embedding in realistic models such as Kim-Shifman-Vainshtein-Zakharov (KSVZ) and Dine-Fischler-Srednicki-Zhitnitsky (DFSZ), highlighting the axion's dual role in solving the strong CP problem and acting as a DM candidate. We then extended the ChPT formalism to incorporate axion interactions, resulting in an effective Lagrangian applicable across astrophysical and collider contexts.

Chapter 3 allowed to explore the role of strange matter in the emission of axions from core-collapse Supernovæ (SNe), a subject hitherto unexplored. By including the full octets of baryons and mesons in our calculations, we quantified axion emissivities arising from baryon-meson scatterings and baryon decays, under various equations of state and thermodynamic conditions. For the first time, we derived constraints on the axion-strange-strange coupling, and improved existing bounds on the axial axion-down-strange coupling, reaching sensitivities at the level of $\mathcal{O}(10^{-2})$ for $f_a = 10^9$ GeV. These results indicate that strange matter can play a significant role in the astrophysical production of axions, and should not be neglected in Supernova (SN) cooling studies.

In Chapter 4, we examined the detectability of a relic axion flux on Earth, originating from a nearby SN, using future large-scale water Cherenkov detectors such as Hyper-Kamiokande (HK). By computing axion-induced processes like $a+N \to N+\gamma$ and $a+N \to N+\pi^0$, we identified a potentially detectable signal even for the QCD axion, particularly through the π^0 channel whose energy spectrum is well separated from SM backgrounds induced by neutrinos. Although interactions involving strange baryons yield weaker signals, they remain phenomenologically relevant if first-generation couplings are suppressed. These findings open a novel detection strategy based on coherent axion signatures across astrophysical production and terrestrial absorption.

Chapter 5 explored the potential of flavor experiments at colliders to constrain axion-like particles via rare kaon decays. While two-body decays like $K \to \pi a$ already provide stringent constraints on the vectorial flavor-changing couplings, we highlighted that axial couplings remain significantly less bounded. We proposed new three-body decay modes such as $K \to \pi\pi a$ and $K \to \mu\mu a$, which, despite lower Branching Ratios (BRs), benefit from favorable kinematic configurations and excellent vertex reconstruction capabilities at Large Hadron Collider beauty (LHCb). Sensitivity projections suggest that these channels could probe f_a scales as high as 10^6 TeV, substantially extending current bounds and accessing otherwise unexplored regions of parameter space.

The work presented here is not intended as a complete phenomenological survey but rather as an exploration of key, previously overlooked contributions, in completely different contexts, and yet within a unifying thread. Several avenues for future research naturally arise. A comprehensive study incorporating all significant SN production and detector-level absorption processes could yield detailed spectral predictions for axion-induced Cherenkov signals, conditional on the axion's parameter space. However, the main source of uncertainty remains the limited understanding of astrophysical sources themselves–particularly their equations of state and thermodynamic profiles. Thus, progress on the theoretical modeling of SNe will be critical for enhancing the predictive power of such studies.

Furthermore, the role of strange matter in neutron stars, where conditions differ from those in SNe, deserves focused attention. Strange baryons could contribute non-trivially to axion emission processes in this environment, complementing nucleon-induced channels and potentially yielding distinctive observational signatures. On the collider side, a deeper exploration of axial flavor-changing interactions, using both existing and novel decay modes, could yield critical constraints.

In summary, this thesis demonstrates the power and necessity of a multi-pronged approach to axion searches. By systematically bridging theoretical modeling with experimental opportunities across energy scales and sectors, we have uncovered new, highly sensitive strategies to constrain axion properties and couplings–particularly involving strange matter–and laid the groundwork for future discovery-oriented investigations. The results support the notion that QCD axions and ALPs remain among the most realistic and theoretically motivated candidates for new physics, whose indirect effects may soon be within reach of our most advanced experimental facilities.

Appendix A

Basic tools and conventions

A.1 Conventions

Throughout this manuscript, we adopt the mostly-minus metric signature convention, which is standard in particle physics. Calculations are performed in natural units, where the fundamental constants c, $\hbar$, ε_0, and k_B are set to unity ($c = \hbar = \varepsilon_0 = k_B = 1$), thereby simplifying the appearance of physical equations. The sign convention for the Levi-Civita tensor is $\epsilon^{0123} = +1$.

The definition of a parameter is denoted by $:=$.

For intervals, we adopt the following notations: $[a, b]$ denotes the closed interval including both endpoints; $]a, b]$ and $[a, b[$ denote semi-open intervals, excluding the left or right endpoint respectively; and $]a, b[$ denotes the open interval excluding both endpoints. The notation $[\![a, b]\!] = [a, b] \cap \mathbb{Z}$ represents the set of integers between a and b, inclusive.

A.2 Pauli and Gell-Mann matrices

The Pauli matrices, which form a basis of the Lie algebra $\mathfrak{su}(2)$ consisting of Hermitian, traceless 2×2 matrices, are given by

$$\sigma^1 = \begin{pmatrix} 0 & 1 \\ 1 & 0 \end{pmatrix} \ , \quad \sigma^2 = \begin{pmatrix} 0 & -i \\ i & 0 \end{pmatrix} \ , \quad \sigma^3 = \begin{pmatrix} 1 & 0 \\ 0 & -1 \end{pmatrix} \ . \tag{A.2.1}$$

The Gell-Mann matrices, which generalize this basis to $\mathfrak{su}(3)$, are

$$\lambda^1 = \begin{pmatrix} 0 & 1 & 0 \\ 1 & 0 & 0 \\ 0 & 0 & 0 \end{pmatrix} \ , \quad \lambda^2 = \begin{pmatrix} 0 & -i & 0 \\ i & 0 & 0 \\ 0 & 0 & 0 \end{pmatrix} \ , \quad \lambda^3 = \begin{pmatrix} 1 & 0 & 0 \\ 0 & -1 & 0 \\ 0 & 0 & 0 \end{pmatrix} \ , \quad \lambda^4 = \begin{pmatrix} 0 & 0 & 1 \\ 0 & 0 & 0 \\ 1 & 0 & 0 \end{pmatrix} \ , \tag{A.2.2}$$
$$\lambda^5 = \begin{pmatrix} 0 & 0 & -i \\ 0 & 0 & 0 \\ i & 0 & 0 \end{pmatrix} \ , \quad \lambda^6 = \begin{pmatrix} 0 & 0 & 0 \\ 0 & 0 & 1 \\ 0 & 1 & 0 \end{pmatrix} \ , \quad \lambda^7 = \begin{pmatrix} 0 & 0 & 0 \\ 0 & 0 & -i \\ 0 & i & 0 \end{pmatrix} \ , \quad \lambda^8 = \frac{1}{\sqrt{3}} \begin{pmatrix} 1 & 0 & 0 \\ 0 & 1 & 0 \\ 0 & 0 & -2 \end{pmatrix} \ .$$

These matrices are normalized such that

$$\mathrm{Tr}(\sigma^a \sigma^b) = 2\delta^{ab} \ , \quad \mathrm{Tr}(\lambda^a \lambda^b) = 2\delta^{ab} \ . \tag{A.2.3}$$

To complete the basis of Hermitian matrices by including the identity matrix (thus extending from traceless Hermitian matrices to all Hermitian matrices), one adds the appropriately normalized identity matrices:

$$\sigma^0 = \begin{pmatrix} 1 & 0 \\ 0 & 1 \end{pmatrix} \ , \quad \lambda^0 = \sqrt{\frac{2}{3}} \begin{pmatrix} 1 & 0 & 0 \\ 0 & 1 & 0 \\ 0 & 0 & 1 \end{pmatrix} \ . \tag{A.2.4}$$

Appendix B

Observables and specific calculations

B.1 Calculations of observables

B.1.1 Rate of observed events

To compute observable quantities in particle physics, we begin by defining the scattering matrix S_{fi}, which encodes the transition probability amplitude from an initial state i to a final state f for a general process involving n_i incoming particles A_i and n_f outgoing particles B_f, $\sum_{i=1}^{n_i} A_i \to \sum_{f=1}^{n_f} B_f$:

$$S_{fi} = i\mathcal{M}_{fi}(2\pi)^4\delta^4(p_i - p_f)\prod_{i=1}^{n_i}\frac{1}{\sqrt{(2\pi)^3 2E_{A_i}}}\prod_{f=1}^{n_f}\frac{1}{\sqrt{(2\pi)^3 2E_{B_f}}}\ . \tag{B.1.1}$$

Here:

- n_i and n_f are the numbers of initial and final particles, respectively.
- P_i and P_f are the total initial and final four-momenta.
- $\mathcal{M}_{fi}$ is the Feynman amplitude, which contains the dynamics of the interaction.

The transition probability is:

$$P_{fi} = |S_{fi}|^2\ . \tag{B.1.2}$$

To handle the square of the delta function, we use the identity:

$$((2\pi)^4\delta^4(p_i - p_f))^2 \to (2\pi)^4\delta^4(p_i - p_f)\cdot(2\pi)^4\delta^4(0)\ . \tag{B.1.3}$$

We then introduce the interaction time T and volume V as:

$$T = 2\pi\delta^1(0)\ ,\quad V = (2\pi)^3\delta^3(\vec{0})\ . \tag{B.1.4}$$

The transition probability becomes:

$$P_{fi} = TV(2\pi)^4\delta^4(p_i - p_f)|\mathcal{M}_{fi}|^2\prod_{i=1}^{n_i}\frac{1}{(2\pi)^3 2E_{A_i}}\prod_{f=1}^{n_f}\frac{1}{(2\pi)^3 2E_{B_f}}\ . \tag{B.1.5}$$

The squared Feynman amplitude depends on the spin states of the external particles. If all spins are specified, one uses

$$|\mathcal{M}_{fi}(s_{A_1},\ldots,s_{A_{n_i}},s_{B_1},\ldots,s_{B_{n_f}})|^2\ . \tag{B.1.6}$$

However, in most realistic scenarios, the spin states of the incoming particles are unknown and those of the outgoing particles are not measured. Therefore, one must sum over all spin configurations:

$$|\mathcal{M}_{fi}|^2 = \sum_{\{s_{A_i}\},\{s_{B_f}\}}|\mathcal{M}_{fi}(s_{A_1},\ldots,s_{A_{n_i}},s_{B_1},\ldots,s_{B_{n_f}})|^2\ . \tag{B.1.7}$$

Since the initial particles are in definite but unobserved spin states, summing over them would lead to overcounting. To correct this, one averages over the initial spin states:

$$\overline{|\mathcal{M}_{fi}|^2} = \left(\prod_{i=1}^{n_i} \frac{1}{g_{A_i}}\right) |\mathcal{M}_{fi}|^2 \ , \tag{B.1.8}$$

where g_{A_i} is the number of spin degrees of freedom of particle A_i. For a particle of spin s, this is typically $g = 2s + 1$, except for massless spin-1 particles (e.g., photons), where $g = 2$ due to the absence of longitudinal polarization.

Therefore Eq. (B.1.5) becomes

$$P_{fi} = TV(2\pi)^4 \delta^4(p_i - p_f) \overline{|\mathcal{M}_{fi}|^2} \prod_{i=1}^{n_i} \frac{1}{(2\pi)^3 2E_{A_i}} \prod_{f=1}^{n_f} \frac{1}{(2\pi)^3 2E_{B_f}} \ . \tag{B.1.9}$$

The general form of a normalized particle wavefunction is given by:

$$\psi(x) = \frac{1}{\sqrt{(2\pi)^3 2E}} Z e^{ik_\mu x^\mu} \ , \tag{B.1.10}$$

where the factor Z depends on the spin. In a finite volume, where momenta are quantized, the wavefunction becomes:

$$\psi_V(x) = \frac{1}{\sqrt{2EV}} Z e^{ik_\mu x^\mu} \ . \tag{B.1.11}$$

The transition rate (probability per unit time) is then:

$$R_{fi} = \frac{P_{fi}}{T} = (2\pi)^4 \delta^4(p_i - p_f)\, V^{1-n_i-n_f} \overline{|\mathcal{M}_{fi}|^2} \prod_{i=1}^{n_i} \frac{1}{2E_{A_i}} \prod_{f=1}^{n_f} \frac{1}{2E_{B_f}} \ . \tag{B.1.12}$$

To compute the number of physical final states, the rate is multiplied by the number of states in a momentum interval:

$$dP = \prod_{a=1}^{N} d^3\vec{p}_a \ , \tag{B.1.13}$$

where, in a volume V,

$$d^3\vec{\mathcal{N}}_a = \frac{V}{(2\pi)^3} d^3\vec{p}_a \ , \tag{B.1.14}$$

and hence,

$$d\mathcal{N} = \prod_{a=1}^{N} d^3\vec{\mathcal{N}}_a = V^N \prod_{a=1}^{N} \frac{d^3\vec{p}_a}{(2\pi)^3} \ , \tag{B.1.15}$$

N represents the number of momentum unspecified particles, those with fixed momentum do not contribute to the phase space integration.

The rate of observed states becomes:

$$dW_{fi} = R_{fi}\, d\mathcal{N} \ . \tag{B.1.16}$$

The phase space of N elements is defined by:

$$d\Phi_N = (2\pi)^4 \delta^4(p_i - p_f) \prod_{a=1}^{N} \frac{d^3\vec{p}_a}{(2\pi)^3 2E_a} \ . \tag{B.1.17}$$

If we write N_{A_i} the number of particles of species A_i initially present, since the differential transition rate for a single interaction is denoted dW_{fi}, then the differential total number of events rate is[1]

$$d\dot{n} = dW_{fi} \prod_{i=1}^{n_i} N_{A_i} \ . \tag{B.1.18}$$

[1]This approximation assumes that W_{fi} is small enough for multiple interactions to be negligible, which is generally valid in particle physics.

In collider experiments, the particle numbers N_{A_i} are determined by the luminosity and beam fluxes, where their momenta are fixed by the experimental setup, then $N = n_f$. The differential transition rate is then given by the standard expression:

$$dW_{fi} = V^{1-n_i} \left(\prod_{i=1}^{n_i} \frac{1}{2E_{A_i}} \right) \left(\prod_{f=1}^{n_f} \frac{d^3\vec{p}_{B_f}}{(2\pi)^3 2E_{B_f}} \right) \overline{|\mathcal{M}_{fi}|^2} (2\pi)^4 \delta^4(p_i - p_f) \ . \tag{B.1.19}$$

For astrophysical environments, the initial particle densities are determined by:

$$n_{A_i} = \int \frac{d^3\vec{p}_{A_i}}{(2\pi)^3} g_{A_i} f_{A_i}(E_{A_i}) \ , \tag{B.1.20}$$

where g_{A_i} accounts for spin multiplicities (assuming an unpolarized system), and $f(E)$ is the quantum statistical distribution function. Under the ideal gas assumption, this reduces to the Bose-Einstein distribution for particles with integer spin and the Fermi-Dirac distribution for particles with half-integer spin:

$$f(E) = \frac{1}{e^{(E-\mu)/T} + (-1)^{2s+1}} \ . \tag{B.1.21}$$

The differential event rate in a medium, including quantum statistical effects for both initial and final particles, reads:

$$d\dot{n} = V \left(\prod_{i=1}^{n_i} \frac{g_{A_i} f_{A_i}(E_{A_i}) d^3\vec{p}_{A_i}}{(2\pi)^3 2E_{A_i}} \right) \left(\prod_{f=1}^{n_f} \frac{\bar{f}_{B_f}(E_{B_f}) d^3\vec{p}_{B_f}}{(2\pi)^3 2E_{B_f}} \right) \overline{|\mathcal{M}_{fi}|^2} (2\pi)^4 \delta^4(p_i - p_f) \ , \tag{B.1.22}$$

where the final-state quantum factor is:

$$\bar{f}(E) = 1 - (-1)^{2s+1} f(E) = \frac{1}{1 + (-1)^{2s+1} e^{-(E-\mu)/T}} \ . \tag{B.1.23}$$

This accounts for Pauli blocking for fermions ($\bar{f} = 1 - f$) and Bose enhancement for bosons ($\bar{f} = 1 + f$).

Alternatively, one may omit the spin degeneracy factors g_{A_i} in the phase-space elements. In this case, to compensate, one must not average over initial spin states, and instead use the fully summed amplitude:

$$d\dot{n} = V \left(\prod_{i=1}^{n_i} \frac{f_{A_i}(E_{A_i}) d^3\vec{p}_{A_i}}{(2\pi)^3 2E_{A_i}} \right) \left(\prod_{f=1}^{n_f} \frac{\bar{f}_{B_f}(E_{B_f}) d^3\vec{p}_{B_f}}{(2\pi)^3 2E_{B_f}} \right) |\mathcal{M}_{fi}|^2 (2\pi)^4 \delta^4(p_i - p_f) \ . \tag{B.1.24}$$

This convention is used, for instance, in the computation of axion emissivity $dQ_a = E_a d\dot{n}/V$ in [Can+25].

A third, equally valid, convention consists of including spin degeneracy factors g in both the initial and final state phase-space elements, while using the squared amplitude averaged over all spin configurations (initial and final). This is the convention adopted in [Car+21; Lel+23] for emissivity calculations.

All three formulations are equivalent and differ only in the bookkeeping of spin degrees of freedom between the amplitude and the phase-space elements.

B.1.2 Feynman amplitude

Each particle interaction process can be represented as an infinite series of Feynman diagrams, where lines are connected at vertices corresponding to interaction terms defined in the Lagrangian. In practice, only a finite number of diagrams are calculated, typically up to a certain loop order, as the contribution of each diagram decreases with the number of loops. The tree-level contribution involves diagrams with no loops.

To compute the amplitude from a Feynman diagram, one traces back along the fermionic lines and multiplies all contributions, following these rules:

- **External lines:**

Initial/final scalar	1
Initial/final fermion	$u_{\vec{p},s}$ / $\bar{u}_{\vec{p},s}$
Initial/final antifermion	$\bar{v}_{\vec{p},s}$ / $v_{\vec{p},s}$
Initial/final vector	$\epsilon^{\mu}_{\vec{k},\lambda}$ / $\left(\epsilon^{\mu}_{\vec{k},\lambda}\right)^*$

- **Internal lines (propagators):**

Scalar propagator	$\dfrac{i}{p^2 - m^2 + i\epsilon}$
Fermion propagator	$i\dfrac{\not{p} + m}{p^2 - m^2 + i\epsilon}$
Massless vector propagator	$\dfrac{-i\eta_{\mu\nu}}{p^2 + i\epsilon}$
Massive vector propagator	$-i\dfrac{\eta_{\mu\nu} + p_\mu p_\nu/m^2}{p^2 - m^2 + i\epsilon} = i\dfrac{\eta_{\mu\nu}}{m^2 - i\epsilon} + \mathcal{O}\left(\dfrac{p^2}{m^2}\right)$

- **Vertex rules:**
  To determine the Feynman rule for a vertex from a given Lagrangian $\mathcal{L}$, proceed as follows:
  - Identify the relevant interaction term from $i\mathcal{L}$ involving the fields at the vertex.
  - Replace $\partial^\mu\phi$ by $-ip^\mu_\phi$ for incoming particles or outgoing antiparticles, and by $+ip^\mu_\phi$ for outgoing particles or incoming antiparticles. This result follows from the formulation of the solutions using Fourier transforms.
  - Sum over permutations for indistinguishable particles.
  - Remove the field operators from the vertex expression.

  For instance, the Quantum Electrodynamics (QED) Lagrangian reads:

$$\mathcal{L}_{QED} = \bar{\psi}(i\gamma^\mu D_\mu - m)\psi = \bar{\psi}(i\gamma^\mu\partial_\mu - m)\psi + q\bar{\psi}\gamma^\mu\psi A_\mu \ . \tag{B.1.25}$$

  The vertex for the $\bar{\psi} - \psi - A_\mu$ interaction is then:

$$V_{\bar{\psi}\psi A_\mu} = iq\gamma^\mu \ . \tag{B.1.26}$$

Once the amplitude is calculated for all diagrams, we sum them and evaluate the squared amplitude:

$$|\mathcal{M}_{fi}|^2 = \mathcal{M}_{fi}\,\mathcal{M}^*_{fi} \ . \tag{B.1.27}$$

To compute $|\mathcal{M}_{fi}|^2$, we make use of spin summation identities:

$$\sum_{s=1}^{2} u_{\vec{p},s}\bar{u}_{\vec{p},s} = \not{p} + m \ , \quad \sum_{s=1}^{2} v_{\vec{p},s}\bar{v}_{\vec{p},s} = \not{p} - m \ , \tag{B.1.28}$$

and trace formulas such as:

$$\sum_{s=1}^{2} \bar{u}_{\vec{p},s} K u_{\vec{p},s} = \mathrm{Tr}[(\not{p} + m)K] \ , \quad \sum_{s=1}^{2} \bar{v}_{\vec{p},s} K v_{\vec{p},s} = \mathrm{Tr}[(\not{p} - m)K] \ . \tag{B.1.29}$$

For vector bosons:

$$\sum_{\lambda=1}^{\lambda_{max}} \epsilon^{\mu}_{\vec{k},\lambda}(\epsilon^{\nu}_{\vec{k},\lambda})^* = -\eta^{\mu\nu} + \frac{k^\mu k^\nu}{m^2} \ , \tag{B.1.30}$$

where the mass term is omitted in the massless case.

To simplify amplitudes involving spin-$\frac{1}{2}$ fermions, one must be familiar with Dirac algebra:

$$\{\gamma^\mu, \gamma^\nu\} = 2\eta^{\mu\nu}, \quad (\gamma^0)^2 = I_4, \quad (\gamma^i)^2 = -I_4 \ , \tag{B.1.31}$$

$$\{\gamma^\mu, \gamma^5\} = 0, \quad \overline{\gamma^\mu} = \gamma^\mu, \quad \overline{\gamma^5} = -\gamma^5 \ , \tag{B.1.32}$$

$$\overline{AB} = \overline{B}\,\overline{A} \ . \tag{B.1.33}$$

This implies:

$$\{\not{p}, \gamma^5\} = 0 \ . \tag{B.1.34}$$

Useful contraction identities:

$$\begin{aligned}
\gamma^\mu\gamma_\mu &= 4I_4 \ , \\
\gamma^\mu\gamma^\nu\gamma_\mu &= -2\gamma^\nu, \\
\gamma^\mu\not{p}\gamma_\mu &= -2\not{p} \ , \\
\gamma^\mu\gamma^\alpha\gamma^\beta\gamma_\mu &= 4\eta^{\alpha\beta}I_4 \ , \\
\gamma^\mu\not{p}\not{k}\gamma_\mu &= 4(p\cdot k)I_4 \ , \\
\gamma^\mu\gamma^\alpha\gamma^\beta\gamma^\nu\gamma_\mu &= -2\gamma^\beta\gamma^\nu\gamma^\alpha \ , \\
\gamma^\mu\not{p}_1\not{p}_2\not{p}_3\gamma_\mu &= -2\not{p}_2\not{p}_3\not{p}_1 \ .
\end{aligned} \tag{B.1.35}$$

And trace identities:

$$\begin{aligned}
\mathrm{Tr}(\gamma^\mu\gamma^\nu) &= 4\eta^{\mu\nu} \ , \\
\mathrm{Tr}(\not{p}\not{k}) &= 4(p\cdot k) \ , \\
\mathrm{Tr}(\gamma^\alpha\gamma^\beta\gamma^\mu\gamma^\nu) &= 4(\eta^{\alpha\beta}\eta^{\mu\nu} - \eta^{\alpha\mu}\eta^{\beta\nu} + \eta^{\alpha\nu}\eta^{\beta\mu}) \ , \\
\mathrm{Tr}(\not{p}_1\not{p}_2\not{p}_3\not{p}_4) &= 4[(p_1\cdot p_2)(p_3\cdot p_4) - (p_1\cdot p_3)(p_2\cdot p_4) + (p_1\cdot p_4)(p_2\cdot p_3)] \ , \\
\mathrm{Tr}(\gamma^5) &= 0 \ , \\
\mathrm{Tr}(\gamma^\alpha\gamma^\beta\gamma^5) &= 0 \ , \\
\mathrm{Tr}(\gamma^\alpha\gamma^\beta\gamma^\mu\gamma^\nu\gamma^5) &= -4i\epsilon^{\alpha\beta\mu\nu} \ .
\end{aligned} \tag{B.1.36}$$

Note: The trace of an odd number of gamma matrices vanishes. Similarly, the presence of γ^5 requires an even number of gamma matrices to yield a nonzero trace.

B.1.3 2-body phase space: example of phase space calculation

A useful formula for calculating the phase space is given by:

$$\begin{aligned}
\int_{\mathbb{R}^4} d^4p\,\delta^1(p^2-m^2)H(p^0) &= \int_{\mathbb{R}^3} d^3\vec{p}\int_{\mathbb{R}} dp^0\,\delta^1((p^0)^2 - |\vec{p}|^2 - m^2)H(p^0) \\
&= \int_{\mathbb{R}^3} d^3\vec{p}\int_{\mathbb{R}} dp_0\,\delta^1((p^0)^2 - E_{\vec{p}}^2)H(p^0) \\
&= \int_{\mathbb{R}^3} d^3\vec{p}\int_{\mathbb{R}} dp_0\left(\frac{\delta^1(p_0-E_{\vec{p}})}{2E_{\vec{p}}}H(p^0) - \frac{\delta^1(p_0+E_{\vec{p}})}{2E_{\vec{p}}}H(p^0)\right) \\
\int_{\mathbb{R}^4} d^4p\,\delta^1(p^2-m^2)H(p^0) &= \int_{\mathbb{R}^3}\frac{d^3\vec{p}}{2E_{\vec{p}}} \ ,
\end{aligned} \tag{B.1.37}$$

where $H(x) = 1$ if $x > 0$ and 0 otherwise, is the Heaviside function.

For a given initial polarization state, the 2-body phase space is:

$$\begin{aligned}
\int_{(\mathbb{R}^3)^2} d\Phi_2 &= \int_{(\mathbb{R}^3)^2}(2\pi)^4\delta^4(P_i - p_1 - p_2)\frac{d^3\vec{p}_1}{(2\pi)^3 2E_1}\frac{d^3\vec{p}_2}{(2\pi)^3 2E_2} \\
&= \frac{1}{4\pi^2}\int_{\mathbb{R}^3}\frac{d^3\vec{p}_1}{2E_1}\int_{\mathbb{R}^4} d^4p_2\,\delta^4(P_i - p_1 - p_2)\delta^1(p_2^2 - m_2^2)H(p_2^0) \\
&= \frac{1}{4\pi^2}\int_{\mathbb{R}^3}\frac{d^3\vec{p}_1}{2E_1}\delta^1((P_i - p_1)^2 - m_2^2)H(E_i - E_1) \ .
\end{aligned} \tag{B.1.38}$$

In spherical coordinates:

$$d^3\vec{p}_1 = |\vec{p}_1|^2 d|\vec{p}_1| d\cos(\theta) d\psi = |\vec{p}_1|^2 d|\vec{p}_1| d\Omega \ , \tag{B.1.39}$$

and using $E_1^2 = m_1^2 + |\vec{p}_1|^2$, one obtains:

$$d^3\vec{p}_1 = E_1|\vec{p}_1| dE_1 d\Omega \ . \tag{B.1.40}$$

In the center-of-mass frame, $P_i = (\sqrt{s}; \vec{0})$, $E_1^* + E_2^* = \sqrt{s}$, $(\vec{p}_1)^* + (\vec{p}_2)^* = \vec{0}$, we get:

$$\begin{aligned}\int_{(\mathbb{R}^3)^2} d\Phi_2 &= \frac{1}{8\pi^2}\int_{\mathbb{R}} dE_1^* \int_{[-1;1]\times[0;2\pi]} d\Omega^* |(\vec{p}_1)^*| \delta^1(s - 2\sqrt{s}E_1^* + m_1^2 - m_2^2) H(\sqrt{s} - E_1^*) \\ &= \frac{1}{8\pi^2}\int_{\mathbb{R}} dE_1^* \int_{[-1;1]\times[0;2\pi]} d\Omega^* |(\vec{p}_1)^*| \frac{\delta^1\left(E_1^* - \dfrac{s + m_1^2 - m_2^2}{2\sqrt{s}}\right)}{2\sqrt{s}} H(\sqrt{s} - E_1^*) \\ &= \frac{1}{16\sqrt{2}\pi^2}\int_0^{\sqrt{s}} dE_1^* \int_{[-1;1]\times[0;2\pi]} d\Omega^* |(\vec{p}_1)^*| \delta^1\left(E_1^* - \frac{s + m_1^2 - m_2^2}{2\sqrt{s}}\right) .\end{aligned} \tag{B.1.41}$$

The integration over dE_1^* fixes the value of E_1^*, leading to:

$$\begin{aligned}|(\vec{p}_1)^*| = |(\vec{p}_2)^*| &= \sqrt{(E_1^*)^2 - m_1^2} \\ &= \sqrt{\left(\frac{s + m_1^2 - m_2^2}{2\sqrt{s}}\right) - m_1^2} \\ &= \sqrt{\frac{\Delta(s; m_1^2; m_2^2)}{4s}} .\end{aligned} \tag{B.1.42}$$

Here, $\Delta(a; b; c) = a^2 + b^2 + c^2 - 2ab - 2ac - 2bc$ is the Källén function, which allows us to express the differential 2-body phase space element as:

$$\frac{d\Phi_2}{d\Omega^*} = \frac{\sqrt{\Delta(s; m_1; m_2)}}{32\pi^2 s} . \tag{B.1.43}$$

For unpolarized particles, if the amplitude is independent of the azimuthal angle ψ, we obtain:

$$\frac{d\Phi_2}{d\cos(\theta^*)} = \frac{\sqrt{\Delta(s; m_1; m_2)}}{16\pi s} . \tag{B.1.44}$$

B.1.4 Decay length

A process $1 \to N$ corresponds to a decay of an unstable particle with mass M into N final-state particles, where the total mass of the final-state particles must be smaller than the initial mass for the decay to be kinematically allowed.

The decay width Γ, defined using Eq. (B.1.19), is given by:

$$d\Gamma = dW_{fi} = \frac{1}{2E}\overline{|\mathcal{M}_{fi}|}^2 d\Phi_N . \tag{B.1.45}$$

Then in the center-of-mass frame:

$$d\Gamma^* = \frac{1}{2M}\overline{|\mathcal{M}_{fi}|}^2 d\Phi_N . \tag{B.1.46}$$

The lifetime τ is defined as:

$$\tau = \frac{1}{\Gamma^*} . \tag{B.1.47}$$

Using the 2-body phase space from Eq. (B.1.43), we obtain:

$$\frac{d\Gamma^*}{d\Omega^*} = \frac{\sqrt{\Delta(M^2; m_1^2; m_2^2)}}{64\pi^2 M^3}\overline{|\mathcal{M}_{fi}|^2} . \tag{B.1.48}$$

If the Feynman amplitude does not depend on the azimuthal angle ψ, we have:

$$\frac{d\Gamma^*}{d\cos(\theta^*)} = \frac{\sqrt{\Delta(M^2; m_1^2; m_2^2)}}{32\pi M^3}\overline{|\mathcal{M}_{fi}|^2} . \tag{B.1.49}$$

B.1.5 Cross-section

A process $2 \to N$ describes the collision between two particles, leading to the production of N final-state particles. The interaction rate is given by:

$$\dot{n} = n_0 \int dW_{fi} \ , \tag{B.1.50}$$

where n_0 denotes the number of possible interactions between two particles.

From a macroscopic perspective, the $2 \to N$ process can be interpreted as the collision of two particle beams. By changing the frame of reference, this can be simplified to a beam-target configuration. The relevant macroscopic parameters include:

- Incident particle flux Φ.
- Target particle density ρ,
- Target thickness ϵ,
- Interaction cross-sectional area ξ.

Typically, the beam is narrower than the target and well-centered, so ξ corresponds to the transverse area of the beam.

The total number of observed interactions per unit time is proportional to the incident flux Φ, the target density ρ, and the effective interaction volume $\epsilon\xi$. The instantaneous luminosity is therefore defined as:

$$L = \Phi\rho\epsilon\xi \ . \tag{B.1.51}$$

Dimensionally, luminosity corresponds to an area per unit time. The cross-section σ is then defined as:

$$\sigma = \frac{\dot{n}}{L} \ . \tag{B.1.52}$$

Here, σ has units of area and encapsulates the microscopic properties of the interaction, while luminosity represents macroscopic beam-target parameters.

Considering a beam with N_A particles and a target with N_B particles in the interaction volume $V_i = \epsilon\xi$, we have:

$$n_0 = N_A N_B \frac{V}{\epsilon\xi} \, , \quad \rho = \frac{N_B}{\epsilon\xi} \, , \quad \Phi = \frac{N_A}{\frac{\epsilon}{\beta}\xi} = \frac{\beta N_A}{\epsilon\xi} \ . \tag{B.1.53}$$

where β denotes the velocity of the incident particles in natural units.

The cross-section can then be expressed as:

$$\sigma = \frac{\dot{n}}{\Phi\rho\epsilon\xi} = \frac{V}{\beta} \int dW_{fi} \ . \tag{B.1.54}$$

Using Eq. (B.1.19), the differential cross-section in the rest frame of particle 2 is:

$$d\sigma = \frac{V}{\beta} dW_{fi} = \frac{1}{4E_1E_2\beta} \overline{|\mathcal{M}_{fi}|^2} d\Phi_N \ . \tag{B.1.55}$$

To express this in a Lorentz-invariant form, we write:

$$d\sigma = \frac{1}{F} \overline{|\mathcal{M}_{fi}|^2} d\Phi_N \ , \tag{B.1.56}$$

where F is the Møller flux factor, defined as:

$$F = 4\sqrt{(p_1 \cdot p_2)^2 - (m_1 m_2)^2} \ , \tag{B.1.57}$$

since in the rest frame of particle 2, this becomes:

$$(p_1 \cdot p_2)^2 - (m_1 m_2)^2 = (E_1 E_2)^2 - (E_1^2 - |\vec{p}_1|^2)E_2^2 = E_1^2 E_2^2 \left(\frac{|\vec{p}_1|}{E_1} \right)^2 = E_1^2 E_2^2 \left(\frac{\gamma m \beta}{\gamma m} \right)^2 = E_1^2 E_2^2 \beta^2 \ . \tag{B.1.58}$$

Using the 2-body phase space expression from Eq. (B.1.43), with $p_i^* = |(\vec{p}_1)^*| = |(\vec{p}_2)^*|$ and $p_f^* = |(\vec{p}_3)^*| = |(\vec{p}_4)^*|$, we get:

$$\frac{d\sigma^*}{d\Omega^*} = \frac{p_f^*}{16\pi^2\sqrt{s}} \frac{\overline{|\mathcal{M}_{fi}|^2}}{F} \ . \tag{B.1.59}$$

From Eq. (B.1.42), we have:

$$p_i^* = \sqrt{\frac{\Delta(s; m_1^2; m_2^2)}{4s}} \ , \quad p_f^* = \sqrt{\frac{\Delta(s; m_3^2; m_4^2)}{4s}} \ . \tag{B.1.60}$$

The flux factor becomes:

$$\begin{aligned} F &= 4\sqrt{(p_1 \cdot p_2) - (m_1 m_2)^2} \\ &= 4\sqrt{(E_1^* E_2^* + (p_i^*)^2)^2 - (m_1 m_2)^2} \\ &= 4\sqrt{(m_1^2 + (p_i^*)^2)(m_2^2 + (p_i^*)^2) + 2(p_i^*)^2 E_1^* E_2^* + (p_i^*)^4 - (m_1 m_2)^2} \\ &= 4p_i^* \sqrt{m_1^2 + m_2^2 + 2E_1^* E_2^* + 2(p_i^*)^2} \\ &= 4p_i^* \sqrt{(p_1 + p_2)^2} \\ &= 4p_i^* \sqrt{s} \ . \end{aligned} \tag{B.1.61}$$

Hence, the differential cross-section simplifies to:

$$\frac{d\sigma^*}{d\Omega^*} = \frac{1}{64\pi^2 s} \frac{p_f^*}{p_i^*} \overline{|\mathcal{M}_{fi}|^2} = \frac{1}{64\pi^2 s} \sqrt{\frac{\Delta(s; m_3^2; m_4^2)}{\Delta(s; m_1^2; m_2^2)}} \overline{|\mathcal{M}_{fi}|^2} \ . \tag{B.1.62}$$

If the Feynman amplitude does not depend on the azimuthal angle ψ, we obtain:

$$\frac{d\sigma^*}{d\cos(\theta^*)} = \frac{1}{32\pi s} \sqrt{\frac{\Delta(s; m_3^2; m_4^2)}{\Delta(s; m_1^2; m_2^2)}} \overline{|\mathcal{M}_{fi}|^2} \ . \tag{B.1.63}$$

B.2 Regularization of loop integrals

In this section, we introduce the key concepts needed to understand regularization. For a more detailed treatment of loop integrals, refer to [PS95].

B.2.1 Generalities

In Quantum Field Theory (QFT), observables are computed from Feynman amplitudes, ideally obtained by summing over all possible diagrams. However, achieving infinite precision is impractical, so we typically perform perturbative expansions, including diagrams with up to n loops.

At tree level ($n = 0$), calculations pose no conceptual difficulties. However, the inclusion of loops ($n \geq 1$) introduces potential non-physical infinities. These divergences arise because loop integrals involve momenta that are not fixed by the initial and final states, leading to ultraviolet divergences that must be addressed through regularization.

B.2.2 Regularization by cutoff

One intuitive approach is to introduce an energy cutoff Λ, under the assumption that physical theories are valid only up to a certain energy scale (e.g., the Planck scale: $E \sim 10^{19}$ GeV). This cutoff renders integrals finite by restricting the range of momenta considered.

However, this method lacks a physical justification for the specific value of the cutoff, is not Lorentz invariant, and breaks gauge symmetry.

B.2.3 Pauli–Villars Regularization

To address divergences more rigorously, the Pauli–Villars method introduces fictitious particles with mass M to modify the propagators $(p^2 - m^2)^{-1}$. Specifically, the propagator is replaced by $(p^2 - m^2)^{-1} - (p^2 - M^2)^{-1}$, which suppresses high-energy contributions effectively.

While this method improves upon cutoff regularization by providing a more controlled regularization parameter (M), it becomes cumbersome in multi-loop diagrams due to the need for multiple fictitious particles. Moreover, it still violates gauge symmetry.

B.2.4 Analytic Regularization

In analytic regularization, the propagators $(p^2 - m^2)^{-1}$ are modified to $(p^2 - m^2)^{-z}$, where $z \in \mathbb{C}$ and $\mathrm{Re}(z)$ is chosen sufficiently large to ensure convergence of the integrals.

A key advantage of this method is that the resulting integrals define holomorphic functions within the convergence domain. By exploiting complex analysis, one can analytically continue the results around $z = 1$, yielding finite expressions.

Although theoretically elegant, analytic regularization is rarely used in practice; dimensional regularization is generally preferred.

B.2.5 Dimensional Regularization

Dimensional regularization is a robust method for handling divergences that arise in loop integrals within QFT. In this approach, we temporarily deviate from the familiar four-dimensional spacetime ($d = 4$) by introducing a small complex parameter ϵ, such that $d = 4 - \epsilon$. This parameter serves to regulate the integrals, allowing us to manage and ultimately eliminate divergences by taking the limit $\epsilon \to 0$.

d-dimensional integrals satisfy several fundamental properties:

- **Linearity:** $\int_{\mathbb{R}^d} (\alpha f(p) + g(p))\, d^d p = \alpha \int_{\mathbb{R}^d} f(p)\, d^d p + \int_{\mathbb{R}^d} g(p)\, d^d p$.
- **Translation invariance:** $\int_{\mathbb{R}^d} f(p+q)\, d^d p = \int_{\mathbb{R}^d} f(p)\, d^d p$.
- **Scaling:** $\forall s \in \mathbb{C},\ \int_{\mathbb{R}^d} f(sp)\, d^d p = s^{-d} \int_{\mathbb{R}^d} f(p)\, d^d p$.
- **Separation of angular and radial parts:** $\int_{\mathbb{R}^d} d^d p = s_d \int_{\mathbb{R}} p^{d-1}\, dp$, where $s_d = 2\pi^{d/2}/\Gamma(d/2)$.

The factor s_d generalizes the volume of a unit sphere in d dimensions by employing the Gamma function $\Gamma(z) := \int_0^{+\infty} t^{z-1} e^{-t}\, dt$, which extends the factorial: $\forall n \in \mathbb{N},\ \Gamma(n+1) = n!$.

This method is particularly noteworthy as it preserves all the symmetries of the theory and provides a systematic framework for identifying divergences.

To manage and eliminate divergences using dimensional regularization, the following procedure is typically employed:

1. Introduction of Feynman parameters:
   We begin by introducing Feynman parameters $(\alpha_k)_{k \in [\![1;n]\!]}$ to re-express the product of propagators in loop integrals. This allows us to rewrite:
   $$\prod_{k=1}^{n} \frac{1}{D_k} = \int_{[0,1]^n} \left(\prod_{k=1}^{n} d\alpha_k \right) \delta\left(\sum_{k=1}^{n} \alpha_k - 1 \right) \frac{(n-1)!}{\left(\sum_{k=1}^{n} \alpha_k D_k\right)^n} \ . \tag{B.2.1}$$
   For two propagators, this simplifies to:
   $$\frac{1}{D_1 D_2} = \int_0^1 \frac{d\alpha}{\left(\alpha D_1 + (1-\alpha) D_2\right)^2} \ . \tag{B.2.2}$$
2. Canonical form and change of variables:
   Once the Feynman parameters are introduced, the denominator becomes a quadratic polynomial in the loop momentum. We then complete the square and perform a change of variables to bring the integral into a suitable form. If needed, we use the standard replacement rules:
   $$p^\mu p^\nu \to \frac{p^2 \eta^{\mu\nu}}{d} \ , \tag{B.2.3}$$
   $$p^\mu p^\nu p^\sigma p^\rho \to \frac{p^4}{d(d+2)} \left(\eta^{\mu\nu}\eta^{\sigma\rho} + \eta^{\mu\sigma}\eta^{\nu\rho} + \eta^{\mu\rho}\eta^{\nu\sigma} \right) \ . \tag{B.2.4}$$

3. Application of dimensional integration formulas:
For each unconstrained momentum p, we apply standard dimensional integration formulas:

$$\int_{\mathbb{R}^d} \frac{d^d p}{(2\pi)^d} \frac{1}{(p^2-\Delta)^n} = \frac{(-1)^n i}{(4\pi)^{d/2}} \frac{\Gamma(n-d/2)}{\Gamma(n)} \frac{1}{\Delta^{n-d/2}} \ , \tag{B.2.5}$$

$$\int_{\mathbb{R}^d} \frac{d^d p}{(2\pi)^d} \frac{p^2}{(p^2-\Delta)^n} = \frac{(-1)^{n-1} i}{(4\pi)^{d/2}} \frac{d}{2} \frac{\Gamma(n-d/2-1)}{\Gamma(n)} \frac{1}{\Delta^{n-d/2-1}} \ , \tag{B.2.6}$$

$$\int_{\mathbb{R}^d} \frac{d^d p}{(2\pi)^d} \frac{p^4}{(p^2-\Delta)^n} = \frac{(-1)^n i}{(4\pi)^{d/2}} \frac{d(d+2)}{4} \frac{\Gamma(n-d/2-2)}{\Gamma(n)} \frac{1}{\Delta^{n-d/2-2}} \ , \tag{B.2.7}$$

$$\int_{\mathbb{R}^d} \frac{d^d p}{(2\pi)^d} \frac{p^{2k}}{(p^2-\Delta)^n} = i \frac{(-1)^{n+k}}{(4\pi)^{d/2} \Delta^{n-d/2-k}} \frac{\prod_{i=0}^{k-1}(d+2i)}{2^k} \frac{\Gamma(n-d/2-k)}{\Gamma(n)} \ . \tag{B.2.8}$$

4. Expansion in ϵ:
We expand the result in powers of ϵ, using the asymptotic behavior of the Gamma function:

$$\Gamma(x) = \frac{(-1)^n}{n!} \left(\frac{1}{x+n} - \gamma + \sum_{k=1}^{n} \frac{1}{k} + \mathcal{O}(x+n) \right) \ , \tag{B.2.9}$$

where

$$\gamma = \sum_{k=1}^{\infty} \left[\frac{1}{k} - \ln\left(1+\frac{1}{k}\right) \right] \simeq 0.5772 \ . \tag{B.2.10}$$

We also use the expansion:

$$\begin{aligned} \frac{\mu^{4-d}}{(4\pi)^{d/2}\Delta^{N-d/2}} &= \frac{1}{(4\pi)^2 \Delta^{N-2}} \left(\frac{\Delta}{4\pi\mu^2} \right)^{-\epsilon/2} \\ &= \frac{1}{(4\pi)^2 \Delta^{N-2}} \left(1 - \frac{\epsilon}{2} \ln\left(\frac{\Delta}{4\pi\mu^2} \right) + \mathcal{O}(\epsilon^2) \right) \ . \end{aligned} \tag{B.2.11}$$

5. Renormalization:
After discarding the non-divergent ϵ-dependent terms, the remaining $1/\epsilon$ poles are absorbed through redefinition of parameters in the Lagrangian. Counterterms are introduced to cancel the divergences and render the theory finite.

This systematic procedure illustrates the power and elegance of dimensional regularization in controlling divergences in QFT computations.

To demonstrate the Eq. (B.2.8), we perform a Wick rotation. That is, we substitute $ip^0 = p_E^0$ and $p^a = p_E^a$, so that $d^d p = i\, d^d p_E$ and $p^2 = -p_E^2$. Applying this rotation and converting to spherical coordinates in $\mathbb{R}^d$, we obtain:

$$\begin{aligned} \int_{\mathbb{R}^d} \frac{d^d p}{(2\pi)^d} \frac{p^{2k}}{(p^2-\Delta)^n} &= \int_{\mathbb{R}^d} \frac{d^d p_E}{(2\pi)^d} \frac{(-1)^k p_E^{2k}}{(-1)^n (p_E^2+\Delta)^n} \\ &= i \frac{(-1)^{n+k}}{(2\pi)^d} \frac{2\pi^{d/2}}{\Gamma(d/2)} \int_{\mathbb{R}_+} \frac{p_E^{2k+d-1} dp_E}{(p_E^2+\Delta)^n} \\ &= i \frac{2(-1)^{n+k}}{(4\pi)^{d/2}\Gamma(d/2)} \int_{\mathbb{R}_+} \frac{p_E^{2k+d-1} dp_E}{(p_E^2+\Delta)^n} \ . \end{aligned} \tag{B.2.12}$$

Now, we change variables to $y = p_E^2$, and then $z = y/\Delta$, giving:

$$\int_{\mathbb{R}^d} \frac{d^d p}{(2\pi)^d} \frac{p^{2k}}{(p^2-\Delta)^n} = i \frac{(-1)^{n+k}}{(4\pi)^{d/2}\Delta^{n-d/2-k}} \frac{1}{\Gamma(d/2)} \int_{\mathbb{R}_+} \frac{z^{d/2+k-1}}{(z+1)^n} dz \ . \tag{B.2.13}$$

Using the substitution $x = \frac{z}{z+1}$, we obtain:

$$\begin{aligned}
\int_{\mathbb{R}^d} \frac{d^d p}{(2\pi)^d} \frac{p^{2k}}{(p^2-\Delta)^n} =& i \frac{(-1)^{n+k}}{(4\pi)^{d/2}\Delta^{n-d/2-k}} \frac{1}{\Gamma(d/2)} \int_0^1 (1-x)^{n-d/2-k-1} x^{d/2+k-1} dx \\
=& i \frac{(-1)^{n+k}}{(4\pi)^{d/2}\Delta^{n-d/2-k}} \frac{1}{\Gamma(d/2)} B(d/2+k, n-d/2-k) \\
=& i \frac{(-1)^{n+k}}{(4\pi)^{d/2}\Delta^{n-d/2-k}} \frac{1}{\Gamma(d/2)} \frac{\Gamma(d/2+k)\Gamma(n-d/2-k)}{\Gamma(d/2+k+n-d/2-k)} \\
=& i \frac{(-1)^{n+k}}{(4\pi)^{d/2}\Delta^{n-d/2-k}} \frac{\Gamma(d/2+k)}{\Gamma(d/2)} \frac{\Gamma(n-d/2-k)}{\Gamma(n)} \\
=& i \frac{(-1)^{n+k}}{(4\pi)^{d/2}\Delta^{n-d/2-k}} \frac{\Gamma(d/2)\prod_{i=0}^{k-1}(d/2+i)}{\Gamma(d/2)} \frac{\Gamma(n-d/2-k)}{\Gamma(n)} \\
=& i \frac{(-1)^{n+k}}{(4\pi)^{d/2}\Delta^{n-d/2-k}} \frac{\prod_{i=0}^{k-1}(d+2i)}{2^k} \frac{\Gamma(n-d/2-k)}{\Gamma(n)} \ .
\end{aligned} \tag{B.2.14}$$

To justify the Euler beta function identity, we recall its definition:

$$B(x,y) = \int_0^1 t^{x-1}(1-t)^{y-1} dt \ , \tag{B.2.15}$$

and use:

$$\begin{aligned}
\Gamma(x)\Gamma(y) &= \int_0^{+\infty} s^{x-1} e^{-s} ds \int_0^{+\infty} t^{y-1} e^{-t} dt \\
&= \int_0^{+\infty} u^{x+y-1} e^{-u} du \int_0^1 v^{x-1}(1-v)^{y-1} dv \\
&= \Gamma(x+y) B(x,y) \ ,
\end{aligned} \tag{B.2.16}$$

where the change of variables $s = uv$, $t = u(1-v)$ was used, along with Fubini's theorem to separate the integrals.

B.2.6 Veltman-Passarino reduction

The Veltman-Passarino reduction method provides a structured approach within dimensional regularization for handling loop integrals in QFT.

Consider a typical loop diagram illustrated as:

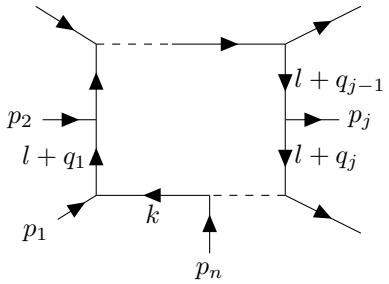

For such a diagram, we define the integral $I_n[f(l)]$ as:

$$I_n[f(l)] := -i(4\pi)^{d/2} \int \frac{d^d l}{(2\pi)^d} \frac{f(l)}{(l^2-m_0^2)((l+q_1)^2-m_1^2)\cdots((l+q_{n-1})^2-m_{n-1}^2)} \ , \tag{B.2.17}$$

where $q_i := \sum_{j=1}^{i} p_j$ denotes the sum of external momenta.

We further define the $(n-1)$-point integrals $I^j_{n-1}[f(l)]$, obtained by removing the jth propagator:

$$I^j_{n-1}[f(l)] := -i(4\pi)^{d/2} \int \frac{d^d l}{(2\pi)^d} \tag{B.2.18}$$
$$\times \frac{f(l)}{(l^2-m_0^2)((l+q_1)^2-m_1^2)\cdots((l+q_{j-1})^2-m_{j-1}^2)((l+q_{j+1})^2-m_{j+1}^2)\cdots((l+q_{n-1})^2-m_{n-1}^2)} \ .$$

The integral $I_n[l^\mu]$ can be expressed in terms of coefficients $C_{n;i}$ as:

$$I_n[l^\mu] = \sum_{i=1}^{n-1} C_{n;i}\, p_i^\mu \ , \tag{B.2.19}$$

which implies:

$$I_n[l \cdot p_j] = \sum_{i=1}^{n-1} C_{n;i}\, \Delta^{ij} \ , \tag{B.2.20}$$

where $\Delta^{ij} = p_i \cdot p_j$ is the so-called Gram matrix.

Since $p_j = q_j - q_{j-1}$, the Veltman–Passarino reduction allows us to rewrite the scalar product in the numerator as:

$$l \cdot p_j = \frac{1}{2}\left((l+q_j)^2 - m_j^2 - (l+q_{j-1})^2 + m_{j-1}^2 + m_j^2 - m_{j-1}^2 - q_j^2 + q_{j-1}^2\right) \ . \tag{B.2.21}$$

Here, the terms $(l+q_j)^2 - m_j^2$ and $(l+q_{j-1})^2 - m_{j-1}^2$ effectively cancel the jth and $(j-1)^{\text{th}}$ propagators, respectively.

The coefficients $C_{n;i}$ can then be determined by solving the linear system:

$$\sum_{i=1}^{n-1} C_{n;i}\, \Delta^{ij} = \frac{1}{2}\left(I^{(j)}_{n-1}[1] - I^{(j-1)}_{n-1}[1] + (m_j^2 - m_{j-1}^2 - q_j^2 + q_{j-1}^2) I_n[1]\right) \ . \tag{B.2.22}$$

This formalism provides a systematic and efficient approach to compute the coefficients $C_{n;i}$ and to handle divergences in loop integrals within the framework of dimensional regularization.

B.3 Resonance

We aim to demonstrate that the replacement of the numerator in the expression

$$(2\pi)\delta(\sqrt{s} - m_B) \quad \longrightarrow \quad \frac{4m^2\Gamma}{(s-m^2)^2 + (m\Gamma)^2} \ , \tag{B.3.1}$$

is well-defined, such that it reproduces the correct integral value in the narrow width limit, i.e., when $\Gamma_B \ll m_B$:

$$\begin{aligned}
\frac{1}{2\pi}\int_{\mathbb{R}} dx \frac{4m^2\Gamma}{(x^2-m^2)^2+(m\Gamma)^2} &= \frac{2m^2\Gamma}{\pi}\int_{\mathbb{R}} dx \frac{1}{(x^2-m^2+im\Gamma)(x^2-m^2-im\Gamma)} \\
&= \frac{m}{i\pi}\int_{\mathbb{R}} dx \left(\frac{1}{x^2-m^2-im\Gamma} - \frac{1}{x^2-m^2+im\Gamma}\right) \\
&= \frac{m}{i\pi}\int_{\mathbb{R}} dx \left(\frac{\frac{-1}{m^2+im\Gamma}}{1+\left(\frac{x}{im-\Gamma/2}\right)^2} + \frac{\frac{1}{m^2-im\Gamma}}{1+\left(\frac{x}{im+\Gamma/2}\right)^2}\right) \\
&= \frac{m}{i\pi}\int_{\mathbb{R}} dy \left(\frac{\frac{im-\Gamma/2}{m^2+im\Gamma}}{1+y^2} + \frac{\frac{im+\Gamma/2}{m^2-im\Gamma}}{1+y^2}\right) \\
&= \frac{m}{2i}\left(\frac{im-\Gamma/2}{m^2+im\Gamma} + \frac{im+\Gamma/2}{m^2-im\Gamma}\right) \\
&= \frac{1}{2}\left(\frac{1+i\Gamma/2m}{1+i\Gamma/m} + \frac{1-\Gamma/2m}{1-i\Gamma/m}\right) \\
&= \frac{1+\Gamma^2/2m^2}{1+\Gamma^2/m^2} \\
&= 1+o\left(\left(\frac{\Gamma}{m}\right)^2\right) .
\end{aligned} \tag{B.3.2}$$

B.4 $g-2$ anomaly calculation and axion contribution

B.4.1 Motivation

The measured value of the muon's anomalous magnetic moment, a_μ, at the Fermilab $g-2$ experiment [Abi+21], used to exceed the Standard Model (SM) prediction [Aoy+20; KKY22]. This discrepancy is quantified as:

$$\Delta a_\mu = a_\mu^{exp} - a_\mu^{SM} = (25.1 \pm 5.9) \times 10^{-10} , \tag{B.4.1}$$

corresponding to a 4.2σ deviation. While this does not exceed the conventional 5σ discovery threshold in particle physics, it still represents a significant tension between theory and experiment.

However, and very importantly, recent developments challenge this tension. Lattice QCD (LQCD) calculations performed by [Bor+21] and by [Ale+23] find a smaller deviation between the SM prediction and the experimental value, so that the two agree to within approximately 1.5σ.

The muon $g-2$ problem can therefore be considered resolved in the sense that there is no longer a statistically significant discrepancy between experiment and theory [Ali+25].

Nevertheless, while the anomaly appeared, a large number of Beyond the Standard Model (BSM) calculations were performed to explain it, e.g. contributions from Axion-like Particles (ALPs) [GMR22; Bue+21]. These computations remain valuable today, not to shift the SM prediction toward a different experimental value, but conversely to state that BSM contributions must not exceed a certain size in order for the SM and experiment to remain consistent. This allows one to derive upper bounds on BSM couplings.

B.4.2 Classical calculation

The magnetic moment $\vec{\mu}$ of a current loop is given by the product of the current I and the area S of the loop, oriented along the z-axis:

$$\vec{\mu} = IS\,\vec{e}_z . \tag{B.4.2}$$

For a circular loop of radius a, the area is $S = \pi a^2$. The current I associated with a rotating particle of charge q and angular frequency ω is:

$$I = \frac{\omega}{2\pi} q . \tag{B.4.3}$$

The angular momentum $\vec{L}$ of the particle rotating around the center of the loop is given by:

$$\vec{L} = m\,\vec{r} \wedge \vec{v} = \omega m a^2\,\vec{e}_z \ , \tag{B.4.4}$$

where $\vec{r}$ is the position vector and $\vec{v}$ is the velocity vector.

Therefore, the magnetic moment can be expressed as:

$$\vec{\mu} = \frac{q}{2m}\vec{L} \ . \tag{B.4.5}$$

B.4.3 Standard Model contribution

B.4.3.1 Loop-free quantum calculation

In QFT, the interaction Hamiltonian $\mathcal{H}_{int} = -\vec{\mu}\cdot\vec{B}$ and the interaction Lagrangian $\mathcal{L}_{int} = -eA_\mu\bar{\ell}\gamma^\mu\ell$ both describe the coupling between a lepton's magnetic moment $\vec{\mu}$ and the external magnetic field $\vec{B}$, via the electromagnetic potential A_μ:

$$-\vec{\mu}\cdot\vec{B} = eA_\mu\bar{\ell}\gamma^\mu\ell \ . \tag{B.4.6}$$

For a static magnetic field described by $A_\mu = (0, \vec{A})$, with $\vec{B} = \nabla\times\vec{A}$, its Fourier transform is given by:

$$\tilde{B}^k = -i\epsilon^{ijk}q^i\tilde{A}^j(\vec{q}) \ , \tag{B.4.7}$$

which leads to:

$$i\langle\mu^k\rangle\epsilon^{ijk}q^i\tilde{A}^j(\vec{q}) = e\bar{u}(p')\gamma^j u(p)\tilde{A}_j(q) \ . \tag{B.4.8}$$

The Dirac spinors yield:

$$\begin{aligned}
\bar{u}(p')\gamma^j u(k) &= \begin{pmatrix}\sqrt{p'\cdot\sigma}\xi'\\ \sqrt{p'\cdot\bar{\sigma}}\xi'\end{pmatrix}^\dagger \begin{pmatrix}0 & 1\\ 1 & 0\end{pmatrix}\begin{pmatrix}0 & \sigma^j\\ \bar{\sigma}^j & 0\end{pmatrix}\begin{pmatrix}\sqrt{k\cdot\sigma}\xi\\ \sqrt{k\cdot\bar{\sigma}}\xi\end{pmatrix}\\
&= m\xi'^\dagger\left(\left(1-\frac{\vec{q}\cdot\vec{\sigma}}{4m}\right)\bar{\sigma}^j\left(1+\frac{\vec{q}\cdot\vec{\sigma}}{4m}\right)+\left(1+\frac{\vec{q}\cdot\vec{\sigma}}{4m}\right)\sigma^j\left(1-\frac{\vec{q}\cdot\vec{\sigma}}{4m}\right)\right)\xi\\
&\simeq m\xi'^\dagger\left(\bar{\sigma}^j+\sigma^j+\frac{\vec{q}\cdot\vec{\sigma}}{4m}(\sigma^j-\bar{\sigma}^j)-(\sigma^j-\bar{\sigma}^j)\frac{\vec{q}\cdot\vec{\sigma}}{4m}\right)\xi\\
&= \frac{1}{2}\xi'^\dagger q^i(\sigma^i\sigma^j-\sigma^j\sigma^i)\xi\\
&= i\epsilon^{ijk}q^i\xi'^\dagger\sigma^k\xi \ .
\end{aligned} \tag{B.4.9}$$

This gives:

$$\langle\mu^k\rangle(i\epsilon^{ijk}q^i\tilde{A}^j(\vec{q})) = \frac{e}{m}\langle S^k\rangle(i\epsilon^{ijk}q^i\tilde{A}^j(\vec{q})) \ , \tag{B.4.10}$$

and therefore:

$$\langle\vec{\mu}\rangle = \frac{e}{m}\langle\vec{S}\rangle = g\frac{e}{2m}\langle\vec{S}\rangle \ , \tag{B.4.11}$$

with $g = 2$, which differs by a factor of 2 from the classical result.

B.4.3.2 Loop corrections

The inclusion of loop corrections modifies the value of g, thereby necessitating the definition of the anomaly:

$$a = \frac{g-2}{2} \ . \tag{B.4.12}$$

The general amplitude can be written as

$$i\mathcal{M}_{fi} = -ie\bar{u}(p')\Gamma^\mu u(k)A_\mu(k) \ , \tag{B.4.13}$$

where the most general form of Γ^μ, consistent with the equations of motion and gauge invariance, is given by

$$\Gamma^\mu = F_1(q^2)\gamma^\mu + F_2(q^2)\frac{i\sigma^{\mu\nu}q_\nu}{2m} \ . \tag{B.4.14}$$

By considering terms linear in q_i, we find

$$\frac{i}{2m}\bar{u}(p')\sigma^{k\nu}q_\nu u(k) = \frac{i}{2m}\xi'^\dagger\left(\frac{-i}{2m}\epsilon^{ijk}q^j\sigma^k\right)\xi \ , \tag{B.4.15}$$

which allows us to write

$$\bar{u}(p')\Gamma^\mu u(k) = \frac{i}{2m}\xi'^\dagger\left(\frac{-i}{2m}\epsilon^{ijk}q^j\sigma^k\right)\xi(F_1(0)+F_2(0)) \ . \tag{B.4.16}$$

From the above result, we deduce that

$$g = 2(F_1(0)+F_2(0)) \ . \tag{B.4.17}$$

Gauge invariance implies that $F_1(0) = 1$, leading to

$$a = \frac{g-2}{2} = F_2(0) \ . \tag{B.4.18}$$

B.4.4 Contribution of the axion

This section explores how an ALP contribute to the muon $g-2$ anomaly. Key references include [GMR22; Bue+21].

Let us consider a Lagrangian in which the axion couples to the SM fermions, written as follows[2]:

$$\mathcal{L}_{aff} = \frac{1}{2}\partial^\mu a\partial_\mu a - \frac{1}{2}m_a^2a^2 - i\sum_f \frac{c_{ff}m_f}{f_a}\bar{f}\gamma_5 f a \tag{B.4.19}$$

The one-loop diagram:

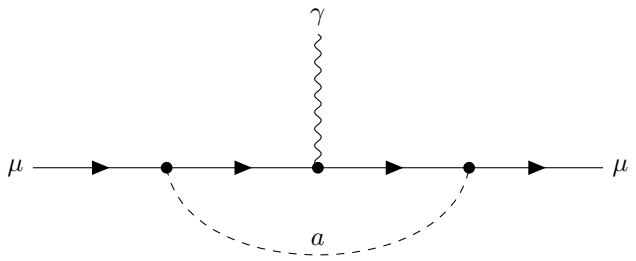

yields:

$$a_\mu^{ALP(1\,\text{loop})} = -\left(\frac{c_{\mu\mu}m_\mu}{f_a}\right)^2\frac{r}{8\pi^2}\int_0^1\frac{x^3dx}{1-x+rx^2} \ , \tag{B.4.20}$$

where $r = m_\mu^2/m_a^2$. Therefore, $a_\mu^{ALP(1\,\text{loop})} < 0$.

The two-loop diagrams:

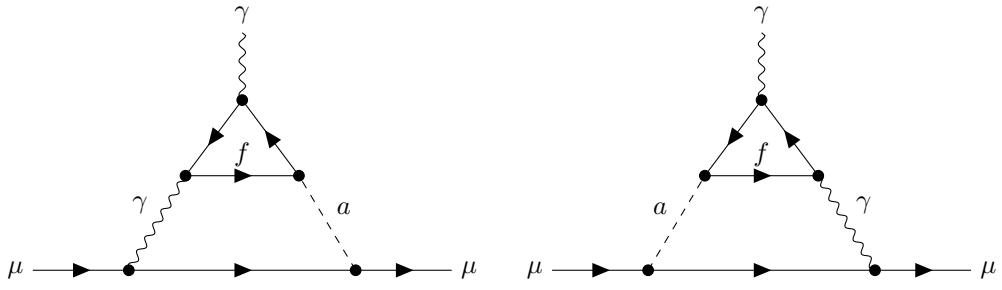

[2]This expression is equivalent to that of Section 1.2, where the axion-fermion couplings are written in a more compact form. It uses the fact that a total derivative in the Lagrangian does not affect the physics: $\partial_\mu a\bar{f}\gamma^\mu\gamma_5 f = \partial_\mu(a\bar{f}\gamma^\mu\gamma_5 f) - a\,\partial_\mu\bar{f}\gamma^\mu\gamma_5 f - a\,\bar{f}\gamma^\mu\gamma_5\partial_\mu f \equiv -a\,\partial_\mu\bar{f}\gamma^\mu\gamma_5 f + a\,\bar{f}\gamma_5\gamma^\mu\partial_\mu f$, and applies the Dirac equation $i\not{\partial}f = m_f f$ to the fermions.

give

$$a_\mu^{ALP(2\,\text{loops})} = \frac{\alpha_{e.m.} m_\mu^2 c_{\mu\mu}}{8\pi^3 f_a} \sum_f \frac{N_c^f q_f^2 c_{ff}}{f_a} \mathcal{F}\left(\frac{m_a^2}{m_\mu^2}; \frac{m_a^2}{m_f^2}\right) , \tag{B.4.21}$$

where N_c^f is the color factor (3 for quarks, 1 for leptons), q_f is the electric charge, and

$$\mathcal{F}(a;b) = \iiint_{[0;1]^3} \frac{axdxdydz}{a(1-x) + abxyz(1-z) + bz(1-z)x^2(1-y)^2} . \tag{B.4.22}$$

We find $a_\mu^{ALP(2\,\text{loops})} > 0$.

The total axion contribution to the muon anomaly is then:

$$a_\mu^{ALP} \simeq a_\mu^{ALP(1\,\text{loop})} + a_\mu^{ALP(2\,\text{loops})} . \tag{B.4.23}$$

It is therefore possible to explore the couplings in Lagrangian (B.4.19) to identify the parameter space in which ALPs is compatible with the experimental measurement.

B.5 Extraction of F_0, D, and F from experimental data in ChPT

B.5.1 Experimental value of F_0

We determine F_0 from the decay $\pi^- \to \mu^- \bar{\nu}_\mu$, which has an experimentally measured Branching Ratio (BR) close to 1. This decay proceeds via the mediation of a W^- boson. First, we calculate the $\pi^- - W^-$ vertex:

$$i\mathcal{M}_{fi} = \left\langle 0 \left| \bar{u} \frac{-ig_W}{2\sqrt{2}} V_{ud} \gamma^\mu (1-\gamma_5) d \right| \pi^- \right\rangle \tag{B.5.1}$$

$$= \frac{-ig_W}{2\sqrt{2}} V_{ud} \left\langle 0 \left| \bar{u}\gamma^\mu(1-\gamma_5)d \right| \pi^- \right\rangle . \tag{B.5.2}$$

Given $|\pi^-\rangle = \frac{1}{\sqrt{2}}\left(|\pi^1\rangle - i|\pi^2\rangle\right)$ and the axial current $J_A^{\mu;b} = \bar{\psi}\gamma^\mu\gamma_5 \frac{1}{2}\sigma^b\psi$, we have:

$$J_A^{\mu;1} + iJ_A^{\mu;2} = \bar{u}\gamma^\mu\gamma_5 d . \tag{B.5.3}$$

Using the one-meson axial current[3]:

$$J_A^{b,\mu} = J_R^{b,\mu} - J_L^{b,\mu} = \frac{F_0}{2}\text{Tr}(\lambda^b \partial^\mu \phi) = \frac{F_0}{2}\partial^\mu\phi^c \text{Tr}(\lambda^b\lambda^c) = F_0 \partial^\mu \phi^c \delta^{bc} = F_0 \partial^\mu \phi^b , \tag{B.5.4}$$

we deduce:

$$\left\langle 0 \left| J_A^{\mu;a} \right| \phi^b \right\rangle = ip_\phi^\mu F_0 \delta^{ab} , \tag{B.5.5}$$

which allows us to write:

$$\begin{aligned} i\mathcal{M}_{fi} &= \frac{-ig_W}{2\sqrt{2}} V_{ud} \left\langle 0 \left| \left(J_A^{\mu;1} + iJ_A^{\mu;2}\right) \frac{|\pi^1\rangle - i|\pi^2\rangle}{\sqrt{2}} \right\rangle \\ &= \frac{-ig_W}{4} V_{ud} \left(\left\langle 0 \left| J_A^{\mu;1} \right| \pi^1 \right\rangle + \left\langle 0 \left| J_A^{\mu;2} \right| \pi^2 \right\rangle \right) \\ &= \frac{g_W}{2} V_{ud} F_0 p^\mu . \end{aligned} \tag{B.5.6}$$

The amplitude for the decay $\pi^- \to \ell^- \nu_\ell$ is:

$$i\mathcal{M}_{fi} = \left(-i\frac{g_W}{2} V_{ud} F_0 p_{\pi^-}^\mu\right) \left(\frac{i\eta_{\mu\nu}}{m_W^2}\right) \left(\bar{u}_\nu \frac{-ig_W}{\sqrt{2}} \gamma^\nu \frac{1}{2}(1-\gamma_5) v_\ell\right) = iG_F F_0 \bar{u}_\nu \not{p}_{\pi^\pm}(1-\gamma_5)v_\ell . \tag{B.5.7}$$

This yields to:

$$|\mathcal{M}_{fi}|^2 = 4|V_{ud}|^2 G_F^2 F_0^2 m_\ell^2 (m_{\pi^\pm}^2 - m_\ell^2) . \tag{B.5.8}$$

[3] The vector part vanishes.

Thus, the decay width is:

$$\Gamma[\pi^- \to \ell^- + \nu_\ell] = \frac{|V_{ud}|^2 G_F^2 F_0^2 [m_\ell (m_{\pi^\pm}^2 - m_\ell^2)]^2}{4\pi m_{\pi^\pm}^3} \ . \tag{B.5.9}$$

This expression can be inverted to extract F_0, yielding

$$F_0 \simeq \sqrt{\frac{4\pi m_{\pi^\pm}^3}{|V_{ud}|^2 G_F^2 [m_\mu (m_{\pi^\pm}^2 - m_\mu^2)]^2} BR[\pi^- \to \mu^- + \nu_\mu] \Gamma[\pi^-]} = 93.07(2) \text{ MeV} \ , \tag{B.5.10}$$

where $\Gamma[\pi^-]$ denotes the experimentally measured total decay width.

B.5.2 Experimental values of D and F

The constants D and F can be extracted by fitting semi-leptonic decays[4] of the form $B_i \to B_f e^- \bar{\nu}_e$ at tree level.

At the quark level, the relevant transition is $q \to u e^- \bar{\nu}_e$ with $q \in \{d, s\}$, yielding the Feynman amplitude

$$\mathcal{M}_{fi}(q \to u e^- \bar{\nu}_e) = i \frac{G_F V_{uq}}{\sqrt{2}} [\bar{u}_q \gamma^\mu (1 - \gamma_5) u_u] [\bar{u}_e \gamma_\mu (1 - \gamma_5) v_\nu] \ . \tag{B.5.11}$$

At the baryon level, this generalizes by replacing the quark currents with baryonic currents:

$$\mathcal{M}_{fi}(B_i \to B_f e^- \bar{\nu}_e) = \frac{G_F V_{uq}}{\sqrt{2}} \left[\bar{u}_{B_f} \gamma^\mu (g_V^{B_i B_f} - g_A^{B_i B_f} \gamma_5) u_{B_i}\right] [\bar{u}_e \gamma_\mu (1 - \gamma_5) v_\nu] \ , \tag{B.5.12}$$

where $g_V^{B_i B_f}$ and $g_A^{B_i B_f}$ are constants associated with the vector and axial-components, respectively.

These couplings are computed by expanding the relevant currents:

$$J_A^{b,\mu} = -\frac{D}{2} \text{Tr}\left(\bar{B} \gamma^\mu \gamma_5 \{\lambda^b, B\}\right) - \frac{F}{2} \text{Tr}\left(\bar{B} \gamma^\mu \gamma_5 [\lambda^b, B]\right) \ , \tag{B.5.13}$$

$$J_V^{b,\mu} = \frac{1}{2} \text{Tr}\left(\bar{B} \gamma^\mu [\lambda^b, B]\right) \ . \tag{B.5.14}$$

For a $d \to u$ transition, the contribution arises from $J^\mu = J^{1,\mu} - i J^{2,\mu}$, while for an $s \to u$ transition, it comes from $J^\mu = J^{4,\mu} - i J^{5,\mu}$.

As an illustration, for neutron beta decay $n \to p e^- \bar{\nu}_e$, one finds $g_V^{np} = 1$ and $g_A^{np} = D + F$.

The decay width can then be expressed as

$$\Gamma(B_i \to B_f e^- \bar{\nu}_e) = \frac{G_F^2 |V_{uq}|^2}{2\pi^3} \left(|g_V^{B_i B_f}|^2 + 3|g_A^{B_i B_f}|^2\right) \int_0^\Delta dE_e \, p_e E_e (\Delta - E_e)^2 \ , \tag{B.5.15}$$

where $\Delta = m_{B_i} - m_{B_f}$.

In the limit $m_e \ll \Delta$ – an approximation that is not valid for neutron decay – one can set $p_e \simeq E_e$, allowing for an analytic evaluation of the integral:

$$\Gamma(B_i \to B_f e^- \bar{\nu}_e) = \frac{G_F^2 |V_{uq}|^2}{60\pi^3} \left(|g_V^{B_i B_f}|^2 + 3|g_A^{B_i B_f}|^2\right) \Delta^5 \ . \tag{B.5.16}$$

Fitting to experimental data yields approximate values $D \simeq 0.8$ and $F \simeq 0.5$ [Sch03][5].

B.6 $K \to \ell^+ \ell^- \pi$ calculation

B.6.1 Tree-level calculation

The tree-level Feynman diagrams for $K \to \pi\gamma$ are shown in Fig. B.1.

In the case of $K_S \to \pi^0 (\gamma \to \ell^+ \ell^-)$, these diagrams each vanish because electromagnetism requires charged particles to mediate a photon interaction.

[4] Studying semi-leptonic processes minimizes uncertainties related to the Quantum Chromodynamics (QCD) structure.

[5] We have provided positive values for D and F; however, their overall sign is irrelevant for these processes. Taking both D and F with the same negative sign would also be consistent with the observed decay rates.

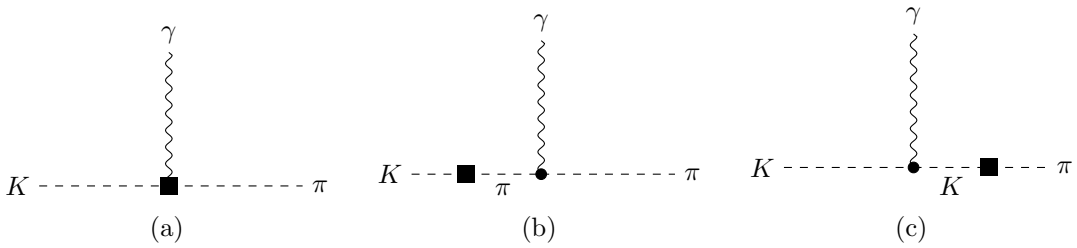

Figure B.1: Tree-level Feynman diagrams for $K \to \pi\gamma$.

For $K^+ \to \pi^+\gamma$, the diagrams do not individually vanish, but their sum still yields a zero contribution. Individually, we have:

$$\mathcal{M}_{fi}^{(a)} = \frac{\sqrt{2}F_0^2 G_F e V_{us} V_{ud}^* g_8 \eta_{\mu\nu}(p_K^\mu + p_\pi^\mu)}{s} \ , \tag{B.6.1}$$

$$\mathcal{M}_{fi}^{(b)} = -\frac{\sqrt{2}F_0^2 G_F e V_{us} V_{ud}^* g_8 \eta_{\mu\nu}(p_K^\mu + p_\pi^\mu)}{s} \frac{m_K^2}{m_K^2 - m_\pi^2} \ , \tag{B.6.2}$$

$$\mathcal{M}_{fi}^{(c)} = -\frac{\sqrt{2}F_0^2 G_F e V_{us} V_{ud}^* g_8 \eta_{\mu\nu}(p_K^\mu + p_\pi^\mu)}{s} \frac{m_\pi^2}{m_\pi^2 - m_K^2} \ . \tag{B.6.3}$$

The sum is:

$$\begin{aligned} \mathcal{M}_{fi} &= \mathcal{M}_{fi}^{(a)} + \mathcal{M}_{fi}^{(b)} + \mathcal{M}_{fi}^{(c)} \\ &= \frac{\sqrt{2}F_0^2 G_F e V_{us} V_{ud}^* g_8 \eta_{\mu\nu}(p_K^\mu + p_\pi^\mu)}{s} \left(1 - \frac{m_K^2}{m_K^2 - m_\pi^2} - \frac{m_\pi^2}{m_\pi^2 - m_K^2}\right) \\ &= 0 \ . \end{aligned} \tag{B.6.4}$$

The fact that there is no possible tree-level diagram for the process $K \to \pi(\gamma \to \ell^+\ell^-)$ implies that a loop-level calculation is required.

B.6.2 Loop calculation

The one-loop Feynman diagrams for $K \to \pi\gamma$ are shown in Fig. B.2.

B.6.2.1 Diagram (a)

The amplitude corresponding to diagram (a) for $K^0 \to \pi^0(\gamma \to \ell^+\ell^-)$ is:

$$i\mathcal{M}_{fi}^{(a)} = \int_{\mathbb{R}^d} \frac{\mu^{4-d} d^d p_{K^+}}{(2\pi)^d} \frac{i}{p_{K^+}^2 - m_{K^\pm}^2} \frac{i}{p_{\pi^-}^2 - m_{\pi^\pm}^2} i(i\sqrt{2}G_F F_0^2 e V_{us} V_{ud}^* g_8 (ip_{\pi^-}^\mu - ip_{K^+}^\mu)) \frac{-i\eta_{\mu\nu}}{s} \bar{u}_{\ell^-}(ie\gamma^\nu) v_{\ell^+} \tag{B.6.5}$$

$$\times\, i\frac{\sqrt{2}}{4}[(p_K \cdot p_{\pi^0}) + (p_{\pi^0} \cdot p_{K^+}) - (p_{\pi^-} \cdot p_{K^+})] \ .$$

To evaluate this integral, we use the Feynman parameter α:

$$\frac{1}{D_1 D_2} = \int_0^1 \frac{d\alpha}{(\alpha D_1 + (1-\alpha)D_2)^2} \ , \tag{B.6.6}$$

which we apply to the two propagators:

$$\begin{aligned} \frac{1}{p_{K^+}^2 - m_{K^\pm}^2} \frac{1}{p_{\pi^-}^2 - m_{\pi^\pm}^2} &= \int_0^1 \frac{d\alpha}{\left(\alpha(p_{K^+}^2 - m_{K^\pm}^2) + (1-\alpha)(p_{\pi^-}^2 - m_{\pi^\pm}^2)\right)^2} \\ &= \int_0^1 \frac{d\alpha}{\left(\alpha(p_{K^+}^2 - m_{K^\pm}^2) + (1-\alpha)((p_\gamma - p_{K^+})^2 - m_{\pi^\pm}^2)\right)^2} \\ &= \int_0^1 \frac{d\alpha}{\left((p_{K^+} - (1-\alpha)p_\gamma)^2 - \Delta\right)^2} \ , \end{aligned} \tag{B.6.7}$$

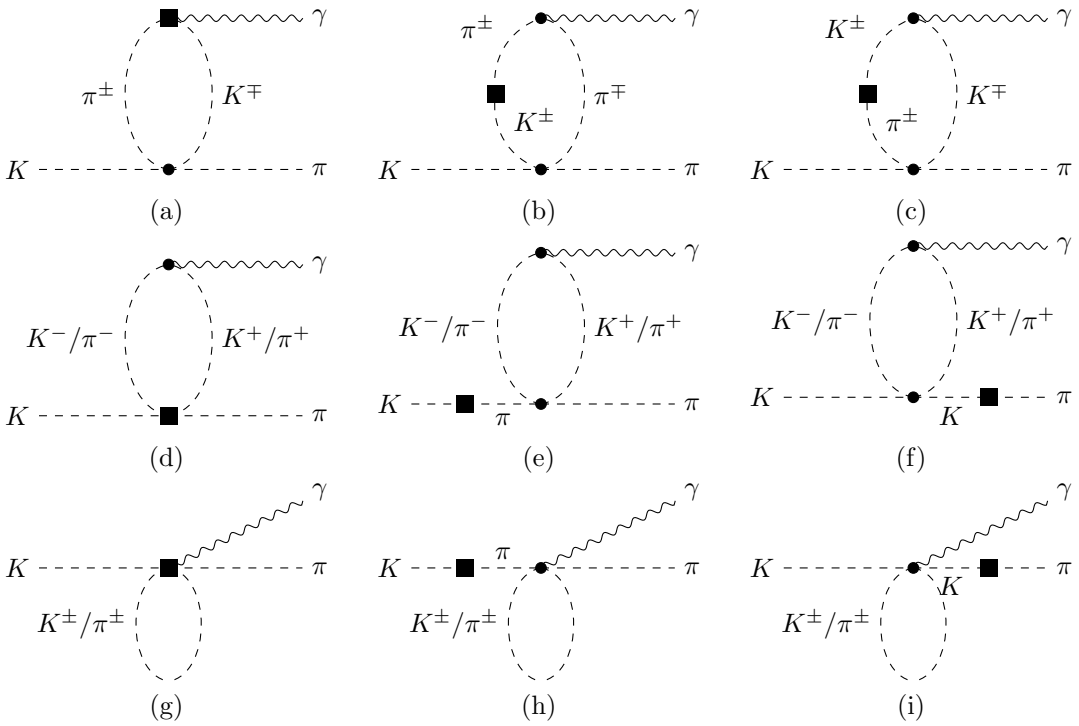

Figure B.2: One-loop Feynman diagrams for $K \to \pi\gamma$.

with

$$\Delta = m_{\pi^\pm}^2 + \alpha(m_{K^\pm}^2 - m_{\pi^\pm}^2) - \alpha(1-\alpha)p_\gamma^2 \ . \tag{B.6.8}$$

Changing variables to $p = p_{K^+} - (1-\alpha)p_\gamma$, discarding odd terms in the integrand (which vanish upon integration), and using the loop integrals provided in Appendix B.2, the part without $\not{p}_\gamma$ (which will cancel, see Section 5.2.3.2 for details) becomes:

$$\begin{aligned} i\mathcal{M}_{fi}^{(a)} = &- i\frac{e^2 G_F V_{us} V_{ud}^* g_8}{(4\pi)^2 s}\bar{u}_{\ell^-}\not{p}_K v_{\ell^+} \\ &\left(\left(-\frac{2}{\epsilon} + \gamma - 1\right)\frac{3(m_{K^\pm}^2 + m_{\pi^\pm}^2) - s}{6} + \int_0^1 \Delta \ln\left(\frac{\Delta}{4\pi\mu^2}\right) d\alpha\right) \ . \end{aligned} \tag{B.6.9}$$

Using the function I defined in Eq. (B.6.38) and the shorthand $G_8 = G_F V_{us} V_{ud}^* g_8/\sqrt{2}$, the final result is:

$$\mathcal{M}_{fi}^{(a)}[K^0 \to \ell^+\ell^-\pi^0] = -\frac{\sqrt{2}G_8 e^2}{s}\bar{u}_{\ell^-}\not{p}_K v_{\ell^+} I(s; m_{K^\pm}^2; m_{\pi^\pm}^2) \ . \tag{B.6.10}$$

B.6.2.2 Diagram (b)

The amplitude corresponding to diagram (b) is given by:

$$\begin{aligned} i\mathcal{M}_{fi}^{(b)} = &- i\frac{e^2 G_F V_{us} V_{ud}^* g_8}{2s}\bar{u}_{\ell^-}\gamma_\mu v_{\ell^+}\int_{\mathbb{R}^d}\frac{\mu^{4-d}d^d p_{\pi^+}}{(2\pi)^d}\frac{p_{\pi^+}^2(p_{\pi^+}^\mu - p_{\pi^-}^\mu)}{(p_{\pi^+}^2 - m_{K^\pm}^2)(p_{\pi^+}^2 - m_{\pi^\pm}^2)(p_{\pi^-}^2 - m_{\pi^\pm}^2)} \\ &\times\left[(p_K \cdot p_{\pi^0}) + (p_{\pi^0} \cdot p_{K^+}) - (p_{\pi^-} \cdot p_{K^+})\right] \ . \end{aligned} \tag{B.6.11}$$

We decompose the numerator:

$$p_{\pi^+}^2 = \frac{m_{K^\pm}^2}{m_{K^\pm}^2 - m_{\pi^\pm}^2}(p_{\pi^+}^2 - m_{\pi^\pm}^2) - \frac{m_{\pi^\pm}^2}{m_{K^\pm}^2 - m_{\pi^\pm}^2}(p_{\pi^+}^2 - m_{K^\pm}^2) \ . \tag{B.6.12}$$

Substituting into the amplitude gives:

$$i\mathcal{M}_{fi}^{(b)} = -i\frac{e^2 G_F V_{us} V_{ud}^* g_8}{2s}\bar{u}_{\ell^-}\gamma_\mu v_{\ell^+}\left(\frac{m_{K^\pm}^2}{m_{K^\pm}^2 - m_{\pi^\pm}^2}F(m_{K^\pm}) - \frac{m_{\pi^\pm}^2}{m_{K^\pm}^2 - m_{\pi^\pm}^2}F(m_{\pi^\pm})\right) \ . \tag{B.6.13}$$

with the loop integral function defined as:

$$F(m_M) = \int_{\mathbb{R}^d} \frac{\mu^{4-d} d^d p_{\pi^+}}{(2\pi)^d} \frac{p^\mu_{\pi^+} - p^\mu_{\pi^-}}{(p^2_{\pi^+} - m^2_M)(p^2_{\pi^-} - m^2_{\pi^\pm})} [(p_K \cdot p_{\pi^0}) + (p_{\pi^0} \cdot p_{K^+}) - (p_{\pi^-} \cdot p_{K^+})] \ . \tag{B.6.14}$$

Discarding odd terms in the integrand and using Feynman parametrization, the part without p^μ_γ is:

$$\begin{aligned} F(m_M) =& 4\frac{p^\mu_K}{d} \int_{\mathbb{R}^d} \frac{\mu^{4-d} d^d p}{(2\pi)^d} \int_0^1 d\alpha \frac{p^2}{(p^2 - \Delta(m_M))^2} \\ =& \frac{-2ip^\mu_K}{(4\pi)^2} \int_0^1 d\alpha \Delta(m_M) \left(\frac{-2}{\epsilon} + \gamma - 1 \right) \left(1 - \frac{\epsilon}{2} \ln \left(\frac{\Delta(m_M)}{4\pi\mu^2} \right) \right) \\ =& \frac{-2ip^\mu_K}{(4\pi)^2} \int_0^1 d\alpha \Delta(m_M) \left(\frac{-2}{\epsilon} + \gamma - 1 + \ln \left(\frac{\Delta(m_M)}{4\pi\mu^2} \right) \right) \ , \end{aligned} \tag{B.6.15}$$

with $\Delta(m_M) = \alpha m^2_M + (1-\alpha) m^2_{\pi^\pm} - \alpha(1-\alpha)s$.

Thus, the total contribution from diagram (b) is:

$$\mathcal{M}^{(b)}_{fi}[K^0 \to \ell^+\ell^-\pi^0] = \frac{\sqrt{2} G_8 e^2}{s} \bar{u}_{\ell^-} \not{p}_{K^0} v_{\ell^+} \frac{m^2_{K^\pm} I(s; m^2_{\pi^\pm}; m^2_{\pi^\pm}) - m^2_{\pi^\pm} I(s; m^2_{K^\pm}; m^2_{\pi^\pm})}{m^2_{K^\pm} - m^2_{\pi^\pm}} \tag{B.6.16}$$

B.6.2.3 Diagram (c)

Diagram (c) is structurally identical to diagram (b), but with the replacement $\pi^\pm \leftrightarrow K^\pm$. As a result, the amplitude can be directly obtained by exchanging the mass arguments in the expression for $\mathcal{M}^{(b)}_{fi}$ in Eq. (B.6.16).

The contribution to the process $K^0 \to \ell^+\ell^-\pi^0$ from diagram (c) is thus given by:

$$\mathcal{M}^{(c)}_{fi}[K^0 \to \ell^+\ell^-\pi^0] = \frac{\sqrt{2} G_8 e^2}{s} \bar{u}_{\ell^-} \not{p}_{K^0} v_{\ell^+} \frac{m^2_{\pi^\pm} I(s; m^2_{K^\pm}; m^2_{K^\pm}) - m^2_{K^\pm} I(s; m^2_{\pi^\pm}; m^2_{K^\pm})}{m^2_{\pi^\pm} - m^2_{K^\pm}} \ . \tag{B.6.17}$$

B.6.2.4 Diagram (d)

The amplitude for diagram (d), corresponding to the case of an intermediate meson $M \in \{\pi, K\}$, is given by:

$$\begin{aligned} i\mathcal{M}^{(d)}_{fi} =& \int_{\mathbb{R}^d} \frac{\mu^{4-d} d^d p_{M^+}}{(2\pi)^d} \frac{i}{p^2_{M^+} - m^2_{M^\pm}} \frac{i}{p^2_{M^-} - m^2_{M^\pm}} ie(ip^\mu_{M^-} - ip^\mu_{M^+}) \frac{-i\eta_{\mu\nu}}{s} \bar{u}_{\ell^-} (ie\gamma^\nu) v_{\ell^+} \\ & i\left(\frac{-1}{3} G_F V_{us} V^*_{ud} g_8 \right) [C_{K\pi^0}(p_K \cdot p_{\pi^0}) + C_{KM^-}(p_K \cdot p_{M^-}) + C_{KM^+}(p_K \cdot p_{M^+}) \\ & - C_{\pi^0 M^-}(p_{\pi^0} \cdot p_{M^-}) - C_{\pi^0 M^+}(p_{\pi^0} \cdot p_{M^+}) - C_{\pi^- M^+}(p_{\pi^-} \cdot p_{M^+})] \ . \end{aligned} \tag{B.6.18}$$

Here, the coefficients C_{ij} are effective couplings extracted from the weak chiral Lagrangian.

We define: $\Delta(m^2_{M^\pm}) = m^2_{M^\pm} - \alpha(1-\alpha)s$. Focusing on the part of the amplitude without $\not{p}_\gamma$, we obtain:

$$i\mathcal{M}^{(d)}_{fi} = -i \frac{e^2 G_F V_{us} V^*_{ud} g_8}{6(4\pi)^2 s} (C_{KM^+} - C_{KM^-} + C_{\pi^0 M^-} - C_{\pi^0 M^+}) \bar{u}_{\ell^-} \not{p}_K v_{\ell^+} \tag{B.6.19}$$

$$\left(\left(-\frac{2}{\epsilon} + \gamma - 1 \right) \frac{6m^2_{M^\pm} - s}{6} + \int_0^1 \Delta(m^2_{M^\pm}) \ln \left(\frac{\Delta(m^2_{M^\pm})}{4\pi\mu^2} \right) d\alpha \right) \ . \tag{B.6.20}$$

Substituting the numerical values of the couplings, we find:

$$\mathcal{M}^{(d)}_{fi}[K^0 \to \ell^+\ell^-\pi^0] = \frac{\sqrt{2} e^2 G_8}{s} \bar{u}_{\ell^-} \not{p}_K v_{\ell^+} I(s; m^2_{K^\pm}; m^2_{K^\pm}) \ . \tag{B.6.21}$$

B.6.2.5 Diagram (e)

The amplitude corresponding to diagram (e) is given by:

$$\begin{aligned} i\mathcal{M}_{fi}^{(e)} =& -G_F F_0^2 V_{us} V_{ud}^* g_8 i m_{K_S}^2 \frac{i}{m_{K_S}^2 - m_{\pi^0}^2} \frac{-i\eta_{\mu\nu}}{s} \bar{u}_{\ell^-}(ie\gamma^\nu) v_{\ell^+} \\ & \int_{\mathbb{R}^d} \frac{\mu^{4-d} d^d p_{M^+}}{(2\pi)^d} ie(ip_{M^-}^\mu - ip_{M^+}^\mu) \frac{i}{p_{M^+}^2 - m_{M^\pm}^2} \frac{i}{p_{M^-}^2 - m_{M^\pm}^2} \\ & i\frac{1}{12F_0^2}[C_{\pi^0\pi^0}(p_K \cdot p_{\pi^0}) - C_{\pi^0 M^+}(p_{\pi^0} \cdot p_{M^+}) + C_{\pi^0 M^+}(p_K \cdot p_{M^+}) \\ & - C_{\pi^0 M^-}(p_{\pi^0} \cdot p_{M^-}) + C_{\pi^0 M^-}(p_K \cdot p_{M^-}) - 2C_{M^+M^-}(p_{M^+} \cdot p_{M^-})] \end{aligned} \tag{B.6.22}$$

The coefficients C_{ij} represent effective couplings derived from the weak chiral Lagrangian.

By expanding and focusing on the part of the amplitude without $\not{p}_\gamma$, we find that it vanishes:

$$\mathcal{M}_{fi}^{(e)} = 0 \ . \tag{B.6.23}$$

B.6.2.6 Diagram (f)

The amplitude corresponding to diagram (f) is given by:

$$\begin{aligned} i\mathcal{M}_{fi}^{(f)} =& -G_F F_0^2 V_{us} V_{ud}^* g_8 i m_{\pi^0}^2 \frac{i}{m_{\pi^0}^2 - m_{K_S}^2} \frac{-i\eta_{\mu\nu}}{s} \bar{u}_{\ell^-}(ie\gamma^\nu) v_{\ell^+} \\ & \int_{\mathbb{R}^d} \frac{\mu^{4-d} d^d p_{M^+}}{(2\pi)^d} ie(ip_{M^-}^\mu - ip_{M^+}^\mu) \frac{i}{p_{M^+}^2 - m_{M^\pm}^2} \frac{i}{p_{M^-}^2 - m_{M^\pm}^2} \\ & i\frac{1}{12F_0^2}[2C_{K\bar{K}}(p_K \cdot p_{\pi^0}) - C_{KM^+}(p_K \cdot p_{M^+}) + C_{\bar{K}M^+}(p_{\pi^0} \cdot p_{M^+}) \\ & - C_{KM^-}(p_K \cdot p_{M^-}) + C_{\bar{K}M^-}(p_{\pi^0} \cdot p_{M^-}) - 2C_{M^+M^-}(p_{M^+} \cdot p_{M^-})] \ . \end{aligned} \tag{B.6.24}$$

The coefficients C_{ij} represent effective couplings in the weak chiral Lagrangian.

Using $\Delta(m_{M^\pm}^2) = m_{M^\pm}^2 - \alpha(1-\alpha)s$, we isolate the contribution without $\not{p}_\gamma$:

$$\begin{aligned} \mathcal{M}_{fi}^{(f)} =& -\frac{e^2 G_F V_{us} V_{ud}^* g_8}{12s} \frac{m_{\pi^0}^2}{m_{K^0}^2 - m_{\pi^0}^2} \bar{u}_{\ell^-} \not{p}_K v_{\ell^+} \\ & [-C_{KM^+} + C_{\bar{K}M^+} + C_{KM^-} - C_{\bar{K}M^-}] \int_0^1 d\alpha \Delta(m_{M^\pm}^2) \left(\frac{-2}{\epsilon} + \gamma - 1 + \ln\left(\frac{\Delta(m_{M^\pm}^2)}{4\pi\mu^2} \right) \right) \ . \end{aligned} \tag{B.6.25}$$

After substituting the coupling values, the final result simplifies to:

$$\mathcal{M}_{fi}^{(f)} = \frac{1}{s} \frac{eG_8}{\sqrt{2}} \frac{m_{\pi^0}^2}{m_{K^0}^2 - m_{\pi^0}^2} \bar{u}_{\ell^-} 2\not{p}_K v_{\ell^+} (I(s; m_{\pi^\pm}^2; m_{\pi^\pm}^2) - I(s; m_{K^\pm}^2; m_{K^\pm}^2)) \ . \tag{B.6.26}$$

B.6.2.7 Diagram (g)

The amplitude corresponding to diagram (g) is given by:

$$i\mathcal{M}_{fi}^{(g)} = \int \frac{\mu^{4-d} d^d p}{(2\pi)^d} ieG_F V_{us} V_{ud}^* g_8 (-iC_K p_K^\mu + iC_{M^+} p^\mu - iC_{M^-} p^\mu + iC_\pi p_\pi^\mu) \frac{i}{p^2 - m_{M^\pm}^2} \frac{-i\eta_{\mu\nu}}{s} \bar{u}_{\ell^-} ie\gamma^\nu v_{\ell^+} \ . \tag{B.6.27}$$

The coefficients C_i represent effective couplings in the weak chiral Lagrangian.

After evaluating the integral, we obtain:

$$i\mathcal{M}_{fi}^{(g)} = -(C_K - C_\pi) \frac{e^2 G_F V_{us} V_{ud}^* g_8}{s} \left(\frac{-2}{\epsilon} + \gamma - 1 + \ln\left(\frac{m_{M^\pm}^2}{4\pi\mu^2} \right) \right) \bar{u}_{\ell^-} \not{p}_K v_{\ell^+} \ . \tag{B.6.28}$$

Substituting the values of the couplings, we find:

$$i\mathcal{M}_{fi}^{(g)} = i \frac{e^2 G_F V_{us} V_{ud}^* g_8}{s} \left(\frac{-2}{\epsilon} + \gamma - 1 + \ln\left(\frac{m_{K^\pm}^2}{4\pi\mu^2} \right) \right) \bar{u}_{\ell^-} \not{p}_K v_{\ell^+} \ . \tag{B.6.29}$$

However, due to gauge invariance, the physical amplitude must be invariant under the subtraction:

$$\mathcal{M}_{fi} \equiv \frac{[s\mathcal{M}_{fi}] - [s\mathcal{M}_{fi}]|_{s=0}}{s} \ . \tag{B.6.30}$$

This prescription ensures gauge invariance of the result. Since $\mathcal{M}_{fi}$ is independent of s in this case, this subtraction yields:

$$\mathcal{M}_{fi}^{(g)} \equiv 0 \ , \tag{B.6.31}$$

and the diagram does not contribute to the physical amplitude.

B.6.2.8 Diagram (h)

The amplitude corresponding to diagram (h) is given by:

$$\begin{aligned} i\mathcal{M}_{fi}^{(h)} = &\int_{\mathbb{R}^d} \frac{\mu^{4-d}d^dp}{(2\pi)^d}(-iG_F F_0^2 V_{us}V_{ud}^* g_8 m_K^2)\frac{i}{m_K^2 - m_\pi^2}\frac{i}{p^2 - m_{M^\pm}^2}\frac{-i\eta_{\mu\nu}}{s}\bar{u}_{\ell^-} ie\gamma^\nu v_{\ell^+} \\ &i\frac{e}{12F_0^2}(-iC_\pi p_K^\mu + iC_{M^+}p^\mu - iC_{M^-}p^\mu + iC_\pi p_\pi^\mu) \ . \end{aligned} \tag{B.6.32}$$

The coefficients C_i represent effective couplings in the weak chiral Lagrangian.

Upon expanding and isolating the part of the amplitude that does not involve $\not{p}_\gamma$, we find that the contribution cancels out completely:

$$\mathcal{M}_{fi}^{(h)} = 0 \ . \tag{B.6.33}$$

B.6.2.9 Diagram (i)

The amplitude corresponding to diagram (i) is given by:

$$\begin{aligned} i\mathcal{M}_{fi}^{(i)} = &\int_{\mathbb{R}^d} \frac{\mu^{4-d}d^dp}{(2\pi)^d}(-iG_F F_0^2 V_{us}V_{ud}^* g_8 m_K^2)\frac{i}{m_\pi^2 - m_K^2}\frac{i}{p^2 - m_{M^\pm}^2}\frac{-i\eta_{\mu\nu}}{s}\bar{u}_{\ell^-} ie\gamma^\nu v_{\ell^+} \\ &i\frac{e}{12F_0^2}(-iC_K p_K^\mu + iC_{M^+}p^\mu - iC_{M^-}p^\mu + iC_{\bar{K}} p_\pi^\mu) \ . \end{aligned} \tag{B.6.34}$$

The coefficients C_i represent effective couplings in the weak chiral Lagrangian.

Evaluating the loop, we obtain:

$$i\mathcal{M}_{fi}^{(i)} = (C_K - C_{\bar{K}})\frac{e^2 G_F V_{us}V_{ud}^* g_8}{12s}\frac{m_K^2}{m_\pi^2 - m_K^2}\left(\frac{-2}{\epsilon} + \gamma - 1 + \ln\left(\frac{m_{M^\pm}^2}{4\pi\mu^2}\right)\right)\bar{u}_{\ell^-}\not{p}_K v_{\ell^+} \ . \tag{B.6.35}$$

Substituting the numerical values of the couplings, we find:

$$i\mathcal{M}_{fi}^{(i)} = 2i\frac{e^2 G_F V_{us}V_{ud}^* g_8}{s}\frac{m_K^2}{m_\pi^2 - m_K^2}\ln\left(\frac{m_{K^\pm}}{m_{\pi^\pm}}\right)\bar{u}_{\ell^-}\not{p}_K v_{\ell^+} \ . \tag{B.6.36}$$

However, since $s\mathcal{M}_{fi}$ is independent of s, the gauge-invariant subtraction yields zero:

$$\mathcal{M}_{fi}^{(i)} \equiv 0 \ . \tag{B.6.37}$$

B.6.2.10 Sum of diagrams

In [EPR87], the loop function is defined as:

$$I(s, M_1^2, M_2^2) = \frac{1}{16\pi^2}\left(\frac{1}{3\hat{\epsilon}}[3(M_1^2 + M_2^2) - s] + J(s, M_1^2, M_2^2, \mu^2)\right) \ , \tag{B.6.38}$$

where

$$\frac{1}{\hat{\epsilon}} = \frac{-1}{\epsilon} + \frac{1}{2}(\gamma - 1 - \ln(4\pi)) + \mathcal{O}(\epsilon) \ , \tag{B.6.39}$$

and

$$J(s, M_1^2, M_2^2, \mu^2) = \int_0^1 dx[M_1^2(1-x) + M_2^2 x - sx(1-x)]\ln\left(\frac{M_1^2(1-x) + M_2^2 x - sx(1-x)}{\mu^2}\right) \ , \tag{B.6.40}$$

Here, M_1 and M_2 are the internal meson masses in the loop, μ is the renormalization scale, and γ is Euler's constant. The function $I(s, M_1^2, M_2^2)$ is symmetric under the interchange $M_1 \leftrightarrow M_2$ and encodes the full s-dependence of the amplitude.

Gauge invariance requires that I be proportional to s, which implies that the physical contribution must vanish at $s = 0$. Therefore, the relevant gauge-invariant quantity is:

$$\hat{I}(s, M_1^2, M_2^2) = I(s, M_1^2, M_2^2) - I(0, M_1^2, M_2^2) \ . \tag{B.6.41}$$

For convenience, we define:

$$F_{\pi\pi} = \hat{I}(s, m_{\pi^\pm}^2, m_{\pi^\pm}^2) \ , \quad F_{KK} = \hat{I}(s, m_{K^\pm}^2, m_{K^\pm}^2) \ , \quad F_{K\pi} = F_{\pi K} = \hat{I}(s, m_{K^\pm}^2, m_{\pi^\pm}^2) \ . \tag{B.6.42}$$

The individual diagram contributions to the amplitude (omitting the spinor structure $\bar{u}_{\ell^-} \not{p}_K v_{\ell^+}$) are summarized as follows:

Diagram	$\sqrt{2}\mathcal{M}_{fi}(K^0 \to \pi^0 + \gamma')/(eG_8)$
(a)	$-F_{K\pi}$
(b)	$\dfrac{m_\pi^2 F_{K\pi} - m_K^2 F_{KK}}{m_\pi^2 - m_K^2}$
(c)	$\dfrac{m_K^2 F_{K\pi} - m_\pi^2 F_{\pi\pi}}{m_K^2 - m_\pi^2}$
(d)	F_{KK}
(e)	0
(f)	$\dfrac{m_\pi^2}{m_K^2 - m_\pi^2}(F_{\pi\pi} - F_{KK})$

with $G_8 = \frac{1}{\sqrt{2}} G_F V_{us} V_{ud}^* g_8$.

These results are in perfect agreement with [EPR87].

Summing all contributions, one finds that the terms involving $F_{\pi\pi}$ and $F_{K\pi}$ cancel exactly. The total amplitude is thus:

$$\mathcal{M}_{fi}(K^0 \to \pi^0 + (\gamma \to \ell^- + \ell^+)) = 2\sqrt{2} e G_8 F_{KK} \bar{u}_{\ell^-} \not{p}_K v_{\ell^+} \ . \tag{B.6.43}$$

B.6.2.11 Renormalisation

In a similar manner to the calculation of $K^0 \to \pi^0 + (\gamma \to \ell^+ + \ell^-)$, one can also determine (see [EPR87]):

$$\mathcal{M}_{fi}(K^+ \to \pi^+ + (\gamma \to \ell^- + \ell^+)) = -2eG_8(F_{KK} + F_{\pi\pi}) \bar{u}_{\ell^-} \not{p}_K v_{\ell^+} \ , \tag{B.6.44}$$

$$\mathcal{M}_{fi}(\eta \to \bar{K}^0 + (\gamma \to \ell^- + \ell^+)) = -2\sqrt{6} e G_8 F_{\pi\pi} \bar{u}_{\ell^-} \not{p}_K v_{\ell^+} \ . \tag{B.6.45}$$

This leads to the relation:

$$\mathcal{M}_{fi}(K^+ \to \pi^+ + (\gamma \to \ell^- + \ell^+)) = -\frac{1}{\sqrt{2}} \mathcal{M}_{fi}(K^0 \to \pi^0 + (\gamma \to \ell^- + \ell^+)) - \frac{1}{\sqrt{6}} \mathcal{M}_{fi}(\eta \to \bar{K}^0 + (\gamma \to \ell^- + \ell^+)) \ . \tag{B.6.46}$$

In the $SU(3)$ limit ($m_K = m_\pi$), this becomes:

$$\mathcal{M}_{fi}(K^+ \to \pi^+ + (\gamma \to \ell^- + \ell^+)) = -\sqrt{2} \mathcal{M}_{fi}(K^0 \to \pi^0 + (\gamma \to \ell^- + \ell^+)) = -\frac{\sqrt{2}}{\sqrt{3}} \mathcal{M}_{fi}(\eta \to \bar{K}^0 + (\gamma \to \ell^- + \ell^+)) \ . \tag{B.6.47}$$

The strong counterterms arise from:

$$\begin{aligned} \mathcal{L}^s &= -ieL_9 F_{\mu\nu} \mathrm{Tr}\left[Q\left(\partial_\mu U \partial_\nu U^\dagger + \partial_\mu U^\dagger \partial_\nu U\right)\right] \\ &\supset -\frac{4ieL_9}{F_0^2} F_{\mu\nu} (\partial^\mu \pi^+ \partial^\nu \pi^- + \partial^\mu K^+ \partial^\nu K^-) \ , \end{aligned} \tag{B.6.48}$$

which gives the contribution:

$$\mathcal{M}_{fi}[K^+ \to \pi^+ \gamma'] = -8 L_9 G_8 e s \bar{u}_{\ell^-} \not{p}_K v_{\ell^+} \ . \tag{B.6.49}$$

The weak counterterms originate from:

$$\begin{aligned}\mathcal{L}^w =& -\frac{ie}{2F_0^2}G_8F^{\mu\nu}\left(w_1\mathrm{Tr}[Q\lambda_{6-i7}\mathcal{L}_\mu\mathcal{L}_\nu]+w_2\mathrm{Tr}[Q\mathcal{L}_\mu\lambda_{6-i7}\mathcal{L}_\nu]+w_3\mathrm{Tr}[Q\mathcal{L}_\mu]\mathrm{Tr}[\lambda_{6-i7}\mathcal{L}_\nu]\right)+\text{h.c.}\\ \supset& -i\frac{2}{3}eG_8F^{\mu\nu}\left((w_1+2w_2)\partial_\mu K^+\partial_\nu\pi^- +\frac{1}{\sqrt{2}}(w_1-w_2+3w_3)\partial_\mu\pi^0\partial_\nu K^0\right.\\ &\left.-\sqrt{\frac{3}{2}}(w_1-w_2-w_3)\partial_\mu\eta\partial_\nu K^0\right)+\text{h.c.}\ ,\end{aligned} \tag{B.6.50}$$

which yields:

$$\begin{aligned}\mathcal{M}_{fi}[K^0\to\pi^0+\gamma'] =& \frac{2}{3}eG_8(w_1+2w_2)\bar{u}_{\ell^-}\not{p}_K v_{\ell^+}s\ ,\\ \mathcal{M}_{fi}[K^+\to\pi^++\gamma'] =& -\frac{2}{3}\frac{1}{\sqrt{2}}eG_8(w_1-w_2+3w_3)\bar{u}_{\ell^-}\not{p}_K v_{\ell^+}s\ ,\\ \mathcal{M}_{fi}[\eta\to\bar{K}^0\gamma'] =& -\frac{2}{\sqrt{6}}eG_8(w_1-w_2-w_3)\bar{u}_{\ell^-}\not{p}_K v_{\ell^+}s\ .\end{aligned} \tag{B.6.51}$$

Imposing CPS symmetry (i.e., CP symmetry combined with $d\leftrightarrow s$ exchange), we must set $w_3=0$.

Combining both strong and weak counterterms:

$$\begin{aligned}\mathcal{M}_{fi}[K^0\to\pi^0+\gamma'] =& \frac{2}{3}eG_8(w_1-w_2+3(w_2-4L_9))\bar{u}_{\ell^-}\not{p}_K v_{\ell^+}s\ ,\\ \mathcal{M}_{fi}[K^+\to\pi^++\gamma'] =& -\frac{2}{3}\frac{1}{\sqrt{2}}eG_8(w_1-w_2+3w_3)\bar{u}_{\ell^-}\not{p}_K v_{\ell^+}s\ ,\\ \mathcal{M}_{fi}[\eta\to\bar{K}^0\gamma'] =& -\frac{2}{\sqrt{6}}eG_8(w_1-w_2-w_3)\bar{u}_{\ell^-}\not{p}_K v_{\ell^+}s\ .\end{aligned} \tag{B.6.52}$$

Then, applying the $SU(3)$ limit from Eq. (B.6.47), we obtain the constraints: $w_2=4L_9$ and $w_3=0$.

If we write

$$L_9=L_9^r+\frac{1}{4}\frac{1}{(4\pi)^2\hat{\epsilon}}\,,\quad w_1=w_1^r-\frac{1}{(4\pi)^2\hat{\epsilon}}\ , \tag{B.6.53}$$

then using

$$w_+=-\frac{(4\pi)^2}{3}(w_1^r-4L_9^r)-\frac{1}{6}\ln\left(\frac{m_K^2m_\pi^2}{m_\eta^4}\right)\ , \tag{B.6.54}$$

we can write

$$\mathcal{M}_{fi}[K^+\to\pi^+\ell^+\ell^-]=\frac{2e^2G_8}{(4\pi)^2}\hat{\phi}_+(s)\bar{u}_{\ell^-}\not{p}_K v_{\ell^+}\ , \tag{B.6.55}$$

$$\mathcal{M}_{fi}[K_S\to\pi^0\ell^+\ell^-]=\frac{2e^2G_8}{(4\pi)^2}\hat{\phi}_S(s)\bar{u}_{\ell^-}\not{p}_K v_{\ell^+}\ , \tag{B.6.56}$$

with

$$\hat{\phi}_+(s)=-(\phi_K(s)+\phi_\pi(s)+w_+)\ , \tag{B.6.57}$$

$$\hat{\phi}_S(s)=2\phi_K(s)+\frac{1}{6}\ln\left(\frac{m_\pi^2}{m_K^2}\right)+w_+\ , \tag{B.6.58}$$

and

$$\phi_i(s)=\int_0^1 dx\left(\frac{m_i^2}{s}-x(1-x)\right)\ln\left(1-\frac{s}{m_i^2}x(1-x)\right)\ . \tag{B.6.59}$$

Here, w_+ is a free parameter to be fixed by experimental input. In order to match the observed branching ratio $\Gamma[K^+\to\pi^+e^+e^-]$, Ref. [EPR87] finds two possible values:

$$w_+=1.16\pm0.08\quad\text{or}\quad w_+=-0.47\pm0.08\ . \tag{B.6.60}$$

Table B.1 compares the branching ratios obtained in our calculation to those presented in [EPR87], showing excellent agreement.

	$w_+ = 1.16 \pm 0.08$			$w_+ = -0.57 \pm 0.08$	
	[EPR87]	This work		[EPR87]	This work
$BR(K^+ \to \pi^+\mu^+\mu^-) \times 10^8$	$6.1^{+1.1}_{-1.0}$	$6.3^{+1.1}_{-1.0}$		$4.5^{+1.0}_{-0.8}$	$4.7^{+1.0}_{-0.9}$
$BR(K^+ \to \pi^+e^+e^-) \times 10^7$	2.7 ± 0.5	2.8 ± 0.5		2.7 ± 0.6	2.8 ± 0.5
$BR(K_S \to \pi^0\mu^+\mu^-) \times 10^9$	0.10 ± 0.04	0.11 ± 0.04		1.0 ± 0.1	1.1 ± 0.1
$BR(K_S \to \pi^0e^+e^-) \times 10^9$	$0.48^{+0.20}_{-0.17}$	$0.49^{+0.21}_{-0.17}$		4.9 ± 0.6	5.0 ± 0.6

Table B.1: Comparison between the predictions of [EPR87] and our results.

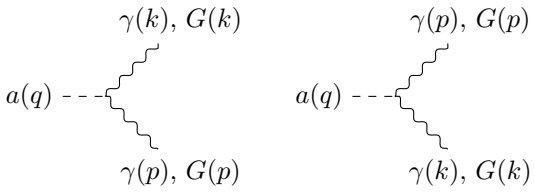

Figure B.3: Tree-level Feynman diagrams for $a \to \gamma\gamma$ and $a \to GG$.

B.7 Calculation of $\hat{c}_{aGG}$ and $\hat{c}_{a\gamma\gamma}$

In processes involving at most one axion, the axial and vector couplings after a chiral rotation are given by:

$$\hat{k}_V = k_V + 2c_{GG}\delta, \quad \hat{k}_A = k_A + 2c_{GG}\kappa \ . \tag{B.7.1}$$

At one loop, the corrected coefficients are:

$$\hat{c}_{GG} = c_{GG}(1 - \mathrm{Tr}[\kappa]) \ , \tag{B.7.2}$$

$$\hat{c}_{\gamma\gamma} = c_{\gamma\gamma} - 2N_c c_{GG}\mathrm{Tr}[Q^2\kappa] \ . \tag{B.7.3}$$

Therefore, to enforce $\hat{c}_{GG} = 0$, one must choose $\mathrm{Tr}[\kappa] = 1$.

To justify Eqs. (B.7.2) and (B.7.3), we sum both the tree-level and one-loop contributions to the processes $a \to GG$ and $a \to \gamma\gamma$, respectively.

At tree level, the axion-gluon-gluon vertex (similarly for two photons) comes from:

$$\begin{aligned}\mathcal{L}_{aGG} &= c_{GG}\frac{\alpha_s}{4\pi}\frac{a}{f_a}G\tilde{G} \\ &= c_{GG}\frac{\alpha_s}{4\pi}\frac{a}{f_a}\epsilon^{\alpha\lambda\beta\nu}(\partial_\alpha G_\lambda - \partial_\lambda G_\alpha)(\partial_\beta G_\nu - \partial_\nu G_\beta) \\ &= c_{GG}\frac{\alpha_s}{2\pi}\frac{a}{f_a}\epsilon^{\alpha\lambda\beta\nu}\partial_\alpha G_\lambda \partial_\beta G_\nu \ ,\end{aligned} \tag{B.7.4}$$

where we used the antisymmetry of the Levi-Civita tensor.

The corresponding tree-level amplitudes (see Fig. B.3) are:

$$i\mathcal{M}_{fi}^{(tree)}(a \to GG) = -ic_{GG}\frac{\alpha_s}{\pi f_a}\epsilon^{\alpha\lambda\beta\nu}k_\alpha p_\beta \delta^{ab}\epsilon^*_{\lambda,a}(k)\epsilon^*_{\nu,b}(p) \ , \tag{B.7.5}$$

$$i\mathcal{M}_{fi}^{(tree)}(a \to \gamma\gamma) = -ic_{\gamma\gamma}\frac{\alpha_{e.m.}}{\pi f_a}\epsilon^{\alpha\lambda\beta\nu}k_\alpha p_\beta \epsilon^*_\lambda(k)\epsilon^*_\nu(p) \ . \tag{B.7.6}$$

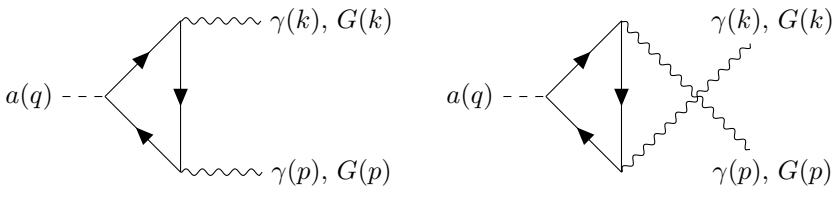

Figure B.4: One-loop Feynman diagrams for $a \to \gamma\gamma$ and $a \to GG$.

At one loop (see Fig. B.4), we use the known result that a fermion loop with an incoming axial vertex $-iq\!\!\!/\gamma_5$ and two outgoing vector vertices $-ig_a\gamma^\mu$ (with $a \in \{s, e.m.\}$) evaluates to (see [PS95]):

$$\frac{g_a^2}{2\pi^2}\epsilon^{\alpha\lambda\beta\nu}k_\alpha p_\beta = \frac{2\alpha_a}{\pi}\epsilon^{\alpha\lambda\beta\nu}k_\alpha p_\beta \ . \tag{B.7.7}$$

The vertex between the axion and a quark i is:

$$\frac{(\hat{k}_A)_{ii}}{2f_a}q\!\!\!/\gamma_5 \ , \tag{B.7.8}$$

while the photon vertex is $iq_i e\gamma^\mu$, and the gluon vertex is $ig_s(\lambda^a)_{cd}\gamma^\mu$.

Thus, for a single quark loop:

- the photon amplitude is multiplied by $i\frac{(\hat{k}_A)_{ii}}{2f_a}q_i^2 N_c$,
- the gluon amplitude is multiplied by $i\frac{(\hat{k}_A)_{ii}}{2f_a}\mathrm{Tr}[\lambda^a\lambda^b] = i\frac{(\hat{k}_A)_{ii}}{f_a}\delta^{ab}$.

Summing over all quark flavors:

- the photon amplitude gains an overall factor $i\frac{N_c}{2f_a}\mathrm{Tr}[Q^2\hat{k}_A]$,
- the gluon amplitude gains $i\frac{1}{f_a}\mathrm{Tr}[\hat{k}_A]$.

We then obtain the one-loop amplitudes:

$$i\mathcal{M}_{fi}^{(loop)}(a \to GG) = +i\frac{\mathrm{Tr}[\hat{k}_A]}{2}\frac{\alpha_s}{\pi f_a}\epsilon^{\alpha\lambda\beta\nu}k_\alpha p_\beta\delta^{ab}\epsilon^*_{\lambda,a}(k)\epsilon^*_{\nu,b}(p) \tag{B.7.9}$$

$$i\mathcal{M}_{fi}^{(loop)}(a \to \gamma\gamma) = +iN_c\mathrm{Tr}[Q^2\hat{k}_A]\frac{\alpha_{e.m.}}{\pi f_a}\epsilon^{\alpha\lambda\beta\nu}k_\alpha p_\beta\epsilon^*_\lambda(k)\epsilon^*_\nu(p) \ . \tag{B.7.10}$$

The overall sign depends on the convention chosen for the Levi-Civita tensor: it is positive for $\epsilon^{0123} = +1$, and negative if $\epsilon^{0123} = -1$.

Substituting the model-independent relation $\hat{k}_A = 2c_{GG}\kappa$ into the above expressions directly yields the results stated in Eqs. (B.7.2) and (B.7.3).

We now verify Eq. (B.7.7) by directly computing the loop diagram for the process $a(q) \to \gamma(k) + \gamma(p)$. Neglecting polarization vectors, the loop amplitude is given by:

$$i\mathcal{M}_{fi}^{loop} = \int\frac{d^4\ell}{(2\pi)^4}\mathrm{Tr}\left[(-iq\!\!\!/\gamma_5)\,i\frac{\ell\!\!\!/ - k\!\!\!/}{(\ell-k)^2}\left(-ie\gamma^\lambda\right)i\frac{\ell\!\!\!/}{\ell^2}\left(-ie\gamma^\nu\right)i\frac{\ell\!\!\!/ + p\!\!\!/}{(\ell+p)^2}\right] \ . \tag{B.7.11}$$

Using momentum conservation $q = p + k$, we write:

$$q\!\!\!/\gamma_5 = (\ell\!\!\!/ + p\!\!\!/ - \ell\!\!\!/ + k\!\!\!/)\gamma_5 = (\ell\!\!\!/ + p\!\!\!/)\gamma_5 + \gamma_5(\ell\!\!\!/ - k\!\!\!/) \ . \tag{B.7.12}$$

Substituting this into the amplitude, we obtain:

$$i\mathcal{M}_{fi}^{loop} = e^2\int\frac{d^4\ell}{(2\pi)^4}\mathrm{Tr}\left[\gamma_5\frac{\ell\!\!\!/ - k\!\!\!/}{(\ell-k)^2}\gamma^\lambda\frac{\ell\!\!\!/}{\ell^2}\gamma^\nu + \gamma_5\gamma^\lambda\frac{\ell\!\!\!/}{\ell^2}\gamma^\nu\frac{\ell\!\!\!/ + p\!\!\!/}{(\ell+p)^2}\right] \ . \tag{B.7.13}$$

After a change of variable $\ell \to \ell + k$ in the first term and using cyclicity of the trace, the amplitude becomes:

$$i\mathcal{M}_{fi}^{loop} = e^2\int\frac{d^4\ell}{(2\pi)^4}\mathrm{Tr}\left[\gamma_5\frac{\ell\!\!\!/}{\ell^2}\gamma^\lambda\frac{\ell\!\!\!/ + k\!\!\!/}{(\ell-k)^2}\gamma^\nu - \gamma_5\frac{\ell\!\!\!/}{\ell^2}\gamma^\nu\frac{\ell\!\!\!/ + p\!\!\!/}{(\ell+p)^2}\gamma^\lambda\right] \ . \tag{B.7.14}$$

This expression is manifestly antisymmetric under the exchange $(p, \nu) \leftrightarrow (k, \lambda)$, which corresponds to interchanging the two photons (or gluons) in the final state. As a result, the sum of the two diagrams in Fig. B.4 naively cancels out, suggesting that the total amplitude vanishes.

The issue with the previous procedure is that it involves subtracting divergent integrals, which is ill-defined. To properly regularize the amplitude, we must compute it using dimensional regularization by splitting the loop momentum as

$$\ell = \ell_\parallel + \ell_\perp \ , \tag{B.7.15}$$

where $\ell_\parallel$ lies in the physical 4-dimensional Minkowski spacetime (i.e., the subspace spanned by $\mu \in \{0,1,2,3\}$) and $\ell_\perp$ lies in the orthogonal $d-4$ extra dimensions introduced by the continuation to d-dimensions.

Since $\gamma_5 = i\gamma^0\gamma^1\gamma^2\gamma^3$, it follows that γ_5 anticommutes with γ^μ for $\mu \in \{0,1,2,3\}$, i.e., $\{\gamma_5, \ell_\parallel\} = 0$, but commutes with γ^μ for $\mu \notin \{0,1,2,3\}$, i.e., $[\gamma_5, \ell_\perp] = 0$.

As a result, Eq. (B.7.12) now reads:

$$\not{q}\gamma_5 = (\not{\ell} + \not{p})\gamma_5 + \gamma_5(\not{\ell} - \not{k}) - 2\gamma_5\not{\ell}_\perp \ , \tag{B.7.16}$$

Importantly, only this third term contributes to the anomaly, since the first two terms cancel out when the second diagram is included. This leaves the amplitude as:

$$i\mathcal{M}_{fi} = -2e^2 \int \frac{\mu^{4-d} d^d\ell}{(2\pi)^d} \mathrm{Tr}\left[\gamma_5 \not{\ell}_\perp \frac{\not{\ell} - \not{k}}{(\ell-k)^2}\gamma^\lambda \frac{\not{\ell}}{\ell^2}\gamma^\nu \frac{\not{\ell} + \not{p}}{(\ell+p)^2}\right] \ . \tag{B.7.17}$$

We now use the standard Feynman parametrization:

$$\begin{aligned}
\frac{1}{(\ell-k)^2(\ell+p)^2\ell^2} &= \int_{[0;1]^3} \frac{2dxdydz\delta(x+y+z-1)}{(x(\ell-k)^2 + y(\ell+p)^2 + z\ell^2)^3} \\
&= \int_{x+y\leq 1} \frac{2dxdy}{\ell^2 - 2\ell\cdot(xk-yp)} \\
&= \int_{x+y\leq 1} \frac{2dxdy}{((\ell-(xk-yp))^2 + 2xy\, p\cdot k)^3} \ ,
\end{aligned} \tag{B.7.18}$$

where we used $k^2 = p^2 = 0$, as the final-state bosons are massless.

We perform the change of variable $\ell \to \ell + P$ with $P = xk - yp$. In the expansion of the Dirac trace, only terms that include exactly one of each among γ^ν, γ^λ, $\not{p}$, and $\not{k}$ contribute, due to the properties of γ_5. Cross-terms such as $\not{\ell}_\perp\not{\ell}_\parallel$ give vanishing traces after angular integration. Therefore, only the quadratic term $\not{\ell}_\perp^2 = \ell_\perp^2$ contributes. Using the fact that $\not{\ell}_\perp$ commutes with all 4D gamma matrices, we can factor it out of the trace. This yields:

$$i\mathcal{M}_{fi} = -4e^2 \int_{x+y\leq 1} dxdy \left(\int \frac{\mu^{d-4} d^d\ell}{(2\pi^d)} \frac{\ell_\perp^2}{(\ell^2-\Delta)^3}\right) \mathrm{Tr}\left[\gamma_5 \not{k}\gamma^\lambda \not{p}\gamma^\nu\right] \ , \tag{B.7.19}$$

where we defined $\Delta = -2xy\, p\cdot k$. The antisymmetry of the trace with γ_5 ensures that reordering the gamma matrices in the trace introduces only signs.

Using the standard projection formula in dimensional regularization, we have:

$$\ell_\perp^2 \to \frac{d-4}{d}\ell^2 \ , \tag{B.7.20}$$

which allows us to express the integral as:

$$\begin{aligned}
\int \frac{\mu^{4-d} d^d\ell}{(2\pi^d)} \frac{\not{\ell}_\perp^2}{(\ell^2-\Delta)^3} &= \mu^{4-d}\frac{d-4}{d}\int \frac{\mu^{4-d} d^d\ell}{(2\pi^d)} \frac{\ell^2}{(\ell^2-\Delta)^3} \\
&= \mu^{4-d}\frac{i(d-4)\Gamma(2-d/2)}{(4\pi)^{d/2}\Delta^{2-d/2}\Gamma(3)} \\
&= \frac{-i}{2(4\pi)^2}\left(\frac{\Delta}{4\pi\mu^2}\right)^{-\epsilon}\epsilon\Gamma(\epsilon/2) \\
&= \frac{-i}{2(4\pi)^2} + \mathcal{O}(\epsilon)
\end{aligned} \tag{B.7.21}$$

where we used the expansion $\Gamma(\epsilon/2) = 2/\epsilon - \gamma + \mathcal{O}(\epsilon)$.

Moreover, the Feynman parameter integral evaluates to:

$$\int_{x+y\leq 1} dxdy = \int_{x=0}^1 \int_{y=0}^{1-x} dydx = \int_0^1 (1-x)dx = \frac{1}{2} \ . \tag{B.7.22}$$

Combining everything, we finally obtain:

$$i\mathcal{M}_{fi} = \frac{ie^2}{(4\pi)^2}\mathrm{Tr}\left[\gamma_5 \not{k}\gamma^\lambda \not{p}\gamma^\nu\right] = \frac{e^2}{4\pi^2}\epsilon^{\alpha\lambda\beta\nu}k_\alpha p_\beta \ . \tag{B.7.23}$$

This expression agrees with Eq. (B.7.12) upon summing the contributions from both diagrams.

B.8 Axion emissivity calculation

The emissivity can be expressed as

$$Q_a = \int dE_a E_a \frac{d\dot{n}_a}{dE_a} \ , \tag{B.8.1}$$

where $d\dot{n}_a/dE_a$ is the differential production rate of axions.

After selecting one of the three momentum vectors, e.g., $\vec{p}_a$, as a reference, the physics will only depend on the relative orientation of the vectors. Different orientations of $\vec{p}_a$ yield the same physical results as long as the relative orientations of the other vectors remain unchanged.

Therefore, the solid angle element $d^2\Omega_a$ associated with $\vec{p}_a$ can be integrated out, contributing a factor of 4π:

$$d^3\vec{p}_a = |p_a| E_a dE_a d^2\Omega_a = 4\pi |p_a| E_a dE_a \ . \tag{B.8.2}$$

For computational convenience, we choose $\vec{p}_a = |p_a|\vec{e}_z$.

B.8.1 $1 \to 2$ decay

B.8.1.1 General calculation

$$\frac{d\dot{n}_a}{dE_a} = \int \frac{d^3\vec{p}_i}{2E_i(2\pi)^3} \frac{d^3\vec{p}_f}{2E_f(2\pi)^3} \frac{4\pi |p_a| E_a}{2E_a(2\pi)^3} |\mathcal{M}_{fi}|^2 (2\pi)^4 \delta^4(p_i - p_f - p_a) f_i \bar{f}_f \tag{B.8.3}$$

$$= \frac{|p_a|}{4(2\pi)^3} \int \frac{|p_i|^2 d\cos(\theta_{ia}) d|p_i|}{E_i E_f} |\mathcal{M}_{fi}|^2 \delta(E_i - E_f - E_a) f_i \bar{f}_f \ . \tag{B.8.4}$$

Using the relation

$$m_f^2 = p_f^2 = (p_i - p_a)^2 = m_i^2 + m_a^2 - 2E_i E_a + 2|p_i||p_a|\cos(\theta_{ia}) \ , \tag{B.8.5}$$

we obtain

$$\cos(\theta_{ia}) = \frac{E_i E_a - (m_i^2 + m_a^2 - m_f^2)/2}{|p_i||p_a|} \ . \tag{B.8.6}$$

In general,

$$E_f = \sqrt{m_f^2 + |p_f|^2} = \sqrt{m_f^2 + |p_i|^2 + |p_a|^2 - 2|p_i||p_a|\cos(\theta_{ia})} \ , \tag{B.8.7}$$

which leads to

$$\frac{\partial(E_i - E_f - E_a)}{\partial \cos(\theta_{ia})} = \frac{|p_i||p_a|}{E_f} \ . \tag{B.8.8}$$

This allows us to express

$$\frac{d\dot{n}_a}{dE_a} = \frac{1}{4(2\pi)^3} \int \frac{|p_i| d|p_i|}{E_i} |\mathcal{M}_{fi}|^2 f_i \bar{f}_f \chi_{[-1;1]}(\cos(\theta_{ia})) \ , \tag{B.8.9}$$

where χ is the characteristic function defined as

$$\chi_A(x) := \begin{cases} 1 \text{ if } x \in A \\ 0 \text{ if } x \notin A \end{cases} \ . \tag{B.8.10}$$

To work in a dimensionless form, we introduce the change of variable $x_i = |p_i|/T$, and define $e_i = E_i/T = \sqrt{(m_i/T)^2 + x_i^2}$, which gives

$$\frac{d\dot{n}_a}{dE_a} = \frac{T}{4(2\pi)^3} \int_0^{+\infty} \frac{x_i dx_i}{e_i} |\mathcal{M}_{fi}|^2 f_i \bar{f}_f \chi_{[-1;1]}(\cos(\theta_{ia})) \ . \tag{B.8.11}$$

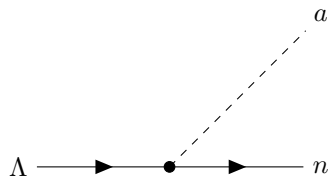

Figure B.5: Feynman diagram contributing to the baryon decay $\Lambda \to na$.

B.8.1.2 Comparison with [Mar+20; Cam+21] for $\Lambda \to na$

We now compare our procedure with the approach used in [Mar+20; Cam+21], applied to the process $\Lambda \to n + a$.

The relevant tree-level Feynman diagram for the $\Lambda \to na$ decay is shown in Fig. B.5.

Results from [Mar+20; Cam+21]

The authors work within the framework of LQCD and use the following Lagrangian:

$$\mathcal{L}_{aff} = \frac{\partial_\mu a}{2f_a}\,\overline{f_i}\gamma^\mu \left(c_{ij}^V + c_{ij}^A\gamma_5\right) f_j \ . \tag{B.8.12}$$

Introducing the notation:

$$F_{ij}^{V,A} \equiv \frac{2f_a}{c_{ij}^{V,A}} \ , \tag{B.8.13}$$

they obtain the decay rate:

$$\Gamma[\Lambda \to n + a] = \frac{m_\Lambda^3}{16\pi}\left(1 - \frac{m_n^2}{m_\Lambda^2}\right)^3 \left(\frac{f_1(0)^2}{|F_{32}^V|^2} + \frac{g_1(0)^2}{|F_{32}^A|^2}\right) \ , \tag{B.8.14}$$

and the corresponding energy emission rate[6]:

$$\frac{Q_a[\Lambda \to n + a]}{\Gamma[\Lambda \to n + a]} = \frac{m_\Lambda^3}{\pi^2(m_\Lambda^2 - m_n^2)} \int_0^\infty p_\Lambda\, dp_\Lambda \int_{p_n^{\min}}^{p_n^{\max}} p_n\, dp_n\, \frac{E_\Lambda - E_n}{E_\Lambda E_n} f_\Lambda(1 - f_n) := \alpha \tag{B.8.15}$$

$$\simeq n_\Lambda(m_\Lambda - m_n) := \beta \ . \tag{B.8.16}$$

This leads to the expression:

$$\epsilon = \frac{Q_a}{\rho_{\rm nuc}} = 3.6 \times 10^{38}\ \frac{\rm erg}{\rm s \cdot g} \cdot {\rm GeV}^2 \left(\frac{f_1(0)^2}{|F_{32}^V|^2} + \frac{g_1(0)^2}{|F_{32}^A|^2}\right) \ . \tag{B.8.17}$$

The bound $\epsilon < 10^{19}$ erg.s^{-1}.g^{-1} then implies:

$$|F_{32}^V| > 7.4 \times 10^9 \ , \quad |F_{32}^A| > 5.4 \times 10^9 \ . \tag{B.8.18}$$

Verification of the Effective Field Theory (EFT)-LQCD equivalence

With our procedure, we can compute:

$$\overline{|\mathcal{M}_{fi}|^2} = 4(p_\Lambda \cdot p_a)^2 \left(\frac{3/2}{|F_{32}^V|^2} + \frac{(3F + D)^2/6}{|F_{32}^A|^2}\right) \ , \tag{B.8.19}$$

and

$$m_n^2 = p_n^2 = (p_\Lambda - p_a)^2 = m_\Lambda^2 - 2p_\Lambda \cdot p_a \Rightarrow p_\Lambda \cdot p_a = \frac{m_\Lambda^2 - m_n^2}{2} \ , \tag{B.8.20}$$

so that

$$\overline{|\mathcal{M}_{fi}|^2} = (m_\Lambda^2 - m_n^2)^2 \left(\frac{3/2}{|F_{32}^V|^2} + \frac{(3F + D)^2/6}{|F_{32}^A|^2}\right) \ . \tag{B.8.21}$$

[6] In Eq. (B.8.15), the numerator in front of the integral contains a factor of m_Λ^3. However, in [Mar+20], this factor appears as m_n^3. As I will show below, this is a typographical error, and the correct term is m_Λ^3. This discrepancy introduces a factor of $(m_\Lambda/m_n)^3 = 1.67$, which does not affect the overall order-of-magnitude (oom). And more importantly, in [Mar+20] they make the assumption $m_n \simeq m_\Lambda$ to obtain Eq. (B.8.16).

Therefore in the center of mass

$$\begin{aligned}\Gamma &= \int_{(\mathbb{R}^3)^2} \frac{1}{2m_\Lambda}\overline{|\mathcal{M}_{fi}|^2}(2\pi)^4\delta^4(p_\Lambda - p_n - p_a)\frac{d^3\vec{p}_n}{2E_n(2\pi)^3}\frac{d^3\vec{p}_a}{2E_a(2\pi)^3} \\ &= \frac{m_\Lambda^2 - m_n^2}{16\pi m_\Lambda^3}\overline{|\mathcal{M}_{fi}|^2} \\ &= \frac{m_\Lambda^3}{16\pi}\left(1 - \left(\frac{m_n}{m_\Lambda}\right)^2\right)^3\left(\frac{3/2}{|F_{32}^V|^2} + \frac{(3F+D)^2/6}{|F_{32}^A|^2}\right) .\end{aligned} \tag{B.8.22}$$

By comparing this with Eq. (B.8.14), we identify:

$$|f_1(0)| = \sqrt{\frac{3}{2}} \simeq 1.22 , \quad |g_1(0)| = \frac{|3F+D|}{\sqrt{6}} \simeq 0.94 . \tag{B.8.23}$$

To check the consistency of these values with the numerical results from [Mar+20; Cam+21], we start from the constraint:

$$\epsilon < 10^{19}\ \frac{\text{erg}}{\text{s.g}} , \tag{B.8.24}$$

and the expression:

$$\epsilon = 3.6 \times 10^{38}\ \frac{\text{erg}}{\text{s}\cdot\text{g}} \cdot \text{GeV}^2 \left(\frac{f_1(0)^2}{|F_{32}^V|^2} + \frac{g_1(0)^2}{|F_{ij}^A|^2}\right) , \tag{B.8.25}$$

which implies:

$$\frac{f_1(0)^2}{|F_{ij}^V|^2} + \frac{g_1(0)^2}{|F_{32}^A|^2} < 2.78 \times 10^{-20}\ \text{GeV}^{-2} . \tag{B.8.26}$$

From this, we obtain the separate bounds:

$$\frac{f_1(0)^2}{|F_{32}^V|^2} < 2.78 \times 10^{-20}\ \text{GeV}^{-2} \ \Leftrightarrow\ |F_{32}^V| > |f_1(0)| \times 6 \times 10^9\ \text{GeV} , \tag{B.8.27}$$

$$\frac{g_1(0)^2}{|F_{32}^A|^2} < 2.78 \times 10^{-20}\ \text{GeV}^{-2} \ \Leftrightarrow\ |F_{32}^A| > |g_1(0)| \times 6 \times 10^9\ \text{GeV} . \tag{B.8.28}$$

Identifying these with the bounds from Eq. (B.8.18), we find:

$$|f_1(0)| = \frac{7.4}{6} \simeq 1.23 , \quad |g_1(0)| = \frac{5.4}{6} \simeq 0.90 , \tag{B.8.29}$$

which is in excellent agreement with the values obtained in Eq. (B.8.23). This confirms the consistency between our EFT-based calculation and the LQCD results from [Mar+20; Cam+21].

Verification of Eqs. (B.8.15)-(B.8.16)
Using Eq. (B.8.9), the change of variables

$$d|p_\Lambda|dE_a = d|p_\Lambda|dE_n = \frac{|p_n|}{E_n}d|p_\Lambda|d|p_n| , \tag{B.8.30}$$

and the link between the averaged Feynman amplitude squared $\overline{|\mathcal{M}_{fi}|^2}$ and the decay rate in the center-of-mass frame Γ in Eq. (B.8.22), we obtain:

$$Q_a = \frac{m_\Lambda^3\Gamma}{\pi^2(m_\Lambda^2 - m_n^2)}\int_0^{+\infty} |p_\Lambda|\, d|p_\Lambda| \int_{p_n^{\min}}^{p_n^{\max}} |p_n|\, d|p_n|\, \frac{E_a}{E_\Lambda E_n} f_\Lambda(1-f_n) , \tag{B.8.31}$$

which is exactly the expression in Eq. (B.8.15) due to energy conservation $E_a = E_\Lambda - E_n$.

A stronger approximation can be made under the condition $|p_\Lambda|, |p_n| \ll m_n \simeq m_\Lambda$, in which case:

$$\frac{m_\Lambda^3}{\pi^2(m_\Lambda^2 - m_n^2)}\frac{E_\Lambda - E_n}{E_\Lambda E_n} \simeq \frac{m_\Lambda^3}{\pi^2(m_\Lambda - m_n)(m_\Lambda + m_n)} \cdot \frac{m_\Lambda - m_n}{m_\Lambda m_n} \simeq \frac{1}{2\pi^2} , \tag{B.8.32}$$

which leads to:

$$Q_a \simeq \Gamma \cdot \frac{1}{2\pi^2} \int_0^\infty f_\Lambda \, |p_\Lambda| \, |dp_\Lambda| \int_{p_n^{\min}}^{p_n^{\max}} (1 - f_n) \, |p_n| \, d|p_n| \ . \tag{B.8.33}$$

In the rest frame of the initial Λ, the neutron momentum is

$$|p_n^*| = \frac{m_\Lambda^2 - m_n^2}{2m_\Lambda} = \frac{(m_\Lambda - m_n)(m_\Lambda + m_n)}{2m_\Lambda} \simeq m_\Lambda - m_n \ . \tag{B.8.34}$$

From the center-of-mass frame quantities, we can deduce the neutron momentum in the boosted frame with

$$\begin{cases} p_{n,||} = \gamma(p^*_{n,||} + vE^*_n) \\ p_{n,\perp} = p^*_{n,\perp} \end{cases} , \tag{B.8.35}$$

where

$$\begin{aligned} |v| &= \frac{|p_\Lambda|}{E_\Lambda} \simeq \frac{|p_\Lambda|}{m_\Lambda} \ , \\ \gamma &= (1 - v^2)^{-1/2} \simeq 1 \ , \\ E^*_n &\simeq m_n \ , \\ p^*_{n,||} &= |p^*_n| \cos(\theta^*_{\Lambda n}) \ , \\ p^*_{n,\perp} &= |p^*_n| \sin(\theta^*_{\Lambda n}) \ . \end{aligned} \tag{B.8.36}$$

Averaging over angles, $\overline{\sin(\theta^*_{\Lambda n})} = \overline{\sin(\theta^*_{\Lambda n})} = 0$, gives:

$$\overline{|p_n|} \simeq |p_\Lambda| \frac{m_n}{m_\Lambda} \simeq |p_\Lambda| \ , \tag{B.8.37}$$

and the variation is approximately

$$\Delta|p_n| = |p_n^{\max}| - |p_n^{\min}| = \gamma(vE^*_n + |p^*_n|) - \gamma(vE^*_n - |p^*_n|) = 2\gamma|p^*_n| \simeq 2|p^*_n| = 2(m_\Lambda - m_n) \ . \tag{B.8.38}$$

Neglecting $1 - f_n \simeq 1$, we then have:

$$\int_{p_n^{\min}}^{p_n^{\max}} (1 - f_n) \, |p_n| \, d|p_n| \simeq \overline{|p_n|} \Delta|p_n| = 2(m_\Lambda - m_n)|p_\Lambda| \ . \tag{B.8.39}$$

Therefore,

$$Q_a \simeq (m_\Lambda - m_n)\Gamma \cdot \frac{1}{\pi^2} \int_0^\infty |p_\Lambda|^2 f_\Lambda d|p_\Lambda| = n_\Lambda (m_\Lambda - m_n)\Gamma \ . \tag{B.8.40}$$

which exactly matches the expression in Eq. (B.8.16).

Numerical comparison

To obtain the numerical values, it is necessary to specify the Supernova (SN) model used in [Mar+20; Cam+21]. The authors consider:

$$\begin{aligned} T &= 30 \text{ MeV} \ , \\ m_n &= 939.57 \text{ MeV}, \quad m_\Lambda = 1115.683 \text{ MeV} \ , \\ \rho_{\text{nuc}} &= 3 \times 10^{17} \text{ kg/m}^3 = 3 \times 10^{14} \text{ g/cm}^3 = 1.3 \times 10^9 \text{ MeV}^4 \ , \\ Y_\ell &= \frac{n_\ell}{n_B} = 0.3, \quad \rho_B = (1 - Y_\ell)\rho_{\text{nuc}}, \quad \rho_n \simeq \rho_B \ , \\ n_n &= \frac{\rho_n}{m_n} \simeq \frac{(1 - Y_\ell)\rho_{\text{nuc}}}{m_n} = 9.62 \times 10^5 \text{ MeV}^3 \ , \\ n_\Lambda &\simeq n_n \, e^{-(m_\Lambda - m_n)/T} = 2.71 \times 10^3 \text{ MeV}^3 \ . \end{aligned} \tag{B.8.41}$$

The justification for the expression of n_n in Eq. (B.8.41) is that the SN core is dominated by neutrons, protons, and electrons. Since charge neutrality implies $n_e = n_p$, we get $Y_p = n_p/n_B = n_e/n_B = Y_e \simeq Y_\ell$. The proton energy density can then be written as $\rho_p \simeq Y_p \rho_{\text{nuc}}$, and since the lepton energy density is negligible ($\rho_\ell \simeq Y_\ell (m_e/m_N)\rho_B \ll \rho_B$), we find $\rho_{\text{nuc}} = \rho_n + \rho_p = \rho_n + Y_p \rho_{\text{nuc}}$, which yields $\rho_n = (1 - Y_\ell)\rho_{\text{nuc}}$.

We can invert the Fermi-Dirac distribution to determine chemical potentials using:

$$n = \iiint_{\mathbb{R}^3} \frac{2d^3\vec{p}}{(2\pi)^3} f(p) = \frac{1}{\pi^2}\int_0^\infty \frac{p^2 dp}{1+\exp\left(\frac{E-\mu}{T}\right)} = \frac{T^3}{\pi^2}\int_0^\infty \frac{x^2 dx}{1+\exp\left(\frac{E-\mu}{T}\right)} \ . \tag{B.8.42}$$

Using a dichotomy algorithm, we find:

$$\mu_n = 966.9 \text{ MeV}, \quad \mu_\Lambda = 944.5 \text{ MeV} \ . \tag{B.8.43}$$

From this and Eqs. (B.8.14), (B.8.15), and (B.8.16), we calculate:

$$\begin{aligned} \Gamma[\Lambda \to n + a] &= 6.79 \times 10^5 \text{ MeV}^3 \left(\frac{f_1(0)^2}{|F_{32}^V|^2} + \frac{g_1(0)^2}{|F_{32}^A|^2}\right) \ , \\ \alpha &= 1.90 \times 10^{53} \ \frac{\text{erg.cm}^{-3}.\text{s}^{-1}}{\text{MeV}} \ , \\ \beta &= 1.51 \times 10^{53} \ \frac{\text{erg.cm}^{-3}.\text{s}^{-1}}{\text{MeV}} \ , \end{aligned} \tag{B.8.44}$$

and thus:

$$\begin{aligned} \alpha\Gamma &= 1.29 \times 10^{52} \text{ erg.cm}^{-3}.\text{s}^{-1}.\text{GeV}^2 \left(\frac{f_1(0)^2}{|F_{32}^V|^2} + \frac{g_1(0)^2}{|F_{32}^A|^2}\right) \ , \\ \beta\Gamma &= 1.03 \times 10^{53} \text{ erg.cm}^{-3}.\text{s}^{-1}.\text{GeV}^2 \left(\frac{f_1(0)^2}{|F_{32}^V|^2} + \frac{g_1(0)^2}{|F_{32}^A|^2}\right) \ . \end{aligned} \tag{B.8.45}$$

Normalizing to the nuclear density, we find:

$$\begin{aligned} \epsilon_\alpha &= \frac{\alpha\Gamma}{\rho_{\text{nuc}}} = 4.29 \times 10^{38} \ \frac{\text{erg}}{\text{s.g}}.\text{GeV}^2 \left(\frac{f_1(0)^2}{|F_{32}^V|^2} + \frac{g_1(0)^2}{|F_{32}^A|^2}\right) \ , \\ \epsilon_\beta &= \frac{\beta\Gamma}{\rho_{\text{nuc}}} = 3.43 \times 10^{38} \ \frac{\text{erg}}{\text{s.g}}.\text{GeV}^2 \left(\frac{f_1(0)^2}{|F_{32}^V|^2} + \frac{g_1(0)^2}{|F_{32}^A|^2}\right) \ . \end{aligned} \tag{B.8.46}$$

Let us denote by $\hat{\epsilon}$ the result obtained in [Mar+20; Cam+21], as given in Eq. (B.8.17). We then find:

$$\frac{\epsilon_\alpha}{\hat{\epsilon}} = 1.2, \quad \frac{\epsilon_\beta}{\hat{\epsilon}} = 0.95 \ . \tag{B.8.47}$$

We observe that, at the oom level, these values are largely consistent with each other. In particular, ϵ_β differs from $\hat{\epsilon}$ by only 5%, indicating that the SN model has been correctly identified. Similarly, ϵ_α differs by about 20%, which reflects the uncertainty associated with the approximations made in [Mar+20; Cam+21], namely $|p_\Lambda|, |p_n| \ll m_n \simeq m_\Lambda$.[7]

B.8.2 $2 \to 2$ scattering

B.8.2.1 General calculation

$$\begin{aligned} \frac{d\dot{n}_a}{dE_a} &= \int \frac{d^3\vec{p}_1}{2E_1(2\pi)^3}\frac{d^3\vec{p}_2}{2E_2(2\pi)^3}\frac{d^3\vec{p}_3}{2E_3(2\pi)^3}\frac{4\pi|p_a|E_a}{2E_a(2\pi)^3}|\mathcal{M}_{fi}|^2(2\pi)^4\delta^4(p_i - p_f)f_1 f_2 \bar{f}_3 \\ &= \frac{|p_a|}{8(2\pi)^7}\int \frac{|p_1|^2 d|p_1| d\cos(\theta_{1a}) d\psi_1 |p_2|^2 d|p_2| d\cos(\theta_{2a}) d\psi_2}{E_1 E_2 E_3}|\mathcal{M}_{fi}|^2\delta(E_i - E_f)f_1 f_2 \bar{f}_3 \end{aligned} \tag{B.8.48}$$

In spherical coordinate

$$\vec{p}_i = \begin{pmatrix} p_i^x \\ p_i^y \\ p_i^z \end{pmatrix} = |p_i| \begin{pmatrix} \cos(\psi_i)\sin(\theta_{ia}) \\ \sin(\psi_i)\sin(\theta_{ia}) \\ \cos(\theta_\alpha) \end{pmatrix} \tag{B.8.49}$$

$|\mathcal{M}_{fi}|^2$ only depends on $p_1 \cdot p_a$, $p_2 \cdot p_a$ and $p_1 \cdot p_2$ and therefore only on $|p_1|$, $|p_2|$, $|p_a|$, $\cos(\theta_{1a})$, $\cos(\theta_{2a})$, $\cos(\theta_{12})$ with $\theta_{\alpha\beta}$ the relative angle between $\vec{p}_\alpha$ and $\vec{p}_\beta$ ($\vec{p}_\alpha \cdot \vec{p}_\beta = |p_\alpha||p_\beta|\cos(\theta_{\alpha\beta})$).

$\cos(\theta_{iM})$ can be expressed in terms of $\cos(\theta_{1a})$, $\cos(\theta_{2a})$, $\psi_1 - \psi_2$, see Eq. (B.8.50).

[7] Interestingly, the oom of the 20% difference is consistent with the approximation $m_n \simeq m_\Lambda$, since $(m_\Lambda - m_n)/m_\Lambda \simeq 16\%$.

$$\begin{aligned}\vec{p}_1\cdot\vec{p}_2 =&|p_1||p_2|(\cos(\psi_1)\sin(\theta_{1a})\cos(\psi_2)\sin(\theta_{2a})+\sin(\psi_1)\sin(\theta_{1a})\sin(\psi_2)\sin(\theta_{2a})+\cos(\theta_{1a})\cos(\theta_{2a}))\\ \Rightarrow\cos(\theta_{12}) =&\cos(\psi_1-\psi_2)\sin(\theta_{1a})\sin(\theta_{2a})+\cos(\theta_{1a})\cos(\theta_{2a})\\ =&\cos(\psi_1-\psi_2)\sqrt{1-\cos^2(\theta_{1a})}\sqrt{1-\cos^2(\theta_{2a})}+\cos(\theta_{1a})\cos(\theta_{2a})\end{aligned}\tag{B.8.50}$$

In the integration, the only dependence on ψ_1 and ψ_2 is on $\cos(\psi_1-\psi_2)$, we pose $\psi_{12}=\psi_1-\psi_2$, therefore the integration is of the type

$$\begin{aligned}\int_0^{2\pi}d\psi_1\int_0^{2\pi}d\psi_2 f(\cos(\psi_1-\psi_2)) &= \int_0^{2\pi}d\psi_1\int_0^{2\pi}d(\psi_1-\psi_2)f(\cos(\psi_1-\psi_2))\\ &= \int_0^{2\pi}d\psi_1\int_{-\psi_1}^{2\pi-\psi_1}d(\psi_1-\psi_2)f(\cos(\psi_1-\psi_2))\\ &= \int_0^{2\pi}d\psi_1\int_0^{2\pi}d\psi_{12}f(\cos(\psi_{12}))\\ &= 2\pi\int_0^{2\pi}d\psi_{12}f(\cos(\psi_{12}))\end{aligned}\tag{B.8.51}$$

therefore

$$\frac{d\dot{n}_a}{dE_a}=\frac{|p_a|}{8(2\pi)^6}\int\frac{|p_1|^2d|p_1|d\cos(\theta_{1a})d\psi_{12}|p_2|^2d|p_2|d\cos(\theta_{2a})}{E_1E_2E_3}|\mathcal{M}_{fi}|^2\delta(E_i-E_f)f_1f_2\bar{f}_3\ .\tag{B.8.52}$$

B.8.2.2 Relativist calculation

Using $\vec{p}_3=\vec{p}_1+\vec{p}_2-\vec{p}_a$, we can write

$$|p_3|^2=|p_1|^2+\alpha|p_1|+\beta\tag{B.8.53}$$

where

$$\alpha=2(|p_2|\cos(\theta_{12})-|p_a|\cos(\theta_{1a}))\ ,\tag{B.8.54}$$

$$\beta=|p_2|^2+|p_a|^2-2|p_2||p_a|\cos(\theta_{2a}))\ .\tag{B.8.55}$$

Thus

$$\begin{aligned}&E_1+E_2=E_3+E_a\\ \Leftrightarrow&\sqrt{m_1^2+|p_1|^2}=\sqrt{m_3^2+|p_1|^2+\alpha|p_1|+\beta}+E_a-E_2\\ \Rightarrow&m_1^2+|p_1|^2=m_3^2+|p_1|^2+\alpha|p_1|+\beta+(E_a-E_2)^2+2(E_a-E_2)\sqrt{m_3+|p_1|^2+\alpha|p_1|+\beta}\\ \Leftrightarrow&m_1^2-m_3^2-\beta-(E_a-E_2)^2-\alpha|p_1|=2(E_a-E_2)\sqrt{m_3^2+|p_1|^2+\alpha|p_1|+\beta}\\ \Rightarrow&\begin{matrix}(m_1^2-m_3^2-\beta-(E_a-E_2)^2)^2+\alpha^2|p_1|^2\\ -2\alpha(m_1^2-m_3^2-\beta-(E_a-E_2)^2)|p_1|\end{matrix}=4(E_a-E_2)^2(m_3^2+|p_1|^2+\alpha|p_1|+\beta)\ ,\end{aligned}\tag{B.8.56}$$

therefore we can write

$$E_1+E_2=E_3+E_a\Rightarrow A|p_1|^2+B|p_1|+C=0\tag{B.8.57}$$

with

$$\begin{aligned}A&=\alpha^2-4(E_a-E_2)^2\ ,\\ B&=-2\alpha(m_a^2+m_2^2+m_1^2-m_3^2-2p_2\cdot p_a)\ ,\\ C&=(m_1^2-m_3^2-\beta-(E_a-E_2)^2)^2-4(m_3^2+\beta)(E_a-E_2)^2\ .\end{aligned}\tag{B.8.58}$$

We define

$$\Delta=B^2-4AC\ ,\tag{B.8.59}$$

if $\Delta>0$ we have two solutions ($\Delta=0$ is of zero measurement and therefore does not contribute to the integration)

$$|p_1^{(\gamma)}|=\frac{-B+(-1)^\gamma\sqrt{\Delta}}{2A}\ ,\quad\gamma\in\{1;2\}\ ,\tag{B.8.60}$$

therefore[8]

$$d|p_1|\delta(E_1+E_2-E_3-E_a)=\sum_{\gamma=1}^{2}\frac{\delta(|p_1|-|p_1^{(\gamma)}|)}{|\Delta E'(|p_1^{(\gamma)}|)|}H(|p_1^{(\gamma)}|)H(E_3-m_3)\ , \tag{B.8.61}$$

with

$$\Delta E'(|p_1|)=\frac{\partial E_1}{\partial|p_1|}-\frac{\partial E_3}{\partial|p_1|}=\frac{|p_1|}{E_1}-\frac{|p_1|+\alpha/2}{E_3}\ , \tag{B.8.62}$$

and $H=\chi_{[0;+\infty[}$ is the Heaviside function.

B.8.2.3 Non-relativist limit

We will use $\delta(E_1+E_2-E_3-E_a)$ in the non-relativistic approximation for particles 1 & 3 to eliminate $\int d|p_1|$

$$E_1+E_2-E_3-E_a=m_1+\frac{|p_1|^2}{2m_1}-m_3-\frac{|p_3|^2}{2m_3}+E_2-E_a\ , \tag{B.8.63}$$

but

$$\begin{aligned}|p_3|^2&=(\vec{p}_1+\vec{p}_2-\vec{p}_a)^2\\&=|p_1|^2+|p_2|^2+|p_a|^2+2|p_1||p_2|\cos(\theta_{iM})-2|p_1||p_a|\cos(\theta_{ia})-2|p_2||p_a|\cos(\theta_{Ma})\ ,\end{aligned} \tag{B.8.64}$$

which allows us to write

$$E_1+E_2-E_3-E_a=A|p_1|^2+B|p_1|+C\ , \tag{B.8.65}$$

with

$$\begin{aligned}A&=\frac{1}{2m_1}-\frac{1}{2m_3}\\B&=\frac{|p_a|\cos(\theta_{ia})-|p_2|\cos(\theta_{iM})}{m_3}\\C&=m_1-m_3+E_2-E_a+\frac{2|p_2||p_a|\cos(\theta_{Ma})-|p_2|^2-|p_a|^2}{2m_3}\ .\end{aligned} \tag{B.8.66}$$

Once $|p_1|$ is determined, we will have

$$E_2=\sqrt{m_2^2+|p_2|^2}\ ,\ E_a=\sqrt{m_a^2+|p_a|^2}\ ,\ E_1=m_1+\frac{|p_1|^2}{2m_1}\ ,\ E_3=E_1+E_2-E_a\ . \tag{B.8.67}$$

If $m_1=m_3$ then $A=0$ which implies

$$|p_1^{(0)}|=-\frac{C}{B}\ , \tag{B.8.68}$$

and

$$d|p_1|\delta(E_1+E_2-E_3-E_a)=\frac{\delta(|p_1|-|p_1^{(0)}|)}{|B|}\ . \tag{B.8.69}$$

If $m_1\neq m_3$ then

$$\Delta=B^2-4AC\ , \tag{B.8.70}$$

if $\Delta>0$ we have two solutions ($\Delta=0$ is of zero measurement and therefore doesn't contribute to the integration)

$$|p_1^{(\gamma)}|=\frac{-B+(-1)^\gamma\sqrt{\Delta}}{2A}\ , \tag{B.8.71}$$

therefore

$$d|p_1|\delta(E_1+E_2-E_3-E_a)=\sum_{\gamma=1}^{2}\frac{\delta(|p_1|-|p_1^{(\gamma)}|)}{|2A|p_1^{(\gamma)}|+B|}H(|p_1^{(\gamma)}|)\ . \tag{B.8.72}$$

[8] We have $H(E_3-m_3)$ in addition to what seems necessary, but the fact that we have implications and not equivalences to solve the equation in $|p_1|$ can pose a problem, it is why we need to add $H(E_3-m_3)$.

B.8.2.4 Low-energy limit

In the low-energy limit, we have $E_1 \simeq m_1$ and $E_3 \simeq m_3$[9].

Using the relation $\delta(E_i - E_f) = \delta(m_1 + E_2 - m_3 - E_a)$, and the fact that $|\mathcal{M}_{fi}|^2$ becomes independent of $|p_1|$, $\cos(\theta_{1a})$, and ψ_{12} in this regime (since $p_1 \cdot p_a \sim m_1 E_a$ and $p_1 \cdot p_2 \sim m_1 E_2$), we can rewrite Eq. (B.8.52) as:

$$\frac{d\dot{n}_a}{dE_a} = \frac{|p_a||p_2| f_2 \bar{f}_3}{4(2\pi)^5 m_1 m_3} \left(\int_0^{+\infty} |p_1|^2 f_1 d|p_1| \right) \left(\int_{-1}^{1} d\cos(\theta_{2a}) |\mathcal{M}_{fi}|^2 \right) . \tag{B.8.73}$$

B.8.2.5 Comparison with [Car+21] for $\pi^- p \to na$

We compare our calculation with that of [Car+21] for the process $\pi^- p \to na$, where only the diagrams shown in Fig. B.6 was considered.

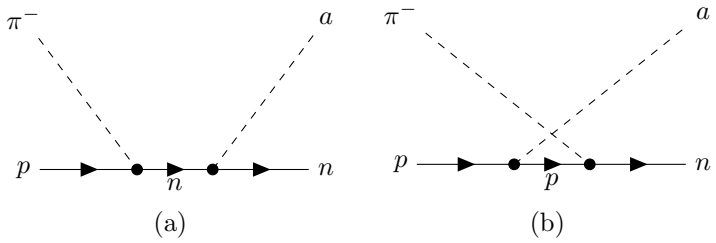

Figure B.6: Feynman diagrams considered in [Car+21] for pion-nucleon scattering $\pi^- p \to na$.

They work in the low-energy approximation of Eq. (B.8.73). They are placed within the limit

$$E_p \simeq E_n \simeq m_N \gg E_\pi \gg m_\pi, \quad p_p \cdot p_a \simeq m_N E_a, \quad p_p \cdot p_M \simeq m_N E_M , \tag{B.8.74}$$

so that

$$p_\pi \cdot p_a = E_\pi E_a - |p_\pi||p_a| \cos(\theta_{\pi a}) \simeq E_\pi E_a (1 - \cos(\theta_{\pi a})) . \tag{B.8.75}$$

The Compton scattering relation gives a link between E_π and $\cos(\theta_{\pi a})$:

$$E_\pi = \frac{m_N E_a}{m_N + E_a(1 - \cos(\theta_{\pi a}))} , \tag{B.8.76}$$

It is then possible to write the squared matrix element as:

$$|\mathcal{M}_{fi}|^2 = \alpha E_\pi + \beta + \frac{\gamma}{E_\pi} \tag{B.8.77}$$

where α, β, and γ are independent of both $\cos(\theta_{\pi a})$ and E_π.

This allows us to integrate directly over $\cos(\theta_{\pi a})$:

Firstly,

$$\begin{aligned} \int E_\pi d\cos(\theta_{\pi a}) &= \int_{-1}^{1} \frac{m_N E_a}{m_N + E_a(1 - \cos(\theta_{\pi a}))} d\cos(\theta_{\pi a}) \\ &= -m_N \left[\ln\left(m_N + E_a - E_a \cos(\theta_{\pi a})\right) \right]_0^1 \\ &= m_N \ln\left(1 + \frac{2E_a}{m_N}\right) \\ &\simeq 2E_a - 2\pi \frac{E_a^2}{m_N} + \frac{8}{3} \frac{E_a^3}{m_N^2} + m_N o\left(\frac{E_a^3}{m_N^3}\right) . \end{aligned} \tag{B.8.78}$$

Secondly,

$$\int \frac{d\cos(\theta_{\pi a})}{E_\pi} = \int_{-1}^{1} \frac{m_N + E_a(1 - \cos(\theta_{\pi a}))}{m_N E_a} d\cos(\theta_{\pi a}) = 2 \frac{m_N + E_a}{m_N E_a} . \tag{B.8.79}$$

[9] We will use this approximation everywhere except in the distribution f_1, since it is f_1 itself that enforces $E_1 \simeq m_1$. However, we can treat $\bar{f}_3$ as a constant.

Therefore:

$$\frac{1}{2}\int_{-1}^{1} |\mathcal{M}_{fi}|^2 d\cos(\theta_{\pi a}) \simeq \alpha E_a + \beta + \gamma \frac{m_N + E_a}{m_N E_a} \ . \tag{B.8.80}$$

From our own calculation, we find:

$$\int |\mathcal{M}_{fi}|^2 d\cos(\theta_{\pi a}) \simeq 16 \frac{g_A^2 E_a^2}{F_0^2} C_{\text{eff}}^2 \ , \tag{B.8.81}$$

with $C_{\text{eff}}^2 = \overline{g}_{aN}^2/2$, where

$$\overline{g}_{aN}^2 = \left(\frac{m_N}{f_a}\right)^2 \left(\frac{1}{2}C_{an}^2 + \frac{1}{2}C_{ap}^2 + \frac{1}{3}C_{an}C_{ap}\right) \ . \tag{B.8.82}$$

However, in [Car+21], with our notations, the authors obtain $C_{\text{eff}}^2 = \overline{g}_{aN}^2$, indicating a discrepancy by a factor of 2[10]. Nevertheless, in a more recent work [Lel+23], which shares some of the same collaborators as [Car+21], this factor-of-two discrepancy has been corrected, and our procedure is therefore consistent with the current literature.

The axion parameters used in their numerical application are for the Kim-Shifman-Vainshtein-Zakharov (KSVZ) model. To allow a proper comparison, we also need to account for the SN model used in [Car+21], which is taken from [FR20]. This model provides:

$$z_n \simeq 0.934, \quad z_p \simeq 0.0726, \quad z_\pi \simeq 0.427 \tag{B.8.83}$$

with $z_i = \exp\left((\mu_i - m_i)/T\right)$.

Table B.2: Numerical values used to compare our results with the literature for $T = 40.56$ MeV, $n_B = n_{\text{sat}}$, $Y_p = 0.3$.

Integration	Amplitude	Model	Q_a (10^{32} erg.cm^{-3}.s^{-1})
[Car+21]	[Car+21]	[FR20]	8.5
Our	[Car+21]	[FR20]	6.4
Our	Our	[FR20]	7.6
Our	Our	DD2Y	7.6

The results in Table B.2 can be compared with the value $Q_a = 7.935 \times 10^{32}$ erg.cm^{-3}.s^{-1} reported in [Car+21][11]. The various lines are designed to isolate the effect of each parameter by changing only one at a time:

1. The first line vs. the reference value of [Car+21] shows a 7% difference, testing the implementation of [FR20] in Eq. (B.8.83).
2. The first and second lines compare our full 5D integration with their 1D×1D integration, revealing a 25% difference, with an overestimation in [Car+21].
3. The second and third lines isolate the effect of the amplitude: using the same model and integration, our unapproximated amplitude yields a 16% lower result.
4. The third and fourth lines compare the models from [FR20] and DD2Y, which yield the same result.

Ultimately, the overall difference between our final estimate and that of [Car+21] is only about 4%.

We also observe that [Car+21] use a more aggressive low-energy approximation (non-relativistic limit). Our calculation, while more computationally expensive due to a 5D phase-space integration, is thus more precise. In contrast, the simplified approach of [Car+21] requires only two 1D integrations, making it much faster.

[10] This factor of 2 may arise from the definition of $\overline{|\mathcal{M}_{fi}|^2}$. In [Car+21], the authors use $\overline{|\mathcal{M}_{fi}|^2}$ instead of $|\mathcal{M}_{fi}|^2$ as we do. If they average over both initial and final spin states, then the two formulas are expected to be equivalent. However, if they average only over initial spin states, this would explain the factor-of-two difference. A detailed explanation of our expression for the emissivity can be found in Section 3.4.4. Nevertheless, this factor-of-two difference does not affect the oom, which is the only relevant quantity in the context of the crude neutrino emissivity estimate used for the constraint $Q_a < Q_\nu$, and the uncertainties in the modeling of the SN core.

[11] The value in [Car+21] is $Q_a = 15.87 \times 10^{32}$ erg.cm^{-3}.s^{-1}; however, to account for the factor-of-2 error, we divided it by 2.

B.8.2.6 $2 \to 3$ scattering

For axion production of the form $P_1 + P_2 \to P_3 + P_4 + a$, the axion emissivity is given by

$$\frac{d\dot{n}_a}{dE_a} = \int_{(\mathbb{R}^3)^4} \frac{d^3\vec{p}_1}{(2\pi)^3 2E_1} \frac{d^3\vec{p}_2}{(2\pi)^3 2E_2} \frac{d^3\vec{p}_3}{(2\pi)^3 2E_3} \frac{d^3\vec{p}_4}{(2\pi)^3 2E_4} \frac{4\pi|p_a|E_a}{(2\pi)^3 2E_a} (2\pi)^4 \delta^4(p_f - p_i) |\mathcal{M}_{fi}|^2 f_1 f_2 \bar{f}_3 \bar{f}_4 \ , \tag{B.8.84}$$

where the f_k are either Fermi-Dirac or Bose-Einstein distributions depending on the spin.

We can eliminate the $d^3\vec{p}_4$ integral using the $\delta^3(\vec{p}_f - \vec{p}_i)$, and write $d\vec{p}_j = |p_j|^2 \, d\cos(\theta_j) \, d\psi_j \, d|p_j|$. However, only the relative azimuthal angles $\psi_{jk} = \psi_j - \psi_k$ appear in the calculation[12]. Therefore, we define $\psi_{12} = \psi_1 - \psi_2$ and $\psi_{13} = \psi_1 - \psi_3$, which allows us to write $\psi_{23} = \psi_{13} - \psi_{12}$ and integrate over one of the azimuthal angles. This gives:

$$\frac{d\dot{n}_a}{dE_a} = \int_{D_8} d^8\Omega \frac{|p_1|^2 |p_2|^2 |p_3|^2 |p_a|}{2^4 (2\pi)^9 E_1 E_2 E_3 E_4} \delta(E_f - E_i) |\mathcal{M}_{fi}|^2 f_1 f_2 \bar{f}_3 \bar{f}_4 \ , \tag{B.8.85}$$

with $d^8\Omega = d|p_1| \, d|p_2| \, d|p_3| \, d\cos(\theta_1) \, d\cos(\theta_2) \, d\cos(\theta_3) \, d\psi_{12} \, d\psi_{13}$ and $D_8 = \mathbb{R}^3 \times [-1, 1]^3 \times [0, 2\pi]^2$.

B.8.2.6.1 Ultra-relativistic calculation

Assuming $|p_j| = E_j$, we can write

$$\begin{aligned} 0 = p_4^2 &= (p_1 + p_2 - p_3 - p_a)^2 \\ &= m_a^2 + 2E_1E_2(1 - \cos\theta_{12}) - 2E_1E_3(1 - \cos\theta_{13}) - 2E_2E_3(1 - \cos\theta_{23}) \\ &\quad - 2E_1(E_a - p_a\cos\theta_1) - 2E_2(E_a - p_a\cos\theta_2) + 2E_3(E_a - p_a\cos\theta_3) \ , \end{aligned} \tag{B.8.86}$$

which allows us to isolate

$$E_3 = \frac{m_a^2 + 2E_1E_2(1 - \cos\theta_{12}) - 2E_1(E_a - |p_a|\cos\theta_1) - 2E_2(E_a - |p_a|\cos\theta_2)}{2E_1(1 - \cos\theta_{13}) + 2E_2(1 - \cos\theta_{23}) - 2E_a(1 - \cos\theta_3)} \ . \tag{B.8.87}$$

Using

$$\begin{aligned} E_4^2 &= (\vec{p}_1 + \vec{p}_2 - \vec{p}_3 - \vec{p}_a)^2 \\ &= E_3^2 + 2E_3(E_a\cos\theta_3 - E_1\cos\theta_{13} - E_2\cos\theta_{23}) \\ &\quad + E_1^2 + E_2^2 + E_a^2 + 2E_1E_2\cos\theta_{12} - 2E_1E_a\cos\theta_1 - 2E_2E_a\cos\theta_2 \ , \end{aligned} \tag{B.8.88}$$

we obtain

$$\frac{\partial(E_f - E_i)}{\partial E_3} = 1 + \frac{\partial E_4}{\partial E_3} = 1 + \frac{E_3 + E_a\cos\theta_3 - E_1\cos\theta_{13} - E_2\cos\theta_{23}}{E_4} \ . \tag{B.8.89}$$

We can thus write

$$\frac{d\dot{n}_a}{dE_a} = \int_{D_7} d^7\Omega \frac{E_1E_2E_3|p_a| \, |\mathcal{M}_{fi}|^2 f_1 f_2 \bar{f}_3 \bar{f}_4 \, H(E_3)}{2^4 (2\pi)^9 (E_4 + E_3 + E_a\cos\theta_3 - E_1\cos\theta_{13} - E_2\cos\theta_{23})} \ , \tag{B.8.90}$$

with $d^7\Omega = dE_1 \, dE_2 \, d\cos\theta_1 \, d\cos\theta_2 \, d\cos\theta_3 \, d\psi_{12} \, d\psi_{13}$, $D_7 = \mathbb{R}^2 \times [-1, 1]^3 \times [0, 2\pi]^2$, and H the Heaviside function.

B.8.2.6.2 Non-relativistic calculation for P_2 and P_4

In the non-relativistic case for P_2 and P_4, we use the relation

$$E = m + \frac{|p|^2}{2m} \ , \tag{B.8.91}$$

which allows us to write

$$E_f - E_i = E_1 - E_3 - E_a + m_2 + \frac{|p_2|^2}{2m_2} - m_4 - \frac{|p_4|^2}{2m_4} \ . \tag{B.8.92}$$

[12] In the $\cos(\theta_{jk})$ terms, as in Eq. (B.8.50)

Now,

$$|p_4|^2 = |p_1|^2 + |p_2|^2 + |p_3|^2 + |p_a|^2 + 2|p_1||p_2|\cos\theta_{12} - 2|p_1||p_3|\cos\theta_{13} \\ - 2|p_1||p_a|\cos\theta_1 - 2|p_2||p_3|\cos\theta_{23} - 2|p_2||p_a|\cos\theta_2 + 2|p_3||p_a|\cos\theta_3 \ , \tag{B.8.93}$$

so we can write

$$E_f - E_i = A|p_2|^2 + B|p_2| + C \ , \tag{B.8.94}$$

with

$$\begin{aligned} A &= \frac{1}{2m_2} - \frac{1}{2m_4} \ , \\ B &= \frac{-|p_1|\cos\theta_{12} + |p_3|\cos\theta_{23} + |p_a|\cos\theta_2}{m_4} \ , \\ C &= E_1 - E_3 - E_a - \frac{|p_1|^2 + |p_3|^2 + |p_a|^2}{2m_4} \ . \end{aligned} \tag{B.8.95}$$

If $m_2 = m_4$, then $A = 0$, and we obtain

$$|p_2| = -\frac{C}{B} \ , \tag{B.8.96}$$

and

$$\frac{d\dot{n}_a}{dE_a} = \int_{D_7} d^7\tilde{\Omega} \frac{|p_1|^2|p_2|^2|p_3|^2|p_a|}{2^4(2\pi)^9 E_1 E_2 E_3 E_4 |B|} |\mathcal{M}_{fi}|^2 f_1 f_2 \bar{f}_3 \bar{f}_4 H(|p_2|) \ , \tag{B.8.97}$$

with $d^7\tilde{\Omega} = d|p_1|\, d|p_3|\, d\cos\theta_1\, d\cos\theta_2\, d\cos\theta_3\, d\psi_{12}\, d\psi_{13}$ and $D_7 = \mathbb{R}^2 \times [-1,1]^3 \times [0,2\pi]^2$.

If $m_2 \neq m_4$, then we have two solutions

$$|p_2^\gamma| = \frac{-B + (-1)^\gamma \sqrt{B^2 - 4AC}}{2A} \ , \tag{B.8.98}$$

and

$$\frac{d\dot{n}_a}{dE_a} = \sum_{\gamma=1}^{2} \int_{D_7} d^7\tilde{\Omega} \frac{|p_1|^2|p_2^\gamma|^2|p_3|^2|p_a|}{2^4(2\pi)^9 E_1 E_2^\gamma E_3 E_4 |2|p_2^\gamma| + B|} |\mathcal{M}_{fi}|^2 f_1 f_2 \bar{f}_3 \bar{f}_4 H(|p_2^\gamma|) \ . \tag{B.8.99}$$

B.9 SN core effective quantities

This section summarizes effective in-medium properties and composition of hot, dense matter relevant for core-collapse Supernovæ (SNe) at fixed charge baryon fraction $Y_{Q_B} = 0.3$. We report, for two Equation of State (EoS) ($DD2(Y)$ and $SFHo(Y)$), two temperatures ($T = 30, 40$ MeV), and two baryon densities ($n_B = n_{\rm sat}$ and $1.5\, n_{\rm sat}$), the effective masses m_i^*, effective chemical potentials μ_i^*, and particle fractions $Y_i = n_i/n_B$ of fermions with strange matter (Table B.3), mesons with strange matter (Table B.4), and first generation particles (Table B.5).

Table B.3: Effective masses m_i^* (MeV), effective chemical potentials μ_i^* (MeV) and particle fractions $Y_i = n_i/n_B$ for the various fermionic species (e^-, n, p, Λ, Σ, Ξ) in core-collapse SNe at $Y_{Q_B} = 0.3$. Results are shown for two EoS ($DD2Y$ and $SFHoY$), two temperatures ($T = 30$ and 40 MeV) and two baryon densities ($n_B = n_{\rm sat}$ and $1.5\,n_{\rm sat}$).

EoS	T	n_B	i	e^-	n	p	Λ	Σ^-	Σ^0	Σ^+	Ξ^-	Ξ^0
$DD2Y$	30	n_{sat}	m_i^*	0.511	528.2	526.9	861.0	994.4	994.4	994.4	1190.1	1183.3
			μ_i^*	208.1	589.8	547.9	716.2	758.1	716.2	674.4	884.5	842.7
			Y_i	0.3	0.7	0.3	0.004	2×10^{-4}	5×10^{-5}	1×10^{-5}	3×10^{-5}	9×10^{-6}
		$1.5\,n_{sat}$	m_i^*	0.511	415.8	414.5	791.4	941.0	941.0	941.0	1154.1	1147.3
			μ_i^*	242.0	523.8	470.1	687.8	741.5	687.8	634.2	905.5	851.9
			Y_i	0.3	0.69	0.3	0.008	4×10^{-4}	7×10^{-5}	1×10^{-5}	1×10^{-4}	2×10^{-5}
	40	n_{sat}	m_i^*	0.511	537.7	536.4	866.9	999.0	999.0	999.0	1193.1	1186.3
			μ_i^*	196.8	584.4	538.5	709.3	755.2	709.3	663.4	880.1	834.2
			Y_i	0.3	0.68	0.3	0.01	0.002	6×10^{-4}	2×10^{-4}	5×10^{-4}	2×10^{-4}
		$1.5\,n_{sat}$	m_i^*	0.511	426.6	425.3	798.2	946.2	946.2	946.2	1157.6	1150.8
			μ_i^*	232.1	520.9	466.6	682.1	736.4	682.1	627.9	897.6	843.4
			Y_i	0.3	0.67	0.3	0.02	0.003	7×10^{-4}	2×10^{-4}	0.001	3×10^{-4}
$SFHoY$	30	n_{sat}	m_i^*	0.511	720.0	718.7	928.1	1061.9	1061.5	1061.1	1209.0	1202.2
			μ_i^*	208.1	759.4	722.3	772.3	803.7	770.0	736.3	883.9	846.0
			Y_i	0.3	0.7	0.3	0.003	1×10^{-4}	4×10^{-5}	1×10^{-5}	1×10^{-5}	5×10^{-6}
		$1.5\,n_{sat}$	m_i^*	0.511	639.8	638.6	859.6	1015.1	1014.6	1014.0	1167.9	1161.1
			μ_i^*	241.9	709.8	665.6	722.2	761.0	720.0	679.0	870.8	825.8
			Y_i	0.3	0.7	0.3	0.003	8×10^{-5}	2×10^{-5}	5×10^{-6}	2×10^{-5}	7×10^{-6}
	40	n_{sat}	m_i^*	0.511	723.3	722.0	930.9	1063.9	1063.4	1063.0	1210.7	1203.9
			μ_i^*	196.7	747.0	704.2	759.1	796.2	756.8	717.4	875.2	831.7
			Y_i	0.29	0.69	0.3	0.01	0.001	5×10^{-4}	2×10^{-4}	3×10^{-4}	1×10^{-4}
		$1.5\,n_{sat}$	m_i^*	0.511	644.1	642.8	863.3	1017.6	1017.1	1016.5	1170.1	1163.3
			μ_i^*	231.9	701.7	652.9	713.1	756.4	710.9	665.3	864.8	815.2
			Y_i	0.3	0.69	0.3	0.01	9×10^{-4}	3×10^{-4}	9×10^{-5}	4×10^{-4}	1×10^{-4}

Table B.4: Same as Table B.3 but for mesons (π, K, η).

EoS	T	n_B	i	π^-	π^0	π^+	K^-	K^+	K^0	$\bar{K}^0$	η_8
$DD2Y$	30	n_{sat}	m_i	139.6	135.0	139.6	493.7	493.7	497.7	497.7	547.3
			μ_i	62.2	0	-62.2	62.2	-62.2	0	-0	0
			Y_i	0.001	2×10^{-4}	2×10^{-5}	6×10^{-8}	9×10^{-10}	7×10^{-9}	7×10^{-9}	1×10^{-9}
		$1.5\,n_{sat}$	m_i	139.6	135.0	139.6	493.7	493.7	497.7	497.7	547.3
			μ_i	62.2	0	-62.2	62.2	-62.2	0	0	0
			Y_i	0.001	1×10^{-4}	2×10^{-5}	4×10^{-8}	6×10^{-10}	4×10^{-9}	4×10^{-9}	10×10^{-10}
	40	n_{sat}	m_i	139.6	135.0	139.6	493.7	493.7	497.7	497.7	547.3
			μ_i	65.5	0	-65.5	65.5	-65.5	0	0	0
			Y_i	0.005	0.001	2×10^{-4}	4×10^{-6}	1×10^{-7}	7×10^{-7}	7×10^{-7}	2×10^{-7}
		$1.5\,n_{sat}$	m_i	139.6	135.0	139.6	493.7	493.7	497.7	497.7	547.3
			μ_i	70.6	0	-70.6	70.6	-70.6	0	0	0
			Y_i	0.004	8×10^{-4}	1×10^{-4}	3×10^{-6}	8×10^{-8}	4×10^{-7}	4×10^{-7}	1×10^{-7}
$SFHoY$	30	n_{sat}	m_i	139.6	135.0	139.6	493.7	493.7	497.7	497.7	547.3
			μ_i	63.7	0	-63.7	63.7	-63.7	0	0	0
			Y_i	0.002	2×10^{-4}	2×10^{-5}	6×10^{-8}	9×10^{-10}	7×10^{-9}	7×10^{-9}	1×10^{-9}
		$1.5\,n_{sat}$	m_i	139.6	135.0	139.6	493.7	493.7	497.7	497.7	547.3
			μ_i	70.0	0	-70.0	70.0	-70.0	0	0	0
			Y_i	0.001	1×10^{-4}	1×10^{-5}	5×10^{-8}	5×10^{-10}	4×10^{-9}	4×10^{-9}	10×10^{-10}
	40	n_{sat}	m_i	139.6	135.0	139.6	493.7	493.7	497.7	497.7	547.3
			μ_i	68.7	0	-68.7	68.7	-68.7	0	0	0
			Y_i	0.006	0.001	2×10^{-4}	4×10^{-6}	1×10^{-7}	7×10^{-7}	7×10^{-7}	2×10^{-7}
		$1.5\,n_{sat}$	m_i	139.6	135.0	139.6	493.7	493.7	497.7	497.7	547.3
			μ_i	74.0	0	-74.0	74.0	-74.0	0	0	0
			Y_i	0.004	8×10^{-4}	1×10^{-4}	3×10^{-6}	8×10^{-8}	4×10^{-7}	4×10^{-7}	1×10^{-7}

Table B.5: Same as Table B.3 but for first generation hadrons.

EoS	T	n_B	i	e^-	n	p	π^-	π^0	π^+
$DD2$	30	n_{sat}	m_i^*	0.511	527.6	526.3	139.6	135.0	139.6
			μ_i^*	208.2	589.7	547.5	62.8	0	-62.8
			Y_i	0.3	0.7	0.3	0.002	2×10^{-4}	2×10^{-5}
		$1.5\, n_{sat}$	m_i^*	0.511	414.6	413.3	139.6	135.0	139.6
			μ_i^*	241.8	523.9	469.0	72.6	0	-72.6
			Y_i	0.3	0.7	0.3	0.001	1×10^{-4}	1×10^{-5}
	40	n_{sat}	m_i^*	0.511	535.4	534.1	139.6	135.0	139.6
			μ_i^*	196.8	584.4	536.3	68.7	0	-68.7
			Y_i	0.29	0.7	0.3	0.006	0.001	2×10^{-4}
		$1.5\, n_{sat}$	m_i^*	0.511	423.4	422.1	139.6	135.0	139.6
			μ_i^*	231.9	522.1	463.2	76.6	0	-76.6
			Y_i	0.3	0.7	0.3	0.005	8×10^{-4}	1×10^{-4}
$SFHo$	30	n_{sat}	m_i^*	0.511	719.9	718.6	139.6	135.0	139.6
			μ_i^*	208.1	759.6	722.2	64.1	0	-64.1
			Y_i	0.3	0.7	0.3	0.002	2×10^{-4}	2×10^{-5}
		$1.5\, n_{sat}$	m_i^*	0.511	639.7	638.4	139.6	135.0	139.6
			μ_i^*	241.9	710.0	665.4	70.6	0	-70.6
			Y_i	0.3	0.7	0.3	0.001	1×10^{-4}	1×10^{-5}
	40	n_{sat}	m_i^*	0.511	723.0	721.7	139.6	135.0	139.6
			μ_i^*	196.7	747.9	703.7	70.9	0	-70.9
			Y_i	0.29	0.7	0.3	0.006	0.001	2×10^{-4}
		$1.5\, n_{sat}$	m_i^*	0.511	643.7	642.4	139.6	135.0	139.6
			μ_i^*	231.9	702.7	652.3	76.4	0	-76.4
			Y_i	0.3	0.7	0.3	0.004	8×10^{-4}	1×10^{-4}

Appendix C

Field theory and Lagrangians

C.1 Zoology of Standard Model particle physics

Fig. C.1 summarizes the elementary particles of the Standard Model (SM), along with their fundamental properties: mass, electric charge, and spin.

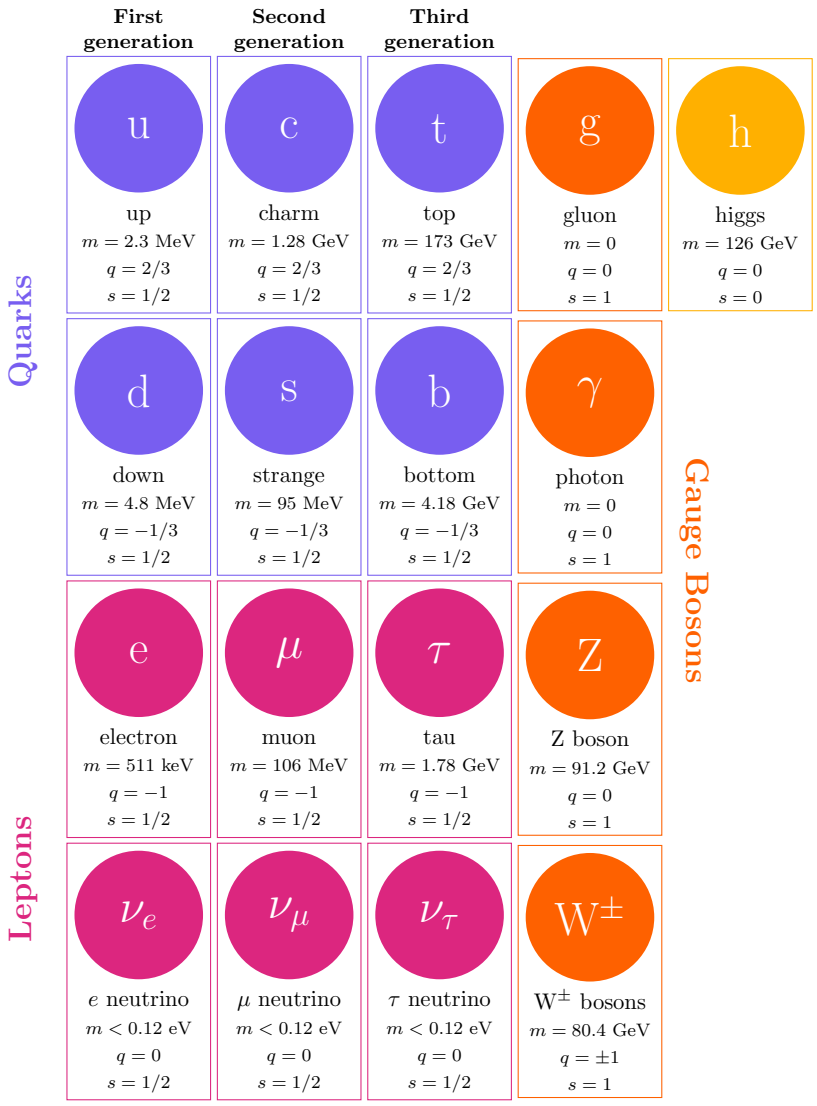

Figure C.1: Elementary particles of the SM.

C.2 Higgs mechanism

C.2.1 Goldstone's theorem

Goldstone's theorem states that for every generator T_a of a continuous symmetry that is spontaneously broken by the vacuum (i.e., $T_a |0\rangle \neq 0$, where $|0\rangle$ denotes the vacuum state), there exists a massless, neutral scalar field known as a Goldstone boson, these Goldstone bosons emerge as a consequence of the broken symmetry.

C.2.2 $U(1)$ case

For a $U(1)$ symmetry, we define a massless complex scalar field ϕ in terms of two real scalar fields, φ_1 and φ_2, as follows:

$$\phi = \frac{\varphi_1 + i\varphi_2}{\sqrt{2}} \ . \tag{C.2.1}$$

The Lagrangian for this field is given by:

$$\mathcal{L} = \partial_\mu \phi^* \partial^\mu \phi - V(\phi) \ , \tag{C.2.2}$$

where the potential $V(\phi)$ must be a function of the invariant combination $\phi^*\phi$ to ensure invariance under $U(1)$ transformations. One such potential is:

$$V(\phi) = -\mu^2 \phi^* \phi + \lambda(\phi^* \phi)^2 \ , \tag{C.2.3}$$

where $\lambda > 0$ ensures the potential has a minimum. To find the Vacuum Expectation Value (vev) v of ϕ, we minimize the potential:

$$\frac{v}{\sqrt{2}} = |\phi|_{\min} = \sqrt{\frac{\mu^2}{\lambda}} \ . \tag{C.2.4}$$

To shift the potential such that $V(v/\sqrt{2}) = 0$, we add a constant term $\lambda v^4/4$. The redefined potential becomes:

$$V(\phi) = \lambda \left(\phi^* \phi - \frac{v^2}{2} \right)^2 \ . \tag{C.2.5}$$

The potential $V(\phi)$ has a characteristic Mexican hat shape, with its minimum lying on a circle of radius $v/\sqrt{2}$. Although the Lagrangian remains invariant under $U(1)$ transformations, the vacuum selects a specific point on this circle, thereby spontaneously breaking the symmetry.

To simplify the analysis without loss of generality, we choose the vacuum such that $\phi^0 = v/\sqrt{2}$, corresponding to $\varphi_1^0 = v$ and $\varphi_2^0 = 0$. This choice aligns the vacuum state along the φ_1-axis.

The symmetry breaking becomes evident through the presence of a non-zero charge:

$$iQ|0\rangle = q \begin{pmatrix} 0 & -1 \\ 1 & 0 \end{pmatrix} \begin{pmatrix} 0 \\ qv \end{pmatrix} \neq \vec{0}. \tag{C.2.6}$$

We now describe the physical state as $\vec{\varphi} = \vec{\varphi}^0 + \vec{h}$, where $\vec{h}$ denotes excitations around the vacuum. The Lagrangian for these excitations becomes after expansion:

$$\mathcal{L} = \frac{1}{2} \partial_\mu h_1 \partial^\mu h_1 + \frac{1}{2} \partial_\mu h_2 \partial^\mu h_2 - V(h_1, h_2) \ , \tag{C.2.7}$$

with the potential:

$$V(h_1, h_2) = \mu^2 h_1^2 + \lambda v \vec{h} \cdot \vec{h} + \frac{\lambda}{4} (\vec{h} \cdot \vec{h})^2 \ . \tag{C.2.8}$$

Here, h_1 represents the radial excitation with mass $\sqrt{2}\mu$, while h_2, the angular excitation, is massless. This massless field h_2 is the Goldstone boson associated with the broken generator Q.

Let h denote the scalar field corresponding to the Higgs boson. By performing a $U(1)$ transformation, we can write:

$$\phi \to \phi' = \frac{v + h}{\sqrt{2}} \ . \tag{C.2.9}$$

Given that:

$$\phi' = e^{i\alpha}\frac{v+h_1+ih_2}{\sqrt{2}} = (1+i\alpha)\frac{v+h_1+ih_2}{\sqrt{2}} + \mathcal{O}(\alpha^2) \tag{C.2.10}$$
$$= \frac{v+(h_1-\alpha h_2)+i(h_2+\alpha v+\alpha h_1)}{\sqrt{2}} + \mathcal{O}(\alpha^2)\ ,$$

we match this to Eq. (C.2.9) by choosing $\alpha = h_2/(v+h_1)$ and redefining $h = h_1 - \alpha h_2$. This allows us to express ϕ in a form consistent with the desired transformation.

We now turn to theories invariant under local gauge transformations, defined by the covariant derivative $D_\mu = \partial_\mu + iqA_\mu$ and the field strength tensor $F_{\mu\nu} = \partial_\mu A_\nu - \partial_\nu A_\mu$. The Lagrangian becomes:

$$\mathcal{L} = D_\mu\phi^\dagger D^\mu\phi - V(\phi) - \frac{1}{4}F_{\mu\nu}F^{\mu\nu}\ . \tag{C.2.11}$$

Expanding the Lagrangian yields:

$$\mathcal{L} = \frac{1}{2}\partial_\mu h\partial^\mu h - \frac{1}{2}(\sqrt{2}\mu)^2h^2 - \frac{1}{4}F_{\mu\nu}F^{\mu\nu} + \frac{1}{2}(qv)^2A_\mu A^\mu + q^2vhA_\mu A^\mu + \frac{1}{2}q^2h^2A_\mu A^\mu - \lambda vh^3 - \frac{\lambda}{4}h^4\ . \tag{C.2.12}$$

This expansion reveals a mass term for the gauge field A_μ, indicating that it acquires a mass $m_A = qv$.

C.2.3 $SO(n)$ case

For the group $SO(n)$, the field $\vec{\varphi}$ belongs to $\mathbb{R}^n$. The Lagrangian is given by:

$$\mathcal{L} = \frac{1}{2}\partial_\mu\vec{\varphi}\cdot\partial^\mu\vec{\varphi} - V(\vec{\varphi})\ , \tag{C.2.13}$$

where the potential takes the form:

$$V(\vec{\varphi}) = \frac{\lambda v^4}{4} - \frac{\mu^2}{2}\vec{\varphi}\cdot\vec{\varphi} + \frac{\lambda}{4}(\vec{\varphi}\cdot\vec{\varphi})^2\ . \tag{C.2.14}$$

The minimum of this potential occurs when:

$$|\vec{\varphi}|_{\min} = v = \sqrt{\frac{\mu^2}{\lambda}}\ . \tag{C.2.15}$$

This defines a $(n-1)$-dimensional surface (a sphere of radius v) in field space.

The system spontaneously evolves toward a specific minimum configuration $\vec{\varphi}_0$. We can write the field as $\vec{\varphi} = \vec{\varphi}_0 + \vec{h}$, where $\vec{h}$ represents fluctuations (excitations) around the vacuum state. Expanding the potential around $\vec{\varphi}_0$, we obtain:

$$V(\vec{\varphi}) = V(\vec{\varphi}_0) + \frac{\partial V}{\partial h_a}(\vec{\varphi}_0)h_a + \frac{1}{2}\frac{\partial^2 V}{\partial h_a\partial h_b}(\vec{\varphi}_0)h_ah_b + o(\|\vec{h}\|^2)\ . \tag{C.2.16}$$

By definition, $V(\vec{\varphi}_0) = 0$, and since $\vec{\varphi}_0$ corresponds to a minimum, the first derivative vanishes: $\partial V/\partial h_a = 0$. Thus, the potential simplifies to:

$$V(\vec{\varphi}) = \frac{1}{2}\vec{h}^T M\vec{h} + o(\|\vec{h}\|^2)\ , \tag{C.2.17}$$

where the mass matrix M is given by:

$$M_{ab} = \left.\frac{\partial^2 V}{\partial\varphi_a\partial\varphi_b}\right|_{\vec{\varphi}_0} = 2\mu^2\frac{\varphi_a^0\varphi_b^0}{v^2}\ . \tag{C.2.18}$$

In the particular case where $\varphi_a^0 = \delta_{a1}v$, the mass matrix becomes $M_{ab} = 2\mu^2\delta_{a1}\delta_{b1}$, indicating that only the field h_1 acquires a mass $m = \sqrt{2}\mu$, while the remaining fields remain massless.

In $\mathbb{R}^n$, there are $C_n^2 = n(n-1)/2$ possible rotation generators. Among these, the generators T_{1b} (with $b \in [\![2;n]\!]$) do not leave the vacuum invariant:

$$\vec{\varphi}_0' - \vec{\varphi}_0 = \left(\exp\left(-i\theta^bT_{1b}\right) - I_n\right)\vec{\varphi}_0 = -i\theta^bT_{1b}\vec{\varphi}_0 + o(\theta) \neq 0\ . \tag{C.2.19}$$

These broken generators correspond to the Goldstone bosons h_b, and there are $n-1$ of them in total. Therefore, the physical vacuum breaks the original $SO(n)$ symmetry down to $SO(n-1)$.

C.2.4 $SU(2)$ Case

Consider the symmetry group $SU(2)$. We define the Higgs doublet as:

$$\vec{H} = \begin{pmatrix} \phi^+ \\ \phi^0 \end{pmatrix} = \frac{1}{\sqrt{2}} \begin{pmatrix} \varphi_3 + i\varphi_4 \\ \varphi_1 + i\varphi_2 \end{pmatrix} \ . \tag{C.2.20}$$

The corresponding Lagrangian is given by:

$$\mathcal{L} = \partial_\mu \vec{H}^\dagger \partial^\mu \vec{H} - V(\vec{H}) \ , \tag{C.2.21}$$

where the potential $V(\vec{H})$ is defined as:

$$V(\vec{H}) = \frac{\lambda v^4}{4} - \mu^2 \vec{H}^\dagger \vec{H} + \lambda (\vec{H}^\dagger \vec{H})^2 \ . \tag{C.2.22}$$

Note that:

$$\vec{H}^\dagger \vec{H} = \frac{1}{2} \vec{\varphi} \cdot \vec{\varphi} \ , \tag{C.2.23}$$

which implies that the Lagrangian exhibits an $SO(4)$ symmetry in terms of the real field components $\vec{\varphi}$.

Under the influence of the potential, the system evolves toward a vacuum state $\vec{\varphi}_0$. The $SU(2)$ symmetry transformation acts as:

$$\vec{H}' = \exp\left(i\vec{\theta} \cdot \frac{\vec{\sigma}}{2} \right) \vec{H} \ . \tag{C.2.24}$$

We define the vev of the Higgs field as:

$$\vec{H}_0 = \frac{v}{\sqrt{2}} \begin{pmatrix} 0 \\ 1 \end{pmatrix} \ . \tag{C.2.25}$$

For an infinitesimal transformation, the variation of the vacuum becomes:

$$\delta \vec{H}_0 = \vec{H}_0' - \vec{H}_0 \simeq \frac{-i}{2\sqrt{2}} \begin{pmatrix} \theta_z & \theta_x - i\theta_y \\ \theta_x + i\theta_y & -\theta_z \end{pmatrix} \begin{pmatrix} 0 \\ v \end{pmatrix} \ . \tag{C.2.26}$$

This leads to:

$$\delta\varphi_1^0 = 0, \quad \delta\varphi_2^0 = \frac{\theta_z v}{2}, \quad \delta\varphi_3^0 = -\frac{\theta_y v}{2}, \quad \delta\varphi_4^0 = -\frac{\theta_x v}{2} \ . \tag{C.2.27}$$

Three generators of the group are broken, leading to the appearance of three Goldstone bosons.

The Lagrangian can be decomposed as:

$$\mathcal{L} = \mathcal{L}_{scalar} + \mathcal{L}_{SU(2)} \ , \tag{C.2.28}$$

where:

$$\mathcal{L}_{SU(2)} = -\frac{1}{4} \left(\partial_\mu \vec{W}_\nu - \partial_\nu \vec{W}_\mu - g \vec{W}_\mu \wedge \vec{W}_\nu \right)^2 \ , \tag{C.2.29}$$

and:

$$\mathcal{L}_{scalar} = \partial_\mu \vec{H}^\dagger \partial^\mu \vec{H} - V(\vec{H}) \ , \tag{C.2.30}$$

with the same scalar potential:

$$V(\vec{H}) = \frac{\lambda v^4}{4} - \mu^2 \vec{H}^\dagger \vec{H} + \lambda (\vec{H}^\dagger \vec{H})^2 \ . \tag{C.2.31}$$

Let g be the $SU(2)$ coupling constant. The covariant derivative is given by:

$$D_\mu \vec{H} = \partial_\mu \vec{H} + ig \left(\vec{W}_\mu \cdot \frac{\vec{\sigma}}{2} \right) \vec{H} \ . \tag{C.2.32}$$

To demonstrate spontaneous symmetry breaking, we show that there exists a gauge transformation aligning any $\vec{H}$ with the vacuum, such that the only nonzero component is $\varphi_1 = v + h$. We write:

$$\vec{H} = \frac{1}{\sqrt{2}} \begin{pmatrix} \varphi_3 + i\varphi_4 \\ \varphi_1 + i\varphi_2 \end{pmatrix} = R\vec{H}' = \begin{pmatrix} \bar{a} & b \\ -\bar{b} & a \end{pmatrix} \begin{pmatrix} 0 \\ (v+h)/\sqrt{2} \end{pmatrix} \ , \tag{C.2.33}$$

where the rotation matrix R must preserve the norm, leading to:

$$a = \cos(\theta/2)e^{i\alpha}, \quad b = \sin(\theta/2)e^{i\beta} \ . \tag{C.2.34}$$

This yields:

$$e^{i\alpha} = \frac{\varphi_1 + i\varphi_2}{\sqrt{\varphi_1^2 + \varphi_2^2}}, \quad e^{i\beta} = \frac{\varphi_3 + i\varphi_4}{\sqrt{\varphi_3^2 + \varphi_4^2}}, \quad \cos(\theta/2) = \frac{\sqrt{\varphi_1^2 + \varphi_2^2}}{v + h}, \quad \sin(\theta/2) = \frac{\sqrt{\varphi_3^2 + \varphi_4^2}}{v + h} \ . \tag{C.2.35}$$

Therefore,

$$\vec{H} = \exp\left(-\frac{ig}{2}\vec{\theta}\cdot\vec{\sigma}\right)\begin{pmatrix}0\\(v+h)/\sqrt{2}\end{pmatrix} \ . \tag{C.2.36}$$

The three Goldstone bosons are absorbed by the gauge bosons W_μ^a, which thereby acquire a mass:

$$m_W = \frac{gv}{2} \ . \tag{C.2.37}$$

C.3 Quark Model

Due to the phenomenon of confinement, quarks are not observed as free particles in nature. It is therefore essential to understand how they combine to form hadrons.

C.3.1 Flavor Symmetry

The isospin symmetry between up quarks ($|u\rangle$) and down quarks ($|d\rangle$) is described by the fundamental representation of $SU(2)$. The corresponding generators are denoted as $I_a = \frac{1}{2}\sigma_a$, where σ_a are the Pauli matrices. Introducing the scaling operators:

$$I_\pm = \frac{1}{\sqrt{2}}(I_1 \pm iI_2) \ , \tag{C.3.1}$$

we obtain the following action on quark states:

$$I_-|u\rangle = |d\rangle \ , \quad I_+|d\rangle = |u\rangle \ . \tag{C.3.2}$$

Representing the quark states explicitly:

$$u \equiv \begin{pmatrix}1\\0\end{pmatrix} \ , \quad d \equiv \begin{pmatrix}0\\1\end{pmatrix} \ , \quad I_3 = \frac{1}{2}\begin{pmatrix}1 & 0\\0 & -1\end{pmatrix} \ , \tag{C.3.3}$$

we find:

$$I_3|u\rangle = \frac{1}{2}|u\rangle \ , \quad I_3|d\rangle = -\frac{1}{2}|d\rangle \ . \tag{C.3.4}$$

Thus, for a particle composed of n_u up quarks and n_d down quarks, the total isospin component is given by:

$$I_3 = \frac{n_u - n_d}{2} \ . \tag{C.3.5}$$

Similarly, the anti-quark states $|\bar{u}\rangle$ and $|\bar{d}\rangle$, which transform under the anti-fundamental representation of $SU(2)$, obey:

$$I_+|\bar{u}\rangle = -|\bar{d}\rangle \ , \quad I_-|\bar{d}\rangle = -|\bar{u}\rangle \ . \tag{C.3.6}$$

To include strange quarks ($|s\rangle$), the flavor symmetry is extended to the fundamental representation of $SU(3)$[1]. This symmetry includes three interrelated $SU(2)$ subgroups, defined via the scaling operators: $I_\pm$ (for $|u\rangle \leftrightarrow |d\rangle$), $V_\pm$ (for $|u\rangle \leftrightarrow |s\rangle$), and $U_\pm$ (for $|d\rangle \leftrightarrow |s\rangle$).

The basis vectors and generators in this representation are:

$$u \equiv \begin{pmatrix}1\\0\\0\end{pmatrix} \ , \quad d \equiv \begin{pmatrix}0\\1\\0\end{pmatrix} \ , \quad s \equiv \begin{pmatrix}0\\0\\1\end{pmatrix} \ , \quad I_3 = \frac{1}{2}\begin{pmatrix}1 & 0 & 0\\0 & -1 & 0\\0 & 0 & 0\end{pmatrix} \ , \quad Y = \frac{1}{3}\begin{pmatrix}1 & 0 & 0\\0 & 1 & 0\\0 & 0 & -2\end{pmatrix} \ , \tag{C.3.7}$$

[1]Note that this $SU(3)$ is completely distinct from the $SU(3)_c$ of Quantum Chromodynamics (QCD). In general, with n quark flavors, the flavor symmetry group is $SU(n)$.

where I_3 is the third component of isospin and Y is the hypercharge.

Their values for a particle composed of n_u, n_d, and n_s quarks are given by:

$$I_3 = \frac{n_u - n_d}{2}, \qquad Y = \frac{n_u + n_d - 2n_s}{3} \ . \tag{C.3.8}$$

The electric charge Q is then defined by the Gell-Mann-Nishijima relation:

$$Q = I_3 + \frac{Y}{2} = \frac{2n_u - n_d - n_s}{3} \ , \tag{C.3.9}$$

which correctly yields the quark charges: $Q_u = 2/3$, and $Q_d = Q_s = -1/3$.

C.3.2 Representation of $SU(n)$

A representation of $SU(n)$ can be described using Young tableaux, which must satisfy the following rules:

- Each box may contain integers from 1 to n.
- Along each row (horizontally connected boxes), the numbers must be non-decreasing.
- Along each column (vertically connected boxes), the numbers must strictly increase. Consequently, there can be at most n boxes in a column.

The number of valid tableaux under these constraints corresponds to the dimension of the representation.

For $SU(2)$, if we denote the number of boxes in the first row by n_{box}, the representation is labeled as $\underline{n}$, where $n = n_{box} + 1$, corresponding to the number of valid tableaux satisfying the above rules. The associated spin $s \in \frac{1}{2}\mathbb{Z}$ is such that $n = 2s + 1$.

The tensor product resulting from spin addition is given by:

$$\underline{2s_1 + 1} \otimes \underline{2s_2 + 1} = \bigoplus_{s=|s_1 - s_2|}^{s_1 + s_2} \underline{2s + 1} \ . \tag{C.3.10}$$

In particular:

$$\underline{2} \otimes \underline{1} = \underline{2}, \quad \underline{2} \otimes \underline{2} = \underline{3} \oplus \underline{1} \ , \quad \underline{2} \otimes \underline{3} = \underline{4} \oplus \underline{2} \ , \tag{C.3.11}$$

and by further decomposition:

$$\underline{2} \otimes \underline{2} \otimes \underline{2} = (\underline{3} \oplus \underline{1}) \otimes \underline{2} = (\underline{3} \otimes \underline{2}) \oplus (\underline{1} \otimes \underline{2}) = \underline{4} \oplus \underline{2} \oplus \underline{2} \ . \tag{C.3.12}$$

For $SU(3)$, there is no simple formula analogous to that of $SU(2)$; however, Young tableaux provide an intuitive method to deduce certain decomposition rules. For example:

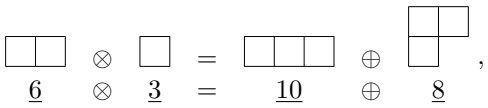

, (C.3.13)

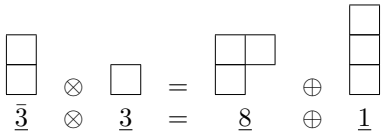

, (C.3.14)

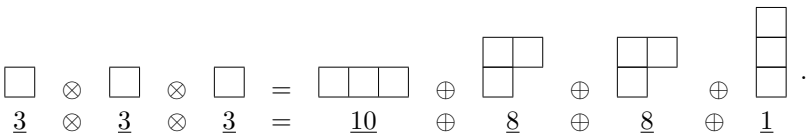

. (C.3.15)

The dimension of each representation can be obtained by listing all the tableaux consistent with the rules outlined above.

C.3.3 Baryons with $\vec{L} = \vec{0}$

Baryons are composed of three quarks, and their total wave function is given by the tensor product of four components: the spatial ($|\eta_{space}\rangle$), spin ($|\chi_{spin}\rangle$), color ($|\xi_{color}\rangle$), and flavor ($|\phi_{flavor}\rangle$) wave functions. Since we consider baryons with zero orbital angular momentum ($\vec{L} = \vec{0}$), the spatial wave function is symmetric. To be consistent with QCD, the color wave function must be totally antisymmetric.

The decomposition of the flavor wave function is given by:

$$\underline{3} \otimes \underline{3} \otimes \underline{3} = \underline{10} \oplus \underline{8}_s \oplus \underline{8}_a \oplus \underline{1} \ , \tag{C.3.16}$$

where:

- $\underline{10}$ corresponds to a totally symmetric decuplet.
- $\underline{8}_s$ denotes a mixed-symmetry octet, symmetric under exchange of the first two indices.
- $\underline{8}_a$ denotes a mixed-symmetry octet, antisymmetric under exchange of the first two indices.
- $\underline{1}$ corresponds to a totally antisymmetric singlet.

The decomposition of the spin wave function is:

$$\underline{2} \otimes \underline{2} \otimes \underline{2} = \underline{4} \oplus \underline{2}_s \oplus \underline{2}_a \ , \tag{C.3.17}$$

where:

- $\underline{4}$ is a totally symmetric quadruplet (spin $s = 3/2$).
- $\underline{2}_s$ is a mixed-symmetry doublet, symmetric under exchange of the first two indices.
- $\underline{2}_a$ is a mixed-symmetry doublet, antisymmetric under exchange of the first two indices.

Since baryons are fermions, their total wave function must be antisymmetric under exchange of any two quarks. As the color wave function is totally antisymmetric and the spatial wave function is symmetric, the combined spin-flavor wave function must be symmetric.

There are two possible combinations that satisfy this condition:

- The decuplet with spin $s = \frac{3}{2}$: $\underline{10} \otimes \underline{4}$.
- The octet with spin $s = \frac{1}{2}$: $\underline{8}_s \otimes \underline{2}_s + \underline{8}_a \otimes \underline{2}_a$.

Baryons can be represented in a weight diagram based on their isospin and hypercharge, as shown in Fig. C.2. This figure illustrates the baryon octet (with $s = 1/2$) and the baryon decuplet (with $s = 3/2$).

C.3.4 Mesons with $\vec{L} = \vec{0}$

A meson is a particle composed of a quark and an antiquark bound together by the strong interaction. Since quarks and antiquarks are distinguishable, mesons do not exhibit symmetric or antisymmetric exchange properties as in the case of baryons.

The flavor wave function decomposition for mesons is given by:

$$\underline{3} \otimes \overline{\underline{3}} = \underline{8} \oplus \underline{1} \ , \tag{C.3.18}$$

where $\underline{8}$ denotes an octet and $\underline{1}$ a singlet representation.

The spin wave function decomposition is:

$$\underline{2} \otimes \underline{2} = \underline{3} \oplus \underline{1} \ , \tag{C.3.19}$$

This leads to 9 states with spin $s = 1$ and 9 states with spin $s = 0$.

Mesons can be represented on a weight diagram. Fig. C.3 shows the meson octets corresponding to spin states $s = 0$ and $s = 1$.

The parity of a meson is given by:

$$P(q\bar{q}) = P(q) \cdot P(\bar{q}) \cdot (-1)^l = -1 \ , \tag{C.3.20}$$

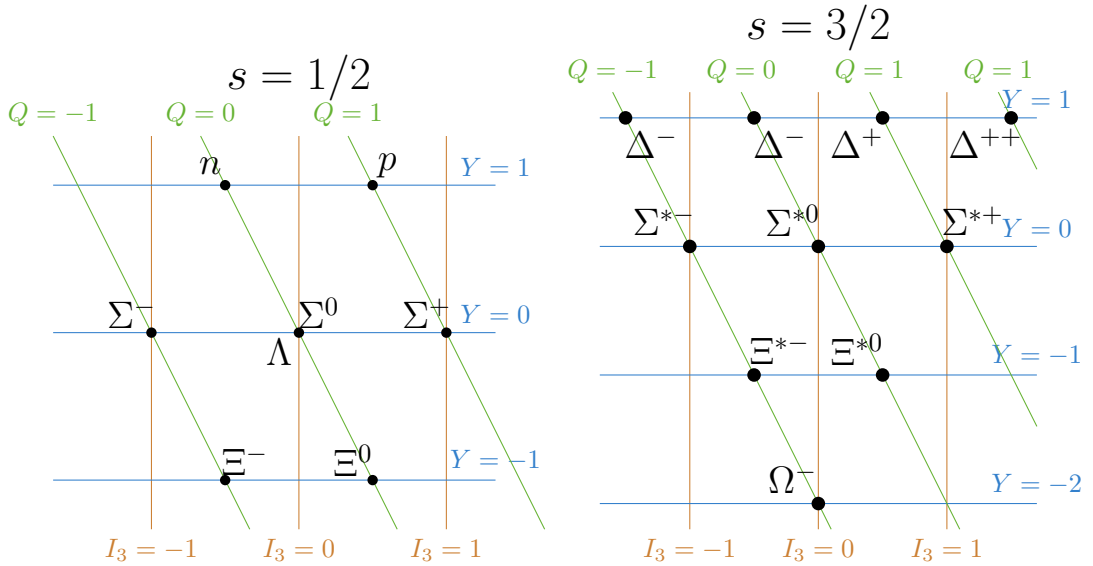

Figure C.2: Weight diagrams of baryons with spin $s = 1/2$ (left, baryon octet) and $s = 3/2$ (right, baryon decuplet), represented in the (I_3, Y) plane.

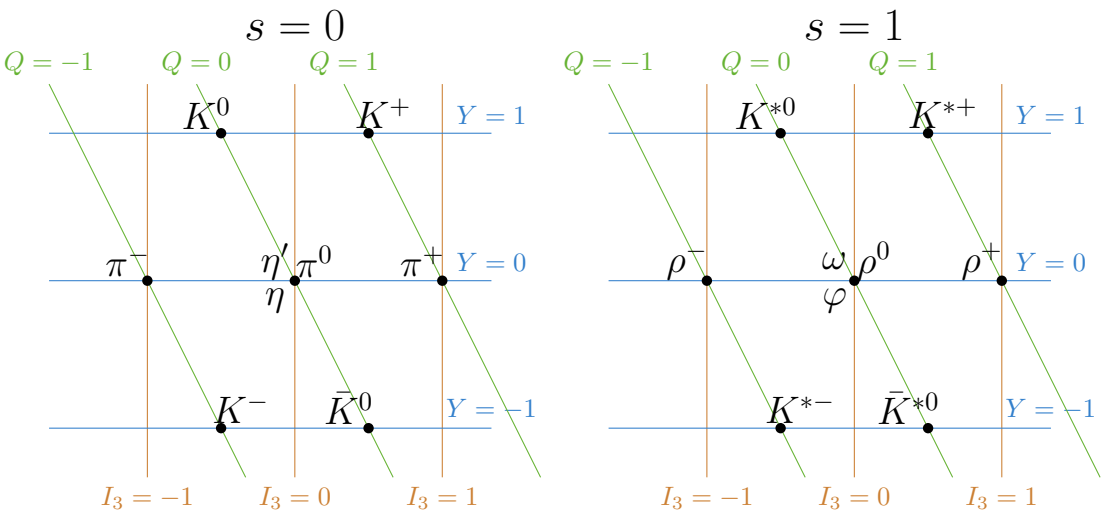

Figure C.3: Weight diagrams of mesons with spin $s = 0$ (left, pseudoscalar mesons) and spin $s = 1$ (right, vector mesons), represented in the (I_3, Y) plane..

since $P(q) = +1$, $P(\bar{q}) = -1$, and we consider $\vec{L} = \vec{0}$. Therefore, mesons with spin $s = 1$ are real vectors, while those with spin $s = 0$ are pseudoscalars.

The charge conjugation quantum number is given by:

$$C(q\bar{q}) = (-1)^{s+l} = (-1)^s \tag{C.3.21}$$

Mesons are commonly classified using the J^{PC} notation, where J is the total angular momentum, P the parity, and C the charge conjugation. Hence, for $\vec{L} = \vec{0}$, vector mesons are denoted as 1^{--} and pseudoscalar mesons as 0^{-+}.

To assign the appropriate flavor wave functions to individual particles:

- For the inner elements of the weight diagram (e.g., π, ρ), use isospin symmetry to determine the appropriate combinations.
- For η, η' and ω, φ (both in the scalar and vector cases), the singlet state is usually associated with the heaviest meson.

However, experimental observations show that $BR(\varphi \to K^0\bar{K}^0) \simeq 1$, suggesting that $|\varphi\rangle = |s\bar{s}\rangle$. This contradicts the expectation that the singlet state should correspond to the heaviest meson. This discrepancy highlights a limitation of the naive quark model and reflects the effect of $SU(3)$ symmetry breaking due to the mass difference $m_s > m_d \simeq m_u$. As a result, the $SU(3)$ symmetry is only approximate and is explicitly broken in nature.

C.3.5 $K^0 - \bar{K}^0$ mixing

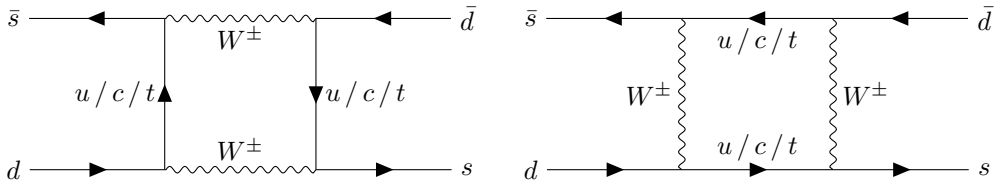

Figure C.4: Box diagrams contributing to $K^0 - \bar{K}^0$ mixing in the SM.

In the SM, K^0 and $\bar{K}^0$ are flavor eigenstates. However, they can mix via weak interactions, as mediated by the box diagrams shown in Fig. C.4. As a result, these states are not necessarily the mass eigenstates.

Next, we discuss how to determine the mass eigenstates. For more details, see [Bur98].

Since K^0 and $\bar{K}^0$ are pseudoscalar mesons, their transformation under CP is given by:

$$CP|K^0\rangle = -|\bar{K}^0\rangle\,, \quad CP|\bar{K}^0\rangle = -|K^0\rangle\,. \tag{C.3.22}$$

Thus, the CP eigenstates are:

$$|K_\mp\rangle = \frac{1}{\sqrt{2}}\left(|K^0\rangle \mp |\bar{K}^0\rangle\right)\,, \tag{C.3.23}$$

since

$$CP|K_\mp\rangle = \frac{1}{\sqrt{2}}\left(CP|K^0\rangle \mp CP|\bar{K}^0\rangle\right) = \frac{1}{\sqrt{2}}\left(-|\bar{K}^0\rangle \pm |K^0\rangle\right) = \pm\frac{1}{\sqrt{2}}\left(|K^0\rangle \mp |\bar{K}^0\rangle\right) = \pm|K_\mp\rangle\,. \tag{C.3.24}$$

The time evolution of the $K^0 - \bar{K}^0$ system is governed by the Schrödinger equation:

$$i\frac{d}{dt}|\psi(t)\rangle = \hat{H}|\psi(t)\rangle\,, \quad |\psi(t)\rangle = \begin{pmatrix}|K^0(t)\rangle\\ |\bar{K}^0(t)\rangle\end{pmatrix}\,, \tag{C.3.25}$$

where

$$\hat{H} = \hat{M} - \frac{i}{2}\hat{\Gamma}\,. \tag{C.3.26}$$

Here, $\hat{M}$ and $\hat{\Gamma}$ are Hermitian matrices. CPT symmetry implies $M_{11} = M_{22} = M$ and $\Gamma_{11} = \Gamma_{22} = \Gamma$, so that:

$$\hat{H} = \begin{pmatrix}M - i\Gamma/2 & M_{12} - i\Gamma_{12}/2\\ M_{12}^* - i\Gamma_{12}^*/2 & M - i\Gamma/2\end{pmatrix}\,. \tag{C.3.27}$$

This matrix can be diagonalized. The resulting mass eigenstates are:

$$|K_{S,L}\rangle = \frac{(1+\bar{\epsilon})|K^0\rangle \mp (1-\bar{\epsilon})|\bar{K}^0\rangle}{\sqrt{2(1+|\bar{\epsilon}|^2)}} = \frac{|K_\mp\rangle + \bar{\epsilon}|K_\pm\rangle}{\sqrt{1+|\bar{\epsilon}|^2}}\,, \tag{C.3.28}$$

where $\bar{\epsilon}$ is a small complex parameter such that:

$$\left(\frac{1-\bar{\epsilon}}{1+\bar{\epsilon}}\right)^2 = \frac{M_{12}^* - i\Gamma_{12}^*/2}{M_{12} - i\Gamma_{12}/2}\,. \tag{C.3.29}$$

The eigenvalues are given by:

$$M_{L/S} = M \pm \mathrm{Re}(Q)\,, \quad \Gamma_{L/S} = \Gamma \mp 2\mathrm{Im}(Q)\,, \tag{C.3.30}$$

with

$$Q^2 = \left(M_{12} - \frac{i}{2}\Gamma_{12}\right)\left(M_{12}^* - \frac{i}{2}\Gamma_{12}^*\right) \ . \tag{C.3.31}$$

Since $\bar{\epsilon} = \mathcal{O}(10^{-3})$, to a good approximation, the mass eigenstates coincide with the CP eigenstates:

$$|K_{S,L}\rangle \simeq |K_{\mp}\rangle = \frac{1}{\sqrt{2}}\left(|K^0\rangle \mp |\bar{K}^0\rangle\right) \ . \tag{C.3.32}$$

C.4 Meson masses and explicit symmetry breaking

The mass term for quarks in the QCD Lagrangian is given by:

$$\mathcal{L}_m = -\bar{q}_L M_q q_R + \text{h.c.} \ , \tag{C.4.1}$$

where the quark mass matrix is $M_q = \text{diag}(m_u; m_d; m_s)$. This term respects chiral symmetry if M_q transforms under $SU(3)_L \times SU(3)_R$ as:

$$M_q \to L M_q R^\dagger \ . \tag{C.4.2}$$

Symmetry-breaking terms in the chiral Lagrangian are constructed to be invariant under the transformation rule in Eq. (C.4.2). The lowest-order term in the effective chiral Lagrangian involving M_q is

$$\mathcal{L}_m = \frac{F_0^2 B_0}{2}\text{Tr}(U^\dagger M_q + M_q^\dagger U) \ , \tag{C.4.3}$$

which lifts the vacuum degeneracy and selects a preferred vacuum alignment. As a result, the vacuum state $U = 1$ minimizes the energy. Expanding around $U = 1$, the mass term becomes:

$$\mathcal{L}_m = -\frac{B_0}{4}\text{Tr}[M_q\phi^2 + \phi^2 M_q] - \frac{1}{2}M_0\eta_0^2 + \mathcal{O}(\phi^4) \ . \tag{C.4.4}$$

Due to the axial anomaly in QCD, η_0 is not a true pseudo-Goldstone boson. We include an additional term that gives mass to the singlet:

$$\mathcal{L}_{anomaly} = \frac{M_0^2 F_0^2}{12}(\ln(\det(U)))^2 = -\frac{1}{2}M_0^2\eta_0^2 \ , \tag{C.4.5}$$

The mass term $-\frac{1}{2}M_0^2\eta_0^2$ is the mass term we intend to add, and the expression involving U is introduced to verify symmetry properties. They are equivalent because:

$$\ln(\det(U)) = \ln(\det(\exp(i\phi/F_0))) = \ln(\exp(\text{Tr}(i\phi/F_0))) = \text{Tr}(i\phi/F_0) = i\sqrt{6}\eta_0/F_0 \ . \tag{C.4.6}$$

Substituting M_q and ϕ into the Lagrangian, we derive the following mass relations:

$$\begin{aligned} m_{\pi^\pm}^2 &= B_0(m_u + m_d) + \Delta M^2 \ , \\ m_{K^\pm}^2 &= B_0(m_u + m_s) + \Delta M^2 \ , \\ m_{K^0,\bar{K}^0}^2 &= B_0(m_d + m_s) \ . \end{aligned} \tag{C.4.7}$$

The mass matrix for the neutral mesons π^0, η, and η' is:

$$M_{\pi^0,\eta,\eta'}^2 = B_0 \begin{pmatrix} m_u + m_d & \frac{1}{\sqrt{3}}(m_u - m_d) & \sqrt{\frac{2}{3}}(m_u - m_d) \\ \frac{1}{\sqrt{3}}(m_u - m_d) & \frac{1}{3}(m_u + m_d + 4m_s) & \frac{\sqrt{2}}{3}(m_u + m_d - 2m_s) \\ \sqrt{\frac{2}{3}}(m_u - m_d) & \frac{\sqrt{2}}{3}(m_u + m_d - 2m_s) & \frac{2}{3}(m_u + m_d + m_s) + M_0^2/B_0 \end{pmatrix} \ . \tag{C.4.8}$$

Neglecting the isospin-breaking parameter $m_u - m_d$, the eigenvalue corresponding to the π^0 mass is:

$$m_{\pi^0}^2 \simeq B_0(m_u + m_d) \ , \tag{C.4.9}$$

with $\pi^0 \simeq \pi^3$ is a good approximation[2]. The η_8 and η_0 states mix even in the isospin-symmetric limit $m_u \simeq m_d$. The corresponding 2×2 mass matrix is:

$$M^2_{\eta,\eta'} = B_0 \begin{pmatrix} \frac{1}{3}(m_u + m_d + 4m_s) & \frac{\sqrt{2}}{3}(m_u + m_d - 2m_s) \\ \frac{\sqrt{2}}{3}(m_u + m_d - 2m_s) & \frac{2}{3}(m_u + m_d + m_s) + M_0^2/B_0 \end{pmatrix} . \tag{C.4.10}$$

This matrix must be diagonalized to obtain the physical states η and η', with the convention $m_{\eta'} > m_\eta$. The physical states are related to the flavor states by:

$$\begin{pmatrix} \eta \\ \eta' \end{pmatrix} = \begin{pmatrix} \cos(\theta) & -\sin(\theta) \\ \sin(\theta) & \cos(\theta) \end{pmatrix} \begin{pmatrix} \eta_8 \\ \eta_0 \end{pmatrix} , \tag{C.4.11}$$

with the mixing angle $\theta \simeq -11.5°$ [GZc20].

Electromagnetic isospin breaking contributes to the masses of charged mesons through the term ΔM^2, which appears in Eq. (C.4.7). This contribution is of comparable magnitude to the isospin-breaking term $m_u - m_d$. At leading order in $SU(3)$ breaking, ΔM^2 is the same for $\pi^\pm$ and $K^\pm$, and vanishes for neutral mesons.

The values of the quark masses cannot be determined from meson masses alone, as they always appear in the product $B_0 m_q$, where B_0 is unknown. However, meson masses allow us to extract ratios of quark masses. From Eqs. (C.4.7) and (C.4.9), we derive:

$$\frac{m_u}{m_d} = \frac{m^2_{K^\pm} - m^2_{K^0} + 2m^2_{\pi^0} - m^2_{\pi^\pm}}{m^2_{K^0} - m^2_{K^\pm} + m^2_{\pi^\pm}} , \tag{C.4.12}$$

$$\frac{m_s}{m_d} = \frac{m^2_{K^0} + m^2_{K^\pm} - m^2_{\pi^\pm}}{m^2_{K^0} - m^2_{K^\pm} + m^2_{\pi^\pm}} . \tag{C.4.13}$$

Experimentally, we have:

$$m_u = 2.16^{+0.49}_{-0.26}\,\text{MeV},\ m_d = 4.67^{+0.48}_{-0.17}\,\text{MeV} \text{ and } m_s = 93.4^{+8.6}_{-3.4}\,\text{MeV}.$$
$$m_{\pi^\pm} = 139.57039(18)\,\text{MeV},\ m_{\pi^0} = 134.9768(5)\,\text{MeV},\ m_\eta = 547.862(17)\,\text{MeV},$$
$$m_{K^\pm} = 493.677(16)\,\text{MeV},\ m_{K^0} = 497.611(13)\,\text{MeV}.$$

Using these values:

$$\frac{m^2_{K^\pm} - m^2_{K^0} + 2m^2_{\pi^0} - m^2_{\pi^\pm}}{m^2_{K^0} - m^2_{K^\pm} + m^2_{\pi^\pm}} = 0.559 \pm 0.001 \quad \& \quad \frac{m_u}{m_d} = 0.46^{+0.11}_{-0.07} , \tag{C.4.14}$$

$$\frac{m^2_{K^0} + m^2_{K^\pm} - m^2_{\pi^\pm}}{m^2_{K^0} - m^2_{K^\pm} + m^2_{\pi^\pm}} = 20.24 \pm 0.02 \quad \& \quad \frac{m_s}{m_d} = 20 \pm 2 . \tag{C.4.15}$$

Finally, an ambiguity arises when extracting second-order corrections to the light quark masses from M_q. The matrices M_q and $\det(M_q)(M_q^\dagger)^{-1}$ transform identically under $SU(3)_L \times SU(3)_R$, and thus cannot be distinguished in the chiral Lagrangian. This leads to the transformation:

$$M_q \to M_q + \lambda \det(M_q)(M_q^\dagger)^{-1} \tag{C.4.16}$$

$$\text{diag}(m_u; m_d; m_s) \to \text{diag}(m_u + \lambda m_d m_s; \lambda m_u m_s; m_s + \lambda m_u m_d) , \tag{C.4.17}$$

where λ parameterizes the ambiguity and refines the comparison between meson and quark masses.

C.5 Chiral Perturbation Theory with an axion Lagrangian

This appendix summarizes the structure of the chiral Lagrangian involving light pseudoscalar mesons and baryons, extended to include axion couplings via derivative interactions.

The leading-order mesonic Lagrangian is

$$\mathcal{L}_U = \frac{F_0^2}{4} \left(\text{Tr}[D_\mu U (D^\mu U)^\dagger] + 2B_0 \text{Tr}[M_q U^\dagger + U M_q^\dagger] \right) , \tag{C.5.1}$$

[2]Strictly speaking, in Eq. (2.7.15), one should write π^3 instead of π^0, which would be the lightest mass eigenstate diagonalizing Eq. (C.4.8).

where $U = \exp(i\phi/F_0)$, and ϕ contains the pseudoscalar octet and singlet states with

$$\phi = \sqrt{2}\begin{pmatrix} \frac{1}{\sqrt{2}}\pi^0 + \frac{1}{\sqrt{6}}\eta_8 + \frac{1}{\sqrt{3}}\eta_0 & \pi^+ & K^+ \\ \pi^- & -\frac{1}{\sqrt{2}}\pi^0 + \frac{1}{\sqrt{6}}\eta_8 + \frac{1}{\sqrt{3}}\eta_0 & K^0 \\ K^- & \bar{K}^0 & -\frac{2}{\sqrt{6}}\eta_8 + \frac{1}{\sqrt{3}}\eta_0 \end{pmatrix} . \tag{C.5.2}$$

The covariant derivative is defined as

$$D_\mu U = \partial_\mu U - ieA_\mu[Q, U] , \tag{C.5.3}$$

where $Q = \mathrm{diag}(q_u, q_d, q_s)$ is the quark charge matrix.

The baryon-meson Lagrangian including the octet baryons is

$$\mathcal{L}_{BU} = \mathrm{Tr}[\bar{B}(i\not{D} - M_B)B] - \frac{D}{2}\mathrm{Tr}[\bar{B}\gamma^\mu\gamma_5\{u_\mu, B\}] - \frac{F}{2}\mathrm{Tr}[\bar{B}\gamma^\mu\gamma_5[u_\mu, B]] + \mathcal{L}_U \tag{C.5.4}$$

where $U = u^2$ and M_B is the baryon mass matrix, and

$$D_\mu B = \partial_\mu B + [\Gamma_\mu, B] , \tag{C.5.5}$$

$$\Gamma_\mu = \frac{1}{2}\left(u(\partial_\mu + eQA_\mu)u^\dagger + u^\dagger(\partial_\mu + eQA_\mu)u\right) , \tag{C.5.6}$$

$$u_\mu = i\left(u^\dagger(\partial_\mu + eQA_\mu)u - u(\partial_\mu + eQA_\mu)u^\dagger\right) . \tag{C.5.7}$$

The baryon octet field B is written as

$$B = \begin{pmatrix} \frac{1}{\sqrt{2}}\Sigma^0 + \frac{1}{\sqrt{6}}\Lambda & \Sigma^+ & p \\ \Sigma^- & -\frac{1}{\sqrt{2}}\Sigma^0 + \frac{1}{\sqrt{6}}\Lambda & n \\ \Xi^- & \Xi^0 & -\frac{2}{\sqrt{6}}\Lambda \end{pmatrix} . \tag{C.5.8}$$

The left- and right-handed Noether currents associated with chiral transformations are:

$$\left(J_L^{(U)}\right)^{b,\mu} = i\frac{F_0^2}{2}\mathrm{Tr}\left[\frac{\lambda^b}{2}(D^\mu U)^\dagger U\right] , \tag{C.5.9}$$

$$\left(J_R^{(U)}\right)^{b,\mu} = -i\frac{F_0^2}{2}\mathrm{Tr}\left[\frac{\lambda^b}{2}U(D^\mu U)^\dagger\right] , \tag{C.5.10}$$

$$\begin{aligned}\left(J_L^{(BU)}\right)^{b,\mu} &= \frac{1}{4}\mathrm{Tr}\left(\bar{B}\gamma^\mu\left[\lambda^b - \frac{f^{\lambda\phi b}}{2F_0}, B\right]\right) \\ &\quad - \frac{1}{8}\mathrm{Tr}\left(\bar{B}\gamma^\mu\left[\left(\lambda^b - \frac{f^{\lambda\phi b}}{2F_0}\right) - u\left(\lambda^b - \frac{f^{\lambda\phi b}}{2F_0}\right)u^\dagger, B\right]\right) \\ &\quad + \frac{D}{4}\mathrm{Tr}\left(\bar{B}\gamma^\mu\gamma_5\{u\lambda^b u^\dagger, B\}\right) + \frac{F}{4}\mathrm{Tr}\left(\bar{B}\gamma^\mu\gamma_5[u\lambda^b u^\dagger, B]\right) ,\end{aligned} \tag{C.5.11}$$

$$\begin{aligned}\left(J_R^{(BU)}\right)^{b,\mu} &= \frac{1}{4}\mathrm{Tr}\left(\bar{B}\gamma^\mu\left[\lambda^b + \frac{f^{\lambda\phi b}}{2F_0}, B\right]\right) \\ &\quad - \frac{1}{8}\mathrm{Tr}\left(\bar{B}\gamma^\mu\left[\left(\lambda^b + \frac{f^{\lambda\phi b}}{2F_0}\right) - u^\dagger\left(\lambda^b + \frac{f^{\lambda\phi b}}{2F_0}\right)u, B\right]\right) \\ &\quad - \frac{D}{4}\mathrm{Tr}\left(\bar{B}\gamma^\mu\gamma_5\{u\lambda^b u^\dagger, B\}\right) - \frac{F}{4}\mathrm{Tr}\left(\bar{B}\gamma^\mu\gamma_5[u\lambda^b u^\dagger, B]\right) ,\end{aligned} \tag{C.5.12}$$

with the shorthand $f^{\lambda\phi b} = \frac{i}{2}[\lambda^b, \phi]$.

The axion-hadron Lagrangian is then given by

$$\begin{aligned}\mathcal{L}_{aBU} &= \frac{\partial_\mu a}{f_a}\left[x_L^b\left(\left(J_L^{(U)}\right)^{b,\mu} + \left(J_L^{(BU)}\right)^{b,\mu}\right) + x_R^b\left(\left(J_R^{(U)}\right)^{b,\mu} + \left(J_R^{(BU)}\right)^{b,\mu}\right)\right] \\ &\quad + \mathrm{Tr}(\hat{k}_A)\frac{S}{6}\frac{\partial_\mu a}{f_a}\mathrm{Tr}\left(\bar{B}\gamma^\mu\gamma_5 B\right) ,\end{aligned} \tag{C.5.13}$$

where $x_{L,R}^b = \mathrm{Tr}[\hat{k}_{L,R}\lambda^b]$, and the couplings $\hat{k}_V = \hat{k}_R + \hat{k}_L$ and $\hat{k}_A = \hat{k}_R - \hat{k}_L$ encode the vector and axial couplings to the axion field.

The numerical parameters used are:

$$F_0 = 93\,\mathrm{MeV}, \quad D = -0.813(43), \quad F = -0.441(26), \quad S = 0.405(62) \tag{C.5.14}$$

C.6 Axion-mesons vertices

The objective of this section is twofold: first, to show that a scalar vertex involving the axion and an even number of light mesons is proportional to the vector part $x_V^b = \mathrm{Tr}[\lambda^b \hat{k}_V]$, whereas a vertex with an odd number of mesons is proportional to the axial part $x_A^b = \mathrm{Tr}[\lambda^b \hat{k}_A]$. Second, we aim to derive an explicit formula for this relation.

The Lagrangian involving the axion and light mesons can be written as:

$$\mathcal{L} \supset \frac{\partial_\mu a}{f_a} \left(x_L^b J_L^{b,\mu} + x_R^b J_R^{b,\mu} \right) , \tag{C.6.1}$$

with

$$J_L^{b,\mu} \supset +i\frac{F_0^2}{2}\mathrm{Tr}\left(\frac{\lambda^b}{2} \left(\partial^\mu U\right)^\dagger U \right) , \tag{C.6.2}$$

$$J_R^{b,\mu} \supset -i\frac{F_0^2}{2}\mathrm{Tr}\left(\frac{\lambda^b}{2} U \left(\partial^\mu U\right)^\dagger \right) . \tag{C.6.3}$$

To compute the interaction vertices, we expand the field U to extract the mesonic degrees of freedom. Using the exponential representation, we have:

$$U(\partial_\mu U)^\dagger = \exp\left(i\frac{\phi}{F_0}\right)\partial_\mu\left(\exp\left(-i\frac{\phi}{F_0}\right)\right) = \sum_{a,b=0}^{+\infty} \frac{i^a\phi^a}{a!F_0^a}\frac{(-1)^b i^b \partial_\mu(\phi^b)}{b!F_0^b} , \tag{C.6.4}$$

$$(\partial_\mu U)^\dagger U = \partial_\mu\left(\exp\left(-i\frac{\phi}{F_0}\right)\right)\exp\left(i\frac{\phi}{F_0}\right) = \sum_{a,b=0}^{+\infty} \frac{i^a\partial_\mu(\phi^a)}{a!F_0^a}\frac{(-1)^b i^b \phi^b}{b!F_0^b} . \tag{C.6.5}$$

To isolate the terms involving exactly n mesons, we extract

$$\frac{i^n}{n!F_0^n}\sum_{a,b=0}^{n}(-1)^b\frac{n!}{a!b!}\phi^a\partial_\mu(\phi^b) = \frac{i^n}{n!F_0^n}\sum_{b=0}^{n}(-1)^b C_n^b \phi^{n-b}\partial_\mu(\phi^b) \subset U(\partial_\mu U)^\dagger , \tag{C.6.6}$$

$$\frac{i^n}{n!F_0^n}\sum_{a,b=0}^{n}(-1)^b\frac{n!}{a!b!}\partial_\mu(\phi^b)\phi^a = \frac{i^n}{n!F_0^n}\sum_{b=0}^{n}(-1)^b C_n^b \partial_\mu(\phi^b)\phi^{n-b} \subset (\partial_\mu U)^\dagger U , \tag{C.6.7}$$

with $C_n^b = b!/(n!(n-b)!)$. Using

$$\partial_\mu(\phi^b) = \sum_{c=0}^{b-1}\phi^{b-c-1}(\partial^\mu\phi)\phi^c = \sum_{c=0}^{b-1}\phi^c(\partial^\mu\phi)\phi^{b-c-1} , \tag{C.6.8}$$

we obtain:

$$\frac{i^n}{n!F_0^n}\sum_{b=1}^{n}\sum_{c=0}^{b-1}(-1)^b C_n^b \phi^{n-c-1}(\partial^\mu\phi)\phi^c \subset U(\partial_\mu U)^\dagger , \tag{C.6.9}$$

$$\frac{i^n}{n!F_0^n}\sum_{b=1}^{n}\sum_{c=0}^{b-1}(-1)^b C_n^b \phi^c(\partial^\mu\phi)\phi^{n-c-1} \subset (\partial_\mu U)^\dagger U . \tag{C.6.10}$$

Rearranging indices, one can show that

$$\sum_{b=1}^{n}\sum_{c=0}^{b-1}(-1)^b C_n^b \phi^{n-c-1}(\partial^\mu\phi)\phi^c = (-1)^n\sum_{b=1}^{n}\sum_{c=0}^{b-1}(-1)^b C_n^b \phi^c(\partial^\mu\phi)\phi^{n-c-1} . \tag{C.6.11}$$

Hence, the contribution to the Lagrangian involving one axion and n mesons is:

$$\mathcal{L}_{a+nM} = i^{n+1}\frac{\partial_\mu a}{f_a}\frac{F_0^{2-n}}{4}\frac{x_L^b + (-1)^n x_R^b}{n!}\mathrm{Tr}\left[\lambda^b\sum_{b=1}^{n}\sum_{c=0}^{b-1}(-1)^b C_n^b\phi^c(\partial^\mu\phi)\phi^{n-c-1}\right] . \tag{C.6.12}$$

It can be shown by induction that

$$\sum_{b=1}^{n}\sum_{c=0}^{b-1}(-1)^b C_n^b \phi^{n-c-1}(\partial^\mu\phi)\phi^c = -C_n(\phi;\partial^\mu\phi)\ , \tag{C.6.13}$$

with the recursive definition

$$C_1(A;B) = B\,, \quad C_{n+1}(A;B) = [A;C_n(A;B)]\ . \tag{C.6.14}$$

- Base case $n = 1$:

$$-C_1(\phi;\partial_\phi) = -\partial^\mu\phi\,, \quad \sum_{b=1}^{1}\sum_{c=0}^{b-1}(-1)^b C_1^b \phi^{1-c-1}(\partial^\mu\phi)\phi^c = -\partial^\mu\phi\ . \tag{C.6.15}$$

- Induction relation:

$$\begin{aligned}
\sum_{b=1}^{n+1}\sum_{c=0}^{b-1}(-1)^b C_{n+1}^b \phi^{n+1-c-1}(\partial^\mu\phi)\phi^c &= \phi\sum_{b=1}^{n}\sum_{c=0}^{b-1}(-1)^b (C_n^b + C_n^{b+1})\phi^{n-c-1}(\partial^\mu\phi)\phi^c + (-1)^{n+1}\sum_{c=0}^{n}\phi^{n-c}(\partial^\mu\phi)\phi^c \\
&= -\phi C_n(\phi;\partial^\mu\phi) - \sum_{b=2}^{n+1}\sum_{c=0}^{b-2}(-1)^b C_n^b \phi^{n+1-c-1}(\partial^\mu\phi)\phi^c + (-1)^{n+1}\sum_{c=0}^{n}\phi^{n-c}(\partial^\mu\phi)\phi^c \\
&= -\phi C_n(\phi;\partial^\mu\phi) - \sum_{b=1}^{n}\sum_{c=1}^{b-1}(-1)^b C_n^b \phi^{n+1-c-1}(\partial^\mu\phi)\phi^c \\
&= -\phi C_n(\phi;\partial^\mu\phi) - \sum_{b=1}^{n}\sum_{c=0}^{b-1}(-1)^b C_n^b \phi^{n-c-1}(\partial^\mu\phi)\phi^{c+1} \\
&= -\phi C_n(\phi;\partial^\mu\phi) - \left(\sum_{b=1}^{n}\sum_{c=0}^{b-1}(-1)^b C_n^b \phi^{n-c-1}(\partial^\mu\phi)\phi^c\right)\phi \\
&= -\phi C_n(\phi;\partial^\mu\phi) + C_n(\phi;\partial^\mu\phi)\phi \\
&= -[\phi;C_n(\phi;\partial^\mu\phi)] \\
&= -C_{n+1}(\phi;\partial^\mu\phi)\ .
\end{aligned} \tag{C.6.16}$$

Therefore, combining Eqs. (C.6.12) and (C.6.13), the interaction vertex involving the axion and n mesons is given by:

$$\mathcal{L}_{a+nM} = (-i)^{n+1}\frac{\partial^\mu a}{f_a}\frac{F_0^{2-n}}{4}\frac{x_R^b + (-1)^n x_L^b}{n!}\mathrm{Tr}[\lambda^b C_n(\phi;\partial^\mu\phi)]\ , \tag{C.6.17}$$

where $C_n(\phi;\partial^\mu\phi)$ is defined by the recursive commutator in Eq. (C.6.14), and we use $x_R^b + x_L^b = x_V^b$, $x_R^b - x_L^b = x_A^b$.

In particular, we find:

$$\mathcal{L}_{a+1M} = -x_A^b\frac{F_0\partial_\mu a}{4f_a}\mathrm{Tr}\left(\lambda^b\partial^\mu\phi\right)\ , \tag{C.6.18}$$

$$\mathcal{L}_{a+2M} = ix_V^b\frac{\partial_\mu a}{8f_a}\mathrm{Tr}\left(\lambda^b[\phi;\partial^\mu\phi]\right)\ , \tag{C.6.19}$$

$$\mathcal{L}_{a+3M} = x_A^b\frac{\partial_\mu a}{24F_0 f_a}\mathrm{Tr}\left(\lambda^b[\phi;[\phi;\partial^\mu\phi]]\right)\ , \tag{C.6.20}$$

$$\mathcal{L}_{a+4M} = -ix_V^b\frac{\partial_\mu a}{96F_0^2 f_a}\mathrm{Tr}\left(\lambda^b[\phi;[\phi;[\phi;\partial^\mu\phi]]]\right)\ . \tag{C.6.21}$$

C.7 Axiflavon/flaxion interactions with quarks

The axiflavon/flaxion-fermion interaction Lagrangian [Ema+17; Cal+17] is given by:

$$\mathcal{L}_{aff} = \lambda_{ij}^f a F_i F_j^c + \text{h.c.}\ , \tag{C.7.1}$$

with couplings:

$$\lambda_{ij}^{u,d,e} = i([L]_i + [R]_j)\frac{v}{V_\Phi} y_{ij}^{u,d,e} \ . \tag{C.7.2}$$

The axiflavon/flaxion's coupling to gluons and photons is described by:

$$\mathcal{L}_{axion-gauge} = c_{aGG}\frac{\alpha_s}{4\pi}\frac{a}{f_a}G\tilde{G} + c_{a\gamma\gamma}\frac{\alpha_{e.m.}}{4\pi}\frac{a}{f_a}F\tilde{F} = \frac{\alpha_s}{8\pi}\frac{a}{f_a}G\tilde{G} + \frac{E}{N}\frac{\alpha_{e.m.}}{8\pi}\frac{a}{f_a}F\tilde{F} \tag{C.7.3}$$

where $f_a = V_\Phi c_{aGG}/N$, and the anomaly coefficients N, E depend on the $U(1)_H$ charges:

$$N = -\frac{1}{2}\sum_i 2[q]_i + [u]_i + [d]_i \ , \tag{C.7.4}$$

$$E = -\sum_i \frac{4}{3}([q]_i + [u]_i) + \frac{1}{3}([q]_i + [d]_i) + [l]_i + [e]_i \ , \tag{C.7.5}$$

with $E/N \in [2.4; 3.0]$, therefore

$$c_{aGG} = -\frac{1}{2} \ , \ c_{a\gamma\gamma} = \frac{c_{aGG}E}{N} \in [-1.5; -1.2] \ . \tag{C.7.6}$$

We label the light quark flavors as follows: 1 for u, 2 for d, and 3 for s. The axiflavon/flaxion-quark Lagrangian (Eq. (C.7.1)) then becomes:

$$\mathcal{L}_{aqq} = a(\lambda_{11}^u uu^c + \lambda_{11}^d dd^c + \lambda_{22}^d ss^c + \lambda_{12}^d ds^c + \lambda_{21}^d sd^c) \tag{C.7.7}$$

$$= a\begin{pmatrix} u^c & d^c & s^c \end{pmatrix}\begin{pmatrix} \lambda_{11}^u & 0 & 0 \\ 0 & \lambda_{11}^d & \lambda_{21}^d \\ 0 & \lambda_{12}^d & \lambda_{22}^d \end{pmatrix}\begin{pmatrix} u \\ d \\ s \end{pmatrix} \ , \tag{C.7.8}$$

with

$$\lambda_{ij}^{u,d} = i([q]_i + [u,d]_j)\frac{v}{V_\Phi} y_{ij}^{u,d} = i([q]_i + [u,d]_j)\frac{v}{2Nf_a} y_{ij}^{u,d} = i\mathcal{O}(1)\frac{v}{2Nf_a} y_{ij}^{u,d} \ . \tag{C.7.9}$$

The CKM-scaled Yukawas are:

$$y_{ij}^{u,d} = \hat{V}_{ij} m_j^{u,d}\sqrt{2}/v \ , \quad \hat{V}_{ij} = V_{ij} \text{ for } i \leqslant j \ , \quad \hat{V}_{ij} = 1/V_{ij} \text{ for } i \geqslant j \ , \tag{C.7.10}$$

so that

$$\lambda_{11}^u \sim i([q]_1 + [u]_1)\frac{m_u}{\sqrt{2}Nf_a}V_{11} = i\mathcal{O}(1)\frac{m_u}{\sqrt{2}Nf_a}V_{11} \ , \tag{C.7.11}$$

$$\lambda_{11}^d \sim i([q]_1 + [d]_1)\frac{m_d}{\sqrt{2}Nf_a}V_{11} = i\mathcal{O}(1)\frac{m_d}{\sqrt{2}Nf_a}V_{11} \ , \tag{C.7.12}$$

$$\lambda_{22}^d \sim i([q]_2 + [d]_2)\frac{m_s}{\sqrt{2}Nf_a}V_{22} = i\mathcal{O}(1)\frac{m_s}{\sqrt{2}Nf_a}V_{22} \ , \tag{C.7.13}$$

$$\lambda_{12}^d \sim i([q]_1 + [d]_2)\frac{m_s}{\sqrt{2}Nf_a}V_{12} = i\mathcal{O}(1)\frac{m_s}{\sqrt{2}Nf_a}V_{12} \ , \tag{C.7.14}$$

$$\lambda_{21}^d \sim i([q]_2 + [d]_1)\frac{m_d}{\sqrt{2}Nf_a}\frac{1}{V_{21}} = i\mathcal{O}(1)\frac{m_d}{\sqrt{2}Nf_a}\frac{1}{V_{21}} \ . \tag{C.7.15}$$

Although λ^d appears non-Hermitian, we find:

$$\frac{\lambda_{12}^d}{(\lambda_{21}^d)^*} = \frac{i([q]_1 + [d]_2)m_s V_{12}/(\sqrt{2}Nf_a)}{-i([q]_2 + [d]_1)m_d/(\sqrt{2}Nf_a V_{21}^*)} = -\frac{[q]_1 + [d]_2}{[q]_2 + [d]_1}\frac{m_s V_{12}V_{21}^*}{m_d} \ . \tag{C.7.16}$$

Using $m_s V_{12}V_{21}^*/m_d = 1$, λ^d is Hermitian if and only if $[q]_1 + [d]_2 = [q]_2 + [d]_1$.

To rewrite the parameters of the general Lagrangian from Section 1.2 in terms of axiflavon/flaxion parameters, we use the Dirac equation:

$$\not{\partial} q = -iM_q q \ , \quad \bar{q}\overleftarrow{\not{\partial}} = i\bar{q}M_q \ , \tag{C.7.17}$$

and rewrite the general Lagrangian for light quarks in terms of $k_R^q = (k_V^q + k_A^q)/2$ and $k_L^q = (k_V^q - k_A^q)/2$ as:

$$\begin{aligned}
\mathcal{L}_{aqq} =& \frac{\partial_\mu a}{f_a} \left(\bar{q}_L k_L^q \gamma^\mu q_L + \bar{q}_R k_R^q \gamma^\mu q_R\right) \\
=& \frac{\partial_\mu a}{f_a} \bar{q} \left(k_L^q P_L \gamma^\mu P_L + k_R^q P_R \gamma^\mu P_R\right) q \\
=& \partial_\mu \left(\frac{a}{f_a} \bar{q} \left(k_L^q P_L \gamma^\mu P_L + k_R^q P_R \gamma^\mu P_R\right) q \right) \\
& - \frac{a}{f_a} \left(\partial_\mu \bar{q} \left(k_L^q P_L \gamma^\mu P_L + k_R^q P_R \gamma^\mu P_R\right) q + \bar{q} \left(k_L^q P_L \gamma^\mu P_L + k_R^q P_R \gamma^\mu P_R\right) \partial_\mu q\right) \\
\equiv& - \frac{a}{f_a} \left(\partial_\mu \bar{q} \left(k_L^q P_L \gamma^\mu P_L + k_R^q P_R \gamma^\mu P_R\right) q + \bar{q} \left(k_L^q P_L \gamma^\mu P_L + k_R^q P_R \gamma^\mu P_R\right) \partial_\mu q\right) \\
=& - \frac{a}{f_a} \left(\overleftarrow{\bar{q}\partial\!\!\!/} \left(k_L^q P_R P_L + k_R^q P_L P_R\right) q + \bar{q} \left(k_L^q P_L P_R + k_R^q P_R P_L\right) \partial\!\!\!/ q \right) \\
=& - i \frac{a}{f_a} \bar{q} \left(M_q k_L^q P_R P_L + M_q k_R^q P_L P_R - k_L^q M_q P_L P_R - k_R^q M_q P_R P_L\right) q \\
=& - i \frac{a}{f_a} \left(\bar{q}_R \left(M_q k_L^q - k_R^q M_q\right) q_L + \bar{q}_L \left(M_q k_R^q - k_L^q M_q\right) q_R\right) \\
=& - i \frac{a}{f_a} [m_u((k_R^q)_{11} - (k_L^q)_{11}) u_L u_R^c + m_d((k_R^q)_{22} - (k_L^q)_{22}) d_L d_R^c + m_s((k_R^q)_{33} - (k_L^q)_{33}) s_L s_R^c \\
& + (m_d (k_R^q)_{23} - m_s (k_L^q)_{23}) d_L s_R^c + (m_s (k_R^q)_{32} - m_d (k_L^q)_{32}) s_L d_R^c] + [L \leftrightarrow R] \ .
\end{aligned} \tag{C.7.18}$$

Matching with Eq. (C.7.7), we identify diagonal terms:

$$\lambda_{11}^u = -i \frac{1}{f_a} m_u ((k_R^q)_{11} - (k_L^q)_{11}) \Rightarrow (k_A^q)_{11} = (k_R^q)_{11} - (k_L^q)_{11} = -([q]_1 + [u]_1) \frac{V_{11}}{\sqrt{2}N} \ , \tag{C.7.19}$$

$$\lambda_{11}^d = -i \frac{1}{f_a} m_d ((k_R^q)_{22} - (k_L^q)_{22}) \Rightarrow (k_A^q)_{22} = (k_R^q)_{22} - (k_L^q)_{22} = -([q]_1 + [d]_1) \frac{V_{22}}{\sqrt{2}N} \ , \tag{C.7.20}$$

$$\lambda_{22}^d = -i \frac{1}{f_a} m_s ((k_R^q)_{33} - (k_L^q)_{33}) \Rightarrow (k_A^q)_{33} = (k_R^q)_{33} - (k_L^q)_{33} = -([q]_2 + [d]_2) \frac{V_{33}}{\sqrt{2}N} \ . \tag{C.7.21}$$

For the off-diagonal terms:

$$\lambda_{12}^d = \frac{-i}{f_a} (m_d (k_R^q)_{23} - m_s (k_L^q)_{23}) \ , \tag{C.7.22}$$

$$\lambda_{21}^d = \frac{-i}{f_a} (m_s (k_R^q)_{32} - m_d (k_L^q)_{32}) \ . \tag{C.7.23}$$

Using hermiticity $(\lambda_{21}^d)^* = \lambda_{12}^d$, we derive:

$$\begin{aligned}
m_d (k_R^q)_{23} - m_s (k_L^q)_{23} = m_s (k_R^q)_{23} - m_d (k_L^q)_{23} \Leftrightarrow (m_d - m_s)(k_R^q)_{23} = (m_s - m_d)(k_L^q)_{23} \\
\Leftrightarrow (k_R^q)_{23} = -(k_L^q)_{23} \Leftrightarrow (k_V^q)_{23} = 0 \ .
\end{aligned} \tag{C.7.24}$$

Thus, Eq. (C.7.22) becomes:

$$(k_L^q)_{23} = -\frac{i f_a \lambda_{12}^d}{m_s + m_d} = ([q]_1 + [d]_2) \frac{V_{12}}{\sqrt{2}N} \frac{m_s}{m_s + m_d} \Leftrightarrow (k_A^q)_{23} = -2([q]_1 + [d]_2) \frac{V_{12}}{\sqrt{2}N} \frac{m_s}{m_s + m_d} \ . \tag{C.7.25}$$

In conclusion, we find

$$(k_V^q)_{23} = 0 \ , \quad |(k_A^q)_{23}| = \mathcal{O}(0.1) \ , \quad (k_A^q)_{ii} = \mathcal{O}(1) \tag{C.7.26}$$

This can be generalized to all quarks: the vectorial terms vanish, the flavor-changing axial terms are of order $\mathcal{O}(0.1)$, and the flavor-conserving axial terms are of order $\mathcal{O}(1)$.

Appendix D

Computational framework for axion emission

D.1 Overview

The program developed in the course of this thesis aims to compute the axion emission spectrum and total emissivity from Supernova (SN) emission under various physical conditions. It allows for the selection and study of a wide range of physical processes, and is currently implemented for baryon-meson scattering, $B_i + M \to B_f + a$, and baryon decay $B_i \to B_f a$, where M is a meson, B_i and B_f are baryons, and a denotes the axion.

The modular structure of the program facilitates the extension to additional processes in the future, including:

- Baryon-baryon scattering: $B_1 + B_2 \to B_3 + B_4 + a$,
- Electron-electron scattering: $e^- + e^- \to e^- + e^- + a$,
- Baryon-electron scattering: $B_i + e^- \to B_f + e^- + a$.

In addition, future developments could include axion detection schemes, such as Cherenkov-based signatures.

D.2 Structure and Usage

The program is composed of several modular Python scripts, each responsible for a specific step of the computation:

- `Info.txt` — Contains all user-defined input parameters including core properties, particle masses and chemical potentials, coupling constants, and numerical integration settings.
- `0_Type_Processes.py` — Allows the user to select the physical processes to include in the calculation.
- `1_Processes.py` — Allows the user to select the physical processes to include in the calculation.
- `2_Amplitude.py` — Computes the squared matrix element for each selected process using the decomposition
$$|\mathcal{M}_{fi}|^2 = \sum_{k=1} C_k P_k,$$
where $C_k \in \{(k_A)_{11}^2, (k_A)_{22}^2, (k_A)_{33}^2, (k_A)_{11}(k_A)_{22}, (k_A)_{11}(k_A)_{33}, (k_A)_{22}(k_A)_{33}, |(k_A)_{23}|^2, |(k_V)_{23}|^2\}$ are coupling constant combinations and P_k are kinematic functions.
- `3_Spectrum.py` — Computes the axion energy spectrum $\frac{dN_a}{dE_a}$ and the corresponding emissivity Q_a, including numerical uncertainties.

- `4_values.py` — Evaluates spectra and emissivities for user-defined values of the coupling constants $(k_{A,V})_{ij}$.
- `5_analyse.py` — Evaluates spectra and emissivities for user-defined values of the coupling constants $(k_{A,V})_{ij}$.
- `main.py` — A wrapper script to control the full computation pipeline from process selection to final outputs.

D.3 Example Input

An example `Info.txt` file is provided below:

```
### Temperature (MeV)
40.0
### Axion mass (MeV)
0
### Meson masses (MeV): \pi^- ; \pi^0 ; \pi^+ ; K^- ; K^+ ; K^0 ; \bar{K}^0 ; \eta
139.57 134.98 139.57 493.68 493.68 497.67 497.67 547.3
### Meson chemical potentials mu_q (MeV) : mu_{\pi^+/-}=mu_{K^+/-}=+/- mu_q
-65.5248735
### Baryon masses (MeV): n ; p ; \Lambda ; \Sigma^- ; \Sigma^0 ; \Sigma^+ ; \Xi^- ; \Xi^0
537.659867 536.362759 866.904097 998.955558 998.955558 998.955558 1193.13456 1186.28456
### Baryon chemical potential (MeV): n ; p ; \Lambda ; \Sigma^- ; \Sigma^0 ; \Sigma^+ ; \Xi^- ; \Xi^0
584.426470 538.549275 709.323547 755.200741 709.323541 663.446350 880.097821 834.220625
### Lagrangian constants: D ; F ; S ; F_0 (MeV) ; f_a (MeV)
-0.813 -0.441 0.405 93 1e+12
### Integration parameters: precision (%) ; max time (h) ; points per integral, spectrum points, max axion energy (MeV)
1 1 1e+6 1e2 1000
### Core properties: core mass (kg), core density (g/cm^3), burst duration (s)
2e+30 2.6e+14 10
```

D.4 Availability

The source code developed in this work is not currently available for public release, as further testing, documentation, and structuring are still ongoing. However, it is intended to be made openly accessible in the near future, with the aim of providing a robust and reusable tool for the scientific community.

A public repository (e.g., GitHub or GitLab) will host the final version, along with comprehensive usage instructions and example files.

Appendix E

Scientific Communication

E.1 Conference presentations

During my PhD, I participated in several national and international conferences to present our work and engage with the scientific community:

- **IRN Terascale – Frascati (Italy), April 2024**[1]: talk in the Beyond the Standard Model (BSM) session on axion emission from core-collapse Supernovæ (SNe), based on the results of [Cav+24] (see Section 3.4).
- **SUPRISE 2025 – Madrid (Spain), March 2025**[2]: presentation in the Axions and Axion-like Particles (ALPs) in SNe session, again focusing on axion emission from core-collapse SNe.
- **IRN Terascale – Strasbourg (France), May 2025**[3]: presentation of a project exploring the detectable signatures of axion emission from a nearby Supernova (SN) in Cherenkov detectors, based on [Cav+25b] (see Section 4.1).
- **JRJC – Saint-Jacut-de-la-Mer (France), November 2024**[4]: outreach-oriented presentation of the results from [Cav+24] to an audience of young researchers from diverse backgrounds. This talk was also included in the theoretical section of the *Book of Proceedings* [Str+25].

E.2 Science outreach

As part of a broader effort to share knowledge and make science more accessible, I have been involved in several public outreach activities:

- Public talks in my laboratory's dedicated outreach space (*Eutopia*), especially during the monthly science events jointly organized by LAPP and LAPTh.
- A public lecture on the philosophy of science, held in the auditorium of my lab during the national *Fête de la science*.
- Participation in the *Ma Thèse en 180 secondes* competition[5], where PhD students present their thesis work in French and in 180 seconds to a general audience.
- Participation in the *Infini à l'école* project[6], introducing primary school children to the scientific method, research careers, and the concept of the infinity small in particle physics.

[1] https://indico.in2p3.fr/event/31806/
[2] https://indico.ift.uam-csic.es/event/26/
[3] https://indico.in2p3.fr/event/35622/
[4] https://indico.in2p3.fr/event/33415/
[5] https://www.youtube.com/watch?v=xONDG3BzBbg
[6] https://ile.in2p3.fr/

My main science outreach project, however, is the co-creation of a science comic book in collaboration with fellow PhD students from Annecy – Nathan Amouroux (LAPP), Margaux Jomain (LAPTh), Léo Le Moigne (LAPP), Cyann Plard (LAPP), Yann Querlioz (LAPP) – and illustrated by Antoine Tassel. The book, entitled *L'odyssée cosmique de Pénélope* (*The Cosmic Odyssey of Pénélope*), is currently in preparation. It tells the story of a young woman, Pénélope, who, intrigued by a mysterious light in the sky, embarks on a journey during which she meets young researchers who each explain their area of research and how it might relate to her observation.

Pages 227-228-229 show pages 11, 12, and 13 of the comic book (current non-final version), which correspond to the section where I popularize my research topic.

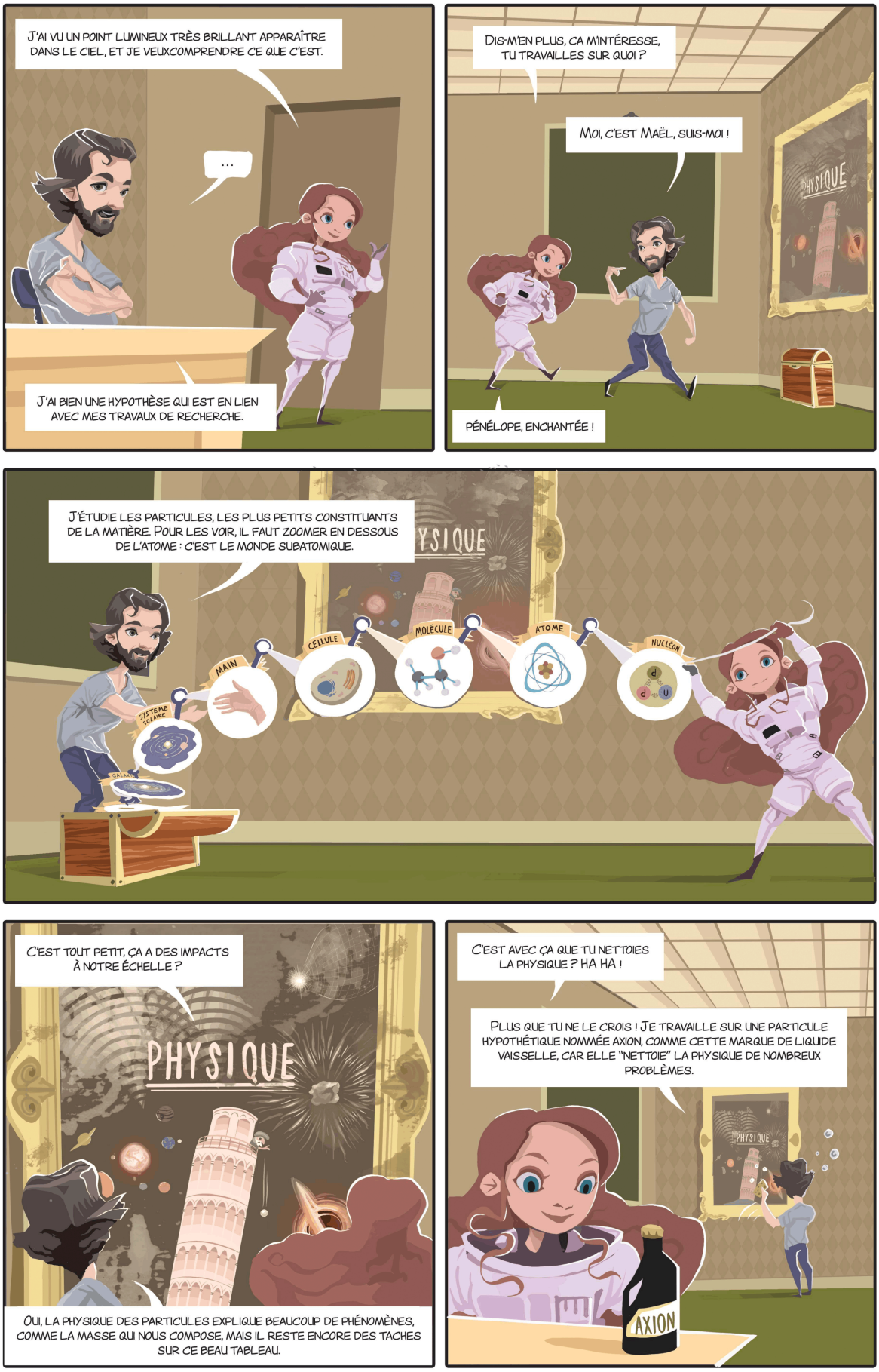
J'AI VU UN POINT LUMINEUX TRÈS BRILLANT APPARAÎTRE DANS LE CIEL, ET JE VEUXCOMPRENDRE CE QUE C'EST.
...
J'AI BIEN UNE HYPOTHÈSE QUI EST EN LIEN AVEC MES TRAVAUX DE RECHERCHE.
DIS-M'EN PLUS, CA M'INTÉRESSE, TU TRAVAILLES SUR QUOI ?
MOI, C'EST MAËL, SUIS-MOI !
PÉNÉLOPE, ENCHANTÉE !
J'ÉTUDIE LES PARTICULES, LES PLUS PETITS CONSTITUANTS DE LA MATIÈRE. POUR LES VOIR, IL FAUT ZOOMER EN DESSOUS DE L'ATOME : C'EST LE MONDE SUBATOMIQUE.
MAIN
CELLULE
MOLÉCULE
ATOME
NUCLÉON
SYSTEME SOLAIRE
C'EST TOUT PETIT, ÇA A DES IMPACTS À NOTRE ÉCHELLE ?
PHYSIQUE
OUI, LA PHYSIQUE DES PARTICULES EXPLIQUE BEAUCOUP DE PHÉNOMÈNES, COMME LA MASSE QUI NOUS COMPOSE, MAIS IL RESTE ENCORE DES TACHES SUR CE BEAU TABLEAU.
C'EST AVEC ÇA QUE TU NETTOIES LA PHYSIQUE ? HA HA !
PLUS QUE TU NE LE CROIS ! JE TRAVAILLE SUR UNE PARTICULE HYPOTHÉTIQUE NOMMÉE AXION, COMME CETTE MARQUE DE LIQUIDE VAISSELLE, CAR ELLE "NETTOIE" LA PHYSIQUE DE NOMBREUX PROBLÈMES.
AXION


ET C'EST QUOI LE RAPPORT AVEC MON OBSERVATION ?
J'AI DEUX ASPECTS DANS MA THÈSE POUR ÉTUDIER LES PARTICULES.
L'UN AVEC DES COLLISIONNEURS COMME LE LHC EN SUISSE.
COLLISIONNEUR
DÉTECTION D'ÉMISSION EXTRA GALACTIQUE
ET L'AUTRE QUI POURRAIT ÊTRE EN LIEN AVEC TON OBSERVATION : D'ABORD L'ÉMISSION EXTRAGALACTIQUE ISSUE D'OBJETS ASTROPHYSIQUES, PUIS LA POTENTIELLE RÉCEPTION TERRESTRE.
QUEL GENRE D'OBJETS ASTROPHYSIQUES ?
POUR TE RÉPONDRE, IL FAUT QUE JE TE PARLE DE LA VIE ET LA MORT DES ÉTOILES.
L'ÉVOLUTION D'UNE ÉTOILE EST UN CONFLIT ENTRE LA GRAVITÉ, QUI VEUT RÉDUIRE SA TAILLE, ET LA PRESSION, QUI VEUT L'AGRANDIR.
GRAVITÉ
PRESSION
SON ÉVOLUTION DÉPEND BEAUCOUP DE SA MASSE. ET ELLE PEUT FINIR EN SUPERNOVA, UNE EXPLOSION CATACLYSMIQUE.
V.I.P
1
2
3
1 ÉTOILE MOYENNE, GÉANTE ROUGE, NÉBULEUSE PLANÉTAIRE, NAINE BLANCHE
2 ÉTOILE LOURDE, SUPERGÉANTE ROUGE, SUPERNOVA, ÉTOILE À NEUTRON
3 ÉTOILE TRÈS LOURDE, SUPERGÉANTE ROUGE, SUPERNOVA, TROU NOIR
AH, ET CETTE EXPLOSION EST POTENTIELLEMENT VISIBLE !

12


ET CA TE SERT À QUOI DANS TES RECHERCHES ?
~ 6 μeV
J'UTILISE LES SUPERNOVAE POUR ÉTUDIER LES PROPRIÉTÉS PROBABLES DE L'AXION.
EN PARTICULIER, COMMENT IL PEUT INTERAGIR AVEC LES PARTICULES CONNUES...
JE PEUX JOUER AVEC VOUS ?
... POUR QUE SON EXISTENCE SOIT COMPATIBLE AVEC L'OBSERVATION D'UNE SUPERNOVA MESURÉE EN 1987.
WAOUH.
MAIS COMMENT TU FAIS EN PRATIQUE ?
TOUT D'ABORD, DES CALCULS À LA MAIN POUR MIEUX COMPRENDRE LE PROBLÈME.
ENSUITE, DES CALCULS INFORMATIQUES POUR OBTENIR DES RÉSULTATS NUMÉRIQUES.
TAP
ET POUR FINIR, JE COMPARE AVEC MES COLLÈGUES.
5,3
5,4
13

List of Figures

1.1 Feynman diagram for axion-gluon-gluon coupling via a heavy quark triangle loop. . . . 24
1.2 The gray region in the f_a-m_a plane corresponds to values consistent with the axion accounting for Dark Matter (DM), assuming $\theta_{osc} \in [10^{-2}, 10^2]$. The red line indicates the Quantum Chromodynamics (QCD) axion relation. 33

2.1 α_s as a function of $\mu/\Lambda_{\rm QCD}$ with Chiral Perturbation Theory (ChPT) limit in brown and perturbative QCD (pQCD) limit in green. 42
2.2 Feynman diagram for $\ell_i \to \nu_i \ell_j \bar{\nu}_j$. 44
2.3 Feynman diagram for $n \to p e^- \bar{\nu}_e$ at the quark level. 45
2.4 One-loop Feynman diagrams contributing to the coupling $\hat{c}_{a\gamma\gamma}$ via the process $a \to \gamma\gamma$. 60
2.5 One-loop Feynman diagram contributing to the axion-lepton-lepton coupling. 60

3.1 The left panel shows in gray the excluded region in the $g_{a\gamma\gamma} - m_a$ plane (see [OHa20]), while the right panel shows in gray the excluded region in the $f_a - m_a$ plane in the model-independent case, see the text for more details. The black lines correspond to the model-independent theoretical prediction derived from Eq. (3.2.5). 73
3.2 Lifetime constraint on axions in the $m_a - |g_{a\gamma\gamma}|$ plane. The color map shows the ratio τ_a/τ_U, where $\tau_a = \tau(a \to \gamma\gamma)$ and τ_U is the age of the universe. The dashed black line corresponds to $\tau_a = \tau_U$, marking the boundary of cosmological stability. 74
3.3 The left panel shows 95% one-sided upper limits in the $C_{ann} - C_{app}$ plane for the reference value $f_a = 10^9$ GeV, with the shaded region consistent with Neutron Star (NS) cooling. The right panel presents the equivalent constraints in the $(\hat{k}_A)_{11} - (\hat{k}_A)_{22}$ plane. See [Bus+22]. 75
3.4 Schematic illustration of the luminosity L_X of a hypothetical light particle X as a function of its coupling g_X to matter, adapted from [Raf90]. The plot is divided into four regions: regions 1 and 2 correspond to the free-streaming regime ($l_X > R_{\rm core}$), where L_X increases with g_X, while regions 3 and 4 correspond to the trapped regime ($l_X < R_{\rm core}$), where L_X decreases with g_X. 77
3.5 Leading-order Feynman diagrams contributing to baryon-meson scattering $B_i M \to B_f a$. 83
3.6 Leading-order Feynman diagrams contributing to baryon decay $B_i \to B_f a$. 83
3.7 Allowed regions for $|(\hat{k}_A)_{ij}|$, with $ij \in \{11, 22, 33, 23\}$, obtained from $Q_a(B_i M \to B_f a)$, $Q_a(B_i \to B_f a)$, and their combination, for $T \in \{30, 40\}$ MeV, $n_B \in \{1, 1.5\}$ $n_{\rm sat}$, and $Y_{Q_B} = 0.3$. The Equation of State (EoS) $DD2Y$ with $f_a = 10^9$ GeV is used. The diagonal plots display the marginalized posterior distributions for the respective k-couplings. 85
3.8 Same as Fig. 3.7, but for $SFHoY$. 85
3.9 Same as Fig. 3.7, but incorporating the NS cooling constraint. 86
3.10 Same as Fig. 3.9, but for $SFHoY$. 86
3.11 Verification of Eq. (3.5.3) for baryon-meson scattering $MB_i \to B_f a$, assuming a constant amplitude $|\mathcal{M}_{fi}|^2$. The Supernova (SN) core is modeled according to Table 3.11. Colors indicate different regimes of the mass difference $\Delta M = m_M + m_{B_i} - m_{B_f}$: blue for $\Delta M > T$, green for $\Delta M \in [0, T]$, and red for $\Delta M < 0$. 92

4.1 Leading-order Feynman diagrams contributing to nucleon-pion scattering $N_i\pi \to N_f a$. 101
4.2 Axion emission spectra from $\pi N \to N'a$ processes in the agnostic case. The line style encodes different temperature and density configurations: solid line ($T = 30$ MeV, $n_B = n_{\rm sat}$, $Y_p = 0.3$), dashed line ($T = 30$ MeV, $n_B = 1.5\ n_{\rm sat}$, $Y_p = 0.3$), dotted line ($T = 40$ MeV, $n_B = n_{\rm sat}$, $Y_p = 0.3$), and dash-dotted line ($T = 40$ MeV, $n_B = 1.5\ n_{\rm sat}$, $Y_p = 0.3$). Colors distinguish between the EoS: pink for $DD2$ and purple for $SFHo$. . 103
4.3 Leading-order Feynman diagrams contributing to $pa \to p\gamma$. 106
4.4 Leading-order Feynman diagrams contributing to $Na \to N\pi^0$. 107
4.5 Comparison between the Cherenkov-light spectra induced by neutrino (dashed blue) vs. axion absorption. The latter includes either a photon (yellow) or a π^0 (purple) as Cherenkov partons, with different line styles denoting the various theoretical scenarios discussed in Section 4.1.3.2—see the legend, which also specifies the total number of events above the π^0 threshold. The first (second) row corresponds to the $DD2$ ($SFHo$) EoS models, while the first (second) column corresponds to $T = 30$ (40) MeV. The remaining thermodynamic parameters are fixed to reference values, as their variations within motivated ranges are imperceptible. 108
4.6 Numerical comparison between Eqs. (4.1.30) and (4.1.32). 111
4.7 Expected number of events (shades of grey) in the C_{app}-C_{ann} plane at a distance of $d = 0.2$ kpc. The blue segment (Dine-Fischler-Srednicki-Zhitnitsky (DFSZ)) extends outward with $\tan(\beta) \in [0.25, 170]$, while the red cross represents the Kim-Shifman-Vainshtein-Zakharov (KSVZ) model with uncertainties. Dotted yellow ellipses and dashed orange lines denote experimental constraints (NSs, Supernovæ (SNe)) and the detectability criterion ($N_{\pi^0} \geq 2$ for a Galactic center SN), respectively. The expected number of events is calculated as λ_{π^0} (central panels), and as $\lambda_{\pi^0} \mp \sqrt{\lambda_{\pi^0}}$ (left/right panels). Top and bottom rows correspond to $T = 30$ and 40 MeV, respectively. . . . 112
4.8 Scaling of the expected number of π^0-initiated Cherenkov cascades with the inverse square of the distance d of a SN candidate from Earth. The left y-axis shows the number of expected events as a function of d (lower x-axis), with SN models matching those in Fig. 4.5-4.7. The grey dashed lines indicate the detectability threshold (≥ 2 events), defining the critical distance $d_2^{(a)}$ below which axion absorption remains observable. The upper y-axis maps d onto the expected number of SNe per century, $\dot{N}(d)$, based on the estimation in [TLS94]. 113
4.9 Posterior probability densities for the axion couplings C_{app} and C_{ann} as a function of the number of observed events N (each row corresponds to a different $N \in \{0, 1, 5\}$). We assume a SN at a distance $d = 0.2$ kpc, considering only first-generation axion production $\pi N \to N'a$ and absorption $ap \to p\pi^0$. The calculation uses the $DD2$ EoS under thermodynamic conditions $T = 30$ MeV, $n_B = n_{\rm sat}$, and $Y_p = 0.3$. The first column shows the joint 2D posterior $P(C_{app}, C_{ann} \,|\, N)$, the second column shows the marginal posterior $P(C_{app} \,|\, N)$, and the third column shows $P(C_{ann} \,|\, N)$. 115
4.10 Axion spectrum from $\Lambda \to na$ emission for two EoS: $DD2Y$ and $SFHoY$, under different thermodynamic conditions: $T \in \{30, 40\}$ MeV, $n_B \in 1, 1.5\ n_{\rm sat}$, and $Y_{Q_B} = 0.3$. 118
4.11 Comparison between the Cherenkov-light spectra induced by neutrinos (dashed blue) and axion (solid purple) absorption through $ap \to \Sigma^+ \to p\pi^0$. The legend also specifies the total number of expected events above the detection threshold $E^* = 194$ MeV. The value of $N[E_{\pi^0} \geq E^*]$ depends on the EoS model and thermodynamic conditions–see Table 4.6. 126

5.1 Baryon decays with Axion-like Particle (ALP) emission. 133
5.2 Constraints on $|(k_V)_{23}|$ (left panel) and $|(k_A)_{23}|$ (right panel) as a function of the ALP mass, assuming $f_a = 1$ TeV, obtained from $B_i \to B_f a$ decays. The different curves correspond to the processes $\Lambda \to na$ (blue, dash-dotted), $\Sigma^+ \to pa$ (pink, dotted), $\Xi^- \to \Sigma^- a$ (orange, dashed), and $\Xi^0 \to \Lambda a$ (yellow, solid). 134
5.3 $K \to \pi a$ decays with an ALP. 135
5.4 $K \to \pi\pi a$ decays with an ALP. 135
5.5 The 90% CL upper limits for the $K_L \to \pi^0 a$ Branching Ratio (BR) [Ahn+19]. 136
5.6 The 90% CL upper limits for the $K^+ \to \pi^+\pi^0 a$ BR [Sad+24]. 137

5.7 Constraints on $|(k_V)_{23}|$ (left panel, for $K \to \pi a$) and $|(k_A)_{23}|$ (right panel, for $K \to \pi\pi a$) as a function of the ALP mass, assuming $f_a = 1$ TeV, derived from meson decays. The different curves correspond to decays of K^+ (blue) and K_L (orange). 138
5.8 Axionic contributions to $K^0 - \bar{K}^0$ mixing up to one loop. 138
5.9 Bounds on $(k_A)_{23}$ for ALPs as a function of the axion mass from $K^0 - \bar{K}^0$ mixing. . . 139
5.10 Bounds on $|(k_{A/V})_{23}|$ for ALPs as a function of the axion mass, derived from the non-observation of hadron decays and $K^0 - \bar{K}^0$ mixing. 140
5.11 Feynman diagrams for $K_S \to a + (\gamma \to \ell^+\ell^-)$. 146
5.12 Visual representation of the Riemann surface of the complex logarithm. Each sheet corresponds to a different branch of $\arg(z)$. 150
5.13 Evaluation of $\hat{J}(s)$ with an incorrect treatment of the logarithmic branches (left), leading to a discontinuity at the branch cut $s = 4m_\pi^2$, versus the correct result obtained with proper branch tracking (right). 150
5.14 Feynman diagrams for $K_S \to \pi^+ + \pi^- + \pi^0$ 151
5.15 Feynman diagrams for $K \to \pi^+\pi^- a$ 152
5.16 Contours of constant f_a (in TeV) in the $\mathrm{Re}(k_A)_{23}$ vs. $\mathrm{Im}(k_A)_{23}$ plane. The upper panels compare $K_S \to \pi^+\pi^- a$ and $K^+ \to \pi^+\pi^0 a$ for $m_a = m_\pi$. The lower panels show the same comparison for $m_a \ll m_\pi$. 155
5.17 Singly differential BRs for the different $K \to \{\pi\pi, \mu\mu\}a$ channels considered. The two panels correspond to $m_a \ll m_\pi$ (upper) or $m_a = m_\pi$ (lower). The couplings are set by assuming saturation of the bounds in (5.2.2), corresponding to a "maximal" coupling value, separately for each channel, as discussed around Table 5.4. 156
5.18 Doubly differential $BR(K^+ \to \pi^+\pi^0 a)$ in the $\{s, t\}$ plane, with $m_a \ll m_\pi$ (left) and $m_a = m_\pi$ (right). In either case we assume the axion coupling strength to saturate the relevant inequality in (5.2.2). 157
5.19 Same as Fig. 5.18, but for the contribution to $BR(K_S \to \pi^+\pi^- a)$ proportional to $\mathrm{Re}(k_A)_{23}$. 158
5.20 Same as Fig. 5.18, but for the contribution to $BR(K_S \to \pi^+\pi^- a)$ proportional to $\mathrm{Im}(k_A)_{23}$. 158
5.21 Same as Fig. 5.18 but for $BR(K_S \to \mu^+\mu^- a)$. 158
5.22 Example of a reconstruction efficiency map, obtained through the fast-simulation code [Cho+20] as detailed in the text. This example corresponds to the case of $K_S \to \mu^+\mu^- X$ with $m_X = m_\pi$, where X is a generic spinless particle, i.e. not necessarily an axion. 159

B.1 Tree-level Feynman diagrams for $K \to \pi\gamma$. 184
B.2 One-loop Feynman diagrams for $K \to \pi\gamma$. 185
B.3 Tree-level Feynman diagrams for $a \to \gamma\gamma$ and $a \to GG$. 191
B.4 One-loop Feynman diagrams for $a \to \gamma\gamma$ and $a \to GG$. 191
B.5 Feynman diagram contributing to the baryon decay $\Lambda \to na$. 195
B.6 Feynman diagrams considered in [Car+21] for pion-nucleon scattering $\pi^- p \to na$. . . . 201

C.1 Elementary particles of the Standard Model (SM). 207
C.2 Weight diagrams of baryons with spin $s = 1/2$ (left, baryon octet) and $s = 3/2$ (right, baryon decuplet), represented in the (I_3, Y) plane. 214
C.3 Weight diagrams of mesons with spin $s = 0$ (left, pseudoscalar mesons) and spin $s = 1$ (right, vector mesons), represented in the (I_3, Y) plane.. 214
C.4 Box diagrams contributing to $K^0 - \bar{K}^0$ mixing in the SM. 215

List of Tables

2.1 Bounds on axion-quark couplings for the Quantum Chromodynamics (QCD) axion ($m_a \ll m_q$). We define $(F_{A,V})_{ij} := 2f_a/(\hat{k}_{A,V})_{ij}$ [Mar+20]. For $(\hat{k}_A)_{23}$ two numbers appear in a cell as $x \mid y$, they correspond to collider | astrophysical bounds, respectively. 68

3.1 Bounds on axion-quark couplings. Constraints on $(\hat{k}_A)_{ii}$ are discussed in Section 3.3, and those on $|(\hat{k}_{V/A})_{23}|$ in Section 5.1. 82
3.2 Supernova (SN) bounds on $|(\hat{k}_A)_{23,11,22,33}|$ depending on the SN core modeling. The lower (resp. upper) value in each entry corresponds to $DD2Y$ (resp. $SFHoY$). Bounds assume $f_a = 10^9$ GeV. 87
3.3 Same as Table 3.2, but including Neutron Star (NS) cooling. 87
3.4 List of processes of the type $B_1B_2 \to B_3B_4a$. 89
3.5 List of processes of the type $B_i \to B_fa$. 89
3.6 List of processes of the type $B_iM \to B_fa$. 90
3.7 List of processes of the type $\ell B_i \to \ell B_fa$. 90
3.8 List of processes of the type $\ell M_i \to \ell M_fa$. 90
3.9 List of processes of the type $M_i \to M_fa$. 90
3.10 List of processes of the type $M_1M_2 \to M_3a$. 91
3.11 Particle fractions (in percent) for the $DD2Y$ Equation of State (EoS) at $T = 40$ MeV, $n_B = n_{\rm sat}$, and $Y_{Q_B} = 0.3$. 91
3.12 List of dominant processes as predicted by Eq. (3.5.3), with numerical input from Table 3.11. The contributions are normalized to the maximum within each type (Transition + Process type). Only relative contributions greater than 10% are shown. . . . 93

4.1 Constraints on the absolute values of the axion couplings to nucleons, $|C_{app}|$ and $|C_{ann}|$, for different EoS models and thermodynamic conditions in the SN core. 102
4.2 Fractions of axion-induced Cherenkov events reconstructed at Hyper-Kamiokande (HK), categorized according to the event types discussed in the main text. Axion emission follows the SN $DD2$ model with $T = 30$ or 40 MeV. The corresponding fractions of $\bar{\nu}$-induced Cherenkov events are omitted as they are always smaller than $\mathcal{O}(10^{-11})$. . . 109
4.3 Statistical significance of observing N events assuming a Poisson background with mean $\lambda = 0.182$. The p-value represents the probability of observing N or more events due to background alone. The corresponding number of σ indicates the equivalent significance in a one-sided Gaussian approximation. 112
4.4 Selection of nearby red supergiant stars (distance < 2 kpc). 114
4.5 Constraints on the absolute value of the axion down-strange coupling, $|(k_A)_{23}|$, for different EoS models and thermodynamic conditions in the SN core. 119
4.6 Maximum average number of particles produced via $ap \to \Sigma^+ \to p\pi^0$, consistent with the Raffelt's bound, for a source at $d = 0.2$ kpc and a detector of the HK type. The result depends on the EoS and the thermodynamic conditions. 124

5.1 Upper bounds on the Branching Ratios (BRs) for baryons based on data from [Nav+24]. 133
5.2 Couplings for different baryon decays $B_i \to B_fa$. 134

5.3 Summary of the 90% C.L. upper limit on the BR as a function of the mass of an invisible particle X in the $K_L \to \pi^0\pi^0 X$ decay [Oga+11]. 136
5.4 Constraints on the ratio of the coupling to f_a, in units of $10^{-3}, \mathrm{TeV}^{-1}$, derived from Eq. (5.2.5). A separate constraint is provided for each of the considered channels (table rows), distinguishing between small and large m_a. Constraints on $\mathrm{Re}(k_A)_{23}$, $\mathrm{Im}(k_A)_{23}$, or $|(k_A)_{23}|$ are reported where applicable (table columns). See the text for more details. 154

B.1 Comparison between the predictions of [EPR87] and our results. 191
B.2 Numerical values used to compare our results with the literature for $T = 40.56$ MeV, $n_B = n_{\mathrm{sat}}$, $Y_p = 0.3$. 202
B.3 Effective masses m_i^* (MeV), effective chemical potentials μ_i^* (MeV) and particle fractions $Y_i = n_i/n_B$ for the various fermionic species (e^-, n, p, Λ, Σ, Ξ) in core-collapse Supernovæ (SNe) at $Y_{Q_B} = 0.3$. Results are shown for two EoS ($DD2Y$ and $SFHoY$), two temperatures ($T = 30$ and 40 MeV) and two baryon densities ($n_B = n_{\mathrm{sat}}$ and $1.5\, n_{\mathrm{sat}}$). 205
B.4 Same as Table B.3 but for mesons (π, K, η). 205
B.5 Same as Table B.3 but for first generation hadrons. 206

List of Acronyms

2HDM Two Higgs Doublet Model.

ALP Axion-like Particle.

BR Branching Ratio.

BSM Beyond the Standard Model.

CCWZ Callan-Coleman-Wess-Zumino.

ChPT Chiral Perturbation Theory.

ChPT+a Chiral Perturbation Theory augmented with an axion.

CKM Cabibbo-Kobayashi-Maskawa.

DFSZ Dine-Fischler-Srednicki-Zhitnitsky.

DM Dark Matter.

EFT Effective Field Theory.

EoS Equation of State.

FCNC Flavor-Changing Neutral Current.

FLRW Friedmann-Lemaître-Robertson-Walker.

HK Hyper-Kamiokande.

IR Infrared.

KSVZ Kim-Shifman-Vainshtein-Zakharov.

LHC Large Hadron Collider.

LHCb Large Hadron Collider beauty.

LQCD Lattice QCD.

MACHO Massive Compact Halo Object.

MIP Minimal Ionizing Particle.

nEDM neutron Electric Dipole Moment.

NS Neutron Star.

oom order-of-magnitude.

PMNS Pontecorvo-Maki-Nakagawa-Sakata.

PQ Peccei-Quinn.

pQCD perturbative QCD.

PQWW Peccei-Quinn-Weinberg-Wilczek.

QCD Quantum Chromodynamics.

QED Quantum Electrodynamics.

QFT Quantum Field Theory.

RMF Relativistic Mean-Field.

SM Standard Model.

SN Supernova.

SNe Supernovæ.

UV Ultraviolet.

vev Vacuum Expectation Value.

WIMP Weakly Interacting Massive Particle.

Bibliography

[Aai+15] Roel Aaij et al. *LHCb Detector Performance*. In: *Int. J. Mod. Phys. A* 30.07 (2015), p. 1530022. DOI: 10.1142/S0217751X15300227. arXiv: 1412.6352 [hep-ex].

[Abe+11] K. Abe et al. *Letter of Intent: The Hyper-Kamiokande Experiment — Detector Design and Physics Potential —*. In: (Sept. 2011). arXiv: 1109.3262 [hep-ex].

[Abe+18] K. Abe et al. *Hyper-Kamiokande Design Report*. In: (May 2018). arXiv: 1805.04163 [physics.ins-det].

[Abi+21] B. Abi et al. *Measurement of the Positive Muon Anomalous Magnetic Moment to 0.46 ppm*. In: *Phys. Rev. Lett.* 126.14 (2021), p. 141801. DOI: 10.1103/PhysRevLett.126.141801. arXiv: 2104.03281 [hep-ex].

[Adl+01] S. Adler et al. *Search for the decay $K^+ \to \pi^+\pi^0\nu\bar{\nu}$*. In: *Phys. Rev. D* 63 (2001), p. 032004. DOI: 10.1103/PhysRevD.63.032004. arXiv: hep-ex/0009055.

[Adl+08] S. Adler et al. *Measurement of the $K^+ \to \pi^+\nu\bar{\nu}$ branching ratio*. In: *Physical Review D* 77.5 (Mar. 2008). ISSN: 1550-2368. DOI: 10.1103/physrevd.77.052003. URL: http://dx.doi.org/10.1103/PhysRevD.77.052003.

[Ahn+19] J. K. Ahn et al. *Search for $K_L \to \pi^0\nu\bar{\nu}$ and $K_L \to \pi^0 X^0$ Decays at the J-PARC KOTO Experiment*. In: *Physical Review Letters* 122.2 (Jan. 2019). ISSN: 1079-7114. DOI: 10.1103/physrevlett.122.021802. URL: http://dx.doi.org/10.1103/PhysRevLett.122.021802.

[Ahn15] Y. H. Ahn. *Flavored Peccei-Quinn symmetry*. In: *Phys. Rev. D* 91 (2015), p. 056005. DOI: 10.1103/PhysRevD.91.056005. arXiv: 1410.1634 [hep-ph].

[Ale+23] C. Alexandrou et al. *Lattice calculation of the short and intermediate time-distance hadronic vacuum polarization contributions to the muon magnetic moment using twisted-mass fermions*. In: *Physical Review D* 107.7 (Apr. 2023). ISSN: 2470-0029. DOI: 10.1103/physrevd.107.074506. URL: http://dx.doi.org/10.1103/PhysRevD.107.074506.

[Ali+25] R. Aliberti et al. *The anomalous magnetic moment of the muon in the Standard Model: an update*. In: *Physics Reports* 1143 (Nov. 2025), pp. 1–158. ISSN: 0370-1573. DOI: 10.1016/j.physrep.2025.08.002. URL: http://dx.doi.org/10.1016/j.physrep.2025.08.002.

[Alo+24a] David Alonso-González et al. *Disentangling axion-like particle couplings to nucleons via a delayed signal in Super-Kamiokande from a future supernova*. In: (Dec. 2024). arXiv: 2412.19890 [hep-ph].

[Alo+24b] David Alonso-González et al. *Probing a diffuse flux of axion-like particles from galactic supernovae with neutrino water Cherenkov detectors*. In: (Dec. 2024). arXiv: 2412.09595 [hep-ph].

[Alv+19] A. A. Alves Junior et al. *Prospects for Measurements with Strange Hadrons at LHCb*. In: *JHEP* 05 (2019), p. 048. DOI: 10.1007/JHEP05(2019)048. arXiv: 1808.03477 [hep-ex].

[Aok+20] S. Aoki et al. *FLAG Review 2019: Flavour Lattice Averaging Group (FLAG)*. In: *The European Physical Journal C* 80.2 (Feb. 2020). ISSN: 1434-6052. DOI: 10.1140/epjc/s10052-019-7354-7. URL: http://dx.doi.org/10.1140/epjc/s10052-019-7354-7.

[Aoy+20] T. Aoyama et al. *The anomalous magnetic moment of the muon in the Standard Model*. In: *Physics Reports* 887 (Dec. 2020), pp. 1–166. ISSN: 0370-1573. DOI: 10.1016/j.physrep.2020.07.006. URL: http://dx.doi.org/10.1016/j.physrep.2020.07.006.

[Ari+24] Fernando Arias-Aragón et al. *Axion-induced pair production: a new strategy for axion detection*. In: (Nov. 2024). arXiv: 2411.19327 [hep-ph].

[Arv+10] Asimina Arvanitaki et al. *String Axiverse*. In: *Phys. Rev. D* 81 (2010), p. 123530. DOI: 10.1103/PhysRevD.81.123530. arXiv: 0905.4720 [hep-th].

[Arv+17] Asimina Arvanitaki et al. *Black hole mergers and the QCD axion at Advanced LIGO*. In: *Phys. Rev. D* 95 (4 Feb. 2017), p. 043001. DOI: 10.1103/PhysRevD.95.043001. URL: https://link.aps.org/doi/10.1103/PhysRevD.95.043001.

[AS83a] L. F. Abbott and P. Sikivie. *A Cosmological Bound on the Invisible Axion*. In: *Phys. Lett. B* 120 (1983). Ed. by M. A. Srednicki, pp. 133–136. DOI: 10.1016/0370-2693(83)90638-X.

[AS83b] L.F. Abbott and P. Sikivie. *A cosmological bound on the invisible axion*. In: *Physics Letters B* 120.1 (1983), pp. 133–136. ISSN: 0370-2693. DOI: https://doi.org/10.1016/0370-2693(83)90638-X. URL: https://www.sciencedirect.com/science/article/pii/037026938390638X.

[Bak+06] C. A. Baker et al. *Improved Experimental Limit on the Electric Dipole Moment of the Neutron*. In: *Physical Review Letters* 97.13 (Sept. 2006). DOI: 10.1103/physrevlett.97.131801. URL: https://doi.org/10.1103%2Fphysrevlett.97.131801.

[Bau+21] Martin Bauer et al. *Consistent Treatment of Axions in the Weak Chiral Lagrangian*. In: *Phys. Rev. Lett.* 127.8 (2021), p. 081803. DOI: 10.1103/PhysRevLett.127.081803. arXiv: 2102.13112 [hep-ph].

[BCK18] Fredrik Björkeroth, Eung Jin Chun, and Stephen F. King. *Accidental Peccei–Quinn symmetry from discrete flavour symmetry and Pati–Salam*. In: *Phys. Lett. B* 777 (2018), pp. 428–434. DOI: 10.1016/j.physletb.2017.12.058. arXiv: 1711.05741 [hep-ph].

[BDB03] Johan Bijnens, Pierre Dhonte, and Fredrik Borg. *$K \to 3\pi$ decays in chiral perturbation theory*. In: *Nucl. Phys. B* 648 (2003), pp. 317–344. DOI: 10.1016/S0550-3213(02)00970-7. arXiv: hep-ph/0205341.

[BGI10] Andrzej J. Buras, Diego Guadagnoli, and Gino Isidori. *On ϵ_K Beyond Lowest Order in the Operator Product Expansion*. In: *Phys. Lett. B* 688 (2010), pp. 309–313. DOI: 10.1016/j.physletb.2010.04.017. arXiv: 1002.3612 [hep-ph].

[BGS20] Joachim Brod, Martin Gorbahn, and Emmanuel Stamou. *Standard-Model Prediction of ϵ_K with Manifest Quark-Mixing Unitarity*. In: *Physical Review Letters* 125.17 (Oct. 2020). ISSN: 1079-7114. DOI: 10.1103/physrevlett.125.171803. URL: http://dx.doi.org/10.1103/PhysRevLett.125.171803.

[Bie+22] Christian Bierlich et al. *A comprehensive guide to the physics and usage of PYTHIA 8.3*. In: *SciPost Phys. Codeb.* 2022 (2022), p. 8. DOI: 10.21468/SciPostPhysCodeb.8. arXiv: 2203.11601 [hep-ph].

[Bio+87] R. M. Bionta et al. *Observation of a Neutrino Burst in Coincidence with Supernova SN 1987a in the Large Magellanic Cloud*. In: *Phys. Rev. Lett.* 58 (1987), p. 1494. DOI: 10.1103/PhysRevLett.58.1494.

[Bjö+20] Fredrik Björkeroth et al. *Axion-electron decoupling in nucleophobic axion models*. In: *Physical Review D* 101.3 (Feb. 2020). ISSN: 2470-0029. DOI: 10.1103/physrevd.101.035027. URL: http://dx.doi.org/10.1103/PhysRevD.101.035027.

[BO22] Aurore Betranhandy and Evan O'Connor. *Neutrino driven explosions aided by axion cooling in multidimensional simulations of core-collapse supernovae*. In: *Phys. Rev. D* 106.6 (2022), p. 063019. DOI: 10.1103/PhysRevD.106.063019. arXiv: 2204.00503 [astro-ph.HE].

[Bon+23] Marcella Bona et al. *New UTfit Analysis of the Unitarity Triangle in the Cabibbo-Kobayashi-Maskawa scheme*. In: *Rend. Lincei Sci. Fis. Nat.* 34 (2023), pp. 37–57. DOI: 10.1007/s12210-023-01137-5. arXiv: 2212.03894 [hep-ph].

[Bor+21] Sz. Borsanyi et al. *Leading hadronic contribution to the muon magnetic moment from lattice QCD*. In: *Nature* 593.7857 (Apr. 2021), pp. 51–55. ISSN: 1476-4687. DOI: 10.1038/s41586-021-03418-1. URL: http://dx.doi.org/10.1038/s41586-021-03418-1.

[Bra+12] G.C. Branco et al. *Theory and phenomenology of two-Higgs-doublet models*. In: *Physics Reports* 516.1–2 (July 2012), pp. 1–102. ISSN: 0370-1573. DOI: 10.1016/j.physrep.2012.02.002. URL: http://dx.doi.org/10.1016/j.physrep.2012.02.002.

[Bru85] Stephen W. Bruenn. *Stellar core collapse: Numerical model and infall epoch*. In: *Astrophys. J. Suppl.* 58 (1985), pp. 771–841. DOI: 10.1086/191056.

[BTB89] Adam Burrows, Michael S. Turner, and R. P. Brinkmann. *Axions and SN 1987A*. In: *Phys. Rev. D* 39 (1989), p. 1020. DOI: 10.1103/PhysRevD.39.1020.

[Bue+21] Manuel A. Buen-Abad et al. *Challenges for an axion explanation of the muon $g-2$ measurement*. In: *Journal of High Energy Physics* 2021.9 (Sept. 2021). DOI: 10.1007/jhep09(2021)101. URL: https://doi.org/10.1007%2Fjhep09%282021%29101.

[Bur00] A. Burrows. *Supernova explosions in the universe*. In: *Nature* 403 (2000), pp. 727–733. DOI: 10.1038/35001501.

[Bur98] Andrzej J. Buras. *Weak Hamiltonian, CP violation and rare decays*. In: *Les Houches Summer School in Theoretical Physics, Session 68: Probing the Standard Model of Particle Interactions*. June 1998, pp. 281–539. arXiv: hep-ph/9806471.

[Bus+22] Malte Buschmann et al. *Upper Limit on the QCD Axion Mass from Isolated Neutron Star Cooling*. In: *Phys. Rev. Lett.* 128.9 (2022), p. 091102. DOI: 10.1103/PhysRevLett.128.091102. arXiv: 2111.09892 [hep-ph].

[Cal+17] Lorenzo Calibbi et al. *Minimal axion model from flavor*. In: *Phys. Rev. D* 95.9 (2017), p. 095009. DOI: 10.1103/PhysRevD.95.095009. arXiv: 1612.08040 [hep-ph].

[Cam+21] Jorge Martin Camalich et al. *Supernova Constraints on Dark Flavored Sectors*. In: *Phys. Rev. D* 103.12 (2021), p. L121301. DOI: 10.1103/PhysRevD.103.L121301. arXiv: 2012.11632 [hep-ph].

[Can+25] Francisco R. Candón et al. *Fresh look at the diffuse ALP background from supernovae*. In: *Phys. Rev. D* 112.1 (2025), p. 015006. DOI: 10.1103/d194-7t6x. arXiv: 2505.05567 [hep-ph].

[Cap+22] Andrea Caputo et al. *Low-Energy Supernovae Severely Constrain Radiative Particle Decays*. In: *Phys. Rev. Lett.* 128.22 (2022), p. 221103. DOI: 10.1103/PhysRevLett.128.221103. arXiv: 2201.09890 [astro-ph.HE].

[Car+19] Pierluca Carenza et al. *Improved axion emissivity from a supernova via nucleon-nucleon bremsstrahlung*. In: *Journal of Cosmology and Astroparticle Physics* 2019.10 (Oct. 2019), p. 016. DOI: 10.1088/1475-7516/2019/10/016. URL: https://dx.doi.org/10.1088/1475-7516/2019/10/016.

[Car+21] Pierluca Carenza et al. *Enhanced Supernova Axion Emission and its Implications*. In: *Phys. Rev. Lett.* 126.7 (2021), p. 071102. DOI: 10.1103/PhysRevLett.126.071102. arXiv: 2010.02943 [hep-ph].

[Car+24] Pierluca Carenza et al. *Cross section for supernova axion observation in neutrino water Čherenkov detectors*. In: *Phys. Rev. C* 109.1 (2024), p. 015501. DOI: 10.1103/PhysRevC.109.015501. arXiv: 2306.17055 [hep-ph].

[Car23] Pierluca Carenza. *Axion emission from supernovae: a cheatsheet*. In: *The European Physical Journal Plus* 138.9 (2023), p. 836. DOI: 10.1140/epjp/s13360-023-04484-2. URL: https://doi.org/10.1140/epjp/s13360-023-04484-2.

[Cav+24] Mael Cavan-Piton et al. *Axion Emission from Strange Matter in Core-Collapse SNe*. In: *Phys. Rev. Lett.* 133.12 (2024), p. 121002. DOI: 10.1103/PhysRevLett.133.121002. arXiv: 2401.10979 [hep-ph].

[Cav+25a] Mael Cavan-Piton et al. *Probing QCD Axions or axion-like particles in three-body K decays*. In: *JHEP* 06 (2025), p. 039. DOI: 10.1007/JHEP06(2025)039. arXiv: 2411.04170 [hep-ph].

[Cav+25b] Mael Cavan-Piton et al. *Probing the general axion-nucleon interaction in water Cherenkov experiments*. In: *JHEP* 07 (2025), p. 070. DOI: 10.1007/JHEP07(2025)070. arXiv: 2503.17490 [hep-ph].

[CC93] Sanghyeon Chang and Kiwoon Choi. *Hadronic axion window and the big bang nucleosynthesis*. In: *Phys. Lett. B* 316 (1993), pp. 51–56. DOI: 10.1016/0370-2693(93)90656-3. arXiv: hep-ph/9306216.

[CFJ24] Wei Chao, Jing-Jing Feng, and Mingjie Jin. *Direct detections of the axionlike particle revisited*. In: *Phys. Rev. D* 109.7 (2024), p. 075044. DOI: 10.1103/PhysRevD.109.075044. arXiv: 2311.09547 [hep-ph].

[CGV24] Sabyasachi Chakraborty, Aritra Gupta, and Miguel Vanvlasselaer. *Photoproduction of heavy QCD axions in supernovae*. In: *Phys. Rev. D* 110.6 (2024), p. 063032. DOI: 10.1103/PhysRevD.110.063032. arXiv: 2403.12169 [hep-ph].

[Cho+16] Veronika Georgieva Chobanova et al. *Sensitivity of LHCb and its upgrade in the measurement of* $\mathcal{B}(K_S^0 \to \pi^0\mu^+\mu^-)$. In: *LHCb-PUB-2016-017* (2016).

[Cho+20] Veronika Chobanova et al. *Fast simulation of a forward detector at 50 and 100 TeV proton-proton colliders*. In: (Dec. 2020). arXiv: 2012.02692 [hep-ex].

[Cho+21] Kiwoon Choi et al. *Precision axion physics with running axion couplings*. In: *JHEP* 08 (2021), p. 058. DOI: 10.1007/JHEP08(2021)058. arXiv: 2106.05816 [hep-ph].

[Cho+22] Kiwoon Choi et al. *Axion emission from supernova with axion-pion-nucleon contact interaction*. In: *JHEP* 02 (2022), p. 143. DOI: 10.1007/JHEP02(2022)143. arXiv: 2110.01972 [hep-ph].

[CIS21] Kiwoon Choi, Sang Hui Im, and Chang Sub Shin. *Recent Progress in the Physics of Axions and Axion-Like Particles*. In: *Ann. Rev. Nucl. Part. Sci.* 71 (2021), pp. 225–252. DOI: 10.1146/annurev-nucl-120720-031147. arXiv: 2012.05029 [hep-ph].

[Clo+06] Douglas Clowe et al. *A Direct Empirical Proof of the Existence of Dark Matter*. In: *The Astrophysical Journal* 648.2 (Aug. 2006), pp. L109–L113. DOI: 10.1086/508162. URL: https://doi.org/10.1086%2F508162.

[Cor+24] Claudia Cornella et al. $K^\pm \to \pi^\pm a$ *at Next-to-Leading Order in Chiral Perturbation Theory and Updated Bounds on ALP Couplings*. 2024. arXiv: 2308.16903 [hep-ph]. URL: https://arxiv.org/abs/2308.16903.

[CPW24] Pierluca Carenza, Roman Pasechnik, and Zhi-Wei Wang. *Glueball Axion-Like Particles*. In: (Nov. 2024). arXiv: 2411.11716 [hep-ph].

[CR20] Francesco Capozzi and Georg Raffelt. *Axion and neutrino bounds improved with new calibrations of the tip of the red-giant branch using geometric distance determinations*. In: *Physical Review D* 102.8 (Oct. 2020). ISSN: 2470-0029. DOI: 10.1103/physrevd.102.083007. URL: http://dx.doi.org/10.1103/PhysRevD.102.083007.

[CR24] Andrea Caputo and Georg Raffelt. *Astrophysical Axion Bounds: The 2024 Edition*. In: *PoS* COSMICWISPers (2024), p. 041. DOI: 10.22323/1.454.0041. arXiv: 2401.13728 [hep-ph].

[Cro67] Jeremiah A. Cronin. *Phenomenological model of strong and weak interactions in chiral* $U(3)\times U(3)$. In: *Phys. Rev.* 161 (1967), pp. 1483–1494. DOI: 10.1103/PhysRev.161.1483.

[CRV22] Andrea Caputo, Georg Raffelt, and Edoardo Vitagliano. *Muonic boson limits: Supernova redux*. In: *Phys. Rev. D* 105.3 (2022), p. 035022. DOI: 10.1103/PhysRevD.105.035022. arXiv: 2109.03244 [hep-ph].

[Dev+24] P. S. Bhupal Dev et al. *First Constraints on the Photon Coupling of Axionlike Particles from Multimessenger Studies of the Neutron Star Merger GW170817*. In: *Phys. Rev. Lett.* 132 (10 Mar. 2024), p. 101003. DOI: 10.1103/PhysRevLett.132.101003. URL: https://link.aps.org/doi/10.1103/PhysRevLett.132.101003.

[DF83] Michael Dine and Willy Fischler. *The Not So Harmless Axion*. In: *Phys. Lett. B* 120 (1983). Ed. by M. A. Srednicki, pp. 137–141. DOI: 10.1016/0370-2693(83)90639-1.

[DFS81] Michael Dine, Willy Fischler, and Mark Srednicki. *A Simple Solution to the Strong CP Problem with a Harmless Axion*. In: *Phys. Lett. B* 104 (1981), pp. 199–202. DOI: 10.1016/0370-2693(81)90590-6.

[DHV22] Matthew J. Dolan, Frederick J. Hiskens, and Raymond R. Volkas. *Advancing globular cluster constraints on the axion-photon coupling*. In: *Journal of Cosmology and Astroparticle Physics* 2022.10 (Oct. 2022), p. 096. ISSN: 1475-7516. DOI: 10.1088/1475-7516/2022/10/096. URL: http://dx.doi.org/10.1088/1475-7516/2022/10/096.

[Di +20] Luca Di Luzio et al. *The landscape of QCD axion models*. In: *Phys. Rept.* 870 (2020), pp. 1–117. DOI: 10.1016/j.physrep.2020.06.002. arXiv: 2003.01100 [hep-ph].

[Di +23] Luca Di Luzio et al. *Running into QCD axion phenomenology*. In: (May 2023). arXiv: 2305.11958 [hep-ph].

[Din+18] Michael Dine et al. *Some Remarks on Anthropic Approaches to the Strong CP Problem*. In: *JHEP* 05 (2018), p. 171. DOI: 10.1007/JHEP05(2018)171. arXiv: 1801.03466 [hep-th].

[EM89] T.E.O. Ericson and J.-F. Mathiot. *Axion emission from $SN1987A$. Nuclear physics constraints*. In: *Physics Letters B* 219.4 (1989), pp. 507–514. ISSN: 0370-2693. DOI: https://doi.org/10.1016/0370-2693(89)91103-9. URL: https://www.sciencedirect.com/science/article/pii/0370269389911039.

[Ema+17] Yohei Ema et al. *Flaxion: a minimal extension to solve puzzles in the standard model*. In: *JHEP* 01 (2017), p. 096. DOI: 10.1007/JHEP01(2017)096. arXiv: 1612.05492 [hep-ph].

[EO83] John Ellis and Keith A. Olive. *Constraints on light particles from stellar evolution*. In: *Nuclear Physics B* 223.1 (1983), pp. 252–268. ISSN: 0550-3213. DOI: https://doi.org/10.1016/0550-3213(83)90104-9. URL: https://www.sciencedirect.com/science/article/pii/0550321383901049.

[EPR87] Gerhard Ecker, Antonio Pich, and Eduardo de Rafael. *$K \to \pi\ell^+\ell^-$ Decays in the Effective Chiral Lagrangian of the Standard Model*. In: *Nucl. Phys. B* 291 (1987), pp. 692–719. DOI: 10.1016/0550-3213(87)90491-3.

[ESH90] J. Engel, D. Seckel, and A. C. Hayes. *Emission and detectability of hadronic axions from SN1987A*. In: *Phys. Rev. Lett.* 65 (1990), pp. 960–963. DOI: 10.1103/PhysRevLett.65.960.

[Fer+23] Pablo Fernandez et al. *Atmospheric Neutrino Monte Carlo Simulations*. Version V1. 2023. DOI: 10.7910/DVN/OS5N7U. URL: https://doi.org/10.7910/DVN/OS5N7U.

[FG89] S. Fajfer and J. M. Gerard. *A Simple Chiral Lagrangian Approach to $K \to \pi\pi\pi$ Decays and ϵ'_{+0-}*. In: *Z. Phys. C* 42 (1989), p. 425. DOI: 10.1007/BF01548447.

[FI22] Damiano F. G. Fiorillo and Fabio Iocco. *Axions from neutron star mergers*. In: *Phys. Rev. D* 105 (12 June 2022), p. 123007. DOI: 10.1103/PhysRevD.105.123007. URL: https://link.aps.org/doi/10.1103/PhysRevD.105.123007.

[Fis+14] Tobias Fischer et al. *Symmetry energy impact in simulations of core-collapse supernovae*. In: *The European Physical Journal A* 50.2 (2014), p. 46. DOI: 10.1140/epja/i2014-14046-5. URL: https://doi.org/10.1140/epja/i2014-14046-5.

[Fis+21] Tobias Fischer et al. *Observable signatures of enhanced axion emission from protoneutron stars*. In: *Phys. Rev. D* 104.10 (2021), p. 103012. DOI: 10.1103/PhysRevD.104.103012. arXiv: 2108.13726 [hep-ph].

[Fog+05] G. L. Fogli et al. *Probing supernova shock waves and neutrino flavor transitions in next-generation water-Cerenkov detectors*. In: *JCAP* 04 (2005), p. 002. DOI: 10.1088/1475-7516/2005/04/002. arXiv: hep-ph/0412046.

[FOP18] M. Fortin, M. Oertel, and C. Providência. *Hyperons in hot dense matter: what do the constraints tell us for equation of state?* In: *Publ. Astron. Soc. Austral.* 35 (2018), p. 44. DOI: 10.1017/pasa.2018.32. arXiv: 1711.09427 [astro-ph.HE].

[FR20] Bryce Fore and Sanjay Reddy. *Pions in hot dense matter and their astrophysical implications*. In: *Phys. Rev. C* 101.3 (2020), p. 035809. DOI: 10.1103/PhysRevC.101.035809. arXiv: 1911.02632 [astro-ph.HE].

[FRV23] Damiano F. G. Fiorillo, Georg G. Raffelt, and Edoardo Vitagliano. *Strong Supernova 1987A Constraints on Bosons Decaying to Neutrinos*. In: *Phys. Rev. Lett.* 131.2 (2023), p. 021001. DOI: 10.1103/PhysRevLett.131.021001. arXiv: 2209.11773 [hep-ph].

[Gai19] Thomas K. Gaisser. *Atmospheric Neutrinos*. 2019. arXiv: 1910.08851 [astro-ph.HE]. URL: https://arxiv.org/abs/1910.08851.

[GKR15] Peter W. Graham, David E. Kaplan, and Surjeet Rajendran. *Cosmological Relaxation of the Electroweak Scale*. In: *Physical Review Letters* 115.22 (Nov. 2015). ISSN: 1079-7114. DOI: 10.1103/physrevlett.115.221801. URL: http://dx.doi.org/10.1103/PhysRevLett.115.221801.

[GKR86] Howard Georgi, David B. Kaplan, and Lisa Randall. *Manifesting the Invisible Axion at Low-energies*. In: *Phys. Lett. B* 169 (1986), pp. 73–78. DOI: 10.1016/0370-2693(86)90688-X.

[GMR22] Sougata Ganguly, Biswarup Mukhopadhyaya, and Sourov Roy. *Axion-Like Particle Interpretation of Dark Matter and Muon* $(g-2)$. 2022. arXiv: 2204.07920 [hep-ph].

[Gri+16] Giovanni Grilli di Cortona et al. *The QCD axion, precisely*. In: *JHEP* 01 (2016), p. 034. DOI: 10.1007/JHEP01(2016)034. arXiv: 1511.02867 [hep-ph].

[GZc20] Particle Data Group, P A Zyla, and co. *Review of Particle Physics*. In: *Progress of Theoretical and Experimental Physics* 2020.8 (Aug. 2020). 083C01. ISSN: 2050-3911. DOI: 10.1093/ptep/ptaa104. URL: https://doi.org/10.1093/ptep/ptaa104.

[Har+20] Steven P. Harris et al. *Axions in neutron star mergers*. In: *Journal of Cosmology and Astroparticle Physics* 2020.07 (July 2020), pp. 023–023. ISSN: 1475-7516. DOI: 10.1088/1475-7516/2020/07/023. URL: http://dx.doi.org/10.1088/1475-7516/2020/07/023.

[HBG08] Graham M. Harper, Alexander Brown, and Edward F. Guinan. *A New VLA-Hipparcos Distance to Betelgeuse and its Implications*. In: *The Astronomical Journal* 135.4 (Mar. 2008), p. 1430. DOI: 10.1088/0004-6256/135/4/1430. URL: https://dx.doi.org/10.1088/0004-6256/135/4/1430.

[Hir+87] K. Hirata et al. *Observation of a Neutrino Burst from the Supernova SN 1987a*. In: *Phys. Rev. Lett.* 58 (1987). Ed. by K. C. Wali, pp. 1490–1493. DOI: 10.1103/PhysRevLett.58.1490.

[Ho+23] Shu-Yu Ho et al. *Supernova axion emissivity with* $\Delta(1232)$ *resonance in heavy baryon chiral perturbation theory*. In: *Phys. Rev. D* 107.7 (2023), p. 075002. DOI: 10.1103/PhysRevD.107.075002. arXiv: 2212.01155 [hep-ph].

[IR18] Igor G. Irastorza and Javier Redondo. *New experimental approaches in the search for axion-like particles*. In: *Prog. Part. Nucl. Phys.* 102 (2018), pp. 89–159. DOI: 10.1016/j.ppnp.2018.05.003. arXiv: 1801.08127 [hep-ph].

[Jan+07] Hans-Thomas Janka et al. *Theory of Core-Collapse Supernovae*. In: *Phys. Rept.* 442 (2007), pp. 38–74. DOI: 10.1016/j.physrep.2007.02.002. arXiv: astro-ph/0612072.

[JM90] R.L. Jaffe and Aneesh Manohar. *The g1 problem: Deep inelastic electron scattering and the spin of the proton*. In: *Nuclear Physics B* 337.3 (1990), pp. 509–546. ISSN: 0550-3213. DOI: https://doi.org/10.1016/0550-3213(90)90506-9. URL: https://www.sciencedirect.com/science/article/pii/0550321390905069.

[JRW22] J. Jaeckel, G. Rybka, and L. Winslow. *Axion Dark Matter*. 2022. DOI: 10.48550/ARXIV.2203.14923. URL: https://arxiv.org/abs/2203.14923.

[KC10] Jihn E. Kim and Gianpaolo Carosi. *Axions and the Strong CP Problem*. In: *Rev. Mod. Phys.* 82 (2010). [Erratum: Rev.Mod.Phys. 91, 049902 (2019)], pp. 557–602. DOI: 10.1103/RevModPhys.82.557. arXiv: 0807.3125 [hep-ph].

[Kim79] Jihn E. Kim. *Weak Interaction Singlet and Strong CP Invariance*. In: *Phys. Rev. Lett.* 43 (1979), p. 103. DOI: 10.1103/PhysRevLett.43.103.

[Kim87] J. E. Kim. *Light pseudoscalars, particle physics and cosmology*. In: *Physics Reports* 150.1 (Jan. 1987), pp. 1–177. DOI: 10.1016/0370-1573(87)90017-2.

[KKY22] Alex Keshavarzi, Kim Siang Khaw, and Tamaki Yoshioka. *Muon* $g-2$*: A review*. In: *Nuclear Physics B* 975 (Feb. 2022), p. 115675. ISSN: 0550-3213. DOI: 10.1016/j.nuclphysb.2022.115675. URL: http://dx.doi.org/10.1016/j.nuclphysb.2022.115675.

[KM88] David B. Kaplan and Aneesh Manohar. *Strange matrix elements in the proton from neutral-current experiments*. In: *Nuclear Physics B* 310.3 (1988), pp. 527–547. ISSN: 0550-3213. DOI: https://doi.org/10.1016/0550-3213(88)90090-9. URL: https://www.sciencedirect.com/science/article/pii/0550321388900909.

[KMW90] J. Kambor, John H. Missimer, and D. Wyler. *The Chiral Loop Expansion of the Non-leptonic Weak Interactions of Mesons*. In: *Nucl. Phys. B* 346 (1990), pp. 17–64. DOI: 10.1016/0550-3213(90)90236-7.

[KRT22] Hristijan Kochankovski, Angels Ramos, and Laura Tolos. *Equation of state for hot hyperonic neutron star matter*. In: *Mon. Not. Roy. Astron. Soc.* 517.1 (2022). [Erratum: Mon.Not.Roy.Astron.Soc. 518, 6376], pp. 507–517. DOI: 10.1093/mnras/stac2671. arXiv: 2206.11266 [astro-ph.HE].

[Lec+25] Francesca Lecce et al. *Probing axionlike particles with multimessenger observations of neutron star mergers*. In: *Physical Review D* 112.2 (July 2025). ISSN: 2470-0029. DOI: 10.1103/krf3-lm4s. URL: http://dx.doi.org/10.1103/krf3-lm4s.

[Lel+23] Alessandro Lella et al. *Protoneutron stars as cosmic factories for massive axionlike particles*. In: *Phys. Rev. D* 107.10 (2023), p. 103017. DOI: 10.1103/PhysRevD.107.103017. arXiv: 2211.13760 [hep-ph].

[Lel+24] Alessandro Lella et al. *Getting the most on supernova axions*. In: *Phys. Rev. D* 109.2 (2024), p. 023001. DOI: 10.1103/PhysRevD.109.023001. arXiv: 2306.01048 [hep-ph].

[Li+11] Weidong Li et al. *Nearby Supernova Rates from the Lick Observatory Supernova Search. III. The Rate-Size Relation, and the Rates as a Function of Galaxy Hubble Type and Colour*. In: *Mon. Not. Roy. Astron. Soc.* 412 (2011), p. 1473. DOI: 10.1111/j.1365-2966.2011.18162.x. arXiv: 1006.4613 [astro-ph.SR].

[Lo 21] Prisco Lo Chiatto. "Theoretical analysis and sensitivity study for the NA62 experiment of the decay of the K meson into two pions and a pseudoscalar particle". MA thesis. U. Modena (main), Oct. 2021.

[Luc+22] Giuseppe Lucente et al. *Axion signatures from supernova explosions through the nucleon electric-dipole portal*. In: *Phys. Rev. D* 105.12 (2022), p. 123020. DOI: 10.1103/PhysRevD.105.123020. arXiv: 2203.15812 [hep-ph].

[LZ22] Tong Li and Rui-Jia Zhang. *Axionlike particles from primordial black hole evaporation and their detection in neutrino experiments*. In: *Phys. Rev. D* 106.9 (2022), p. 095034. DOI: 10.1103/PhysRevD.106.095034. arXiv: 2208.02696 [hep-ph].

[Man] Aneesh V. Manohar. *Effective field theories*. In: *Perturbative and Nonperturbative Aspects of Quantum Field Theory*. Springer Berlin Heidelberg, pp. 311–362. DOI: 10.1007/bfb0104294. URL: https://doi.org/10.1007%2Fbfb0104294.

[Mar+12] G. Martinez-Pinedo et al. *Charged-current weak interaction processes in hot and dense matter and its impact on the spectra of neutrinos emitted from proto-neutron star cooling*. In: *Phys. Rev. Lett.* 109 (2012), p. 251104. DOI: 10.1103/PhysRevLett.109.251104. arXiv: 1205.2793 [astro-ph.HE].

[Mar+17] Miguel Marques et al. *New temperature dependent hyperonic equation of state: Application to rotating neutron star models and $I-Q$ relations*. In: *Phys. Rev. C* 96.4 (2017), p. 045806. DOI: 10.1103/PhysRevC.96.045806. arXiv: 1706.02913 [nucl-th].

[Mar+20] Jorge Martin Camalich et al. *Quark Flavor Phenomenology of the QCD Axion*. In: *Phys. Rev. D* 102.1 (2020), p. 015023. DOI: 10.1103/PhysRevD.102.015023. arXiv: 2002.04623 [hep-ph].

[Mar16] David J. E. Marsh. *Axion Cosmology*. In: *Phys. Rept.* 643 (2016), pp. 1–79. DOI: 10.1016/j.physrep.2016.06.005. arXiv: 1510.07633 [astro-ph.CO].

[Mas+20] Leonardo Mastrototaro et al. *Heavy sterile neutrino emission in core-collapse supernovae: Constraints and signatures*. In: *JCAP* 01 (2020), p. 010. DOI: 10.1088/1475-7516/2020/01/010. arXiv: 1910.10249 [hep-ph].

[MBB21] Tuhin Malik, Sarmistha Banik, and Debades Bandyopadhyay. *New equation of state involving Bose-Einstein condensate of antikaon for supernova and neutron star merger simulations*. In: *Eur. Phys. J. ST* 230.2 (2021), pp. 561–566. DOI: 10.1140/epjs/s11734-021-00006-2. arXiv: 2012.10127 [astro-ph.HE].

[Mor+22] Kanji Mori et al. *Shock revival in core-collapse supernovae assisted by heavy axionlike particles*. In: *Phys. Rev. D* 105.6 (2022), p. 063009. DOI: 10.1103/PhysRevD.105.063009. arXiv: 2112.03613 [astro-ph.HE].

[Mor+23] Kanji Mori et al. *Multimessenger signals of heavy axionlike particles in core-collapse supernovae: Two-dimensional simulations*. In: *Phys. Rev. D* 108.6 (2023), p. 063027. DOI: 10.1103/PhysRevD.108.063027. arXiv: 2304.11360 [astro-ph.HE].

[MP22] Tuhin Malik and Constan ça Providência. *Bayesian inference of signatures of hyperons inside neutron stars*. In: *Phys. Rev. D* 106 (6 Sept. 2022), p. 063024. DOI: 10.1103/PhysRevD.106.063024. URL: https://link.aps.org/doi/10.1103/PhysRevD.106.063024.

[MS14] Ken Mimasu and Verónica Sanz. *ALPs at Colliders*. In: (2014). DOI: 10.48550/arxiv.1409.4792. URL: https://arxiv.org/abs/1409.4792.

[Nav+24] S. Navas et al. *Review of particle physics*. In: *Phys. Rev. D* 110.3 (2024), p. 030001. DOI: 10.1103/PhysRevD.110.030001.

[Oer+16] Micaela Oertel et al. *Hyperons in neutron stars and supernova cores*. In: *Eur. Phys. J. A* 52.3 (2016), p. 50. DOI: 10.1140/epja/i2016-16050-1. arXiv: 1601.00435 [nucl-th].

[Oer+17] M. Oertel et al. *Equations of state for supernovae and compact stars*. In: *Rev. Mod. Phys.* 89.1 (2017), p. 015007. DOI: 10.1103/RevModPhys.89.015007. arXiv: 1610.03361 [astro-ph.HE].

[Oer+20] M. Oertel et al. *Improved neutrino-nucleon interactions in dense and hot matter for numerical simulations*. In: *Physical Review C* 102.3, 035802 (Sept. 2020), p. 035802. DOI: 10.1103/PhysRevC.102.035802. arXiv: 2003.02152 [astro-ph.HE].

[Oga+11] R. Ogata et al. *Study of the $K_L^0 \to \pi^0\pi^0\nu\bar{\nu}$ decay*. In: *Physical Review D* 84.5 (Sept. 2011). ISSN: 1550-2368. DOI: 10.1103/physrevd.84.052009. URL: http://dx.doi.org/10.1103/PhysRevD.84.052009.

[OHa20] C. O'Hare. *Axion Limits*. Accessed: 2025-03-07. 2020. URL: https://cajohare.github.io/AxionLimits/docs/ap.html.

[PNO22] A. Pascal, J. Novak, and M. Oertel. *Proto-neutron star evolution with improved charged-current neutrino–nucleon interactions*. In: *Mon. Not. Roy. Astron. Soc.* 511.1 (2022), pp. 356–370. DOI: 10.1093/mnras/stac016. arXiv: 2201.01955 [nucl-th].

[Pon+99] J. A. Pons et al. *Evolution of protoneutron stars*. In: *Astrophys. J.* 513 (1999), p. 780. DOI: 10.1086/306889. arXiv: astro-ph/9807040.

[PQ77a] R. D. Peccei and Helen R. Quinn. *Constraints imposed by CP conservation in the presence of pseudoparticles*. In: *Phys. Rev. D* 16 (6 Sept. 1977), pp. 1791–1797. DOI: 10.1103/PhysRevD.16.1791. URL: https://link.aps.org/doi/10.1103/PhysRevD.16.1791.

[PQ77b] R. D. Peccei and Helen R. Quinn. *CP Conservation in the Presence of Instantons*. In: *Phys. Rev. Lett.* 38 (1977), pp. 1440–1443. DOI: 10.1103/PhysRevLett.38.1440.

[PS95] Michael E. Peskin and Daniel V. Schroeder. *An Introduction to quantum field theory*. Reading, USA: Addison-Wesley, 1995. ISBN: 978-0-201-50397-5.

[PWW83a] John Preskill, Mark B. Wise, and Frank Wilczek. *Cosmology of the Invisible Axion*. In: *Phys. Lett. B* 120 (1983). Ed. by M. A. Srednicki, pp. 127–132. DOI: 10.1016/0370-2693(83)90637-8.

[PWW83b] John Preskill, Mark B. Wise, and Frank Wilczek. *Cosmology of the invisible axion*. In: *Physics Letters B* 120.1 (1983), pp. 127–132. ISSN: 0370-2693. DOI: https://doi.org/10.1016/0370-2693(83)90637-8. URL: https://www.sciencedirect.com/science/article/pii/0370269383906378.

[QS19] Jérémie Quevillon and Christopher Smith. *Axions are blind to anomalies*. en. In: *The European Physical Journal C* 79.10 (Oct. 2019), p. 822. ISSN: 1434-6044, 1434-6052. DOI: 10.1140/epjc/s10052-019-7304-4. URL: http://link.springer.com/10.1140/epjc/s10052-019-7304-4 (visited on 06/28/2022).

[QS20] Jérémie Quevillon and Christopher Smith. *Baryon and lepton number intricacies in axion models*. en. In: *Physical Review D* 102.7 (Oct. 2020), p. 075031. ISSN: 2470-0010, 2470-0029. DOI: 10.1103/PhysRevD.102.075031. URL: https://link.aps.org/doi/10.1103/PhysRevD.102.075031 (visited on 06/28/2022).

[Rad22] Adriana R. Raduta. *Equations of state for hot neutron stars-II. The role of exotic particle degrees of freedom*. In: *Eur. Phys. J. A* 58.6 (2022), p. 115. DOI: 10.1140/epja/s10050-022-00772-0. arXiv: 2205.03177 [nucl-th].

[Raf] Georg G. Raffelt. *Astrophysical Axion Bounds*. In: *Axions*. Springer Berlin Heidelberg, pp. 51–71. ISBN: 9783540735182. DOI: 10.1007/978-3-540-73518-2_3. URL: http://dx.doi.org/10.1007/978-3-540-73518-2_3.

[Raf08] Georg G. Raffelt. *Astrophysical axion bounds*. In: *Lect. Notes Phys.* 741 (2008). Ed. by Markus Kuster, Georg Raffelt, and Berta Beltran, pp. 51–71. DOI: 10.1007/978-3-540-73518-2_3. arXiv: hep-ph/0611350.

[Raf90] Georg G. Raffelt. *Astrophysical methods to constrain axions and other novel particle phenomena*. In: *Phys. Rept.* 198 (1990), pp. 1–113. DOI: 10.1016/0370-1573(90)90054-6.

[Raf96] G. G. Raffelt. *Stars as laboratories for fundamental physics: The astrophysics of neutrinos, axions, and other weakly interacting particles*. May 1996. ISBN: 978-0-226-70272-8.

[RC24] G. Raffelt and A. Caputo. *Astrophysical Axion Bounds: The 2024 Edition*. In: *Proceedings of 1st General Meeting and 1st Training School of the COST Action COSMIC WSIPers — PoS(COSMICWISPers). COSMICWISPers*. Sissa Medialab, Mar. 2024. DOI: 10.22323/1.454.0041. URL: http://dx.doi.org/10.22323/1.454.0041.

[Rei82] David B. Reiss. *Can the Family Group Be a Global Symmetry?* In: *Phys. Lett. B* 115 (1982), pp. 217–220. DOI: 10.1016/0370-2693(82)90647-5.

[Rob12] L. F. Roberts. *A New Code for Proto-Neutron Star Evolution*. In: *Astrophys. J.* 755 (2012), p. 126. DOI: 10.1088/0004-637X/755/2/126. arXiv: 1205.3228 [astro-ph.HE].

[RPL98] Sanjay Reddy, Madappa Prakash, and James M Lattimer. *Neutrino interactions in hot and dense matter*. In: *Phys. Rev.* D58 (1998), p. 013009. DOI: 10.1103/PhysRevD.58.013009.

[RRS12] L. F. Roberts, Sanjay Reddy, and Gang Shen. *Medium modification of the charged current neutrino opacity and its implications*. In: *Phys. Rev. C* 86 (2012), p. 065803. DOI: 10.1103/PhysRevC.86.065803. arXiv: 1205.4066 [astro-ph.HE].

[RS88] Georg Raffelt and David Seckel. *Bounds on Exotic Particle Interactions from SN 1987a*. In: *Phys. Rev. Lett.* 60 (1988), p. 1793. DOI: 10.1103/PhysRevLett.60.1793.

[RVC21] Karolina Rozwadowska, Francesco Vissani, and Enrico Cappellaro. *On the rate of core collapse supernovae in the milky way*. In: *New Astron.* 83 (2021), p. 101498. DOI: 10.1016/j.newast.2020.101498. arXiv: 2009.03438 [astro-ph.HE].

[Sad+24] A. S. Sadovsky et al. *Searches for the light invisible axion-like particle in $K^+ \to \pi^+\pi^0 a$ decay*. In: *Eur. Phys. J. C* 84.3 (2024), p. 266. DOI: 10.1140/epjc/s10052-024-12444-y. arXiv: 2310.16429 [hep-ex].

[Sch03] Stefan Scherer. *Introduction to chiral perturbation theory*. In: *Adv. Nucl. Phys.* 27 (2003). Ed. by John W. Negele and E. W. Vogt, p. 277. arXiv: hep-ph/0210398.

[Sik21] Pierre Sikivie. *Invisible Axion Search Methods*. In: *Rev. Mod. Phys.* 93.1 (2021), p. 015004. DOI: 10.1103/RevModPhys.93.015004. arXiv: 2003.02206 [hep-ph].

[Sil+20] André da Silva Schneider et al. *Equation of State and Progenitor Dependence of Stellar-mass Black Hole Formation*. In: *Astrophys. J.* 894.1 (2020), p. 4. DOI: 10.3847/1538-4357/ab8308. arXiv: 2001.10434 [astro-ph.HE].

[SLW23] Armen Sedrakian, Jia-Jie Li, and Fridolin Weber. *Heavy baryons in compact stars*. In: *Prog. Part. Nucl. Phys.* 131 (2023), p. 104041. DOI: 10.1016/j.ppnp.2023.104041. arXiv: 2212.01086 [nucl-th].

[Str+25] *JRJC 2024 - Journées de Rencontres Jeunes Chercheurs. Book of Proceedings*. Saint-Jacut-de-la-Mer, France, June 2025. URL: https://hal.science/hal-05110108.

[SVZ80] Mikhail A. Shifman, A. I. Vainshtein, and Valentin I. Zakharov. *Can Confinement Ensure Natural CP Invariance of Strong Interactions?* In: *Nucl. Phys. B* 166 (1980), pp. 493–506. DOI: 10.1016/0550-3213(80)90209-6.

[SW06] Peter Svrcek and Edward Witten. *Axions In String Theory*. In: *JHEP* 06 (2006), p. 051. DOI: 10.1088/1126-6708/2006/06/051. arXiv: hep-th/0605206.

[Tam+17] Irene Tamborra et al. *Flavor-dependent neutrino angular distribution in core-collapse supernovae*. In: *Astrophys. J.* 839 (2017), p. 132. DOI: 10.3847/1538-4357/aa6a18. arXiv: 1702.00060 [astro-ph.HE].

[Tch+04] O. G. Tchikilev et al. *Search for light pseudoscalar sgoldstino in K- decays*. In: *Phys. Lett. B* 602 (2004), pp. 149–156. DOI: 10.1016/j.physletb.2004.10.002. arXiv: hep-ex/0308061.

[TLS94] G. A. Tammann, W. Loeffler, and A. Schroder. *The Galactic supernova rate*. In: *Astrophys. J. Suppl.* 92 (1994), pp. 487–493. DOI: 10.1086/192002.

[TOK15] S. Typel, M. Oertel, and T. Klähn. *CompOSE CompStar online supernova equations of state harmonising the concert of nuclear physics and astrophysics compose.obspm.fr*. In: *Phys. Part. Nucl.* 46.4 (2015), pp. 633–664. DOI: 10.1134/S1063779615040061. arXiv: 1307.5715 [astro-ph.SR].

[Tur88] Michael S. Turner. *Axions from SN 1987A*. In: *Phys. Rev. Lett.* 60 (1988), p. 1797. DOI: 10.1103/PhysRevLett.60.1797.

[Typ+22] S. Typel et al. *CompOSE Reference Manual*. In: *Eur. Phys. J. A* 58.11 (2022), p. 221. DOI: 10.1140/epja/s10050-022-00847-y. arXiv: 2203.03209 [astro-ph.HE].

[Uba10] Lorenzo Ubaldi. *Effects of theta on the deuteron binding energy and the triple-alpha process*. In: *Phys. Rev. D* 81 (2010), p. 025011. DOI: 10.1103/PhysRevD.81.025011. arXiv: 0811.1599 [hep-ph].

[VGM21] Thomas Vonk, Feng-Kun Guo, and Ulf-G. Meißner. *The axion-baryon coupling in SU(3) heavy baryon chiral perturbation theory*. In: *JHEP* 08 (2021), p. 024. DOI: 10.1007/JHEP08(2021)024. arXiv: 2104.10413 [hep-ph].

[VGM22] Thomas Vonk, Feng-Kun Guo, and Ulf-G. Meißner. *Pion axioproduction: The Δ resonance contribution*. In: *Phys. Rev. D* 105.5 (2022), p. 054029. DOI: 10.1103/PhysRevD.105.054029. arXiv: 2202.00268 [hep-ph].

[VMP21] Pablo Villanueva-Domingo, Olga Mena, and Sergio Palomares-Ruiz. *A Brief Review on Primordial Black Holes as Dark Matter*. In: *Frontiers in Astronomy and Space Sciences* 8 (May 2021). ISSN: 2296-987X. DOI: 10.3389/fspas.2021.681084. URL: http://dx.doi.org/10.3389/fspas.2021.681084.

[Wei00] Stefan Weinzierl. *Introduction to Monte Carlo methods*. 2000. arXiv: hep-ph/0006269 [hep-ph]. URL: https://arxiv.org/abs/hep-ph/0006269.

[Wei78] Steven Weinberg. *A New Light Boson?* In: *Phys. Rev. Lett.* 40 (4 Jan. 1978), pp. 223–226. DOI: 10.1103/PhysRevLett.40.223. URL: https://link.aps.org/doi/10.1103/PhysRevLett.40.223.

[Wes+24] T. Wester et al. *Atmospheric neutrino oscillation analysis with neutron tagging and an expanded fiducial volume in Super-Kamiokande I-V*. In: *Physical Review D* 109.7 (Apr. 2024). ISSN: 2470-0029. DOI: 10.1103/physrevd.109.072014. URL: http://dx.doi.org/10.1103/PhysRevD.109.072014.

[Wil78] Frank Wilczek. *Problem of Strong P and T Invariance in the Presence of Instantons*. In: *Phys. Rev. Lett.* 40 (1978), pp. 279–282. DOI: 10.1103/PhysRevLett.40.279.

[Wil82] Frank Wilczek. *Axions and Family Symmetry Breaking*. In: *Phys. Rev. Lett.* 49 (1982), pp. 1549–1552. DOI: 10.1103/PhysRevLett.49.1549.

[WJ05] Stan Woosley and Thomas Janka. *The physics of core-collapse supernovae*. In: *Nature Phys.* 1 (2005), p. 147. DOI: 10.1038/nphys172. arXiv: astro-ph/0601261.

[Zha+21] Jun Zhang et al. *First Constraints on Nuclear Coupling of Axionlike Particles from the Binary Neutron Star Gravitational Wave Event GW170817*. In: *Physical Review Letters* 127.16 (Oct. 2021). ISSN: 1079-7114. DOI: 10.1103/physrevlett.127.161101. URL: http://dx.doi.org/10.1103/PhysRevLett.127.161101.

[Zhi80] A P Zhitnitskii. *Possible suppression of axion-hadron interactions*. In: *Sov. J. Nucl. Phys. (Engl. Transl.); (United States)* 31 (Feb. 1980). URL: https://www.osti.gov/biblio/7063072.